Investigation of Transitional and Turbulent Pipe Flow of Non-Newtonian Fluids

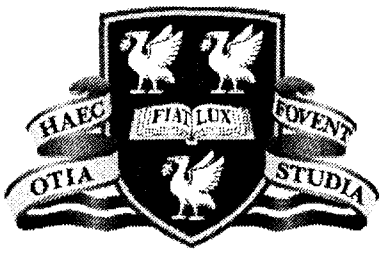

Thesis submitted in accordance with the requirements of the University of Liverpool for the degree of Doctor in Philosophy by

Felice Presti

August 2000

DEDICATIONS

I would like to dedicate this thesis to my dearest family, particularly my parents, *Antonio* and *Filomena Presti,* who have supported me throughout my life and career. Through this study I hope to have made them proud of me by example of the devotion and commitment confined within the covers of this thesis.

I would also like to dedicate this thesis to my dear wife, *Susan,* who has always been there for me, supporting and inspiring me towards this accomplishment.

Thankyou All.

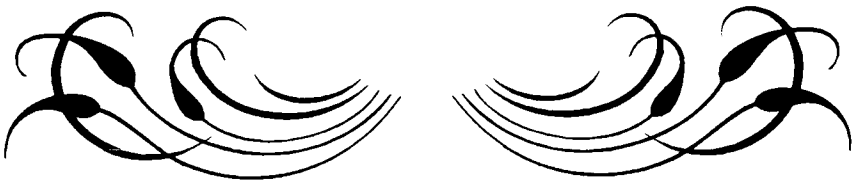

ACKNOWLEDGEMENTS

First and foremost, my sincerest gratitude goes to my supervisor Professor M.P.Escudier who offered me the opportunity to work on this challenging project. Throughout the research programme, Professor M.P.Escudier has shown continuous interest in my work and has supported me throughout by providing valuable advice, direction and positive criticism.

I am extremely grateful to all the technicians who have contributed to the design and construction of the various experimental apparatus, which ensured the successful completion of this work, especially Messrs. N. Beaumont, D. Neary, F. Hayes, D. Smith, D. Miller and A. Davies.

I am particularly thankful for my association with all my colleagues from the Department of Mechanical Engineering at the University of Liverpool, who have provided me with moral, technical and secretarial support and have also shared in my successes and disappointments over the years, in particular Dr. I.W. Gouldson, Dr. J.L. Sproston, Dr. J.W. Cleaver, Dr. M.W. Johnston, Prof. I. Owen, Mr. S. Bode and Mrs. J. O'Rourke.

Finally, I wish to express my appreciation to my sponsors S.E.R.C. (Science and Engineering Research Council), who have financially made this work possible for me.

SUMMARY

This report details an experimental study of fully developed pipe flow of several different aqueous polymer solutions that have been widely used in previous drag reduction studies: 0.24%, 0.25% and 0.4% carboxymethylcellulose (CMC), 0.2% xanthan gum (XG), a 0.09%/0.09% CMC/XG blend, 0.14% Carbopol 934, 0.1% Carbopol EZ1 and 0.125% and 0.2% polyacrylamide (PAA). In addition to the polymer solutions, a non-polymeric test fluid (1.5% Laponite - also classed as a thixotropic fluid) was also analysed in order to account for the wide ranging behaviour associated with drilling muds. All fluids showed various levels of degradation over a period of time. However, the level of degradation, principally due to mechanical shearing effects associated with the set-up of the recirculating flow loop used in this study, were found to be negligible after comparing the viscometric data carried out before and after each flow test.

The study presents new experimental data of concentrated polymer and non-polymeric solutions in rheological laminar flows as well as in laminar, transitional and turbulent drag reduced pipe flows. This was done in order to find the relevant rheological properties causing drag reduction in the turbulent flow regime. For concentrated polymer solutions, the first normal stress difference of these solutions could be measured, which is normally impossible for dilute polymer solutions because the resulting forces are too low be resolved by commercial rheometers.

For all test fluids, detailed measurements of mean velocity and velocity fluctuation levels (axial, tangential and radial) were carried out using a laser Doppler anemometer. The high spatial resolution of the flow facility enabled detailed velocity measurements to be carried out in the vicinity of the wall, extending into the viscous sublayer for all fluids. Laminar profiles were also measured, which for all fluids with the exception of Laponite, were characterised by simple power-law fits. In the case of Laponite, the equilibrium rheological structure is well characterised by the Herschel-Bulkley model. Velocity profiles calculated for a Herschel-Bulkley fluid proved to be a very accurate representation of the measurements for laminar flow at Reynolds numbers below about

1,500. Again, for Laponite, it was evident that under all flow conditions the fluid rheology was far from structural equilibrium, with values for the apparent yield stress and effective viscosity determined from near-wall velocity measurements considerably below those obtained from a rheometer.

For 0.2% XG, 0.09% XG/0.09% CMC, 0.2% PAA, 0.1% Carbopol EZ1 and 1.5% Laponite, the measured profiles develop an unexplained asymmetry for Reynolds numbers approaching the onset of transitional flow. The same asymmetries disappear for higher Reynolds numbers as the flow undergoes a transition to turbulent flow, thus suggesting the fluids are sensitive to flow instabilities near to transition - this has not been reported previously in literature. The Reynolds numbers for which the asymmetric velocity profiles become evident, correlate well with the early transition identification ($Re < 2{,}000$) monitored by using u'/U (measured at 80% of the pipe diameter) as a sensitive transition indicator.

All fluids were drag reducing under turbulent flow conditions with relative levels of tangential and radial turbulence intensity suppressed in comparison with water whilst the axial turbulence intensity varied depending on whether the normalisation of the rms levels were based on either the mean bulk velocity or the friction velocity. Universal velocity distributions indicated that all fluids displayed an upward shift from the Newtonian profile within the turbulent core flow region, though the shift was not parallel for the highly elastic fluids. The extent of upshift in the semi-logarithmic velocity profile was consistent with the level of drag reduction for each test fluid.

A comparison of the rheological behaviour of the polymer test fluids with the drag-reducing experiments suggests that 'ranking' additives according to elasticity provides information about drag-reducing effectiveness. Consequently, for the more concentrated polymer solutions a correspondence between the drag reduction and the rheological behaviour was found. The established correlation further suggested that the drag reduction process is associated with the behaviour occurring within the buffer region of flow.

TABLE OF CONTENTS

LIST OF TABLES AND FIGURES

NOMENCLATURE

Latin Letters

A, B constants in the law-of-the-wall, **Equation (5.9)**;

ΔB upshift of turbulent profile in core region of flow, **Equation (5.11)**;

c concentration of solvent additive;

D diameter of pipe (m);

DR drag reduction (%), **Equation (5.5)**;

d_f fringe spacing of measurement control volume (m), **Figure 3.6**;

f frequency of oscillation in oscillatory test (Hz);

f friction factor, **Equation (5.1)**;

f_B Blasius friction factor, **Equation (5.3)**;

f_D Doppler frequency (Hz), **Figure 3.6**;

f_{DM} friction factor determined from Dodge and Metzner, **Equation (5.12)**;

Δf total reduction in friction factor $f_B - f$;

Δf_E reduction in friction factor due to elastic effects $\Delta f - \Delta f_{ST}$;

Δf_{ST} reduction in friction factor due to shear-thinning $\Delta f - \Delta f_E$;

G' storage modulus (Pa);

G'' loss modulus (Pa);

K constant in Herschel-Bulkley and power-law models ($Pa.s^n$), **Table 4.1**;

l_m length of principal axis of measurement control volume (m);

m Cross model constant, **Equation (4.3)**;

M molecular weight, **Equation (5.7)**;

n power-law exponent, **Table 4.1**;

n refractive index;

N_1 first normal stress difference (Pa);

ΔP pressure drop (Pa);

Q volumetric flow rate (m^3/s);

r radial location within pipe (m);

r_P radius of constant-velocity plastic plug (m);

R pipe radius (m);

R universal gas constant, **Equation (5.7)**;

Re Reynolds number $2\rho UR/\eta_S$;

Re_N generalised Reynolds number, **Equation (5.12a)**;

Re_1 onset of transitional flow;

Re_2 onset of turbulent flow;

T temperature of fluid (°C);

u local axial velocity (m/s);

U bulk mean velocity $Q/\pi R^2$ (m/s);

u′ rms value of turbulent velocity fluctuations in axial direction (m/s);

U^+ non-dimensional velocity u/u_τ, **Equation (5.9)**;

u_τ friction velocity $\sqrt{\tau_S/\rho}$ (m/s);

v′ rms value of turbulent velocity fluctuations in radial direction (m/s);

w′ rms value of turbulent velocity fluctuations in tangential direction (m/s);

x distance from inlet of test section to point of ΔP measurement (m);

y distance from pipe wall (m);

y^+ non-dimensional distance from pipe wall $\rho u_\tau y/\mu_S$;

y_1^+ non-dimensional wall layer thickness;

Greek Letters

$\dot{\gamma}$ shear rate (s^{-1}), **Equation (4.1)**;

$\dot{\gamma}_S$ wall velocity gradient (s^{-1});

δ phase shift angle in oscillatory test (°), **Appendix 3**;

$\dot{\varepsilon}$ extensional strain rate (s^{-1});

η non-Newtonian solution viscosity (Pa.s);

η_E uniaxial extensional viscosity (Pa.s);

η_S viscosity based on conditions at the wall $\tau_S/\dot{\gamma}_S$ (Pa.s);

η_{sol} solvent viscosity (Pa.s);

η_{sol} solvent viscosity (Pa.s);

η_0 non-Newtonian dynamic viscosity at zero shear rate (Pa.s);

η_∞ non-Newtonian dynamic viscosity at infinitely large shear rate (Pa.s);

λ wavelength of LDA laser beams (m), **Figure (3.6)**;

λ_c Cross model constant, **Equation (4.3)**;

μ dynamic Newtonian viscosity (Pa.s), **Equation (4.1)**;

η_S dynamic viscosity of fluid at pipe wall (Pa.s);

ρ fluid density (kg/m^3);

τ shear stress (Pa);

τ_S surface shear stress (Pa);

τ_{S1} surface shear stress at onset of transitional flow (Pa);

τ_{S2} surface shear stress at onset of turbulent flow (Pa);

τ_Y yield stress (Pa);

ϑ intersection angle of LDA laser beams (°), **Figure (3.6)**;

ν kinematic viscosity μ/ρ (m^2/s);

ξ r_P/R;

1.0 INTRODUCTION

The underlying motivation for this study is the need to develop a better understanding of the mechanics of the flow of drilling fluids ('muds'), which are pumped down the drill-pipe, through the drill-bit, and up the annulus between the drill-pipe and the bore-hole wall during the drilling of oil and gas wells. As will be discussed in the following sections, drilling muds are among the fluids which exhibit a wide range of phenomena associated with the flow of non-Newtonian fluids. A parallel study carried out by the author's colleagues has been concerned with the flow of a range of slightly elastic, shear-thinning liquids in an annular geometry with and without centrebody rotation [Escudier *et al.* (1995a, b and c)]. These experimental studies provided partial simulations of mud flow in a well-bore during drilling operations. In the course of that work it became increasingly evident that more fundamental pipe-flow investigations of the fluids being used were required if progress was to be made in analysing and understanding the more complex situation of flow in an annulus.

1.1 Background

It is well known that most fluids of industrial importance (in food, pharmaceutical and oil industries) exhibit complex *rheological* behaviour. For liquids dosed with high molecular weight polymers such as Separan (polyacrylamide), transition to turbulent flow is delayed to much higher Reynolds numbers and the resulting turbulent flow is accompanied by considerable reduction in frictional drag [see e.g. Virk *et al.* (1970), Pinho (1990)]. Moreover, there exist several viscometric flows in which interesting phenomena associated with polymer fluids are completely different from their Newtonian counterparts (for example, paint climbing the stem of a stirring paddle when being mixed). This fact provides a means for qualitative distinction between these two classes of fluids.

Although these effects have been known for almost half a century, the most challenging and unresolved phenomena is that associated with the physical mechanism that causes drag reduction. Drag reduction by additives in pipe flow is pre-eminently a phenomenon involving the reduction of friction drag at the pipe

surface. This result is made more remarkable by the fact that the laminar flow behaviour of very dilute solvent-additive solutions is very little different from that of the base solvent alone, i.e. the density and viscosity of the polymer solutions are not very different from those of the base solvent. However, such dilute solutions can have a dramatic effect in turbulent flow. Apart from the obvious practical and economical applications, the phenomenon of drag reduction is also interesting from a fundamental point of view. Namely, the fact that small changes in the fluid composition can so drastically alter the turbulent flow characteristics strongly hint that the polymer interferes with an essential mechanism of turbulent transport. That means that a study of polymeric drag reduction should help in gaining more insight into turbulence itself. Consequently, the rheological understanding of these non-Newtonian fluids has attracted considerable attention primarily due to the economic implications of achieving drag reduction by the addition of polymer additives. However, despite these economical benefits, detailed studies on non-Newtonian fluids have been limited in contrast to Newtonian fluids. This is primarily due to one of the important problems in rheology, which is the lack of well-defined experiments by which one can measure properties of non-Newtonian fluids pertinent to the behaviour in non-viscometric flows. In this case conventional viscometric techniques fail to provide adequate information on the behaviour of polymer solutions. Gadd (1965) concluded that although the drag-reducing and turbulent-damping properties of dilute long-chain-molecule solutions may seem paradoxical at first sight, since the density and steady shear-flow viscosity are little different from those of water, the viscoelastic characteristics, which some solutions seem to possess, provide at least a partial explanation. There is a clear challenge, therefore, in trying to link drag-reducing behaviour with the viscoelastic characteristics using rheometrical techniques.

Such a challenge, however, does not address the important issues related to the mechanism of drag-reduction or the theory of turbulence. It does, however, provide some insight into the rheology of drag-reducing fluids, an essential ingredient to understanding the interaction of polymers with turbulent flows.

All of the above considerations have further motivated the present work, from which the following basic requirements were identified, which have contributed to the

understanding of fully-developed transitional and turbulent pipe flow of non-Newtonian fluids:

- Non-intrusive flow-measurement technique, such as laser-Doppler anemometry [Durst *et al.* (1976)], because conventional intrusive probes are either difficult to calibrate or totally unable to function (e.g., in a fluid such as Laponite which gels at low shear rates [Escudier *et al.* (1992)]).
- Sufficiently large flow facility to provide high relative spatial resolution.
- Rheometer of sufficient sophistication to characterise the fluid at the time of the flow measurements.

The latter facility is vital since many polymer based fluids are susceptible to degradation, due to either mechanical effects and/or biological influences [see e.g. Pinho (1990)].

The remainder of this chapter provides a basic understanding of well-bore drilling operations and in particular, the use of drilling muds in this process. It then identifies the detailed aims of this study and its present contribution and ends with an outline of this thesis.

1.2 Well-bore Drilling Operations

For many years, the petroleum industry has been interested in the development of specialist drilling fluids. These fluids, which have the appearance of mud, serve many useful purposes in rotary drilling of which some are illustrated in **Figure 1.1**. The mud is circulated downwards through the drill-stem, around the bit, and upward around the annular spacing between the drill-stem and the wall of the well-bore. The main use of drilling mud is for cuttings transport and pressure build up at increased depths. This pressure build up is also important in preventing oil-well 'blowouts' from occurring. Blowouts are caused by an uncontrolled flow of formation fluid (gas in the subsurface rock formations) emitted from the well-bore due to a combination of advection with the drilling mud and the buoyancy driven force due the density difference [International Association of Drilling Contractors (1980)]. If the formation pressure (which can be as

high as 14,000 kPa) is not counteracted by a larger hydrostatic pressure of the drilling mud, the formation fluid will rise and expand due to a decrease in pressure further up the well-bore, thus leading to a blow-out.

Under most circumstances various forms of drilling 'muds' are used, which are either oil-based, non-liquid based (e.g. foam), or more commonly water based. Nevertheless, they are more than just muds; literally scores of chemical additives and weighting materials (e.g. Barite or Calcium Chloride) are added to the drilling mud. These chemicals affect certain physical properties of the drilling mud, which profoundly determine its effectiveness in practical drilling situations. An increase in density and viscosity for example, particularly in boreholes, can improve the cuttings transport at the drill bit, but will slow the settling process at the surface. Conversely, a reduction in density may well result in inadequate formation of the borehole lining. Many other characteristics and properties are associated with drilling muds, some of which will be discussed later in Chapter 4.2.

During drilling operations, there is a widespread need for the direct analysis of the internal flow behaviour of fluids within the various types of industrial plants used respectively, in order to improve the design and operation of equipment. The measuring instruments for such applications must be robust non-invasive sensors, which if required, can operate in aggressive and fast moving fluids and multi-phase mixtures. Historically, the monitoring and control of drilling mud physical properties has been undertaken by simplistic off-line sampling techniques, e.g. the examination of cuttings at the surface. However, in recent years, there has been increasing interest in the field of process tomography - a non-invasive visualisation technique used in multi-phase flows through pipelines. This method uses tomographic imaging methods to manipulate data from remote sensors in order to obtain precise quantitative information from inaccessible locations, including through opaque slurries and solid-wall vessels.

X-Ray Computed Tomography [Vinegar *et al* (1997); Hove *et al.* (1990)], *microtomography* [Flannery *et al.* (1987)], *gamma-ray tomography* [Ursin (1992) and Brown (1993)], *Nuclear Magnetic Resonance Imaging* [Li *et al.* (1995)] and *ultrasound mapping* [Soucemarianadin (1989)] are other means of non-invasive flow measurement.

Such methodologies allows the verification and development of process theories and models. All these methods optimise production and utilisation of gas and oil wells, which is increasingly important as petroleum resources are finite and becoming even more elusive. In this study, laser Doppler anemometry (LDA) was used, as previously mentioned, to measure the local, instantaneous velocities of the test fluids, which is also a non-invasive flow measurement technique though requires fluids to be optically transparent.

1.3 Aim of Study

This study aims to clearly quantify the turbulent flow structure and rheological behaviour for a carefully selected range of non-Newtonian liquids in order to provide a definitive set of dynamic flow data that can ultimately be used for computer modelling purposes.

Mean velocity-distribution data are needed to establish "wall-" and "velocity-defect" functions, which quantify the near-surface behaviour for non-Newtonian class fluids in turbulent flow. Just as for *Newtonian fluids*, such wall-functions are an essential part of the foundations of any engineering approach to the calculation of turbulent flows of non-Newtonian fluids in the vicinity of a solid surface. It is anticipated that the wall functions will be incorporated into Computational Fluid Dynamics (CFD) codes in order to formulate a turbulence model which generates the correct flow behaviour in the vicinity of the surface. The respective data is also needed to establish the limitations of the wall-function approach for non-Newtonian liquids and to assist the interpretation of data obtained in more complex flows as well as simple straight pipe-flow. Analysis of data corresponding to the fluctuations in velocity are also needed to establish reliable transition criteria and advance the understanding of non-Newtonian liquids generally. Turbulence intensity distributions (axial, tangential and radial) are also necessary to characterise the complete turbulent flow structure associated with non-Newtonian fluids.

A quantitative analysis of the rheological behaviour of all test fluids used, other than the dynamic flow measurements, is also required in an attempt to correlate measurable

rheometrical functions with the observed flow behaviour in a pipe. All test fluids selected must exhibit flow properties analogous to those found in drilling fluids whilst conforming to experimental constraints introduced by the various flow measurement techniques employed.

1.4 Present Contribution

An extensive database has been built up from experiments on the flow of CMC, xanthan gum, polyacrylamide, Carbopol and Laponite (time dependent) solutions as well as an aqueous blend of xanthan gum and CMC. The data includes mean velocity distributions, turbulence intensities and surface shear stresses for flow rates corresponding to the laminar, transitional and turbulent flow regimes. Also, an extensive rheological characterisation of each liquid has been carried out: viscosity and first normal stress difference *versus* shear rate; storage and loss moduli *versus* frequency. Attempts were then made to correlate the hydrodynamic flow properties with the extensive range of rheological data obtained for each fluid.

From each hydrodynamic flow test, the level of drag reduction was analysed by separating the shear-thinning and elastic contribution to the total reduction in friction drag, thereby allowing a basis for further rheological correlations to be quantitatively assessed.

Detailed analyses of the turbulent flow structure have also been described using quantitative representations of "wall-functions", with measurements extending into the viscous sublayer. Very little other work has been published: this study provides the most comprehensive, extensive and detailed to date. Two journal papers related to this study have been published, and for reference purposes, have been included within **Appendix 1**.

1.5 Thesis Outline

The remainder of this thesis is presented in six further chapters. Chapter 2 provides a literature review of relevant work performed to date, which encapsulates a wide spectrum of subject areas that have provided a forum for discussion concerning the unexplained drag-reduction phenomena. Pipe flow of non-Newtonian fluids under turbulent conditions and historical developments in rheology provide the main subject areas presented in this chapter.

Chapter 3 describes the experimental set-up and procedures used in acquiring all experimental data, the results of which are detailed in later chapters.

The rheology of the test fluids is discussed in Chapter 4. A review of the relevant rheological models and concepts is presented, followed by a description of the chemical properties of each test fluid analysed in this study. Justification for their use has also been provided. Relevance to well-bore hydraulics is also mentioned where a comparative (rheological) example of a typical drilling mud has been illustrated. A discussion of the measurements carried out includes the characterisation of viscous, shear-thinning, elastic and thixotropic properties.

Chapter 5 discusses the hydrodynamic flow measurements and velocity characteristics for all the time-independent polymeric fluids used in this study. After comparing the Newtonian fluid results with similar pipe flow data obtained in literature, the present measurements are compared and the influence of Reynolds Number and non-Newtonian behaviour are discussed. An attempt is made to correlate the pipe flow experimental data with the rheology of these fluids.

Since the analysis of the pipe flow of a thixotropic (time-thinning) fluid was different to that of the above, a separate discussion was warranted. This analysis is discussed in detail in Chapter 6. Conclusions of this work are summarised in Chapter 7. The final sections of this thesis include suggestions for further investigations in areas deemed supportive to the work carried out in this study.

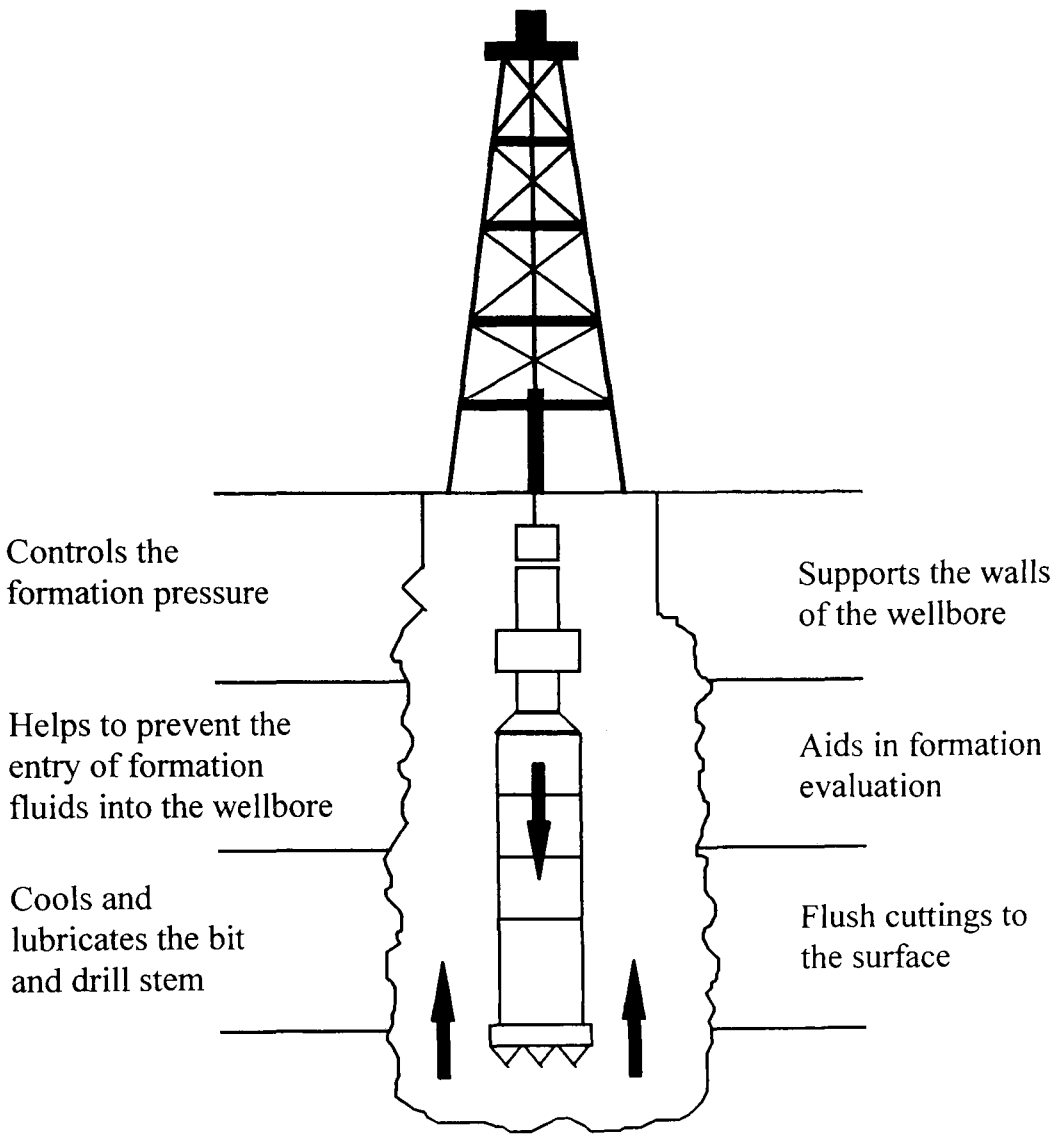

Figure 1.1 *Functions of Drilling Mud [International Association of Drilling Contractors (1980)].*

2.0 LITERATURE REVIEW

It has been found that very small traces of certain long-chain-molecule contaminants added to water can greatly reduce turbulent friction on the surfaces past which the fluid flows [Shaver and Merrill (1959)]. Reductions as much as 40% can be obtained by additions of as little as a 10 ppm by weight [Gadd (1965)]. This is at first sight very puzzling, since the density and viscosity may be very little different for those found in uncontaminated water, and the hydrodynamicist normally regards the density and viscosity as the only relevant properties of a fluid. The explanation has often been linked to the effects associated with viscoelasticity, though as will be discussed below, various other hypotheses and a variety of methodologies have been cited in literature over the past 30 years, which have aimed to resolve the drag reduction phenomenon.

2.1 Drag Reduction in Turbulent Pipe flow

The drag reduction phenomenon was initially observed by Toms (1949) and has subsequently been the subject of investigations by many authors, especially related to pipe flow. Review articles on the drag reduction phenomenon began to appear in 1969 when Lumley (1969) discussed the major phenomenological features of drag-reducing flows obtained from pressure drop, flow rate data and from mean velocity profiles. Hoyt (1972) provided a comprehensive review of the effect of various solvent-additives on frictional drag, particularly over flat plates and in pipe flow, and summarised the various (and often conflicting) theories that attempted to explain the drag reduction phenomena. Hoyt clearly demonstrated the complexity of such flows and their sensitivity to flow configurations, rheology and measurement techniques. Virk's (1975) review in 1975 also provided a comprehensive account of the literature and highlighted that there were only a few experiments prior to 1976, which reported either structural features or velocity statistics for drag-reduced flows.

One of the principal reasons for the lack of such measurements is due to complex rheological characteristics inherent in non-linear viscous fluids. These characteristics have often precluded the use of earlier available instruments (pitot tubes and hot-film anemometers), which were difficult to use and prone to physical and statistical errors.

However, significant technological advancements in rheometry and laser velocimetry in the last 20 years have resolved some of the conflicting hypotheses that have attempted to explain the drag-reduction phenomenon.

Earlier work by Allan *et al.* (1984) is limited in scope as is the more recent work of Park *et al.* (1989) on slurry flow. The work carried out by Shaver and Merrill (1959) and Dodge and Metzner (1959), had been with more concentrated solutions, which were shear-thinning. Such non-linear shear-stress *versus* shear-rate relations have often been approximated to by a power law of the form $\tau \propto (\partial u/\partial y)^n$, where n is 1 for a Newtonian fluid and less than 1 for a shear-thinning fluid. Dodge and Metzner (1959) correlated the friction factors for turbulent flow through pipes by producing a family of curves plotted against a generalised Reynolds number (see Chapter 5.6.2 and **Eq. (5.12)** for explanation), one curve for each value of n. However, Dodge and Metzner's correlation, which was based only on purely viscous fluids, was unable to adequately represent viscoelastic fluids, which show much greater levels of drag reduction. One such anomalous fluid was that of CMC, which was investigated by Shaver and Merrill (1959). They showed by injecting dye into a tube containing flowing CMC solution (0.25% w/w concentration), that the additive appeared to suppress turbulence. They attempted to relate this to the shear-thinning effect, attributing it to the viscosity being less at the wall of the tube, where the vortices are mainly formed, than at the centre. However, this explanation cannot be more than partially true, since later work [see e.g. Hartnett and Kostic (1988)] with very weak solutions has shown that large drag reductions are possible even though the fluid is not shear-thinning, often indeed having a viscosity barely distinguishable from that of water. A subsequent paper by Gadd (1965), illustrated that weak solutions (<60ppm by weight) of 'Polyox' (polyethyleneoxide) and of guar gum, which are regarded as highly elastic solvent additives, displayed first normal stress differences although they were not shear-thinning and displayed viscosities not too dissimilar to that of water. This suggests a correlation of the drag reducing effect with first normal stress difference, which could account for the anomalies in fluid behaviour when comparing data for highly elastic fluids with Dodge and Metzner's correlation. Gadd's observations were however limited and despite hypothesising that the turbulence suppression in viscoelastic turbulent flows is a function of elasticity, his experimental

observations were limited and inconclusive. Gadd's work directly followed that of Metzner and Park (1964), who achieved what they termed indicative success in attempting to correlate the degree of drag reduction in the turbulent pipe flow of viscoelastic polymer solutions with the ratio of elastic to viscous stress i.e. with N_1/τ_S where N_1 is the first normal-stress difference for a given wall shear rate $\dot{\gamma}$ and τ_S the corresponding wall shear stress. Their experimental correlation indicated that drag reduction should be a unique function of N_1/τ_S, where $N_1/2\tau_S$ is often referred to as the 'recoverable shear' [Barnes *et al.* (1989)], with Reynolds number also as a parameter. However, since only one viscoelastic fluid was used (0.3% J-100), their hypothesis remained inconclusive.

In order to clarify the wall structure of drag-reducing fluids in turbulent flow, Virk *et al.* (1970) proposed that the mean velocity profile can be described by a three layer model, which was subsequently derived from experimental pressure drop measurements. The model, comprises of a viscous sublayer, an 'elastic' or 'interactive' layer over which the 'effective slip' (upshift in data) occurs and the Newtonian plug. This wall representation has been illustrated in **Figure 2.1** (described in further detail in Chapter 5). This model is analogous to that of a Newtonian fluid [McComb (1990)], which is represented as:

$$U^+ = A \ln y^+ + B \tag{2.1}$$

For the three layer model as described by Virk *et al.*, an increase in drag reduction leads to an extended elastic layer at the expense of the Newtonian plug. The maximum possible drag reduction occurs when the elastic layer extends over the entire cross-section of the pipe, which can be represented by an ultimate mean velocity profile, based on an averaged envelope of experimental data, given by:

$$U^+ = 11.7 ln y^+ - 17 \tag{2.2}$$

This three-layer profile of mean axial velocity was later confirmed by Tiederman (1988), who agreed that for polymer solutions, constant A (see **Eq. (2.1)**) should be

unchanged, though constant B should be increased with increasing drag reduction. However, recent measurements [see e.g. den Toonder *et al.* (1997)] in polyacrylamide solutions show changes of between 10% and 40%, in both the intercept, A, and the slope, B, of the logarithmic region at drag reducing levels. Lumley (1969) suggested that a universal description for fully-developed turbulent flow should be more straightforward: 'A' should be a universal constant whilst 'B' should be a function of the rheology (e.g. power-law exponent) to be determined empirically. The recent study of Dimitropoulos *et al.* (1998) using a direct numerical simulation (DNS) technique, which will be further discussed in Section 2.4, had also shown an increase in the B-constant for highly drag-reducing and concentrated polymer solutions.

It is only recently that extensive detailed measurements of mean velocity and turbulent-stress distributions for fully developed pipe-flow of a non-Newtonian liquid have been published by Pinho and Whitelaw (1990). Their measurements were for aqueous solutions of the polymer sodium carboxymethylcellulose (CMC) with w/w concentrations in the range 0.1 - 0.4%, which they characterised by a power-law model. Their data showed a progressive approach with increasing polymer concentration to the asymptotic behaviour identified by Virk *et al.* (1970), i.e. a mean velocity distribution with an extended sublayer and an increased additive constant B (in the range of 8 - 12) in the law of the wall compared with the value of 5.5 for a Newtonian fluid whilst the Kármán constant A ($\equiv 1/\kappa$) was unchanged at 2.5.

Similar measurements to those of Pinho and Whitelaw (1990) have been made at the University of Liverpool for several shear-thinning and thixotropic (time-thinning) liquids [Escudier *et al.* (1992)]. The results confirmed that polymers such as CMC and Xanthan gum bear little relationship to the base fluid (filtered tap water) and behave in a similar way to low concentration drag-reducing solutions. However, when using a thixotropic (time-thinning) fluid such as Laponite, which is a non-polymeric synthetic clay, little drag-reduction was exhibited. Also, the viscous sub-layer observed indicated slip behaviour with an inflexion of velocity gradient in the vicinity of the wall. These measurements were, however, limited and inconclusive.

The study of Pereira and Pinho (1994) was very similar in approach to that of Pinho and Whitelaw (1990) but concerned with aqueous solutions (0.4-0.6% w/w concentration) of the low molecular weight polymer Tylose, a methylhydroxilcellulose. Pereira and Pinho concluded that their Tylose solutions, for which the viscometric data are well represented by the Carreau model, could be considered essentially inelastic, as is also the case for CMC at low concentrations. The hydrodynamic data showed turbulent-flow drag reductions of about half that for CMC together with a concomitant upshift in the log-law (i.e. an increase in B). The extent of recent studies associated with drag reducing pipe flows is exemplified by the work of den Toonder *et al.* (1997), Sureshkumar *et al.* (1997) and Beris *et al.* (2000). Numerical simulations incorporating flow and rheological parameters were compared by den Toonder *et al.* with experimental studies using LDA techniques. The main conclusion from their study supported the hypothesis that the key property in drag reduction is related to a purely viscous anisotropic stress introduced by extended polymers. Furthermore, the numerical simulation results also suggested that the elastic behaviour of non-Newtonian fluids reduces the drag-reducing effectiveness, counter to what will be described later.

The numerical study of Dimitropoulos *et al.* (1997) further demonstrated that the mechanism for drag reduction is attributed to a partial inhibition of eddies within the buffer layer caused by the macromolecules. This inhibition of turbulence activity, which results in drag reduction, was found to be primarily related to a sufficiently enhanced extensional viscosity, which was also later supported by the work of Beris *et al.* (1999). Further numerical studies are discussed in Section 2.4.

2.2 Drag-Reducing Test Fluids

From various experimental studies [see e.g. Hoyt and Fabula (1964)] it can be concluded that, in order to reduce turbulent drag, polymers should have:

- Very long molecular chain structure with little branching corresponding to a large number of monomer units
- Flexible chain structure
- Excellent hydration properties.

Many polymer-solvent combinations fit these requirements but the most effective in aqueous solution are polyethyleneoxides (PEOs) such as Polyox WSR 301 [*Merrill et al.* (1959)] and polyacrylamides such as Separan AP-273 [Tung *et al.* (1978)], both supplied by the Dow Chemical Company. Many other non-Newtonian fluids have also been used in turbulent flow experiments, which do not encapsulate all of the above features or even fall outside those identified above. For example, xanthan gum, which is extensively used in research [see e.g. Escudier *et al.* (1995a-c)], is a rod-like fluid and relatively inflexible (see also Chapter 4.7 and **Table 4.4**). Another popular test fluid that has also been extensively investigated over the years is CMC [see e.g. Pinho and Whitelaw (1990)]. These polymer solutions have in common that they are time-independent (see Chapter 4.1.2), hence do not account for unique characteristics normally associated with, for example, thixotropic (time-thinning) fluids.

Given the widespread nature of thixotropic materials (e.g. paints, clays, cement slurries, drilling muds, blood, ketchup, mayonnaise, toothpaste, shaving cream, crude oil and printing inks [Collyer (1973), Mewis (1979), Huang (1988)], and the commercial and technical significance of these materials, it is not surprising that numerous papers have been published on the rheological characteristics of thixotropic fluids. Mewis (1979) put the figure at about a thousand nearly two decades ago. In contrast, the number of papers which are concerned with the flow of thixotropic fluids is small, a consequence of the extreme theoretical and experimental problems involved. The mathematical difficulty of dealing with such flows is exemplified by Pearson (1994) who considers the general physics of the flow of thixotropic fluids and also from a later paper by Billingham and Ferguson (1993), which analysed the relatively simple situation of laminar, unidirectional flow of a thixotropic fluid in a circular pipe. The experimental

difficulties associated with the flow of thixotropic fluids are also readily apparent. For most laboratory installations and many practical situations, it can be anticipated that, except in the immediate vicinity of the surface, the time-scales associated with structural breakdown and build-up for the fluid will be greatly in excess of residence times. An inevitable consequence is that the fluid viscosity is likely to be quite different from what would be consistent with the local shear stress if equilibrium had been reached. Global measurements of pressure drop versus flow rate for flow through pipes and fittings, such as reported by Cheng *et al.* (1965), are clearly inadequate for such complex situations but the very nature of thixotropic fluids precludes detailed measurements using conventional intrusive instrumentation such as pitot tubes or hot-wire anemometers. Since nearly all thixotropic fluids of practical interest are opaque, non-intrusive optical measuring techniques such as laser Doppler anemometry are also ruled out in most instances. The work of Li and McCarthy (1995) on the flow of polyacrylamide is primarily of interest because they utilised nuclear magnetic resonance imaging, a technique that is not limited to optically transparent liquids. However, an exception to the statement about opacity is Laponite, a test fluid investigated within this study.

Further discussions associated with the characteristics of test fluids, in particular those specifically used in this study, will be discussed in detail in Chapter 4.

2.3 Turbulence Intensities

Amongst the recent studies of turbulent flow are those of Pinho and Whitelaw (1990) and the work of Harder and Tiederman (1991), investigations which have in common that they make use of laser Doppler velocimetry (LDV) to measure the turbulence statistics. Pinho and Whitelaw measured all three velocity components in a pipe flow, while Harder and Tiederman used a two-dimensional LDV system in a channel flow. One of the most striking results found in these papers is that polymer additives do not simply suppress the turbulent motion. On the contrary, the stream-wise turbulence intensity is increased. This means that the turbulence structure is changed, rather than attenuated.

Laser velocimetry measurements of the turbulence axial intensity, u`, have been in the most part consistent over the years. Most data illustrates that the peak levels of u` for drag-reducing fluids tended to spread out more and towards the centre of the flow compared to a narrow peak region occurring near the wall in the Newtonian case, with peak values essentially the same [Tiederman (1988)]. However, Allan *et al.* (1984) plotted u`/U as a function of the distance from the wall, for various concentrations of polymer solutions in pipe flow, and concluded that the axial fluctuating velocity component had increased relative to the Newtonian case. Similar increases were also found by Willmarth and Wei (1987) and Usui *et al.* (1988) [cited in McComb (1990)]. However, a surprising feature of the turbulence measurements carried out by Pinho and Pereira (1994) was an almost uniform distribution of both the radial and tangential turbulence intensities in the central core (80% of the diameter) of the flow at levels above those for a Newtonian fluid, contrary to most findings in the literature. Measurements of turbulence intensities normal (w`) and radial (v`) to the stream-wise flow direction are, in contrast, rare, as presumably they are deemed as less important factors in accounting for the drag reduction phenomenon. However, results cited in the literature consistently show reduced levels of v` and w` in the extended buffer layer (elastic layer) and in the core regions of dilute polymer pipe flows [e.g. see review of Tiederman (1988)].

The investigation of Reynolds stresses has become one of the dominant themes of research in turbulence [Schlichting (1978)]. The Reynolds stresses represent the turbulent transport of momentum due to turbulent fluctuations, which is responsible for equilibrating the pressure gradient in a fluid flow field. In turbulent pipe flow, the predominant Reynolds stress is $\tau'_{yx} (\equiv -\rho\overline{u'v'})$, which is extensively used in turbulence modelling. The stress component exemplified here can be interpreted as the transport of x-momentum through a surface normal to the y-axis. In turbulent flows, the momentum transport is dominated by the turbulent Reynolds shear stress and so this becomes a critical quantity, both to measure and to model. The Reynolds stresses effectively alters the viscous stresses due to random molecular motion. This has led to the hypothesis that an analogy exists between these two processes i.e. the

sum of the viscous stress ($\mu du/dy$) and the Reynolds stress ($-\rho\overline{u'v'}$) yields the expected linear variation in total shear stress [Schlichting (1978)]. That is:

$$\tau = \mu\frac{du}{dy} - \rho\overline{u'v'} \qquad \textbf{(2.3)}$$

The measurement of Reynolds stress in dilute polymer channel flows, show that in most cases, reductions occur (in comparison with Newtonian fluids) in the extended buffer region and that **Eq. (2.3)** remains valid [see e.g. Harder and Tiederman (1991)]. However, there are instances, particularly for highly elastic polymer flows such as the channel flow of polyethylene oxide solution [see e.g. Willmarth *et al.* (1987)], where the Reynolds stresses are significantly reduced and **Eq. (2.3)** no longer yields the total shear stress i.e. a Reynolds stress deficit exists. This deficit has been associated with viscoelastic effects. For example, Bewersdorff and Berman (1988) suggested that the Reynolds stress deficit could be compensated by an extensional component, which contributes to the shear viscosity. It is important to note that the above measurements are for channel flows where the LDA can be easily used because there is no curvature effect (see Chapter 3.1). Pipe flow measurements are much more difficult but possible if special precautions are taken (e.g. refractive index matching or by utilising an ultra-thin section of pipe surrounded by the same liquid as that flowing).

Despite the relative importance of Reynolds stresses (τ'_{xy}) in investigating turbulent pipe flows, particularly in turbulence modelling, their experimental determination requires the instantaneous measurement of two velocity components. Such a measurement can be carried out, for example, by using a two-component laser Doppler anemometer. Such an instrument was not available during this study and hence no Reynolds stress data has been investigated nor discussed herein after.

2.4 Numerical Modelling

In spite of the large quantity of observational data available, the mechanism of drag reduction by polymers still remains unclear. As a consequence, investigators have sought other means of trying to solve the drag-reduction phenomena. In the case of Orlandi (1995) and den Toonder *et al.* (1997), this was to use direct numerical simulation (DNS) in an attempt to obtain more insight into the mechanism of polymeric drag reduction in a rational way. Contrary to what is possible in experiments, one can try in numerical simulations to isolate certain properties of the polymer by using a specific constitutive equation, and to study in detail the effects that these properties have on the flow. In this way, the importance of these isolated properties for the phenomenon of drag reduction can be estimated, at least qualitatively.

The suitability of DNS for such a purpose was already made clear in a previous paper (den Toonder *et al.* (1995)) where the role of extensional viscosity in the mechanism of drag reduction by polymer additives was investigated. The aim of that paper was to test a hypothesis introduced by Lumley (1969), who was the first to suggest that the molecular extension of polymers is responsible for drag reduction. Lumley argued that this extension would take place in the flow outside the viscous sublayer, causing an increase in effective viscosity there. Using general scaling arguments, Lumley showed that then a reduction in overall drag would occur. This was later criticised by den Toonder *et al.* (1997) using DNS, which showed that a mere increase in effective viscosity outside the viscous sub-layer is in itself not enough to produce significant drag reduction. Hence, anisotropic effects (molecular changes induced by fluid stresses and chemical actions) became of interest to investigators such as Virk and Wagger (1990) who varied the molecular formation of polymers, from extended to coiled, by the addition of salt to the solvent. The result led to a higher drag reduction in extended polymers, whilst the onset to turbulence occurred at a lower Reynolds number. The increase in drag reduction suggests that polymers are only effective when extended like a rod or thread, thereby introducing anisotropic effects in the fluid. Den Toonder *et al.* (1997) concluded, from DNS, that elastic effects associated with polymer fluids (modelled as an extensional component) reduced the drag-

reducing effectiveness though speculated that these elastic forces could play a significant role in the onset of transition. Den Toonder *et al.* found that the purely viscous anisotropic stresses, introduced by extended polymers, influenced the drag-reducing effectiveness, a similar conclusion to that of Lumley (1969). Achia and Thompson (1977) support the view that drag reduction stems from an increased resistance to deformation of stretched molecules and its consequent effects on turbulence production.

As previously discussed in Section 2.2, the more recent studies of Dimitropoulos *et al.* (1998) and Beris *et al.* (1999), have provided further substantiating evidence that the extensional viscosity decreases the production of the Reynolds stress in all components. They concluded that these changes, which led to a decreased eddy activity, was attributable to the enhanced extensional viscosity of the polymer solution, a hypothesis first advanced by Lumley (1969) and Metzner (1964). Their simulations, including those demonstrated by Sureshkumar *et al.* (1997), also suggested that this partial inhibition of turbulence activity would occur after the onset of drag reduction.

However, in order to validate the predictions provided through using DNS, comparisons must be made with experimental data, which is reliable, extensive and quantitative. Without this, Direct Numerical Simulations provide mere speculative predictions without a solid grounding. It is part of the intention of this work to provide such a database that can be compared, for example, with computational predictions from either DNS or CFD studies; this aspect of work has not been carried out during the course of this study to date.

2.5 The Importance of the Region Near the Wall

It has been traditional in the study of turbulence to attach a lot of importance to the region near the wall. The main turbulence generation and dissipation processes in turbulent shear flows are believed to occur in the buffer region close to the wall. Naturally, therefore, the essential mechanism of drag reduction has been thought to reside in or near the buffer layer. However, there is no conclusive evidence that this is the case and therefore remains indicative only. Polymer injection techniques have been used in the past in an attempt to clarify whether polymer presence in the buffer region has any effect on drag-reduction or whether injecting polymers into the centre of the flow had any influence. Wells and Spangler (1967) found that, when polymers were introduced into the flow near the wall, the wall shear stress was reduced immediately downstream of the injection point, whereas when the polymer was injected at the centre of the flow, no effect was observed until it had diffused to the neighbourhood of the wall. In view of the rather incomplete nature of this investigation, it could be regarded as a direct, but only qualitative, demonstration of this point. Later, Tiederman and Reischman (1975) confirmed this general conclusion by deducing that the polymer solutions had their largest effect on the mean velocity profile in the buffer region ($10 < y^+ < 100$). Later, Tiederman *et al.* (1988) also concluded that the polymer influence was restricted to the buffer layer, decreasing the rate of interaction between high and low momentum fluid close to the wall via lateral vortex stretching.

However, the work of Vleggaar and Tels (1973) poses a question whether drag-reduction produced by polymer injection (also known as heterogeneous flows) is different, or unrepresentative, to conventional drag-reduction with premixed solutions (homogeneous flows), which we are trying to understand. Their work concluded that injecting concentrated polymer solutions into the core region of the turbulent pipe flow, formed long threads, which resisted dispersion for a distance of more than 200 tube diameters. The resultant effect was that a substantial reduction in drag occurred before the polymer reached the wall region without producing any transitional onset effect as reported by many investigators [Virk *et al.* (1970), Park *et al.* (1989)]. However, McComb (1990) later found that the polymer concentration had followed a

Gaussian distribution over the entire cross-section of the pipe. Hence, this would not support the idea of discreet polymer threads and further investigations are required. Also, Bewersdorff (1982) found that there was a difference in the universal velocity distribution measurements within the turbulent core when comparing heterogeneous and homogeneous drag-reducing flows using similar fluid concentrations of polyacrylamide. He found that heterogeneous drag-reducing flows produced a greater slope in the semi-logarithmic velocity profile within the turbulent core than the premixed solutions, therefore indicating that comparisons between both flow conditions should be limited.

More experimental results reported in the literature will be discussed in the following chapters.

Figures

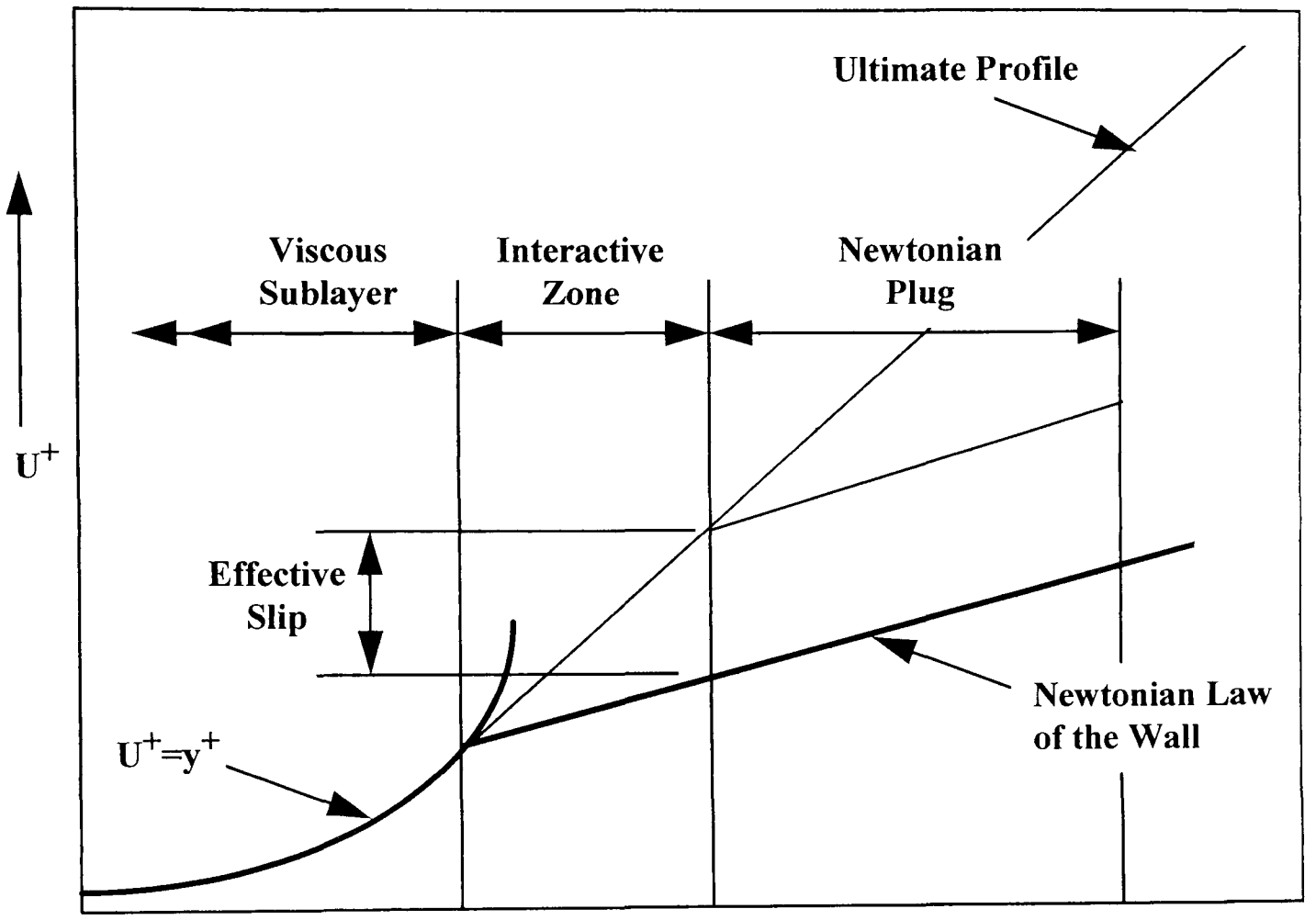

Figure 2.1 *Schematic of three-zone mean flow model [Virk et al. (1970)].*

3.0 EXPERIMENTAL METHODS AND PROCEDURES

This section describes in detail the experimental methods used within this study. The first section of this chapter describes the experimental flow rig used in all the pipe flow experiments. Section 3.2 details the selection, usage and calibration of all instruments employed in this study. In Section 3.3, a description of the LDA set-up is provided, which also details the bias correction methods used to collate and analyse all velocity measurement data. Finally, Section 3.4 provides a brief account of the uncertainty levels associated with the measurements carried out in this study.

3.1 Pipe Flow Rig

The flow loop used for the experiments is shown schematically in **Figure 3.1**. The flow loop consists of a pipe flow arrangement with associated instrumentation, mixing and pumping facilities. Flow was provided by a progressive cavity pump (1)* (Mono type E101, maximum flowrate 0.026m^3/s) fed directly from a 500*l* capacity stainless steel tank (2). The tank was supported at a height of 0.55m above the test section (3) to provide enough head to fill the system with the required test-fluid. Three dampers (4) located immediately after the Mono pump outlet act to remove pulsations in the flow before entry into the test section. The latter consists of thirteen precision-bore borosilicate glass tubes (ID 100.4 ± 0.1 mm), each of which were assembled into modules with matched male/female stainless-steel flanges at alternate ends fixed to a rigid table. Each glass tube was separated from the stainless steel flanges by a thin PTFE ring, and each end of a module (assembled in a jig) was fixed using Devcon urethane rubber. The Devcon rubber (Shore hardness 80) was used to compensate for any expansion or contraction of the stainless steel and glass whilst also reducing any risk of damage during handling. Much attention was devoted to the quality of the connection between the connected flanges, ensuring they were smooth and invisible to the fluid. The modules were 1.027m (± 3 mm) in length, which gave an overall length of 13.356 m and a length:hydraulic diameter ratio of 133. However, measurements were only taken over the initial 12 modules since disturbances in the flow were created at the final

The numbers in parentheses refer to the components shown in* ***Figure 3.1.*

outlet module due to the abrupt change in flow direction. Consequently, this gave the test-section an overall length:hydraulic diameter ratio of effectively 123 from the inlet. Fully developed flow conditions were achieved as will be discussed towards the end of this section.

Linear alignment of the flanged glass pipe assemblies was carried out using a specially configured laser and target arrangement. A Neon-Argon laser device was centrally positioned at one extreme of the test section within one pipe length and the target was manually placed at the other extremity. This enabled the laser beam to have its axis fixed along the entire length of the test section. After the first pipe length was configured, it was possible to add subsequent pipe lengths using the laser and target to set their position. This procedure produced a linear alignment (of the centreline of each pipe) to within ±0.1mm of the first pipe.

Piping to and from the stainless steel tank (2) was by way of a 50mm diameter UPVC pipe with an expansion to 75mm prior to the return side of the tank to reduce velocities and hence turbulence within the tank.

To permit filtering of the base solvent (tap water) prior to the addition of a Newtonian or non-Newtonian additive (typically in powder form), a 125 μm filter (13) was incorporated into a by-pass loop through which the liquid could be diverted. Mixing of the solvent additives was accomplished by circulating the fluid through a small return loop (14) incorporated just before the pulsation dampers after the flow valves were correctly operated. A pressure relief (safety) valve was located immediately after the pump outlet. The valve was set with a limiting pressure of 3 Bar, which provided a minimum 200% safety margin against the maximum operating pressures of the various components integral to the flow.

A second return loop (15) was also incorporated as a means of providing a greater range of flowrates within the test section by carefully regulating the ball-valve.

Pressure tappings of 1 mm diameter were provided on each mating flange pair with 2 mm internal diameter clear vinyl tubing (5), filled with de-ionised water, connecting

each pressure tapping via a series of valves (6) to a differential pressure transducer (see **Figure 3.2**). The valves were connected to the tappings in such a way as to permit measurement of the pressure drop over increasing numbers of pipe sections. The location at which the rate of flow development became negligible could therefore be assessed using the above valve configuration, whilst also enabling the determination of the wall shear stress, τ_S to be computed:

$$\tau_S = \left(\frac{\Delta P}{L}\right)\left(\frac{D}{4}\right) \tag{3.1}$$

where $\Delta P/L$ is the pressure drop over a specified length L of pipe and D is the diameter of the test pipe. Filling the pressure lines with de-ionised water eliminated corrections for specific gravity, though for denser test fluids, the pressure lines were filled with the same working fluid.

A 'zero pressure' reading (under no flow conditions) was made at the beginning and at the end of each flow experiment to account for any drifts in pressure readings. During a flow experiment, these drifts were random and limited to 0.075% of full-scale reading.

Special care was taken to ensure that the edge of each pressure tapping was not rounded and remained flush with the inner wall of the test-section as it has been well documented that large errors can be generated if the hole has burrs, rounded edges or other imperfections [Franklin *et al.* (1969)]. Consequently, all pressure tappings were surface polished. It has been reported, however, that even if the hole is near perfect a residual error remains as a result of the viscoelastic effects associated with non-Newtonian fluids, which could affect the measurements of wall shear stress [Shaw (1959), Franklin *et al.* (1969), Novotny and Eckert (1973)]. This residual error was attributable to a local change in boundary conditions and the consequence disturbance of the boundary layer. For a viscoelastic fluid, Novotny and Eckert (1973) found that this pressure error was proportional to the first normal stress difference (a non-Newtonian effect discussed in Chapter 4.4.2 (b)) when measuring that stress, though Higashitani *et al.* (1975) concluded that these non-Newtonian effects can be ignored when used specifically in determining the wall shear stress. Hence, these hole pressure errors have been ignored

in this study.

Figures 3.3 illustrates the pressure drop over the entire length of the test pipe for all test fluids used in this study. Tung *et al.* (1978), who worked with similar fluids and in particular 0.2% Polyacrylamide solutions, found that entrance lengths of 100 pipe diameters were sufficient to achieve fully developed flow conditions. From **Figure 3.3**, it may be ascertained that fully developed flow conditions have been achieved here for entrance lengths x/D > 90, thus confirming the work of Tung *et al.*.

A flat-faced optical box (10), initially filled with paraffin oil, was positioned over the pipe at 107 hydraulic pipe diameters from the inlet section. The optical box was used to minimise the refraction of the LDA laser beams at the curved surfaces by matching their refractive indices [Bicen (1990)]. However, with the presence of oil in the light-box, there was a loss of modulation signal of the LDA system, which led to lower data rates and poor signal quality. The loss of modulation signal was identified to be due to the absorption properties of the oil used. However, the absorptivity of the oil was not measured nor regarded as important at that stage. The oil in the optical box was then substituted with tap water, which resulted in significantly higher data rates and signal quality of the LDA measurements. The quality of the LDA modulation signal was suitably retained at both the inner-wall and far-wall of the test section. The refractive index of water was also adequate in overcoming any undulations in the external surface of the test-pipe, whilst ensuring that 'blind spots' [Kehoe and Desai (1987)] were not introduced at near-wall locations. The front of the light-box consisted of an optical glass fascia measuring 168×143×8mm (flat to 30 seconds/175mm). Distance dial gauges were used to align the traverse system (housing the LDA probe head) to the test section. **Table 3.1** presents the various refracting medium used within the optical box section.

The variation of refractive indices due to small changes in temperatures were negligible (<0.005% for ±5°C @20°C) and hence ignored.

3.2 Instrumentation

3.2.1 Description of Instrumentation

Pressure drop measurements were made using a Validyne differential pressure transducer (7) (DP15-26, 3448Pa fsd). Signal conditioning for the pressure transducer was provided by a Validyne CD223 digital transducer indicator with a BCD output connected to a data logging computer (RCL 386 5X-33). The accuracy of the Validyne transducer was estimated to be better than ± 0.25% of full-scale reading as quoted by the manufacturer.

A platinum resistance thermometer (8) mounted in the end-housing downstream of the test section was used to monitor the fluid temperature to an accuracy of ± 0.1°C. The range of temperatures measured during a hydrodynamic flow test was used to set the upper and lower operating temperature limits on the rheometer. Linear interpolation was then used to associate a value of viscosity for each value of temperature measured, thus providing a viscosity-temperature profile during the test. However, all test fluids used in this study displayed non-linear temperature relationships with viscosity, which can be represented by the following exponential equation:

$$\eta = C e^{-D/T} \tag{3.2}$$

where T is the absolute temperature and C and D are numerical constants [Massey (1990)]. **Figure 3.4** illustrates the temperature sensitivity for both a Newtonian (50% w/w glucose) and a non-Newtonian fluid (0.2% w/w xanthan gum). The temperature sensitivity for the glucose mixture at 20°C was 3.6% per °C, and 1.9% (at 9.055Pa constant shear stress) and 1.8% per °C (4.934Pa) for xanthan gum. Thus a required accuracy of ±1% in the measured viscosity for 0.2% xanthan gum requires the fluid sample to be maintained to within ±0.54°C at room temperature and similarly at ±0.28°C for the glucose mixture. The rheometers used (see below) were of sufficient sophistication to maintain fluid samples to within ±0.1°C of the set temperature. Therefore, based on small variations in temperature (<3°C) during a typical flow test,

which were recorded, and precluding the means of exponentially characterising the temperature dependency of viscosity for all fluids, the use of linear interpolation produced insignificant errors that were hence ignored.

A Fischer and Porter electromagnetic flowmeter (12) (model 10 DI, maximum capacity $0.0333m^3/s$) was incorporated in the return arm of the flow loop with straight sections corresponding to ×7 and ×5 hydraulic pipe-diameters (ID), upstream and downstream respectively, which complied with the manufacturer's installation specification. The flowmeter output signal was recorded via an Amplicon PC 30AT A/D converter on an RCL 386 5X-33 PC. The corresponding accuracy was specified as 0.07% (average) by the manufacturer when operating between 5-100% of maximum capacity; the operating range used in this study was between 8% and 72% of fsd. Existing in-house software [Escudier *et al.* (1991)] was used to record flowrate, pressure drop and fluid temperature, whilst new software was configured to control and record the LDA probe location (see Section 3.3.3).

Density measurements were taken using both a specific volume density bottle (100ml±0.1ml capacity) and an Oertling RB153 electronic weighing scale (1500g fsd with a resolution of 0.001g in the range 0-150g and 0.01g for 150-1500g). The Oertling balance was also used to weigh the additive to achieve the concentration required for producing the various solutions utilised in this study.

Fluid refractive indices displayed in **Table 3.1** were determined using an ABBE 60/ED high-accuracy refractometer (Type Degree Scale, ±0.001%).

A Spirax Sarco conductivity meter (model MS1, ±0.1mS/cm) was used to measure the conductivity of the test fluids. A pH meter (RS, Model 3051) was also used to monitor the pH balance to an accuracy of ±0.02pH.

The rheological characteristics of the test fluids used were determined using both a CarriMed controlled-stress rheometer (CSL 100) with either a cone-and-plate or a parallel-plate geometry, and also a Bohlin VOR controlled shear-rate rheometer with similar geometries (see **Figure 3.5**). The first rheometer was controlled from a CAF

386SX PC employing CarriMed's flow equilibrium software whilst the Bohlin VOR was controlled by a Compaq 486 DX2 PC running Bohlin's BRS software. The Bohlin VOR was used to measure the first normal stress difference of fluids including measurements of their elastic moduli under oscillatory flow conditions. Viscometric data were obtained from both rheometers for comparison reasons.

Mean velocity and turbulence intensity measurements were determined using a Dantec Fibre-flow laser Doppler anemometer (LDA) system comprising of a 60×10 probe and 55×12 beam expander (8) in conjunction with a Dantec BSA 57N20 Enhanced Burst Spectrum Analyser signal processor. The Spectrum Analyser, which utilised a data reduction procedure and provided values of velocity as well as all the necessary statistical information, was linked to a Hewlett Packard 286/12 microcomputer. This enabled all LDA data to be effectively processed and stored within a library type database. To ensure accurate long-time averaging of the superimposed velocity signals, 2000 data points were processed per measurement. Timiron seed particles (a pearlescent pigment of 20μm mean diameter) were added to the test fluid to produce detectable Doppler bursts. A seeding level of 1ppm was found to be appropriate to provide a good data rate (typically 60-100Hz for $y/R<0.2$, 100Hz-400Hz for $y/R>0.2$) and a high quality Doppler Burst. It should be noted that the addition of the seeding particles did not affect the rheology of any of the test fluids used in this study.

The LDA optics were specially configured by the manufacturer (Dantec) to produce the highest spatial resolution practically possible (see **Table 3.2**), which allowed detailed near-wall measurements extending into the viscous sub-layer of most fluids to be made. **Figure 3.6** illustrates the basic principles applied to laser Doppler anemometry.

The probe head, housing both the transmitting and receiving optics, was mounted on a traverse (9) (see **Figure 3.11(a)**) perpendicular to the stream-wise flow direction. The traverse motion was controlled by a software programme, devised in-house, using an IBM XT PS2 (Model 30) microcomputer. The programme incorporated refraction calculations which allowed the measurement volume to be located accurately within the test section (see Section 3.3.1).

Each traversing axis was fitted with an AC motor (Model 0240-04-005) connected in series to a 2 stage reducing gear-box (gearing ratio - 36:1). The gear-boxes were specially configured to overcome any thread backlash thus enabling fully reversible traverses without loss of positioning accuracy. The pitch of thread on each shaft was determined to an accuracy of ±2μm using a combination of metric slip gauges and a dial testing indicator (x-axis - 1.506mm, y-axis - 1.506mm and z-axis - 2.004mm). An optical rotary encoder (Type E6A2-CW3, 200 pulses/revolution) was then mounted on each shaft, thus providing an accurate measure of distance traversed to within a spatial resolution of 15μm.

Figure 3.7 illustrates the measurement collection and control system setup used in this study.

3.2.2 Calibration of Instruments and Support Measurements

The pressure transducers were calibrated at periodic intervals using air against a Baratron 398HD-01000SP05 (1000 torr fsd) high-precision differential pressure transducer. The accuracy over the calibration range was 0.01% of reading. A schematic representation of the calibration method is shown in **Figure 3.8(a)**. The change in calibration over a 6 month period was within 0.5% of full-scale reading (**Figure 3.8(b)**).

Flow rate measurements were assessed periodically by comparison with the values computed from the integration of the velocity profiles obtained from the LDA mean velocity distribution data, using the relationship:

$$Q = 2\pi \int_0^R urdr \qquad \textbf{(3.3)}$$

which were found to be within 1% of each other. A standby Coriolis Mass Flow meter (25kg/s fsd, resolution of 0.025kg/s), located in series with the principal electromagnetic flow meter, yielded consistent results with the volume flow meter (±0.25%).

The platinum resistance thermometer was calibrated against a glass-tube mercury

thermometer (accuracy ±0.1°C) for temperatures covering its working range (0°C - 35°C). The resistive losses within the A/D converter (attached to the measurement device) were compensated for during calibration. Between calibration periods, a drift limited to less than 0.1°C in measured values was noted. Given the temperature dependence of viscosity and a temperature sensitivity limited to approximately <2% per °C for most fluids used in this study, this drift was regarded as negligible to the overall measurement accuracy of viscosity.

The Carrimed and Bohlin VOR rheometers were calibrated against a 'Standard Fluid' - Dekalin (2% w/v Polyisobutylene, 98% decahydronaphthalene). The measurements of viscosity and first normal stress difference were in excellent agreement with a standard set of measurements issued from the Rheology Centre at Bristol University (UK). These results are presented in **Figures 3.9(a)** and **3.9(b)**. The viscosity measurements illustrated an average discrepancy with the Dekalin sample of less than 3% and 4% for the first normal stress difference. **Figure 3.9(c)** presents the elastic moduli measured under oscillatory flow conditions for Dekalin using the Bohlin VOR, though no standard data were available for comparison purposes.

3.3 LDA Setup - Measurements and Processing

3.3.1 Measurement Volume Location

The major inaccuracy in positioning resulted from the zero location of the measurement control volume at the inner-wall. To obtain the zero location reliably, the volume was traversed into the wall by visual observation, and thereafter, in the close proximity of the inner-wall, the signal due to light scattering by very small particles attached to the wall was recorded by the photodiode current output display. The location of the maximum output signal of the photodiode was recorded and taken as the zero position of the measurement control volume from the inner-wall of the test section.

Using the above procedure provided a means of locating the measurement control volume at the inner-wall to within ±180μm (length of measurement control volume),

which was adequate for velocity distribution measurements to be carried out. However, in order to obtain information on the universality of the $U^+ = f(y^+)$ distribution, the precise knowledge of the measurement control volume relative to the pipe wall was required. This was obtained by observing a distinct change in slope of the velocity profile caused by a partial intrusion of the measuring control volume into the test section wall, as exemplified in **Figure 3.10**. Consequently, the major contribution of the LDA signal was from the scattering particles that flowed passed the measurement control volume, assuming the wall remained clean i.e. relatively few particles at the wall. The resultant velocity should be located at the centre part of the control volume which is covered by the fluid. However, the centre part of the control volume was the centre of the total control volume, and, hence, too high velocity components were measured. Thus, the slope of the velocity profile at the near-wall changes when the measuring volume is less than 1/2 of its total length (<90μm in water). Therefore, by linearly extrapolating the velocity distribution measurements, prior to change in the slope, the zero-velocity point was found, which was taken to be the wall location.

After adjustment, a traverse from the inner-wall to the outer-wall verified this method by yielding a diameter of the test-section to within ±45μm.

The orientation of the laser beams relative to the axis of flow was determined by using a precision made aluminium block with vertical and horizontal cross-hairs inscribed on one face (see **Figure 3.11(b)**). This block, of semi-circular construction, was positioned parallel to the test section adjacent to the optical-box. The probe head, mounted on PTFE rings, was then rotated until the beams intersected the cross-hairs centrally (viewed as an equal distribution of light intensity for both beams on each side of the inscribed line). This method enabled the measurement volume to be accurately placed in a vertical or horizontal plane depending on the traverse required (see Section 3.3.2).

3.3.2 Direction and Orientation of Traverse

By placing the beams in the horizontal plane, the axial velocity component (stream-wise direction) was measured by traversing the probe into the test section from the inner-wall. The same traverse action, though with the beams placed in the vertical plane, allowed the tangential velocity component to be measured. In determining the radial component of velocity, the beams were placed in the vertical plane and the probe volume positioned at the centre of the test pipe. A vertical traverse in both directions was then carried out. These traverse motions are clarified in the illustration given in **Figure 3.12**.

3.3.3 Refraction of Beams

Due to a change in refractive index as the laser beams passed through the measurement test-section, the beams were refracted and therefore the refracted position of the probe volume was calculated. These calculations were based on a ray tracing method that was previously demonstrated by Bicen (1990) and Broadway *et al.* (1981) for LDA measurements at curved boundaries. The derivations of these position corrections for axial, tangential and radial traverses applicable to this study are given in **Appendix 2**. These position corrections were incorporated within the traverse program.

For traverses measuring the axial component of velocity, there was no change to the interference fringe spacing of the probe volume caused by the refraction of beams, therefore no corrections to these measured velocities were required. However, for the tangential and radial velocity components, velocity corrections were required due to a modification of the probe volume dimensions (see **Appendix 2**). These corrections were applied to the measured velocities in a separate computer program.

3.3.4 Bias Correction Methods

In evaluating statistical quantities of the flow velocity from random samples, systematic deviations (bias) from the real values, superimposed on other experimental errors, can occur. To obtain accurate laser Doppler measurements, and thus enable definitive conclusions to be made, the application of appropriate bias correction

methods must be assessed. Firstly, the main sources of statistical bias of LDA measurements must be identified and these are best described using the terminology used by Edwards *et al.* (1987). Here, four areas of bias were identified: *velocity bias, gradient bias, filter bias* and *angle bias*.

3.3.4(a) Velocity Bias

Velocity bias is caused by a dependence of particle velocity on the arrival rate within the boundary of the control volume. As pointed out by McLaughin and Tiederman (1973), when particles arrive individually in the scattering volume, the LDA provides velocity information averaged according to the occurrence of particles. Thus the distribution of velocity can be biased in favour of higher particle velocities because of the more frequent arrival of faster particles in a fluid containing uniformly or randomly distributed scatters. This can be compensated by processing the signals using a time-averaged velocity bias correction method as suggested by Edwards *et al.* (1987):

$$u = \frac{\sum u_n t_n}{\sum t_n} \quad , \qquad u'^2 = \frac{\sum (u_n - u)^2 t_n}{\sum t_n} \tag{3.4}$$

where u_n is the velocity of the n^{th} particle along the x direction, t_n is the residence time of the n^{th} particle and u` is the rms. velocity fluctuation component. The use of residence time weighting was employed in this study using the Burstware software from the LDA system.

3.3.4(b) Gradient Bias

Gradient bias occurs if a measurement volume of finite size covers a region of flow where a mean velocity gradient exists. As a result, particles traversing the measurement volume have a range of velocities, independent of any turbulent fluctuations which may exist, and as a consequence the arithmetical average velocity becomes biased. In the near-wall region where large velocity gradients are present, this bias effect becomes significant. Durst, Melling and Whitelaw (1976) proposed a

method for correcting gradient biased data based on the truncated Taylor expansion method which allows the measured mean velocity (U_i) and turbulence intensity (u_i`) data to be corrected using the following expressions:

$$\overline{u}_{i\ meas} = \overline{u}_{i\ true} + \frac{l_m^{\ 2}}{32}\left(\frac{d^2\overline{u}_{i\ true}}{dy^2}\right) + \ldots\ldots \qquad \textbf{(3.5)}$$

and

$$\overline{u}_i'^{2}_{\ meas} = \overline{u}_i'^{2}_{\ true} + \frac{l_m^{\ 2}}{16}\left(\frac{d\overline{u}_{i\ true}}{dy}\right)^2 + \ldots\ldots \qquad \textbf{(3.6)}$$

where l_m corresponds to the principal length of the measurement volume and y is the distance from the inner-wall of the pipe. **Eq. (3.5)** and **(3.6)** can only be evaluated if the coefficients for a polynomial fit to the true mean velocity profile are known, which allows the derivatives to be assessed. As gradient bias effects are predominant close to the wall, curve fit models were weighted towards points located in the near-wall region. Durst, Jovanovic and Sender (1995), also demonstrated that these bias errors are dependent on probe volume dimensions, where large probe volumes lead to higher values of turbulence intensity in the near-wall region.

In this study, the LDA optical system was specially configured to provide a high spatial resolution of the measurement volume (see Section 3.2), which minimised the effect of gradient bias. Therefore, for a probe length of 180μm, errors due to gradient biasing effects under highly turbulent conditions were limited to <0.1% of the measured velocity at a distance of 1mm from the inner-wall. Errors in the values for velocity fluctuations were much greater at 7% at 1mm from the inner-wall, though reduced to 2% at 3mm. Hence, no corrections were applied to the mean velocities. Corrections were made to the velocity fluctuations when the magnitude of error was significant and an accurate function of velocity could be determined.

3.3.4(c) Filter and Angle Bias

Finally, statistical errors due to filter and angle bias should also be assessed. Filter bias occurs because of the tendency of real systems to have a measurement efficiency that is dependent on the speed of the measured particle. However, for this study, the frequency response of the detection system and the filter settings on the burst processor enabled all particle frequencies to be measured and thus no filter bias correction was necessary.

Angle bias is caused by the fact that real processors cannot measure all speeds at all angles. For instance, the processor can be set to validate a measurement once the particle passes through a given number of fringes within the measurement volume. For this study the system was properly configured to ensure that all attainable velocities were within the measurable range set by the processor's criteria; hence, no angle bias corrections were necessary.

3.4 Uncertainties

3.4.1 Consistency of Measurement Data

The determination of the overall uncertainty of a measurement requires the analysis of the complete measuring system and the assessment of the uncertainties of each component and its sensitivity relative to the quantity under investigation. According to Moffat (1988) the relationship between the uncertainty in any measured quantity ($\Delta\Omega$) and the uncertainties (Δx_i) of the various independent variables x_i is given by:

$$\Delta\Omega = \sqrt{\left(\frac{\partial\Omega}{\partial x_1}\Delta x_1\right)^2 + \ldots\ldots + \left(\frac{\partial\Omega}{\partial x_i}\Delta x_i\right)^2} \qquad (3.7)$$

where the derivatives are the sensitivities. However, the concept of uncertainty can often be complicated and incomplete particularly if not all the information is at hand which contributes towards the overall level of uncertainty. For example, in a measurement device, it may be that the exact performance of an integral component of

the system cannot be obtained by the user, which contributes to its overall uncertainty level. Hence the overall uncertainty for that piece of equipment cannot be assessed accurately and is somewhat incomplete and at times misleading. It can also be dependent on the information provided by the manufacturer. For the present study we rely on the 'consistency' of the measurements, which increased the confidence level of all measured quantities. Consequently, by measuring a physical quantity, in situ, by alternative means and observing the outcome, its consistency or repeatability is appropriately assessed. If the same result was achieved by alternative means, then the level of uncertainty is regarded as low, the extent of which depends on the discrepancy between the measured values. The acceptability of these variations was reviewed with reference to the relative importance of the quantity measured, its effect on other parameters, and the methodology used. This approach was used throughout this study.

Therefore, using the above methodology i.e. the consistency of a measurement, the level of uncertainty may be estimated. Hence, typical uncertainty levels for the main parameters measured and discussed in this study have been estimated and are presented in **Table 3.3**.

3.4.2 Rheological Considerations and Solvent Chemistry

The variability of the rheology of dilute shear-thinning fluids is an important consideration when comparing experimental data from the tests used in this study or data obtained from literature. When comparing such data uncertainties are introduced if their rheological characterisation is incomplete and in particular, if there is no assessment of the various factors that could influence the fluid properties such as solvent chemistry, storage conditions, chemical additives and history (age, mixing process, etc.). For example, the incomplete fluid characterisation of Allan *et al* (1984) and Luchik and Tiederman (1988) prevent the reader from comparing the rheology of theoretically identical polyacrylamide solutions with, say, the data of Hartnett (1992), who has clearly demonstrated that changes in solvent chemistry can effect the viscosity of a given solution by as much as one order of magnitude. Unfortunately, the rheometric techniques required to fully characterise non-Newtonian fluids are not a matter of routine particularly for dilute fluids which exhibit a low viscometric viscosity. During

the course of the research programme, an additional rheometer was purchased and utilised - Bohlin VOR controlled-strain rheometer - in addition to the previous rheometer - Carrimed controlled stress rheometer. By utilising both rheometers, two independent techniques were effectively used to measure various rheological parameters. However, since the overall uncertainty of these measurements was not limited to the measurement system alone as mentioned above, the concept of consistency was not straight forward in this case. Also, the Bohlin VOR controlled-strain rheometer allowed for further detailed rheological studies (i.e. the measurement of first normal stress), which the Carrimed controlled stress rheometer was unable to measure. In this case, the first normal stress measurements were compared with a 'Standard fluid' as discussed in Section 3.2.2, in order to gain confidence in these measured values. Therefore, care was taken to ensure a consistent approach was used when preparing test fluids (see Chapter 4.3.3), particularly when using similar polymers from different batches.

For completeness, the chemical composition of Liverpool tap water was investigated and the results are tabulated (**Table 3.4**) and discussed below.

Such details may preclude any comparison of data obtained in this study with other work if it can be quantitatively shown that the physical characteristics and chemical content of water do influence the rheology of aqueous based non-Newtonian fluids. However, there was no evidence of any rheological effect associated with water during the course of the 3 years research programme, with no data available in literature, thus the effects of solvent chemistry should not have biased the conclusions made in this study.

Tables and Figures

Table 3.1 *Refractive Indices of Measuring Test-Section (@ 20 ℃)*

Refractive Medium	Air	Optical Glass	Paraffin Oil	Water	Glass Tube	Test Fluid
Refractive Index, n	1.000	1.478	1.476	1.333	1.478	1.333 *

* The refractive indices of all test fluids were similar except for 60% w/w aqueous glucose - 1.387.

Table 3.2 *Beam dimensions in LDA system* †

Beam Separation @ Front Lens	Focal Length	Length of Principal Axis		Length of Minor Axis	
		Air	Water	Air	Water
51.487	160.000	0.135	0.180	0.022	0.016

† All dimensions shown are in millimetres.

Table 3.3 *Estimated Uncertainty Levels*

Item	Measured Parameter	Measurement Device	Estimated Uncertainty	Comments
1	τ_s [Pa]	Differential Pressure Transducer	3 %	Compares well with the theoretical Newtonian *f*-Re relationship under both laminar (f=16/Re) and turbulent (Blasius equation) flow conditions.
2	η [Pa]	Rheometer	3 %	From the measured velocity profile at the wall (using the LDA), and using the wall shear stress obtained from the measured pressure drop (see item 1 above), the viscosity can be determined and compares well with the values provided on the rheometer. This was further supported by a comparison made with the Standard A1 Fluid.
3	Q [m^3/s]	Volume Flowmeter	1 %	The integration of the measured velocity profile using the LDA, yields a volume flowrate to within 1% of the flowmeter device. This was further supported by ad hoc measurements carried out by a mass flowmeter located in series with the volume flowmeter.
4	T [°C]	Temperature Probe	0.2 %	The probe was calibrated against a high accuracy mercury thermometer, displaying excellent repeatability. This was further supported by the rheometric measurement of viscosity at the measured temperature specified using the temperature probe and comparing it with that measured at the wall (see item 2).
5	N_1 [Pa]	First Normal Stress Transducer	10 %	The transducer was compared with measurements obtained from a Standard A1 Fluid. The measurements yielded good repeatability and closely matched the data for the Standard A1 Fluid.
6	ρ [kg/m^3]	Density Bottle and Digital Scales	0.2 %	From the *f*-Re observations carried out (see item 1 above), the density was viewed as an accurate measurement, which was used in determining the Reynolds number.
7	n [-]	Refractometer	0.1 %	The refractive index was required for positional corrections, which were programmed into the traverse controller. A full traverse, moving from the inner-wall to the outer-wall, yielded a calculated distance, which was comparable with the measured pipe diameter.
8	u	LDA	3 %	The uncertainty level for the axial velocity component is predominantly associated with the biasing corrections applied and the signal-to-noise ratio of the measured data. The uncertainty level shown here (and for items 9-11 below) are also based on the level of repeatability obtained.
9	u'	LDA	5 %	Axial turbulence intensity. See item 8 above.
10	v'	LDA	10 %	Radial turbulence intensity. See item 8 above.
11	w'	LDA	8 %	Tangential turbulence intensity. See item 8 above.

Table 3.4 *Typical Chemical Composition of Liverpool Tap Water*

Chemical Content and Physical Characteristics ‡		
Parameter	**Average Value**	**Units**
Conductivity	140	µS/cm
Hydrogen Ion (pH)	7.66	pH UNI
Sulphate	12.6	mg/l
Calcium	16.9	mg/l
Iron	73.6	µg/l
Magnesium	2.48	mg/l
Nitrates	4.7187	mg/l
Pottasium	1.68	mg/l
Sodium	9.63	mg/l
Chloride	14.6	mg/l

‡ Data obtained from North West Water Limited (1998), Liverpool (UK).

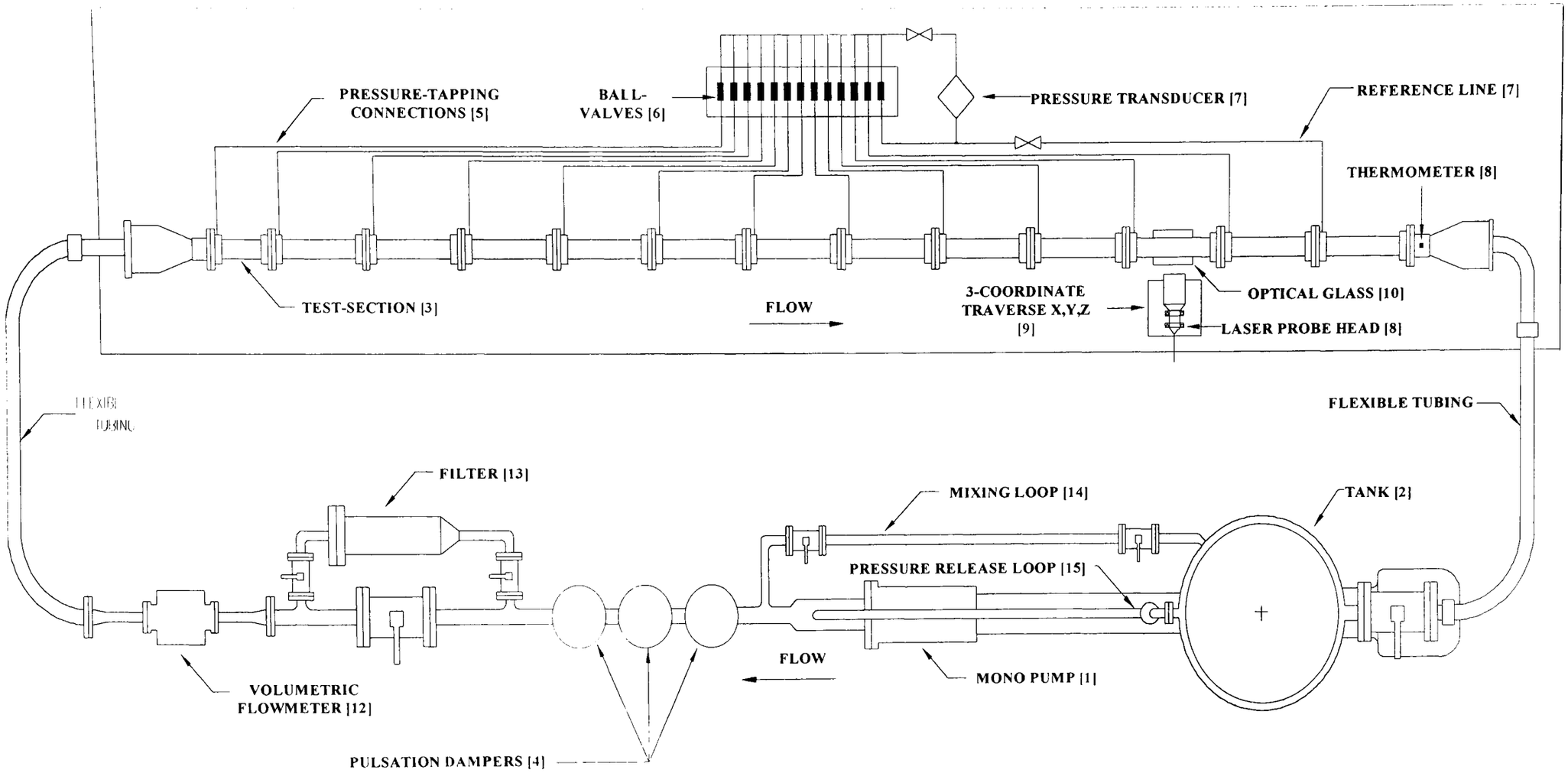

Figure 3.1 *Schematic of pipe flow rig (plan view).*

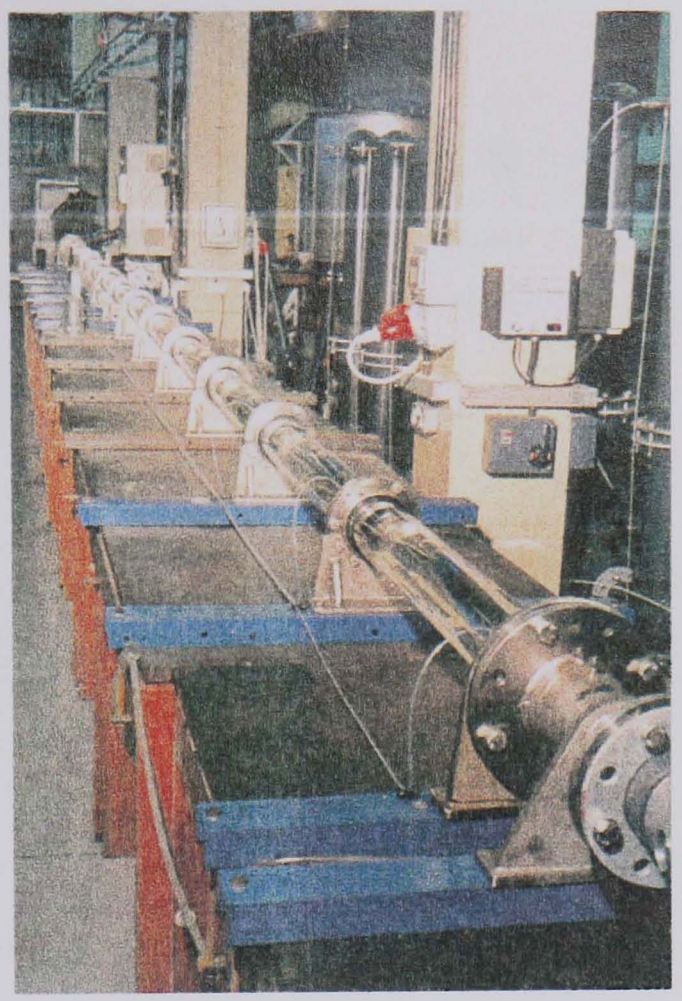

(a)

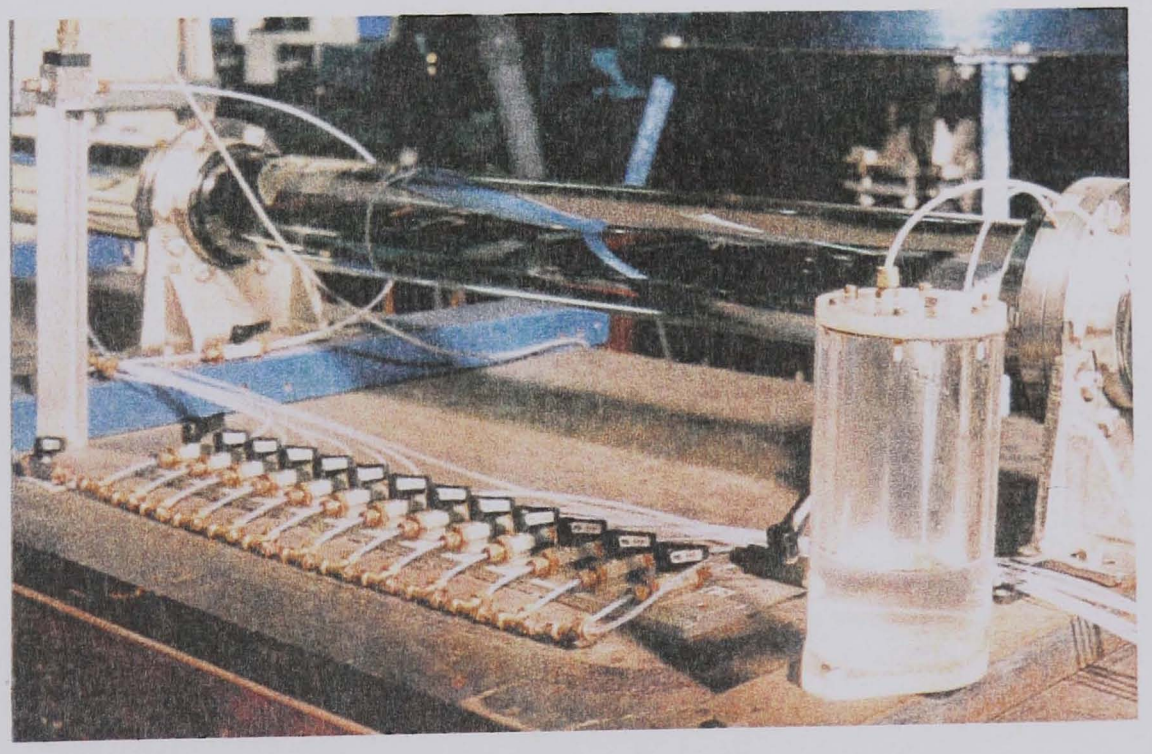

(b)

Figure 3.2 *Photographs illustrating (a) the pipe flow rig and (b) the valves used in determining the pressure drop over sections of pipe.*

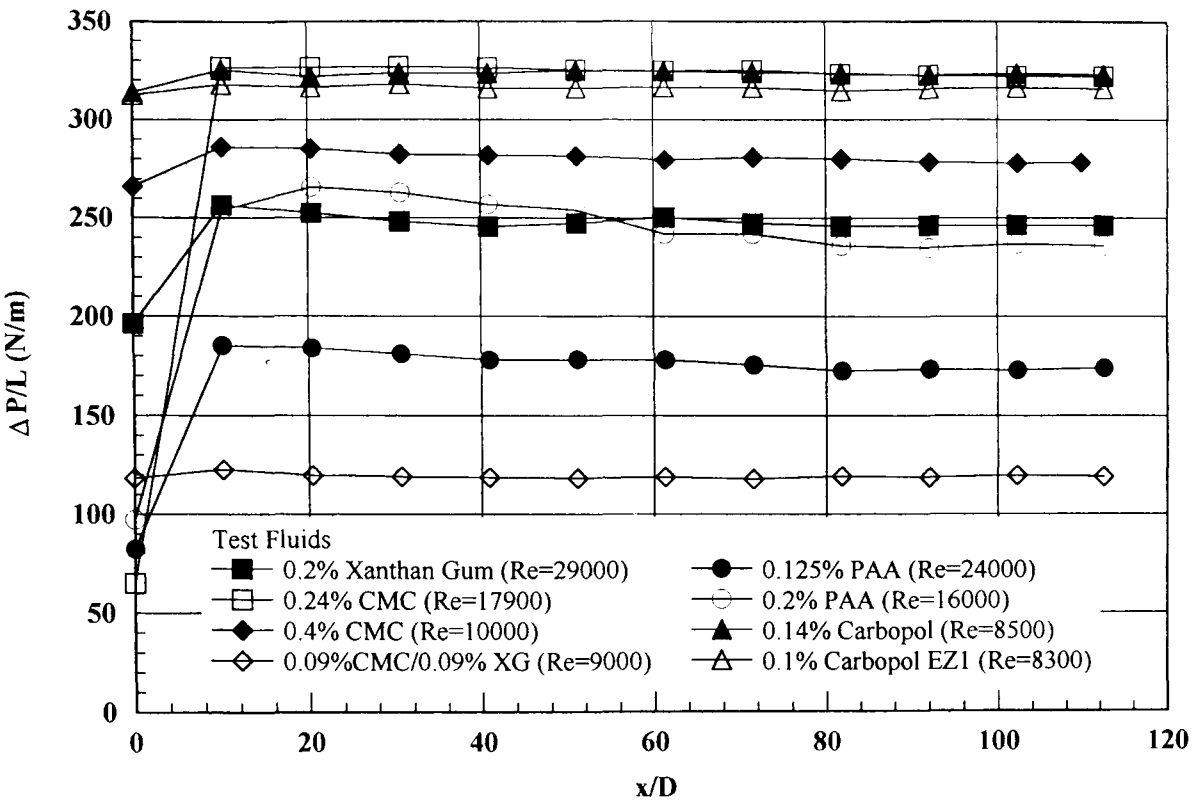

Figure 3.3 *Pressure drop flow characteristics for all test fluids.*

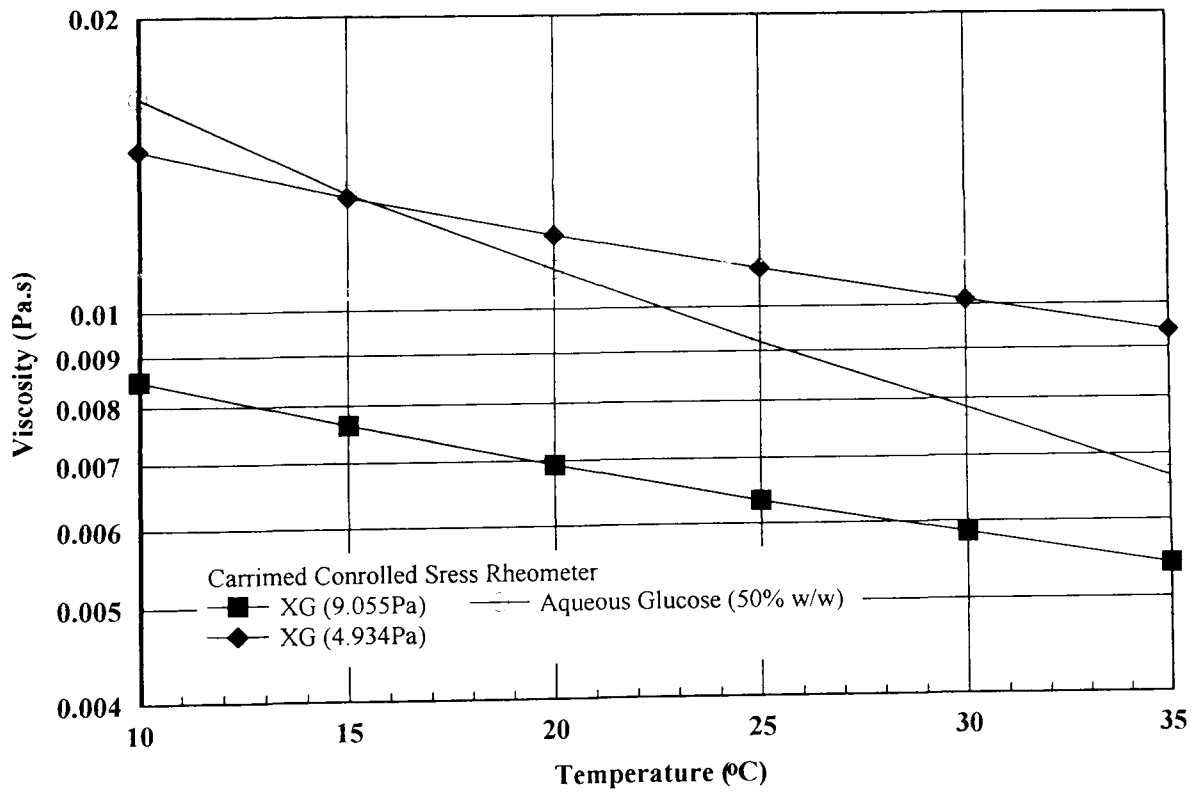

Figure 3.4 *Temperature sensitivity of viscosity for xanthan gum and aqueous glucose.*

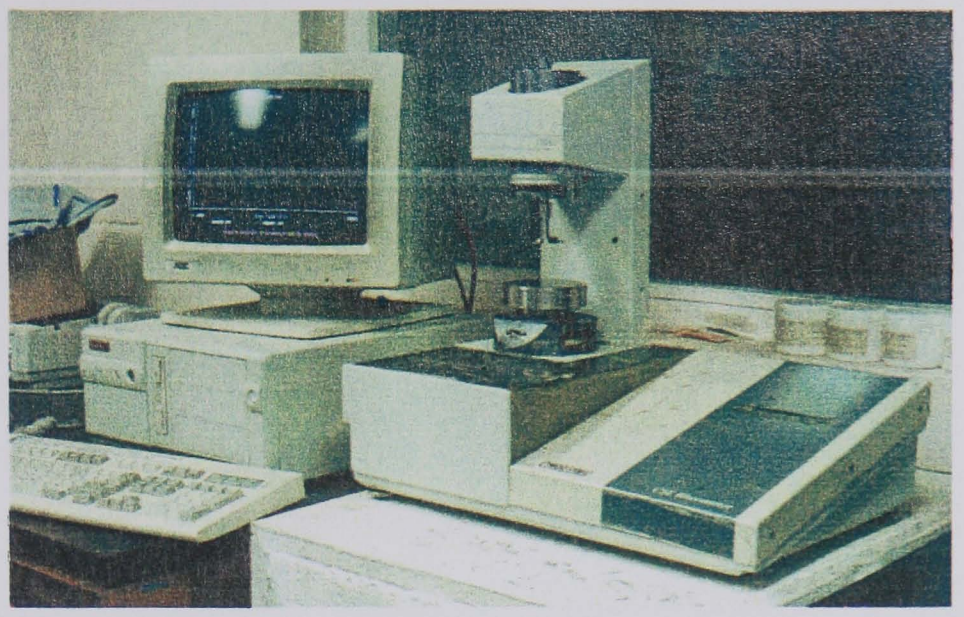

(a)

(b)

Figure 3.5 *Rheometers used in determining rheological characteristics for all fluids: (a) CarriMed Controlled Stress Rheometer and (b) Bohlin VOR Rheometer.*

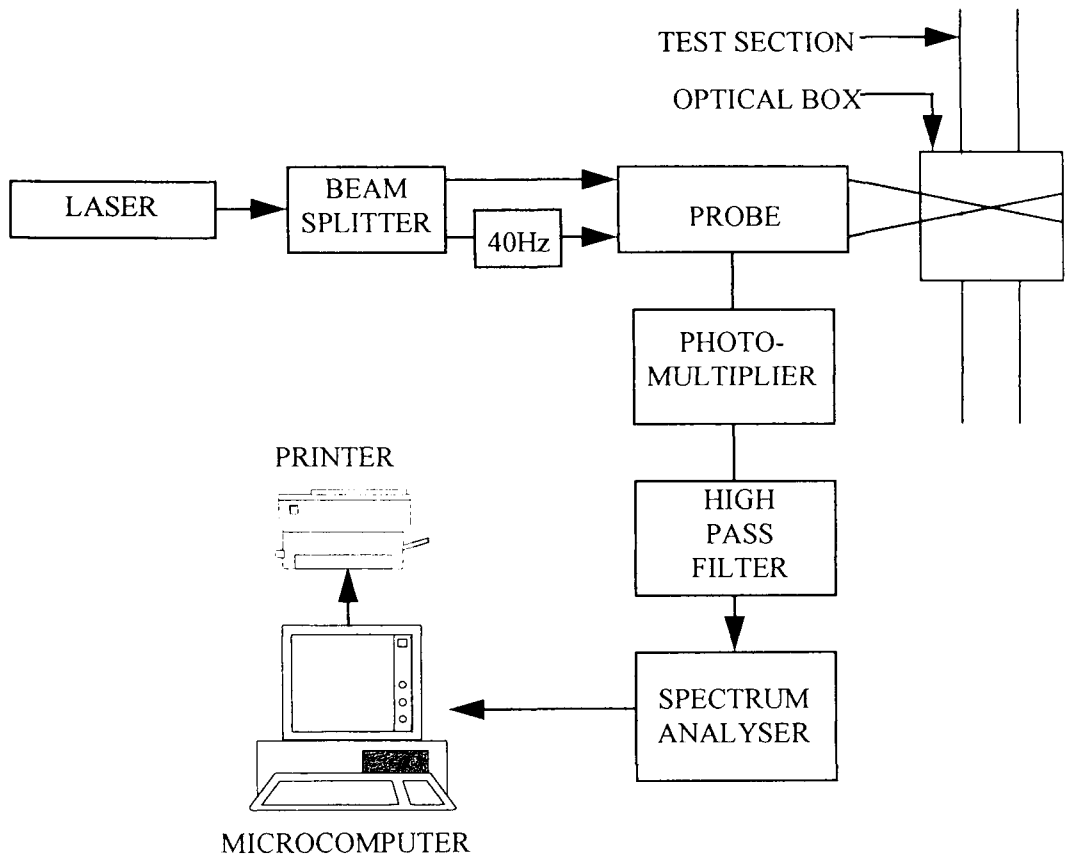

(a)

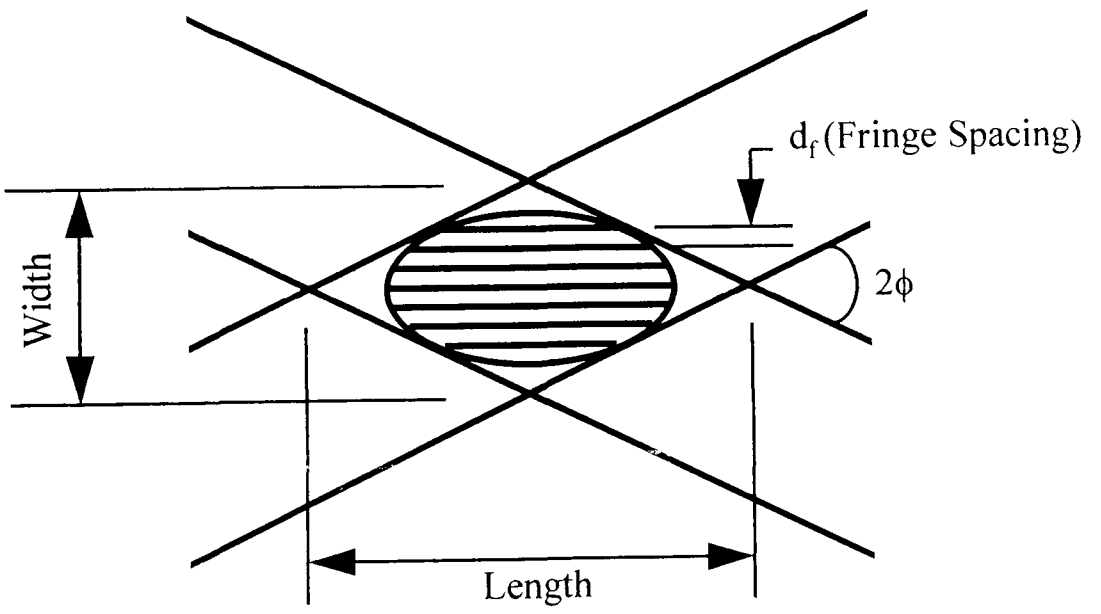

$$\text{Fringe Spacing} \quad d_f = \frac{\lambda}{2 . n . \sin \phi}$$

$$\text{Velocity,} \quad u = f_D . d_f$$

where λ = laser beam wavelength
f_D = Doppler frequency

(b)

Figure 3.6 *Laser Doppler Anemometry: (a) Experimental setup (b) LDA principles.*

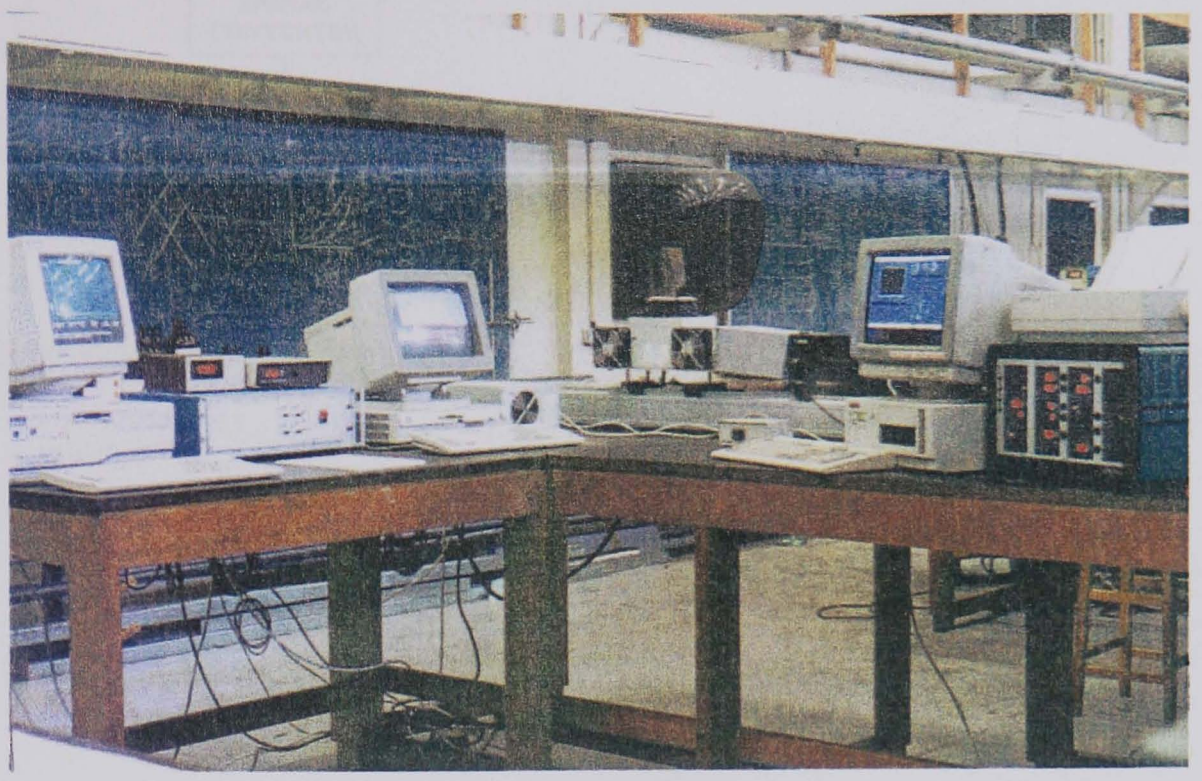

(a)

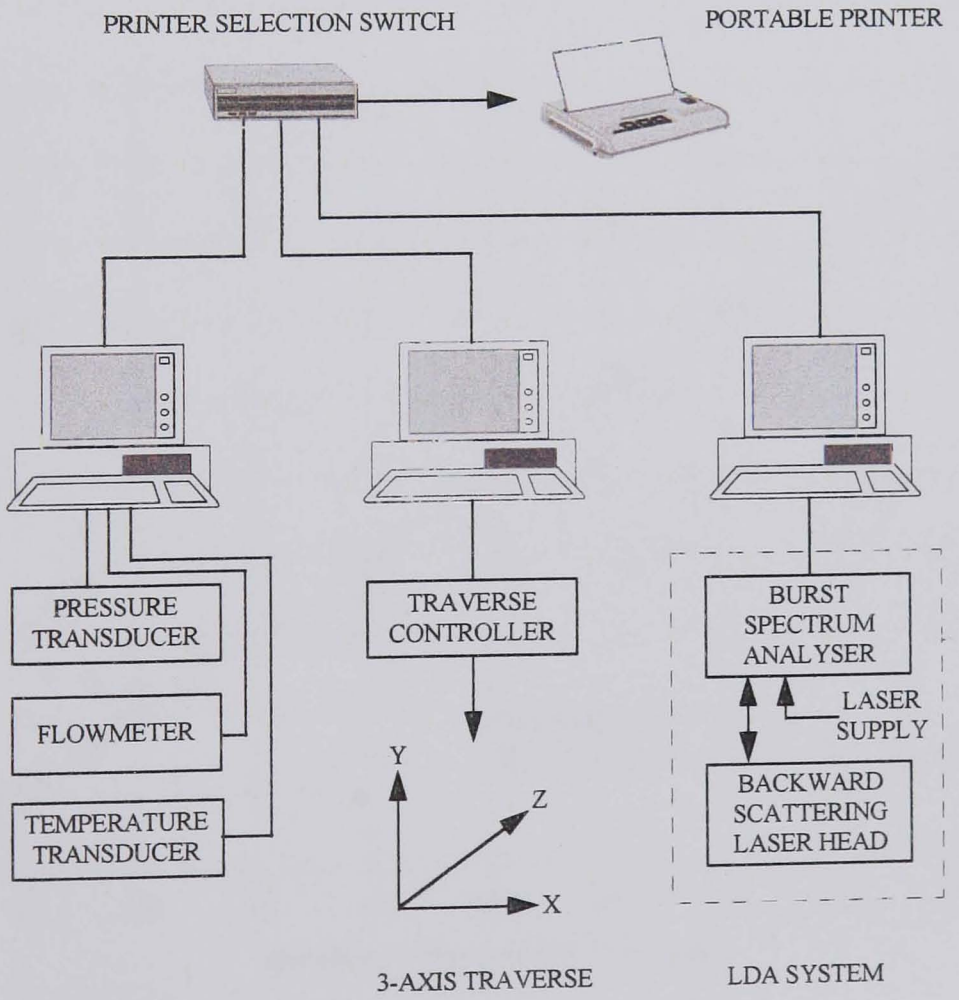

(b)

Figure 3.7 *Experimental System Setup: (a) Photograph of system (b) Schematic of data control and measurement collection system.*

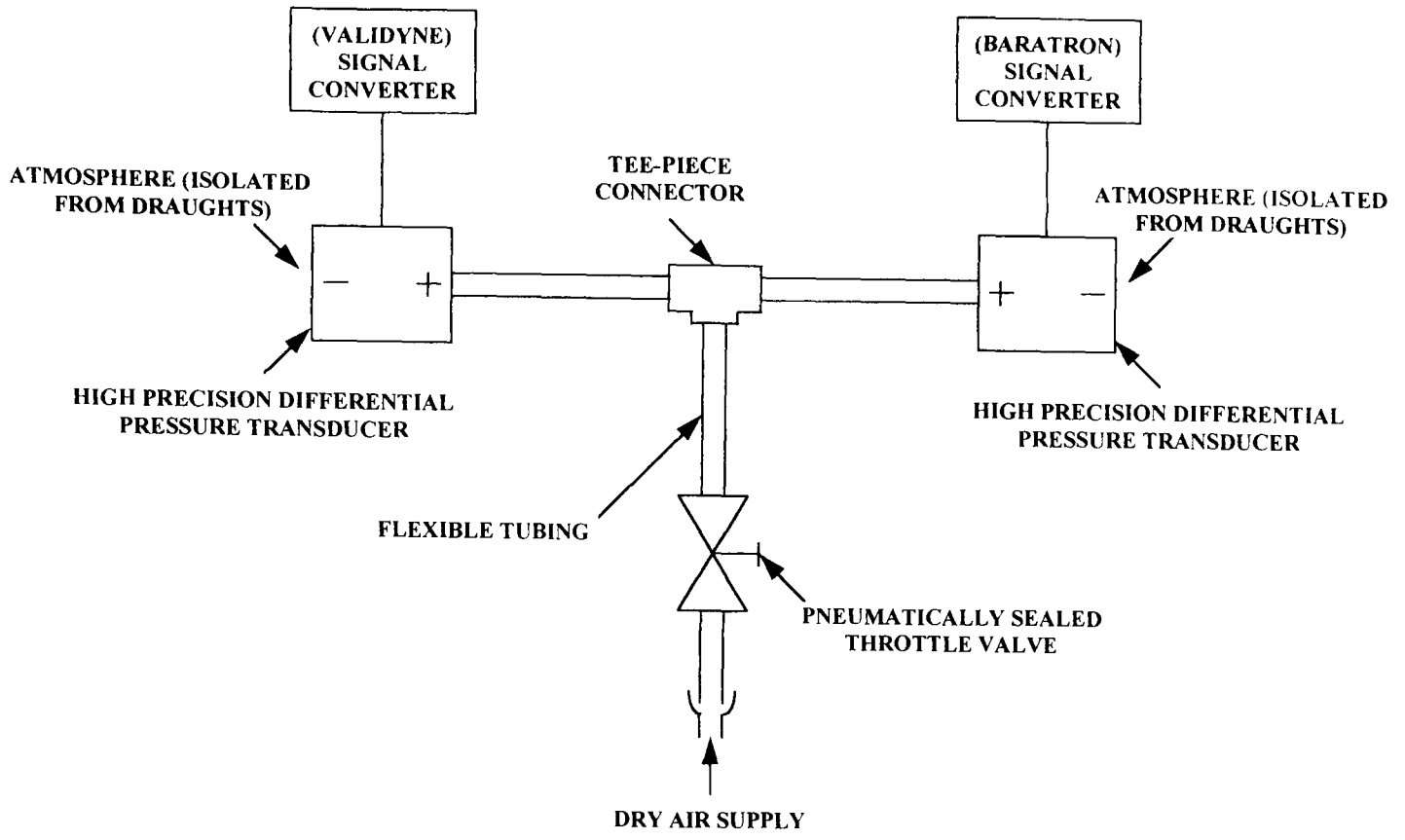

(a)

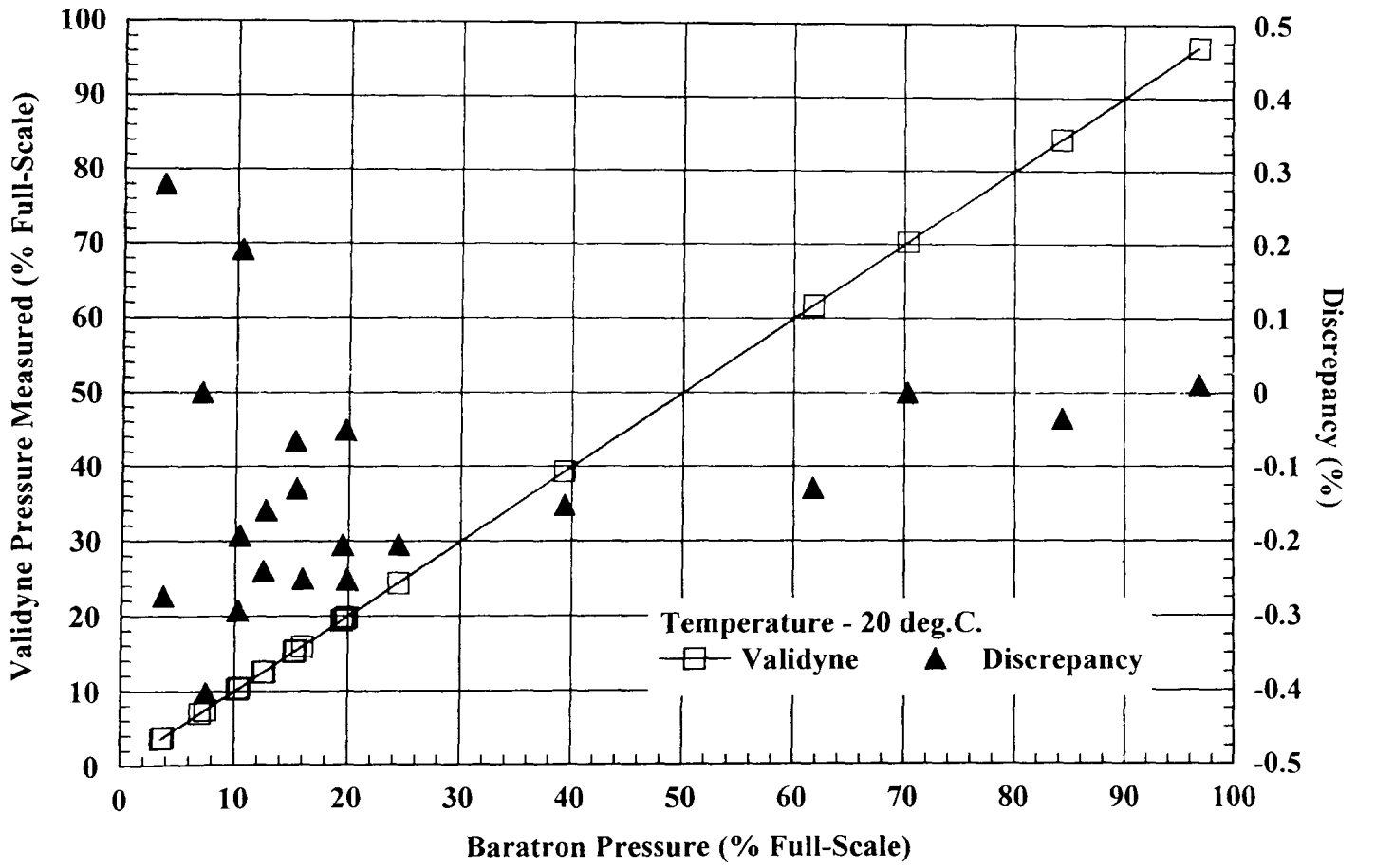

(b)

Figure 3.8 *Calibration of Pressure Transducer. (a) Experimental setup (b) Typical Calibration after 6 months.*

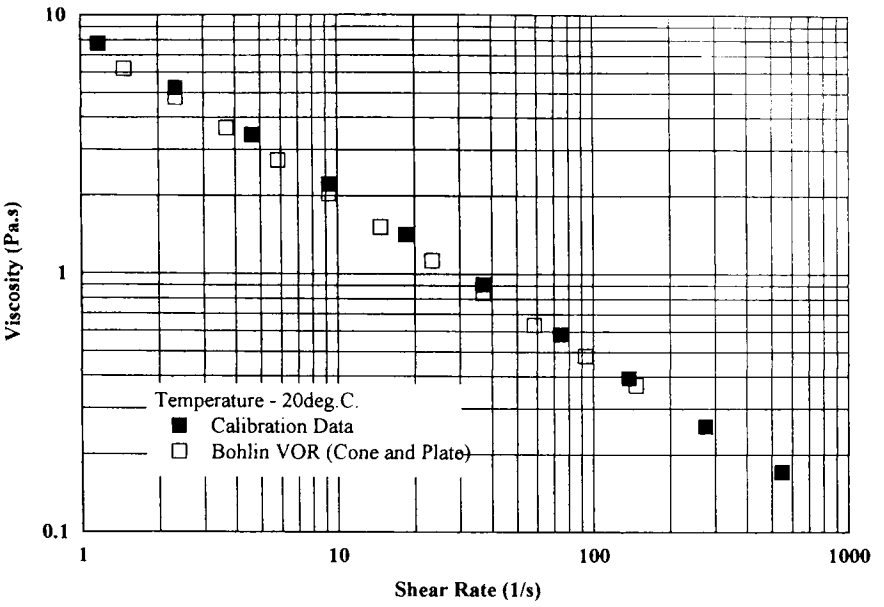

(a)

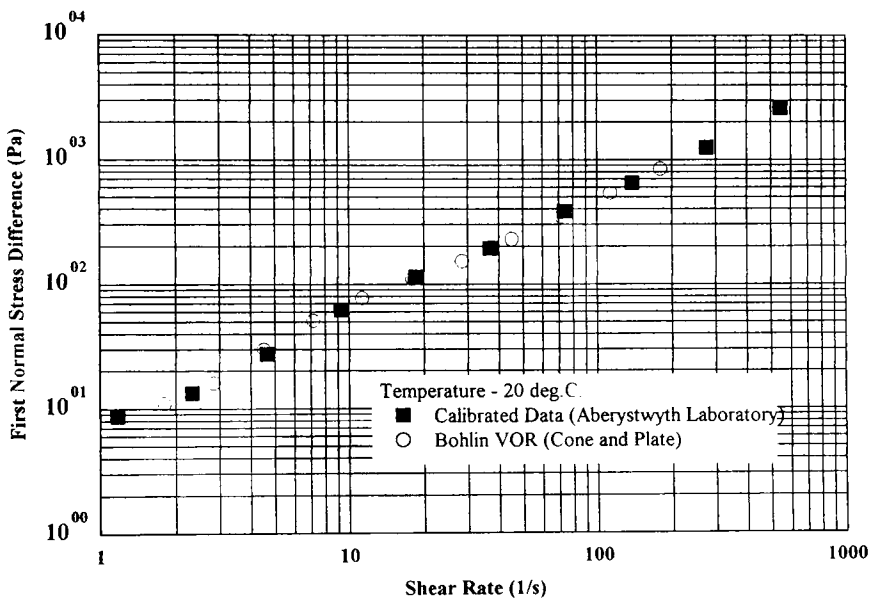

(b)

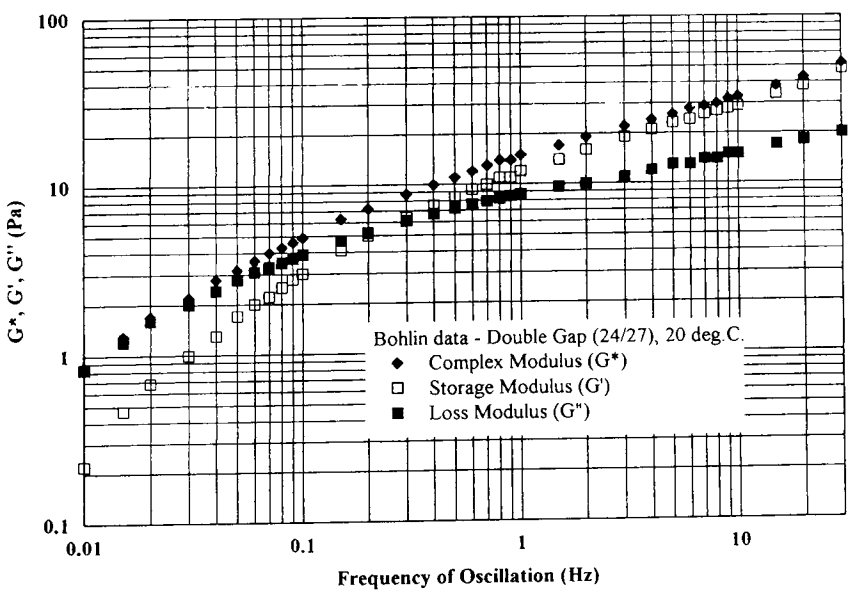

(c)

Figure 3.9 *Rheological Characteristics for Dekalin: (a) Viscosity vs shear rate (b) First normal stress difference vs shear rate and (c) Oscillatory shear flow data.*

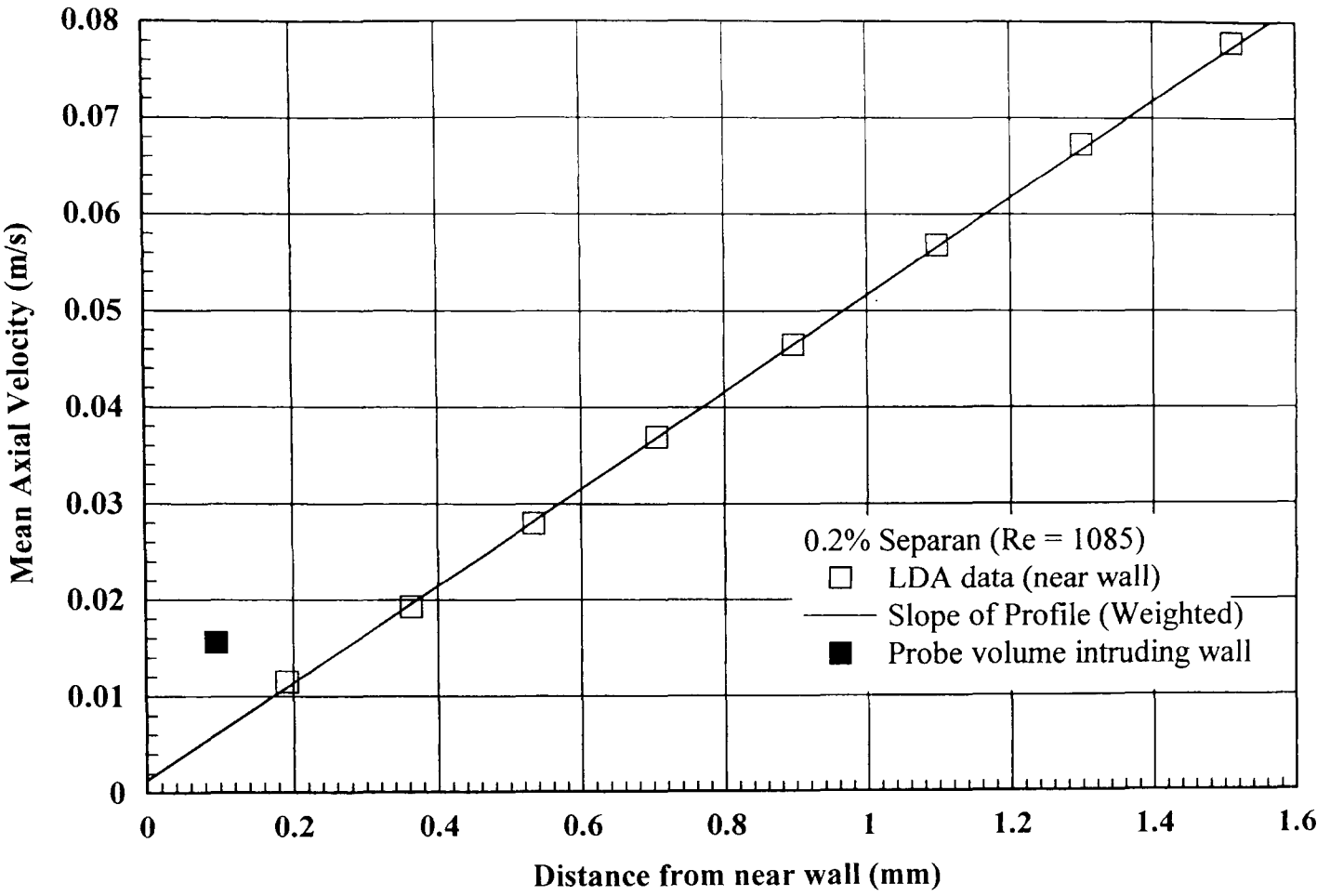

Figure 3.10 *Velocity profile at the near wall of the test-section for 0.2% Separan AP-273.*

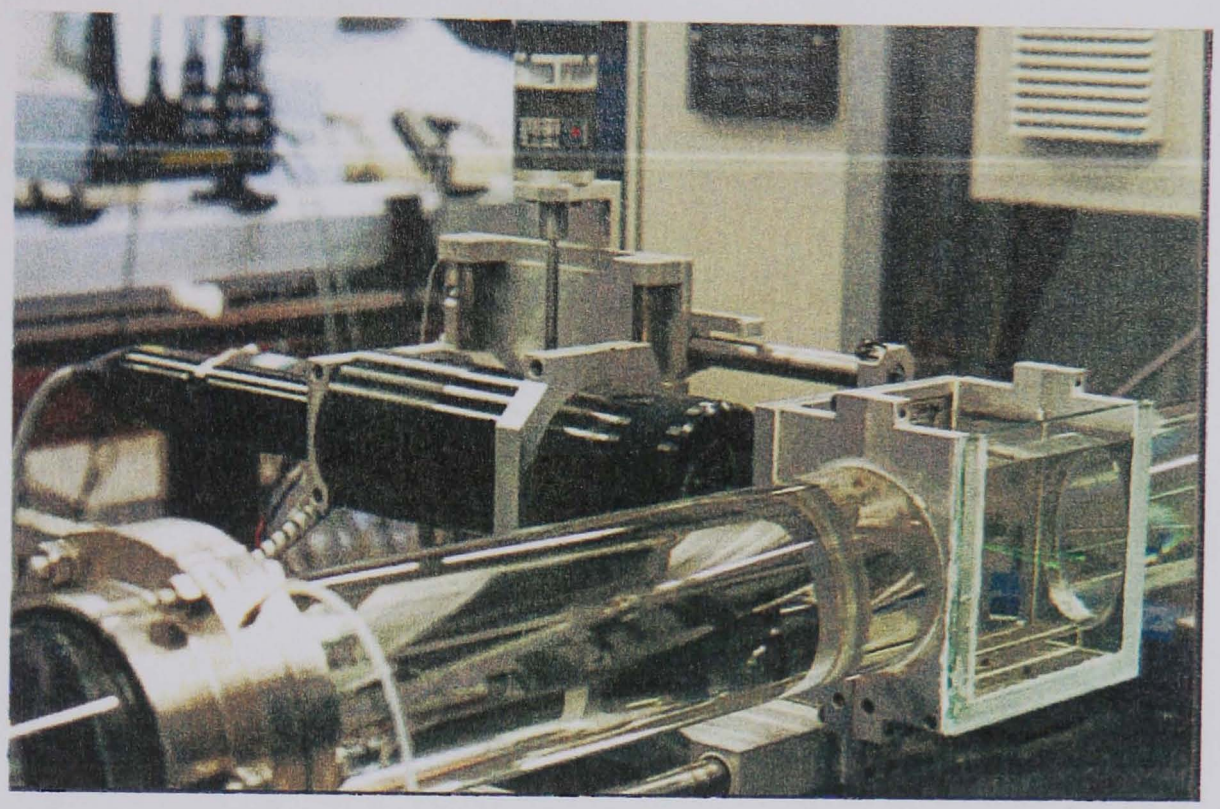

(a)

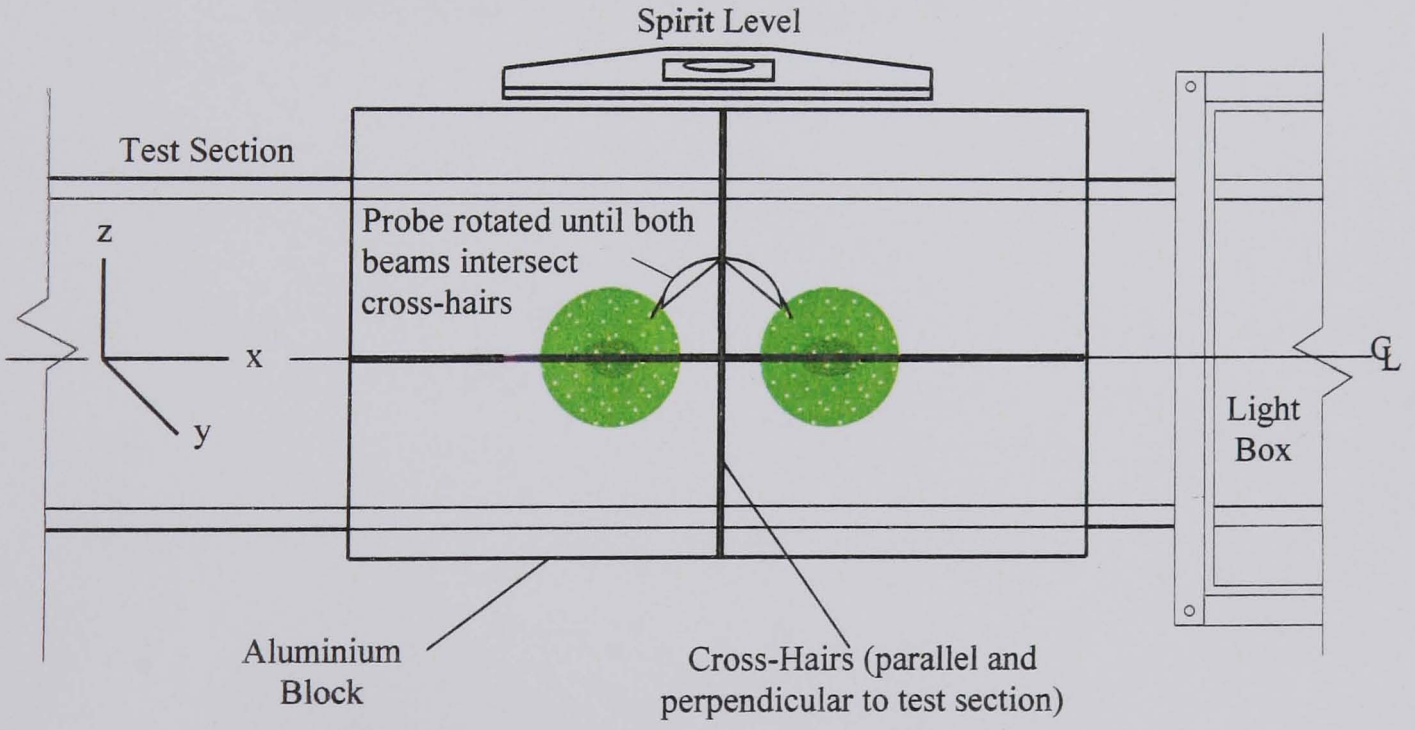

(b)

Figure 3.11 Configuration of LDA Probe: *(a) LDA probe carrying out an axial traverse (b) Alignment of LDA probe.*

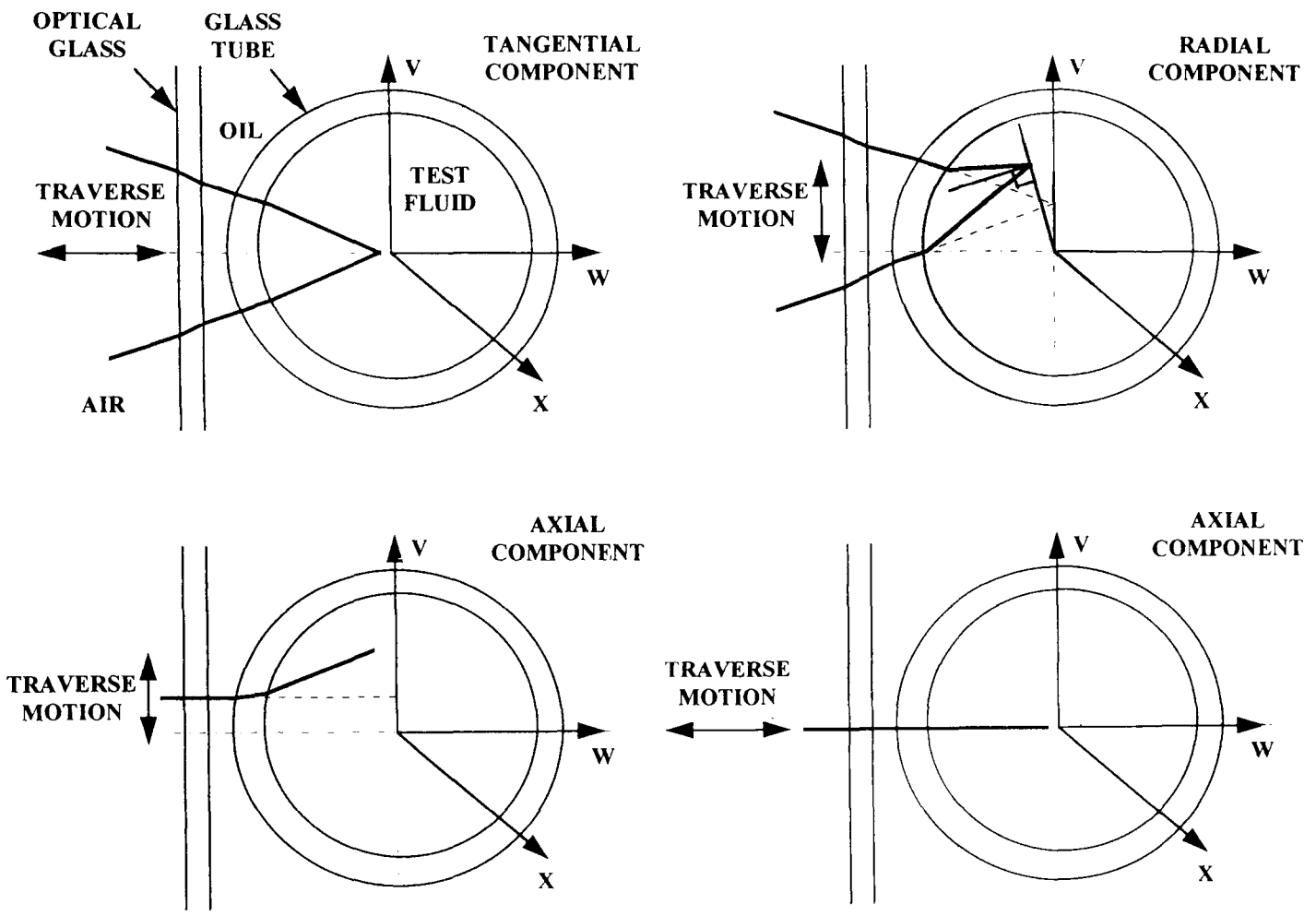

Figure 3.12 *Schematic illustrating the traverse setup required to measure the axial, tangential and radial velocity components.*

4.0 TEST FLUIDS - SELECTION AND RHEOLOGY

This chapter introduces the scientific field of 'Rheology', together with the various fluid characterisation and modelling techniques that fully define the test fluids used in this study. The various terminology and concepts introduced in this chapter must be borne in mind in order to assist in the interpretation of the hydrodynamic and velocity distribution measurements that are discussed in Chapter 5: *Pipe Flow - Results and Discussion.* Details are also given on the selection process for the test fluids investigated based upon criteria primarily determined by the measurement techniques employed. The rheology of these test fluids are discussed in detail and a rheological comparison is made with a typical drilling mud (Wyoming Bentonite).

4.1 Rheology and Definitions

The term 'Rheology' is used to describe the *'.....study of the deformation and flow of matter'*, and was officially introduced by Professor Bingham after its definition was accepted by the newly founded American Society of Rheology in 1929 [Barnes *et al.* (1989)]. The motivation for rheological studies is often the hope that observed behaviour in any fluid-flow process can be correlated with some easily measured rheometrical function. This leads to the concept of rheometry, where fluids are investigated in simple flows like the steady simple shear flow of a fluid between parallel plates [Barnes *et al.*]. Thus quantitative measurements of various flow characteristics can be made to differentiate one fluid behaviour from another by using a rheometer. These techniques are discussed in Section 4.4.2.

In the following sections, the distinction between Newtonian and non-Newtonian fluids will be made in the context of the shear viscosity.

4.1.1 Newtonian Fluids

The equations which describe the flow of any fluid are the equations of conservation, momentum and energy. They cannot be resolved without assuming one or more

constitutive equations which relate the deformation of the fluid (*strain*) to the imposed forces (*stress*). One such equation relates the *shear stress* to the *shear rate*:

$$\tau = \mu \frac{\partial u_x}{\partial y} \equiv \mu \dot{\gamma} \qquad \textbf{(4.1)}$$

This equation [Bird (1965)] represents a Newtonian fluid in laminar flow where the shear stress is proportional to the velocity gradient. The constant of proportionality, μ, is called the Newtonian viscosity and depends only on temperature and pressure and is independent of the rate of shear. The 'flow curve' relating the shear stress with the rate of shear is shown in **Figure 4.1(a)**.

4.1.2 Non-Newtonian Fluids

Non-Newtonian fluids are those for which the flow curve is not linear, i.e. the 'viscosity' of the non-Newtonian fluid is not constant and depends on other factors such as the shear rate, the apparatus in which the fluid is contained or even on the previous history of the fluid. Their rheological behaviour can be classified as viscous or viscoelastic and as time-dependent or not. The relationship between shear rate and shear stress for typical viscous fluids ('shear-thinning' and 'shear-thickening') are shown in **Figures 4.1(b-c)** and time-dependence of viscosity in **Figure 4.2**.

Time dependent fluids ('thixotropic' and 'rheopectic' fluids, see **Figure 4.2**) are more complex in that the relation between the shear rate and the shear stress, for example, depends also on the time the fluid has been sheared or on its previous history.

Viscoeolastic fluids have characteristics of both solids and liquids and exhibit partial elastic recovery after deformation. Viscoelasticity manifest itself in terms of normal stresses, for instance, in flows where they would be zero for Newtonian fluids. Examples of elastic behaviour are normal stresses in steady shear flows and the formation of prolate-shaped gas bubbles rising in an unconfined medium of a viscoelastic fluid.

Yield (or apparent yield) stresses can often be associated with the above fluids and is usually described as the minimum stress required to produce a flow. The term apparent is associated with the idea that a true yield stress does not exist, merely that the strain rate is too small to be measured.

The various combinations of the above properties are typical of many non-Newtonian fluids and since their effects are not evident in every type of flow, their complete characterisation requires the analysis of a set of basic laminar flows as will be discussed in Section 4.4.2. The working fluids adopted for this research encapsulated all the above features in various degrees, with characteristic properties similar to those found in drilling muds. A typical rheological example of a drilling mud is discussed next, in Section 4.2.

4.2 Rheology of a Typical Drilling Mud

As discussed in Section 1.2, a number of chemical additives are added to drilling muds to tailor their performance to specific drilling operating conditions. However, a typical reference fluid is required for a comparison to be made with the test fluids used in this study. Consequently, a viscometric representation of a typical drilling mud under equilibrium conditions - 6% w/w Wyoming Bentonite clay (85% sodium montmorrillonite), a trioctehedral smectite diluted in deionised water [Darley and Gray (1988)] - has been given in **Figure 4.3** for this purpose. The primary clay platelets of the Bentonite interact electrostatically to form a cross-linked 'house of cards' structure, which gives rise to an 'apparent yield stress' and 'thixotropic' behaviour.

Thixotropic cement systems have several important applications. One of the important applications of thixotropic drilling muds is the treatment of lost circulation during drilling. When a thixotropic slurry enters an enlarged area or cross-passage ('thief zone'), the velocity of the leading edge decreases and a gel structure begins to develop. Eventually, the zone becomes plugged because of the increased flow resistance. Once the cements sets, the zone is effectively consolidated. Other uses

include wellbore grouting to prevent gas migration under certain circumstances [Nelson (1990)].

From **Figure 4.3**, the viscosity *versus* shear rate behaviour of the Bentonite mud clearly indicates a shear-thinning characteristic along with other characteristics associated with drilling muds as described by Darley and Gray (1988).

Consequently, the test fluids to be investigated in this study must be systematically selected to represent some of these complex rheological variations. The following sections discusses the selection of the test fluids in more detail.

4.3 Test Fluids - Selection, Description and Preparation

4.3.1 Selection Criteria

Since laser Doppler anemometry was to be the main measurement technique in investigating the flow structure of fully developed pipe flows of non-Newtonian fluids, optical transparency was a basic requirement of any working liquid (actual drilling muds are opaque). As indicated below, two of the five test fluids were slightly turbid, which restricted some test measurements. The oil-based aerosil liquid anticipated as a test fluid was not used since it was found to turn opaque in the presence of minute amounts of water and it was impossible to dry such a large flow facility (capacity ca 800*l*) as that used. In addition to optical transparency, the test fluids must also exhibit well-defined non-Newtonian characteristics at least quantitatively similar to those found in drilling muds.

All test fluids must be relatively resistant to mechanical degradation [see den Toonder *et al.* (1995)]. Mechanical degradation is the breaking up of the polymers by mechanical action, which reduces their molecular weight and hence their effectiveness in reducing drag [Virk *et al.* (1975)]. This is an important point, since this study used a 're-circulatory' experimental set-up in which the polymers were continuously subjected to deformations, especially in the pump, which may cause some scission of polymers. Severe mechanical degradation during a test would lead to unacceptable

changes in flow conditions that would ultimately invalidate the LDA measurements, hence all test fluids must fulfil this criteria. Gadd (1965) also postulated that mechanical action applied to polymer solutions renders the molecules susceptible to oxidation, thus partly explaining one of the causes of degradation. Gadd also found that when solutions of guar gum were exposed to sunlight over a period of three days, considerable levels of degradation took place. Evidently, the sunlight had some action on the guar gum molecules, either a direct photochemical one or by simply promoting bacteriological action. His work was consistent with that of Hoyt and Fabula (1964), who described successfully drag-reducing additives as long molecules of high molecular weight, with few side branches and good solubility.

All test fluids must also exhibit low levels of toxicity, thus permitting easy disposal and safe handling and be of relatively low cost. A further criterion was that all fluids must have a conductivity ≥20μS/cm to be detectable by the electromagnetic flowmeter.

In addition to a Newtonian reference fluid (aqueous mixture of glucose and tap water), the following non-Newtonian liquids (all shear-thinning) were selected:

- Carbopol 934 (0.14%) and Carbopol EZ1 (0.1%) - practically inelastic, slightly turbid.
- Laponite (1.5%) - thixotropic, practically inelastic, very slightly turbid.
- Carboxymethylcellulose (CMC) (0.24%, 0.25%, 0.4%) - slightly elastic, clear.
- Xanthan gum (0.2%) - moderately elastic, slightly turbid.
- Xanthan gum (0.09%)/CMC (0.09%) blend - moderately elastic, very slightly turbid.
- Polyacrylamide (Separan AP273) (0.125%, 0.2%) - highly elastic, clear.

The concentrations indicated refer to the amount of material in water according to weight. The concentrations of the test fluids were limited by the need to obtain detectable non-Newtonian behaviour (by means of current rheometrical techniques available to this study) at viscosities sufficiently low for laminar, transitional and turbulent flow conditions to be achievable at the pump flow rates attainable. The elastic

influences of the test fluids were determined by specific rheometrical techniques as discussed in Section 4.5.

All of the aforementioned test fluids were well-characterised solutions of drag-reducing polymers that have formed the basis of many years of research associated with the phenomenon of turbulent drag-reduction.

4.3.2 Description of Test Fluids

4.3.2 (a) Sodium Carboxymethylcellulose (CMC)

Sodium Carboxymethylcellulose (CMC, supplied by BDH Ltd.) is a semi-synthetic gum produced by the chemical modification of cellulose. It is an anionic polyelectrolyte which forms a colourless, odourless, non-toxic solution in water. Pinho and Whitelaw (1987) have reported moderate resistance to mechanical degradation, with approximately a 10% decrease in viscosity of a 0.4% aqueous solution after prolonged shearing at a high rate. However, Pinho and Whitelaw's CMC polymer (supplied by Hercules) was lower in molecular weight (3×10^5) compared to the CMC (BDH) used in this study (7×10^5). Hence, comparisons between these fluid types should be treated with caution due to the molecular weight influence on rheological behaviour as reported by many previous investigators [see e.g. Fabula (1964)].

4.3.2 (b) Xanthan Gum (XG)

Xanthan gum is a high-molecular-weight natural carbohydrate, or more specifically, a polysaccharide, which appears as a dry, cream-coloured powder in its physical state. The primary structure is based on a linear 1,4β-D-glucose backbone, as in cellulose, with charged trisaccharide side-chains on every second residue [Jeanes *et al.* (1961)]. The secondary (backbone) configuration is influenced by solvent ionic strength and temperature. The backbone changes from being disordered with highly extendible side-chains (due to charge repulsion) in a non-ionic solution at low temperature (<25°C) to an ordered helical configuration with side-chains collapsed onto the

backbone (due to charge screening) as the solvent ionic strength is increased [Pastor *et al.* (1994)]. In the rod-like configuration the molecules are easily aligned and strongly associate to form a gel-like structure [Rochefort and Middleman (1987)]. According to the manufacturer (Kelco), xanthan gum solutions show remarkable resistance to mechanical degradation. The xanthan gum used in this study is better known as Keltrol TF, which is a non-irritant, non-toxic, and most generally used food grade of xanthan gum.

The general characteristics of xanthan gum are illustrated in **Figure 4.4** [cited in Kelco (1991)]. Aqueous solutions of xanthan gum are extremely shear-thinning. Upon release of shear, total viscosity recovery occurs almost instantly due to its helix structure (see **Figure 4.4(d)**). This structure creates a yield stress, which is required to dissociate some of the junction zones and shear thinning results from further dissociation by continuous application; but when the shear stress falls to zero, the junction zones reform to produce a high viscosity fluid.

4.3.2 (c) CMC/XG Blend

An equal quantity of CMC and xanthan gum were blended in solution to investigate whether the resultant flow behaviour in a pipe exhibited combined effects similar or anomalous to the solvent additives when used alone. The chemical interaction of the blend, from a molecular viewpoint, was not known during the course of this investigation.

4.3.2 (d) Separan AP273 (Polyacrylamide, PAA)

The polyacrylamide used in this study is better known as Separan AP273, which is a highly flexible water soluble synthetic polyacrylamide made by Dow Chemical Ltd. (USA), in which about 25% of the amide groups have been hydrolysed and neutralised. Although the exact molecular weight and molecular weight distribution was not known, the mean molecular weight was estimated by the supplier (Floerger) to be approximately 4×10^6. The supplier also stated that an aqueous solution of Separan offered moderate

resistance to mechanical degradation and should not be subjected to high shear rates for a prolonged duration of time.

4.3.2 (e) Carbopol 934 and EZ1 (Polyacrylic Acid)

Carbopol 934 (carboxypolymethylene) is a white powder with a helix coil structure in dry form. When hydrated, the resultant solution thickens as the molecular structure uncoils (straightening effect) due to the slight repulsion of the side branches, thus expanding the molecules whilst hydrogen bonding occurs within the solution. At this stage the pH balance is acidic (pH<4). The basic working fluid was prepared in a similar manner as that described in Section 4.3.3, by slowly adding Carbopol powder to cold (ca 15°C) filtered tap-water being circulated through the mixing loop of the flow facility. However, when neutralised (pH→7) using laboratory grade 2N sodium hydroxide (BDH Ltd., U.K.), cross-linking occurs between the large molecular chains (though not at all atomic points), thus producing a well-structured solution exhibiting non-Newtonian characteristics. The average molecular weight distribution for Carbopol (934 and EZ1) was $<1\times10^6$ (as stated by the supplier, Sursachem Ltd., U.K.).

Despite the apparent simplicity in its preparation, difficulties were encountered in keeping the solution stable. It was found that the calcium salts within tap water were attacking the gel structure, resulting in a sudden decrease in viscosity over a 2 day period. To overcome this, di-Sodium EDTA was used as a chelate agent, which assisted the prevention of the calcium atoms attacking the structure. Problems were also encountered with the transparency of the resultant solution, which was slightly turbid and therefore limited LDA measurements at the far wall of the pipe. Carbopol EZ1 was identical to Carbopol 934 (according to the supplier), though offered greater resistance to calcium salts and was generally simpler to hydrate. However, the slightly turbid appearance in both solutions was never overcome and was presumably caused by an incomplete hydration of the solution within the flow loop [Sursachem Ltd. (1995)]. The pipeflow loop was limited to turbulent mixing at high pump speeds, which may not have caused the solvent additive to completely hydrate within the

solution. However, a degree of stability in solution viscosity was achieved as discussed in Section 4.5.2.

4.3.2 (f) Laponite RD

Laponite is the trade name for a synthetic hectorite clay with a structure similar to that of sodium montmorillonite, a principal constituent in Wyoming Bentonite. When Laponite is dispersed in water, the exchangeable sodium ions hydrate, causing the clay to swell initially and to separate completely. The resulting effect provides a clear colloidal dispersion (a sol) of anionic Laponite platelets and hydrated sodium ions in solution. The platelets carry a surface negative charge (due to lattice substitution) and a small positive charge on the edge due to the disruption of the lattice. In dilute solutions the surface negative charges are much larger than the small edge charges and repulsion occurs between the platelets so that no thickening occurs. As the ionic content of the water increases (either due to the addition of salt or to increasing Laponite level) the surface negative charge is reduced due to increasing association between this charge and the cations in solution. Repulsion between platelets, the primary Laponite clay particle, is reduced and the dominant force becomes the surface to edge attraction causing the dispersion to gel. The particle/particle bonds break down under the application of a shear stress giving rise to a highly thixotropic behaviour. In consequence, the rheology of Laponite suspensions is influenced greatly by solvent ionic strength and shear history.

The basic working fluid was prepared in a similar manner as that described in Section 4.3.3, by slowly adding Laponite powder to filtered tap-water being circulated through the mixing loop of the flow facility. However, in order to increase the yield stress of the fluid to simulate the gel like behaviour inherent of many drilling muds, 60 ppm laboratory grade salt (Fisons S/3120/60) was added to produce a conductivity of about 0.74 mS/cm. This resulted in an immediate increase in viscosity at low shear rates.

4.3.3 Preparation of Test Fluids

Two types of fluid preparation were used in this study. Firstly, solutions that were used in pipe flow experiments were prepared within the pipe flow rig (700*l*). Secondly, 5*l* sample solutions, which were used in determining normal stresses at high concentration levels (0.6% - 1.5% w/w), were prepared in large beakers using a three blade paddle stirrer. All solutions were prepared with care to avoid shear degradation at high shear rates.

The 700*l* test fluids were prepared by filtering tap water within the flow loop prior to the direct dissolution of the solvent additives, which were in powder form. For each solution, weighed amounts of the additives were then sprinkled on the water surface in the tank whilst low speed agitation within the mixing-loop was used to disperse the powder. From preliminary experience, there was a tendency for the powder to coagulate into large lumps when dispersed quickly, which were then difficult to dissolve so great care was taken in order to avoid agglomeration. Timiron seeds (used as LDA tracer particles) were also added (1ppm) to improve LDA data rates and signal quality for all test fluids used.

In the case of the 5*l* sample solutions, good dissolution was ensured by means of a three blade paddle stirrer, which created a large vortex with only moderate shear. Also, for each material, a master aqueous solution was prepared and lower concentrations were obtained by successive dilution.

Formaldehyde (bactericide), at concentration 0.015 % vol., was used as a preservative in all solutions, and twice that amount for the aqueous glucose solution. Finally, when the additives appeared to be completely dissolved, the solutions were left to equilibrate for two days. This was necessary in order to allow time for the solutions to fully homogenise, with low speed agitation being used from time to time to assist this process and to allow small air bubbles to escape. It is important to note that the addition of seed particles and bactericide did not appear to influence the rheology of the test fluids, which were confirmed by a series of rheological tests (see Section 4.4.2) before and after their

addition. Any differences between the rheological data were within the repeatability of the measurement system.

4.4 Fluid Modelling and Characterisation Techniques

4.4.1 Fluid Modelling

A principal aim of this work is to correlate measurable rheometrical functions of the test fluids with the data analysed from the hydrodynamic flow experiments. In order to do this, the fluids need to be accurately represented by constitutive equations. For this study, equations associated with generalised Newtonian fluids (time-independent and inelastic fluids - the theoretical limit of weakly elastic fluids) were used. These equations only need to model the viscosity as a function of shear rate.

Normally, the viscosity of a shear-thinning fluid varies with shear rate in the following manner. At low and high shear rates, the viscosity is normally constant and these regions are denoted as the first and second Newtonian plateau respectively, as their behaviour is not dissimilar to that of a Newtonian fluid (see insert within **Figure 4.5**). However, there is an intermediate range over which the viscosity decreases with shear rate and this region is often described by a power-law equation:

$$\eta = k\dot{\gamma}^{n-1} \tag{4.2}$$

where n is the power-law index and k is the consistency index (units of $Pa.s^n$). The power-law is extensively used in theoretical analyses, though is generally limited to two or three decades of shear rate and fails at extremely low or high shear rates since n ultimately approaches unity i.e. the first and second Newtonian plateau. However, a least-squares fit of the Cross model was well suited to represent the fluids used in this study over the entire shear rate range:

$$\frac{\eta - \eta_\infty}{\eta_0 - \eta_\infty} = \frac{1}{1 + (\lambda_c \dot{\gamma})^m} \tag{4.3}$$

where η_o and η_∞ refer to the asymptotic values of viscosity at very low and very high shear rates respectively, λ_c is a constant parameter with the dimensions of time and m is a dimensionless constant. The Cross model is one of numerous constitutive equations, which are associated with generalised Newtonian fluids. Allen (1995) published an excellent review of other widely used viscosity equations, examples of which are shown in **Table 4.1**.

These laws must be seen as being empirical in nature and arising from curve fitting exercises, and are particularly helpful in making practical engineering flow calculations. The curve fits were conducted using the least squares fit method.

4.4.2 Fluid Characterisation Techniques

Due to the complex combination of various properties associated with non-Newtonian fluids, their effects are not always evident in every type of flow and hence their complete characterisation requires the analysis of a set of basic rheometrical tests. The rheometrical tests used in this study are discussed below.

4.4.2 (a) Viscometric Measurements

The viscometric characteristics (viscosity *versus* shear rate or shear stress) were determined using both the CarriMed controlled-stress rheometer (CSL 100) with either a cone-and-plate or a parallel-plate geometry, and also a Bohlin VOR controlled shear-rate rheometer with similar geometries. The viscometric measurements covered the shear rate range and temperature variations obtained during each pipe flow test

Using the Bohlin VOR rheometer, it was possible to accurately determine viscosities at very low shear rates (tending towards the zero-shear viscosity for some fluids) using a double-gap geometry, which was not available for the CarriMed. Despite the relatively complex set-up required in using the Bohlin VOR as opposed to the CarriMed, a high level of repeatability was achieved. The CarriMed instrument was not sensitive enough to measure these viscosities at low shear rates, which can be seen

illustrated by the number of scattered data shown in **Figure 4.5**. However, it is evident that consistency in viscosity data was obtained between the rheometers, using a combination of geometries, when operating above the low end of their dynamic range (>1 s^{-1}). The deviation in results for the measurements taken with the CarriMed is due to the onset of secondary flows within the geometry. Secondary flows occur at different values of shear rate depending on the geometry used ($\dot{\gamma}$ >400 s^{-1} for cone and plate, $\dot{\gamma}$ >1000s^{-1} for parallel plate) [Barnes *et al.* (1989)].

4.4.2 (b) First Normal Stress Difference

The determination of first normal stress difference, N_1, was obtained from a load cell (150g cm) incorporated into the Bohlin VOR rheometer. N_1 is a non-linear characteristic that is associated with the effects of viscoelasticity [Barnes *et al.* (1989)]. Unfortunately, for the concentrations used for the flow experiments, with the exception of Separan AP273, the first normal stress differences were below the sensitivity of the instrument even at the highest shear rates. Since it is generally accepted that drag reduction in turbulent flow of non-Newtonian fluids is related to viscoelasticity, it was regarded as essential to estimate N_1 for all polymeric fluids tested. However, as suggested by Barnes *et al.*, at higher concentrations it was found that $N_1(\tau)$ followed a power-law master curve for most polymer fluids, from which it was possible to extrapolate to lower concentrations. In the case of CMC and xanthan gum, the extrapolation was relatively straightforward since the dependence of N_1/τ on $\dot{\gamma}$ was found to be practically independent of concentration. For the polyacrylamide (Separan AP273) solutions there was a clear dependence on concentration and the extrapolation was less satisfactory; these results are discussed in Section 4.5.3.

The possibility of quantifying N_1, by relating a measurable linear elastic function from oscillatory flow measurements (e.g. the storage modulus, G′, as discussed in the next section) with a non-linear steady shear flow elastic function (N_1) at low concentrations, would clearly be useful here. From continuum mechanics, it can be shown that a relationhip between G′ when $(\omega)\rightarrow 0$, and N_1 when $(\dot{\gamma})\rightarrow 0$, does indeed

exist and can be empirically represented as [Barnes *et al.* (1989)]:

$$\frac{G'}{\omega^2\big|_{\omega\to 0}} = \frac{N_1}{2\dot{\gamma}^2\big|_{\dot{\gamma}\to 0}} \tag{4.4}$$

However, for moderate to high shear rates (as those encountered within turbulent pipeflow), the above relationship does not hold and no other relationship has been reported to date. Therefore, the extrapolation procedure, though not ideal, has to suffice in the absence of either a direct measurement or a more sophisticated extrapolation algorithm.

4.4.2 (c) Oscillatory Shear Flow Measurements

Oscillatory shear flow provides an assessment of the elastic characteristics of fluids in which the loss (G′′) and storage moduli (G′) are measured. These two moduli depend on the viscous and elastic behaviour, respectively, as a function of oscillation frequency (see **Appendix 3** for further explanation). Both the CarriMed and Bohlin rheometers were capable of carrying out oscillatory flow measurements with a high level of consistency between the measurements (<5% difference). These tests were, however, limited to amplitudes of strain (typically 0.0015) that are characteristic of the linear viscoelastic region (Hookean region). Small amplitudes of strain are therefore necessary to prevent the disruption of molecular entanglements within viscoelastic fluids [Barnes *at al.* (1989)]. However, these conditions are not representative of transitional and turbulent pipeflow of non-Newtonian fluids, hence direct comparisons cannot be made with the experimental flow data discussed in Chapter 5. In any case, the loss and storage moduli will be used for comparison purposes and to 'rank' the test fluids, in order of elasticity, as will be discussed in Section 4.6.

4.5 Results and Discussion

4.5.1 Viscometric Measurements

This section details the viscosity *versus* shear rate behaviour of all test fluids. The values for the four parameters used in the Cross model fit (see **Eq. (4.3)**) are given in **Table 4.2**.

4.5.1 (a) XG

The viscosity *versus* shear rate behaviour of xanthan gum is given in **Figure 4.6**. The corresponding Cross model fit is also shown. The rheological example shown here exhibits an almost power-law structure over three decades of shear (10-1000 s^{-1}), except at high shear rates (>1000 s^{-1}) where the flow curve tends towards its infinite value of viscosity, η_∞. There is no evidence of the viscosity tending towards a Newtonian plateau ($\eta \rightarrow \eta_0$) within the lower shear-rate range of the measurements taken, indicating that XG exhibits an apparent yield stress characteristic. However, this observation is based on the shear rate range shown illustrated in **Figure 4.6**, where measurements of viscosity at lower shear rates may have indeed provided evidence of a first Newtonian plateau. The range of shear rates covered are, however, sufficient to interpret the conditions encountered within the flow experiments as discussed in Chapter 5 and therefore justified.

4.5.1 (b) CMC

The viscosity characteristics for various concentrations of CMC (0.24%, 0.25% and 0.4%) are illustrated in **Figure 4.7**. The extent of shear-thinning for all CMC solutions was less than for 0.2% XG. A tendency towards a Newtonian plateau ($\eta \rightarrow \eta_0$) at low shear rates (<10 s^{-1}) is evident for all three CMC solutions. The value of η_0 increases with concentration as indicated by the values shown in **Table 4.2**. However, there is no evidence of a second Newtonian plateau ($\eta \rightarrow \eta_\infty$) for any of the solutions. Viscosity measurements were limited within the low dynamic range of the CarriMed rheometer, as

shown by the number of scattered data for 0.4% CMC at $\dot{\gamma}$ <3 s^{-1}. The double gap geometry on the Bohlin VOR would have provided improved data within this range due to its greater instrument and geometry sensitivity, but the instrument was not available during the course of this study for CMC (and XG).

The viscosities of the solutions were also a function of concentration, whereby an increase in the concentration of the additive led to an increase in shear viscosity. However, for $\dot{\gamma}$ >85 s^{-1}, the viscosity of 0.25% CMC was lower than that for 0.24% CMC, for which there is no qualitative explanation. As these fluids were prepared from different batches and at significantly different times within the research programme (12 months apart), conditions in rheology, preparation and the cleanliness of the flow loop may have altered slightly. These parameters are difficult to monitor and may therefore result in differing flow curve characteristics as illustrated here for 0.24% and 0.25% CMC.

From **Figure 4.7**, it is also evident that the onset of non-Newtonian behaviour is a function of concentration and is shifted to lower shear rates as the CMC concentration increases.

4.5.1 (c) XG/CMC

The viscosity *versus* shear rate behaviour for 0.09% CMC/0.09% XG is illustrated in **Figure 4.8**. This solution displays a shear-thinning characteristic that is intermediate between the CMC and XG solutions discussed above. The flow curve for 0.09% CMC/0.09% XG is interesting in that it displays a tendency towards both the first and second Newtonian plateau over a similar range of shear rates to those used above, a feature that was only present in either one or other solution.

4.5.1 (d) Separan AP273 (PAA)

The flow curves for 0.125% and 0.2% Separan AP273 are illustrated in **Figure 4.9**. Both concentrations display similar degrees of shear-thinning in the power-law region,

with the onset of non-Newtonian behaviour similar to that of CMC i.e. shifting to lower shear rates for the larger concentration fluid. The constant zero-shear value η_0 also increases with concentration and both flow curves display a convergence towards the infinite shear viscosity η_∞. The viscosity characteristics for 0.125% PAA is very similar to that of 0.09% CMC/0.09% XG (see **Figure 4.8**), whilst 0.2% PAA displays the same level of shear-thinning as 0.2% XG, though with a slightly larger viscosity (5-10%) over the entire shear rate range. These comparisons are important when comparing their corresponding flow behaviour in a pipe, which therefore allows the relative importance of fluid rheology to be investigated.

4.5.1 (e) Carbopol (934 and EZ1)

The viscosity behaviour of both 0.14% Carbopol 934 and 0.1% Carbopol EZ1 are illustrated in **Figure 4.10**. Carbopol 934 yielded larger values of viscosity than EZ1 for $\dot{\gamma} > 5\ s^{-1}$, based on comparatively fresh samples of each solution (less than 3 days old from initial preparation). However, as will be discussed in Section 4.5.2, both fluids were unstable (with Carbopol 934 displaying the larger level of instability), which resulted in significant reductions in viscosity over a period of 7 days. This manifested itself for each solution as a turbid appearance, which was greater for Carbopol 934 than EZ1, thus limiting LDA measurements at the far wall of the test pipe.

The fresh sample solutions differ in that 0.14% Carbopol 934 displays a slight convergence towards the first and second Newtonian plateau for low and high shear rates ($<10\ s^{-1}$ and $>1000\ s^{-1}$ respectively) as where 0.1% Carbopol EZ1 displays a power-law characteristic over the entire range of shear rates ($0.2<\dot{\gamma}<1000\ s^{-1}$), similar to that of XG and Separan. The unavailability of the Bohlin VOR rheometer during the investigation of 0.1385% Carbopol 934 meant that the determination of viscosity at low shear rates were not possible using the CarriMed rheometer alone. However, degradation effects caused noticeable reductions in viscosity for both solutions (see Section 4.5.2), particularly at low shear rates, resulting in a convergence of viscosity towards the first Newtonian plateau η_0 for 0.1% Carbopol EZ1 (see **Figure 4.11**).

Both solutions were however shear-thinning (similar levels to 0.24% CMC) and the undetectable levels of degradation in solution viscosity during a flow experiment (typically <1½ hours in duration), meant that their selection and analysis was justified for this study.

4.5.1 (f) Laponite RD

The viscosity *versus* shear rate behaviour for Laponite is shown in **Figure 4.12**. The data corresponds to a curve fit, which as exemplified below, was not a matter of routine.

Measurements of the viscometric properties were repeated at daily intervals over a period of about one week until their rate of change was negligible over the time required to carry out a single flow experiment. **Figure 4.13** shows the variation of shear stress *versus* shear rate from data obtained using both the CarriMed controlled stress (□ 50 mm ϕ parallel plate) and the Bohlin controlled strain rate (▼ 25 mm ϕ high shear bob and cup, ◆ 5° cone/30 mm ϕ plate, ▲ 24 mm ϕ/27 mm ϕ double gap) rheometers. The fitted curve corresponds to a Herschel-Bulkley fluid (see **Figure 4.1(e)** and **Table 4.1**), represented by:

$$\tau = \tau_y + K\dot{\gamma}^n \qquad \textbf{(4.5)}$$

where, for the Laponite used here, $\tau_Y = 4.4$ Pa, $K = 0.24$ Pa.s^n and $n = 0.535$. These data correspond to equilibrium conditions whereby the fluid was sheared at a given shear stress until the shear rate remained essentially unchanged (ca 30 minutes for each point) and are consistent for shear rates above 30 s^{-1} but become increasingly scattered for shear stresses close to the yield stress. The data presented in **Figure 4.13** will be further discussed in more detail in Chapter 6.

In addition to the anticipated difficulties of working with a shear-thinning thixotropic liquid, a further complication was associated with the tendency (confirmed by the manufacturer) for the viscosity of Laponite to gradually increase with time. This was particularly noticeable at low shear rates where a 30% increase in viscosity occurred over a period of 7 days. This noticeable characteristic is also experienced in wellbore

drilling operations when using thixotropic slurries, where after each static-dynamic cycle, the gel strength and yield point tend to increase [Nelson (1990)]. The increased yield point could pose problems because, after repeated stops, excessive pump pressures may be required to restart movement. Also included in **Figure 4.13** are data deduced from measured velocity profiles (●, ■, ○), which will be further discussed in Chapter 6. The thixotropic nature of Laponite is evident from **Figure 4.14**, which shows the reduction in shear rate when the shear stress was reduced to 12 Pa after pre-shearing at 19 Pa for 15 minutes at 20°C. The two levels of shear stress correspond, respectively, to a typical wall shear stress for the pipe flow and the corresponding equilibrium stress for an asymptotic shear rate of 560 s^{-1}.

4.5.2 Degradation of Fluid Viscosity

Over a 7 day period, the fluids were subjected to approximately 30 hours of shearing during the flow experiments. The extent of shearing was dependent on the pump speeds utilised within each flow test, which was varied to suit the Reynolds number requirement. In addition to mechanical shearing, the fluids were also exposed to bacteriological influences within and around the flow facility, a quantitative assessment of which was practically impossible during the entire programme of this investigation. It is also important to highlight the impracticality of using a once-through experimental system, because of the extremely large amounts of polymer solution required, hence the only alternative was to use a re-circulating system as used in this study. Collectively, these influences inevitably caused the test fluids to degrade (seen as a reduction in shear viscosity) as evident in **Figure 4.15**. However, the precautionary measures in place to minimise these effects (bactericide, mono-progressive cavity pump, etc.), were such that the flow curves for viscosity were indistinguishable before and after each flow test.

For the CMC solutions (0.24%, 0.25%, see **Figures 4.15(c-d)**), degradation effects reduced the low shear viscosities ($\dot{\gamma}$ <50 s^{-1}) by approximately 21% over a 7 day period, where as the high shear viscosities above 500 s^{-1} were reduced by less than 10%. Interestingly, the higher concentration solution of CMC (0.4%, **Figure 4.15(e)**) showed much greater resistance to degradation (<6%) over the entire shear rate range

($10<\dot{\gamma}<1000\ s^{-1}$), which agrees with the work carried out by Nakano and Minoura [(1975), cited in Reddy and Singh (1985)]. Nakano and Minoura found higher polymer concentrations to be more resistant to mechanical shearing because of a reduction in local shear rates brought about by a more intense molecular interaction so that, at high concentrations, the rate of degradation becomes independent of concentration.

XG (0.2%) was particularly resistant to degradation effects (**Figure 4.15(b)**), with degradation levels less than 5% on average over the entire range of shear rates. By comparison, the CMC and XG (**Figure 4.15(a)**) illustrated greater levels of degradation than their respective solutions alone; approximately 20% over the entire shear rate range. This linear additive behaviour has also been reported by Reddy and Singh (1985), who investigated the shear stability and drag-reduction effectiveness of various polymer-polymer and polymer-fibre mixtures in turbulent flow of water. They concluded that the extent of polymer interaction with other polymers or fibres, determines their ability to resist mechanical stress fields where, generally, fluids exhibiting complex molecular geometries and high molecular weights are less resistant to mechanical degradation.

Separan AP273 (0.125% and 0.2%, **Figures 4.15(h-i)**) displayed the greatest resistance to degradation effects, which were limited to less than 4% over moderate to high shear rates ($50<\dot{\gamma}<1000\ s^{-1}$).

Finally, the degradation levels associated with the Carbopol solutions were greater than any other solution, with levels as high as 25-43% at low shear rates ($\dot{\gamma}<50\ s^{-1}$), reducing to 7-20% for high shear viscosities ($\dot{\gamma}>1000\ s^{-1}$). These trends are clearly evident from **Figures 4.15(f-g)**.

Despite the levels of degradation highlighted in this section (based on a 7 day period from initial preparation), no detectable levels were monitored between the start and the finish of any individual flow test. It is also important to note that degradation levels were only monitored as a function of viscosity and not for any elastic function of the test fluid (e.g. N_1 or G'). It was therefore assumed that the elastic effects had also degraded,

the extent of which was not known and would thus benefit from a quantitative assessment. Chang and Darby (1983) investigated the effects of degradation on the viscous and elastic properties of an aqueous solution of Separan AP-30. They concluded that the low shear viscosity was reduced by about an order of magnitude for all concentrations (100, 250 and 500ppm), where as the high shear viscosity was virtually unaffected. However, the first normal stress function was reduced by about the same degree at all shear rates. These considerations must be borne in mind when assessing the elastic properties of these fluids as discussed in the proceeding sections. As insurance against the need to carry out further rheological assessments of the test fluids, samples of each working fluid were frozen. No data have been found in literature concerning the effects of freezing on fluid rheology, but tests carried out during this study (see **Appendix 4**) indicated that single additive fluids could be subjected to numerous freezing/thawing cycles without degradation, although this was not true for blends. When blends were subjected to freezing and thawing cycles, the measured shear viscosities over a range of shear rates reduced successively.

4.5.3 Normal Force Measurements

This section details the normal force measurements for highly concentrated solutions of XG, CMC, XG/CMC blend and PAA. First normal stress difference data were not carried out for Laponite due to its complex time-dependent nature, which would otherwise yield data with complex rheological variations and high levels of uncertainty. Also, due to the complexity in preparing solutions of Carbopol, particularly at high concentrations (>1.0%), and their corresponding instability and high levels of degradation, no elastic measurements ($N_1(\dot{\gamma})$ and $G'(f)$) were taken for Carbopol. It is important to note that all first normal stress difference data presented here are based on fresh fluid samples and hence do not account for the longer exposure to degradation effects associated with the working fluids used for the flow tests.

4.5.3 (a) XG

The first normal stress difference data for 1.0-1.5% xanthan gum solutions are illustrated in **Figures 4.16(a-c)**. In the limited range in which the first normal stress difference data could be obtained, it appeared that the first normal stress difference (N_1) increased with respect to shear rate and also increased with concentration (**Figure 4.16(a)**). However, anomalies were associated with the 1.1-1.3% aqueous solutions of XG, which did not follow this trend.

After the superimposition of the first normal stress difference data with the shear stress data on logarithmic co-ordinates (see **Figure 4.16(b)**), a remarkable correlation was observed for all concentrations in that all the data collapsed on to a straight line. This relationship agrees with the work carried out by Barnes *et al.* (1989) as previously mentioned in Section 4.4.2(b). After establishing the power-law master curve fit for the data plotted, it was then possible to extrapolate the normal force data to corresponding shear stress values, which were obtained from the pipe-flow experiments. This allows a possible correlation to be established between an elastic function and the pipe flow data (*f*, ΔP, DR, etc.). This correlation will be discussed in Chapter 5.4.

The data plotted in **Figure 4.16(b)** resulted in the following empirical expression:

$$N_1 = 0.97\,\tau^{1.47} \qquad \text{1.0-1.5\% XG} \qquad \textbf{(4.6)}$$

According to Barnes *et al.* a recoverable shear (i.e. $N_1/2\tau$) greater than 0.5 indicates a highly elastic state. The recoverable shear is due to the elastic component of the fluid, which reaches an equilibrium state when subjected to continuous simple shear. For xanthan gum, the above condition corresponded to shear stresses in excess of 1.07 Pa. **Figure 4.16(c)** illustrates N_1/τ *versus* shear rate for all concentrations, indicating that N_1 is consistently greater (up to 4 times) than the shear stress for $1<\dot{\gamma}<300\ s^{-1}$.

4.5.3 (b) CMC

The first normal stress difference data for 0.6-1.5% CMC solutions, have been presented in **Figures 4.17(a-c)**. N_1 increased with shear rate and also with concentration as seen in **Figure 4.17(a)**. After the superimposition of the first normal stress difference data with the shear stress data on logarithmic co-ordinates (**Figure 4.17(b)**), a correlation similar to that for XG was observed for all concentrations in that all the data (with the practical exception of scattered data points) collapsed on to a straight line. This agrees with data provided by Kotaka *et al.* (1959). This power-law relationship was expressed with the following parameters:

$$N_1 = 0.85\,\tau^{1.25} \qquad \text{0.6-1.5\% CMC} \qquad \textbf{(4.7)}$$

Figure 4.17(c) illustrates the variation of the non-dimensionalised normal stress difference (N_1/τ) plotted as a function of shear rate. For all shear rates ($1.8<\dot{\gamma}<200$ s^{-1}), the magnitude of the first normal stress difference was consistently higher than the shear stress for all concentrations with the exception of 0.9% CMC, which showed an anomaly at low shear rates $\dot{\gamma}<4.5s^{-1}$. At a shear rate of 180 s^{-1}, N_1/τ increased consistently from 2 to 2.9 for 0.6%-1.5% CMC respectively.

For comparison purposes, the condition defining a highly elastic fluid ($N_1/2\tau > 0.5$) was also identified for CMC and corresponded to shear stresses in excess of 1.916 Pa, compared with 1.07Pa for XG.

4.5.3 (c) XG/CMC

The first normal stress difference relationships with shear stress and shear rate for the XG/CMC blends are given in **Figures 4.18(a-c)**. These solutions behaved similarly to CMC and XG. The first normal stress difference increased with shear rate and with concentration, almost linearly as evident in **Figure 4.18(a)**. After the superimposition of the first normal stress difference data with the shear stress data on log co-ordinates, the data also collapsed onto a single line (**Figure 4.18(b)**). The parameters below

define the power-law curve fit used to empirically model the experimental relationship between N_1 and τ for the XG/CMC blends:

$$N_1 = 1.35\,\tau^{1.18} \qquad 0.4/0.4\text{-}1.5/1.5\%\ \text{CMC/XG} \qquad \textbf{(4.8)}$$

Figure 4.18(c) illustrates N_1/τ versus shear rate for all concentrations. As for the XG/CMC aqueous blends, this stress ratio was consistently larger than 1 (typically between 2 and 3) for all shear rates ($1.8<\dot{\gamma}<180\ s^{-1}$), thereby indicating the dominance of N_1 over τ over this range.

The recoverable shear condition, indicating a highly elastic fluid ($N_1/2\tau>0.5$) for XG/CMC, corresponded to shear stresses in excess of 0.189 Pa.

4.5.3 (d) Separan (PAA)

For the 0.2-1.5% polyacrylamide solutions, **Figure 4.19(a)** shows an increase in N_1 as a function of increasing shear rate and fluid concentration. However, the first normal stress difference data at constant concentration superimposed with shear stress, but those at different concentrations fell on different curves as opposed to the trends observed in the CMC and xanthan gum solutions (**Figure 4.19(b)**). Such observations leads to the idea that structural differences exist between the solvent additives that can influence the rheological characteristics. It is important to note, however, that the rheological assessment of $\eta(\dot{\gamma})$ for PAA and XG, were very similar in terms of viscosity and extent of shear-thinning, yet their elastic influences are noticeably different here. Kokini and Surmay (1994) attempted to explain a similar relationship observed for 0.5-1.25% guar gum solutions (a neutral polysaccharide, prepared in distilled de-ionised water), from a molecular standpoint. They attributed this behaviour to the interchange relaxation processes (due to temporary junction (entanglement) breakage and formation as well as rearrangements of distorted chains) within guar gum. The formation of a network structure through entanglements, which could be positively influenced if significant charge densities were present, was deemed as less dominant than the inter-chain relaxation processes for guar gum.

Their argument was further substantiated by the fact that the interchain relaxation processes are a function of collision frequency, which in turn is a function of concentration, hence the N_1 data at different concentrations fell on different curves. Based on the molecular information provided for each test fluid used in this study, a qualitative assessment of the molecular influence on rheology could not be carried out. However, this should form the basis of investigation for future work.

Also, from **Figure 4.19(b)**, the first normal stress difference data (as a function of shear stress) for lower concentrations was systematically greater than those at higher concentrations, a further anomalous behaviour compared to the test fluids discussed above. However, the reverse is true if these data are plotted in terms of shear rate due to viscous effects as previously shown in **Figure 4.19(a)**.

From the relatively large values of N_1 for the PAA solutions compared with XG and CMC (up to 1520Pa at $180s^{-1}$ for 1.5% PAA), it was possible to obtain $N_1(\dot{\gamma})$ directly for the lower concentration solutions used in the flow experiments (0.125% and 0.2%), since the N_1 values were above the resolution of the rheometer. The data was well represented by:

$$N_1 = 16.3\,\tau^{1.48} \qquad 0.125\%\ \text{PAA} \qquad \textbf{(4.9)}$$

$$N_1 = 6.07\,\tau^{1.90} \qquad 0.2\%\ \text{PAA} \qquad \textbf{(4.10)}$$

as seen in **Figure 4.19(d)**, so that 0.125% PAA can be said to be highly elastic for $\tau>0.003$ Pa and 0.2% PAA for $\tau>0.135$ Pa. The greater dominance of first normal stress difference compared with shear stress is evident in **Figure 4.19(c)** where stress ratios increase from 6 to 40 for shear rates ranging from $1.8s^{-1}$ to $180s^{-1}$ respectively. These ratios are considerably larger than the XG and CMC solutions discussed above.

4.5.4 Oscillatory Flow Measurements

Oscillatory flow measurements were performed for aqueous solutions of XG (0.2%, 1.0-1.5%), CMC (0.6-1.5%), XG/CMC blend (0.18%, 0.8-1.5%), PAA (0.125%, 0.2-1.5%,) and Carbopol EZ1 (0.1%). No measurements were carried out for Laponite due to time-dependent complexities nor for Carbopol 934 due to instabilities in solvent viscosity, particularly at high concentrations. Measurements for Carbopol EZ1 were taken at 0.1% concentration, as that used in the flow tests.

Figures 4.20 - 4.23, illustrates the dynamic shear flow measurements (storage modulus, G′ *versus* frequency) for the high concentration test fluids listed above. For all fluids, the storage modulus (elastic component of the fluid) increased with frequency for $0.001<f<30$Hz. It is also evident from **Figures 4.20 - 4.23** that the storage modulus increases with increasing fluid concentration, with the exception of XG, for which there did not seem to be a particular dependence on concentration. For XG, the following ranking ($G'(f)$) was displayed: 1.1%, 1.0%, 1.5%, 1.2%, 1.4% and 1.3%. This was probably attributable to degradation effects associated with mechanical shearing influences during preparation and bacteriological influences, rather than rheological characteristics, as various containers were used to store the sample solutions during the tests. These re-usable containers (laboratory type beakers and jars) may have contained minute quantities of foreign matter or bacteria that were difficult to control and monitor, thus sensitising the fluids to various degrees of bacteriological influence. All containers were thoroughly cleansed, as practically possible, between each rheological test. Also, the extent of mechanical shearing for each sample fluid may have varied slightly (between 2 and 6 hours), the effect of which is not known. No further qualitative assessment could be made with respect to this anomaly associated with XG.

For comparison purposes, **Figure 4.24** collectively illustrates the frequency response of the storage modulus for all aqueous solutions mentioned above at 1.5% concentration. Such data assists in establishing comparisons between all test fluids under similar flow conditions, from which the results here generally confirm that the elasticity ranking (most → least elastic) is PAA, XG, XG/CMC and CMC. At higher frequencies (>5Hz), the CMC solution exceeds the elasticity levels for other fluids and consequently the

ranking changes here. Again, it is important to note that these solutions were exposed to relatively little shear (<6 hours) as opposed to the test fluids used in the flow tests. Therefore, the influence of mechanical degradation is greater for these sample fluids, thus potentially leading to comparative anomalies between solutions of similar concentration.

Figure 4.25 provides an illustrative comparison of the storage modulus, $G'(f)$, for the test fluids used in the flow tests. Unfortunately, a quantitative assessment for the CMC solutions (0.24%, 0.25% and 0.4%) was not carried out due to the unavailability of a rheometer during the early stages of this investigation. From **Figure 4.25**, the following elastic ranking was deduced: 0.2% PAA, 0.2% XG, 0.125% PAA ≡ 0.09% CMC/0.09% XG and 0.1% Carbopol EZ1. From the observations made from previous data ($N_1(\dot{\gamma})$ and G' for high concentrations), it may be assumed that the CMC solutions, under oscillatory flow conditions, would probably rank between the XG/CMC blend and the Carbopol EZ1 solution.

Figure 4.26 illustrates the corresponding phase angle *versus* frequency behaviour for these test fluids. The phase angle (or loss tangent, $\tan \delta = G''/G'$), indicates the relative contributions of viscous and elastic properties for the fluid. A phase angle of 90° suggests a purely viscous (Newtonian fluid) and 0° indicates a purely elastic fluid; thus a viscoelastic fluid would lie between these extremes.

The data shows that the viscous influences are dominant at low frequencies (f<0.1Hz) for all working fluids, though at higher frequencies the elastic component becomes more effective. Interestingly, 0.1% Carbopol EZ1 shows an anomalous behaviour where by at low frequencies, the elastic component is more dominant, with the viscous influence becoming stronger at higher oscillation frequencies. For all test fluids, a limiting frequency was reached at approximately 6-10Hz, in which a considerable break down in structure occurred and the viscous components became more predominant.

The results discussed in this section are summarised in Section 4.7.

4.6 Role of Extensional Viscosity

Apart from the shear-thinning behaviour of viscoelastic fluids, and elastic characteristics deduced from first normal stress difference and oscillatory flow data, the extensional viscosity η_E is also a function related to viscoelasticity i.e. η_E is a function of the extensional strain rate $\dot{\varepsilon}$ just as shear viscosity η is a function of shear rate $\dot{\gamma}$ [Barnes *et al.* (1989)]. Therefore, a question arises to whether the extensional viscosity of polymer solutions play any part of the process associated with drag-reduction in turbulent pipe flow, since as reported by Metzner and Metzner (1970) and later confirmed by other investigators (e.g. Bragg and Oliver (1973)), the extensional viscosity of polymer solutions can be as large as 10000 times the shear viscosity. This result was found in polyacrylamide and polyethyleneoxide (PEO) solutions, and, even at drag-reducing concentrations, ratios as high as 1000 (often called the Trouton ratio) were found. Even though these measurements are not a matter of routine, the ratios found are large enough to make it seem clear that this creates a non-Newtonian effect that may well be relevant to drag-reduction in turbulent flow. It was later found by Mewis and Metzner (1974) that extensional flow of suspensions of macroscopic fibres led to similar anomalous results. Despite the hypotheses that extensional viscosity plays an important role in drag-reducing turbulent flows, the instrumentation required to carry out such extensional flow measurements was not available in this research programme. Thus quantitative assumptions related to extensional effects cannot be made. However, consideration related to extensional viscous effects will be made based on citations from previous studies.

4.7 Summary

All test fluids exhibited shear-thinning behaviour and were well represented by the Cross model using the least squares fit method. The extent of shear-thinning was greatest for the 0.2% XG and PAA solutions, with the exception of Laponite, which also displayed apparent yield stress and time-dependent characteristics. The test fluids selected for this study encapsulated the rheological behaviour displayed by a typical

drilling mud (Bentonite mud). **Figure 4.27** collectively illustrates the behaviour of $\eta(\dot{\gamma})$ for all working test fluids used in this study.

Degradation levels varied between the working fluids and from **Figure 4.15**, the extent of degradation was dependent on fluid type, polymer blend, concentration and magnitude of shear. The extent of bacteriological influence on degradation levels was not quantitatively assessed, though a bactericide was added, of equal concentration (0.015% vol.), to all working fluids. The following ranking was established based on resistance to degradation (most → least resistant): 0.2% and 0.125% PAA, 0.2% XG, 0.4% CMC, 0.25% and 0.24% CMC, 0.09% CMC/0.09% XG blend, 0.1% Carbopol EZ1 and 0.14% Carbopol 934. The fluid viscosity of Laponite increased with time, behaviour which was substantiated by the manufacturer (Laporte, U.K.).

For XG, CMC and XG/CMC blend, there was a high dependence of N_1 on shear stress, though for PAA there was a strong dependence of N_1 on concentration, deemed to be due to structural changes associated with the solvent additives within the solution. It may therefore be qualitatively assumed, without the direct measurement of anisotropic effects, that the elastic effects and associated drag reducing effectiveness of solvent additives, are highly dependent on physical molecular structures.

With the exception of the CMC/XG blend, for which previous data are unavailable, the first normal stress difference results confirm that the elasticity ranking (most → least elastic) was PAA, XG, XG/CMC and CMC, though with the lower concentration for PAA (0.125%) being the more elastic when N_1 is shown as a function of shear stress. The normal-stress characteristics $N_1(\dot{\gamma})$ for all of the working fluids are shown in **Figure 4.28**.

From the normal-stress data, measurable rheometrical functions of $N_1(\tau)$, were established in the form of power-law master curves for each test fluid, with the exception of Laponite and Carbopol solutions. A rheological correlation with the hydrodynamic pipeflow measurements can therefore be assessed, as will be investigated in the next chapter.

The elasticity ranking deduced from the first normal stress difference data was further supported by oscillatory flow measurement data, which were established under small oscillating strain amplitudes within the linear viscoelastic region of the respective fluids. Although such conditions are not representative of transitional and turbulent flows, they do however provide some consistency in the respective elasticity levels when compared with non-linear elastic measurements ($N_1(\dot{\gamma}, \tau)$).

Table 4.3 provides a summary of the rheological properties for all working test fluids and **Table 4.4** classifies the same fluids in terms of their molecular structure. It may be concluded that the viscoelastic components for all these test fluids were more sensitive to the type of fluid i.e. whether the fluid was rod-like, highly-branched or had a large molecular weight, than its steady shear viscosity.

Tables and Figures

Table 4.1 *Generalised Newtonian Models*

Model	Mathematical Representation	Comments†
Power Law	$\eta = k\dot{\gamma}^{n-1}$	Adequate for viscosities in the power-law region though fails at high and low shear viscosities ($\eta \rightarrow \eta_0$ or η_∞). Useful for practical engineering flow calculations.
Cross‡	$\frac{\eta - \eta_\infty}{\eta_0 - \eta_\infty} = \frac{1}{1 + (\lambda_c \dot{\gamma})^m}$	Represents shear-thinning fluids over entire shear rate range, displaying appropriate asymptotic behaviour (η_0 and η_∞) and a power-law region. Only three parameters required, easily obtained from viscometric data.
Carreau‡	$\frac{\eta - \eta_\infty}{\eta_0 - \eta_\infty} = \frac{1}{\left[1 + (\lambda\dot{\gamma})^2\right]^{\frac{1-n}{2}}}$	Provides the same advantages as the Cross equation, though four parameters are required. Weakness is that the characteristic time, λ, is not specifically related to fluid behaviour and is strictly a non-linear curve-fitting parameter.
Powell-Eyring	$\eta = C + \frac{A\,sinh^{-1}(B\dot{\gamma})}{\dot{\gamma}}$	Based on Prandtl-Eyring and Newtonian laws. At low shear rates it reduces to η=C+AB and at high shear rates η=C. At intermediate shear rates, the shear stress varies in approximately an exponential way.
Herschel-Buckley	$\eta = \frac{\tau_y + K\dot{\gamma}^n}{\dot{\gamma}}$	Used to accurately characterise fluids with yield stress and shear-thinning characteristics (e.g. polymer melts and drilling muds). However, the extrapolated yield stress may be too high, and the true value could be as low as zero.

† Referenced from Barnes *et al.* (1989) and Allen (1995).

‡ Note that for the Cross model, $(d\mu/d\dot{\gamma}) \rightarrow \infty$ for $\dot{\gamma} \rightarrow 0$. For the Carreau model, $(d\mu/d\dot{\gamma}) \rightarrow 0$ for $\dot{\gamma} \rightarrow 0$; but for both models, $d(ln\mu)/d(ln\dot{\gamma}) \rightarrow 0$.

Table 4.2 *Cross Model Parameters for all Test Fluids*

Fluid	η_0 [Pa.s]	η_∞ [Pa.s]	λ_c [s]	m [-]
0.24 % CMC	0.04990	0.00104	0.00257	0.58676
0.25% CMC	0.06286	0.00481	0.00959	0.60017
0.4% CMC	0.14380	0.00100	0.01446	0.51205
0.2% XG	1.14147	0.00243	2.82461	0.69009
0.09% CMC/0.09% XG	0.42493	0.00222	6.60699	0.51048
0.125% PAA	0.26958	0.00293	0.80428	0.64599
0.2% PAA	3.36900	0.00346	4.6445	0.66235
0.1385 % Carbopol 934	0.26949	0.00578	0.77079	0.48021
0.1% Carbopol EZ1	7.13388	0.00250	12955.07	0.39129

Table 4.3 *Summary of Rheological Properties*

Fluid	Turbity	Visco-elasticity[1]	Degradation [%][2]
CMC (0.24, 0.25 & 0.4%)	Clear	Slightly elastic [4]	[3]
XG (0.2%)	Slightly turbid	Moderately elastic [2]	[2]
CMC (0.09%)/ XG (0.09%)	Very slightly turbid	Moderately elastic [3]	[4]
PAA (0.125 & 0.2%)	Clear	Highly elastic [1]	[1]
Carbopol (0.1% 934, 0.14% EZ1)	Slightly turbid	Practically inelastic [5]	[5]
Laponite (1.5%)	Very slightly turbid	Practically inelastic [*]	[-]

NOTES [1] Degree of elasticity based on the following ranking: 1 (most elastic) - 5 (least elastic).

[2] Level of degradation based on the following ranking: 1 (low) - 5 (high).

[*] Based on qualitative assessment.

[-] Not measured.

Table 4.4 *Classification of Test Fluids*

Fluid	Rod-Like	Highly-Branched	Long Molecule ($MW > 10^6$)	Highly Flexible	Comment
XG (Keltrol TF)	Yes	No	Yes	No	Rod-like molecules cannot be flexible. XG has a molecular weight ca 2×10^6.
CMC (BDH)	No	No	No	Yes	CMC is a linear-flexible-molecule with a molecular weight $< 10^6$.
PAA (Separan AP273)	No	No	Yes	Yes	PAA has a molecular weight ca 4×10^6.
Carbopol (EZ1 and 934)	No	Yes	No	No	Being highly branched, it can never be very long although it also uncoils as a linear molecule.
Laponite RD	N/A	N/A	N/A	N/A	Laponite is a 'suspension' fluid and hence cannot be categorised using the classification shown here.

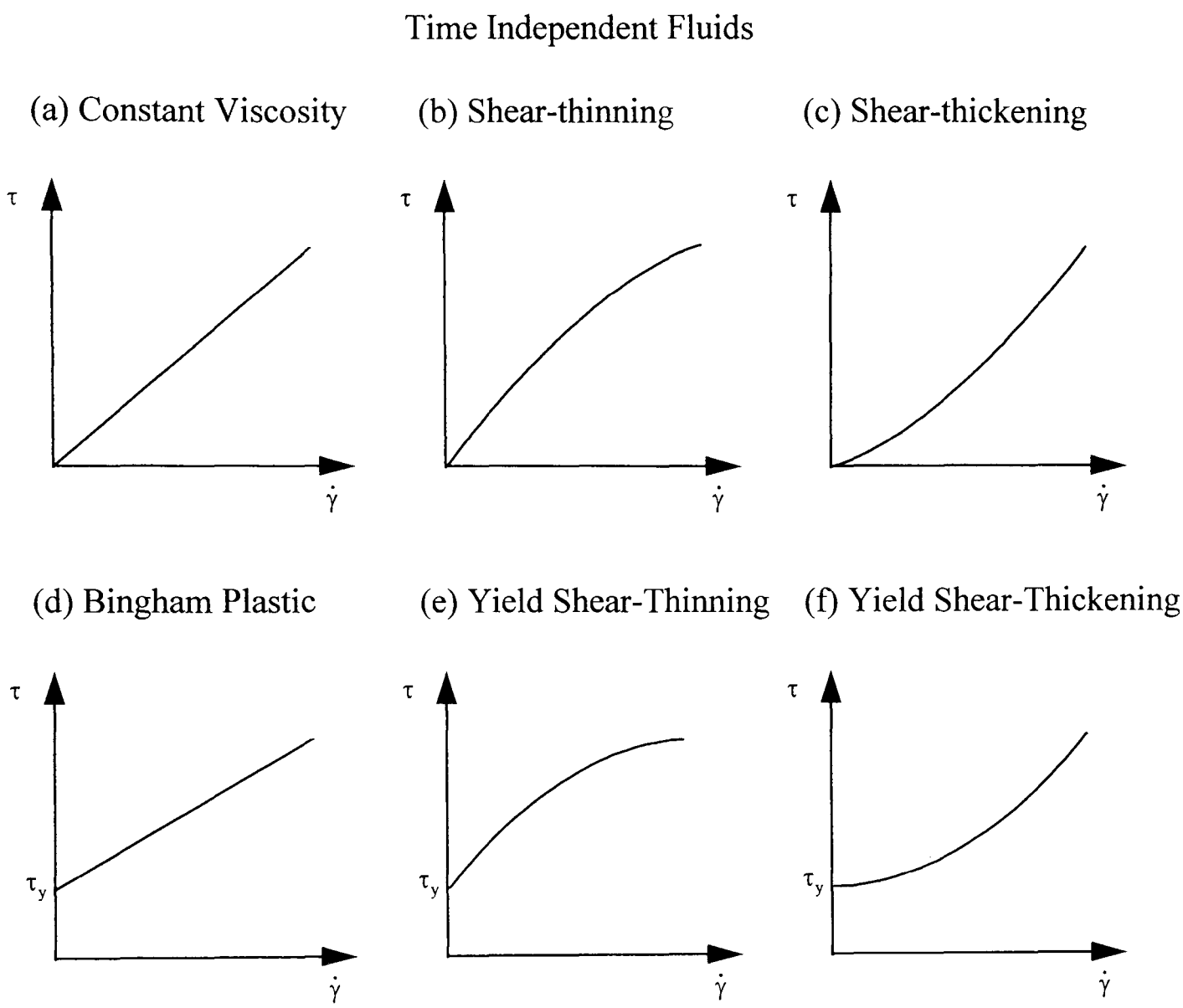

Figure 4.1 *Characteristics of purely viscous time independent fluids.*

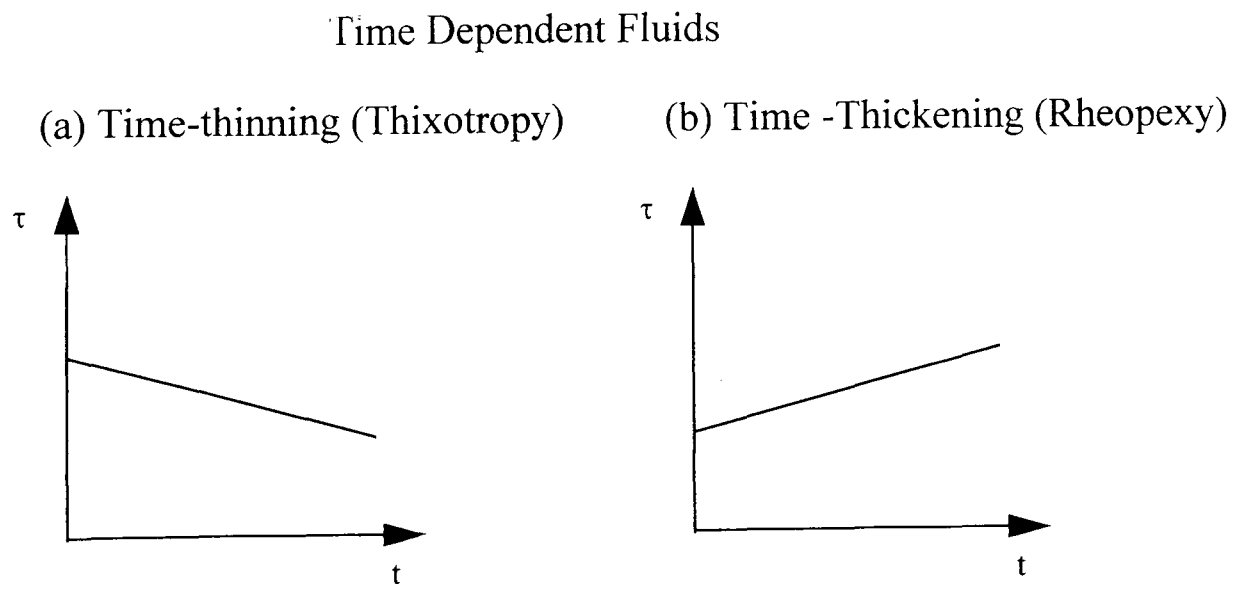

Figure 4.2 *Characteristics of time dependent fluids.*

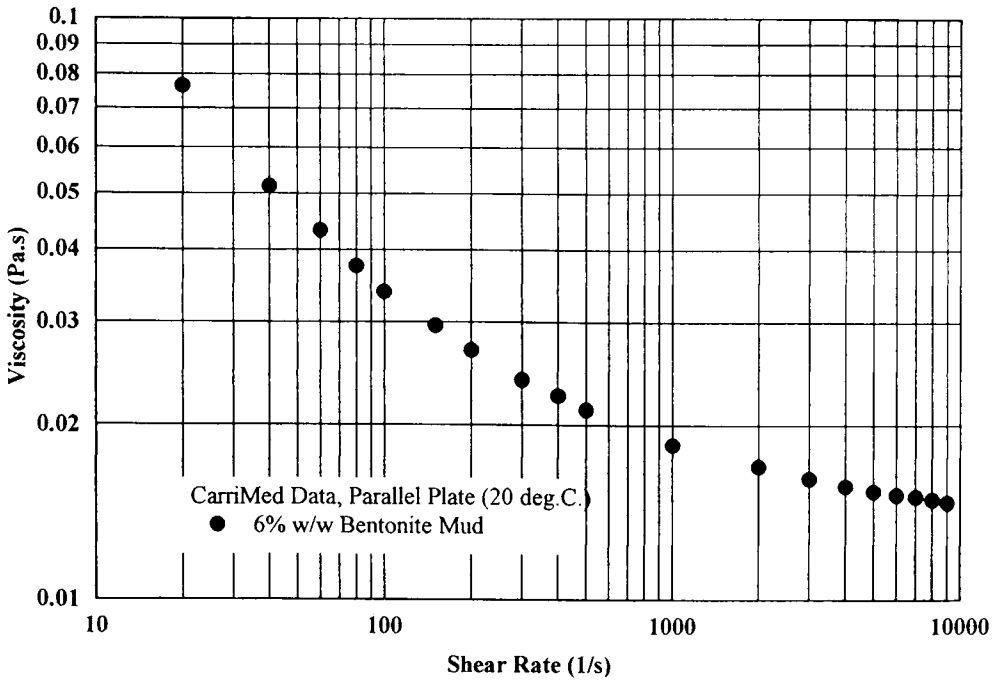

Figure 4.3 *Viscosity versus Shear Rate for a Typical Drilling Mud (Wyoming Bentonite).*

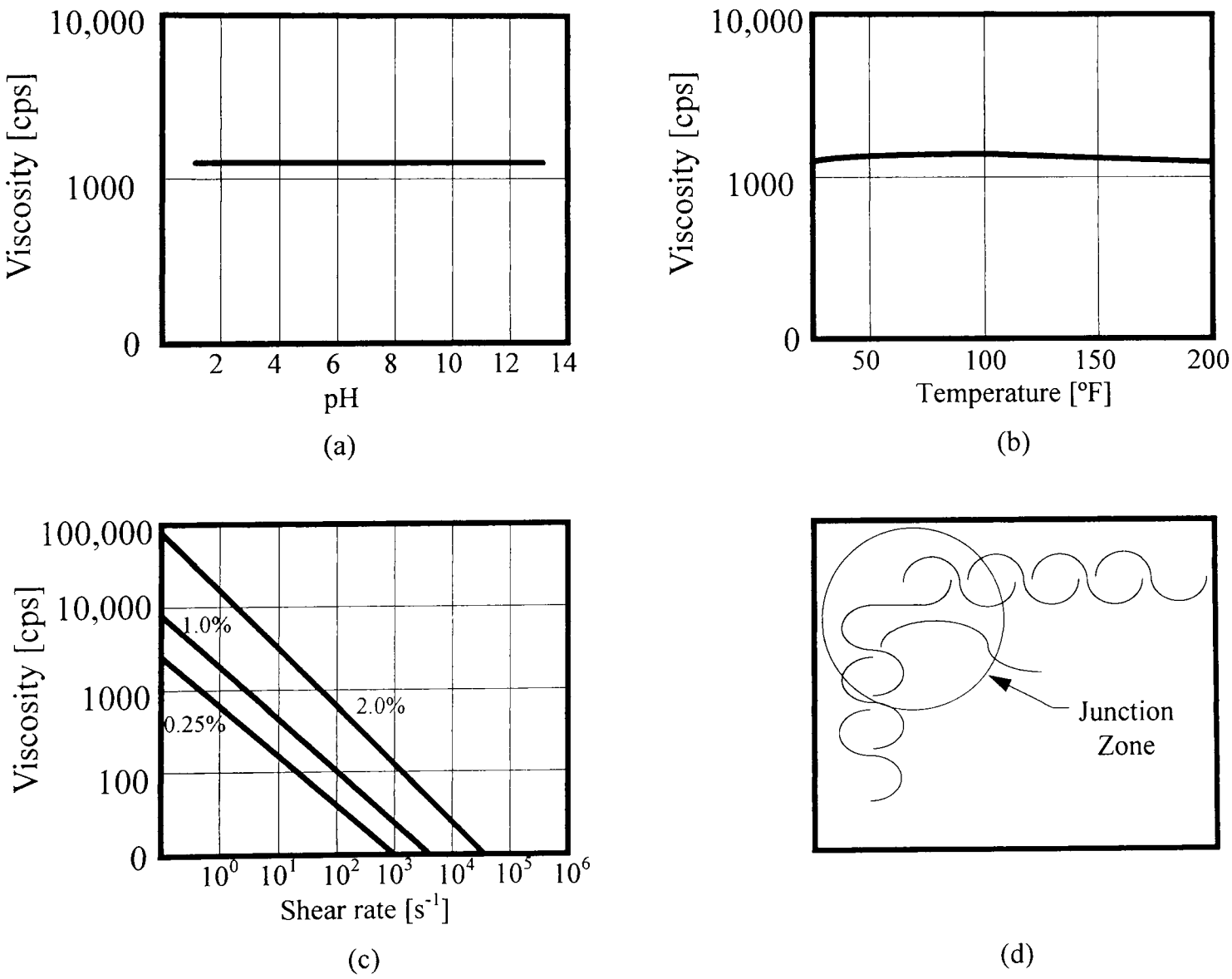

Figure 4.4 *Characteristics of Xanthan Gum: (a) Viscosity vs pH (b) Viscosity vs temperature (c) Viscosity vs shear rate, and (d) Helix structure for xanthan gum [Kelco (1991)].*

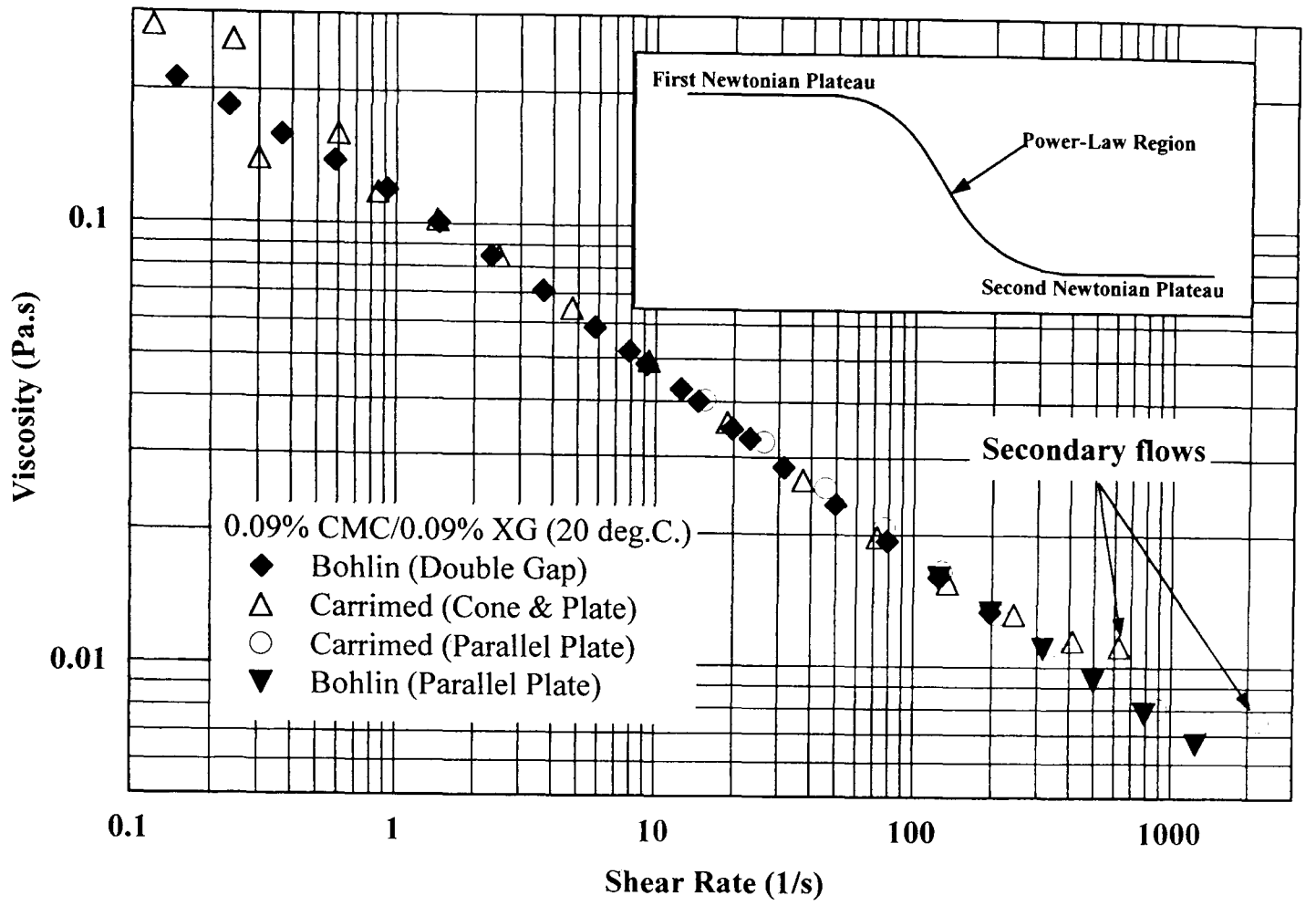

Figure 4.5 *Comparison of the Viscometric Data Obtained from the Bohlin VOR and CarriMed Rheometers.*

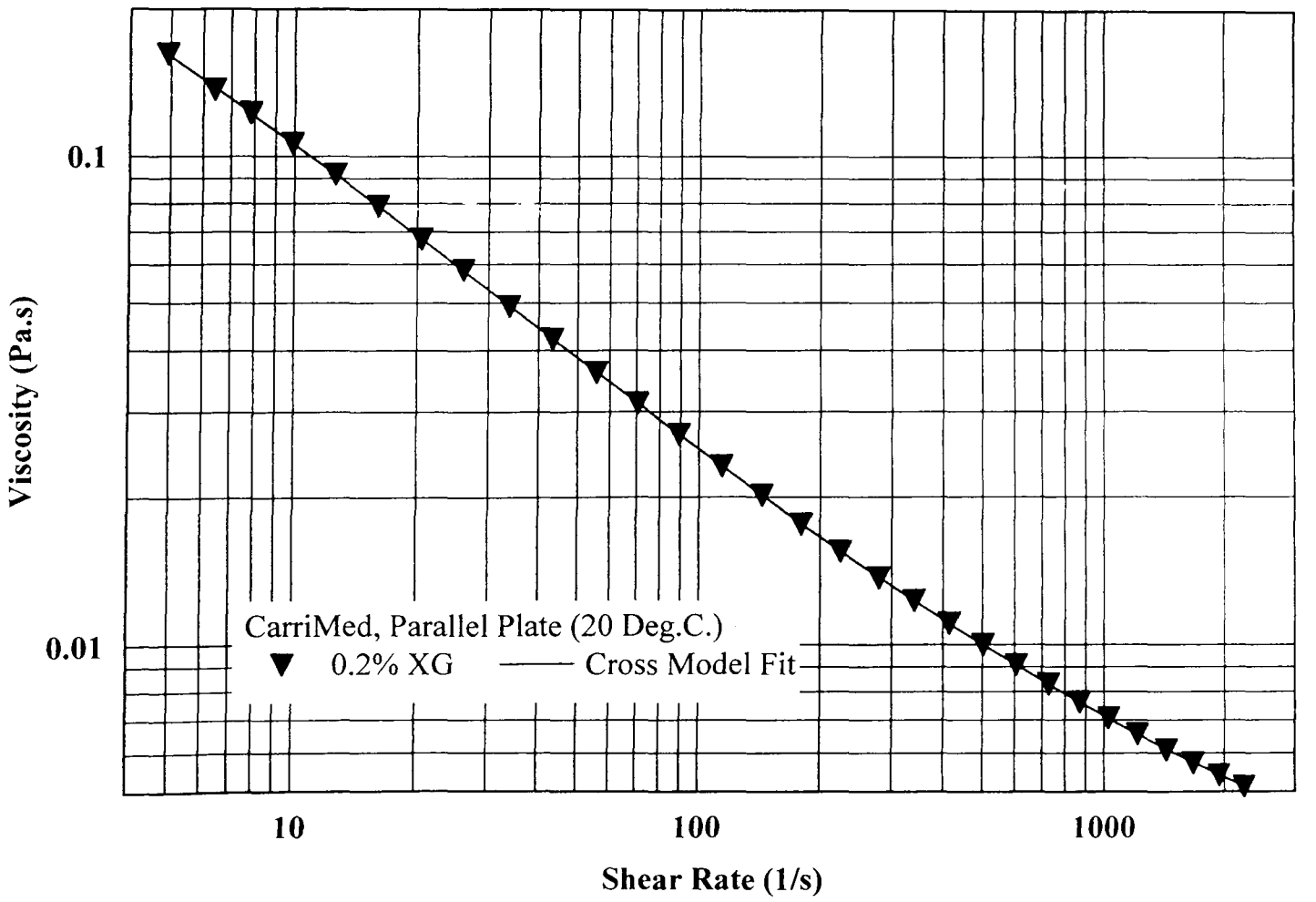

Figure 4.6 *Viscometric Data for 0.2% XG.*

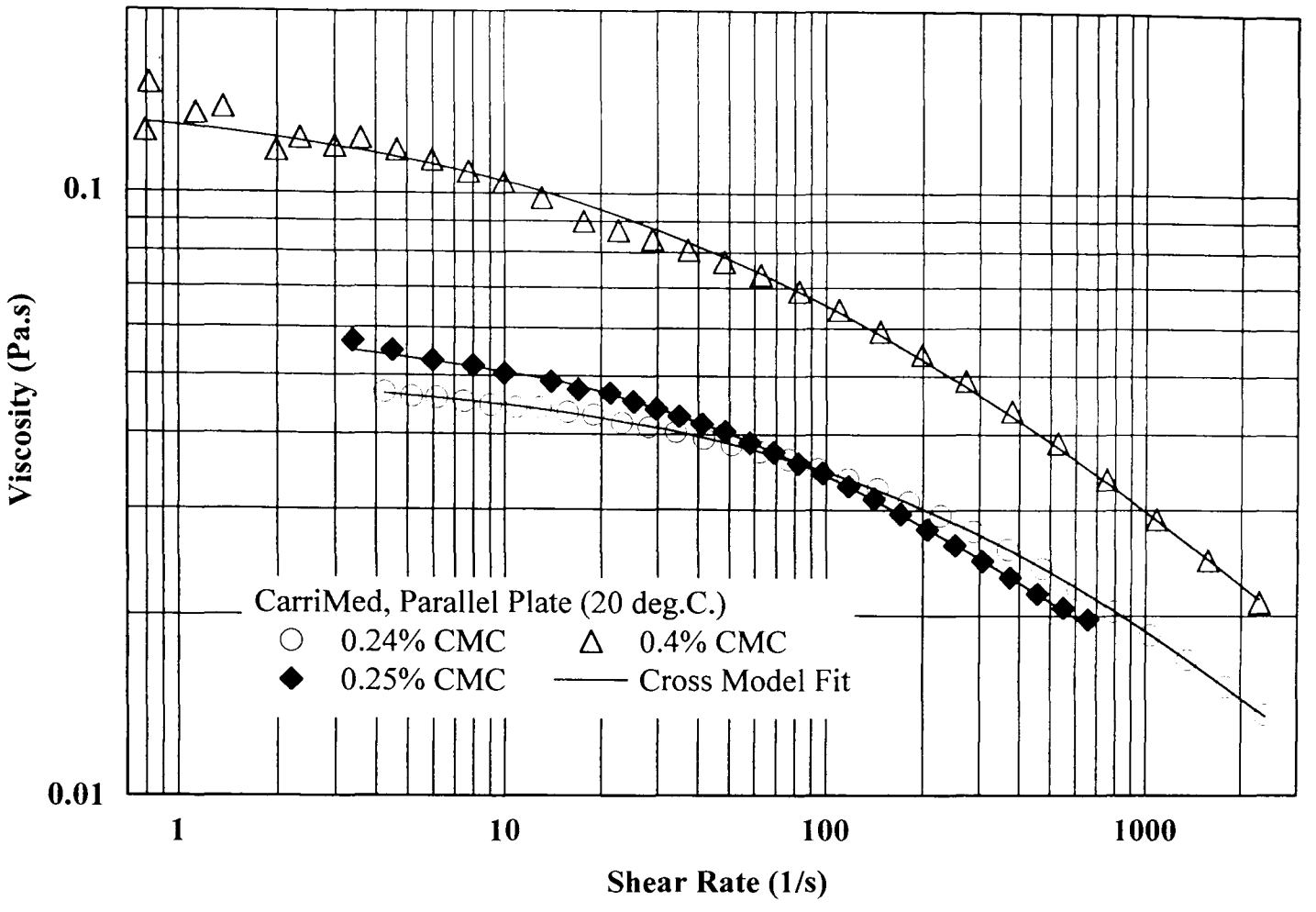

Figure 4.7 *Viscometric Data for 0.24%, 0.25% and 0.4% CMC.*

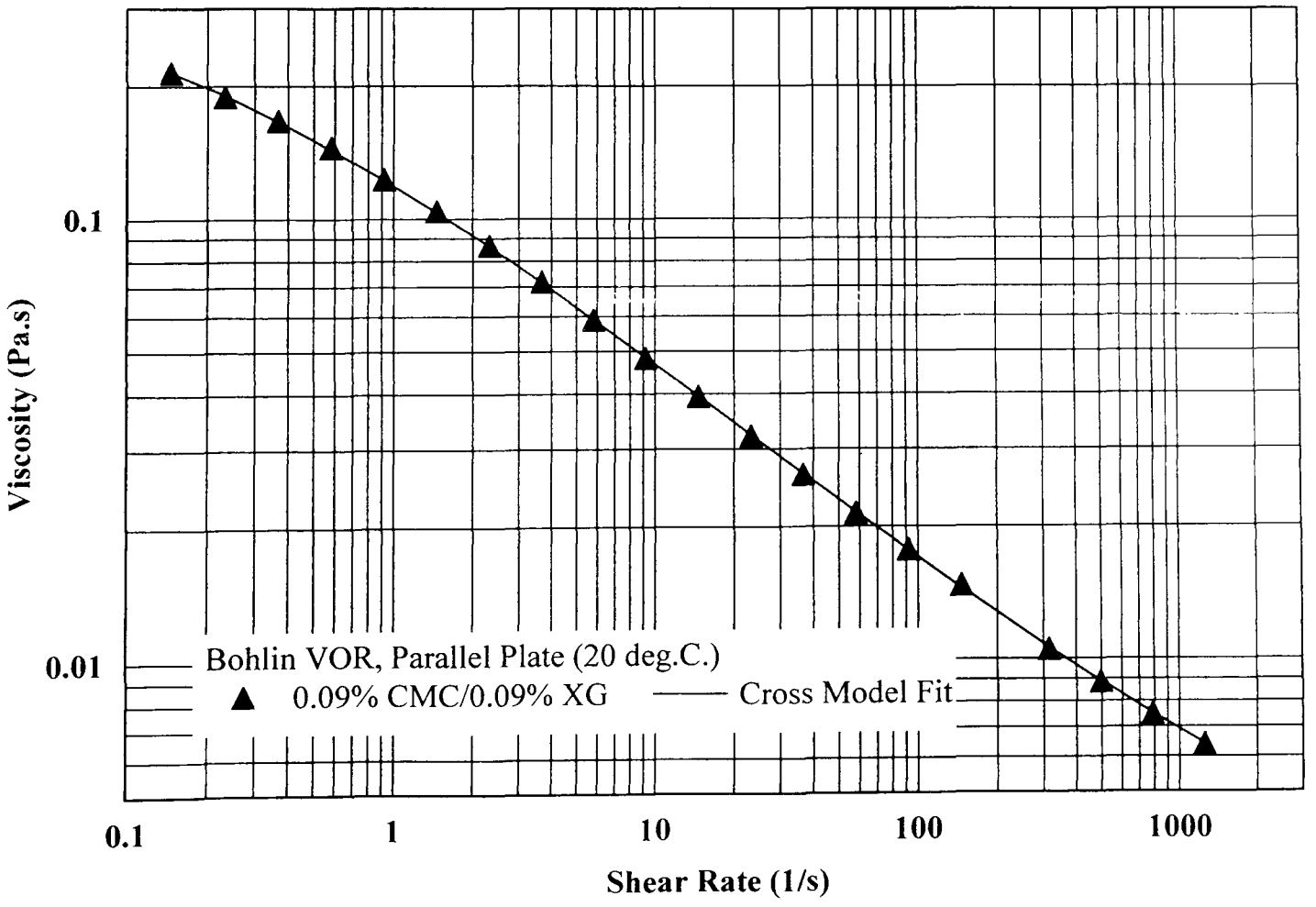

Figure 4.8 *Viscometric Data for 0.09% CMC/0.09% XG.*

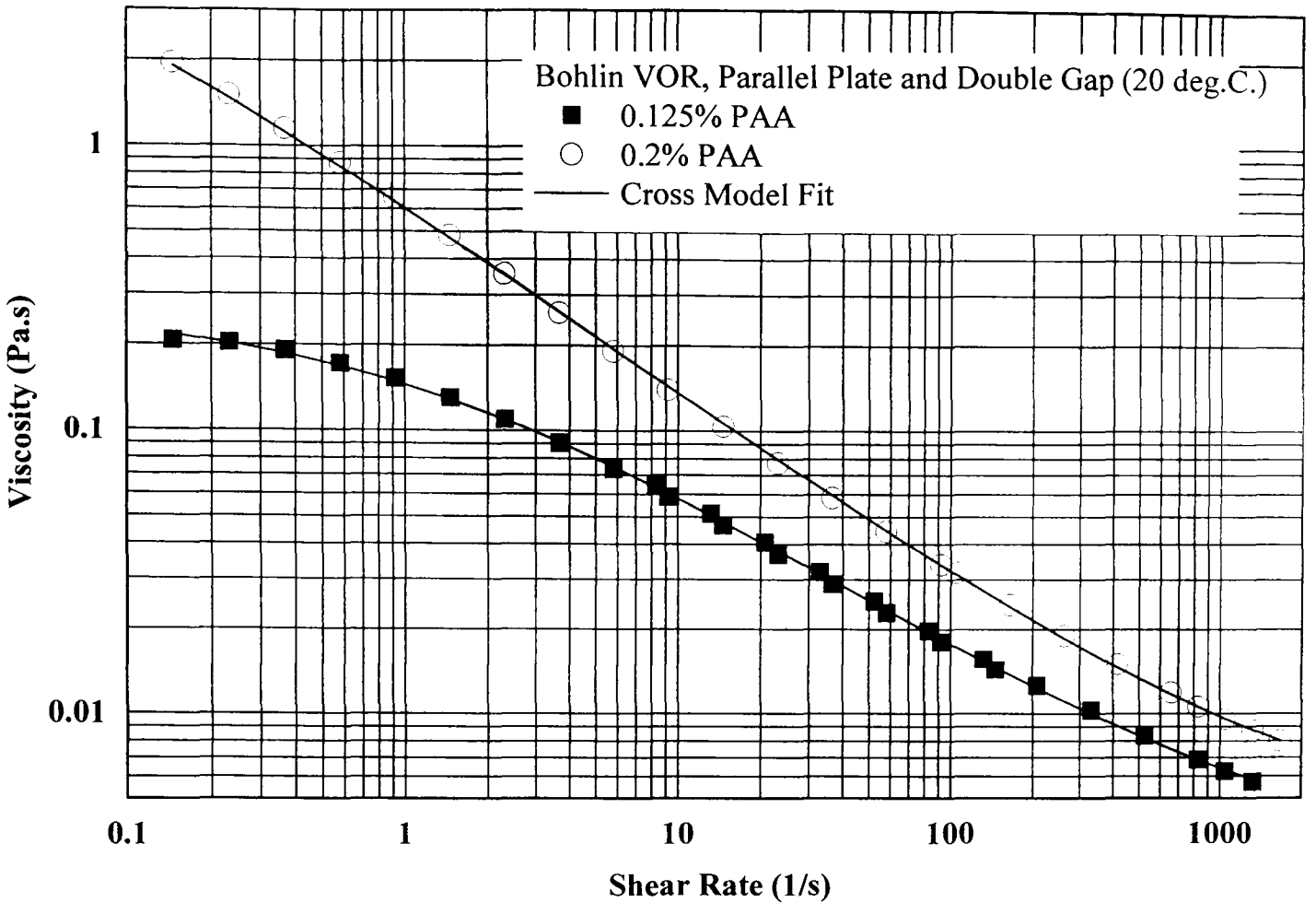

Figure 4.9 *Viscometric Data for 0.125% and 0.2% PAA.*

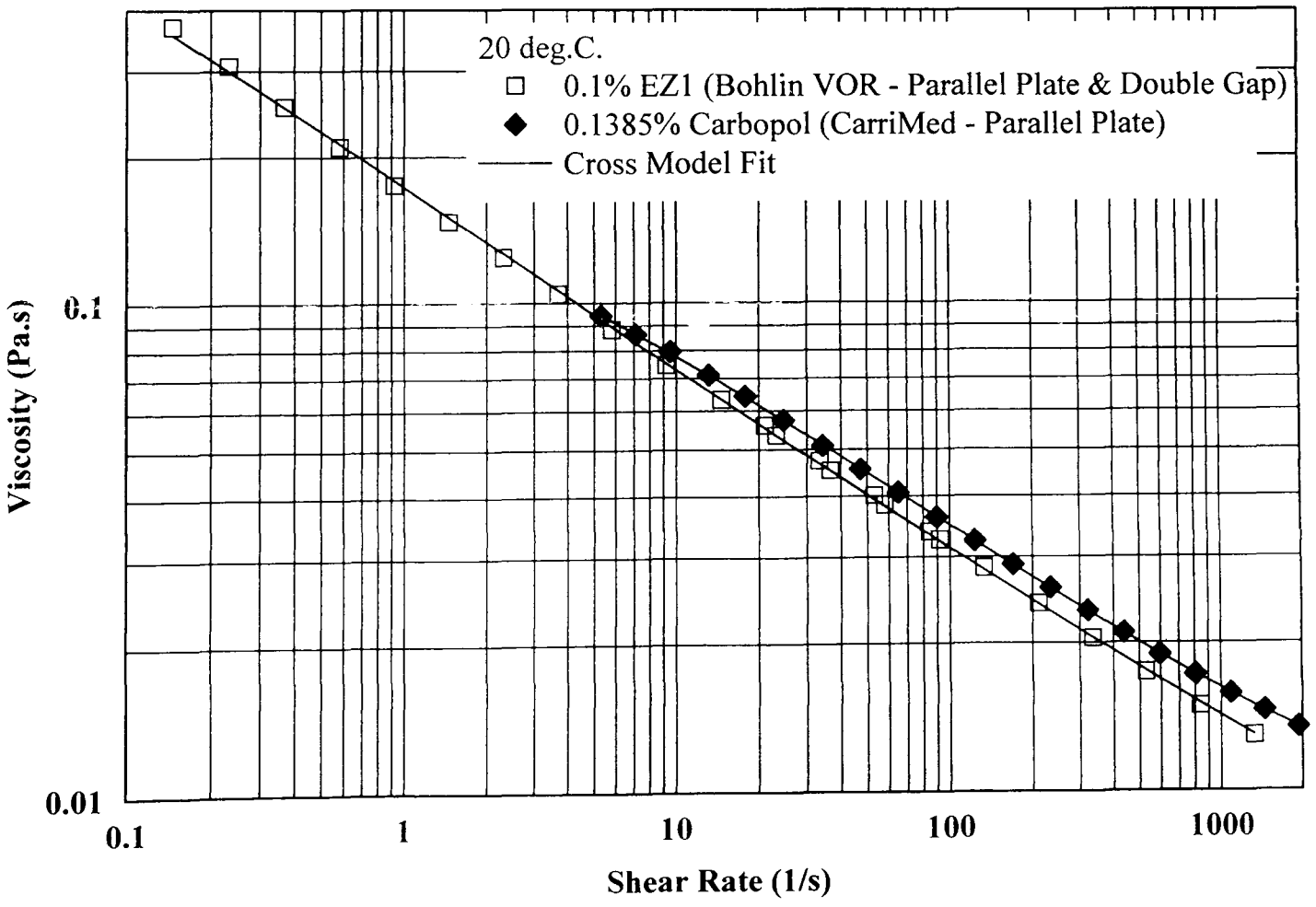

Figure 4.10 *Viscometric Data for 0.14% Carbopol 934 and 0.1% Carbopol EZ1.*

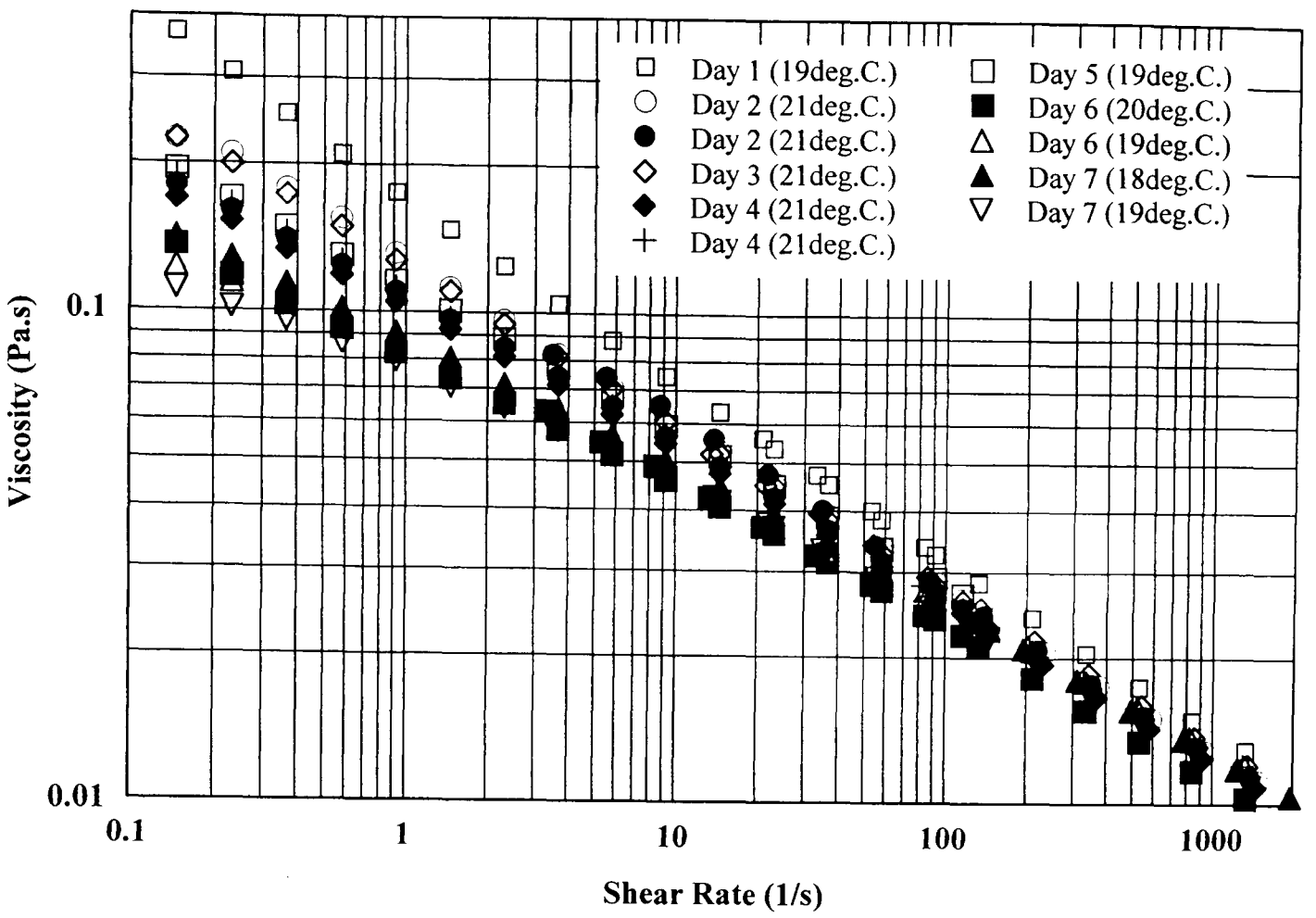

Figure 4.11 *Viscometric Data for 0.1% Carbopol EZ1 over a 7 day Period.*

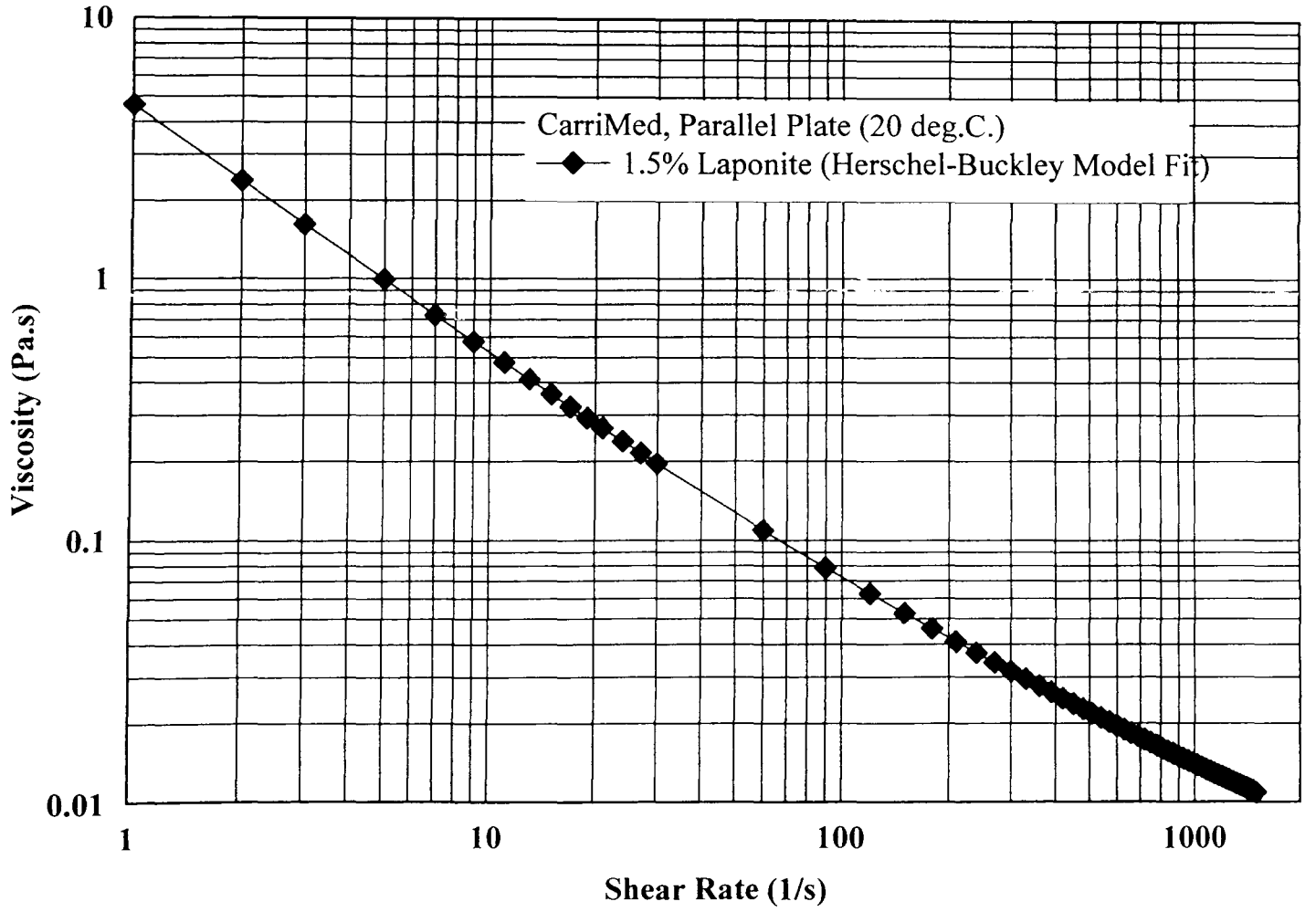

Figure 4.12 *Viscometric Data for 1.5% Laponite RD.*

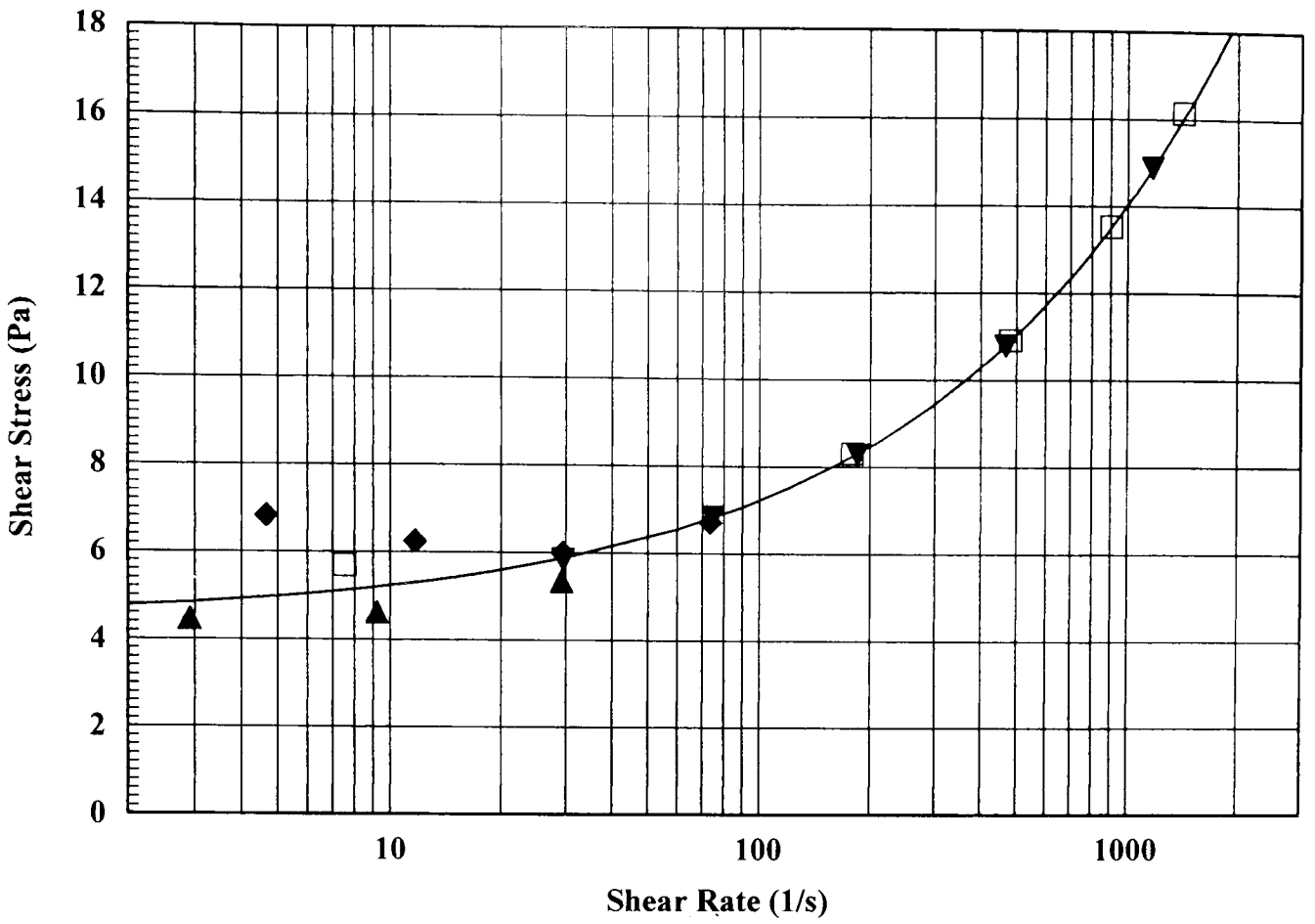

Figure 4.13 *Viscometric Data for 1.5% Laponite RD:* ▼, ▲, ◆, □ *rheometer data.*

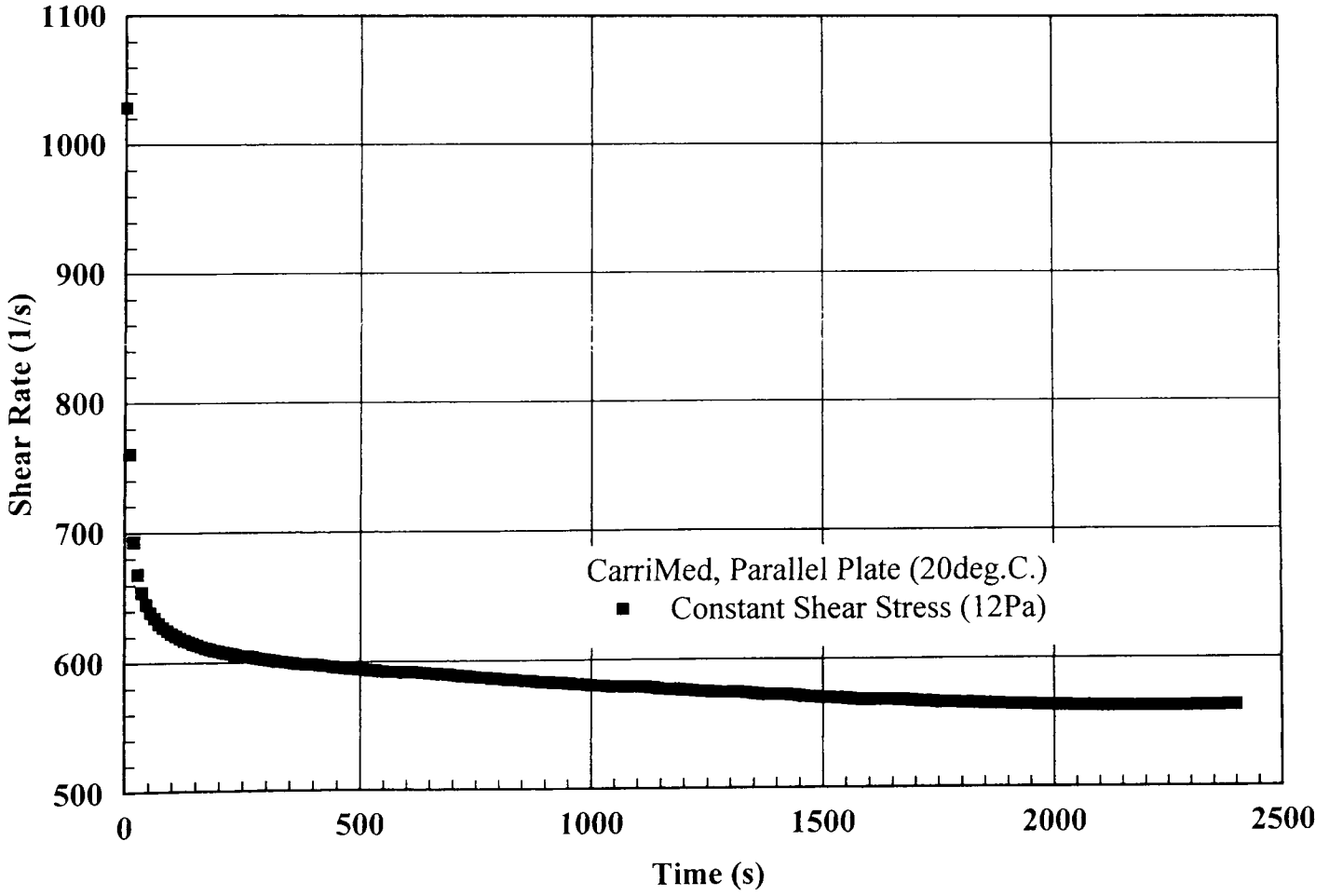

Figure 4.14 *Thixotropic Behaviour of 1.5% Laponite RD.*

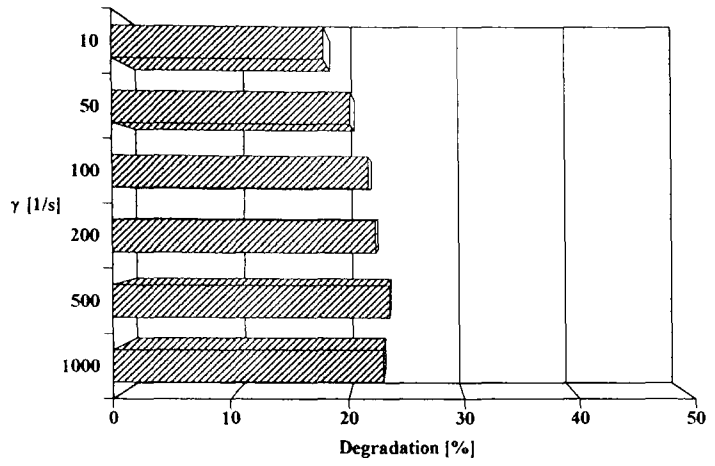

(a) 0.09% CMC/0.09% XG

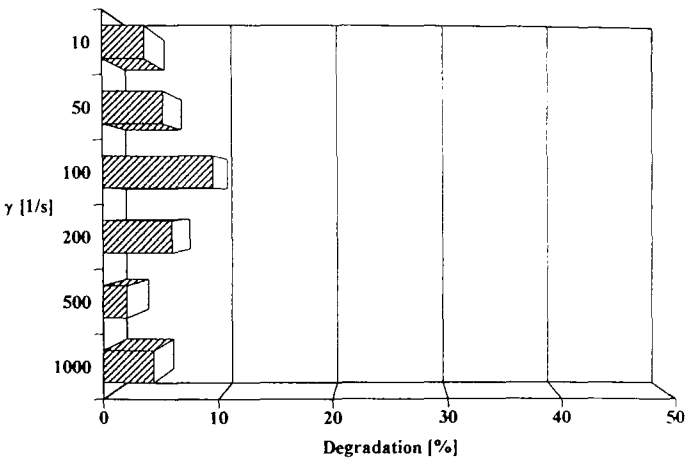

(b) 0.2% XG

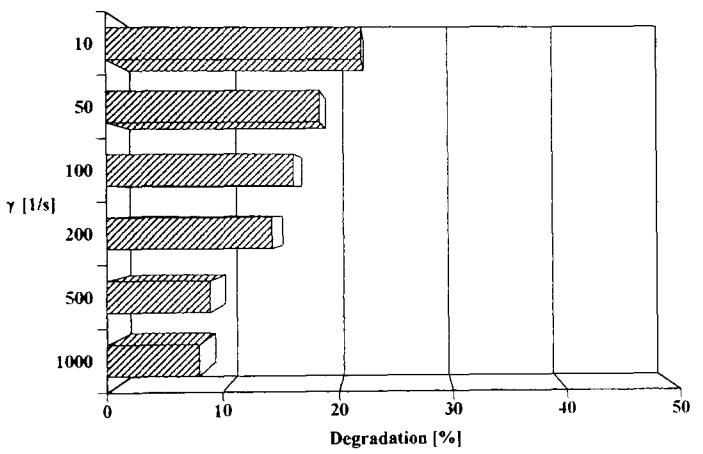

(c) 0.24% CMC

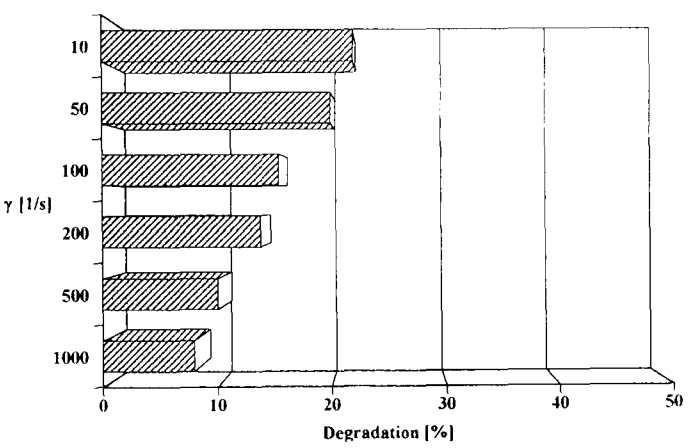

(d) 0.25% CMC

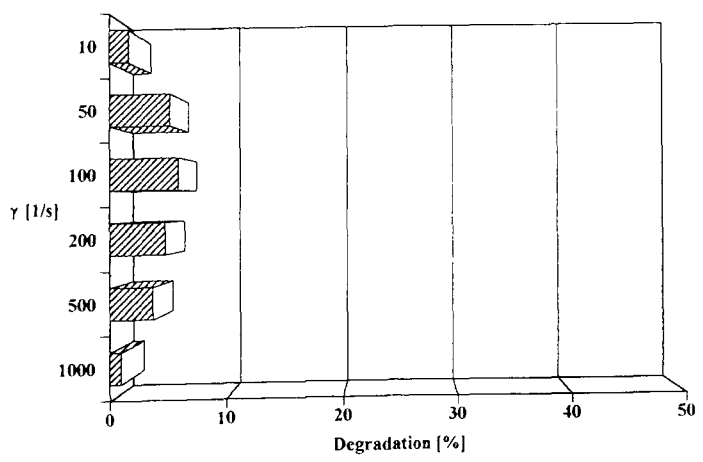

(e) 0.4% CMC

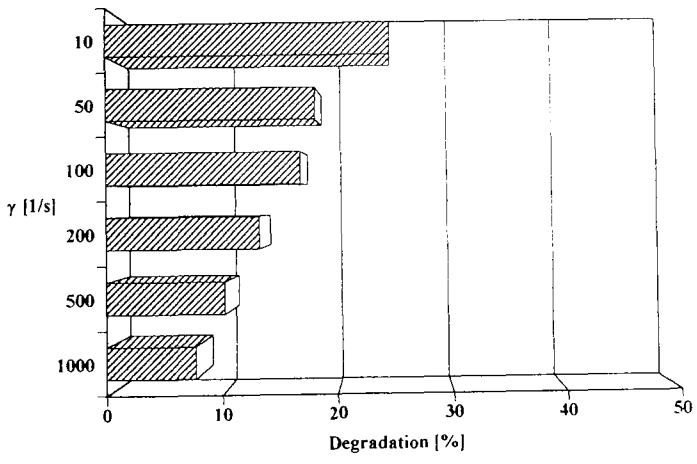

(f) 0.1% EZ1

Figure 4.15 *Degradation Levels for all Test Fluids over 7 Days (continued overleaf).*

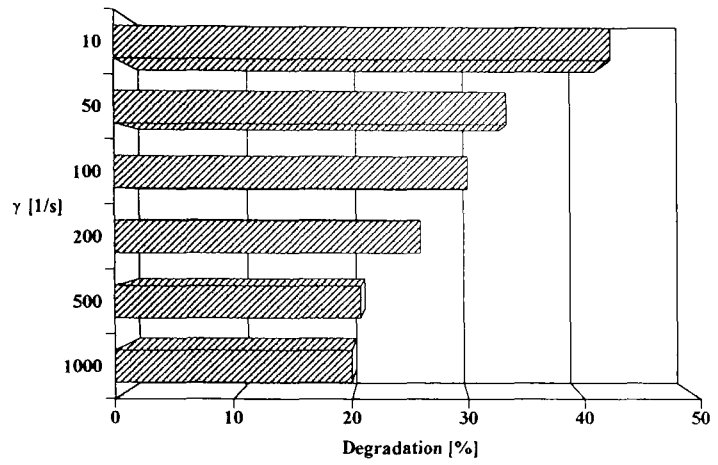

(g) 0.1385% Carbopol

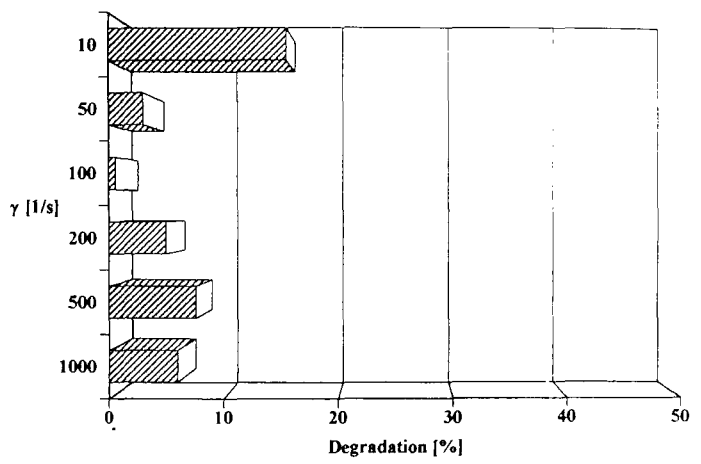

(h) 0.125% PAA

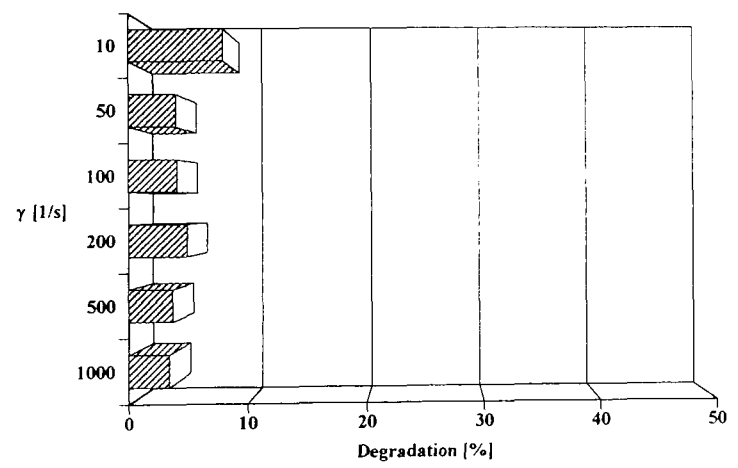

(h) 0.2% PAA

NOTE

For a given shear rate, $\dot{\gamma}$:

$$\text{Degradation Level} = \left(\frac{\eta(\dot{\gamma})_{\text{Fresh Sample}} - \eta(\dot{\gamma})_{\text{n Days Old}}}{\eta(\dot{\gamma})_{\text{Fresh Sample}}} \right) \times 100\%$$

Figure 4.15 *Degradation Levels for all Test Fluids over 7 Days.*

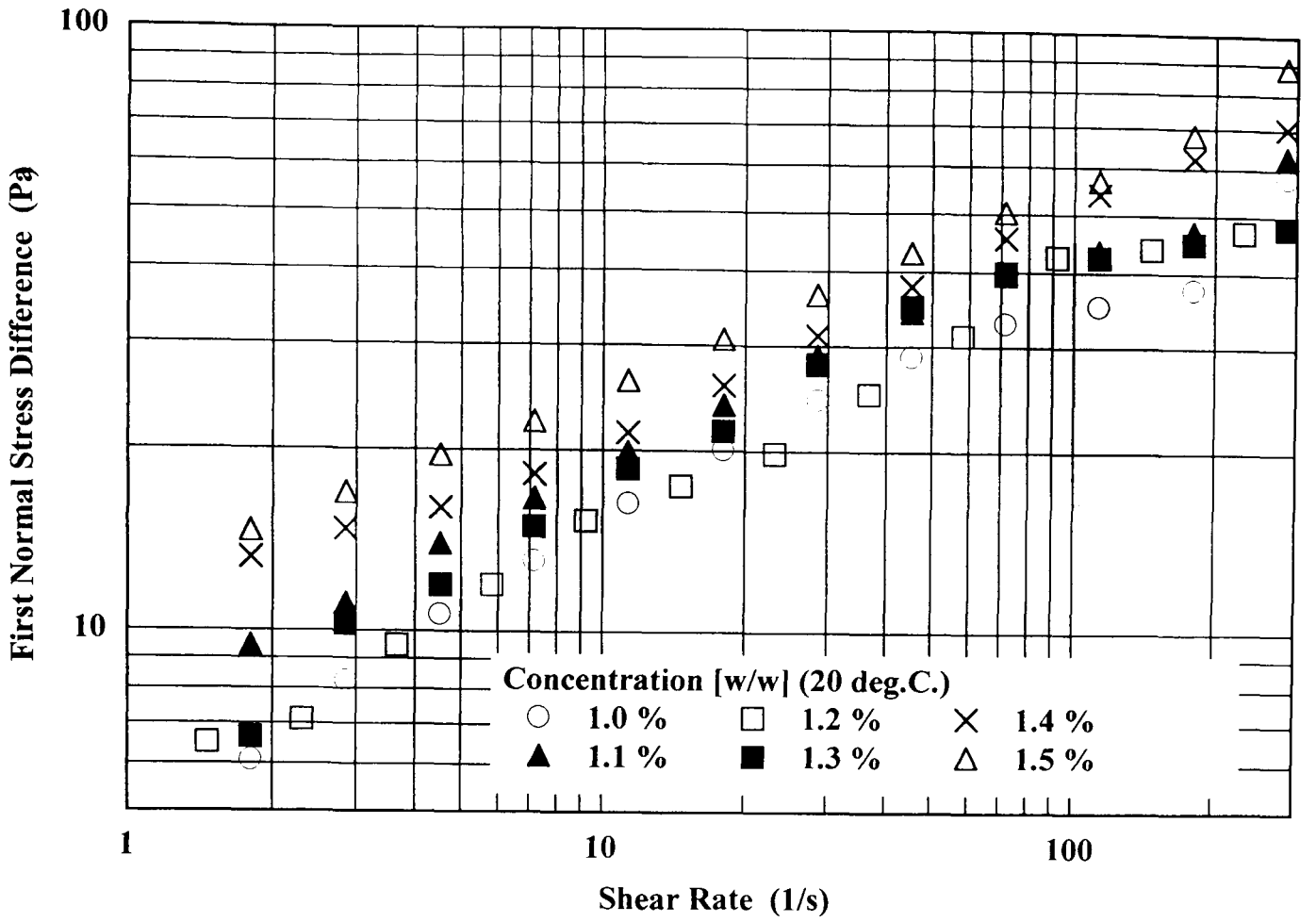

Figure 4.16(a) *First Normal Stress Difference Against Shear Rate for Xanthan Gum.*

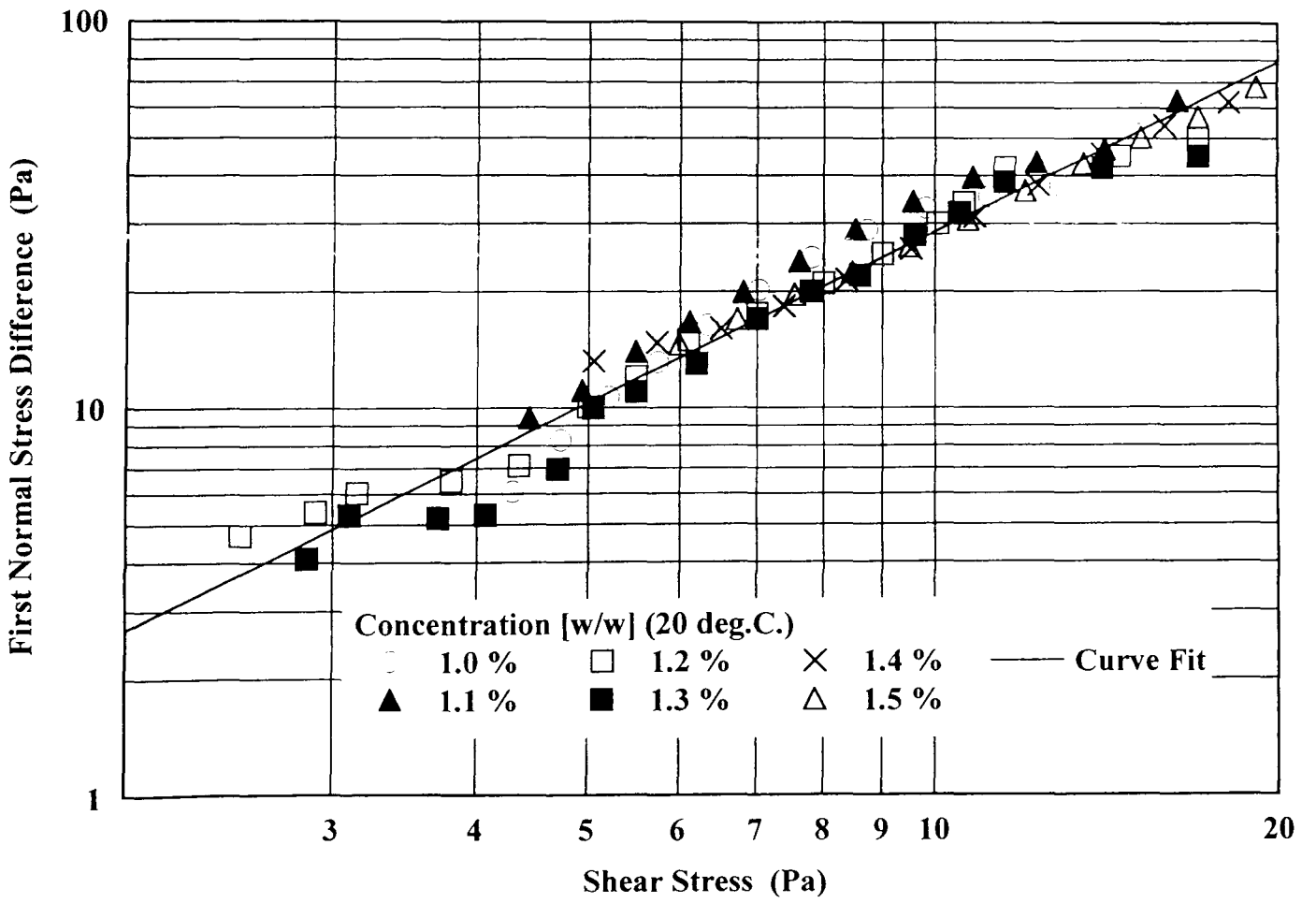

Figure 4.16(b) *First Normal Stress Difference Against Shear Stress for Xanthan Gum.*

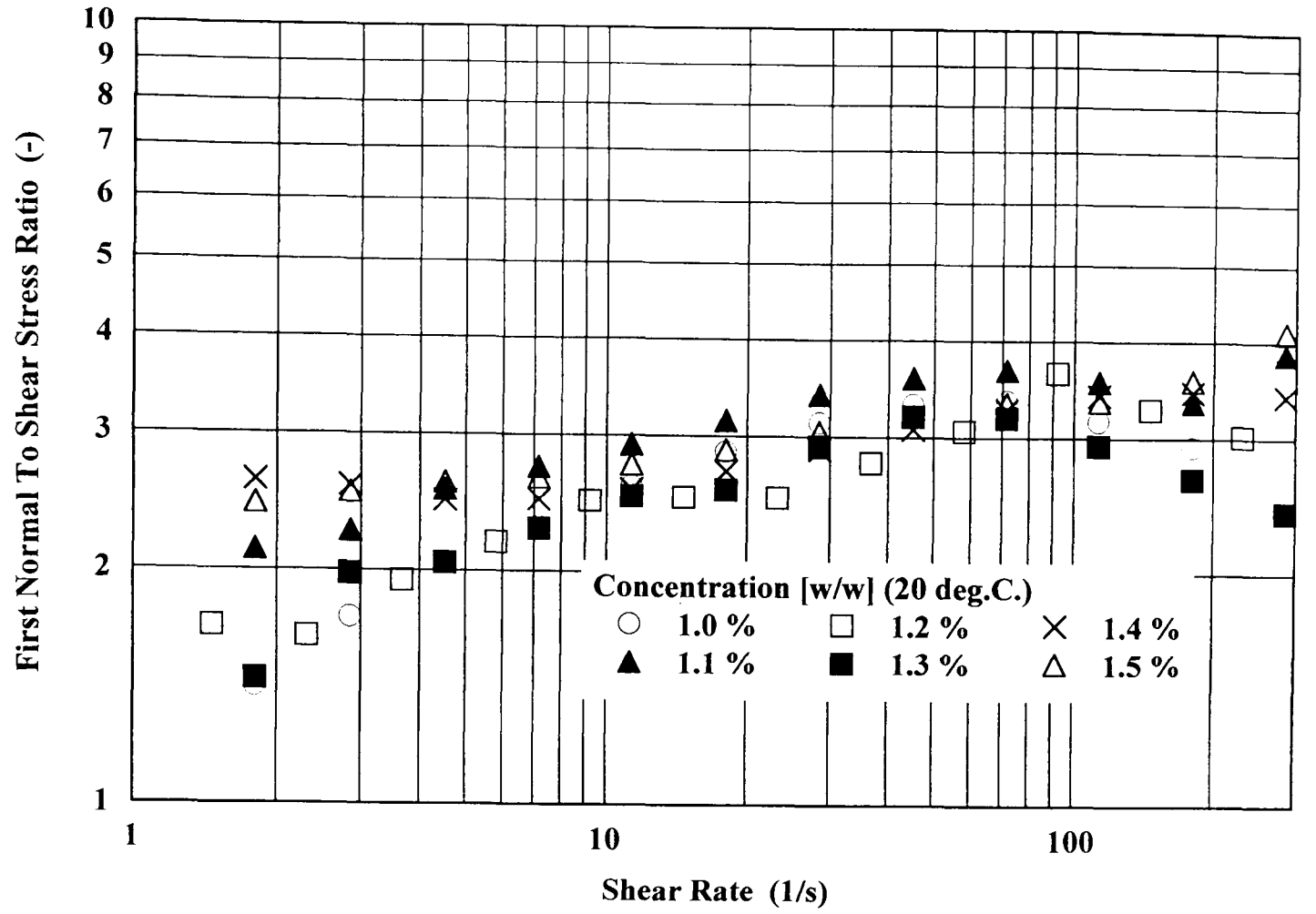

Figure 4.16(c) *First Normal Stress Difference To Shear Stress Ratio Against Shear Rate for Xanthan Gum.*

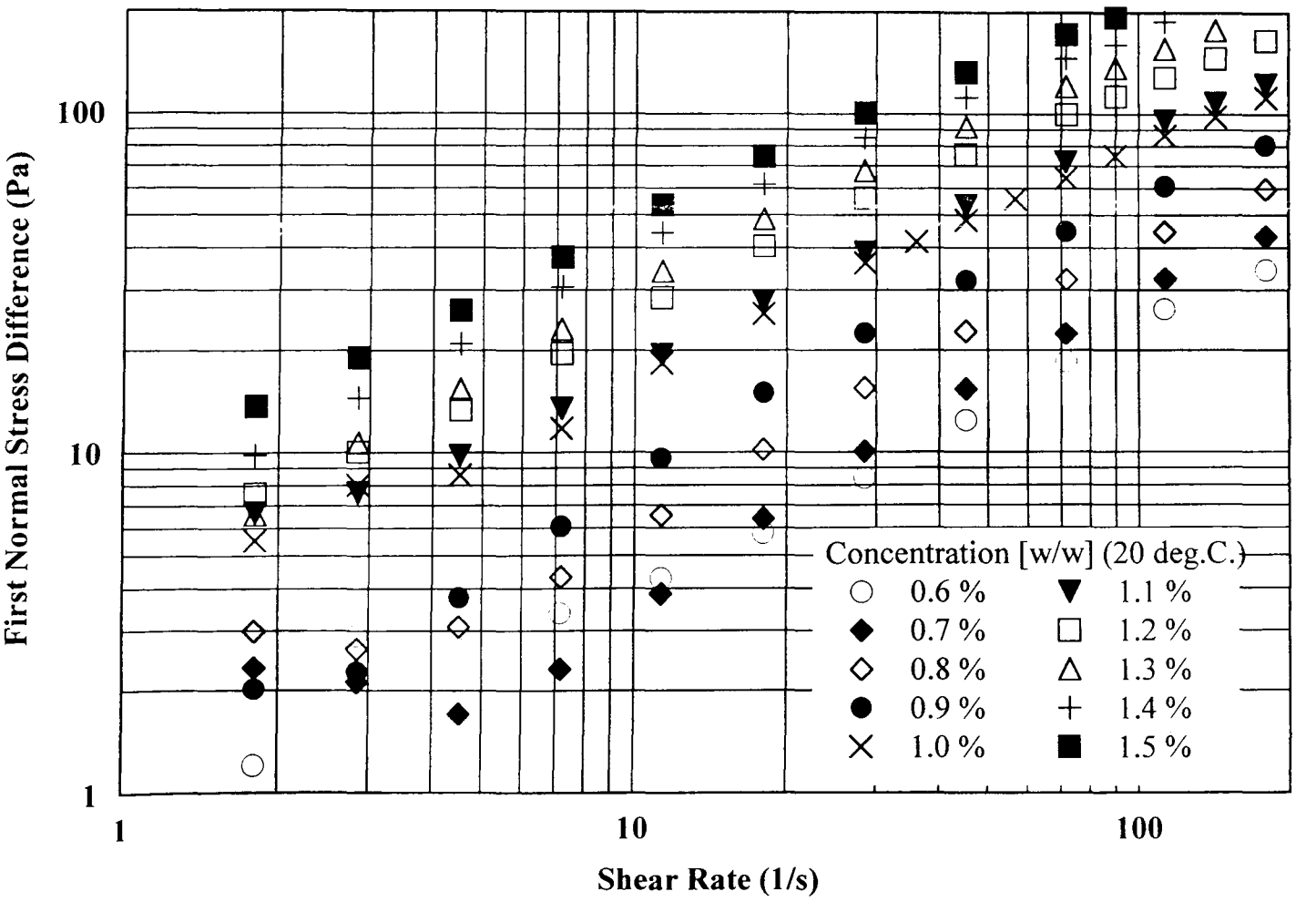

Figure 4.17(a) *First Normal Stress Difference Against Shear Rate for CMC.*

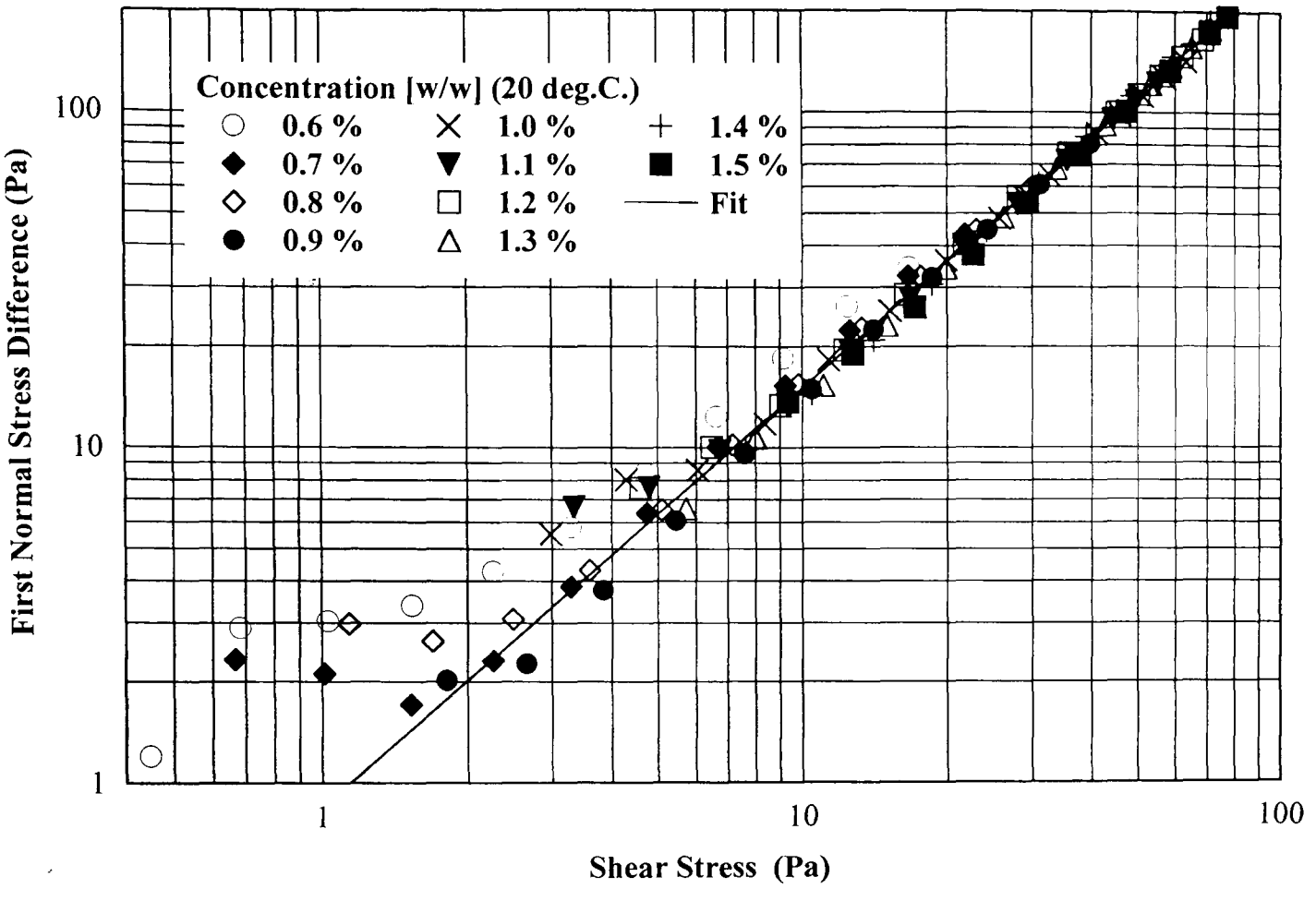

Figure 4.17(b) *First Normal Stress Difference Against Shear Stress for CMC.*

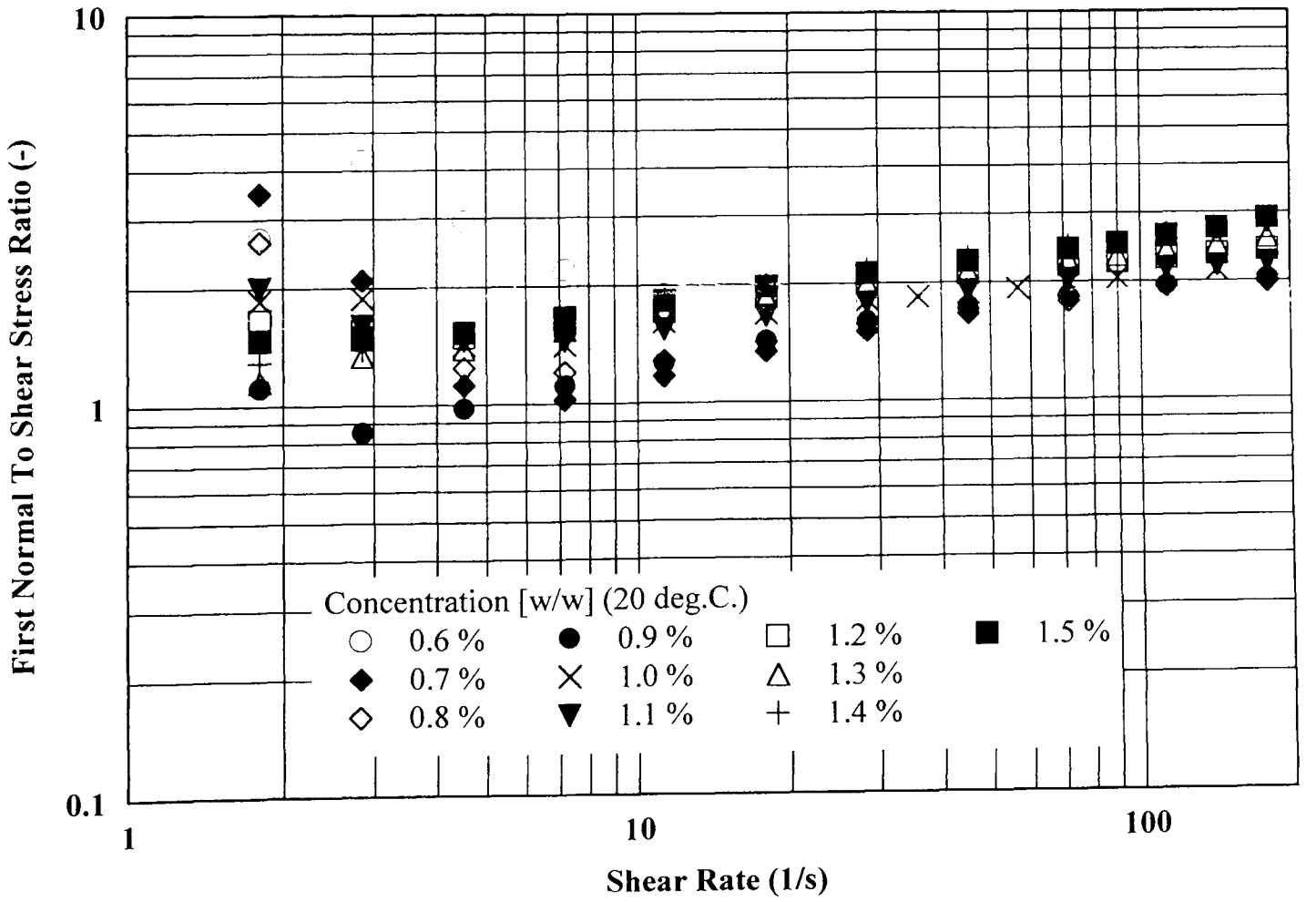

Figure 4.17(c) *First Normal Stress Difference To Shear Stress Ratio Against Shear Rate for CMC.*

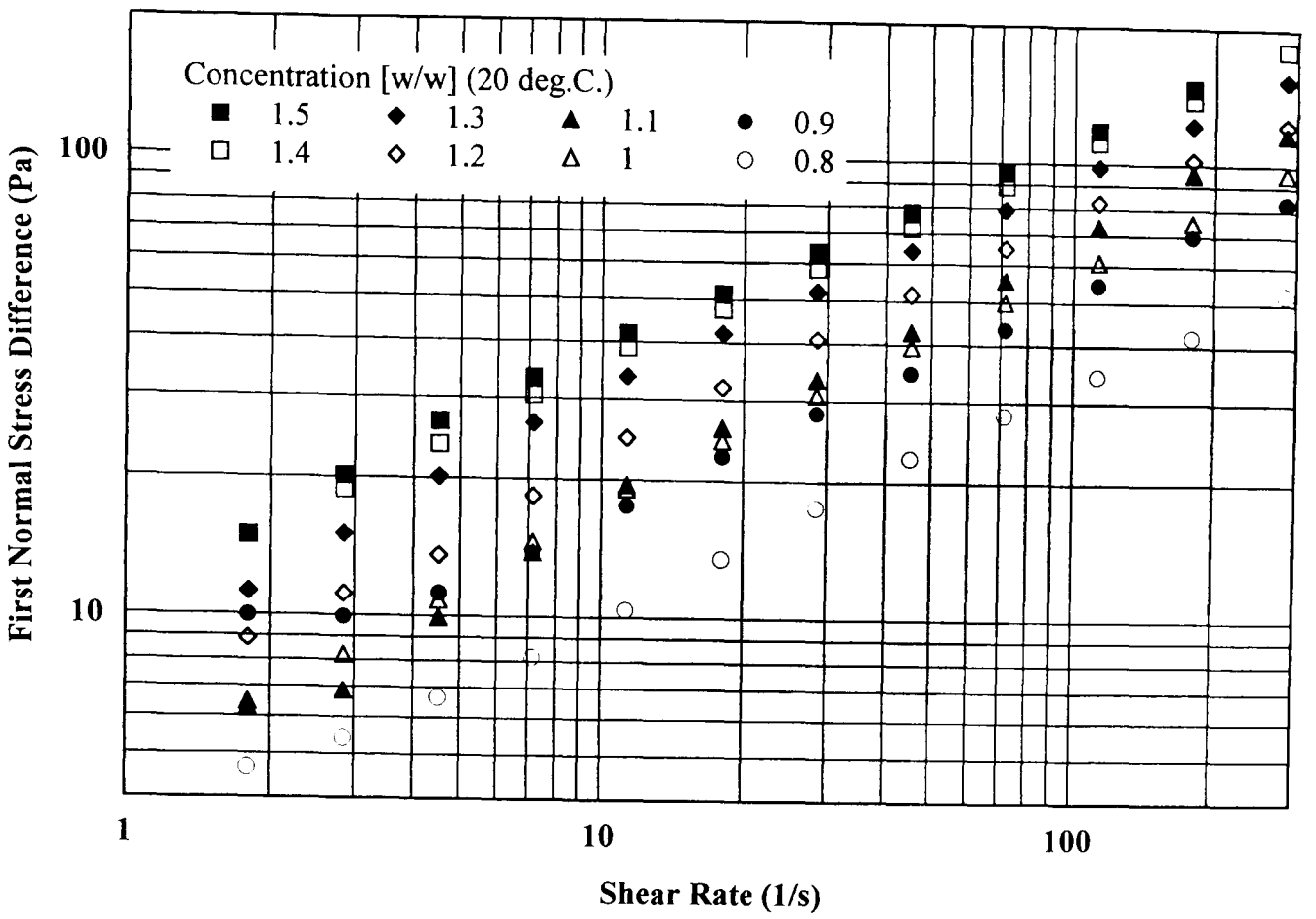

Figure 4.18(a) *First Normal Stress Difference Against Shear Rate for XG/CMC Blend.*

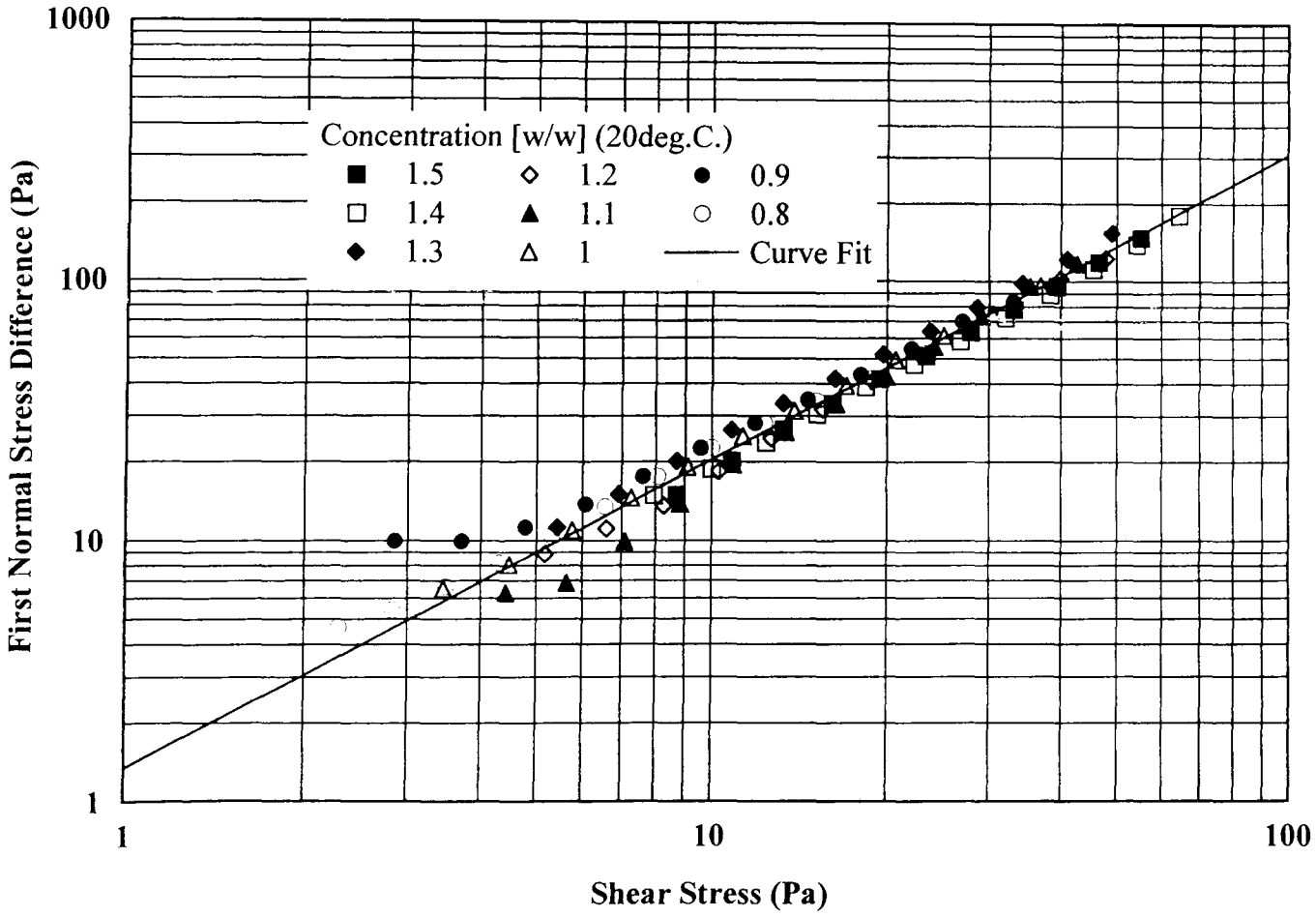

Figure 4.18(b) *First Normal Stress Difference Against Shear Stress for XG/CMC Blend.*

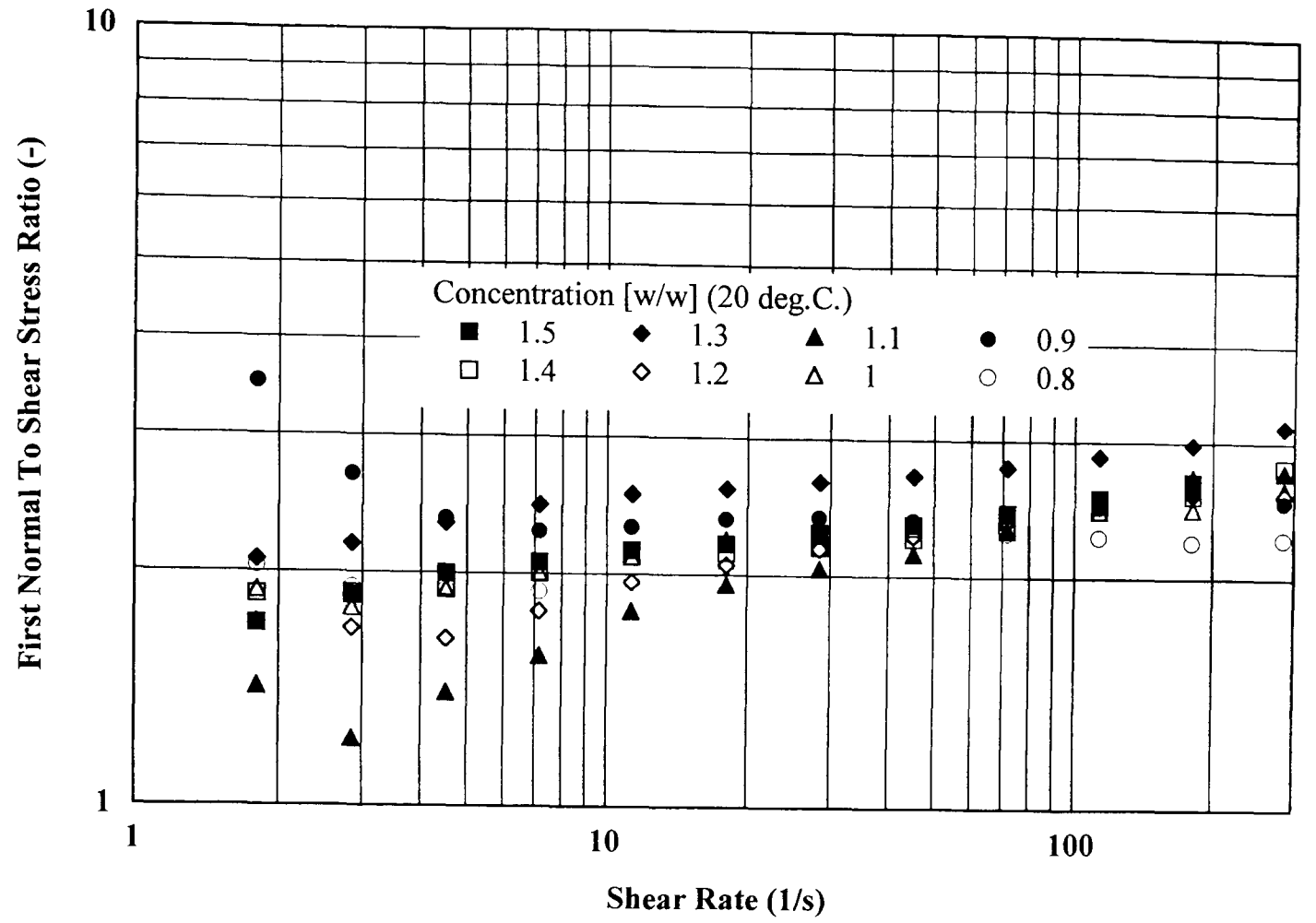

Figure 4.18(c) *First Normal Stress Difference To Shear Stress Ratio Against Shear Rate for XG/CMC Blend.*

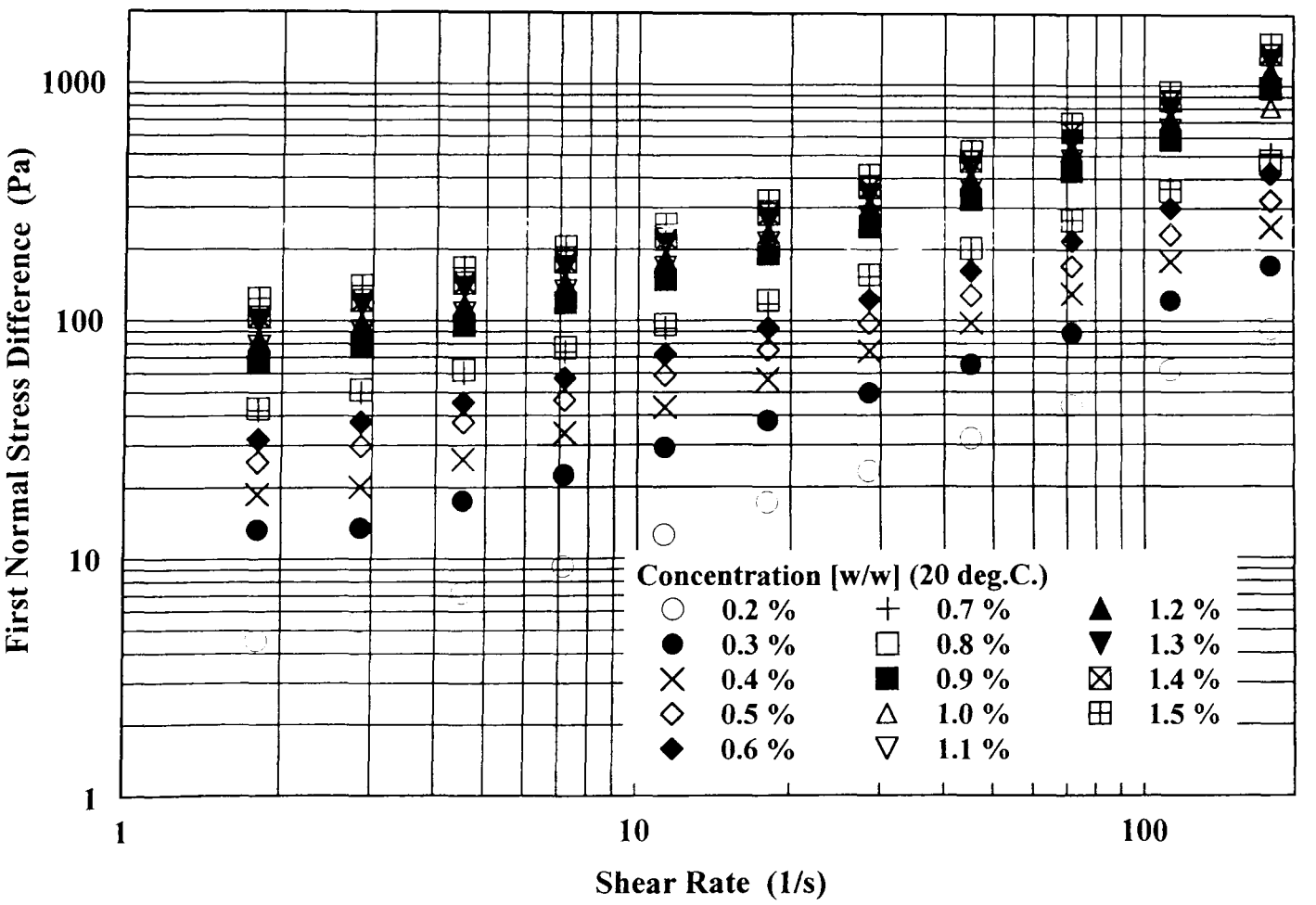

Figure 4.19(a) *First Normal Stress Difference Against Shear Rate for PAA.*

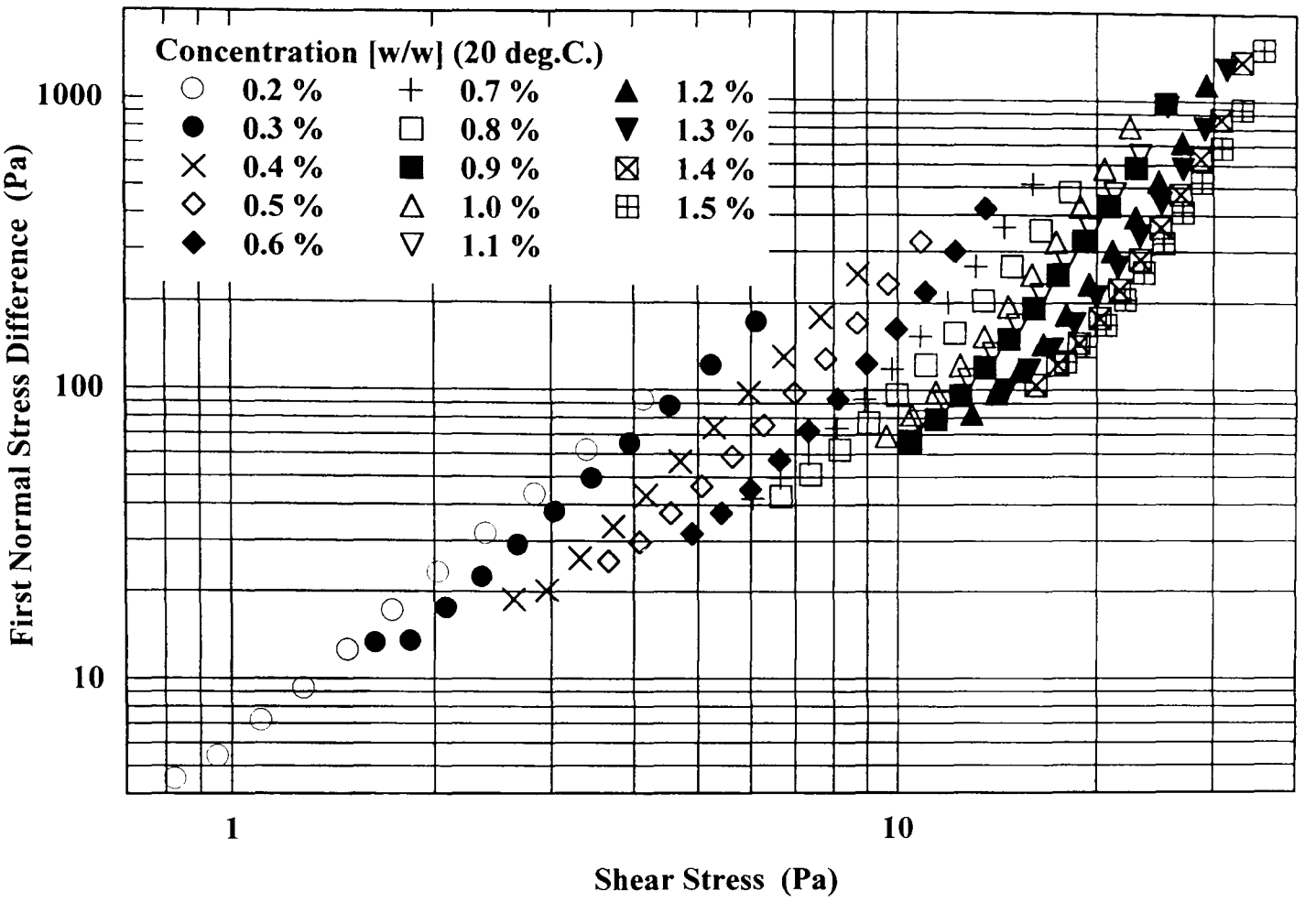

Figure 4.19(b) *First Normal Stress Difference Against Shear Stress for PAA.*

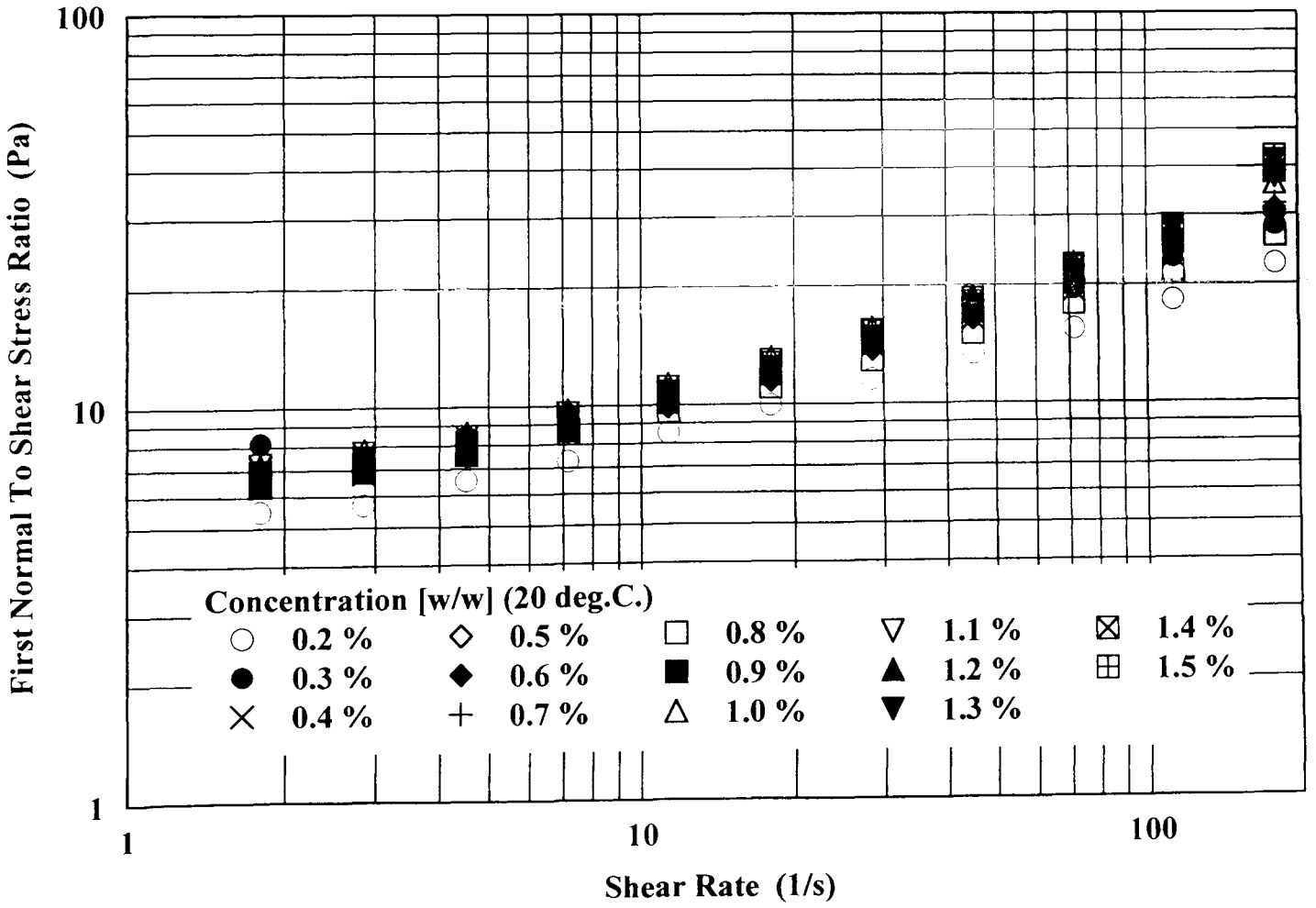

Figure 4.19(c) *First Normal Stress Difference To Shear Stress Ratio Against Shear Rate for PAA.*

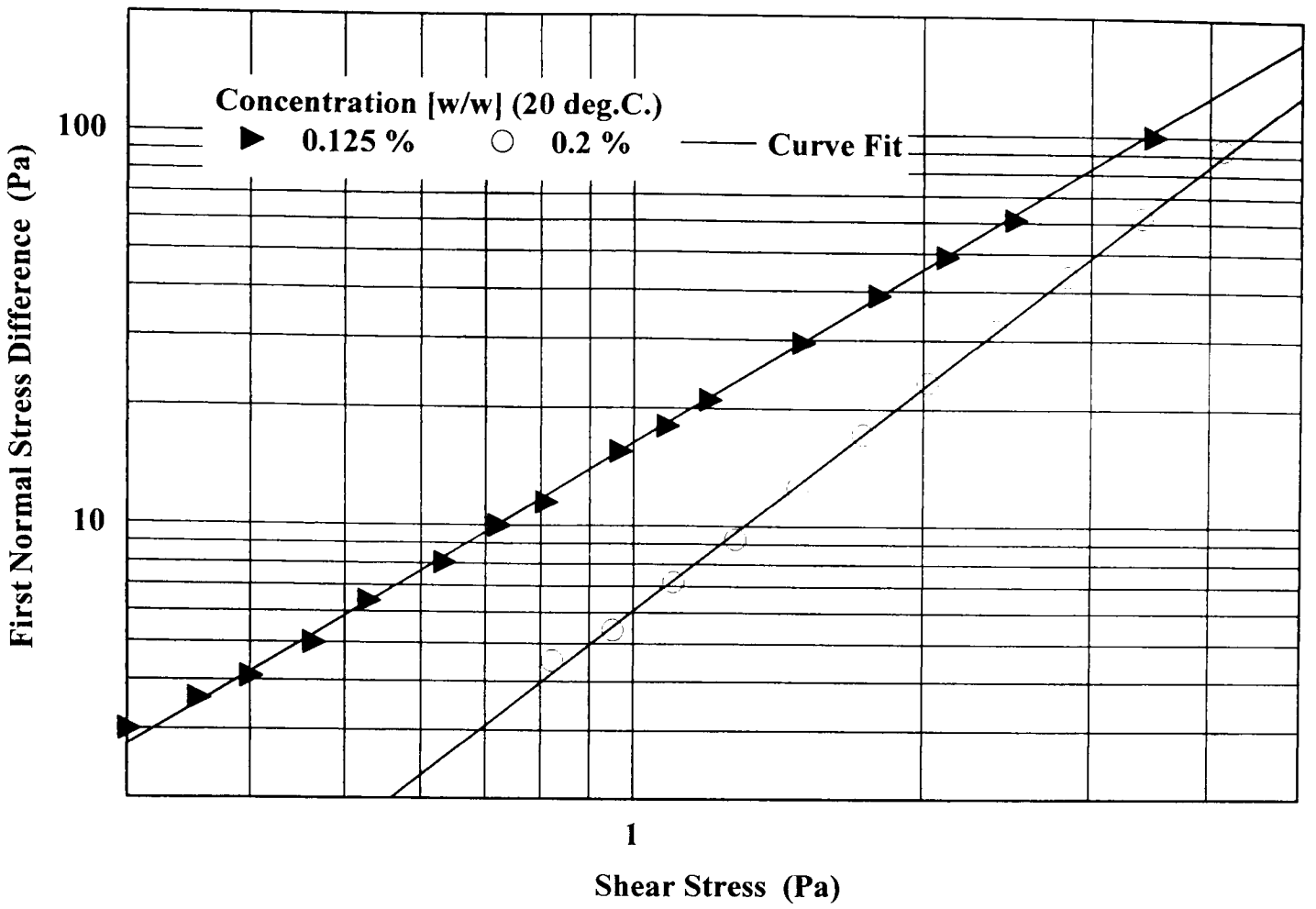

Figure 4.19(d) *First Normal Stress Difference Against Shear Stress for 0.125% and 0.2% PAA.*

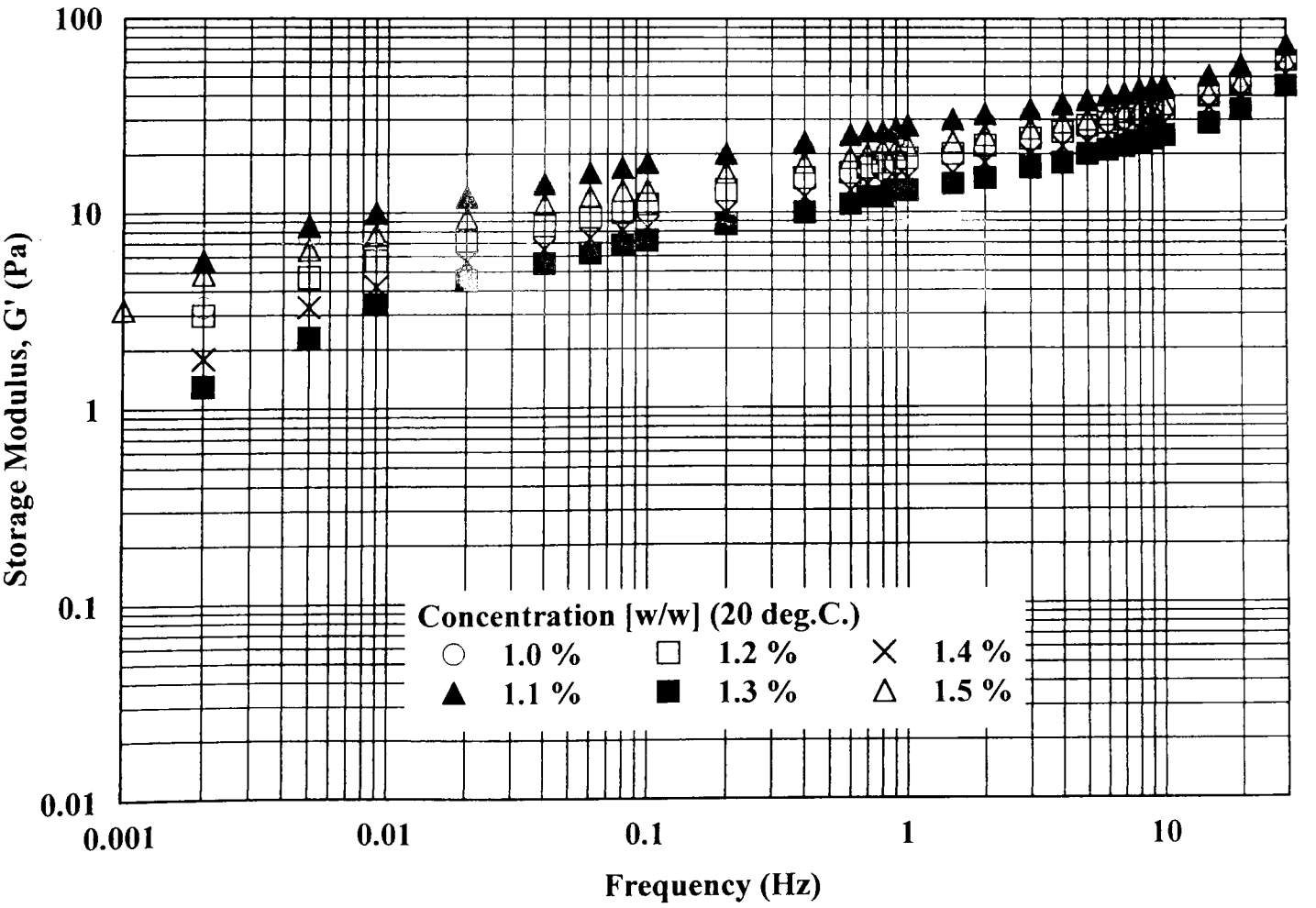

Figure 4.20 *Storage Modulus versus Frequency of Oscillation for XG.*

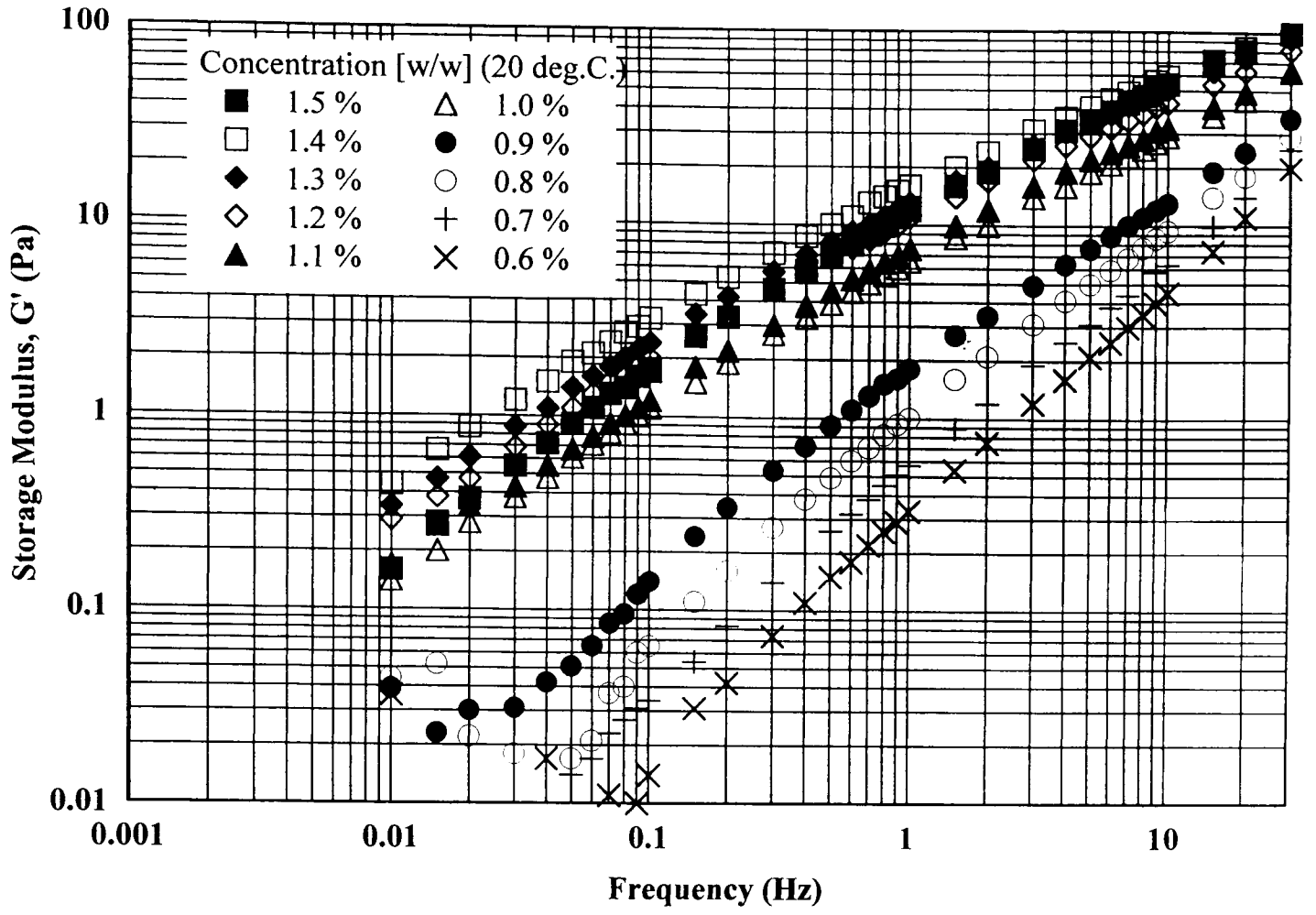

Figure 4.21 *Storage Modulus versus Frequency of Oscillation for CMC.*

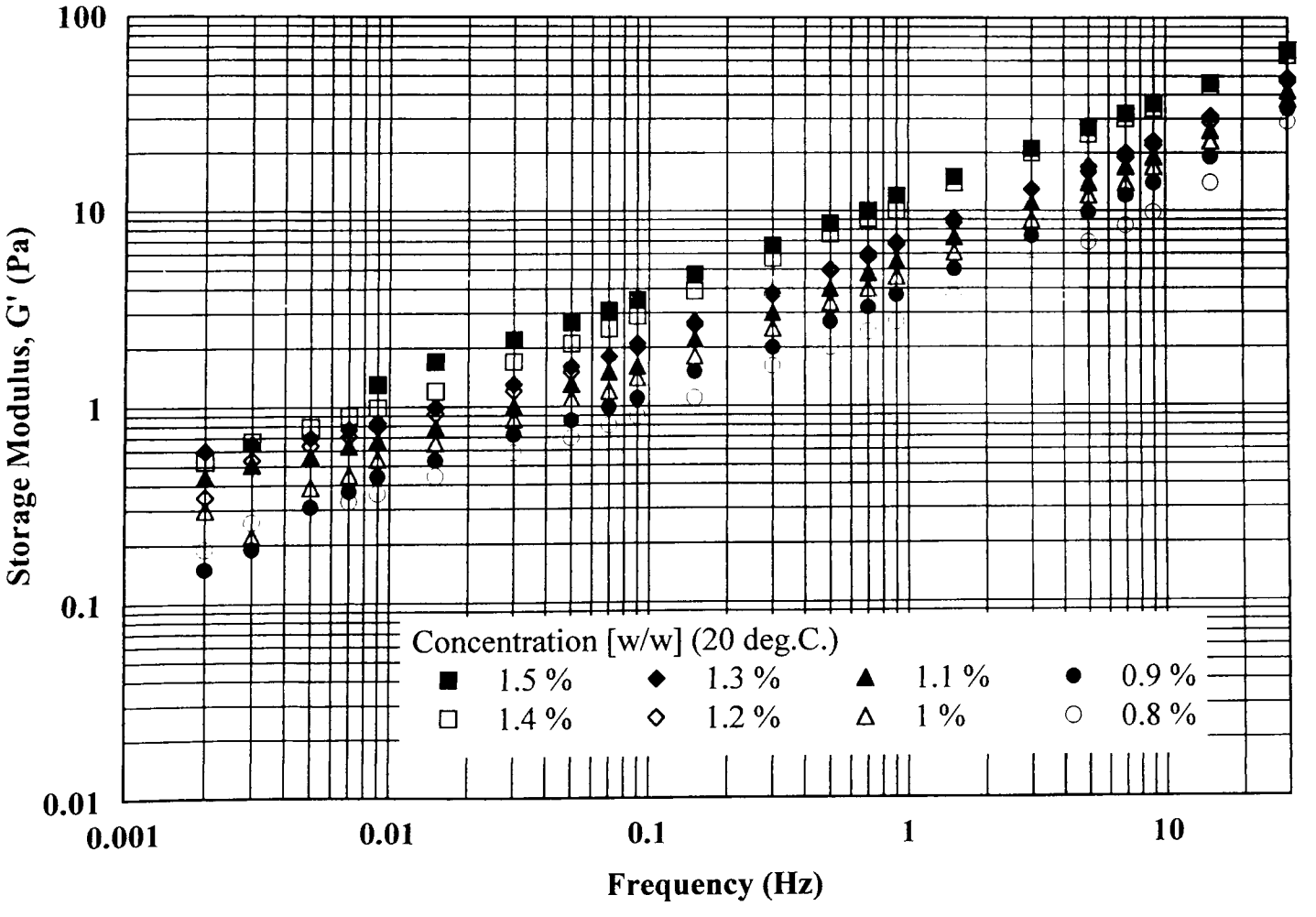

Figure 4.22 *Storage Modulus versus Frequency of Oscillation for XG/CMC Blend.*

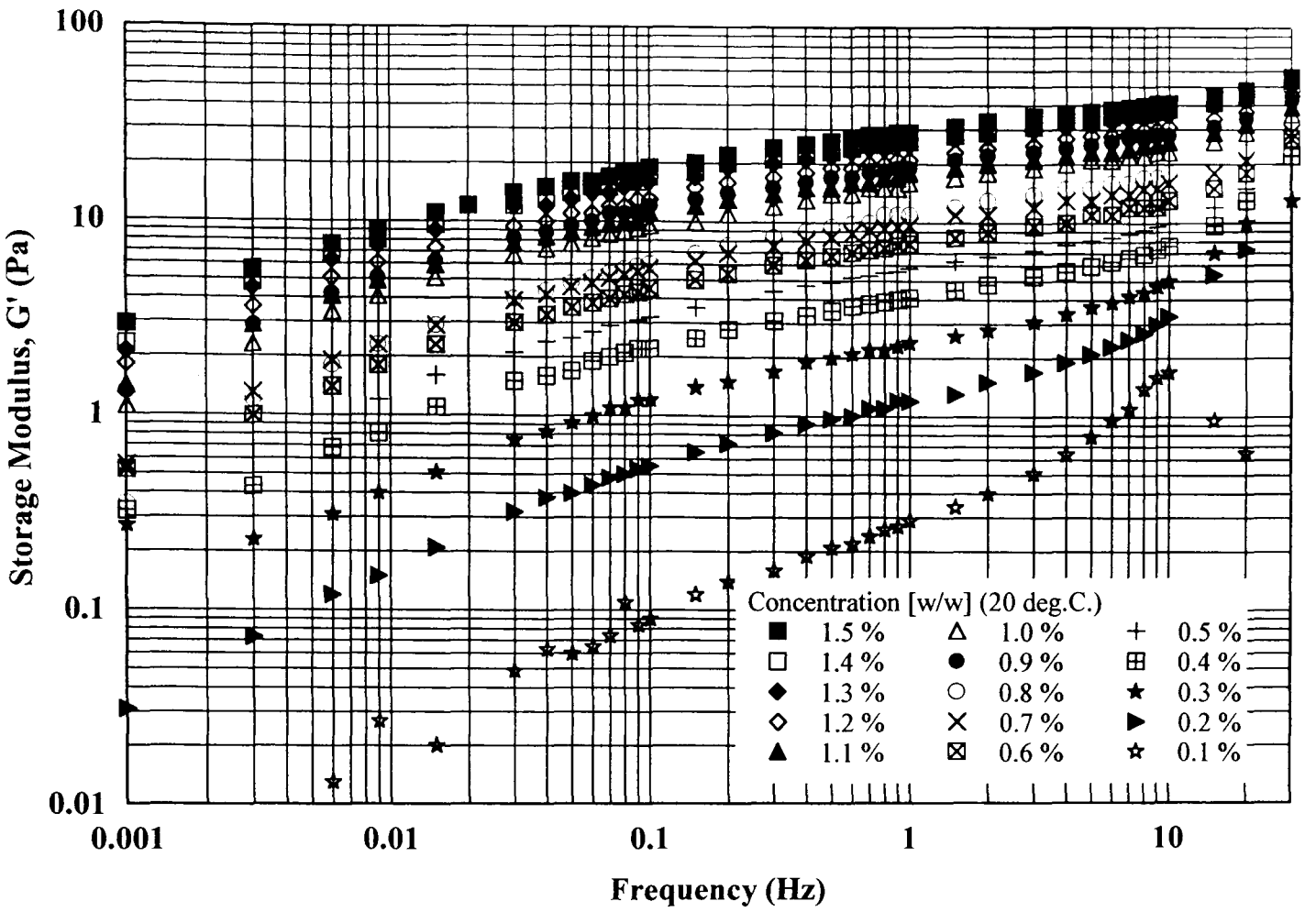

Figure 4.23 *Storage Modulus versus Frequency of Oscillation for PAA.*

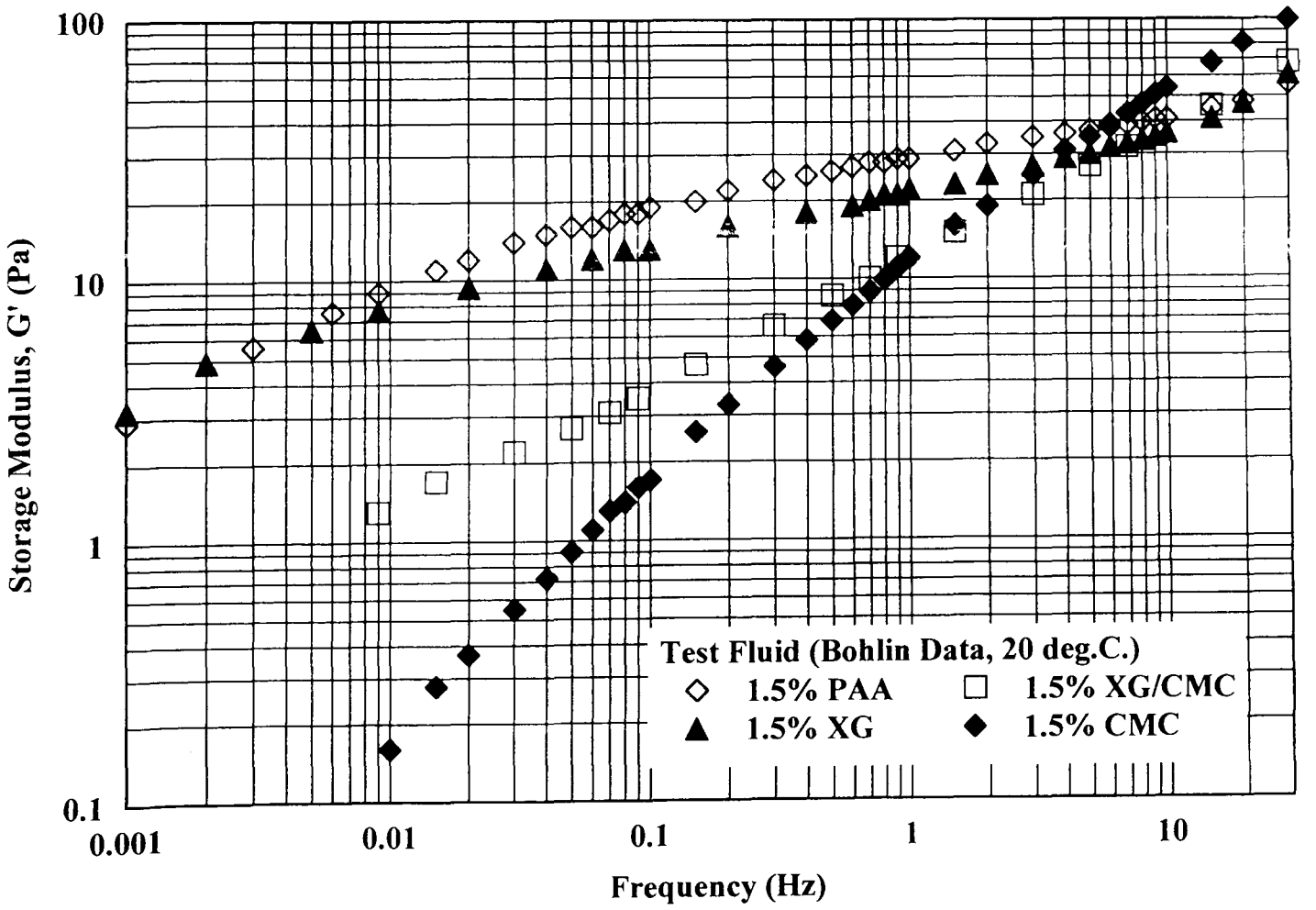

Figure 4.24 *Storage Modulus versus Frequency of Oscillation for 1.5% XG, 1.5% CMC, 1.5% XG/CMC Blend and 1.5% PAA.*

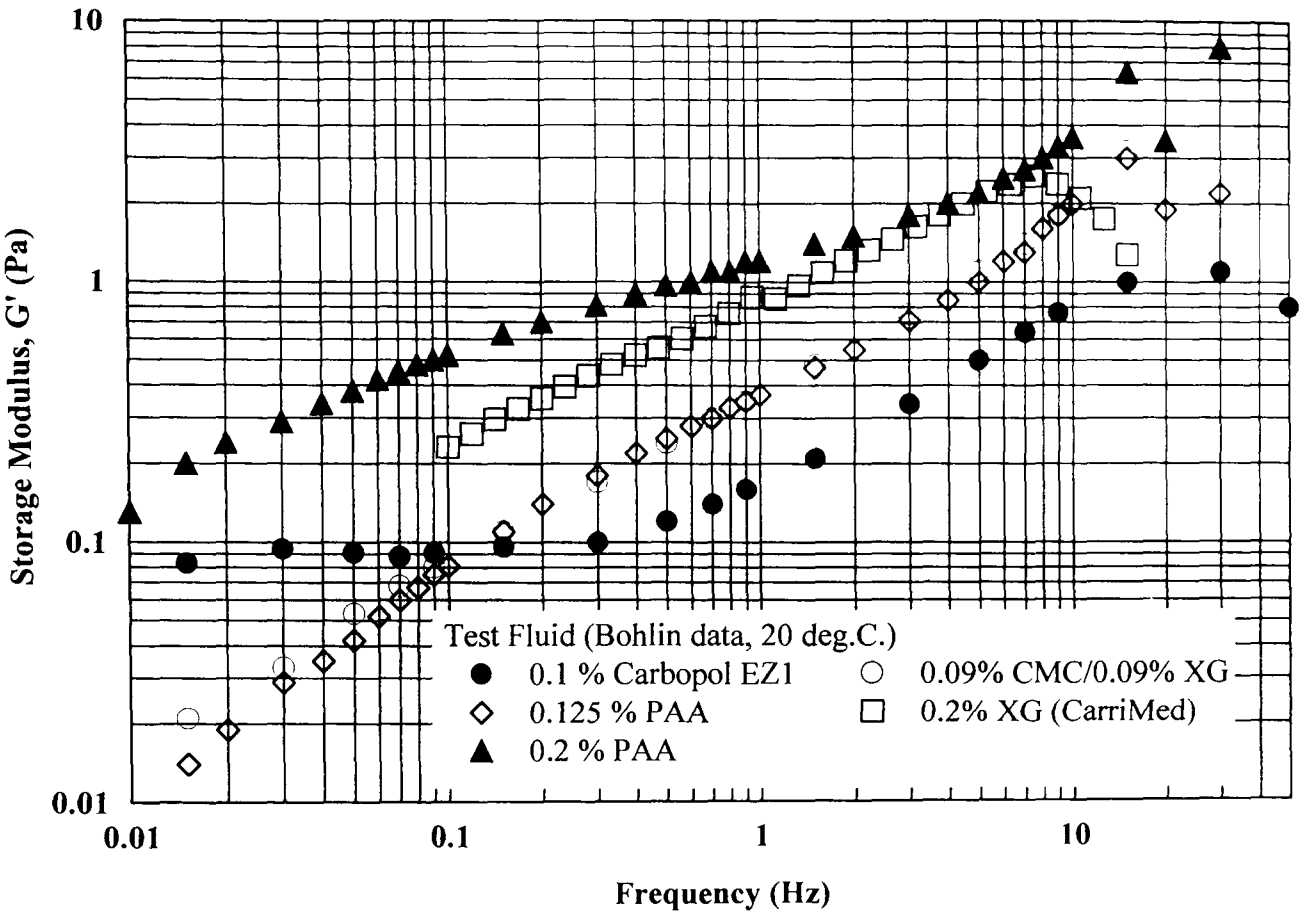

Figure 4.25 *Storage Modulus versus Frequency of Oscillation for 0.2% XG, 0.09% CMC/0.09% XG, 0.125% PAA, 0.2% PAA and 0.1% Carbopol EZ1.*

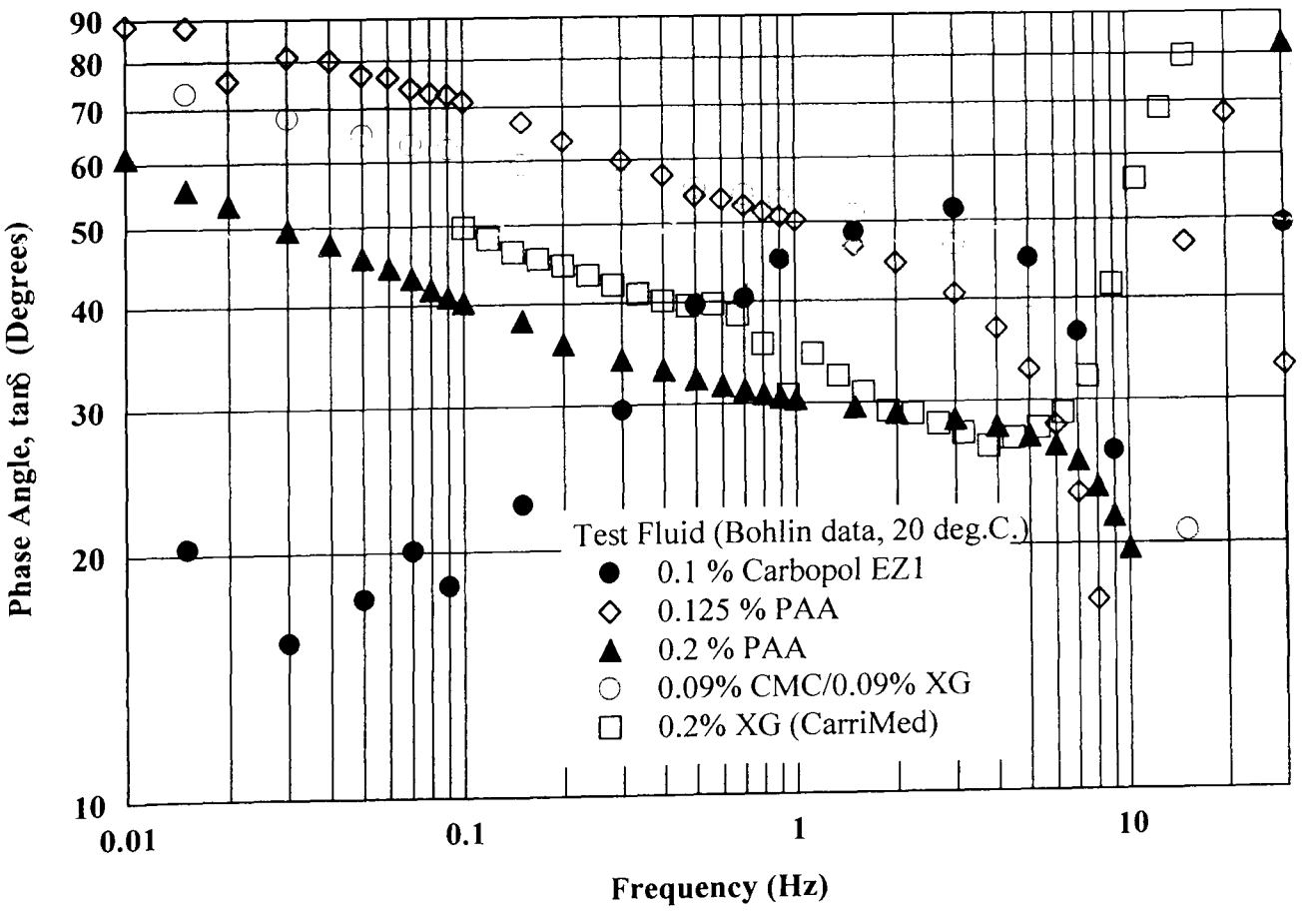

Figure 4.26 *Phase Angle versus Frequency of Oscillation for 0.2% XG, 0.09% CMC/0.09% XG, 0.125% PAA, 0.2% PAA and 0.1% Carbopol EZ1.*

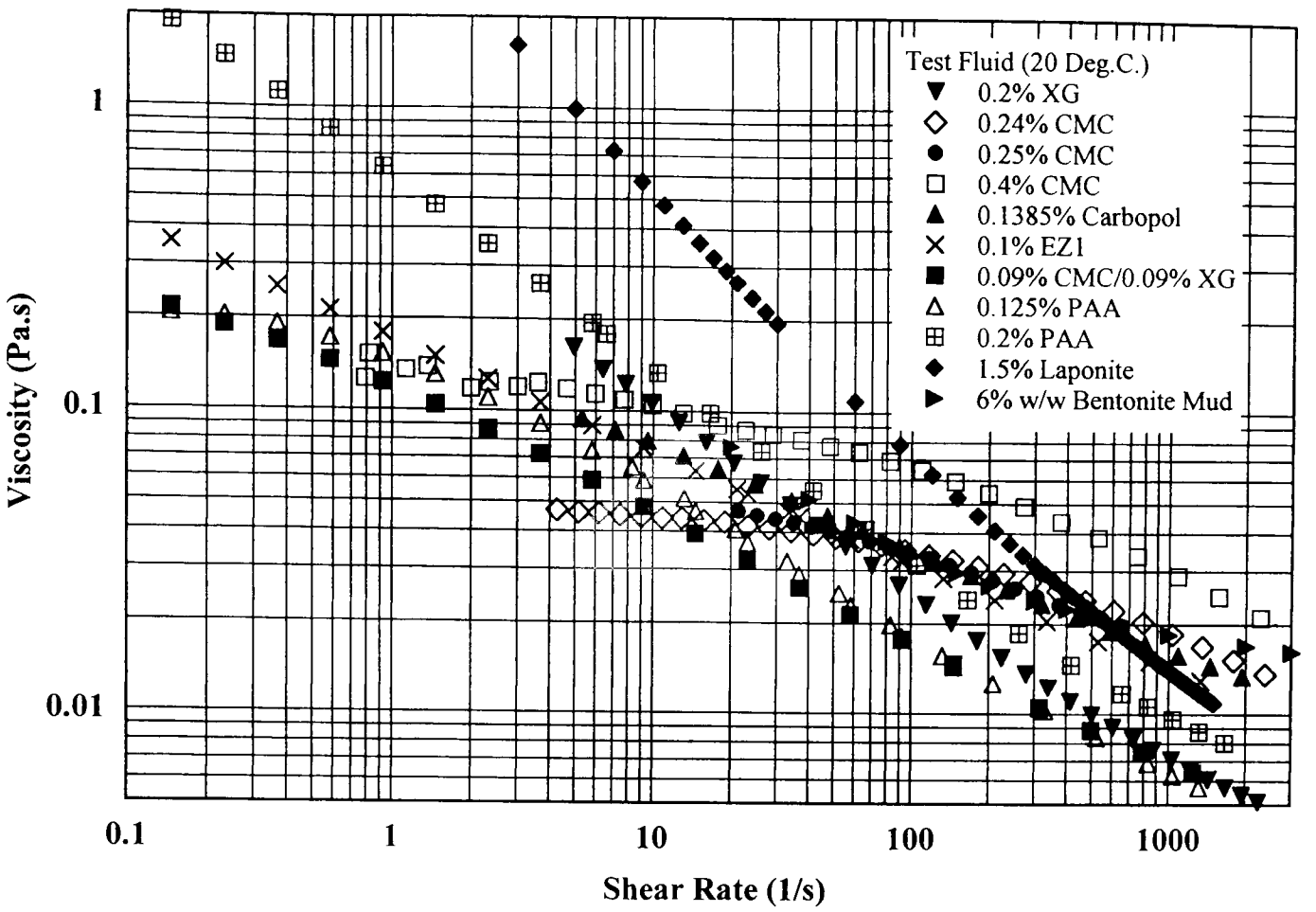

Figure 4.27 *Viscometric Data for all Test Fluids.*

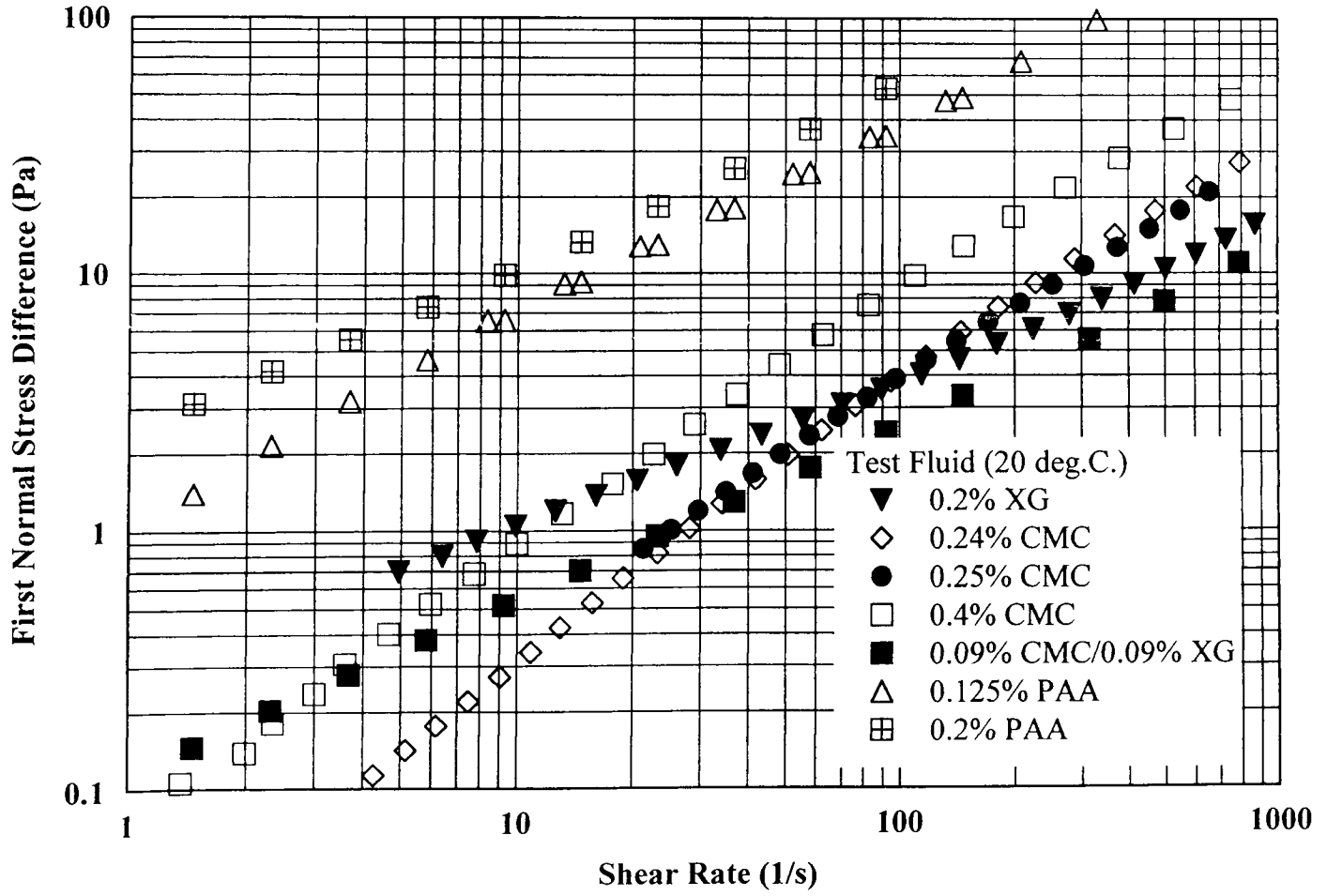

Figure 4.28 *First Normal Stress Difference versus Shear Rate for Working Test Fluids.*

5.0 PIPE FLOW - RESULTS AND DISCUSSION

Distributions of mean axial velocity, axial, tangential and radial turbulence intensities together with friction factor *versus* Reynolds number (*f*-Re) data have been collected for ten non-Newtonian fluids. Similar data has also been collected for two Newtonian test fluids for comparison reasons, in particular with reference to established theories and measurements available from literature. The data are representative of fully-developed laminar, transitional and turbulent pipe-flow conditions.

The first section of this chapter describes the *f*-Re data for all test fluids, which is then followed by a discussion on the identification of transitional and fully developed turbulent flow conditions. The remaining sections analyse the pipe flow measurements of all test fluids. Their analysis have been categorised into velocity distribution data, universal law of the wall representations, turbulence intensities and drag reduction. Finally, using the rheological data from the previous chapter, an attempt is made to correlate a measurable function of rheology with the hydrodynamic pipeflow behaviour for these fluids.

The pipe flow results for Laponite have warranted a separate discussion in Chapter 6.0 as its flow characteristics showed marked deviations compared with the working fluids discussed in this chapter and hence a different analysis was required.

5.1 Friction Factor *versus* Reynolds Number

5.1.1 Newtonian Fluid

The friction factor *versus* Reynolds number behaviour for 60% w/w aqueous glucose syrup, has been illustrated in **Figure 5.1**. The *f*-Re data in both the laminar and turbulent regime follow their respective theoretical relationships with a clear demarcation at transition, which is also confirmed by an abrupt increase in the axial turbulence intensities measured 10mm (y/R=0.8) from the inner wall of the test-section.

The definition for friction factor f and pipe Reynolds number Re used here is as follows:

$$f = \frac{2\tau_S}{\rho U^2} \tag{5.1}$$

and

$$\mathrm{Re} \equiv \frac{\rho UD}{\eta} \tag{5.2}$$

where ρ is the liquid density, U is the mean bulk velocity, D is the internal diameter of the pipe, η is the dynamic viscosity at the pipe wall obtained directly from the viscometric flow curve and τ_S is the wall shear stress as previously defined in **Eq. (3.1)**.

For turbulent flow, the relationship between friction factor and Reynolds number can be expressed using the Blasius equation [McComb (1990)]:

$$f_B = 0.079\mathrm{Re}^{-1/4} \tag{5.3}$$

Studies have shown that at high values of Reynolds number (>100,000), Blasius' equation deviates progressively more from the results of previous measurements [Schlichting (1978)]. Therefore, the Kàrmàn-Nikuradse equation [McComb (1990)], which maintains good agreement with previous data at all values of Reynolds number, could be used:

$$\frac{1}{\sqrt{f/2}} = 2.46ln(\mathrm{Re}\sqrt{f/2}) + 0.30 \tag{5.4}$$

However, the limiting Reynolds number used in this study (Re<60,000) ensured the validity of using the simple Blasius correlation, which closely represented the Newtonian experimental data as shown in **Figure 5.1**.

The transition from laminar to turbulent flow appears to occur for 2,000<Re<3,000, though definitive values require further investigation. Patel and Head (1969) clarified the difficulty in defining the boundaries between the laminar and turbulent flow regimes, using mean velocity profiles and wall shear stresses. They found that the onset of fully developed turbulent flow varied for pipes and channels, with the onset of turbulent flow in pipes characterised by a rapid adjustment of the *f*-Re data to the accepted Blasius friction law [**Eq. (5.3)**].

5.1.2 Non-Newtonian Fluids

From a practical engineering viewpoint, it is the friction factor *versus* Reynolds number behaviour for non-Newtonian fluids, which is of greatest interest as a result of drag reduction. The key unresolved problem is to be able to relate the flow rate to the pressure drop of the liquid with a measurable rheometrical function through a pipe of a specific diameter. This correlation has been attempted and is discussed in Section 5.7.

The plots of friction factor *versus* Reynolds number for all non-Newtonian test fluids are illustrated in **Figures 5.2 - 5.10**. These illustrations clearly indicate that drag reduction in the turbulent flow regime is dependent on fluid type and Reynolds number.

The definition of drag reduction DR can be expressed as the reduction in skin friction in turbulent flow by the addition of additives, which results in the following expression [Lumley (1969)]:

$$\mathrm{DR} = \left(\frac{f_B - f}{f_B} \right) \times 100\% \tag{5.5}$$

where f_B is the Newtonian friction factor determined from **Eq. (5.3)** and f is the measured friction factor (see **Eq. (5.1)**) of the non-Newtonian fluid.

All *f*-Re data indicated good agreement with theoretical predictions for a power law fluid in the laminar flow regime (except Laponite as discussed in Chapter 6), with clear evidence of drag reduction occurring in turbulent flow.

The transition from laminar to turbulent flow was smooth in contrast to the abrupt change in data observed for the Newtonian case (see **Figure 5.1**). However, for XG (**Figure 5.2**), XG/CMC (**Figure 5.6**) and PAA (**Figures 5.7** and **5.8**), the *f*-Re data did not provide a clear indication of transition. In order to gain more insight into the mechanism for transition, measurements of the amplitude of the axial velocity component u′ were carried out during the flow test. These velocity fluctuations were non-dimensionalised with the bulk velocity U and superimposed on all *f*-Re data as also presented in **Figures 5.2 - 5.10**. This representation of data clearly establishes the onset and termination point of transition as will be discussed next, in Section 5.2.

The analysis of the drag reduction (DR) levels for all test fluids is discussed in more detail in Section 5.6.

5.2 Transition Identification

It is frequently impossible to detect from an *f*-Re curve the Reynolds number corresponding to transition from laminar to turbulent flow for non-Newtonian fluids. In fact, for strong drag-reducing polymers, such as 0.2% PAA (see **Figure 5.8**), it is not apparent that transition has occurred, therefore an alternative analysis is required to identify the onset of transitional and turbulent flow. For this study, the suggestion of Park *et al.* (1989) has been used, in that the axial-velocity fluctuation turbulence intensity u′ measured at a near-wall location provides a sensitive indicator of laminar/turbulence transition.

Figures 5.11 illustrates an example of u′/U *versus* Re for 0.125% PAA measured at various distances from the inner-wall (2mm, 5mm, 10mm, 20mm and 30mm). Under laminar flow conditions (Re = 700 and 1,600), the level of axial turbulence intensity increases as the measurement point proceeds towards the centre of the pipe. However,

as will be discussed in Section 5.5, the maximum level of turbulence intensity (u′/U) under fully developed turbulent flow conditions occur at distances closer to the pipe wall for increasing Reynolds numbers. This trend has been identified for all test fluids. Hence monitoring axial turbulence intensity levels at 80% of the pipe radius (y = 10mm) provided a suitable location that was sensitive to transitional and turbulent flow identification.

Figure 5.12 shows the u′/U *versus* Re behaviour for all test fluids based on the *f*-Re data discussed in Section 5.1 (based on a 0.04 scaled increment between the divisions shown on the y-axis). In spite of a considerable degree of scatter in the data plotted, also evident in the paper of Park *et al.*, it is clear that transition to turbulent flow does occur in all cases.

Table 5.1 summarises the data for each test fluid in terms of two Reynolds numbers: the first is used to identify the onset of transition seen as a noticeable change in turbulence activity (u′/U) and is denoted as Re_1; the subsequent 'peak' in u′/U is denoted as Re_2, which corresponds to the onset of turbulent flow qualitatively assessed from the trend in data. The generally accepted values for a Newtonian fluid are Re_1 = 2,000 and Re_2 = 3,000 (see **Figure 5.1**). Thus by comparison, this suggests that the onset of turbulent flow is indeed delayed to higher Reynolds numbers for non-Newtonian fluids.

From **Table 5.1**, it is evident that the onset of turbulent flow (Re_2) is influenced by polymer concentration i.e. a larger concentration of similar fluid tends to delay the onset of turbulent flow to higher Reynolds numbers. What is also apparent is that the onset of turbulent flow is slightly but progressively delayed in the sequence 0.24% CMC, 0.1% Carbopol EZ1, 0.14% Carbopol 934, 0.25% CMC, 0.09% CMC/0.09% XG, 0.125% PAA and 0.2% PAA by a factor of about two-to-three in Reynolds number i.e. similar to the low shear rate ranking of the elasticity. Also apparent is that the peak level of u′/U is very much the same in all cases.

The corresponding DR values for each test fluid at Re_2 have also been given in **Table 5.1**, from which, by comparison, a correlation between the level of drag reduction DR and the onset of turbulent flow Re_2 has been established.

In contrast, the onset of transitional flow (Re_1) for all fluids have occurred within a smaller range of Reynolds numbers than Re_2. Based on the definition of Re_1 used here in this study, the onset of transitional flow for PAA, XG and Carbopol is indeed lower than the Newtonian case from which no qualitative explanation exists; this behaviour has not been reported previously in literature. However, from the mean velocity distribution measurements carried out for these fluids (and also for Laponite as will be discussed in Chapter 6), a strong mean-flow asymmetry inexplicably developed in this region of flow. It may be postulated that for these drag reducing fluids, their mean-flow distributions may be sensitive to entry conditions or any slight asymmetry associated with the pipe flow test section for $Re \rightarrow Re_1$. However, for $Re<Re_1$ and $Re>>Re_1$, the mean axial velocity distributions remain symmetrical. Interestingly, this effect was not seen for the Newtonian fluids, the consequence of which is discussed in more detail in Section 5.3.

According to Hoyt (1972), drag reduction occurs when a threshold wall shear stress, only dependent on the test fluid, is exceeded. Consequently, the 'onset wall shear stresses' (τ_{S1} and τ_{S2}) at Re_1 and Re_2 respectively, have been analysed for all test fluids as shown in **Table 5.1**. From the data presented, it is evident that for similar fluids, the 'onset wall shear stresses' increase with fluid concentration. When comparing different fluids, τ_{S1} and τ_{S2} are greater for fluids displaying the largest levels of drag reduction. However, these observations have been based on the limited comparisons made from the data presented in **Table 5.1** and therefore there is no conclusive evidence at this stage, which supports (or even challenges) Hoyt's theory that a threshold wall shear stress exists for each test fluid.

Probably the most widely used and challenged onset theory cited in literature is that of Lumley (1969). According to Lumley, the onset of drag-reduction occurs when:

$$\left(\frac{u_\tau^{\,2}}{\nu}\right)\times\tau_1 \geq \frac{3}{2} \tag{5.6}$$

where u_τ^2/ν is the reciprocal of the characteristic time scale of the flow and τ_1 is the terminal relaxation time associated with the molecule. Molecular theories for polymer rheology [Ferry (1970)] indicate that

$$\tau_1 \propto \frac{(\eta - \eta_{solvent})M}{cRT} \tag{5.7}$$

where M is the molecular weight, T is the absolute temperature, η is the solution viscosity, $\eta_{solvent}$ is the solvent viscosity, c is the polymer concentration and R is the universal gas constant.

However, as Berman (1977) pointed out, the determination of τ_1 is difficult to assess as it depends on numerous factors such as Reynolds number, pipe diameter, degradation, molecular weight and distribution [also supported by Hunston and Reischman (1975)], etc.. Thus consistency in defining a critical Reynolds number associated with the onset of drag reduction has been difficult to achieve for any particular non-Newtonian fluid. Also, Lumley [(1973), cited in den Toonder *et al.* (1997)] proposed that the molecules for a randomly coiled polymer in a pipe flow must be extended for drag reduction to occur. This extension and hence the onset of drag reduction occurs when the ratio of turbulence and polymer time scales is of one order. From this, it may be assumed that the onset phenomena is determined by elastic effects, particularly in relation to the extensional viscosity, which as previously discussed in Chapter 4.5, was not able to be determined during the course of this study. However, due to a lack of understanding of the quantitative relationships between molecular parameters and drag reduction, the proposed theory by Lumley was not investigated herein after.

5.3 Mean Velocity Distribution

5.3.1 Newtonian Fluid

For comparison purposes, the pipe flow characteristics for water and a more viscous Newtonian fluid were investigated under turbulent flow conditions. The latter fluid was a 60% w/w aqueous glucose (syrup) mixture, produced by Cerestar (UK). The resultant solution provided a dynamic viscosity μ of 5.44×10^{-3} Pa.s, a density ρ of 1143 kg/m^3, a refractive index n of 1.38734 at 20°C and a maximum Reynolds number of 60,000. For water, due to its low shear viscosity, the lowest possible Reynolds number attainable within the limits of the experimental set-up was 61,000. These conditions encapsulated the maximum Reynolds numbers obtained from each of the non-Newtonian flow tests ($Re_{max.} \approx 55{,}000$).

Figure 5.13 shows the axial mean velocity profiles obtained form these preliminary flow tests as u/U *versus* r/R, where u is local instantaneous axial velocity, U is the bulk mean velocity and r/R is the non-dimensionalised distance from the centre of the pipe. The variety of Reynolds numbers shown here (8,000, 36,000 and 61,000) are not too widely separated to show large marked deviations between the respective profiles. These profiles are however, characteristic of turbulent flow, displaying steeper velocity gradients near the wall and flatter profiles in the central core of the pipe than parabolic laminar velocity profiles. This behaviour becomes more marked as the Reynolds number is increased [Patel and Head (1969), Laufer (1954)].

The ratio of the mean to maximum velocity provides an indication of the degree of development of the flow. These results are summarised in **Table 5.2**.

A comparison with previous measurements [Laufer (1954), Lawn (1971) and Pinho (1990)] indicates that these ratios are somewhat larger, though generally within 3% of one another.

5.3.2 XG

The axial mean velocity profiles for XG are shown in **Figure 5.14** for 1,600<Re<40,500. It is evident that for flow conditions approaching transition (i.e. Re→Re_l ≈ 1,600; see Section 5.2), an asymmetry in the profile is developed. For larger Reynolds numbers extending into fully developed turbulent flow conditions (Re>6,000), the mean velocity profiles become symmetrical - a phenomena that has not been reported previously in literature for any non-Newtonian fluid. It may be assumed, therefore, that as the flow approaches transition, the velocity profile becomes sensitive to either entrance effects or imperfections in the alignment of the test pipe. At this stage, no other qualitative explanation for such behaviour exists. However, as explained below (in Sections 5.3.5 and 5.3.6), a similar behaviour was observed for PAA and Carbopol, which eliminated the possibility that the asymmetry in the velocity profiles, under similar flow conditions, were attributable to entrance effects.

For velocity profile a (Re=1,600), a direct comparison with a simple power law curve fit is shown. The curve fit, which is normally used to represent laminar velocity profiles, is represented using the following expression [Barnes *et al.* (1989)]:

$$\frac{u}{U} = \frac{(3n+1)}{(n+1)}\left(1-\left(\frac{r}{R}\right)^{\frac{n+1}{n}}\right) \qquad \textbf{(5.8)}$$

where n is the power law index (see **Table 4.1**). This representation is merely used to identify any asymmetry within the flow, which is clearly evident for profile a. The level of asymmetry was difficult to quantify without directly mapping the velocity profile at all radial locations within the test pipe. This was not carried out during the course of this study nor seen as necessary at this stage.

It is also evident from **Figure 5.14** that turbulent velocity profiles b (Re=6,500), c (Re=14,100) and d (Re=40,500) become progressively flatter towards the centre of the pipe as Reynolds number increases. The extent of flattening for these profiles is larger

than that for a Newtonian fluid, which has also been illustrated in **Figure 5.14** for comparison reasons (Water, Re=61,000).

The remaining sections (Sections 5.3.3 - 5.3.6) detail the same analysis as that applied here to XG (i.e. u/U *versus* r/R behaviour). Further detailed analyses of the mean axial velocity profiles will be discussed in Section 5.4 for all fluids, based on 'universal law of the wall form' representations.

5.3.3 CMC

Figures 5.15 - 5.17 illustrates the mean axial velocity distribution data for various concentrations of CMC (0.24%, 0.25% and 0.4% respectively). The velocity profiles are symmetrical for all ranges of Reynolds number. For 0.24% CMC, the data was limited to only four flow experiments, which correspond to the four Reynolds numbers indicated on **Figure 5.15**. This was due to noticeable degradation effects occurring during the period of investigation for 0.24% CMC, which resulted in a reduction in solution viscosity and an appearance of increased opacity. The degradation of the fluid was assumed to be caused by bacteriological influences related to undetectable minute quantities of aqueous glucose solution that may have resided within the flow loop from the previous flow tests. Despite the degradation effect on the fluid, the limited number of flow tests were continued to be analysed.

From **Figure 5.15**, it is evident that the laminar velocity profile a for 0.24% CMC shows a slight flattening of the profile occurring within the central portion of the pipe when compared with the parabolic Newtonian profile for laminar flow. For fully developed flow conditions (Re>4,000), the turbulent profiles become flatter as the Reynolds number is increased (see e.g. profiles c and d). For profile d (Re=14,100), the data is not too dissimilar to that of a Newtonian fluid (Water, Re=61,000) when shown as u/U *versus* r/R. However, when plotted in law of the wall form as explained within Section 5.4, the flow structure is different to that of a Newtonian fluid. Also, when comparing velocity profiles for 0.24% CMC and 0.2% XG at similar Reynolds

number (see e.g. profiles d (CMC) and c (XG) respectively at Re=14,100), it is evident that XG displays a flatter profile than CMC at the centre of the pipe.

A fresh solution of 0.25% CMC was then prepared in order to acquire further velocity distribution data, which can be seen in **Figure 5.16**. The mean velocity distributions become slightly scattered for flow conditions within or near to transition (1,900<Re<5,500). For higher Reynolds numbers, the velocity profiles flatten towards the centre of the pipe with a resultant increase in velocity gradient at the wall, a trend that is observed for all Newtonian and non-Newtonian fluids. However, the corresponding trend for 0.25% CMC would suggest that the profile would be flatter than the Newtonian fluid at similar Reynolds number if velocity measurements were taken for flows at higher Reynolds numbers.

Finally, a 0.4% CMC solution was tested in order to analyse the effect of fluid concentration on velocity distribution data; these results are shown in **Figure 5.17**. Due to a more viscous solution, the range of Reynolds number were limited (Re<5,500) for safety reasons associated with the maximum permissible pressures allowable within the system. Hence very little data was established for 0.4% CMC, which limited comparisons with fluids of lower concentration, for flows extending to higher Reynolds numbers. Interestingly, however, the u/U *versus* r/R behaviour did not show significant deviations when compared with 0.25% CMC.

5.3.4 XG/CMC

The u/U *versus* r/R behaviour for 0.09% CMC/0.09% XG is shown in **Figure 5.18**. A slight asymmetry in mean velocity distribution data occurs for profiles c (Re= 3,400) and d (Re=5,500), which is analogous to that previously observed for 0.2% XG during transitional flow. However, symmetrical profiles are observed for all other Re, which are representative of fully developed laminar and turbulent flow conditions.

The velocity profile (a) under laminar flow conditions for 0.09% CMC/0.09% XG is flatter than that for CMC alone, which is simply caused by a larger degree of shear-

thinning (denoted by the power-law index, n [Barnes *at al.* (1989)]) than CMC (see **Eq. (5.8)** and **Table 4.1**). Thus, by progressively decreasing the power-law index i.e. increasing the degree of shear-thinning, the flow becomes increasingly plug-like in nature. This behaviour can be qualitatively assessed by comparing the viscometric flow curves in **Figure 4.27** with the laminar velocity profiles presented in these sections (5.3.2-5.3.6).

5.3.5 PAA

Figures 5.19 and **5.20** represents the mean velocity distribution data for 0.125% PAA and 0.2% PAA respectively. Again the data for the more viscous solution is limited to a smaller range of Reynolds numbers due to the maximum permissible pressures allowable within the system (for 0.2% PAA, Re<23,000).

For 0.125% PAA (**Figure 5.19**), the velocity profiles become progressively flatter with a resultant increase in velocity gradient near the pipe wall as Reynolds number is increased and are again much flatter than those for water. Also, the velocity profiles remain relatively symmetrical.

However, for 0.2% PAA (**Figure 5.20**) and as previously seen for XG, a level of asymmetry under transitional flow conditions (denoted previously in Section 5.2 as 1,500<Re<11,000 for 0.2% PAA) is clearly evident. This supports the suggestion made in Section 5.2 that transition does indeed occur at Reynolds numbers lower than 2,000. What is interesting from **Figure 5.20** is that the asymmetry occurs towards the far wall section of the test pipe (right-hand-side of the u/U *versus* r/R plots) i.e. the centreline peak velocity is shifted to the right, contrary to that for 0.2% XG (see Section 5.3.2). This would suggest that the stability of the mean velocity profiles (defined here as the degree of symmetry) is generally sensitive to transition effects and is therefore not associated with any adverse entrance effects nor pipe misalignment as previously mentioned in Section 5.3.2 for 0.2% XG. This phenomena has not been reported previously in literature and may be used to ascertain transitional flow conditions for such non-Newtonian fluids. However, this is limited by the fact that

there does not seem to be any qualitative explanation for why this observed behaviour does not occur in all drag reducing fluids. Without carrying out further flow tests for each fluid within their respective transitional flow regions, the asymmetrical behaviour of the flow must be limited to the flow arrangement, fluid type and concentrations discussed here for specific Reynolds numbers.

5.3.6 Carbopol

The mean velocity distribution data for 0.14% Carbopol 934 is given in **Figure 5.21**. Due to the turbid appearance of the solution (as explained in Chapter 4.3.1), the LDA measurements were limited to the near wall section of the pipe (50% of the pipe diameter) and therefore a full profile was not achieved. The opened symbols in **Figure 5.21** are purely a reflection of the velocity data measured at the near wall, which are denoted by the corresponding closed symbols. Subsequently, any asymmetry in the velocity profiles cannot be identified from the data provided, though a qualitative assessment of the trend would suggest that the velocity profiles would appear to be symmetrical.

Once again, the laminar velocity profiles (a $\rightarrow$ Re = 1,450 and b $\rightarrow$ Re = 2,000) are flatter than that for a Newtonian fluid, with no evidence of any irregularity in shape associated with transitional effects. However, at larger Reynolds numbers, the profiles become slightly perturbed at $r/R \approx 0.8$ for profile c (Re = 4,130) and d (Re = 5,220), which is indicative of transitional flow. In comparison with the observations made from the *f*-Re data in Section 5.2, the transition region for 0.14% Carbopol 934 was identified as $1{,}000 < Re < 5{,}000$. However, due to the measured velocity data being limited to 50% of the pipe diameter, a correlation between asymmetry of velocity profile data and transitional effects can not be quantitatively assessed for 0.14% Carbopol 934 and certainly there is no definite indication that this would be the case.

For the turbulent profiles (e-h), the mean velocity distribution data progressively approaches a similar trend, for increasing Reynolds number, not too dissimilar for that of the Newtonian fluid.

Figure 5.22 shows the u/U *versus* r/R behaviour for 0.1% Carbopol EZ1, which due to a lesser turbid appearance compared with 0.14% Carbopol 934, allowed LDA measurements to be taken across the entire section of the test pipe. For flow conditions approaching transition, the data clearly shows velocity profiles with various levels of asymmetry for a (Re=950, slight), b (Re=1,400-1,200, significant) and c (Re=3,100, slight). The flow conditions from which the asymmetric profiles were observed correlate quite well with the transition region predicted from the *f*-Re data discussed in Section 5.2 i.e. 1,000<Re<5,000 for 0.1% Carbopol EZ1.

Under turbulent flow conditions for 0.1% Carbopol EZ1 (Re>5,000), the mean velocity distribution profiles approach that for a Newtonian fluid as the Reynolds number is increased. This behaviour was also seen for 0.14% Carbopol 934.

The ratio of the maximum instantaneous velocity (U_0) to the mean bulk velocity (U) is shown in **Figure 5.23** for all fluids as a function of Reynolds number. The data clearly indicates flatter profiles compared with Newtonian fluids and compares well with the data of Pinho (1990). For Newtonian fluids, U_0/U takes the value of 2.0 for the laminar parabolic profile and 1.224 for the turbulent 1/7 power-law profile [Schlichting (1978)]. The Newtonian data shown in **Figure 5.23** has been extracted from the paper of Patel and Head (1969) for comparison reasons. Subsequently, it is evident that the non-Newtonian velocity profiles become flatter in a steady manner as the Reynolds is increased from laminar to turbulent flow, compared to a relatively abrupt change in U_0/U for Newtonian fluids [Patel and Head (1969)].

5.4 Universal Law of The Wall

This section analyses the turbulent mean velocity distribution data discussed in Section 5.3 using semi-logarithmic law of the wall coordinates. Such representations are a foundation of any practical approach to calculating the near wall turbulent flow behaviour of fluids. The first section introduces the analysis applied to the Newtonian

fluids, which is then directly compared within the following sections for all non-Newtonian fluids used in this study.

5.4.1 Newtonian Fluid

The mean velocity for the Newtonian fluids have been reduced to the universal 'law of the wall form' [e.g. see McComb (1990)], as demonstrated in **Figure 5.24**. Here, the entire velocity distribution constitutes three distinct regions: (i) the *viscous sublayer* ($0<y^+<5$), (ii) the *transition* or *buffer layer* ($5<y^+<30$) and finally (iii) the *turbulent layer* ($y^+>30$). It should be noted that the values quoted for y^+ to classify the various layers varies from one source to another in literature, which reflects the difficulty in establishing precisely the criteria for the boundary between each layer as clearly pointed out by many investigators [see e.g. Patel and Head (1969)].

In the turbulent core, the velocity distribution is represented by the logarithmic law:

$$U^+ = 2.5 ln\, y^+ + 5.5 \qquad \textbf{(5.9)}$$

where $U^+ \equiv u/u_\tau$, $y+ \equiv u_\tau y/\nu$, u_τ is the friction velocity given by $\sqrt{(\tau_s/\rho)}$, ν is the kinematic viscosity ($=\mu_s/\rho$) and y is the distance from the wall [Schlichting (1978)]. In the viscous sublayer, the linear law:

$$U^+ = y^+ \qquad \textbf{(5.10)}$$

is applicable. The numerical constants used in **Eq. (5.9)** (i.e. A=2.5 and B=5.5) represent averages over many experiments as discussed below.

The abscissa in **Figure 5.24**, is the natural logarithm (i.e. logarithm to the base e, see **Eq. (5.9)**) of y^+, which indicates a satisfactory logarithmic dependence for most of the data. This result has been confirmed by many investigators [see e.g. review by Hinze (1975)] and means that the velocity distribution given by **Eq. (5.9)** is in good agreement with the experimental data, except close to the wall. However, from

numerous experimental reviews [see e.g. Tennekes and Lumley (1972), Hinze (1975)], there is considerable uncertainty over the precise value of the von Kàrmàn constant κ ($\equiv 1/A$), the experimental scatter of which is shown in **Figure 5.25**. However, the values for the numerical constants used in **Eq. (5.9)** are in excellent agreement with the experimental data obtained from this study and confirm the original conclusions based on Nikuradse's results [cited in McComb (1990)].

In contrast, the part of the mean velocity profile in the viscous sublayer is well represented by the linear relationship given in **Eq. (5.10)**. The results shown in **Figure 5.24** agree well with the data of Laufer (1954).

5.4.2 XG

For many additive-solvent systems, comparisons of their drag reducing profiles with Newtonian profiles, using semi-logarithmic law of the wall coordinates, can yield significant changes that are not immediately evident from their corresponding u/U *versus* r/R behaviour.

Subsequently, mean velocity profiles in the universal U^+ form for 0.2% XG are shown in **Figure 5.26**. Both the velocity variation within the viscous sublayer and also the extent of the sublayer are not significantly different from the standard $U^+=y^+$ ($y^+\leq 10$) form, thus suggesting that this region does not play a major role in the drag-reduction process. This latter postulation will be challenged further in the following sections.

The velocity distribution close to the wall ($y^+<30$) extended partially onto Virk's (1970) ultimate drag reducing asymptote (see **Eq. (2.2)**). As many previous studies have shown [see e.g. Pinho and Whitelaw (1990) and Tiederman (1997)], this clearly indicates that the buffer region increases in thickness with increasing levels of drag reduction.

An upshifted log-law region of limited extent can be identified for 0.2% XG for $y^+>70$, which is consistent with the extent of drag reduction. The level of upward shift ΔB can be expressed as follows:

$$U^+ = 2.5 ln y^+ + 5.5 + \Delta B \qquad \textbf{(5.11)}$$

Although the progressive increase in the upward shift is consistent with earlier work [see e.g. Pinho (1990)], the slope in each case is subject to qualitative assessment as will be discussed in Section 5.4.5. Previous opinion on this issue has been divided, with the majority of workers inferring that the log-law was negligibly affected by drag-reducing polymers. However, den Toonder *et al.* (1997) also reported both measurements and numerical simulations showing a significantly increased slope.

Observations from the mean distribution data given in **Figure 5.26** have been summarised in **Table 5.3**.

5.4.3 CMC

Figures 5.27 - 5.29 illustrate the universal law of the wall plots for fully developed turbulent flows of 0.24% CMC, 0.25% CMC and 0.4% CMC. For all concentrations, the data reduced to $U^+=y^+$ at the near vicinity of the wall as that for the Newtonian fluid.

For 0.24% CMC (**Figure 5.27**), the data illustrates a clear upward shift within the turbulent core region ($\Delta B \approx 3.7$) with respect to the Newtonian data for Re=14,100, again consistent with earlier work. The mean velocity distribution data for profile c (Re = 4,300) shows this upward shift to a limited extent with an increase in slope, which is primarily related to the flow being close to transition (see e.g. Patel and Head (1969)]. The increased slope in data within the turbulent core does not allow for an acceptable assessment of the wall layer thickness i.e. the sum of the viscous sublayer and buffer region [Tiederman (1988)]. The wall layer thickness can be defined as the distance from the wall to the point where the data intercepts with the parallel upward

shift within the turbulent core (y_1^+). These subjective observations have been utilised for comparison reasons and are purely based on qualitative assessments from the data plotted in **Figures 5.27 -5.34**. These results are included within **Table 5.3**.

Figure 5.28 illustrates the universal distribution data for 0.25% CMC. In the turbulent core region, the upward shift in data from the Newtonian characteristic remains almost constant for the limited range of Reynolds numbers shown (3,750<Re<16,600), despite a progressive increase in DR (see **Table 5.3**). This is not consistent with previous data [see e.g. Pinho (1990)] and could therefore have been partially influenced by degradation effects during the 2 week period of testing (see Chapter 4.5.2). However, the extent of the buffer region (y_1^+) had increased consistently with Reynolds number and DR.

The universal mean distribution data for 0.4% CMC is shown in **Figure 5.29**. The data shows a larger upward shift in data within the turbulent core ($\Delta B \approx 6.0$) compared with 0.24% and 0.25% CMC, thus indicating a concentration dependence on ΔB. This behaviour is consistent with the corresponding larger DR compared with the lower concentrations for CMC. The wall layer thickness had also increased compared with the Newtonian fluid ($5<y^+<30$), though at a similar extent as for the lower fluid concentrations (see **Table 5.3**).

5.4.4 XG/CMC

Universal mean distribution data for 0.09% CMC/0.09% XG is shown in **Figure 5.30** for Re=10,700, 26,100 and 45,300. The extent of the buffer region (y_1^+) and level of upward shift for each Reynolds number is given in **Table 5.3**. The data clearly shows a larger upward shift within the turbulent core compared with 0.4% (and lower concentrations of) CMC, though to a lesser extent than 0.2% XG, thus generally consistent with the overall level of DR. For all Reynolds numbers (10,700<Re<45,300), ΔB remained relatively constant, which is analogous to the behaviour of 0.24% CMC. The wall layer thickness had extended further into the pipe (y_1^+) compared with CMC and to a similar extent as that for 0.2% XG (see **Table 5.3**).

5.4.5 PAA

Law of the wall plots for fully developed turbulent flows of 0.125% PAA and 0.2% PAA are shown in **Figures 5.31 - 5.32**. The data clearly indicates an extended buffer region for both concentrations and for all ranges of Reynolds number, with a resultant upward shift of the logarithmic profile within the turbulent core. The upward shift (ΔB) is consistent with higher Reynolds numbers and corresponding larger values of DR (see **Table 5.3**). The values of ΔB for PAA are larger than any other test fluid identified in this study. Subsequently, for PAA, the mean distribution data near the wall region closely follows Virk's ultimate drag reducing asymptote (see **Eq. (2.2)**) for greater wall distances (y^+) than the less drag reducing fluids discussed above.

For 0.2% PAA at Re = 23,100 (**Figure 5.32**), it is clear that the upward shift is not quite parallel to the Newtonian data. This has been previously mentioned in Section 5.4.2, from which after the careful investigation of the recent measurements of Pinho and Whitelaw (1990) (pipe flow), Harder and Tiederman (1992) (channel flow), Wei and Willmarth (1992) (channel flow) and den Toonder (1997) (pipe flow), their data also showed that the slope is actually somewhat increased thus consistent with the experimental data presented here.

5.4.6 Carbopol

Figures 5.33 and **5.34** illustrate the universal distribution data for 0.14% Carbopol 934 and 0.1% Carbopol EZ1 respectively. In comparison with the XG, CMC and PAA, the data shows lower upward shifts within the logarithmic flow region ($\Delta B<3.0$) for $5{,}200<Re<24{,}000$. Interestingly, this upward shift reduces and becomes near parallel to the Newtonian data as Reynolds number increases, which is consistent with the drag reduction behaviour for Carbopol as discussed in Section 5.6.

The extent of the buffer region (interactive layer) compares closely with that for a Newtonian fluid ($5<y^+<30$) with only a slight extension of the wall layer thickness for

lower Reynolds numbers. The data extracted from **Figures 5.33** and **5.34** have been tabulated in **Table 5.3** along with the other test fluids.

5.5 Turbulence Intensities

5.5.1 Newtonian Fluid

Figures 5.35(a-c) illustrate the profiles of the non-dimensionalised root-mean-square (r.m.s.) values of the axial velocity fluctuations (u′/U) against r/R and y^+. **Figure 5.35(a)** clearly shows that the profile peaks towards the wall and is lower at the centre of the pipe. The data corresponding to Reynolds numbers of 36,000 and 61,000 are almost indistinguishable, with peaks occurring within the boundaries of the transition layer ($5<y^+<30$), as seen from **Figure 5.35(b)**. The data has also been non-dimensionalised using the friction velocity u_τ as shown in **Figure 5.35(c)**, thus allowing comparisons to be made with previous data presented by Pinho (1990) and Laufer (1954), with which the data compares well.

Figure 5.36 provides a comparison of the axial r.m.s. (u′) velocity component with the radial (v′) and tangential (w′) velocity fluctuations for water (Re ≈ 61,000). It is clearly evident that v′ and w′ are lower than the axial velocity fluctuating component everywhere across the entire section of the pipe. Their maximum values also occur towards the wall of the pipe, with w′ displaying peaks larger than v′ and also at distances much closer to the wall respectively. This data follows the trends made from numerous investigators [see e.g. Laufer (1954), Clark (1968), Lawn (1971), Pinho (1990) and den Toonder (1995)].

Clark (1968) provided a detailed study of turbulent boundary layers in channel flow using a hot-wire anemometer and suggested that the mean velocity profiles in the log-law region is independent of Reynolds number, though the fluctuating velocities within the buffer region were Reynolds number dependent. The former has been identified as not being the case for non-Newtonian fluids as discussed in the previous section.

5.5.2 XG

Figures 5.37(a-c) illustrates the distribution of the normalised rms velocities (u′/U, w′/U and v′/U) *versus* r/R for 0.2% XG in turbulent flow. For velocity fluctuations in the axial direction (**Figure 5.37(a)**), the data shows a reduction in u′/U over 80% of the pipe diameter as the Reynolds number is increased. The distribution of normalised rms values for the axial velocity fluctuation at Re = 6,500, confirms once again that the transitional state (identified as approximately 1,600 < Re < 6,000 in **Table 5.1**) is characterised by much higher levels than is typical for the fully developed turbulent flow of Newtonian or non-Newtonian fluids except in the immediate vicinity of the pipe surface. It is also evident that the peak value of u′/U tends nearer towards the wall with a corresponding peak broadening effect as the Reynolds number increases. The results are lower over the majority of the pipe section than that for a Newtonian fluid (Re = 61,000) for a Reynolds number of similar order of magnitude (Re = 40,500). The relative decrease (though minimal) in the axial velocity fluctuation relative to the Newtonian fluid contradicts the works of Allan *et al.* (1984) and Willmarth *et al.* (1987), though the peak broadening effect is however, consistent with their results. Generally, in the most part, the turbulence axial intensity data have been consistent with work over the more recent years [see e.g. review by Tiederman (1988)].

The normalised distribution data given in **Figures 5.37(b-c)**, show significantly reduced velocity rms levels in both the tangential (w′/U) and radial (v′/U) directions compared with u′/U as shown in **Figure 5.37a**. This dampening effect occurred throughout the pipe section, even at the centreline where drag-reduction had a minimal effect on u′. The tangential and radial r.m.s. data are also noticeably less than that for a Newtonian fluid, which has also been included for comparison reasons. These observations are consistent with the behaviour associated with polymer solutions in turbulent pipe-flow [see e.g. Pinho and Whitelaw (1990), Harder and Tiederman (1991)]. It is important to note that experimental results for w′ and v′ are rare in literature in contrast to u′, which are also often contradicting. For example, Pereira and Pinho (1994) found that the turbulent pipe flow of Tylose solution displayed an almost uniform distribution of both the radial and tangential turbulence intensities in

the central core (varying from 50% to 80% of the diameter) at levels above those for a Newtonian fluid, contrary to most findings in literature. Such anomalies are investigated in detail in this study.

It was also considered instructive here to present the normalised distribution data for the velocity fluctuations in law of the wall coordinates in order to assess their behaviour in terms of the three-layer wall model: viscous sublayer, extended wall layer or buffer region and turbulent core. This data is presented in **Figures 5.38(a-c)** for u'/u_τ, w'/u_τ and v'/u_τ *versus* y^+ for 0.2% XG. There is an important aspect of these results that deserve a mention. From the plots of normalised distribution of the various components of velocity with friction velocity (u_τ), it is not possible to assert that the turbulence has not been suppressed by the additive, because the increase in u'/u_τ for example, with increasing drag reduction may be due to the corresponding reduction in friction velocity. Hence the true turbulence intensity may be assumed as being that which is normalised with the mean bulk velocity (i.e. u'/U, w'/U and v'/U). For comparison reasons, both sets of data have been presented for all test fluids.

Figure 5.38(a) indicates that u'/u_τ increases with Reynolds number (and DR as will be explained in Section 5.6), with the peak range occurring within the extent of the wall-layer thickness as previously identified in **Table 5.3**. A similar trend has been identified for the tangential velocity distribution as shown in **Figure 5.38(b)**, though with peak values much reduced in comparison with the corresponding u'/u_τ values for similar Reynolds number. The peaks in w'/u_τ also occur at progressively larger distances from the wall than u'/u_τ as Reynolds number increases, which is consistent with the findings of Willmarth *et al.* (1987) and Tiederman (1988). For the radial velocity component (**Figure 5.38(c)**), the peak values of v'/u_τ occur at similar distances from the wall as that for the tangential, though at slightly reduced levels by comparison respectively. These results have been summarised in **Tables 5.4 - 5.5**. Also, from **Figure 5.38(c)**, it is evident that the radial measurement data displays an increased level of scatter compared with the measured axial and tangential velocity fluctuation data. The increased level of scatter applies to all radial velocity

measurements discussed here in this study and is related to the refraction of the LDA laser beams during a radial traverse as explained in detail in **Appendix A2.3**.

5.5.3 CMC

The normalised distribution data for the axial velocity fluctuation is shown in **Figure 5.39(a)**. The data shown is limited to low Reynolds numbers, which with the exception of the results for Re=14,100, are within the influence of transitional flow. As previously mentioned, it is evident that the transitional region of flow is characterised by much higher levels of axial turbulence intensity than that for fully developed turbulent flow. Therefore, excluding the data for Re=4,300, 0.24% CMC illustrates a similar behaviour as that for the Newtonian fluid over the majority of the pipe section (approximately 80% of the pipe diameter). However, a peak broadening effect is evident at $0.8<r/R<0.95$, which is of similar magnitude to that for the Newtonian fluid though occurring at larger distances from the wall. This agrees with the work of Allan *et al.* (1984) and is very similar to the flow behaviour of 0.2% XG at an identical Reynolds number. However, this behaviour is restricted by comparison to the Reynolds numbers shown, which as demonstrated for 0.2% XG, the peak in u'/U eventually decreases to below that for the Newtonian fluid as Reynolds number increases.

Figures 5.39(b-c) illustrates the w'/U and v'/U *versus* r/R behaviour for 0.24% CMC. The data clearly shows that the tangential and radial velocity fluctuating components are significantly reduced compared with u'/U. Interestingly, their behaviour is comparable with that for the Newtonian fluid except near the wall ($0.8<r/R<0.95$). In this region, the peak values of w'/U and v'/U are reduced in comparison with the Newtonian fluid, which also occur at larger distances from the wall (see **Table 5.5**).

Figures 5.40(a-c) presents the data for 0.24% CMC in wall coordinates. The peak value and location of u'/u_τ are similar to that for a Newtonian fluid, which occurs within the buffer region of the flow. However, for w'/u_τ, the data is significantly reduced compared to the Newtonian fluid, though again with peak values occurring at

similar wall distances within the buffer region (see **Table 5.4**). As for 0.2% XG, v'/u_τ is lower than the corresponding w'/u_τ profile (see **Figure 5.40(c)**), with a respective peak broadening effect occurring at larger distances from the wall as also summarised in **Tables 5.4 - 5.5**.

A similar set of data, to that of the above, have been presented in **Figures 5.41-5.42** for 0.25% CMC, though with a larger distribution of Reynolds numbers in turbulent flow than that for 0.24% CMC. The results presented have substantiated the comments made for 0.24% CMC, from which there were no discernible differences. The corresponding results for 0.25% CMC have been summarised in **Table 5.4**.

Figure 5.43 shows the normalised axial fluctuation turbulence intensity for 0.4% CMC. Comparisons with the Newtonian fluid can not be carried out satisfactorily as the flow for 0.4% CMC was restricted to very low Reynolds numbers, which were within or close to the zone of influence associated with transitional flow effects. This has been characterised by much higher values of u'/U compared to fully developed turbulent flow as illustrated in **Figure 5.43(a)**. From the limited data shown in **Figure 5.43(b)** as u'/u_τ *versus* y^+, there is some evidence that suggests the effect of concentration has little influence on the peak value of u'/u_τ and its corresponding location from the wall. The concentration effect of the solvent additive solution on normalised turbulence intensities will be further investigated using the two distinct concentrations for PAA (0.125% and 0.2%).

Due to the limiting Reynolds number of the more viscous flow for 0.4% CMC, no further investigations were carried out.

5.5.4 XG/CMC

The turbulence intensity profiles (u'/U, w'/U and v'/U *versus* r/R) for 0.09% CMC/0.09% XG are illustrated in **Figures 5.44(a-c)** respectively. For Re<26,800, u'/U (**Figure 5.44(a)**) is comparable with the Newtonian data shown except near the wall, with peaks of similar magnitude respectively. However, for Re=45,300, the data

consistently falls below the Newtonian reference, thus once again indicating a Reynolds number dependence on the turbulent structure of flow. Generally, for increasing Reynolds number, the peak in u′/U tends towards the wall with correspondingly less peak broadening effects. In contrast, the tangential (w′/U) and radial (v′/U) turbulence intensities are lower than the Newtonian fluid, with corresponding peak turbulence intensities occurring further away from the wall (r/R≈0.92 and 0.75 respectively). The peak values in w′/U and v′/U are similar (≈0.50-0.56), with individual profiles indicating little or no Reynolds number dependence based on the representation of data given.

Figures 5.45(a-c) presents the turbulence intensities normalised with friction velocity (u_τ) using wall coordinates. Unlike XG and CMC, u'/u_τ *versus* y^+ for the XG/CMC blend shown in **Figure 5.45(a)** indicates levels of normalised axial turbulence intensity that are comparable and even greater than the Newtonian fluid which is consistent with the findings of Tiederman and Reischman (1975). The peaks in u'/u_τ also occur at slightly larger wall distances than the Newtonian fluid, the locations of which are summarised in **Table 5.4**. For tangential and radial turbulence intensities (**Figures 5.45(b-c)** respectively), the peaks in w'/u_τ and v'/u_τ are significantly lower than the corresponding peak in u'/u_τ for similar Reynolds numbers (see **Figure 5.45(a)**). These peaks are also lower than that for a Newtonian fluid, and occur at larger distances away from the wall as Reynolds number increases when compared with the axial turbulence intensity distribution for XG/CMC. Once again, the peaks in v'/u_τ are slightly lower than the corresponding tangential (w'/u_τ) values. These results are summarised in **Tables 5.4 - 5.5**.

5.5.5 PAA

Figures 5.46(a-c) illustrates u′/U, w′/U and v′/U *versus* r/R for 0.125% PAA. For the axial turbulence intensities (u′/U) shown in **Figure 5.46(a)**, the data in the central section of flow (-0.4<r/R<0.4) are indistinguishable from one another and comparable with the Newtonian data. However at distances closer to the wall (0.6<r/R<0.95), the peaks in turbulence intensity are greater than that for a Newtonian fluid. This

difference becomes less noticeable as Reynolds number increases, with the corresponding peaks in u′/U tending closer towards the wall respectively.

In contrast, the tangential (w′/U) and radial (v′/U) turbulence intensities, which are shown in **Figures 5.46(b-c)** respectively, are significantly lower than u′/U throughout the entire pipe section. The data presented in these figures are almost indistinguishable from another, showing little or no dependence on Reynolds number. As with previous fluids, their corresponding peaks occur at distances further away from the wall compared with that of a Newtonian fluid.

Figures 5.47(a-c) illustrates the turbulence intensities normalised with the friction velocity in wall coordinates for 0.125% PAA. For u'/u_τ (see **Figure 5.47(a)**), the peak in data occurs within the extent of the interactive layer at levels larger than that for a Newtonian fluid. The peak locations also extend further into the pipe section, which is consistent with Virk's (1970) three-layer model i.e. extended interaction region (y_I^+; see **Table 5.3**). Due to degradation effects becoming apparent (seen as a reduction in solution viscosity), the number of flow tests were limited to the higher Reynolds numbers in the case of the tangential and radial flow measurements. These results are illustrated in **Figures 5.47(b-c)** for w'/u_τ and v'/u_τ respectively. For the tangential case (**Figure 5.47(b)**), there is little difference between the measured data for Re=37,500 and 43,100, though is significantly reduced compared with the Newtonian reference fluid. The peak in data also occurs at larger distances away from the wall than the Newtonian fluid, from which a similar trend is shown for the radial measurements in **Figure 5.47(c)**. The above data for 0.125% PAA has been summarised in **Table 5.4**.

Normalised axial turbulence intensity measurements for 0.2% PAA are illustrated in **Figures 5.48(a-b)**. No data was obtained in the tangential and radial measurement planes due to equipment related problems at the time of its investigation.

It is evident from **Figure 5.48(a)** that the normalised axial fluctuations (u′/U) are greater than the Newtonian fluid except for a small region near the wall (r/R>0.95),

with also a similar magnitude of peak intensity at the centre of the pipe. The peak in u'/U also occurred at larger distances away from the wall in comparison with a narrower peak intensity for a Newtonian fluid, which is closer to the wall.

The data shown in **Figure 5.48(b)** indicates that u'/u_τ is larger than that for a Newtonian fluid within the extended buffer region of flow ($y^+>10$), which is consistent with the findings of Reischman and Tiederman (1975). The peak intensity profile was also shifted further away from the wall in comparison with the Newtonian reference data provided. These results have been summarised in **Tables 5.4 - 5.5**.

5.5.6 Carbopol

The normalised distribution data (u'/U and w'/U versus r/R) for 0.14% Carbopol 934 are shown in **Figures 5.49(a-b)**. Due to the turbid appearance of 0.14% Carbopol 934 solution (as mentioned previously in Chapter 4.3.1), low data rates and reduced signal quality of the LDA signal were obtained. This inhibited any satisfactory LDA measurement data for radial turbulence intensities. The turbidity of the solution also affected the axial and tangential flow measurements for distances beyond the centreline of the pipe ($0<r/R<1$), hence the data presented in **Figures 5.49(a-b)** (shown as open symbols) are merely a reflection of the near wall data for clarification purposes.

From **Figure 5.49(a)**, the data for 0.14% Carbopol 934 indicates much higher levels of axial turbulence intensity for $Re<12{,}700$. At higher Reynolds number (18,600), the normalised turbulence data is very similar to that for a Newtonian fluid, which is consistent with its low drag reducing behaviour (as detailed further in Section 5.6). Also, from **Figure 5.49(b)**, the tangential velocity fluctuations (w'/U) are very similar to that for a Newtonian fluid for the majority of the pipe section ($-0.9<r/R<0.9$). The corresponding smaller peak intensities also occured at larger distances from the wall by comparison respectively (see **Table 5.5**).

From the axial normalised turbulence distributions (u'/u_τ *versus* y^+) presented in wall coordinates in **Figure 5.50(a)**, the data suggests that u'/u_τ is almost independent of the

Reynolds number. Also, the peak intensity profiles are essentially identical to that for a Newtonian fluid for $y^+<50$, which again is consistent with the low drag reducing behaviour associated with Carbopol in comparison with the other non-Newtonian fluids investigated in this study. However, beyond the buffer region of flow ($y^+>40$; see **Table 5.3**), the data falls below the Newtonian reference fluid. In contrast to the similarity of the axial turbulence intensity data with the Newtonian data for flow regions limited to the extent of the buffer region, the tangential normalised profiles (w'/u_τ) were lower than the Newtonian fluid. However, it is evident that despite the peak intensities being lower by comparison for 0.14% Carbopol 934, the peak broadening effect and peak location is not too dissimilar from that for the Newtonian fluid; this data has been summarised in **Tables 5.4 - 5.5**.

The normalised velocity fluctuations (u'/U, w'/U and v'/U *versus* r/R) for 0.1% Carbopol EZ1, are shown in **Figures 5.51(a-c)**. The same discussion applies for 0.1% Carbopol EZ1 as that given above for 0.14% Carbopol 934, where the data remained relatively unchanged. However, the less turbid nature of the solution for 0.1% Carbopol EZ1, allowed radial turbulence intensities to be measured, though a certain degree of scatter in data was still evident (see **Figure 5.51(c)**). For Re < 28,000, v'/U displayed slightly larger turbulence intensity levels over the majority of the pipe section ($-0.6<r/R<0.6$) beyond which, the scatter in data close to the wall (due to lower LDA data rates caused by the slight turbidity of the solution), made any comparison with the Newtonian fluid difficult. However, for Re=28,000, the data closely followed that for the Newtonian fluid within the restricted range of reduced scatter as just mentioned. The radial turbulence intensity profiles (v'/u_τ *versus* y^+) shown in **Figure 5.52(c)**, shows peak intensities occurring at distances beyond the buffer region of flow, with a corresponding increase in peak intensity as the Reynolds number is increased. However, the analysis of data (summarised in **Tables 5.4 - 5.5**) has been based on subjective assessments of the trend in data using the illustrations shown, which for the radial case, has been difficult.

Finally, **Table 5.6** summarises the 'centre-line' turbulent velocity fluctuations for all test fluids, which have been normalised using both the mean bulk flow velocity (U) and the friction velocity (u_τ). The data given in **Table 5.6** represents the highest

Reynolds number flows for each test fluid, with the Newtonian data also provided for comparison purposes. When comparing the data for the Newtonian fluids, the differences when normalised with U are ca 2.5% maximum – well within experimental uncertainty. However, when u_τ is used the differences become significant (ca 10%). Therefore, it may be concluded that the determination of u_τ has a greater level of uncertainty associated with it, which is not a Reynolds number effect since at such high Re values the change with Re is small. It may also be concluded that the turbulence intensity data for water are correct based on comparisons made with the data found in literature. Hence, as the measurement technique was the same for all test fluids, the turbulence data for the non-Newtonian fluids may also be assumed to be correct. For the non-Newtonian fluids, the tangential and radial velocity fluctuations normalised using U are for the most part lower than the values provided for the Newtonian reference fluid. For the test fluids displaying greater levels of drag reduction, the normalised axial velocity fluctuations (u'/u_τ) are greater than those for the Newtonian fluid. The remaining data provided in **Table 5.6** shows a random variation of values when compared with the Newtonian data thus limiting any further conclusions to be made.

5.6 Drag Reduction

5.6.1 Drag Reduction Levels of Test Fluids

Drag reduction (DR) (see **Eq. (5.5)**) values for all test fluids have been summarised in **Table 5.7** for a range of Reynolds numbers. The drag reduction data have been extracted from the *f*-Re curves, which are collectively illustrated in **Figure 5.53**. The drag reduction ranking of these fluids is discussed in Section 5.6.3. The data clearly shows an increase of DR with concentration and Reynolds number for all fluids. However, an anomalous behaviour was observed for Carbopol (and Laponite, as discussed in Chapter 6) where DR reduced with Reynolds number.

The anomalous behaviour of Carbopol has often been compared to clay suspensions such as Attagel, which are classified as purely viscous non-Newtonian fluids [Hartnett

and Kostic (1988)]. Hartnett and Kostic challenged this classification for Carbopol and indeed discovered that despite large differences in *f*-Re data when comparing equal concentrations of Carbopol and a highly viscoelastic solution of Separan in turbulent flow, their enhanced heat transfer rates were similar thus indicating that Carbopol was indeed viscoelastic. Their data on oscillatory shear flows indicated phase shifts (tanδ) of 60°, hence also providing further evidence that Carbopol was viscoelastic. From **Figure 5.53**, it would suggest that for turbulent flow, the *f*-Re behaviour for Carbopol (and Laponite - platelet clay suspensions), progressively tends towards that of a Newtonian fluid as Reynolds number increases. An interesting analogy arises when comparing this behaviour with the oscillatory shear flow assessment made previously in this study for 0.1% Carbopol EZ1 (see **Figures 4.25 - 4.26**). At high oscillation frequencies, despite increases in the elastic component (G′) of the fluid, the resulting increase in phase shift indicates a behaviour tending towards that of a purely viscous fluid response. Without the means of directly quantifying the level of molecular interaction within the solution, it may therefore be assumed that the *f*-Re behaviour is associated with the dissociation of interactive bonds within the solution (both physical and polar type) due to high frequency turbulence. The resulting breakdown of structure reduces the level of DR, the effect of which becomes further pronounced at higher Reynolds numbers. This postulated behaviour is specific to the physical molecular arrangement for Carbopol (and Laponite).

5.6.2 Separation of Shear-Thinning and Elastic Influences

The level of drag reduction observed for the test fluids used in this study is partly a consequence of the shear-thinning effect of each fluid, particularly within the power-law region of their respective flow curves (see **Figure 4.27**). The shear-thinning influence on DR can be deduced from the Dodge and Metzner (1959) model for a purely viscous power-law fluid using the following correlation:

$$\frac{1}{\sqrt{f_{DM}}} = \frac{4.0}{n^{0.75}} log\left(Re_N f_{DM}^{1-\frac{n}{2}} \right) \qquad \textbf{(5.12a)}$$

where n is the power law index obtained directly from the viscometric data (see **Table 4.1**), f_{DM} is the reduced friction factor due to shear-thinning and Re_N is the generalised Reynolds number defined as:

$$Re_N = \frac{10^{\left(\frac{\frac{1}{\sqrt{f_{DM}}}+C}{A}\right)}}{B} \quad \text{and} \quad A = \frac{4}{n^{0.75}},\ B = f_{DM}^{\left(1-\frac{n}{2}\right)},\ C = \frac{0.4}{n^{1.2}} \qquad \textbf{(5.12b)}$$

The remaining reduction in friction factor (Δf_E) is presumably due to other non-Newtonian effects, which are assumed to be related to elasticity. Therefore, by separating the elastic (Δf_E) and shear-thinning (Δf_{ST}) influences, their relative effects can be investigated as a function of Reynolds number as shown in **Figure 5.54**, where the total reduction in frictional drag (Δf) is given by:

$$\Delta f(\mathrm{Re}) = f_B(\mathrm{Re}) - f(\mathrm{Re}) = \Delta f_E(\mathrm{Re}) + \Delta f_{ST}(\mathrm{Re}) \qquad \textbf{(5.13)}$$

wherein Δf_{ST} (Re) is the shear-thinning influence ($\equiv f_B$ (Re) - f_{DM} (Re)) where f_{DM} (Re) is determined from the Dodge-Metzner formula given in Eq. **(5.12a-b)**.

From **Figure 5.54**, it is clear that the elastic influence on drag reduction is greater than the shear-thinning influences for all fluids when Re > 10,000, with the exception of 0.1% Carbopol EZ1, which is predominantly dominated by shear-thinning influences for Re<20,000. It is important to note that the relationship of $\Delta f_E/\Delta f$ *versus* Re is purely an indication of the relative influence of the assumed elastic effect on drag reduction and is not an indication of the degree of elasticity inherent within the fluid. Therefore, based on the ranking deduced from the rheological assessments discussed in Chapter 4 (N_1 and G′), it may be assumed at first sight that the larger the level of viscoelasticity associated with a fluid, the greater is its role in reducing frictional drag in turbulent pipe flow. However, when comparing the data for 0.25% CMC (moderately elastic) and 0.2% PAA (highly elastic) in **Figure 5.54**, the elastic

influence is greater for CMC than PAA in reducing drag, contrary to what may be expected from ranking fluids on their relative viscoelastic levels.

Based on the hypothesis that separating the elastic and shear-thinning influences of a fluid enables their relative effects on reducing drag to be assessed, the following ranking has been deduced based on the magnitude of $\Delta f_E/\Delta f$ for 5,000<Re<10,000: 0.2% XG, 0.2% PAA, 0.125% PAA, 0.09% CMC/0.09% XG, 0.24% CMC, 0.4% CMC and 0.25% CMC. The data for 0.1% Carbopol has been excluded from this ranking due to large changes in $\Delta f_E/\Delta f$ within the Reynolds number range quoted, which is a consequence of the data being exposed to transitional effects. For Re>10,000, the ranking changes slightly and due to the limited range of Reynolds number for some data, the ranking is incomplete. It may be concluded from **Figure 5.54**, that the elastic influence (Δf_E) on drag reduction increases with Reynolds number, which is consistent with an increase in DR, though remains quite steady for the CMC and Carbopol solutions compared with other test fluids, which otherwise show a steady increase with Reynolds number.

5.6.3 Drag-Reduction Ranking

As for the rheological properties of the polymer solutions, it is instructive to identify the drag-reduction ranking for the same test fluids based on the DR levels. For Re>18,000, this is 0.1% Carbopol EZ1, 0.14% Carbopol 934, 0.24% CMC, 0.09% CMC/0.09% XG, 0.25% CMC, 0.4% CMC (based on qualitative assumption), 0.2% XG, 0.125% PAA and 0.2% PAA. At lower Reynolds numbers the curves for 0.2% XG and 0.125% PAA cross over, as do the curves for 0.25% CMC and 0.09% CMC/0.09% XG.

Based on the rankings devised above and from the previous chapter, including the tabulations of results obtained from the universal law of the wall and normalised turbulence intensity distribution profiles, correlations between various data may be deduced. These correlations are specifically based on both quantitative analyses and

qualitative comparisons between the pipeflow and rheological data, which are discussed in detail in the following section.

5.7 Correlations between Elasticity and Pipe Flow Characteristics

The collection, collation and analysis of results for the hydrodynamic flow tests (f-Re data), including the rheological assessments carried out in the previous chapter, have been summarised in terms of 'ranking' in **Table 5.8**. The table ranks the non-Newtonian solutions used in this study with respect to decreasing levels of viscoelasticity; it also ranks the same solutions with respect to decreasing DR effectiveness and resistance to degradation.

It is evident from **Table 5.8** that there is a clear correlation between viscoelasticity and drag-reducing performance, particularly when comparing columns (1-3) and (5-6). The correlation is however, not complete; for example, anomalies exist when comparing columns (1) and (2). Also, quantitative correlations between the data presented are further required when comparing results obtained from various measurement techniques i.e. under different flow conditions.

Considering the above, the results in columns (5-7) of **Table 5.8** would be more meaningful if the frequency of oscillation could be correlated with drag reduction, and in particular with the turbulent flow characteristics. Such a correlation is not obvious at this stage, particularly the relationship between frequency of oscillation and Reynolds number in pipe flow and hence the oscillatory flow data, despite being seemingly supportive of the ranking deduced from DR values and normal-stress data, is not conclusive.

In Chapter 4.7, the ranking of various rheological parameters were discussed in terms of viscoelastic levels in an attempt to provide information that may be correlated with drag reduction. These rheological parameters (namely the first normal stress difference, N_1), were assessed as functions of shear rate ($\dot{\gamma}$) and shear stress (τ_S). From **Table 5.8**, the drag reduction ranking for Re > 18,000 matches that for the first

normal stress difference at low shear rates (<$20s^{-1}$). The first of these conclusions partially confirms that of Vlassopoulos and Schowalter (1993) '...that ranking additives according to elasticity provides information about drag-reducing effectiveness...'. From this, it seems appropriate from a ranking consideration based on observations only, to conclude that the mechanism for drag reduction is associated with shear rates of order $20s^{-1}$ or lower. It was therefore postulated that by identifying the span-wise location (y^+) of shear rates of this order of magnitude ($20s^{-1}$) using law of the wall coordinates, further supporting evidence related to the mechanism behind drag reduction may be discovered.

Figure 5.55 shows the near-wall distribution of the shear rate ($\dot{\gamma}$) *versus* y^+ evaluated from the mean velocity profiles for the highest Reynolds numbers for each fluid i.e. profiles corresponding with the highest levels of drag reduction (except for Carbopol where the level of drag reduction is less at higher Reynolds numbers). Using linear interpolation between consecutive data points, plotted as u *versus* y, the shear rate was determined. It becomes apparent from **Figures 5.26 - 5.34** and **Figure 5.55** that shear rates of the order of $20s^{-1}$ are considerably lower than the wall shear rates and are comparable to what can be estimated from the mean velocity distributions just within or beyond the buffer region ($80<y^+<250$), thus also extending into the log-law region itself.

At this point, these observations seem to be consistent with the view of Tiederman *et al.* (1985) who argued that the viscous sublayer plays a passive role in the drag-reduction process and that polymer additives have a direct effect on flow structures in the buffer layer. This is consistent with the findings made from the previous sections (Sections 5.4 and 5.5), which also indicated that the viscous sublayer plays a passive role in the flow of drag-reducing non-Newtonian fluids. It was evident that significant differences between non-Newtonian and Newtonian fluids only existed within the buffer and turbulent core regions of flow based on the analyses presented in this study. For the non-Newtonian fluids, the buffer region was extended towards the centre of the pipe, the extent of which was consistent with the level of DR and upward shift in

the logarithmic profile within the turbulent core (ΔB). These observations form part of the conclusions discussed in Chapter 7.

Interestingly, also from **Table 5.8**, the resistance to degradation seems to be correlated to DR effectiveness and viscoelasticity, apart from the lower ranked data as previously explained in Chapter 4.5.2. The correlation between these variables substantiates the argument that the macromolecular structures of the test fluids are fundamental in quantifying turbulent flow characteristics of non-Newtonian fluids in pipe flow.

Attempts were then made to quantitatively correlate measurable functions of elasticity - primarily the first normal stress difference as a function of shear stress - with the isolated effects of elasticity (Δf_E) in a pressure drop *versus* flowrate experiment. It was anticipated that Δf_E should depend on N_1/τ, hence their relationship was investigated for all test fluids (except for Carbopol and Laponite) as shown in **Figure 5.56**. It is clear from **Figure 5.56**, that this did not seem to be the case and therefore, other correlations between Δf_E and N_1 were investigated:

$$\frac{\Delta f_E}{\Delta f} \; versus \; \frac{N_1}{\rho U^2} \qquad \textbf{(5.14)}$$

The above expression is a correlation between the elastic contribution to drag reduction and the first normal stress difference non-dimensionalised with the pressure stresses. This relationship is shown in **Figure 5.57**. The trend for individual fluids was for a decrease in the elastic contribution to the overall drag reduction ($\Delta f_E/\Delta f$) with increasing $N_1/\rho U^2$. It may therefore be concluded that N_1 is not the principal factor in drag reduction and that another viscoelastic characteristic must be investigated. The most likely candidate is the extensional viscosity (see Chapter 4.5), as has also been suggested by Durst *et al.* (1982) and by den Toonder *et al.* (1995); although this hypothesis remains unproved.

Tables and Figures

Table 5.1 *Onset of Transition and Turbulent Flow*†

Test Fluid	Re_1	τ_{S1} [Pa]	Re_2	τ_{S2} [Pa]	DR [%]
0.2% PAA	1,500	2.63	11,000	5.10	61
0.125% PAA	1,700	1.21	10,000	2.68	52
0.2% XG	1,600	1.88	6,000	2.90	46
0.4% CMC	2,000	7.65	6,000	18.00	37
0.09% CMC/0.09% XG	2,000	1.13	6,000	2.22	36
0.25% CMC	1,900	2.64	5,500	6.65	32
0.14% Carbopol 934	1,000	1.82	5,000	5.86	21
0.1% Carbopol EZ1	1,000	1.61	5,000	5.20	20
0.24% CMC	2,000	2.60	4,000	5.92	20

† Data obtained from **Figures 5.7-5.15**.

Table 5.2 *Velocity Characteristics of Newtonian Pipe Flow*†

Reference	Fluid	Re	$U/U_{max.}$	Pipe Diameter [mm]	Technique
This Work	Glucose	8,000	0.78	100.46	LDA
This Work	Glucose	36,000	0.82	100.46	LDA
This Work	Water	61,000	0.83	100.46	LDA
Pinho (1990)	Water	32,000	0.79	25.4	LDA
Pinho (1990)	Water	62,000	0.81	25.4	LDA
Laufer (1954)	Air	40,000	0.80	254	Hot-Wire
Lawn (1971)	Air	35,000	0.81	144.3	Hot-Wire

† Based on representation given by Pinho (1990).

Table 5.3 *Universal Law of the Wall Data for all Test Fluids*

Fluid	Re	$\Delta B^{\dagger}$	y_1^+	DR [%]
0.2% PAA	18,800	17.0	90	64.8
	23,100	17.5	160	65.0
0.125% PAA	15,000	13.0	110	57.0
	26,400	15.3	110	61.0
	35,900	16.5	110	64.7
	42,900	18.3	110	66.1
0.2% XG	6,500	10.5	80	48.0
	14,100	12.0	100	58.0
	40,500	14.0	120	61.0
0.09% CMC/0.09% XG	10,700	7.5	110	38.5
	26,100	6.5	130	41.7
	45,300	7.5	150	45.0
0.4% CMC	5,500	6.0	70	39.0
0.25% CMC	3,7500	5.4	52	23.5
	4,500	5.5	80	27.0
	7,300	5.3	85	32.0
	8,900	6.0	90	35.0
	16,600	5.7	110	36.5
0.24% CMC	4,300	3.7	>60	21.0
	14,100	3.7	60	32.4
0.14% Carbopol 934	5,200	2.5	40	20.0
	6,600	2.5	40	19.8
	12,600	1.7	40	15.8
	18,600	1.4	40	15.3
0.1% Carbopol EZ1	5,600	3.0	80	17.6
	9,600	1.7	60	13.8
	14,700	1.4	50	13.5
	24,000	1.0	40	11.9

† See Equation **(5.11)**.

Table 5.4 *Summary of Normalised Velocity Fluctuations (normalised against u_τ)*[†]

Fluid	Axial			Tangential			Radial[‡]		
	Re	u'/u_τ	y^+	Re	w'/u_τ	y^+	Re	v'/u_τ	y^+
0.2% XG	6500	3.1	31	6600	0.60	40	6600	0.65	40
	14100	3.5	26	13800	0.88	70	13900	0.78	60
	40500	3.8	23	39000	1.10	100	39700	0.85	80
0.24% CMC	4300	3.0	18	4850	1.08	40	4700	0.90	65
	14100	3.3	12	16500	1.40	40	16100	1.10	105
0.25% CMC	3750	2.8	13	-	-	-	-	-	-
	4500	3.0	14	-	-	-	-	-	-
	7320	3.3	22	7900	1.24	60	8200	0.95	60
	8900	3.3	21	10000	1.30	50	10200	1.00	60
	16600	3.3	18	18400	1.33	50	20500	1.12	100
0.4% CMC	5500	3.0	20	-	-	-	-	-	-
0.09% XG/	10700	3.6	14	12900	1.25	40	16800	1.10	100
0.09% CMC	26100	3.7	21	26150	1.32	50	29500	1.20	140
	45300	3.75	18	50000	1.45	60	53200	1.30	250
0.125% PAA	15000	4.6	35	-	-	-	-	-	-
	26400	4.4	45	-	-	-	-	-	-
	35900	4.7	45	37500	1.25	100	41100	1.00	200
	42900	4.8	32	43100	1.28	105	52000	1.10	210
0.2% PAA	18800	5.2	40	-	-	-	-	-	-
	23100	5.5	40	-	-	-	-	-	-
0.14% Carb. 934	4100	3.1	15	7600	1.30	40	-	-	-
	5200	3.1	15	8900	1.32	47	-	-	-
	6600	3.1	15	14300	1.40	40	-	-	-
	12650	3.1	15	18300	1.44	47	-	-	-
	18600	3.1	15	20700	1.50	41	-	-	-
0.1% Carb. EZ1	5600	3.2	15	-	-	-	-	-	-
	9600	3.2	15	9400	1.30	50	9800	1.20	100
	14800	3.4	14	18500	1.35	50	16500	1.25	105
	24000	3.3	15	30200	1.44	50	28000	1.35	130

† The data shown are maximum values and their corresponding wall location (y^+) were determined from a subjective assessment of the trend in normalised velocity fluctuation data plotted in wall coordinates.

‡ Subjective assessments of the trend in data were difficult due to a large degree of scatter associated with low data rates and reduced quality of the LDA signal when taking radial measurements. The scatter in data is particularly evident when shown in wall coordinates (v'/u_τ *vs* y^+).

Table 5.5 *Summary of Normalised Velocity Fluctuations (normalised against U)**

Fluid	Axial			Tangential			Radial‡		
	Re	u′/U	r/R	Re	w′/U	r/R	Re	v′/U	r/R
0.2% XG	6500	0.145	0.80	6600	0.028	0.70	6600	0.030	0.90
	14100	0.145	0.92	13800	0.032	0.78	13900	0.030	0.90
	40500	0.127	0.95	39000	0.038	0.87	39700	0.030	0.90
0.24% CMC	4300	0.185	0.90	4850	0.068	0.80	4700	0.060	0.68
	14100	0.165	0.96	16500	0.070	0.92	16100	0.055	0.66
0.25% CMC	3750	0.185	0.90	-	-	-	-	-	-
	4500	0.178	0.89	-	-	-	-	-	-
	7320	0.182	0.90	7900	0.066	0.76	8200	0.052	0.76
	8900	0.170	0.92	10000	0.066	0.78	10200	0.052	0.78
	16600	0.152	0.96	18400	0.060	0.82	20500	0.051	0.77
0.4% CMC	5500	0.172	0.86	-	-	-	-	-	-
0.09% XG/	10700	0.165	0.93	12900	0.057	0.81	16800	0.050	0.74
0.09% CMC	26100	0.157	0.96	26150	0.056	0.90	29500	0.050	0.74
	45300	0.141	0.97	50000	0.057	0.93	53200	0.050	0.74
0.125% PAA	15000	0.145	0.87	-	-	-	-	-	-
	26400	0.150	0.91	-	-	-	-	-	-
	35900	0.146	0.89	37500	0.036	0.87	41100	0.035	0.80
	42900	0.138	0.96	43100	0.036	0.87	52000	0.035	0.80
0.2% PAA	18800	0.174	0.88	-	-	-	-	-	-
	23100	0.190	0.92	-	-	-	-	-	-
0.14% Carb. 934	4100	0.192	0.86	7600	0.075	0.80	-	-	-
	5200	0.192	0.88	8900	0.075	0.86	-	-	-
	6600	0.182	0.93	14300	0.076	0.92	-	-	-
	12650	0.178	0.94	18300	0.080	0.90	-	-	-
	18600	0.168	0.94	20700	0.076	0.92	-	-	-
0.1% Carb. EZ1	5600	0.197	0.92	-	-	-	-	-	-
	9600	0.188	0.94	9400	0.076	0.84	9800	0.068	0.76
	14700	0.195	0.96	18500	0.073	0.90	16500	0.068	0.76
	24000	0.186	0.97	30200	0.072	0.92	28000	0.068	0.76

* The data shown are maximum values and their corresponding location within the pipe (r/R) were determined from a subjective assessment of the trend in normalised velocity fluctuation data plotted as (u′,w′ or v′)/U *vs* r/R.

‡ See comment in **Table 5.4**.

Table 5.6 *Summary of Normalised Centreline Velocity Fluctuations*

Fluid	Axial			Tangential			Radial		
	Re	u′/U	u'/u_τ	Re	w′/U	w'/u_τ	Re	v′/U	v'/u_τ
NON-NEWTONIAN									
0.2% XG	40500	0.048	1.50	39000	0.026	0.78	39700	0.023	0.65
0.24% CMC	14100	0.060	1.25	16500	0.037	0.72	16100	0.038	0.71
0.25% CMC	16600	0.060	1.35	18400	0.034	0.72	20500	0.038	0.72
0.4% CMC	5500	0.080	1.75	-	-	-	-	-	-
0.09%XG/0.09%CMC	45300	0.050	1.35	50000	0.033	0.84	53200	0.035	0.80
0.125% PAA	42900	0.056	1.90	43100	0.027	0.90	52000	0.025	0.86
0.2% PAA	23100	0.062	2.00	-	-	-	-	-	-
0.14% Carb. 934	18600	0.054	1.00	20700	0.042	0.84	-	-	-
0.1% Carb. EZ1	24000	0.052	1.10	30200	0.036	0.72	28000	0.040	0.75
1.5% Laponite †	25300	0.055	0.96	30200	0.026	0.52	28000	0.021	0.48
NEWTONIAN									
Newtonian (This study)	61000	0.060	1.20	61500	0.039	0.83	61500	0.038	0.77
Newtonian (Other) ‡	90000	0.061*	0.96	90000	0.040*	0.76	90000	0.040*	0.76

† See Chapter 6.4.

‡ Data obtained from Lawn (1971) for Air except where stated (see below).

* Data obtained from Pereira and Pinho (1994) for Water at Re = 31000.

Table 5.7 *Drag Reduction Levels for Test Fluids*

Fluid / Re	Drag Reduction, DR (%)			
	5,000	**10,000**	**20,000**	**40,000**
0.2% XG	46	53	59	61
0.24% CMC	22	29	35	-
0.25% CMC	31	40	46	-
0.4% CMC	39	43*	-	-
0.09% XG/0.09% CMC	36	38	41	47
0.125% PAA	42	53	61	66
0.2% PAA	48	60	70	-
0.14% Carbopol 934	21	17	15	-
0.1% Carbopol EZ1	20	15	12	9
1.5% Laponite	18	16	15	13

* Re = 8,000.

Table 5.8 *Ranking of Test Fluids*

Figure 5.53		**Figure 4.28**		**Figure 4.25**	**Figure 4.24**		**Figure 5.54**	**Figure 4.15**
Drag Reduction		**$N_1(\dot{\gamma})$**		**G´ (f)**			**$\Delta f_E/\Delta f$**	**Degradation**
Re < 10,000	**Re > 20,000**	**$\dot{\gamma} < 20s^{-1}$**	**$\dot{\gamma} > 100s^{-1}$**	**f>0.1Hz**	**1.5%, f<1Hz**	**1.5%, f>10Hz**	**5,000<Re<10,000**	**7 Days**
0.2% PAA	0.2% PAA	0.2% PAA	0.2% PAA	0.2% PAA	PAA	CMC	0.1% Carb. EZ1	0.2% PAA
0.2% XG	0.125% PAA	0.125% PAA	0.125% PAA	0.125% PAA	XG	XG/CMC	0.14% Carb. 934*	0.125% PAA
0.125% PAA	0.2% XG	0.2% XG	0.4% CMC	0.2% XG	XG/CMC	XG	0.25% CMC	0.2% XG
0.4% CMC	0.4% CMC	0.4% CMC	0.24% CMC	0.4% CMC*	CMC	PAA	0.4% CMC	0.4% CMC
0.09% XG/ 0.09% CMC	0.25% CMC	0.09% XG/ 0.09% CMC	0.25% CMC	0.09% XG/ 0.09% CMC			0.24% CMC	0.25% CMC
0.25% CMC	0.09% XG/ 0.09% CMC	0.25% CMC	0.2% XG	0.25% CMC*			0.09% XG/ 0.09% CMC	0.24% CMC
0.24% CMC	0.24% CMC	0.24% CMC	0.09% XG/ 0.09% CMC	0.24% CMC*			0.125% PAA	0.09% XG/ 0.09% CMC
0.14% Carb. 934	0.14% Carb. 934			0.14% Carb. 934*			0.2% PAA	0.1% Carb. EZ1
0.1% Carb. EZ1	0.1% Carb. EZ1			0.1% Carb. EZ1			0.2% XG	0.14% Carb. 934
(1)	**(2)**	**(3)**	**(4)**	**(5)**	**(6)**	**(7)**	**(8)**	**(9)**

* Not measured ∴ qualitative assumption.

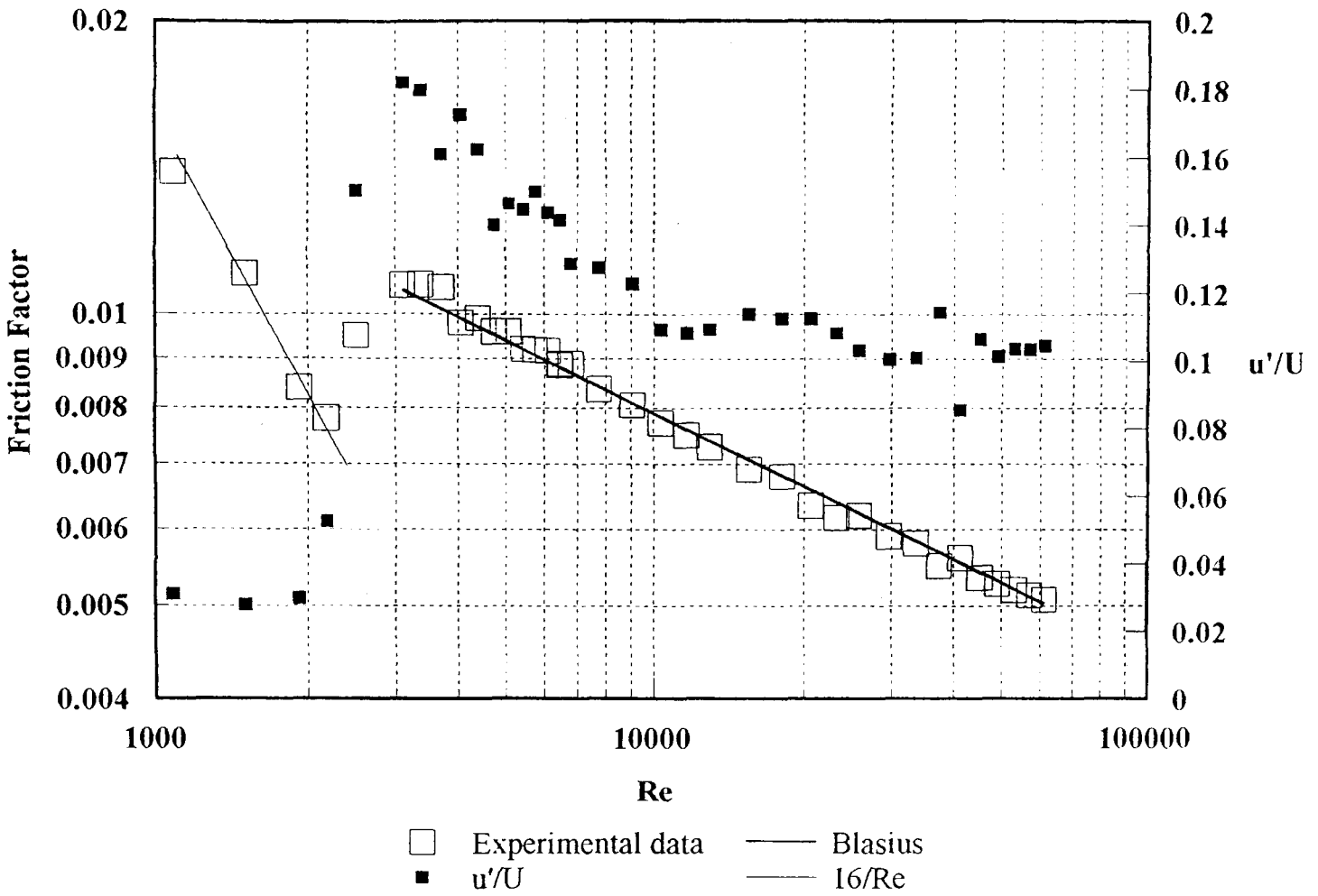

Figure 5.1 *Friction Factor versus Reynolds Number for 60% w/w Aqueous Glucose Solution.*

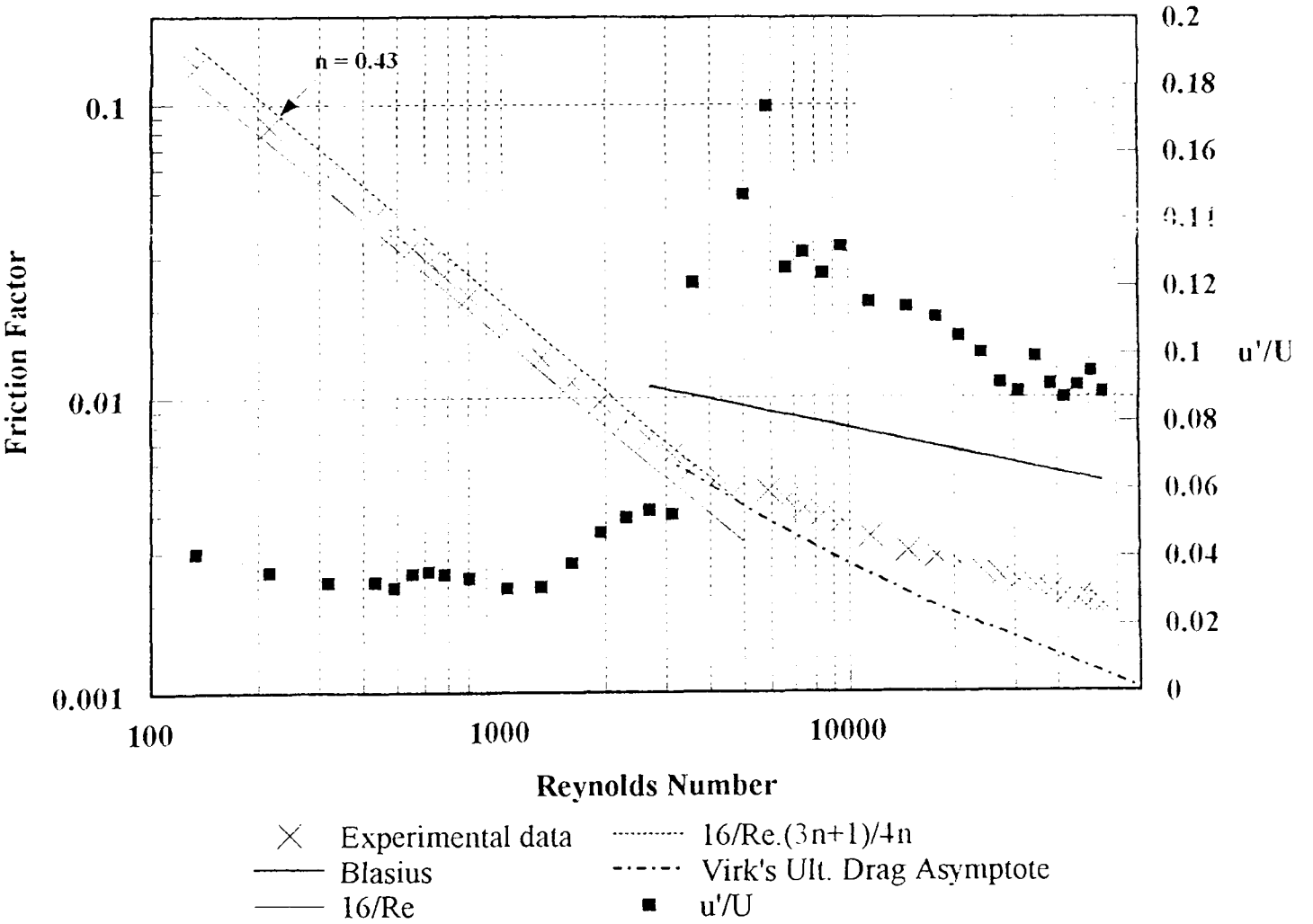

Figure 5.2 *Friction Factor versus Reynolds Number for 0.2% XG.*

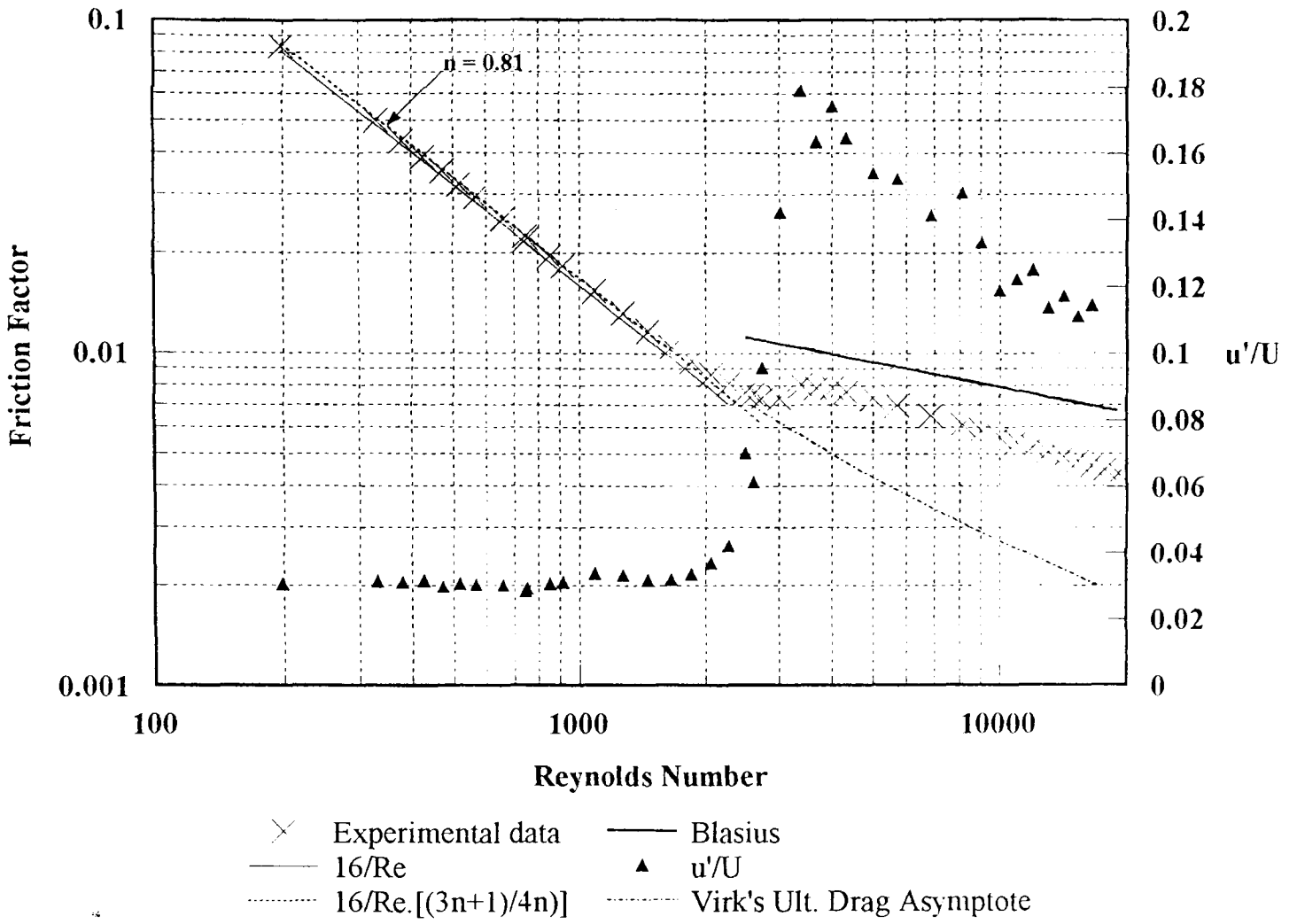

Figure 5.3 *Friction Factor versus Reynolds Number for 0.24% CMC.*

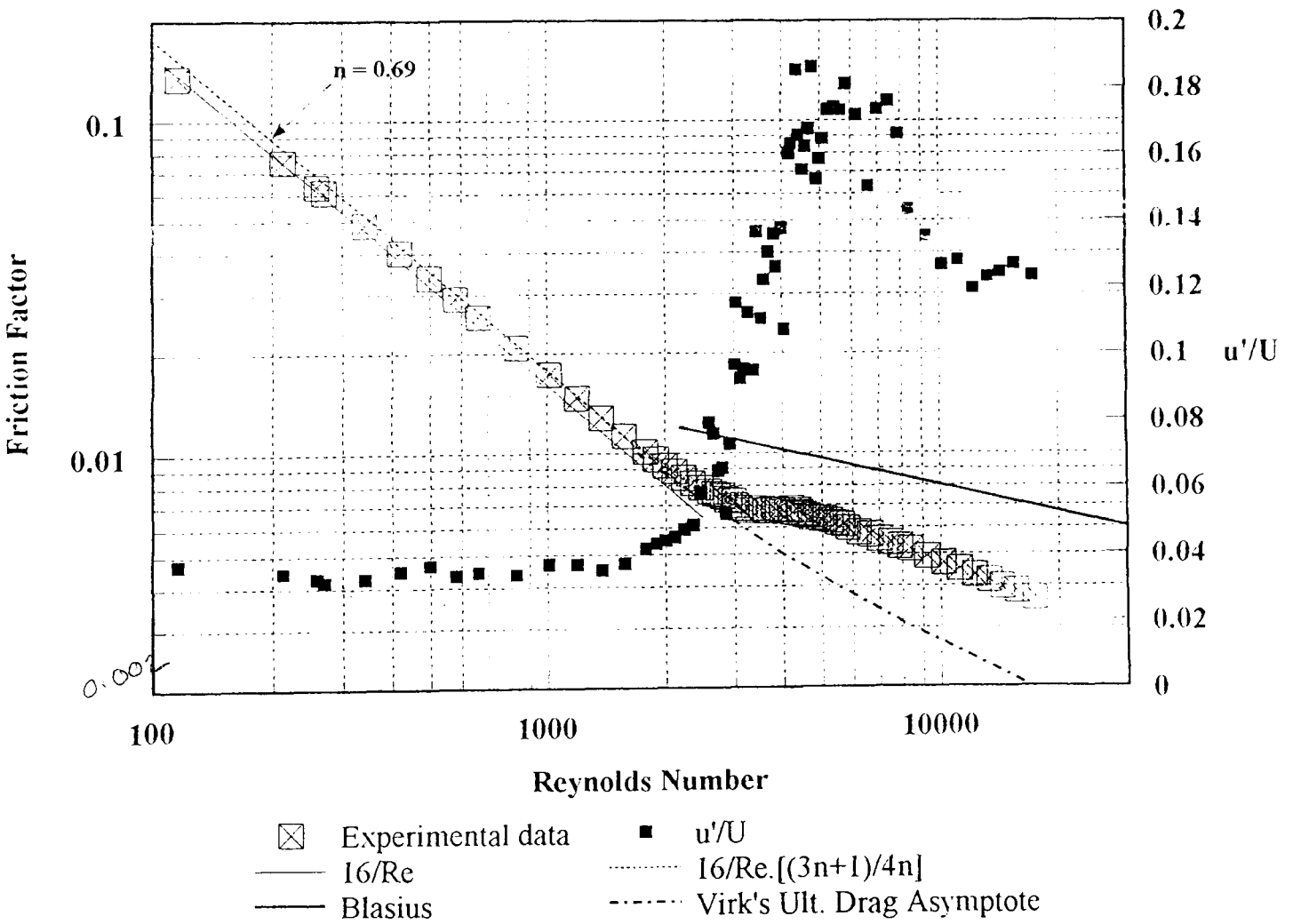

Figure 5.4 *Friction Factor versus Reynolds Number for 0.25% CMC.*

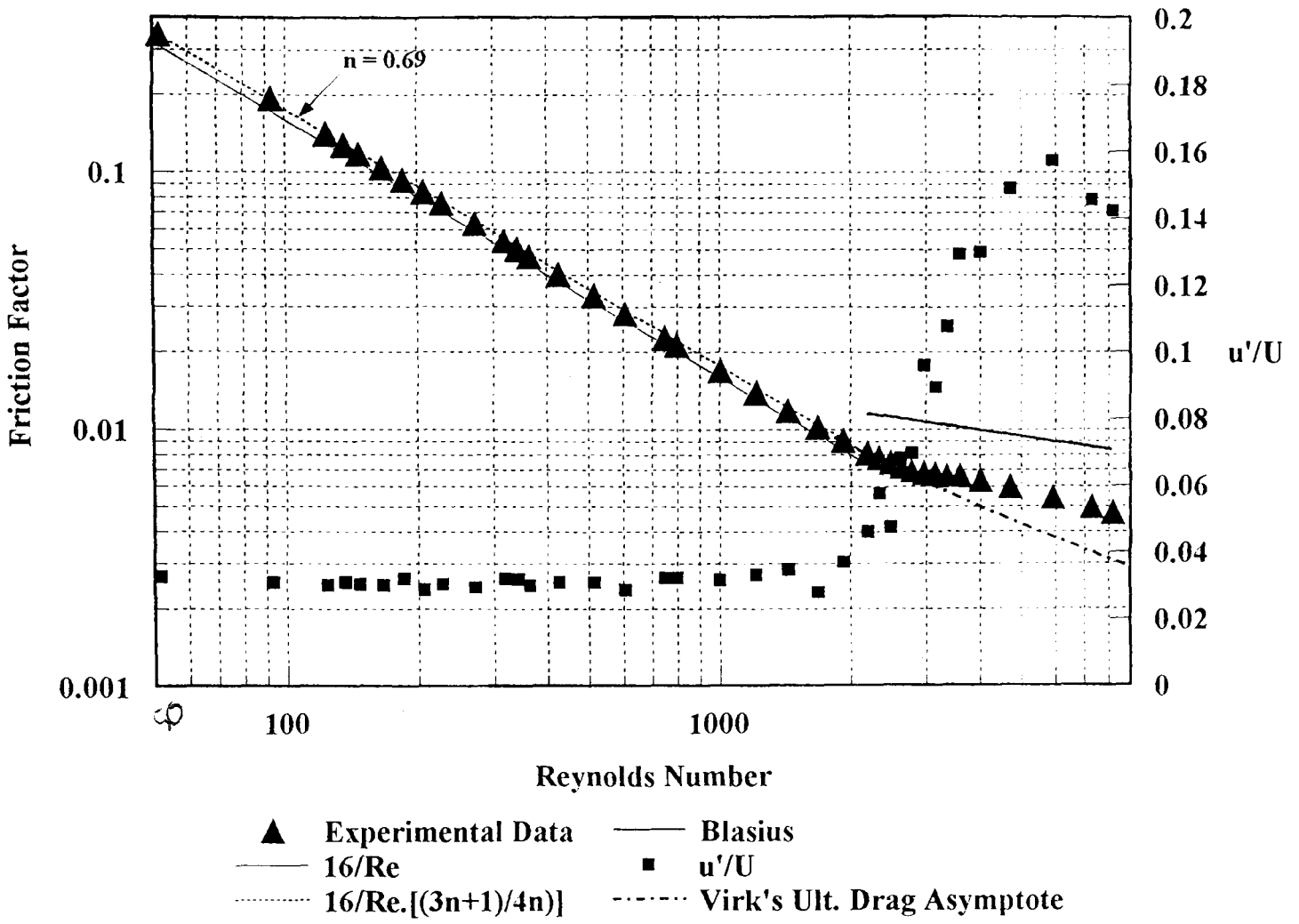

Figure 5.5 *Friction Factor versus Reynolds Number for 0.4% CMC.*

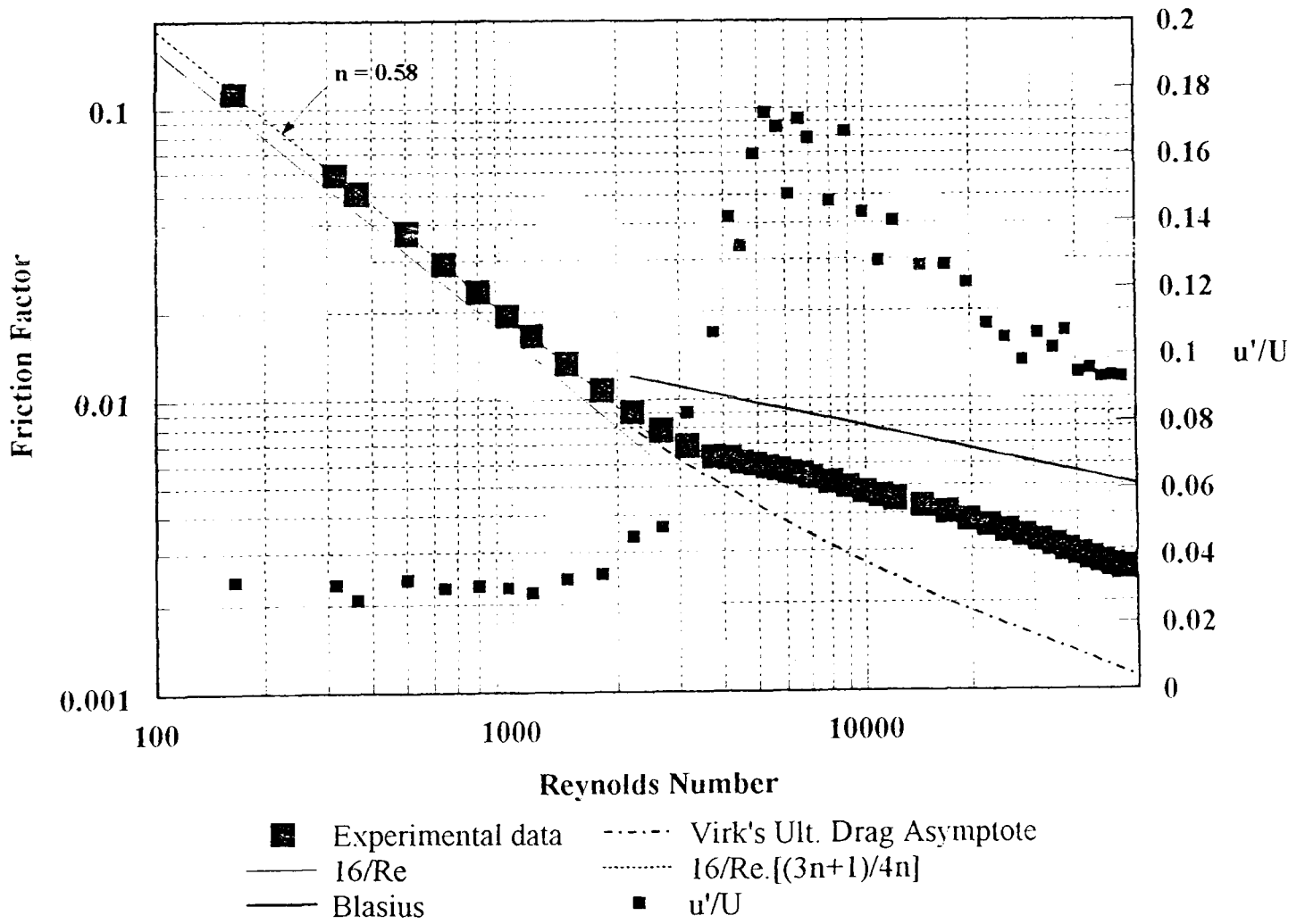

Figure 5.6 *Friction Factor versus Reynolds Number for 0.09% CMC/0.09% XG.*

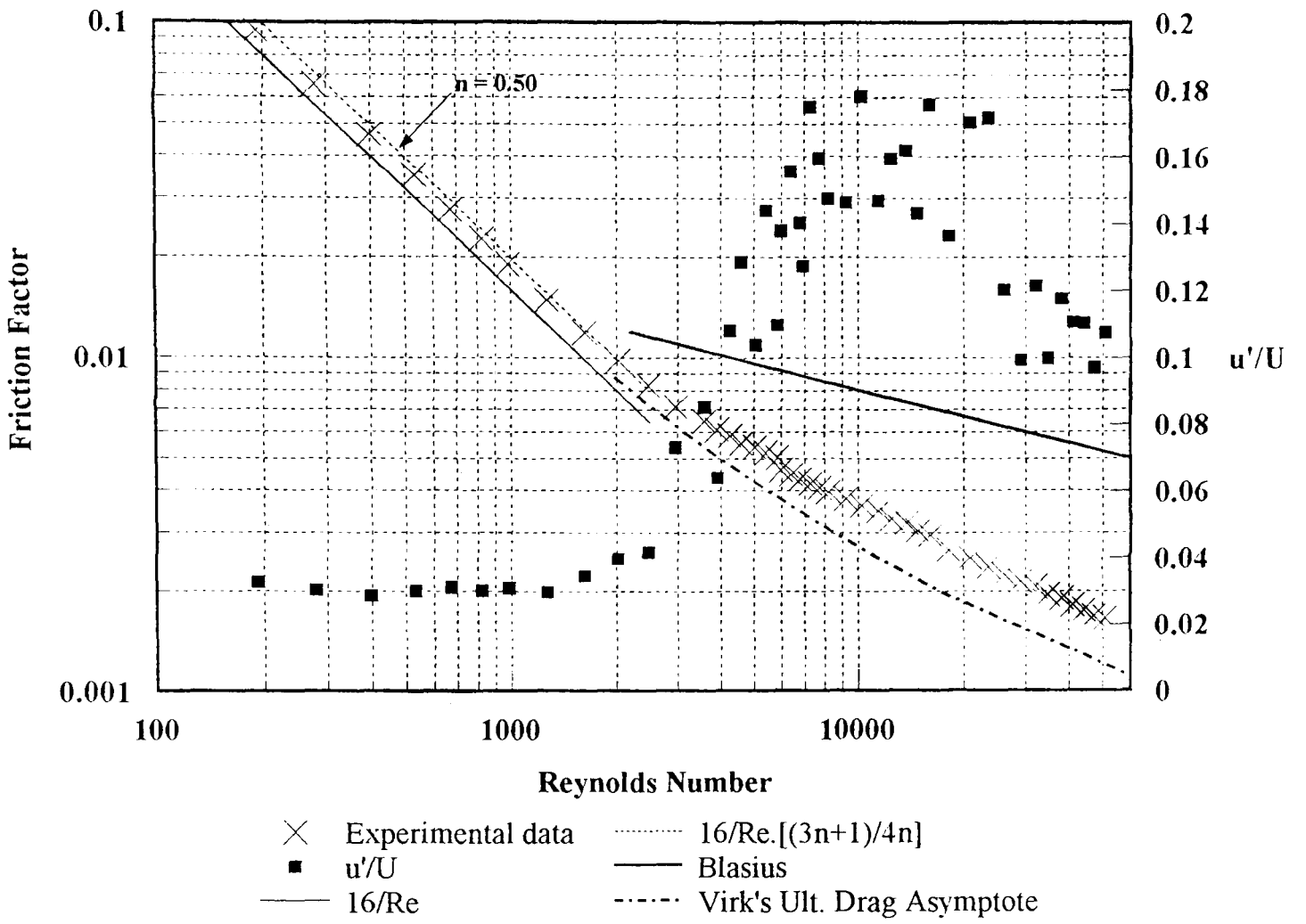

Figure 5.7 *Friction Factor versus Reynolds Number for 0.125% PAA.*

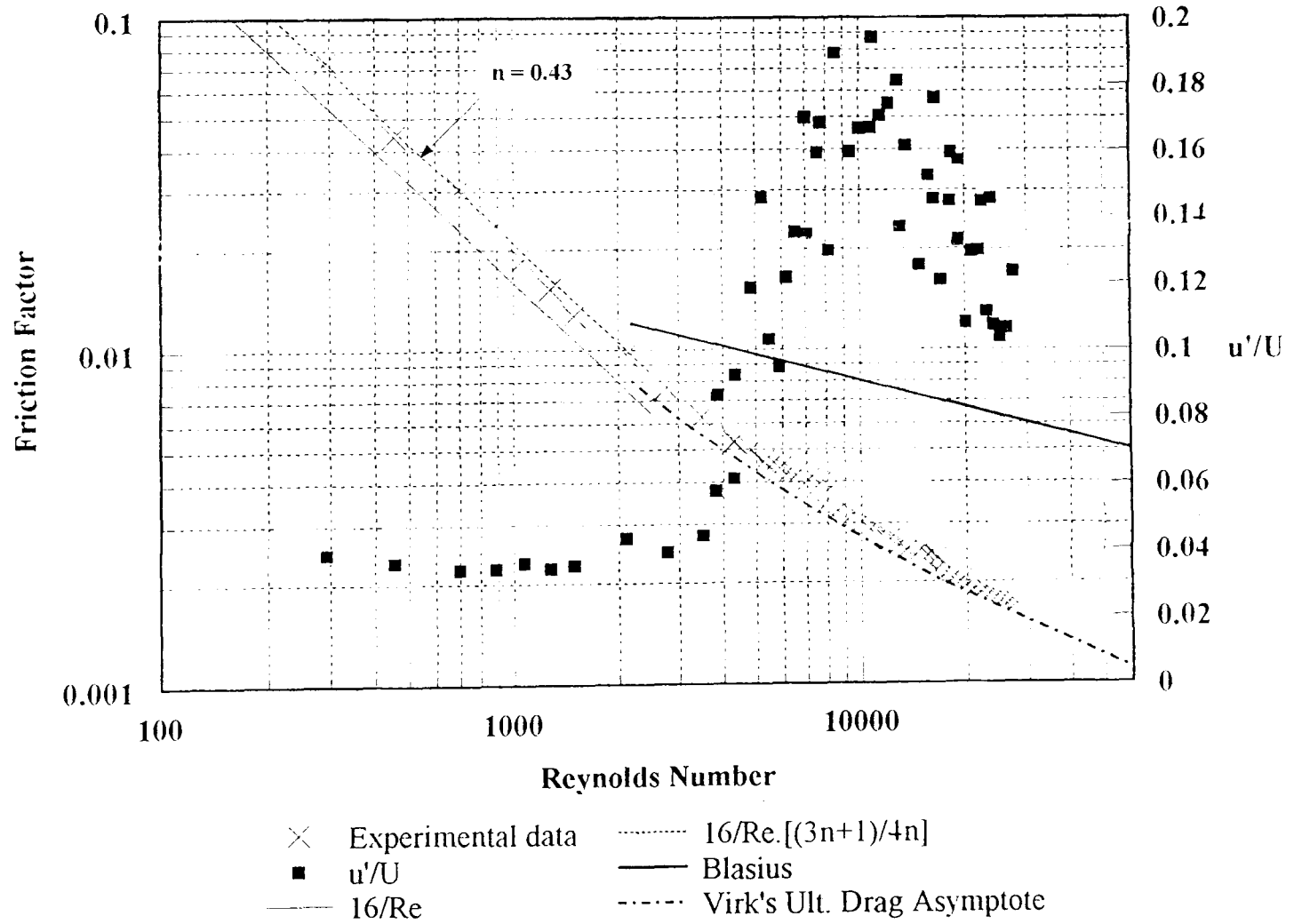

Figure 5.8 *Friction Factor versus Reynolds Number for 0.2% PAA.*

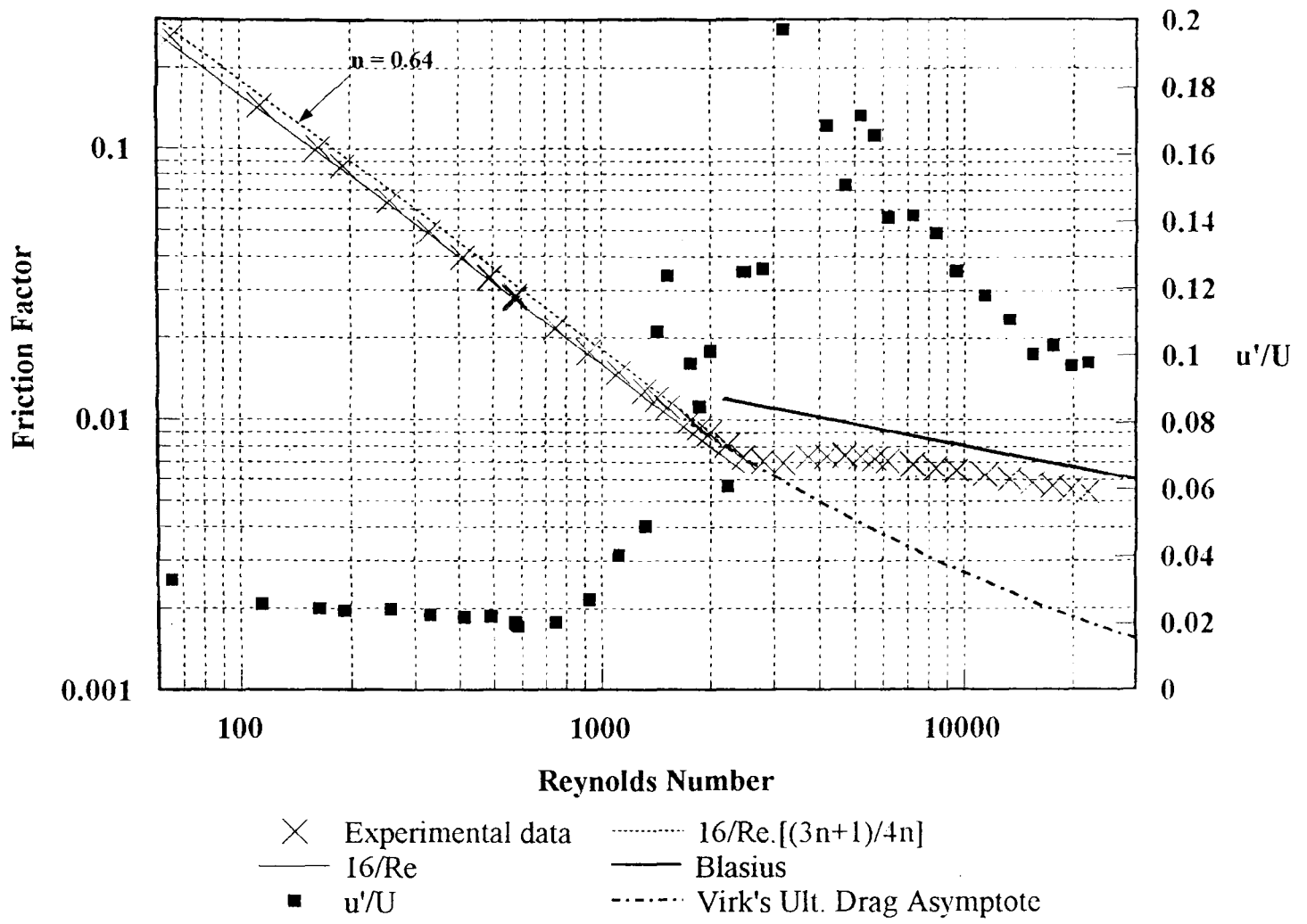

Figure 5.9 *Friction Factor versus Reynolds Number for 0.14 % Carbopol 934.*

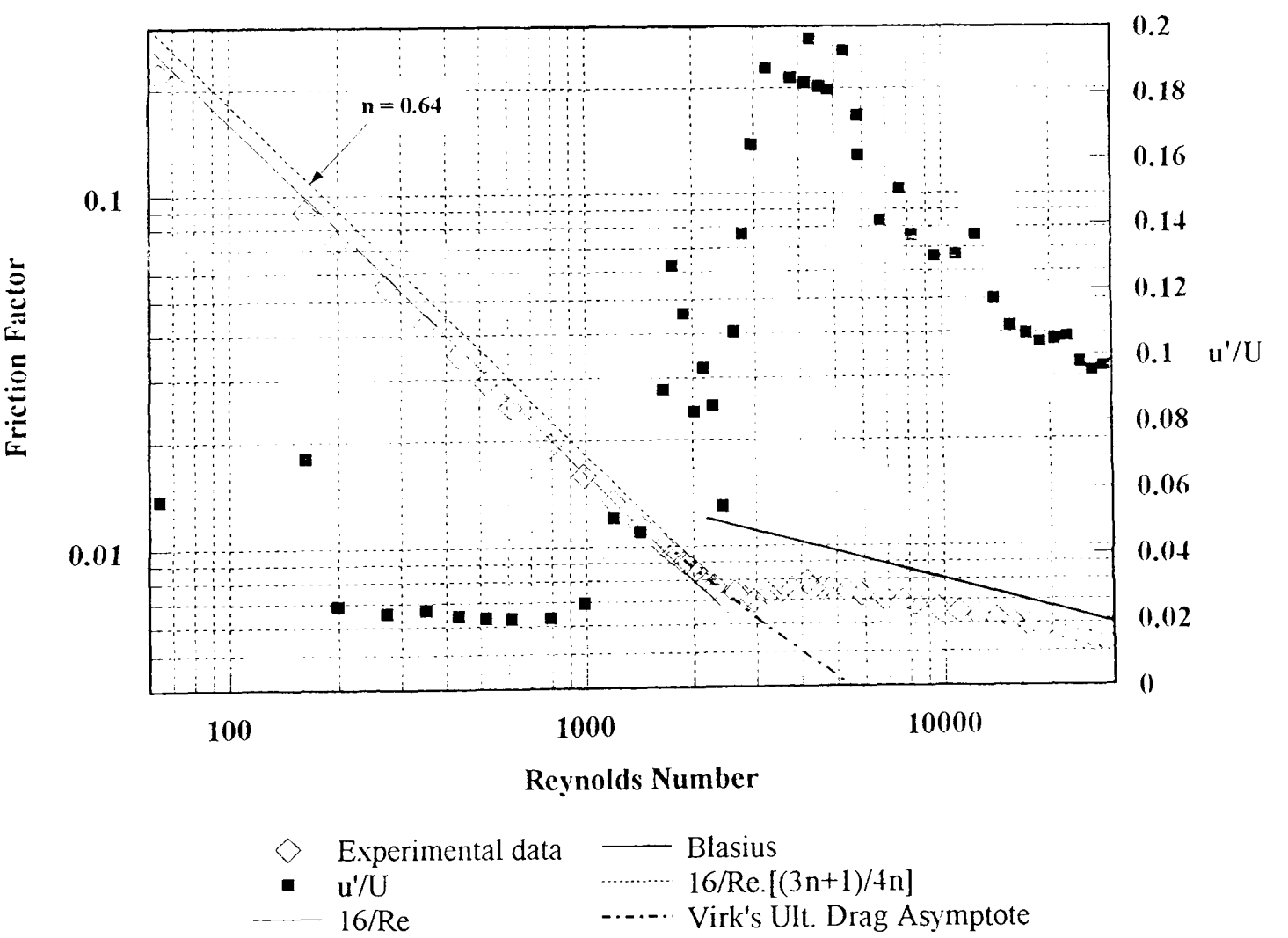

Figure 5.10 *Friction Factor versus Reynolds Number for 0.1 % Carbopol EZ1.*

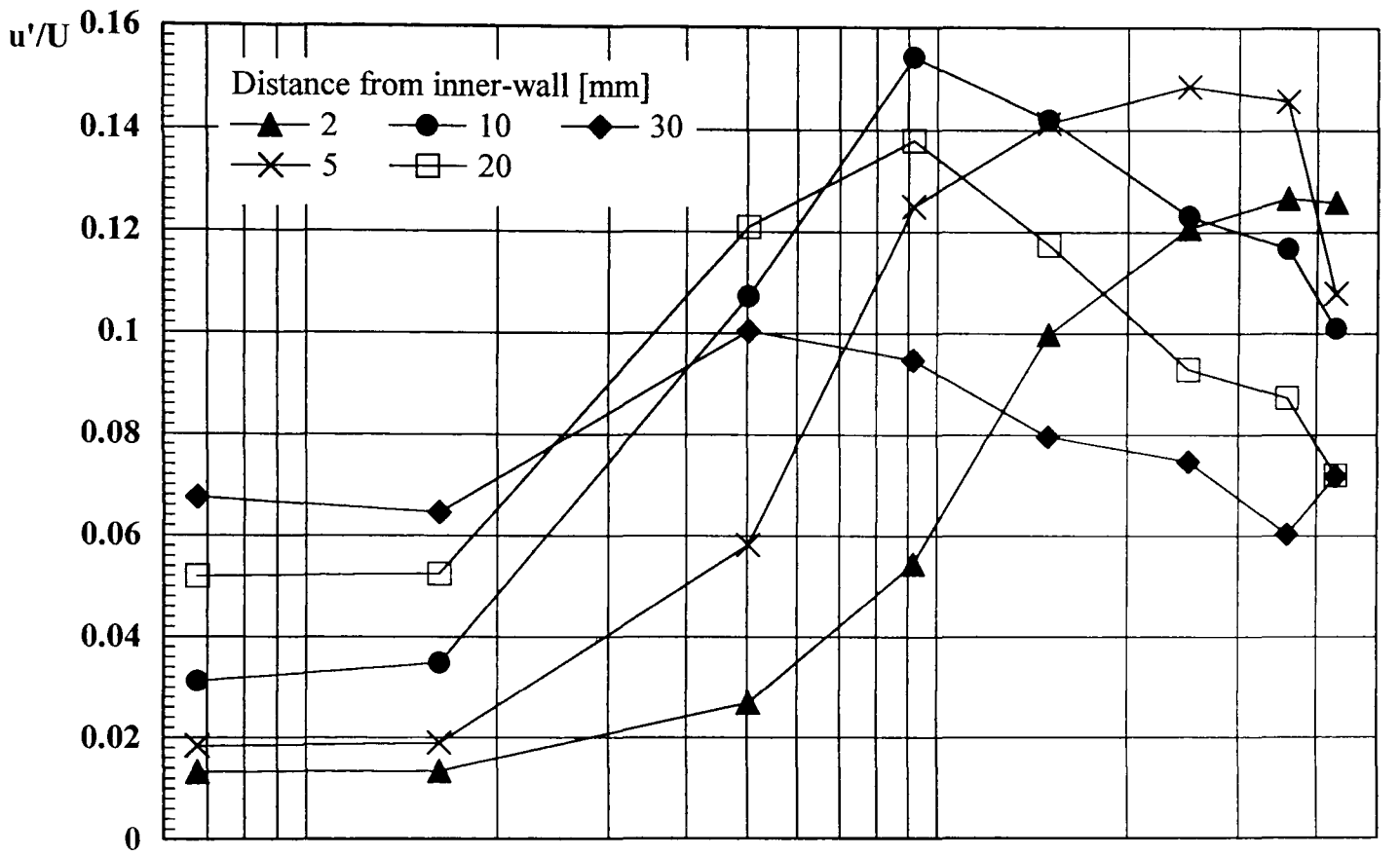

Figure 5.11 *Axial Turbulence Intensities At Various Wall Distances (0.125% PAA).*

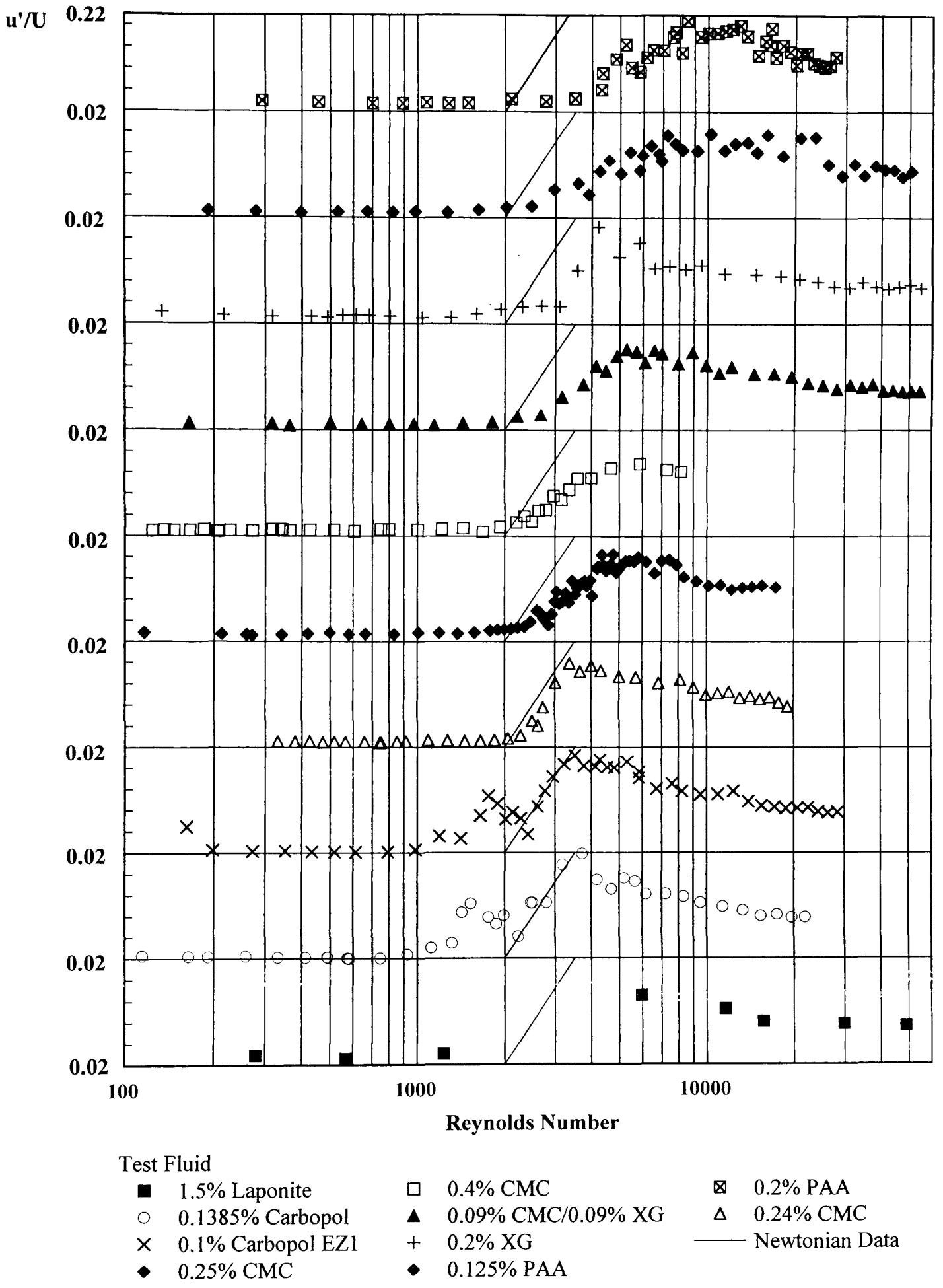

Figure 5.12 *Use of u′/U at y = 10 mm To Indicate Transition.*

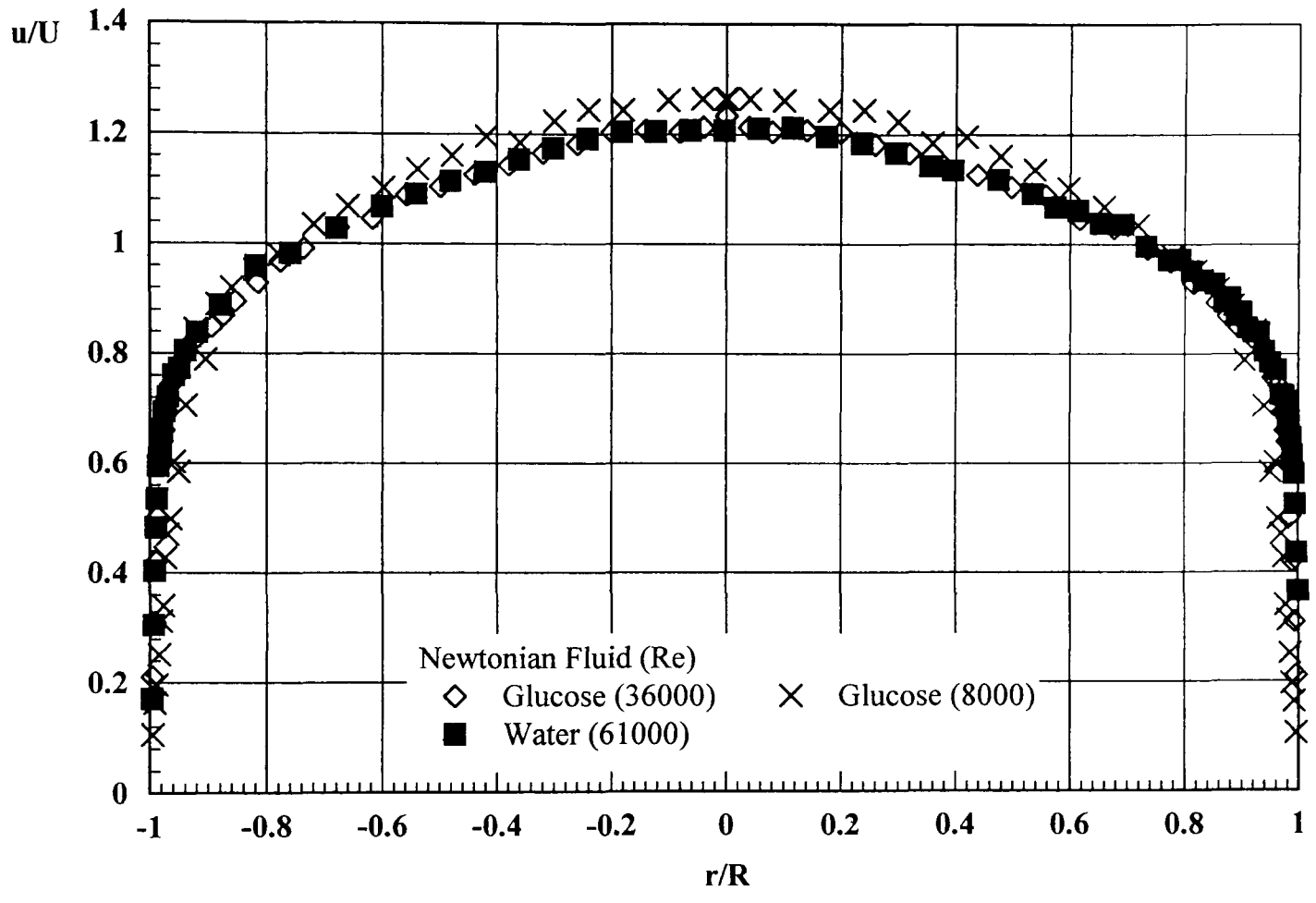

Figure 5.13 *Mean Velocity Distributions in Turbulent Flow For Newtonian Fluids.*

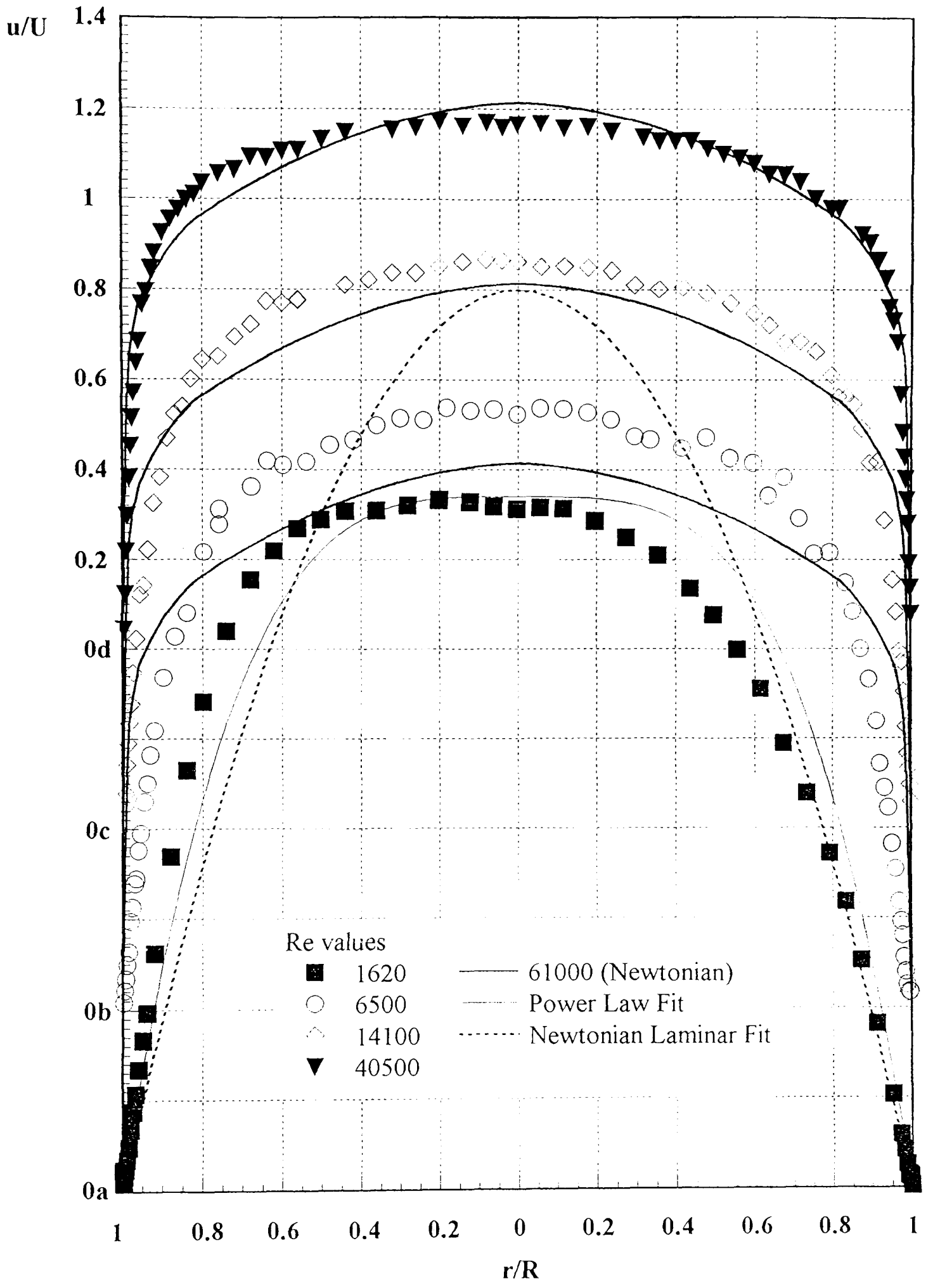

Figure 5.14 *Mean Velocity Distributions For 0.2% XG.*

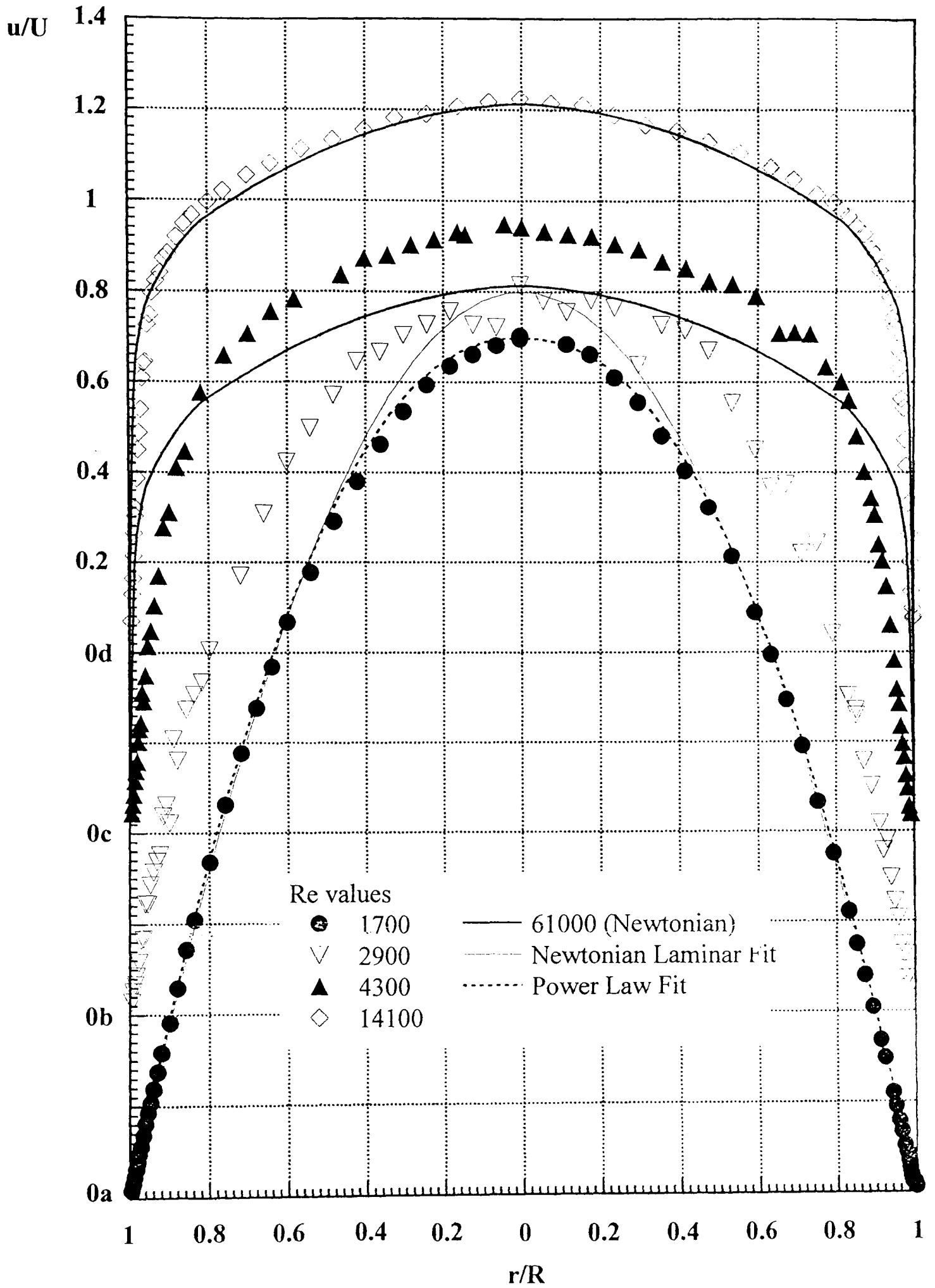

Figure 5.15 *Mean Velocity Distributions For 0.24% CMC.*

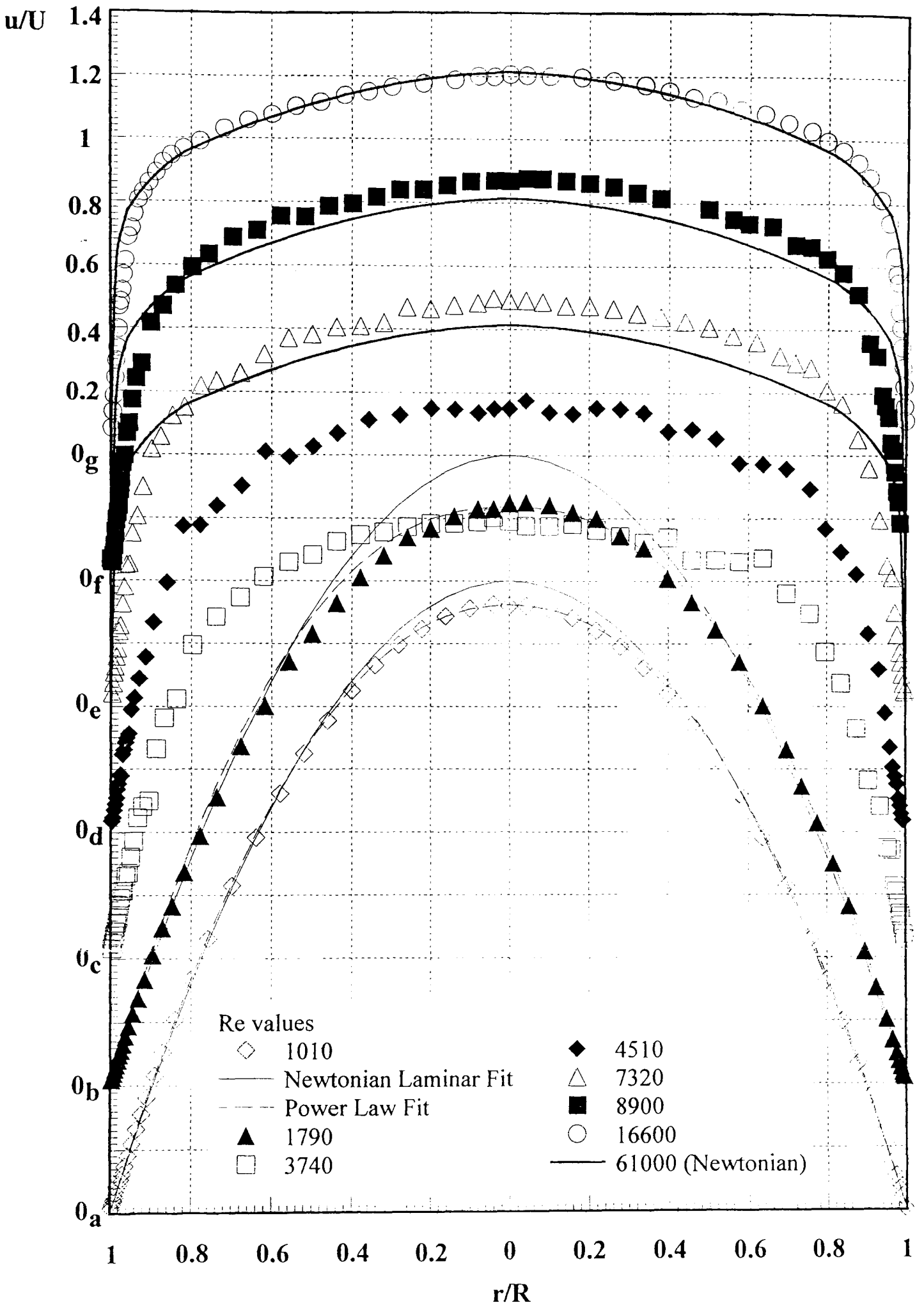

Figure 5.16 *Mean Velocity Distributions For 0.25% CMC.*

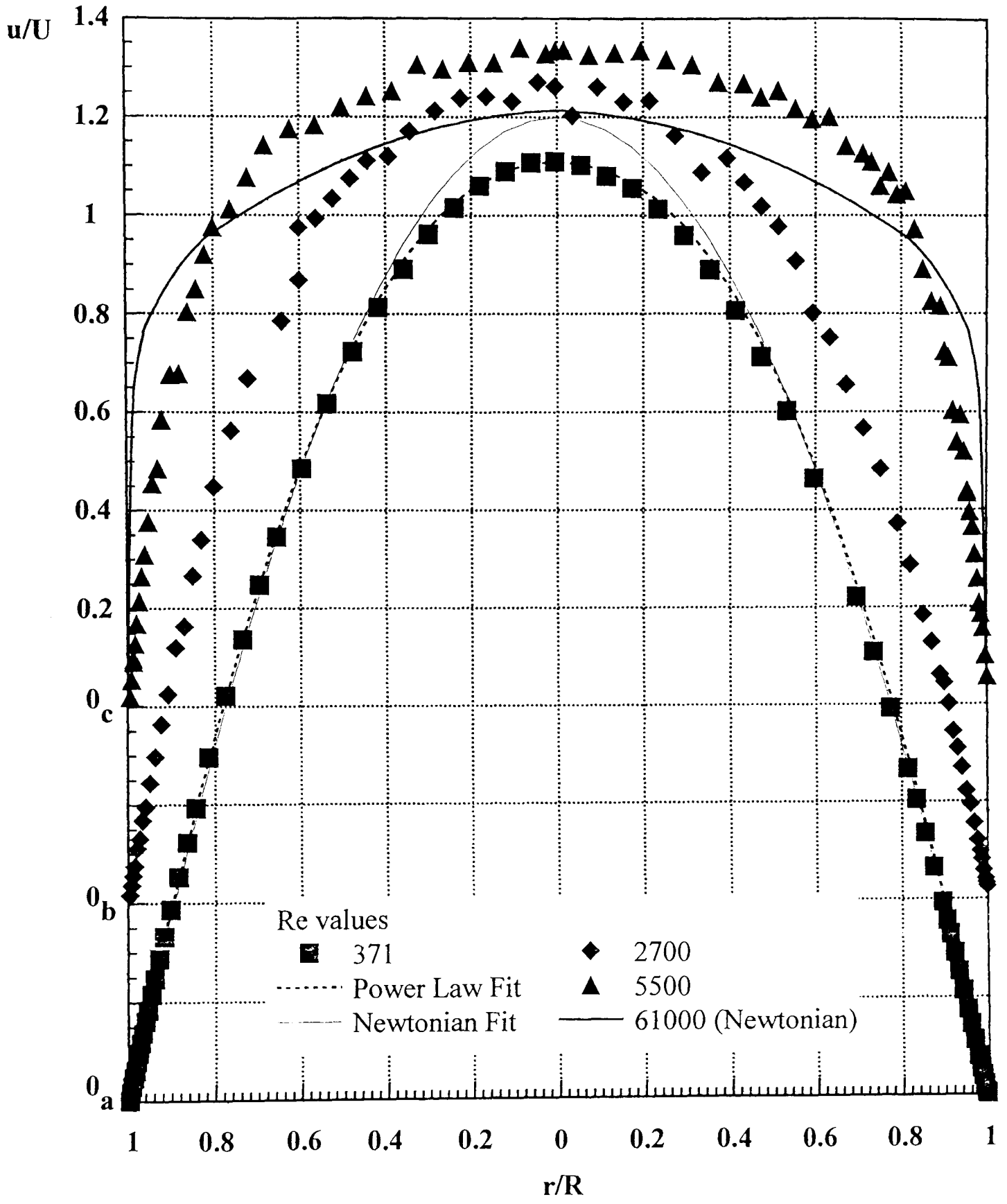

Figure 5.17 *Mean Velocity Distributions For 0.4% CMC.*

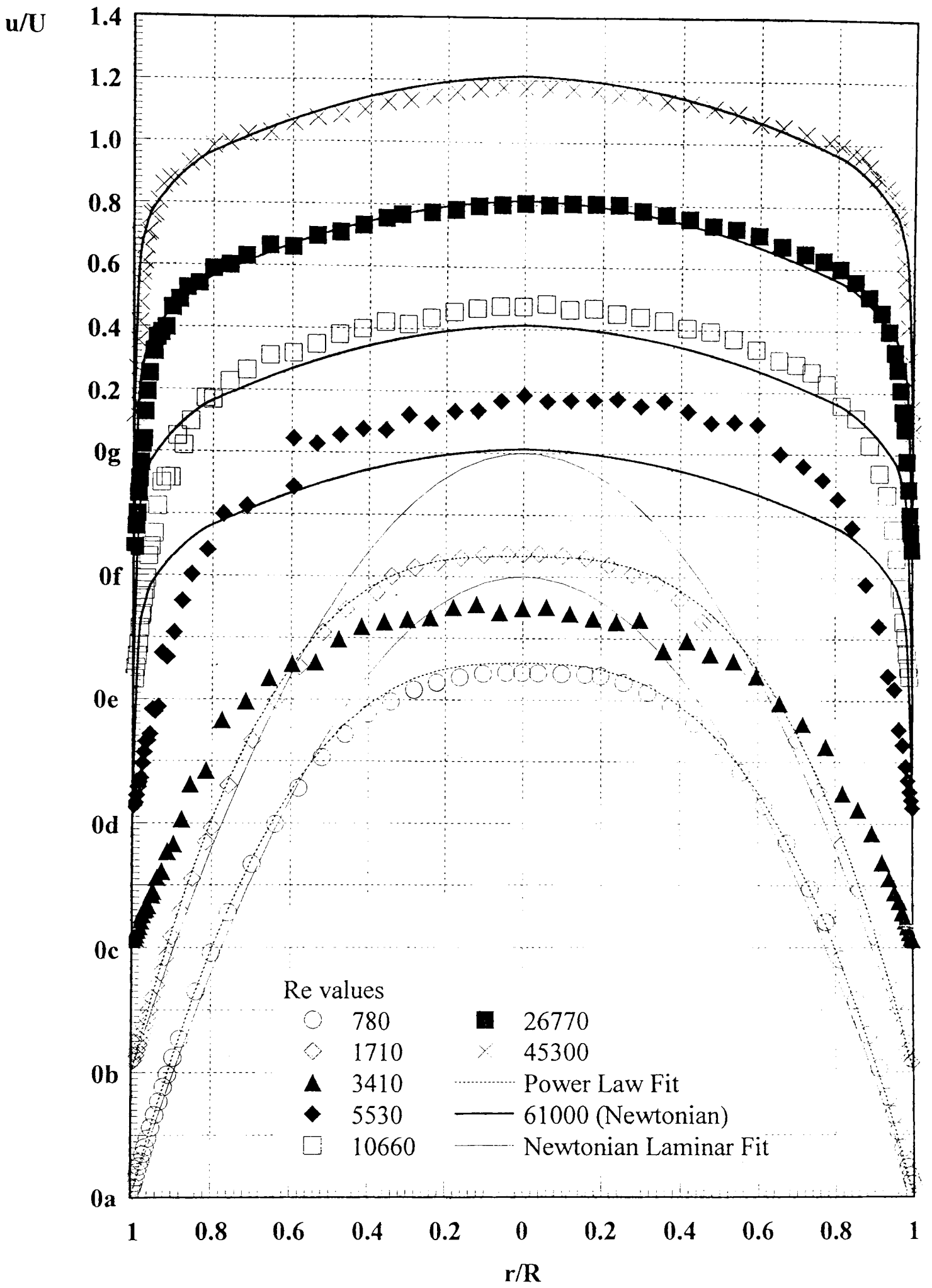

Figure 5.18 *Mean Velocity Distributions For 0.09% CMC/0.09% XG.*

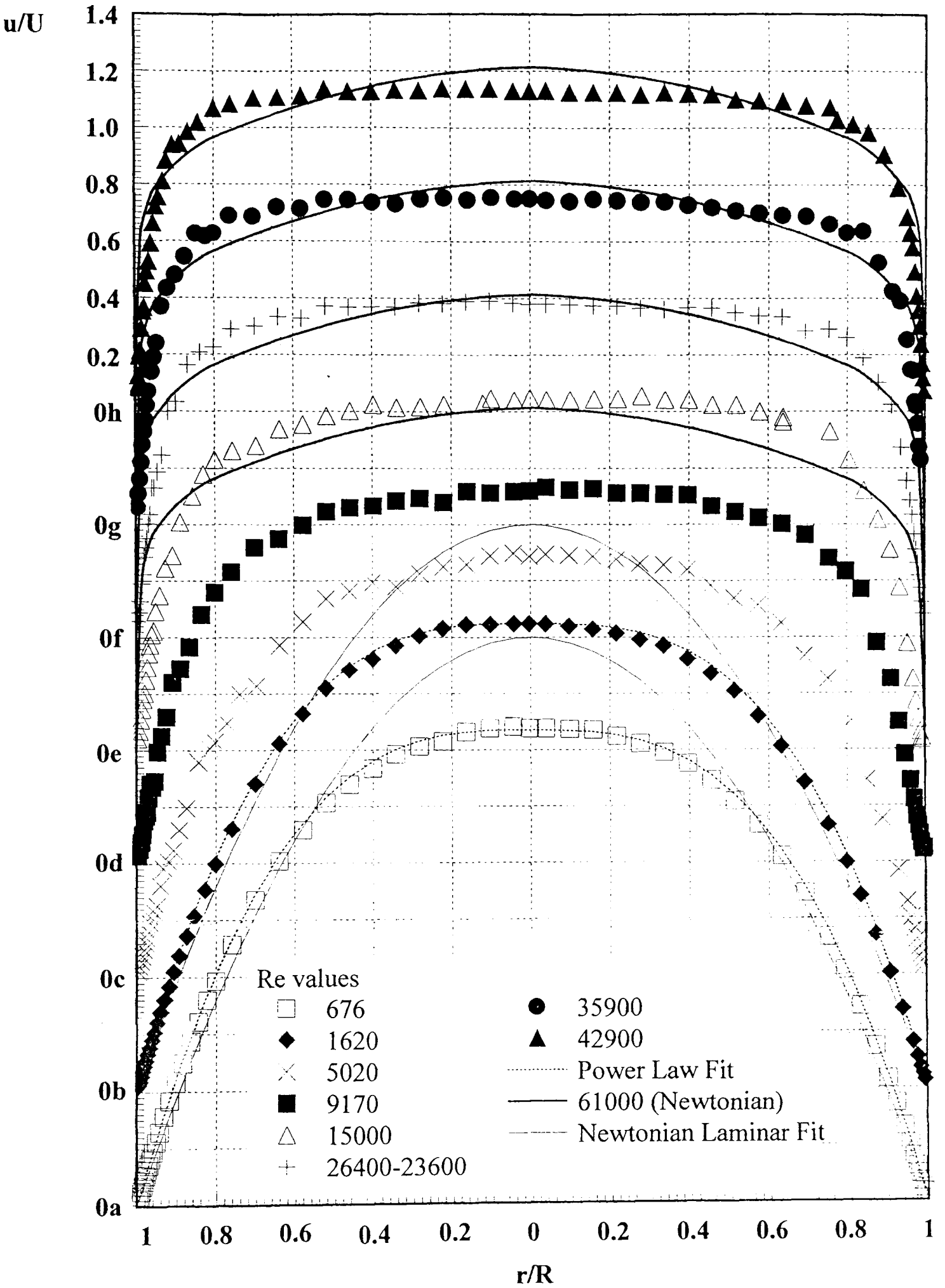

Figure 5.19 *Mean Velocity Distributions For 0.125% PAA.*

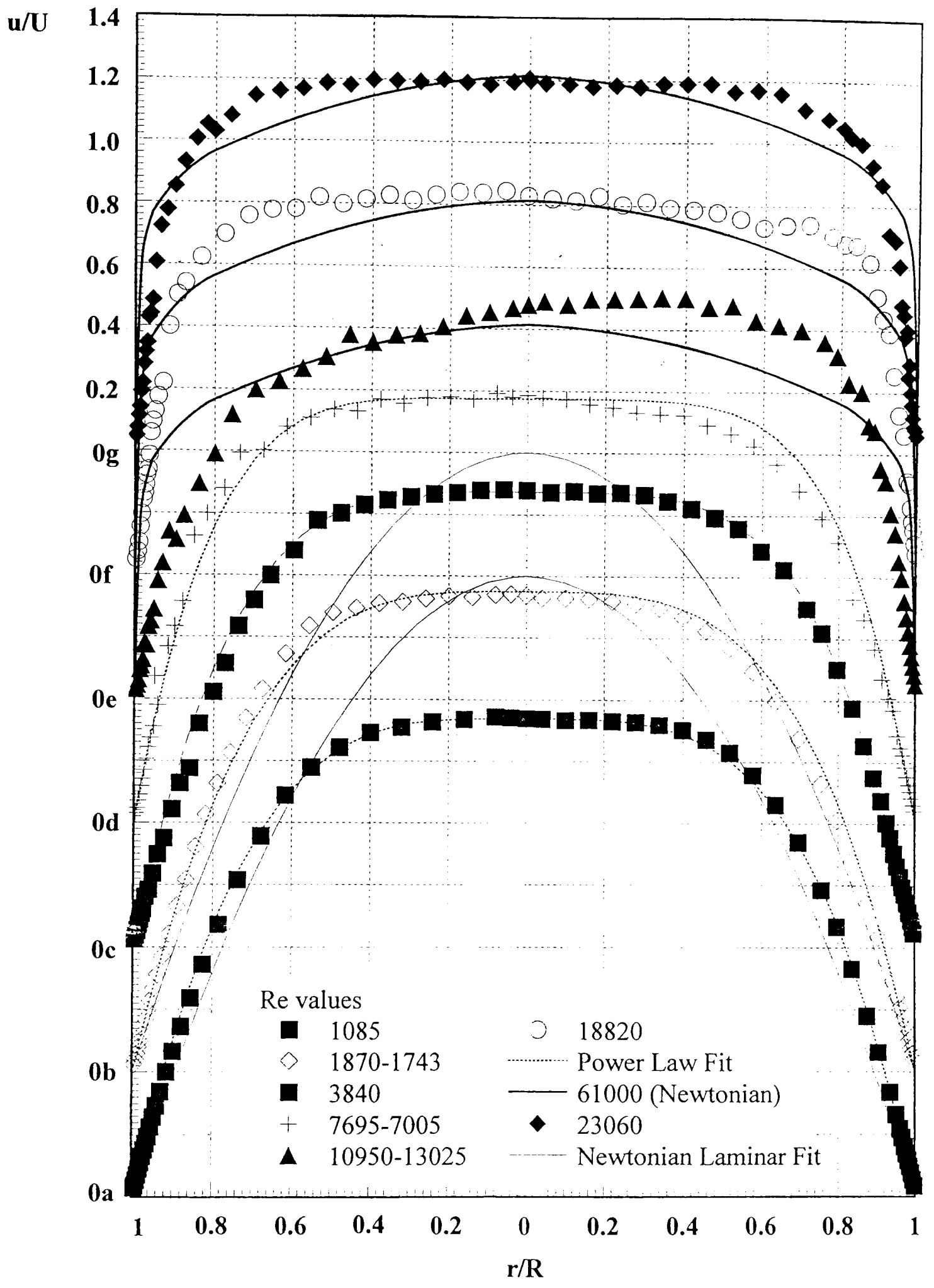

Figure 5.20 *Mean Velocity Distributions For 0.2% PAA.*

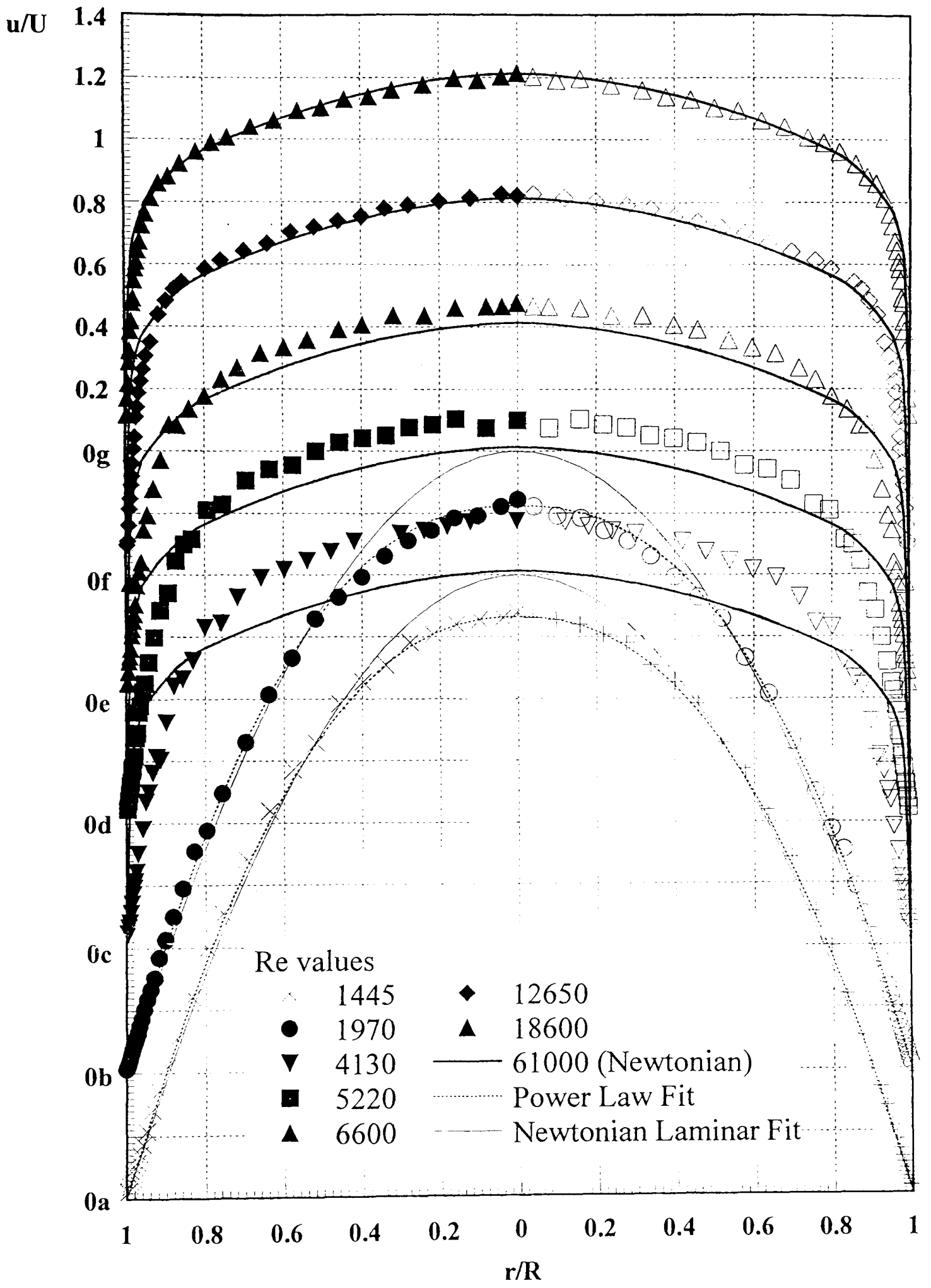

Figure 5.21 *Mean Velocity Distributions For 0.14% Carbopol 934.*

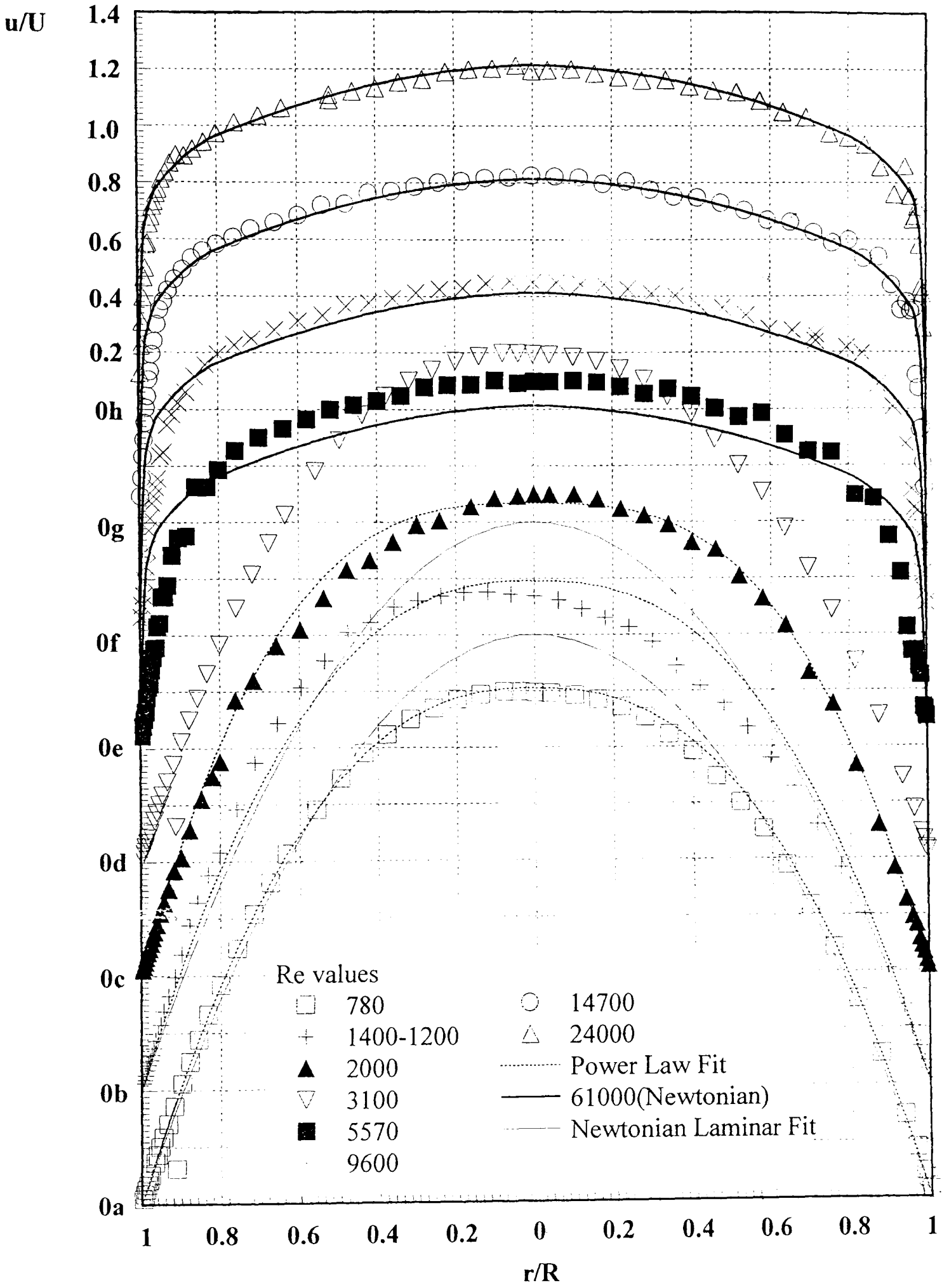

Figure 5.22 *Mean Velocity Distributions For 0.1% Carbopol EZ1.*

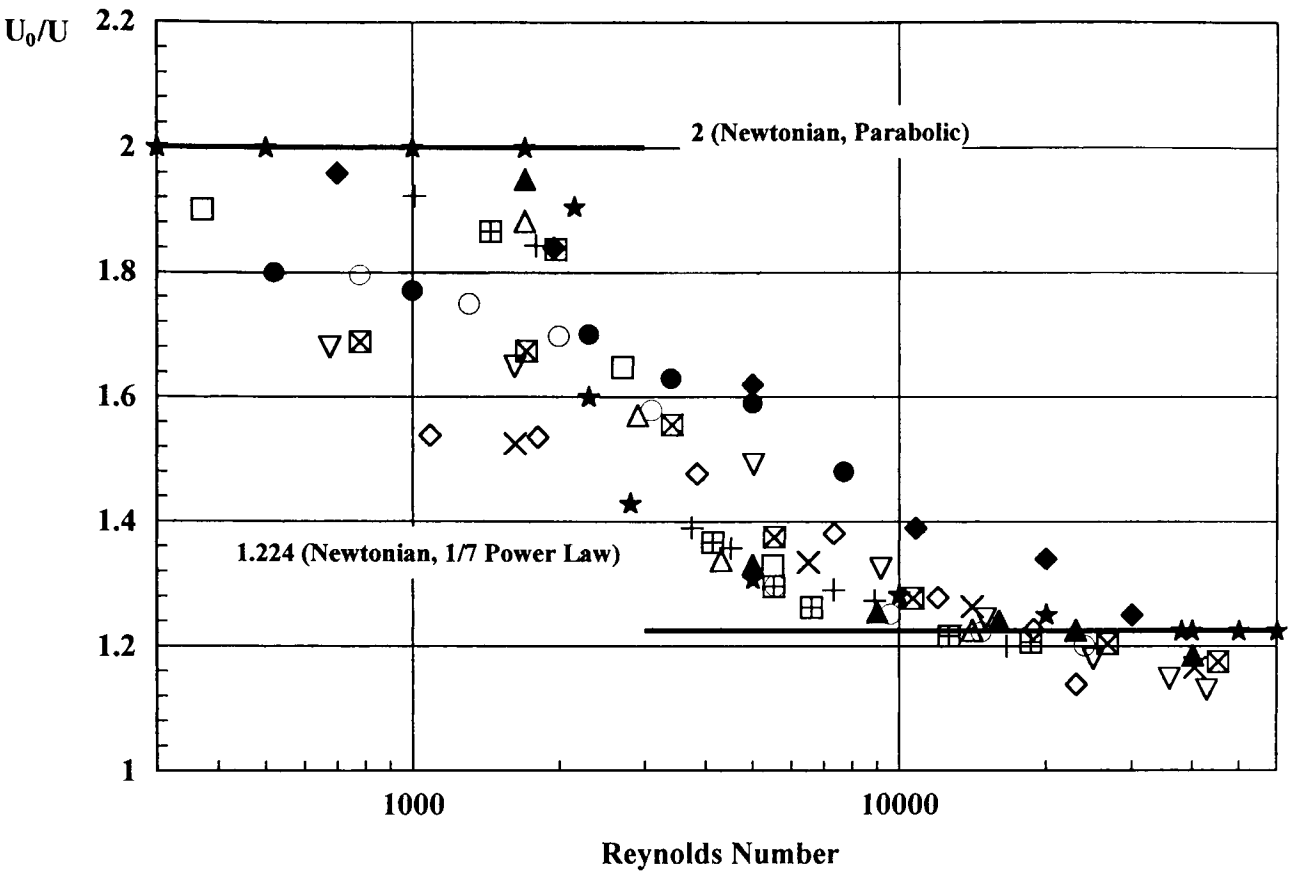

Figure 5.23 *Non-Dimensional Centre-Line Velocity versus Reynolds Number.*

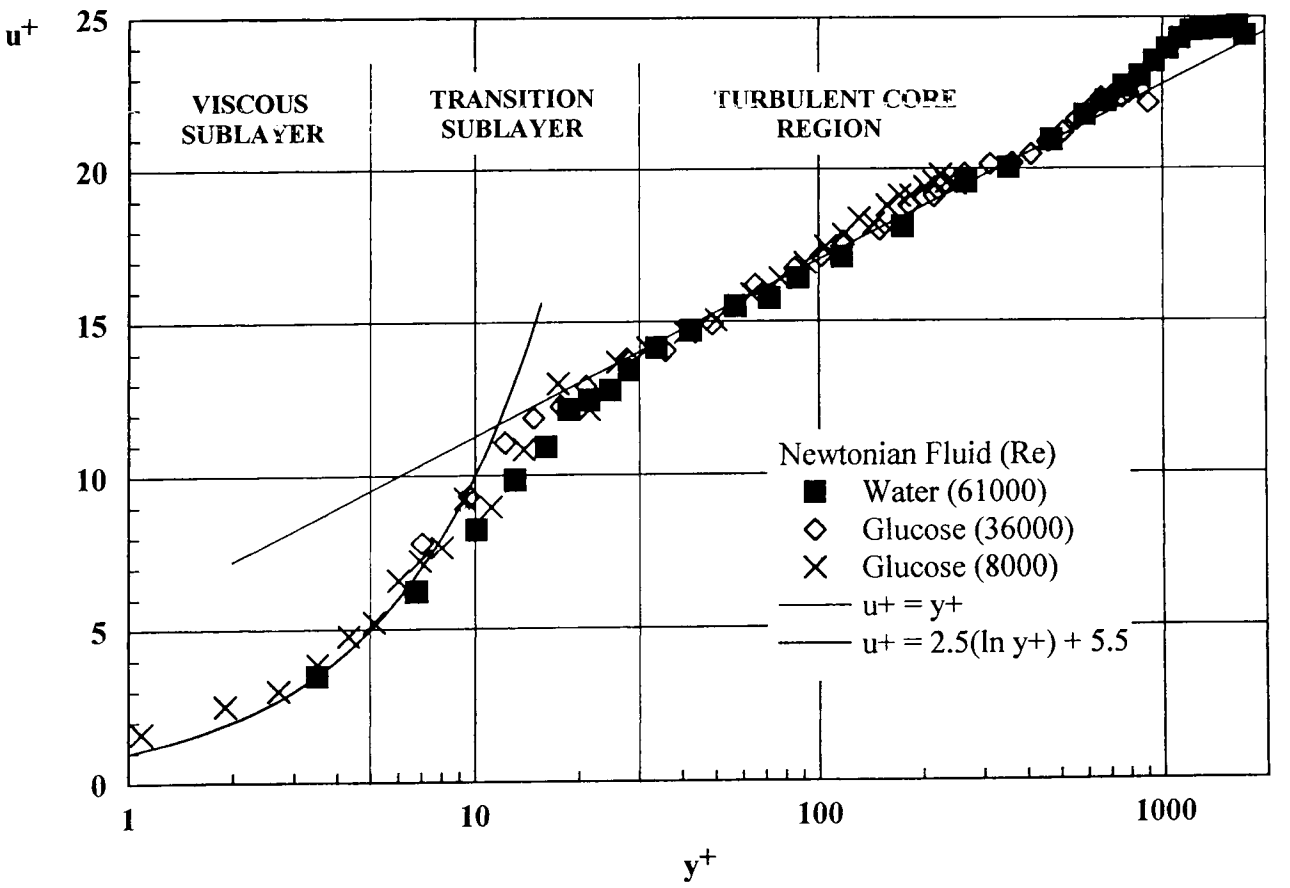

Figure 5.24 *Universal Velocity Distribution For Aqueous Glucose and Water.*

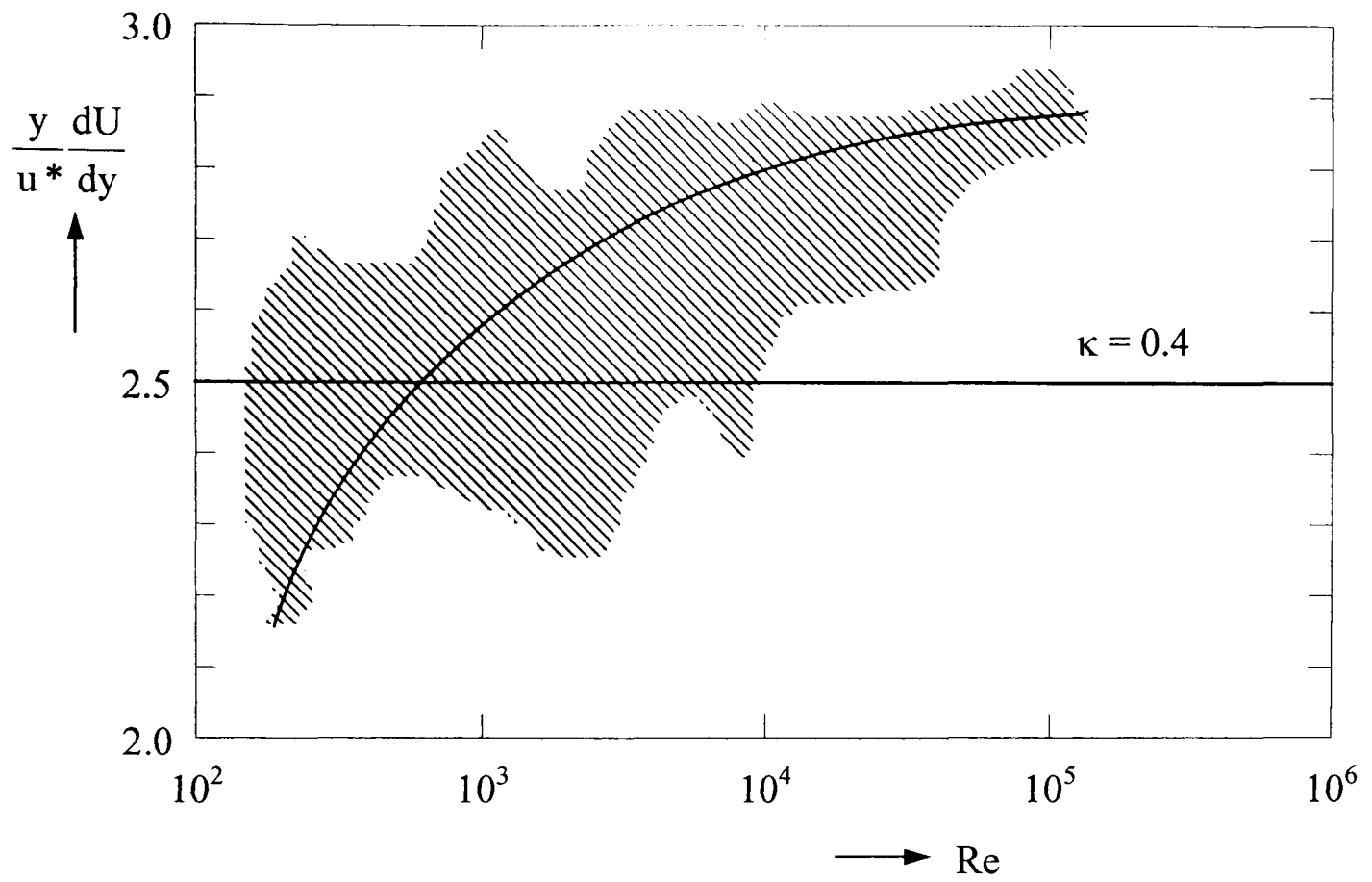

Figure 5.25 *Near wall gradient. Experimental scatter indicated by shaded area [adapted from Tennekes and Lumley (1972)].*

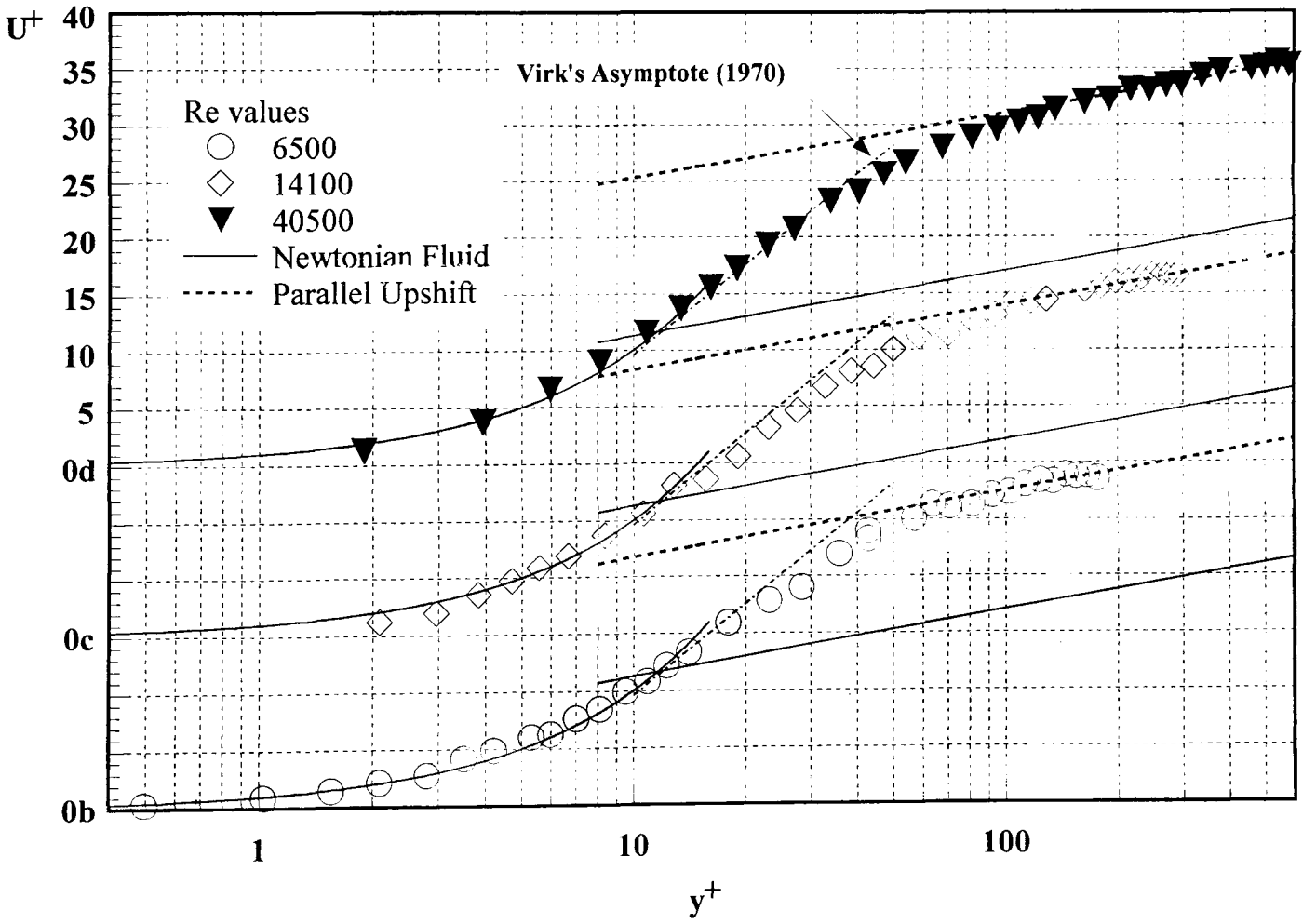

Figure 5.26 *Universal Velocity Distribution For 0.2% XG.*

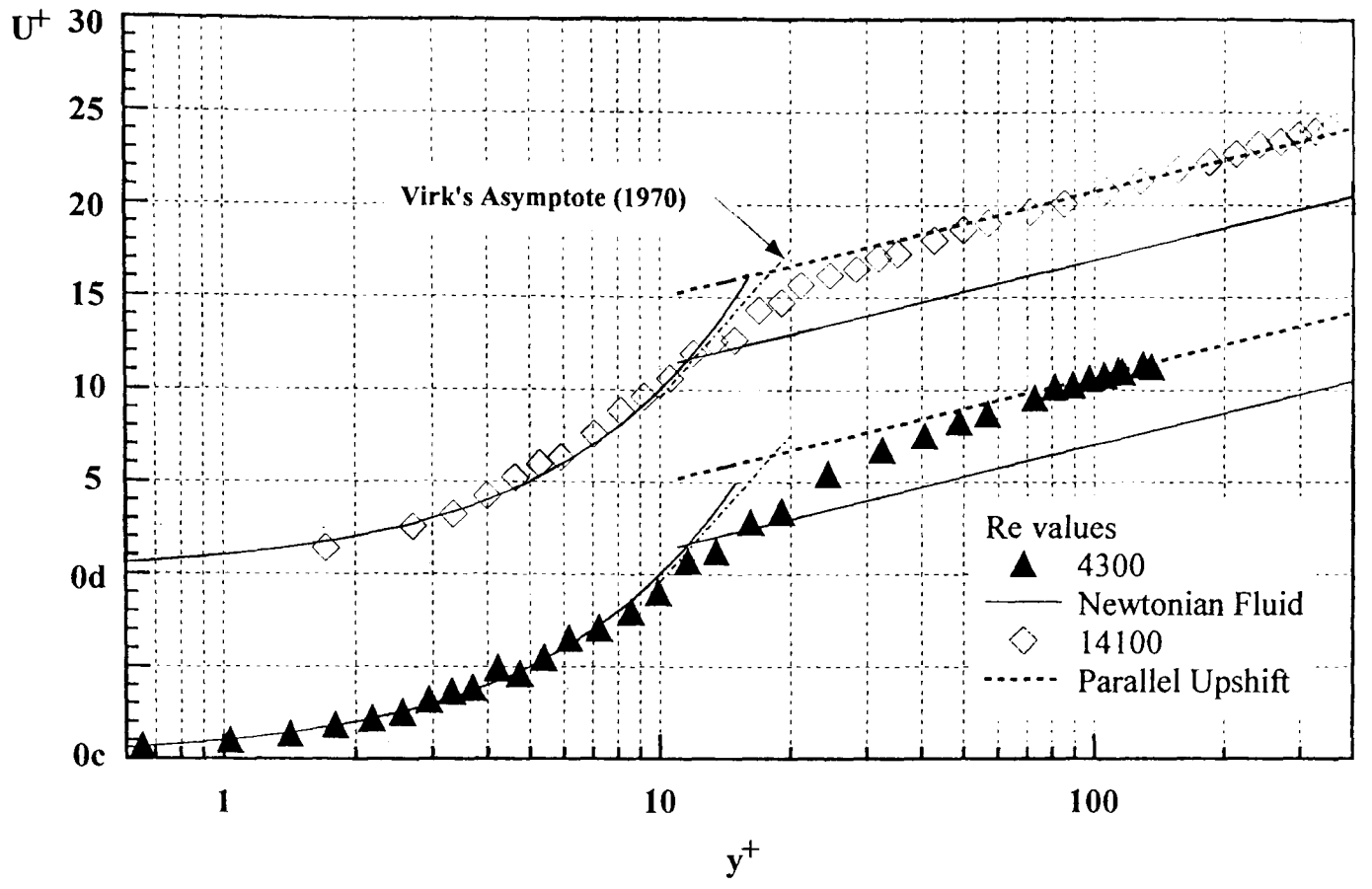

Figure 5.27 *Universal Velocity Distribution For 0.24% CMC.*

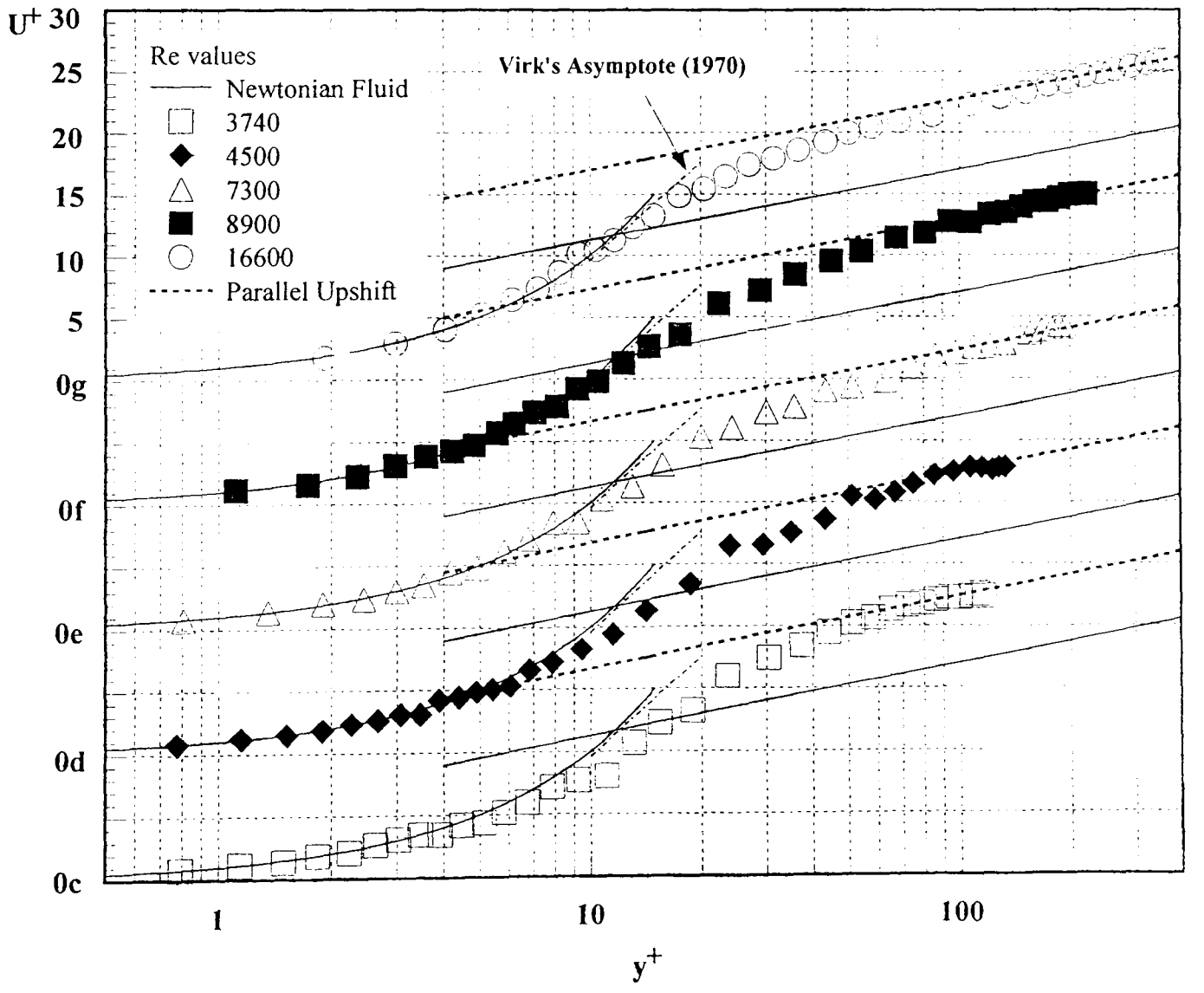

Figure 5.28 *Universal Velocity Distribution For 0.25% CMC.*

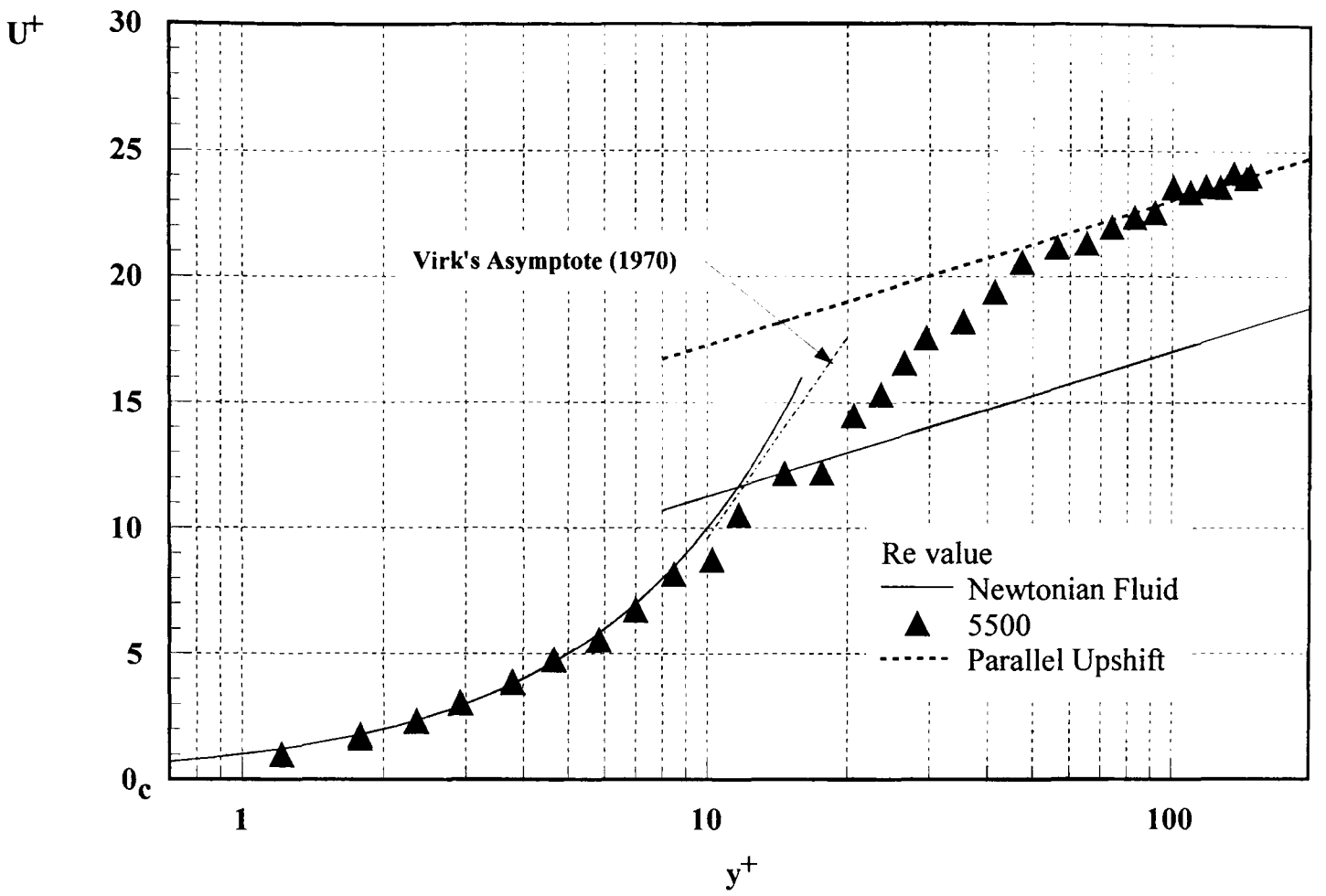

Figure 5.29 *Universal Velocity Distribution For 0.4% CMC.*

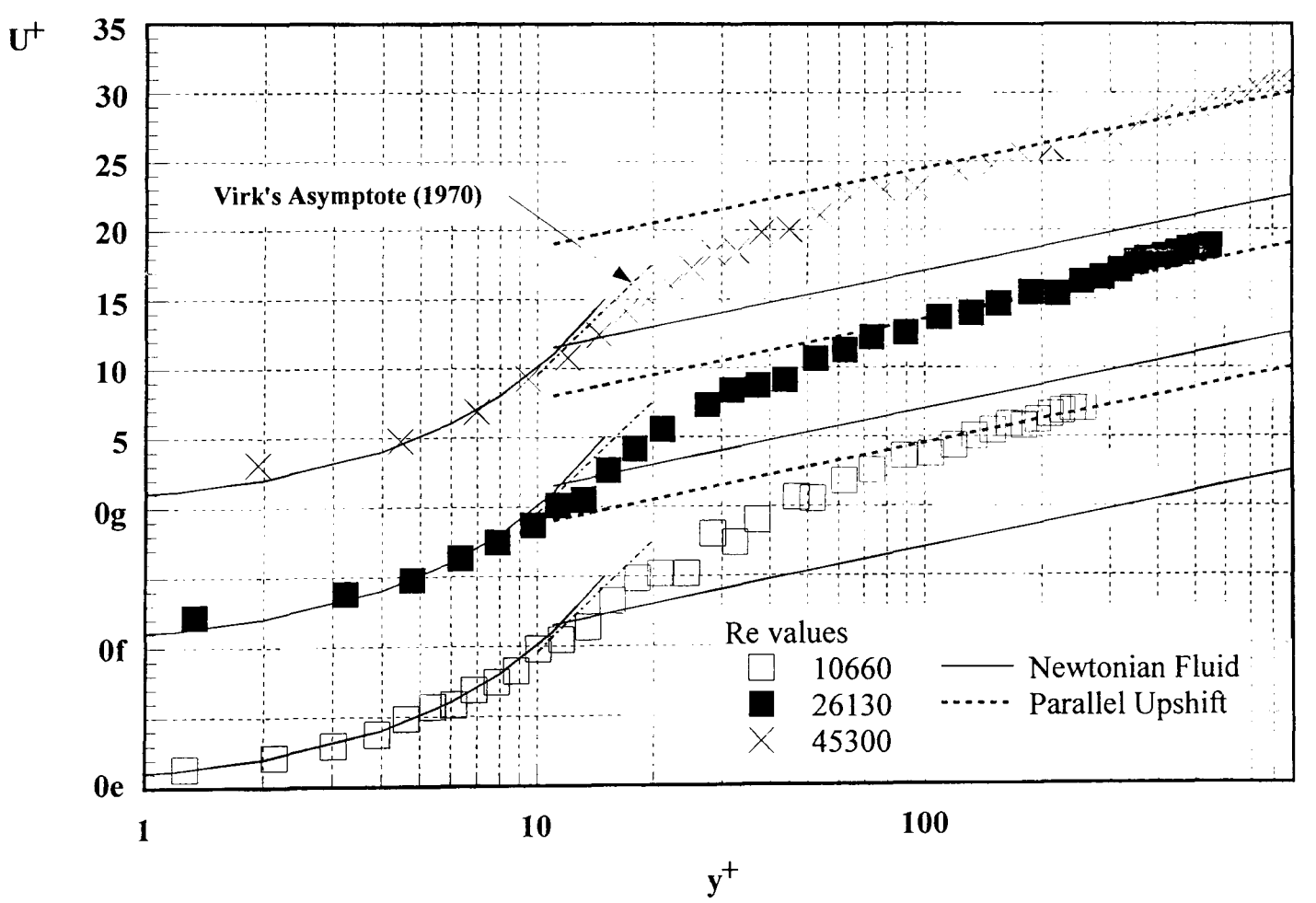

Figure 5.30 *Universal Velocity Distribution For 0.09% CMC/0.09% XG.*

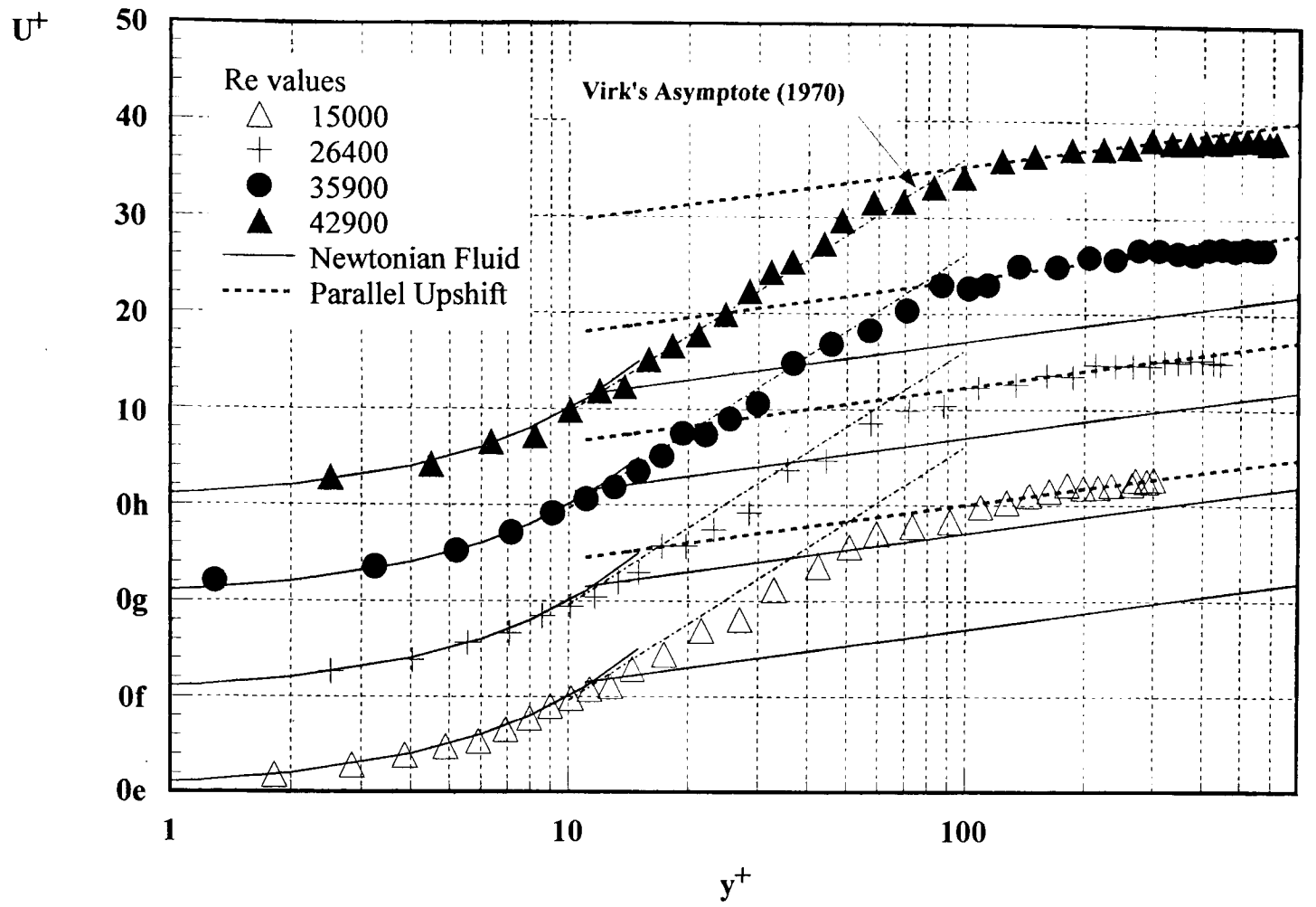

Figure 5.31 *Universal Velocity Distribution For 0.125% PAA.*

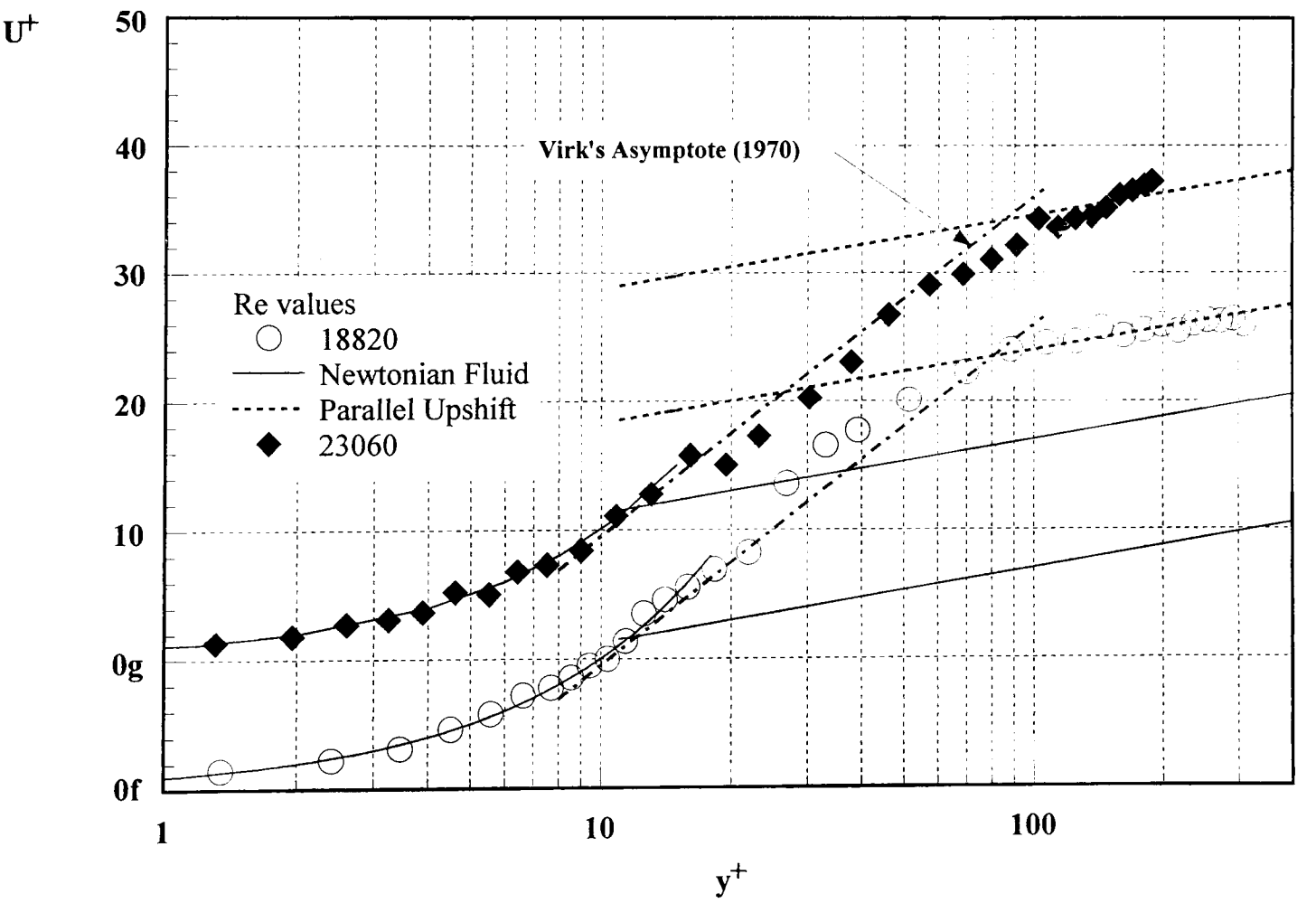

Figure 5.32 *Universal Velocity Distribution For 0.2% PAA.*

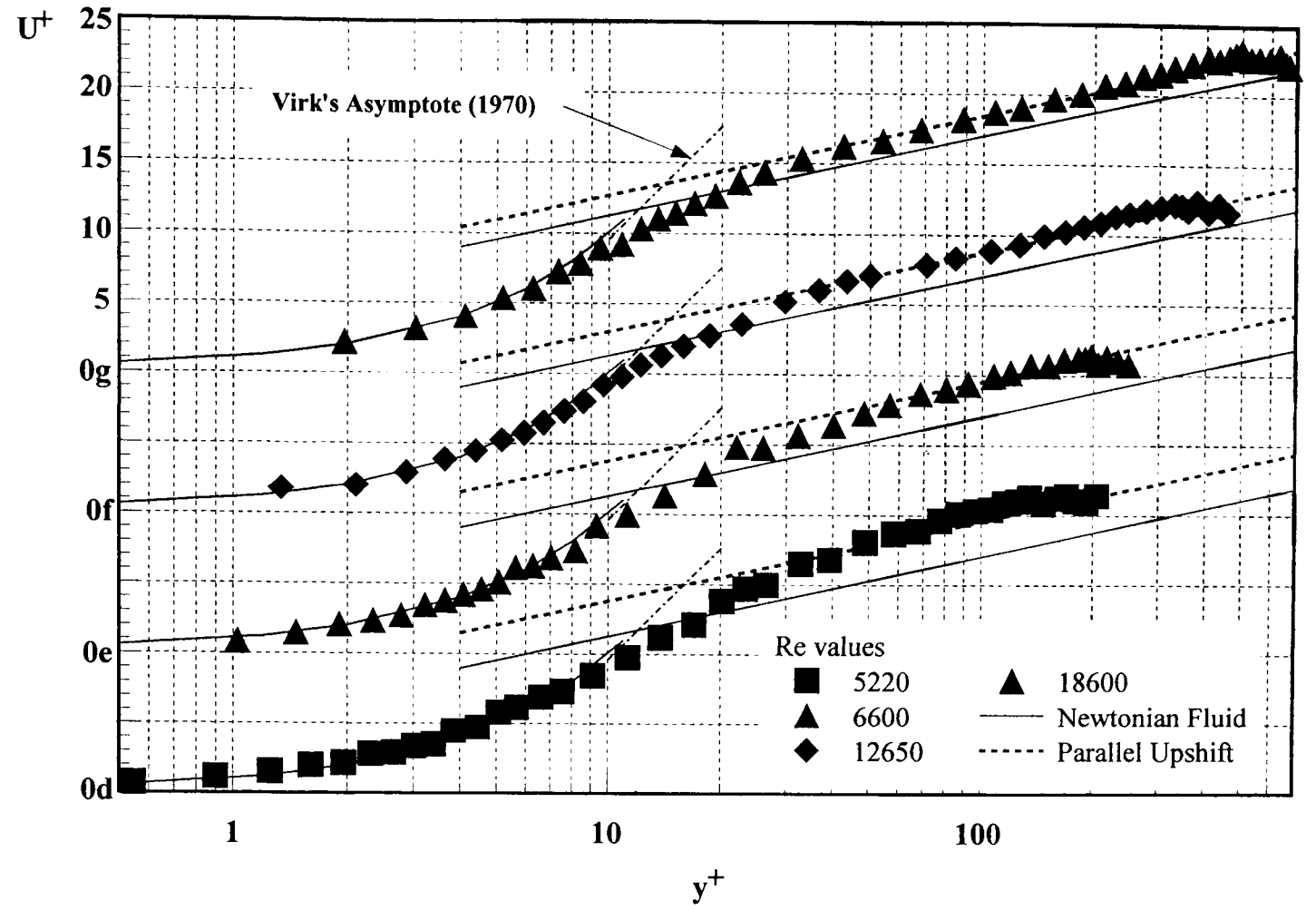

Figure 5.33 *Universal Velocity Distribution For 0.14% Carbopol 934.*

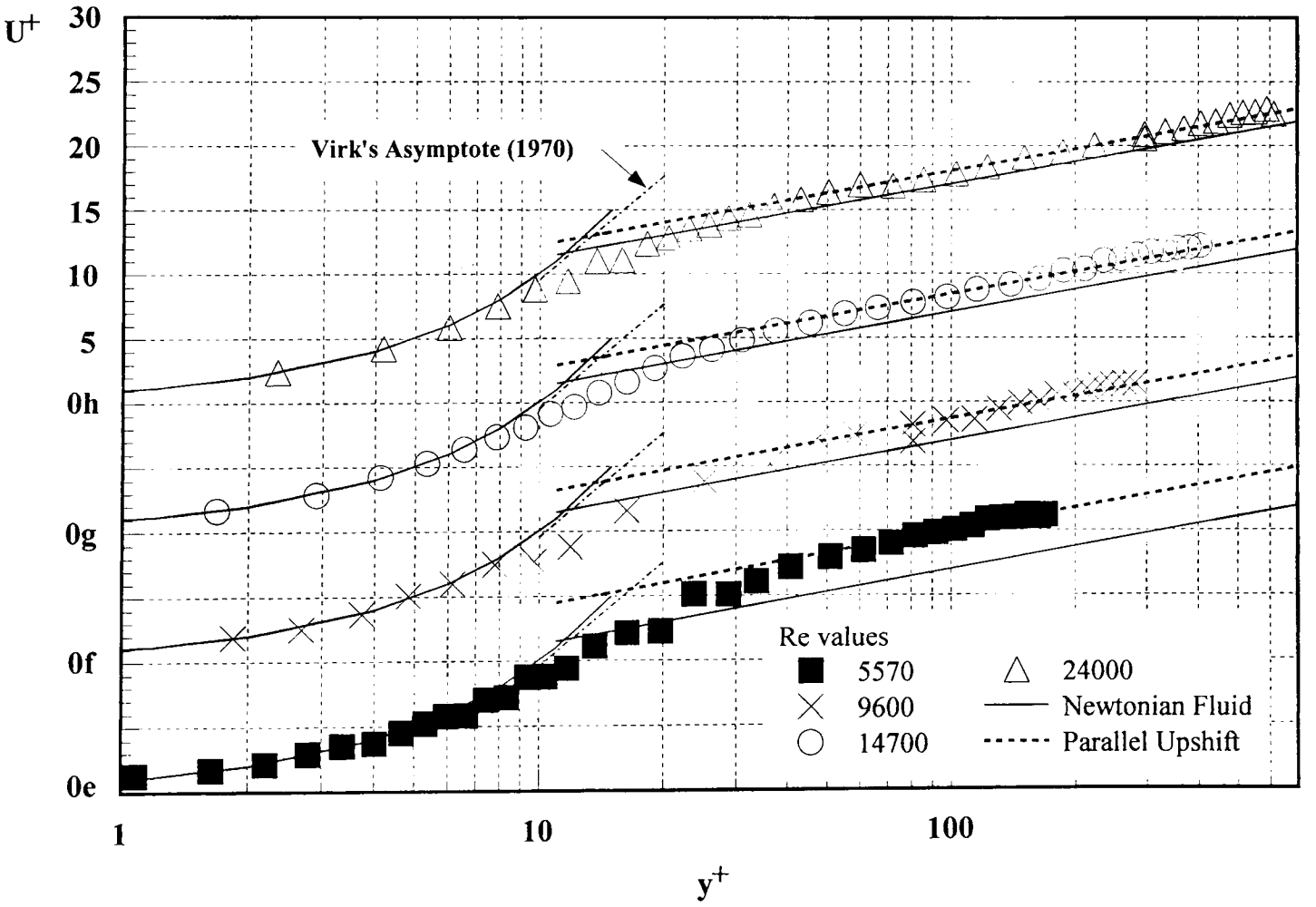

Figure 5.34 *Universal Velocity Distribution For 0.1% Carbopol EZ1.*

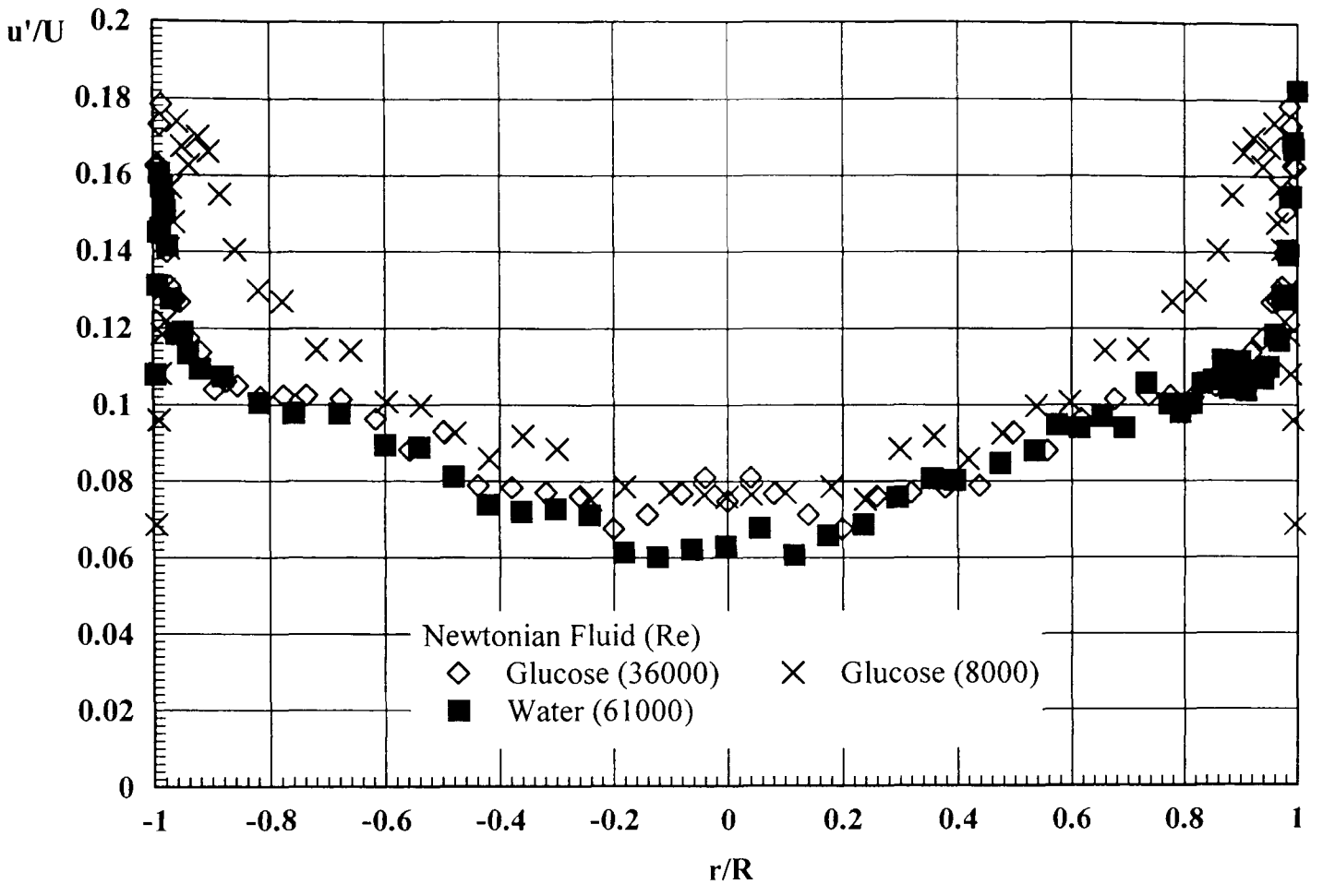

Figure 5.35(a) *Axial Turbulence Intensities For Newtonian Fluids.*

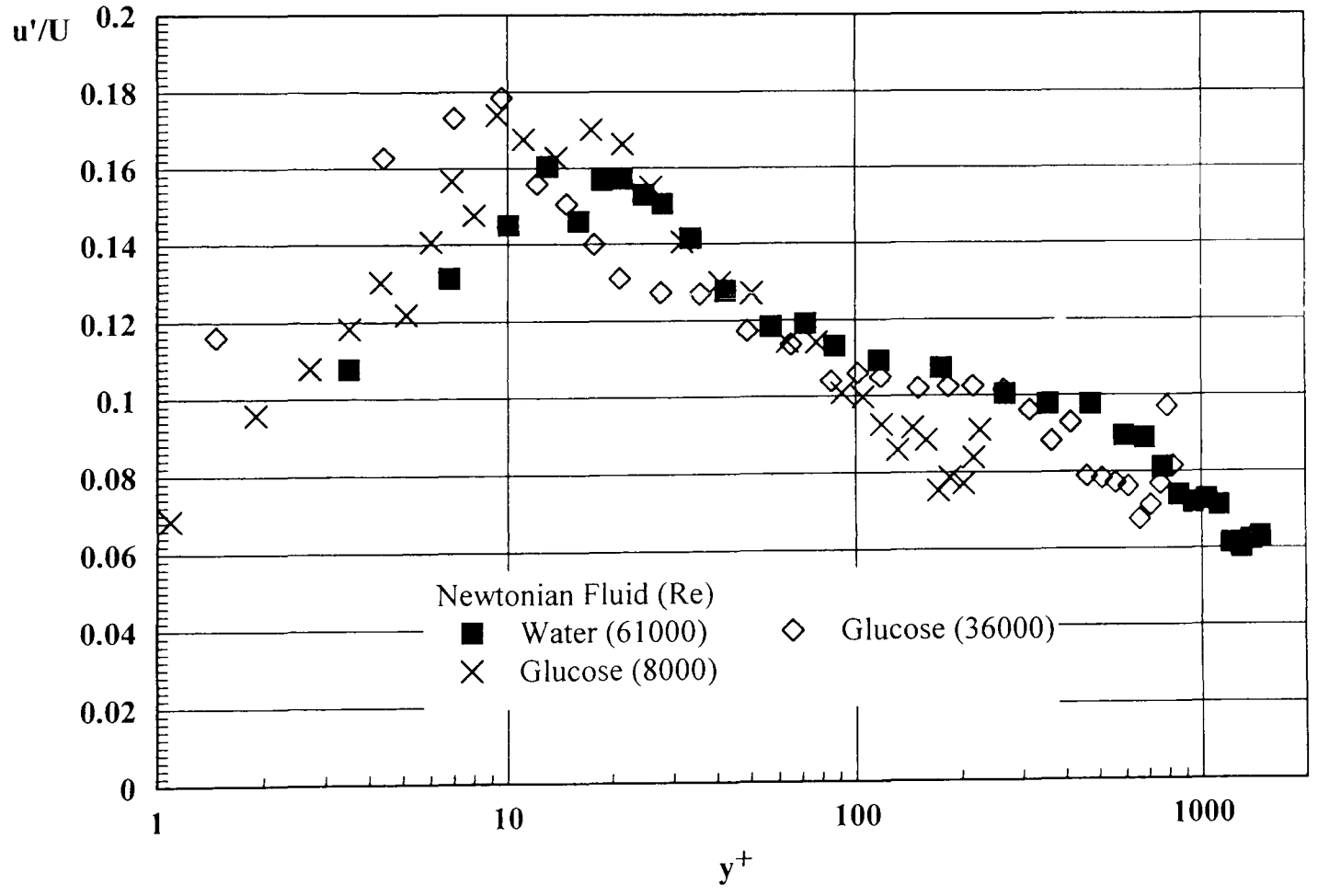

Figure 5.35(b) *Axial Turbulence Intensities in Wall Coordinates (y^+) For Newtonian Fluids.*

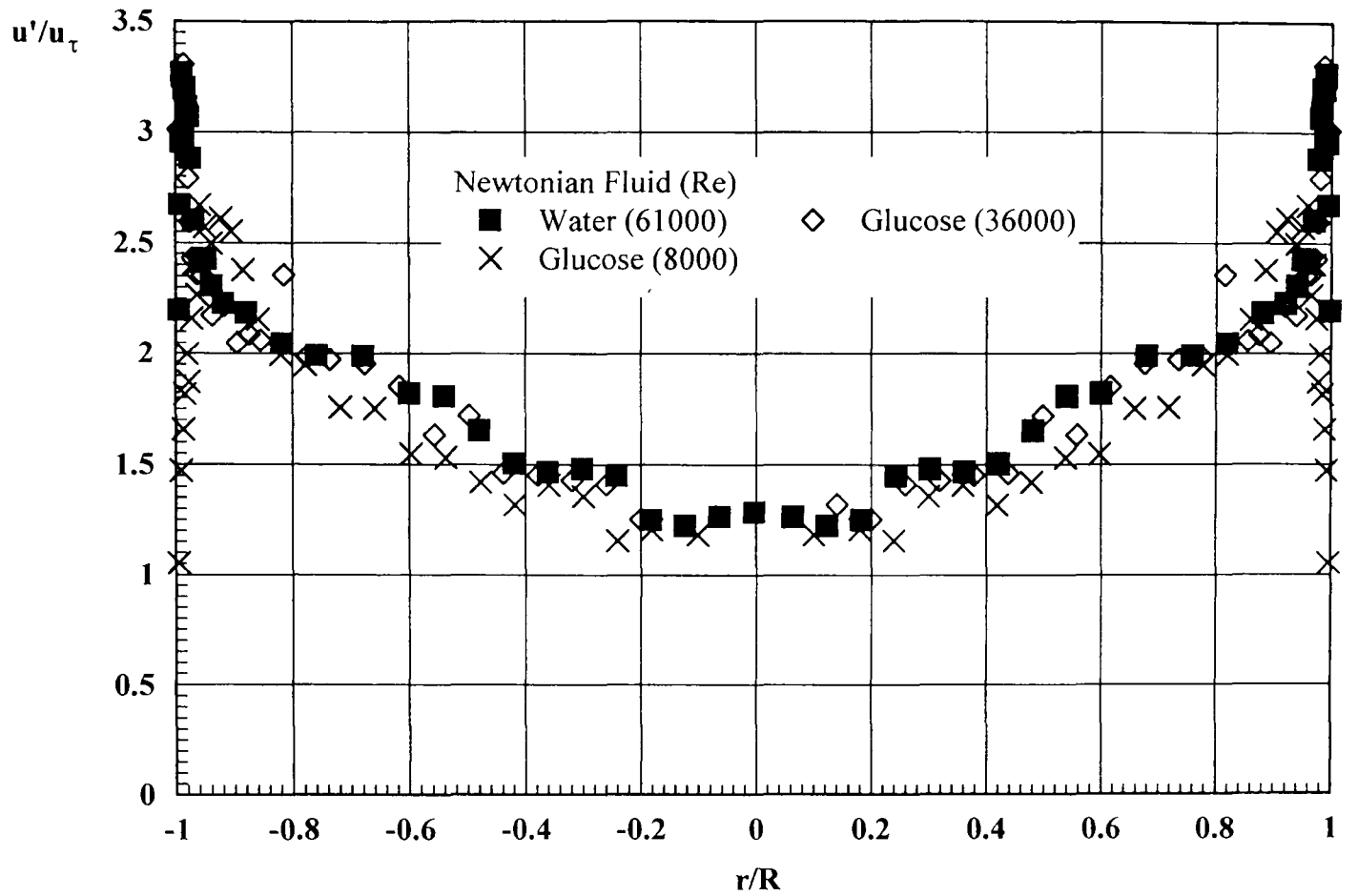

Figure 5.35(c) *Axial Turbulence Intensities Normalised With Friction Velocity For Newtonian Fluids.*

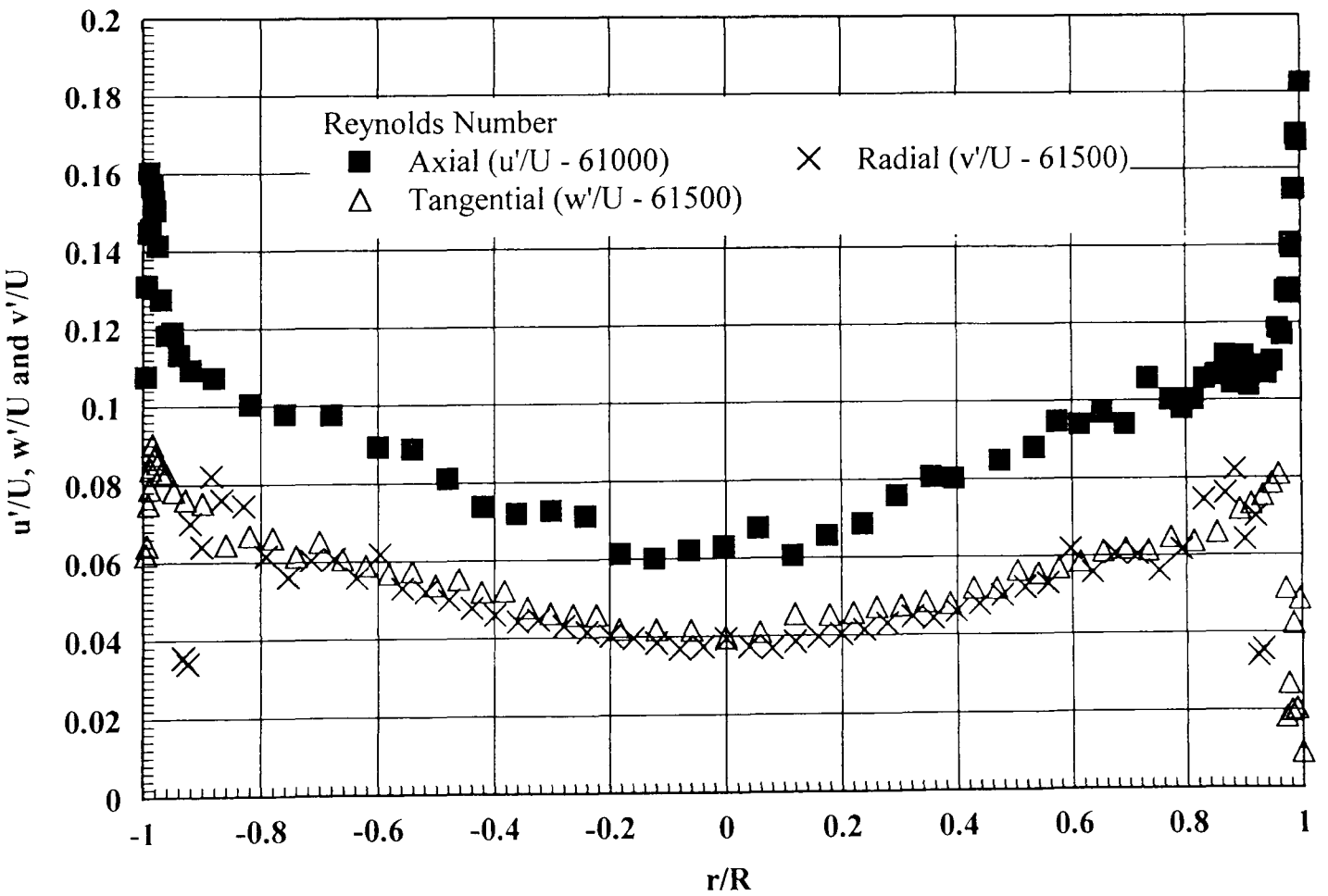

Figure 5.36 *Axial, Tangential and Radial Turbulence Intensities For a Newtonian Fluid (Water).*

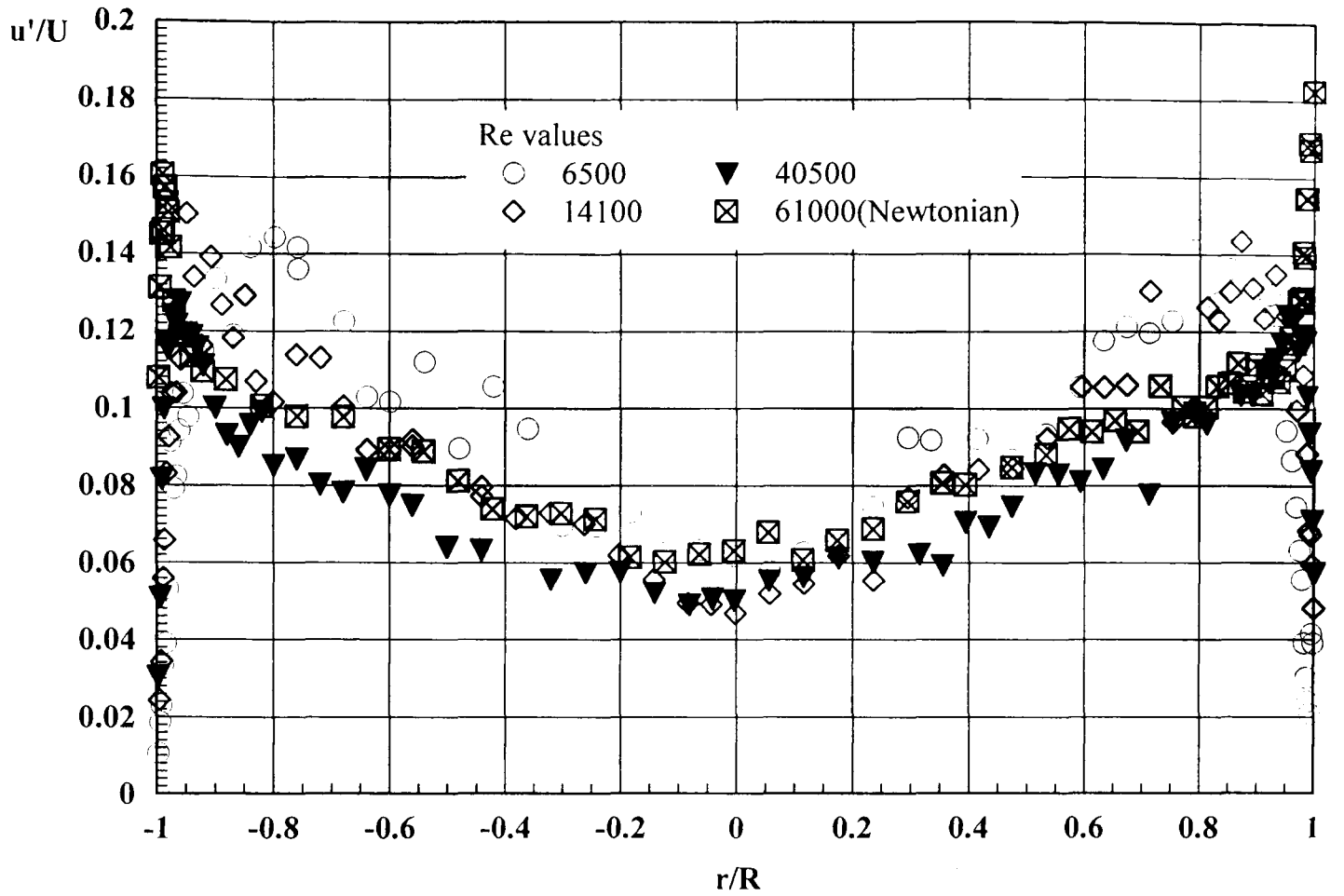

Figure 5.37(a) *Axial Turbulence Intensities For 0.2% XG.*

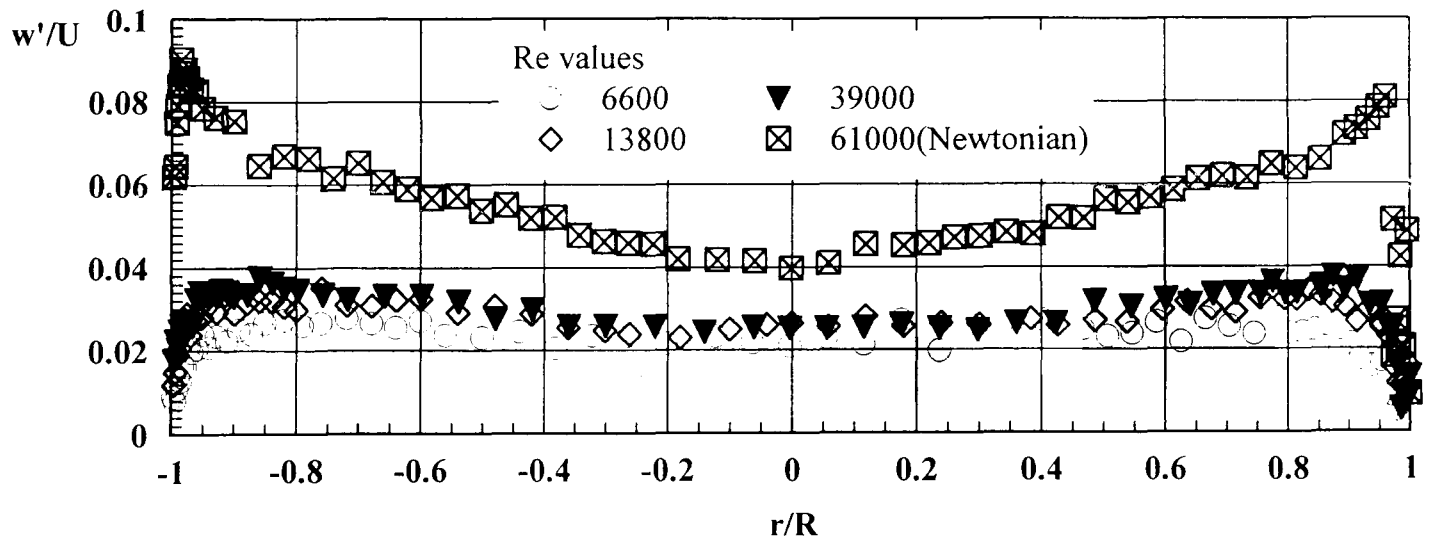

Figure 5.37(b) *Tangential Turbulence Intensities For 0.2% XG.*

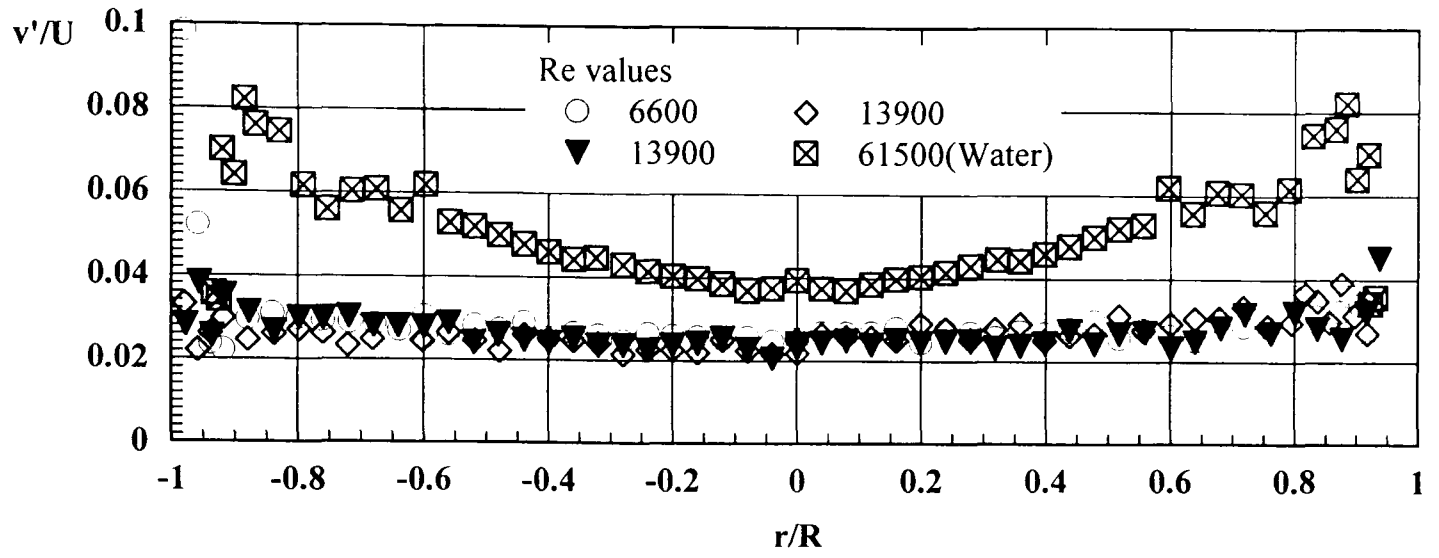

Figure 5.37(c) *Tangential Turbulence Intensities For 0.2% XG.*

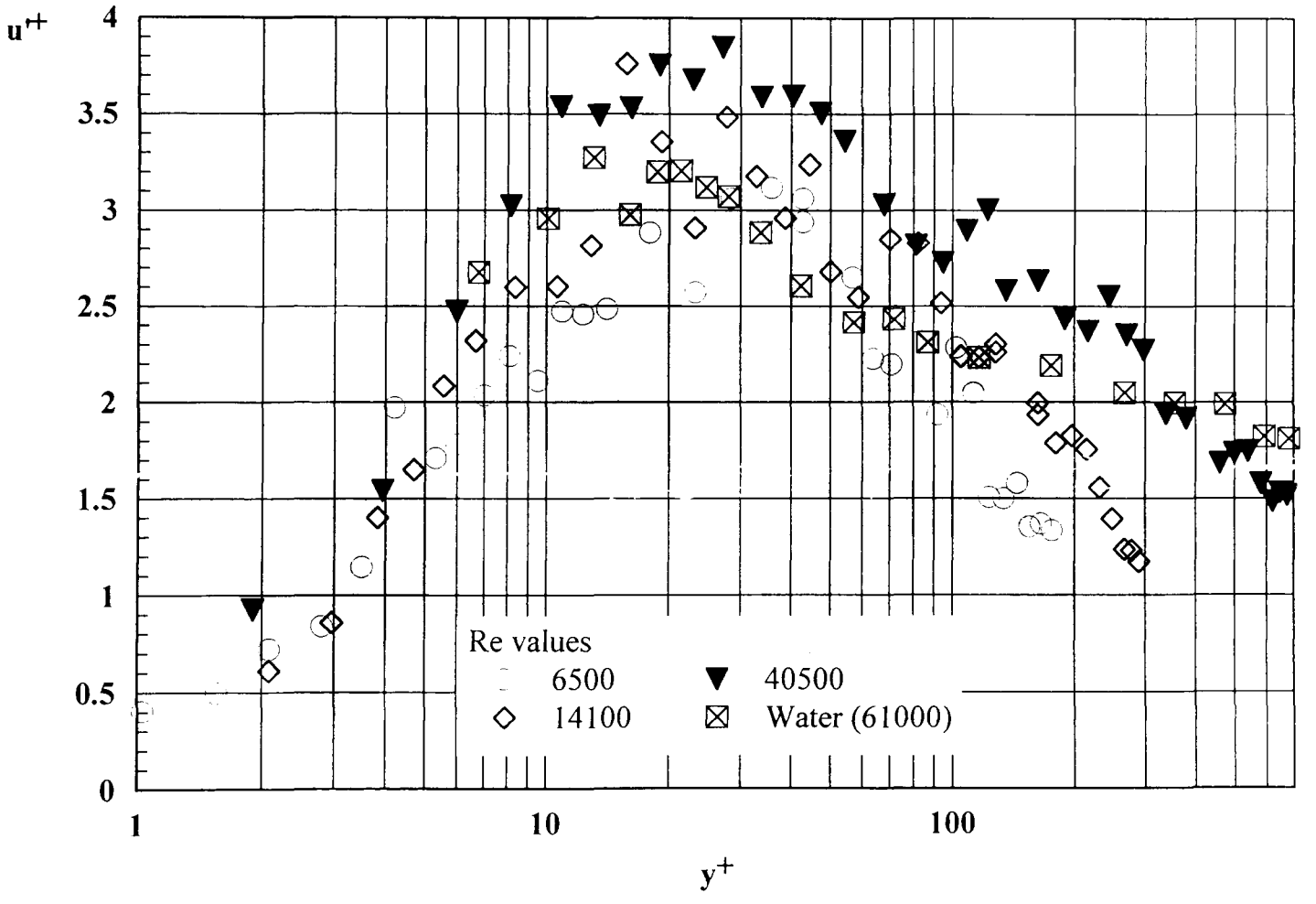

Figure 5.38(a) *Axial Turbulence Intensities in Wall Coordinates For 0.2% XG.*

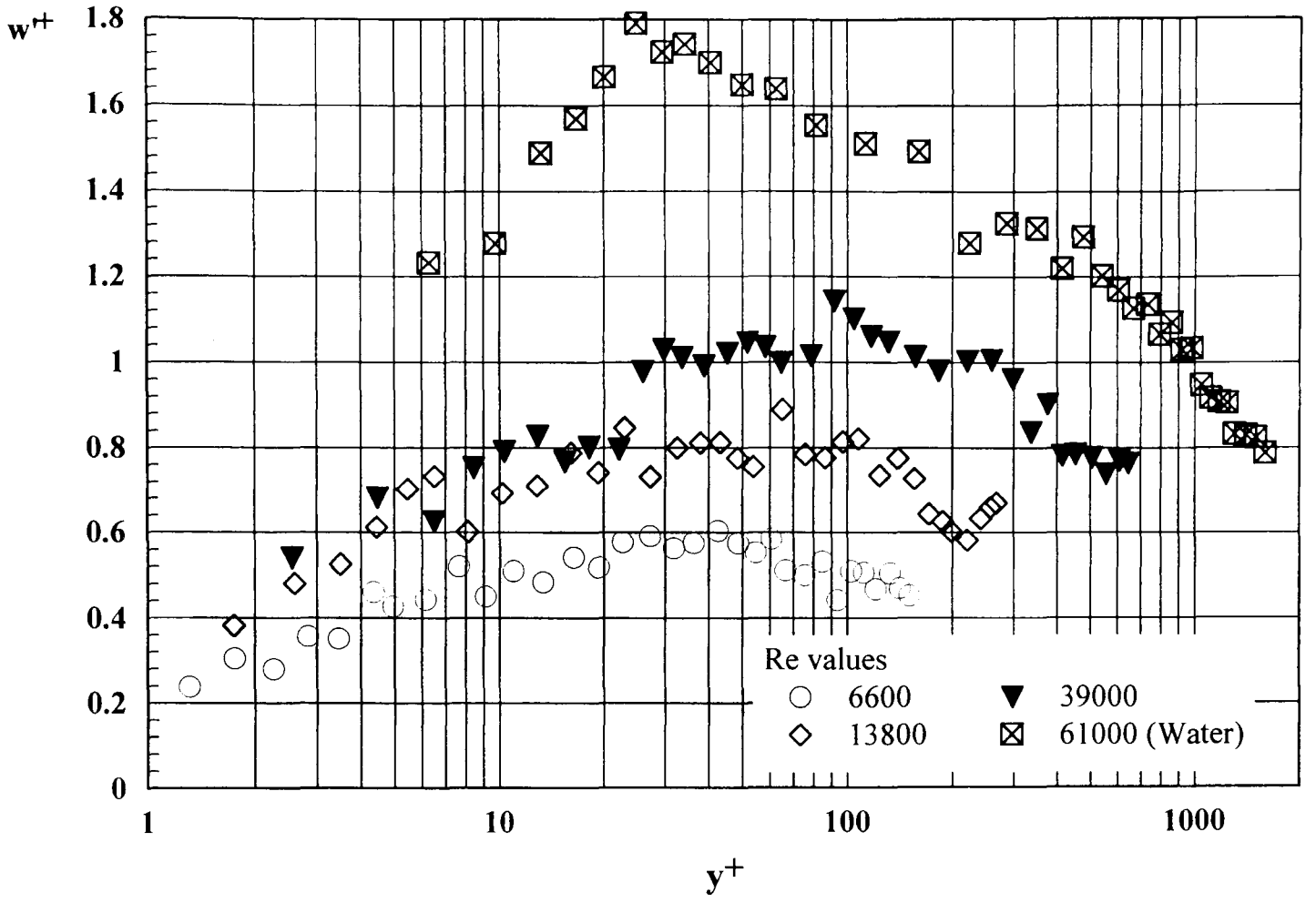

Figure 5.38(b) *Tangential Turbulence Intensities in Wall Coordinates For 0.2% XG.*

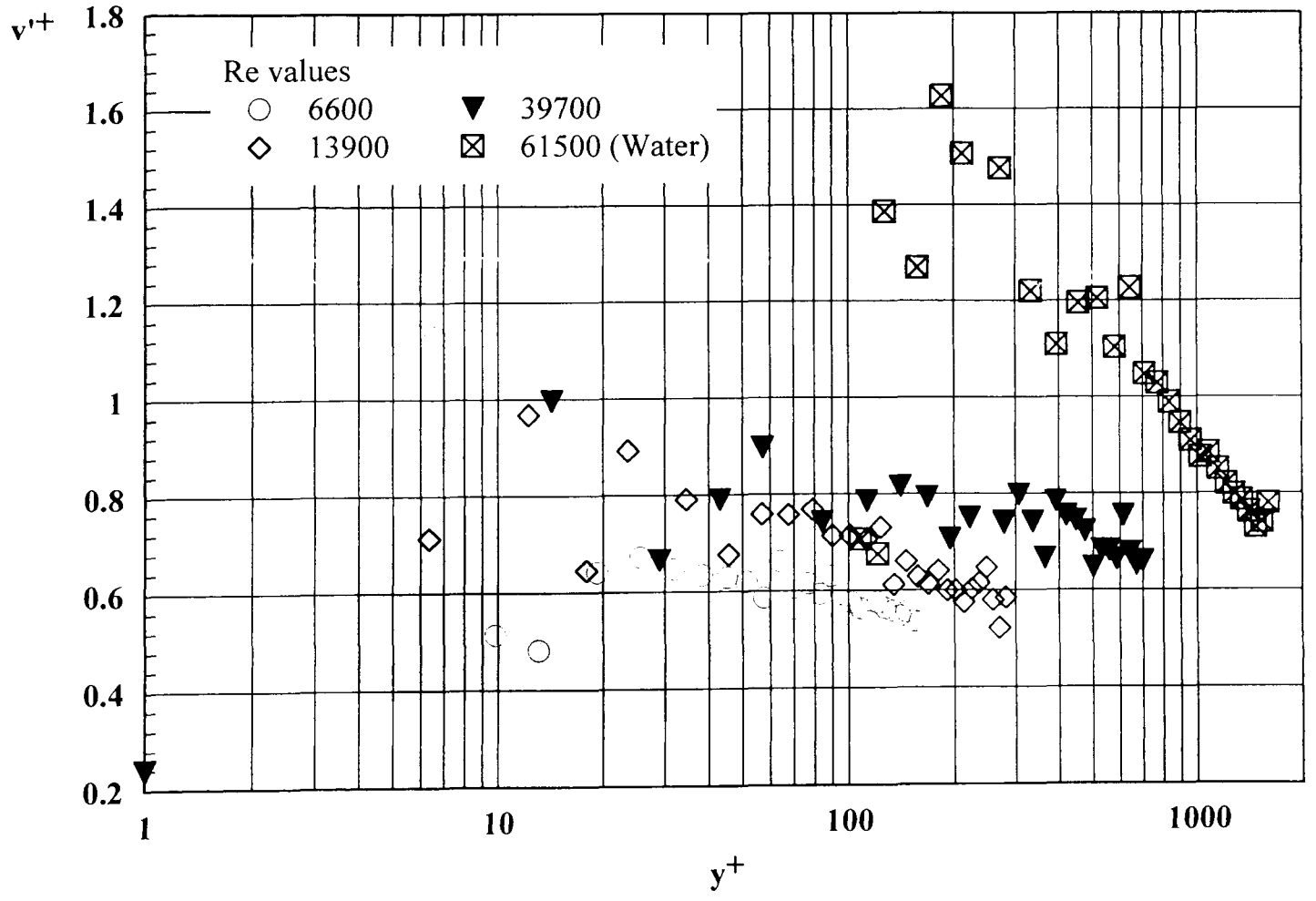

Figure 5.38(c) *Radial Turbulence Intensities in Wall Coordinates For 0.2% XG.*

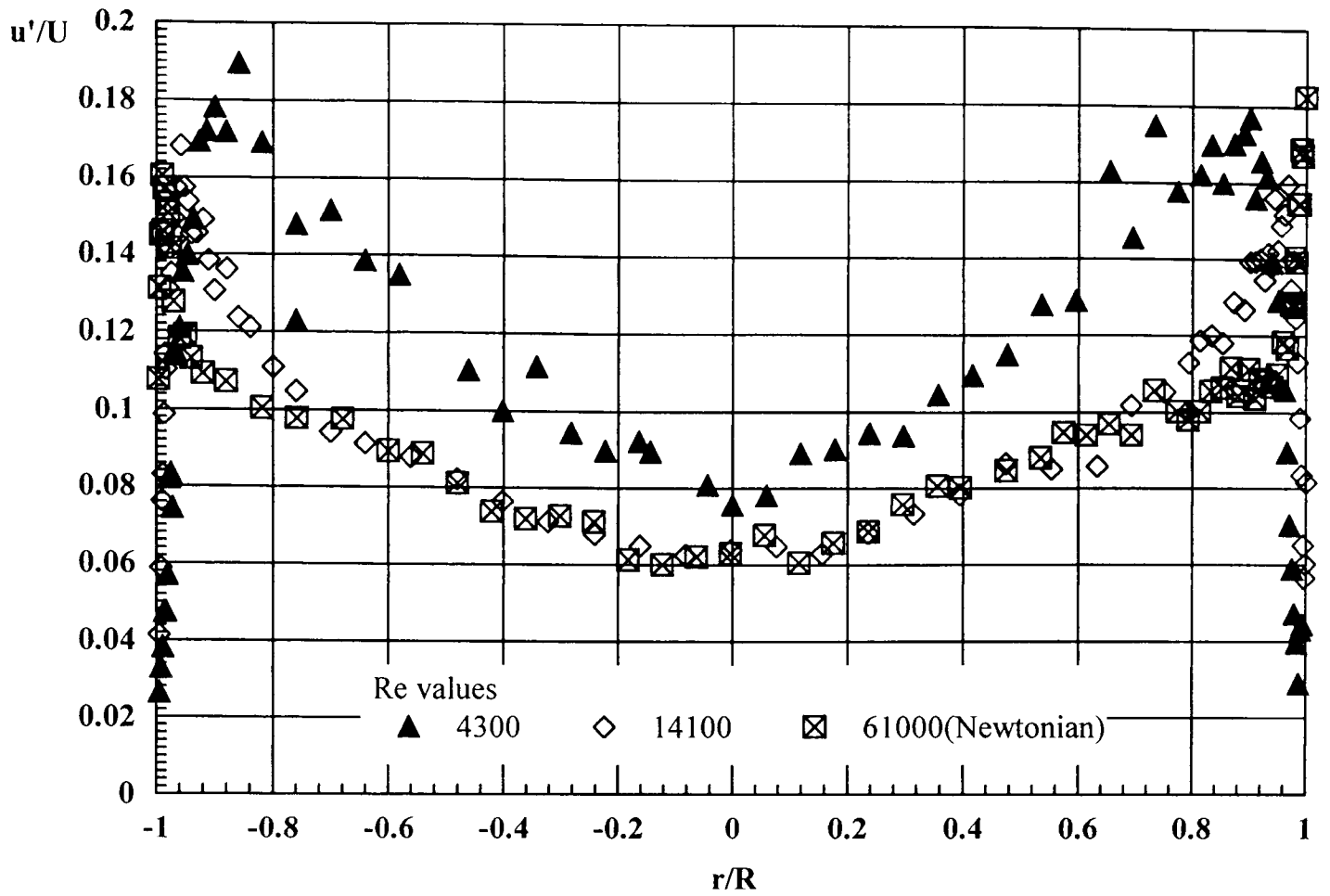

Figure 5.39(a) *Axial Turbulence Intensities For 0.24% CMC.*

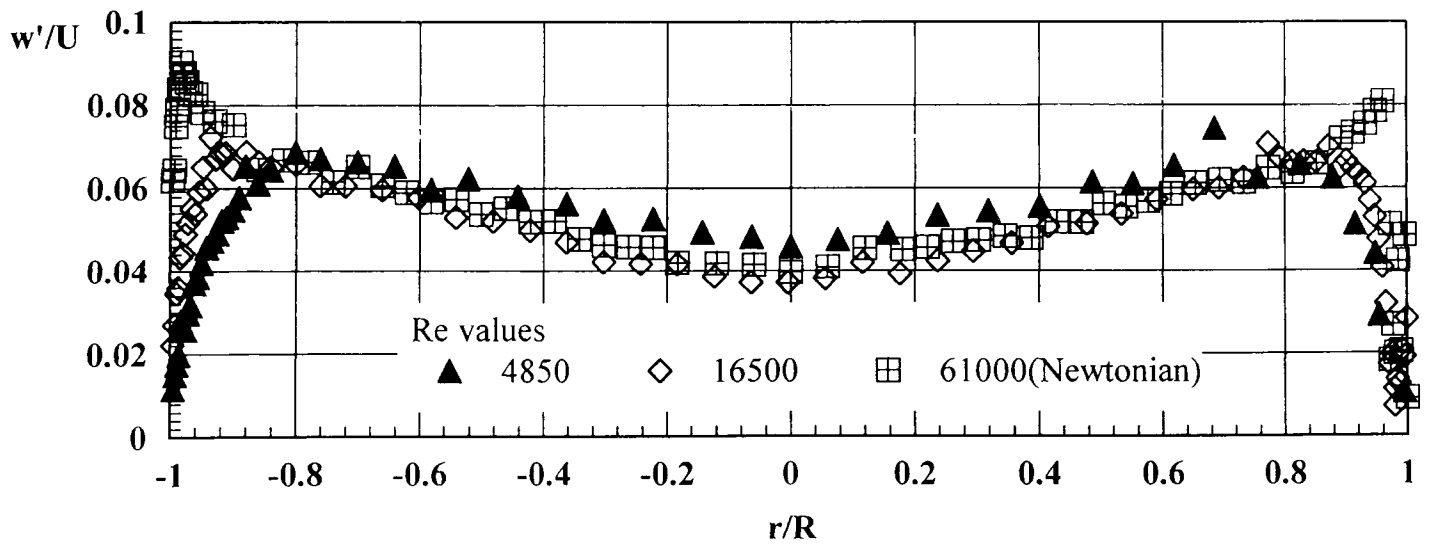

Figure 5.39(b) *Tangential Turbulence Intensities For 0.24% CMC.*

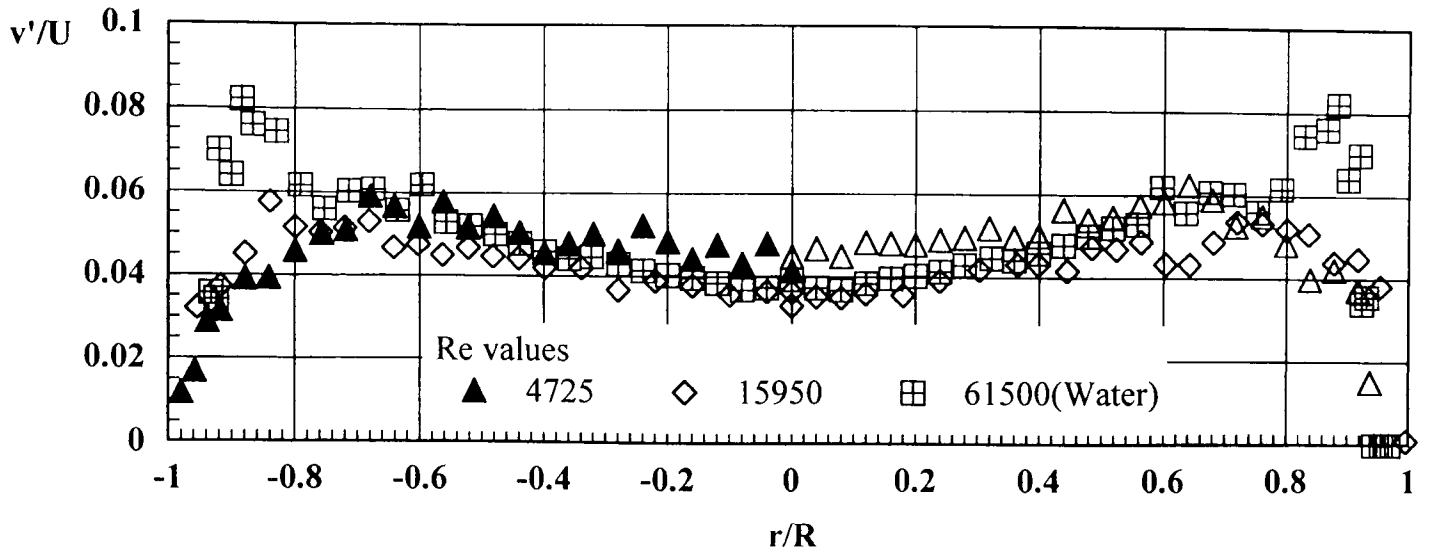

Figure 5.39(c) *Radial Turbulence Intensities For 0.24% CMC.*

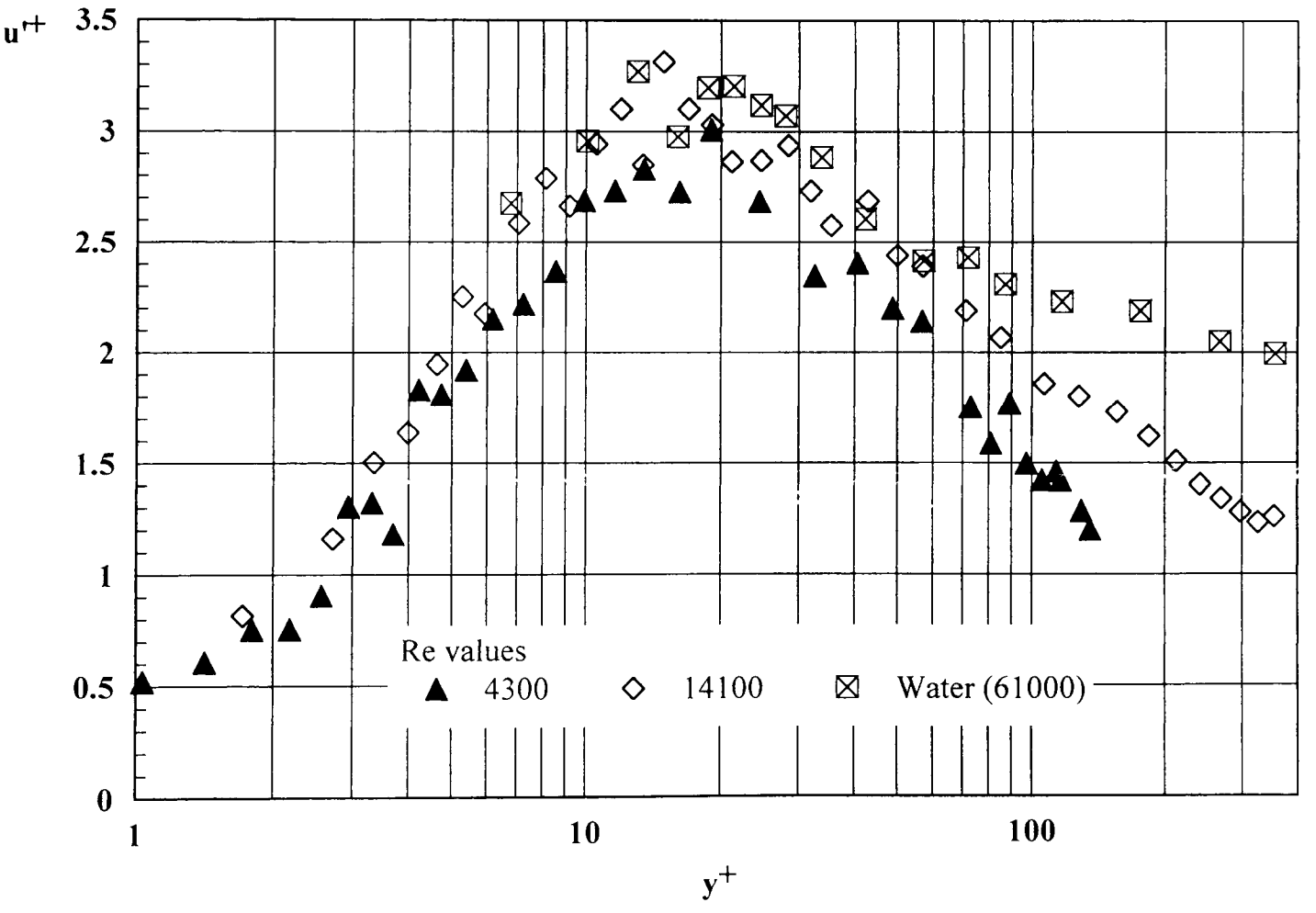

Figure 5.40(a) *Axial Turbulence Intensities in Wall Coordinates For 0.24% CMC.*

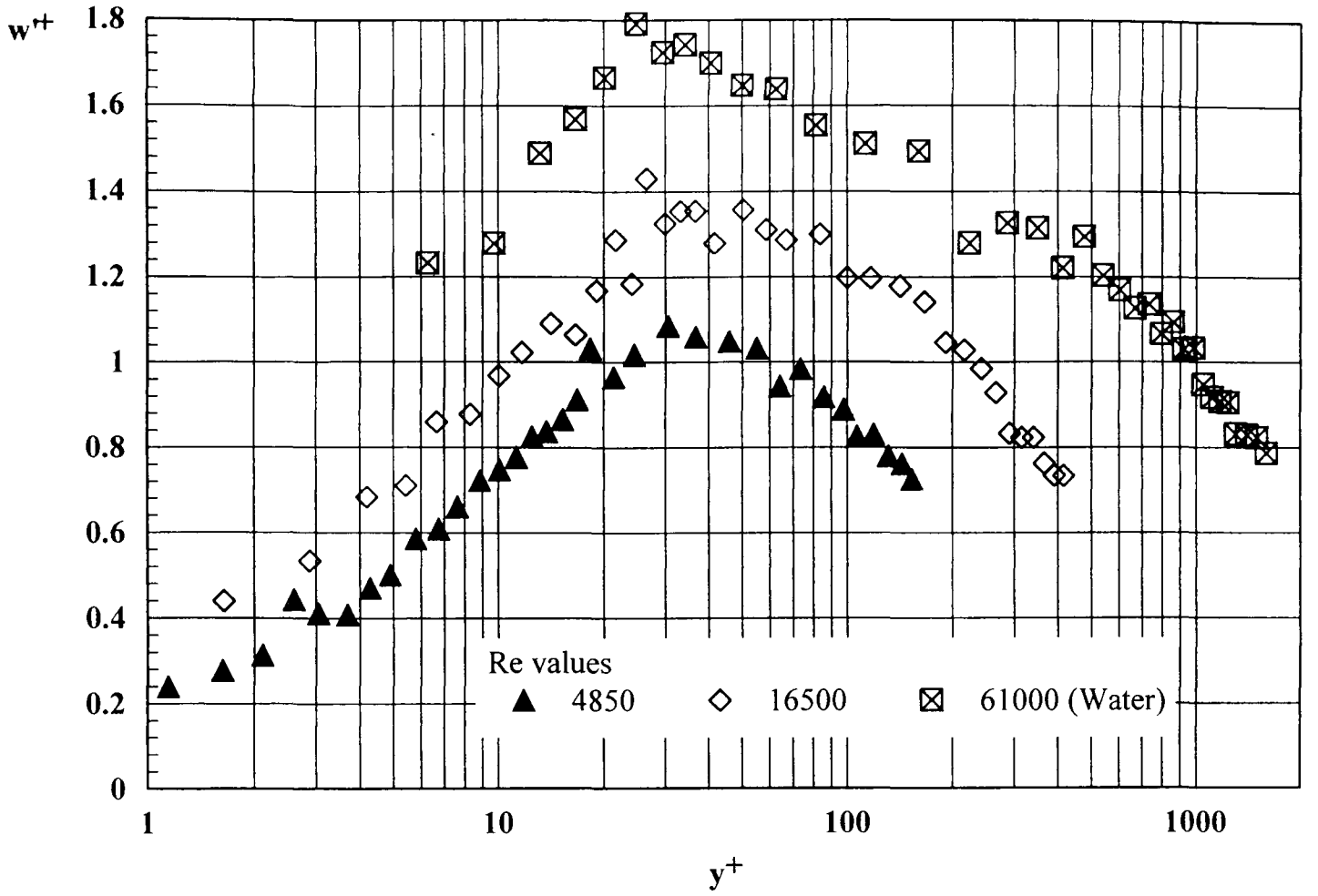

Figure 5.40(b) *Tangential Turbulence Intensities in Wall Coordinates For 0.24% CMC.*

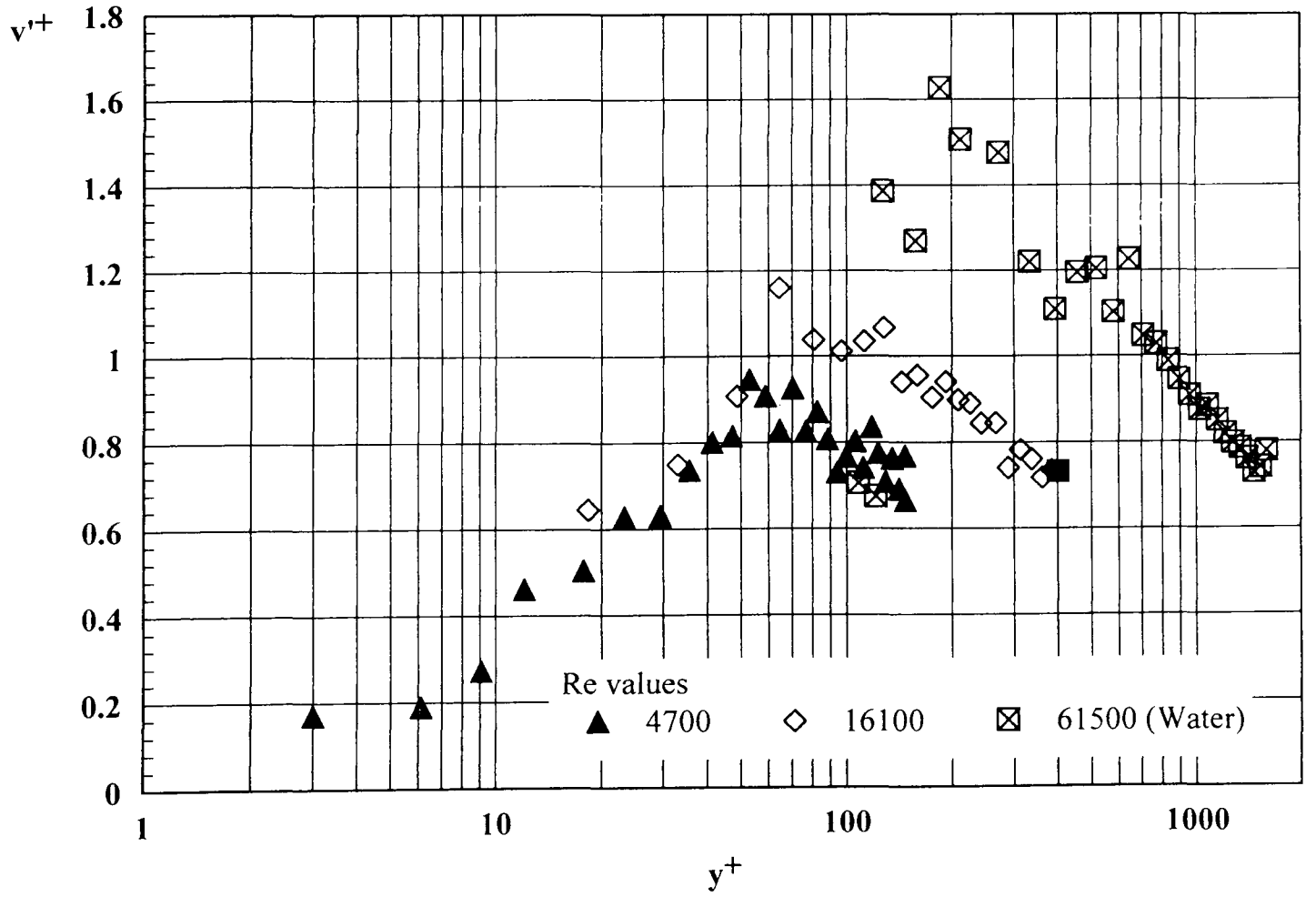

Figure 5.40(c) *Radial Turbulence Intensities in Wall Coordinates For 0.24% CMC.*

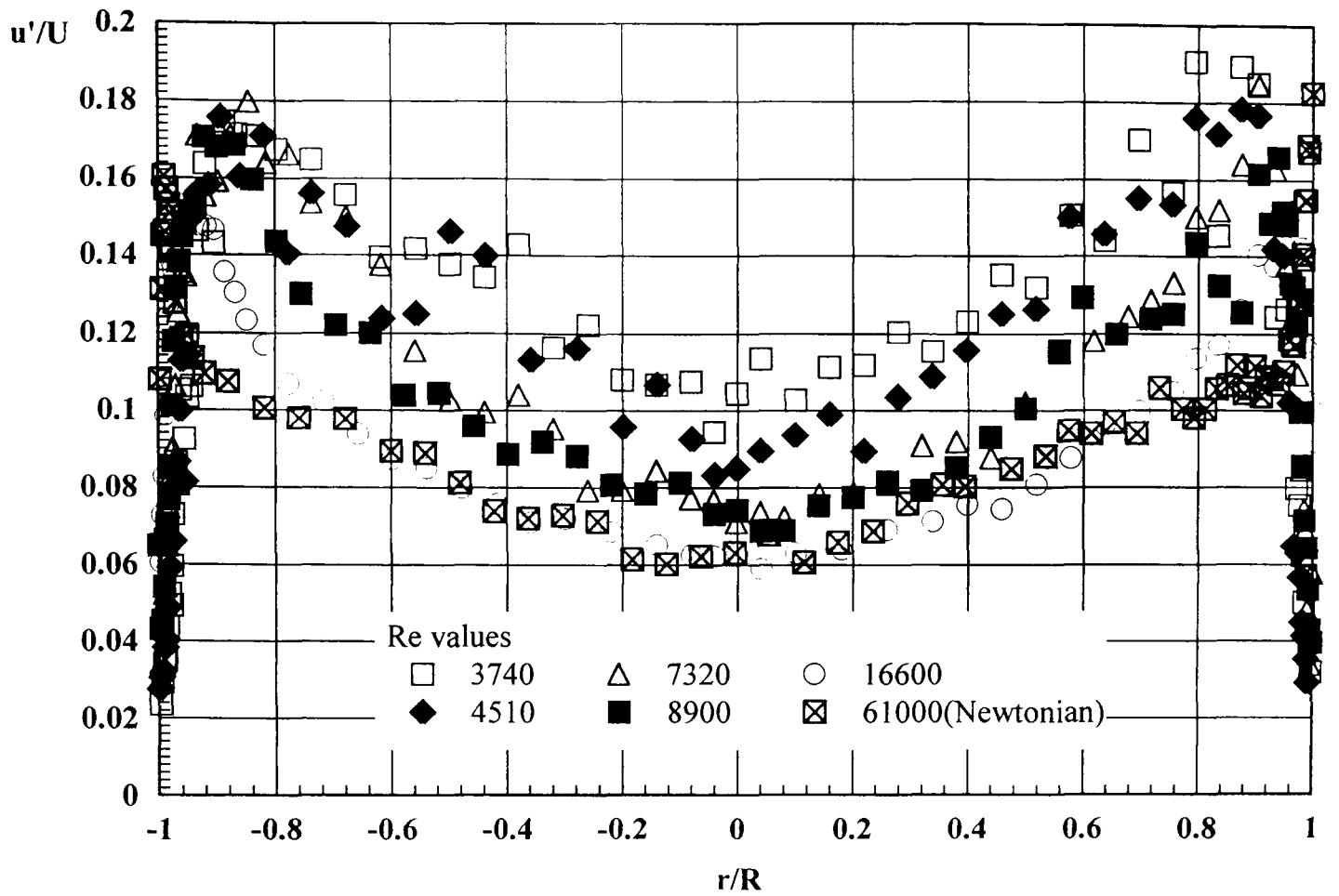

Figure 5.41(a) *Axial Turbulence Intensities For 0.25% CMC.*

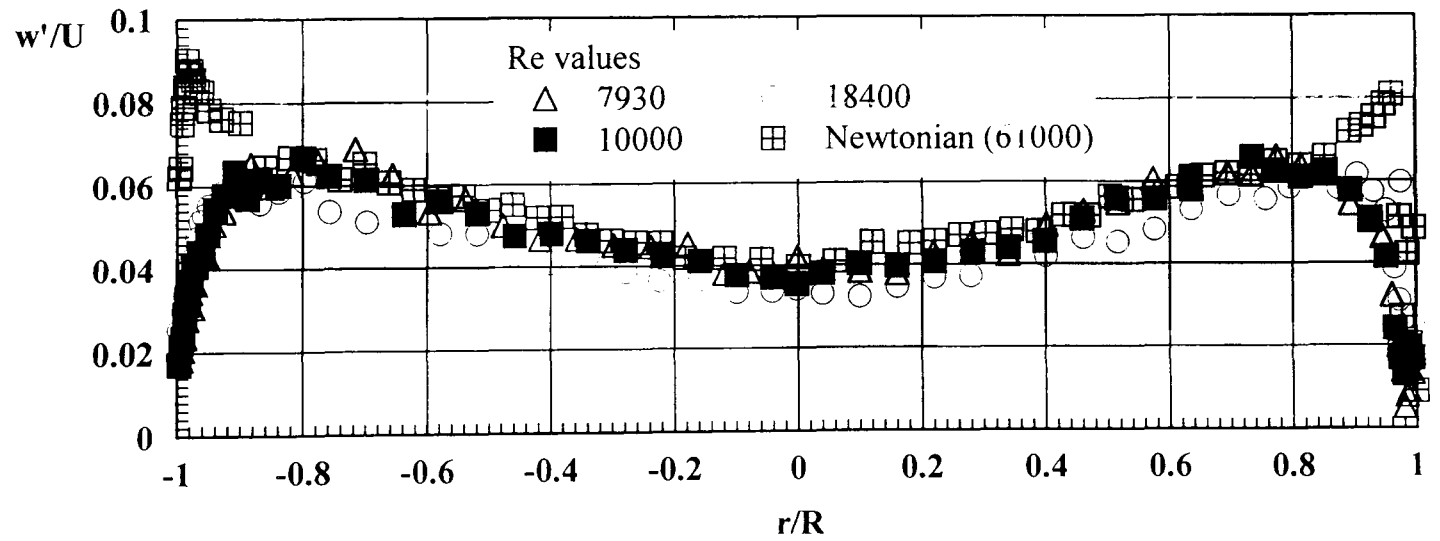

Figure 5.41(b) *Tangential Turbulence Intensities For 0.25% CMC.*

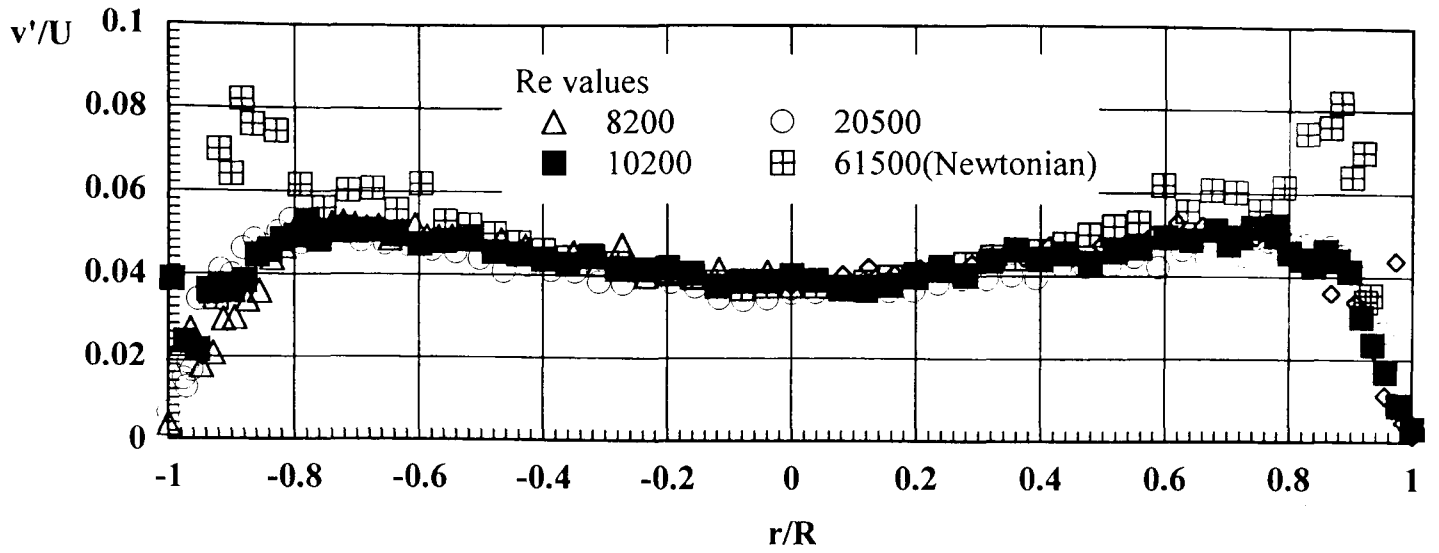

Figure 5.41(c) *Radial Turbulence Intensities For 0.25% CMC.*

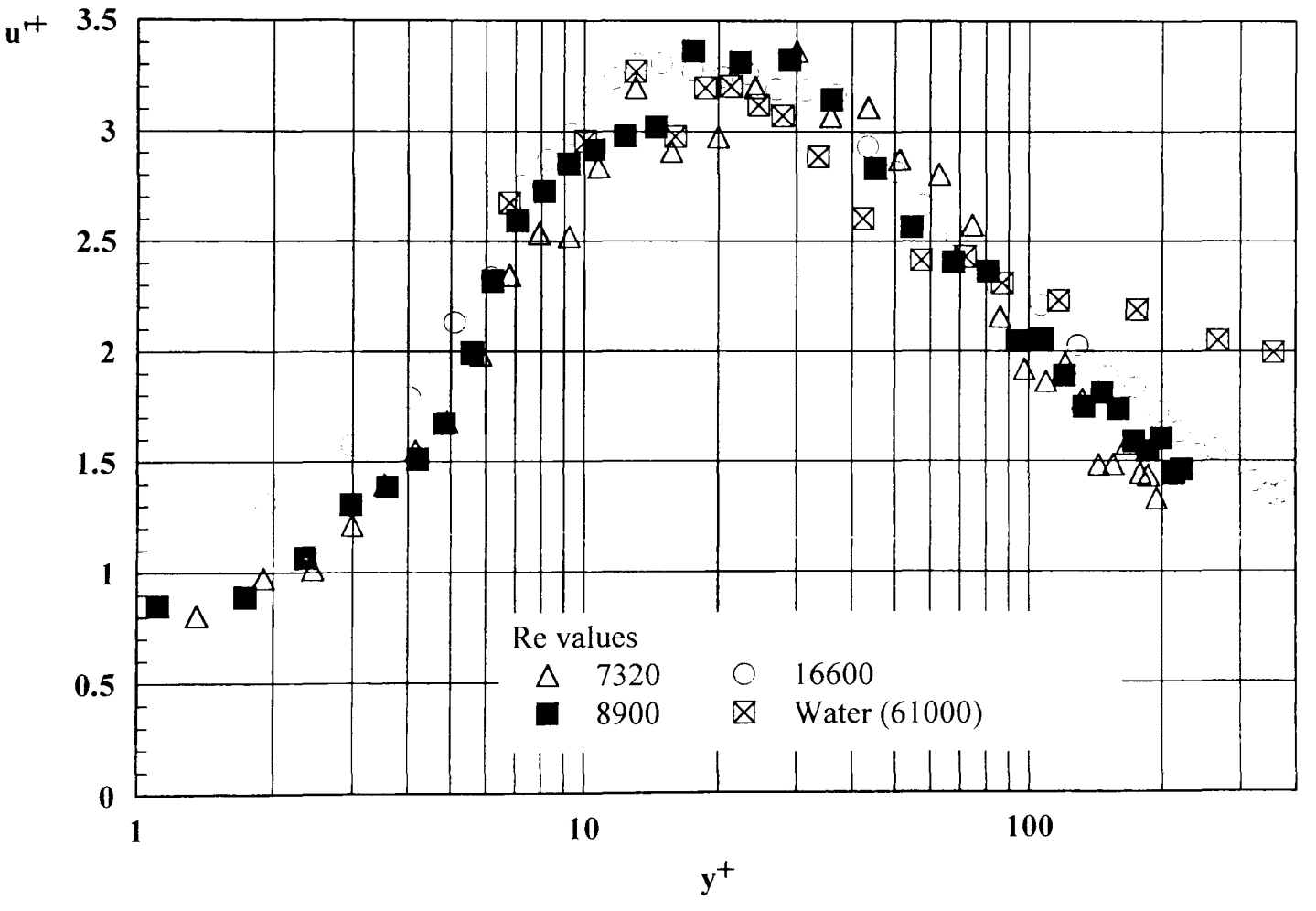

Figure 5.42(a) *Axial Turbulence Intensities in Wall Coordinates For 0.25% CMC.*

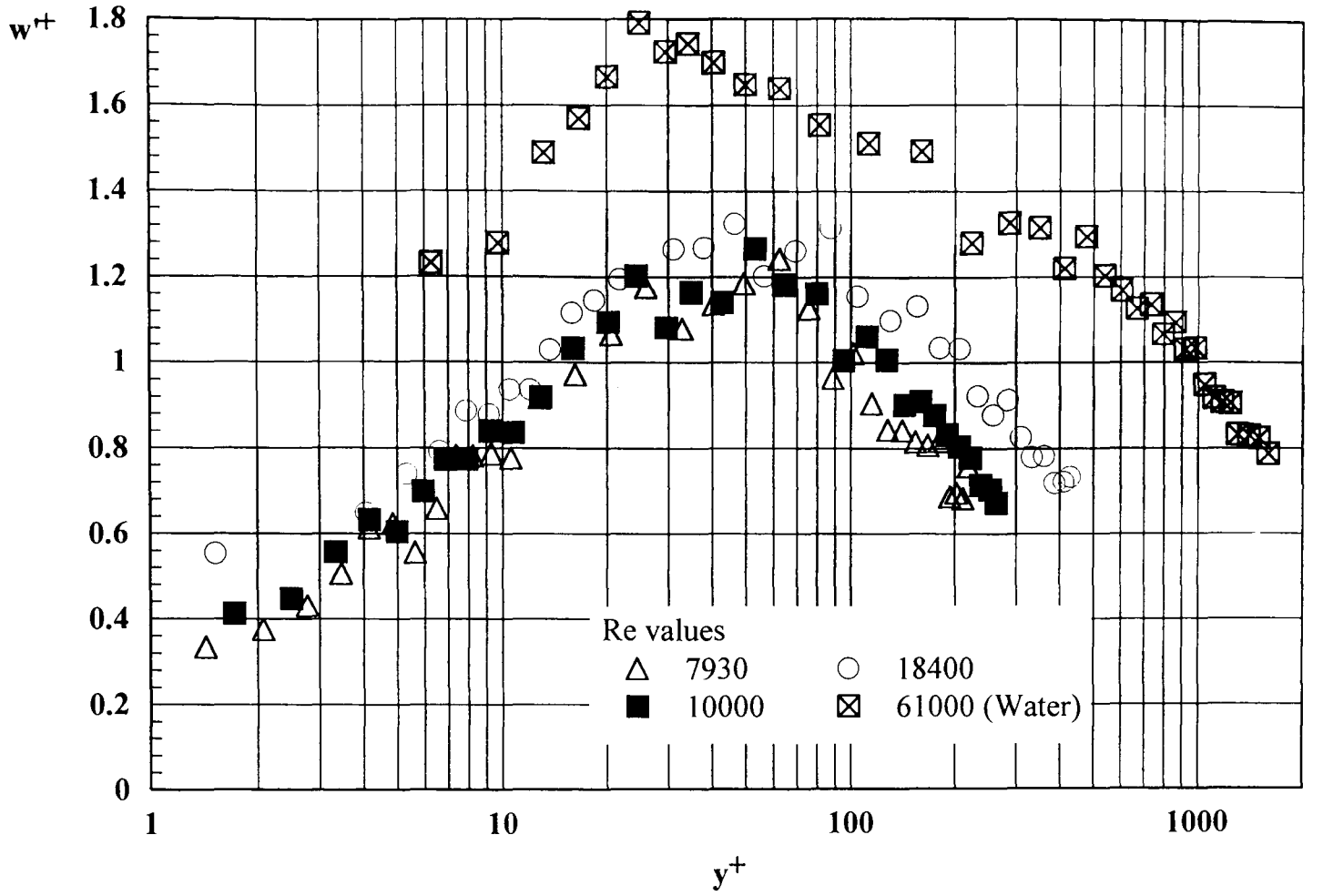

Figure 5.42(b) *Tangential Turbulence Intensities in Wall Coordinates For 0.25% CMC.*

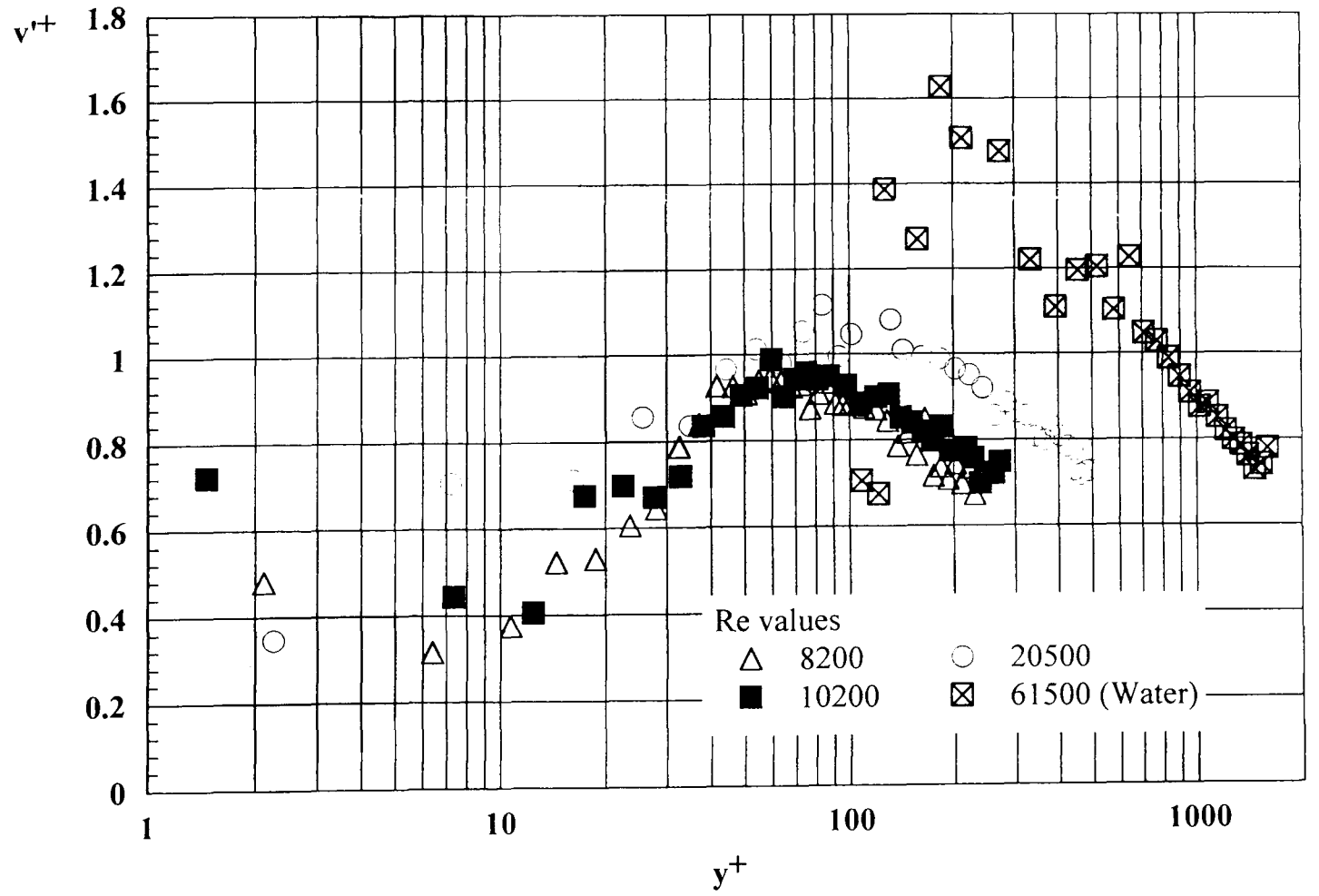

Figure 5.42(c) *Radial Turbulence Intensities in Wall Coordinates For 0.25% CMC.*

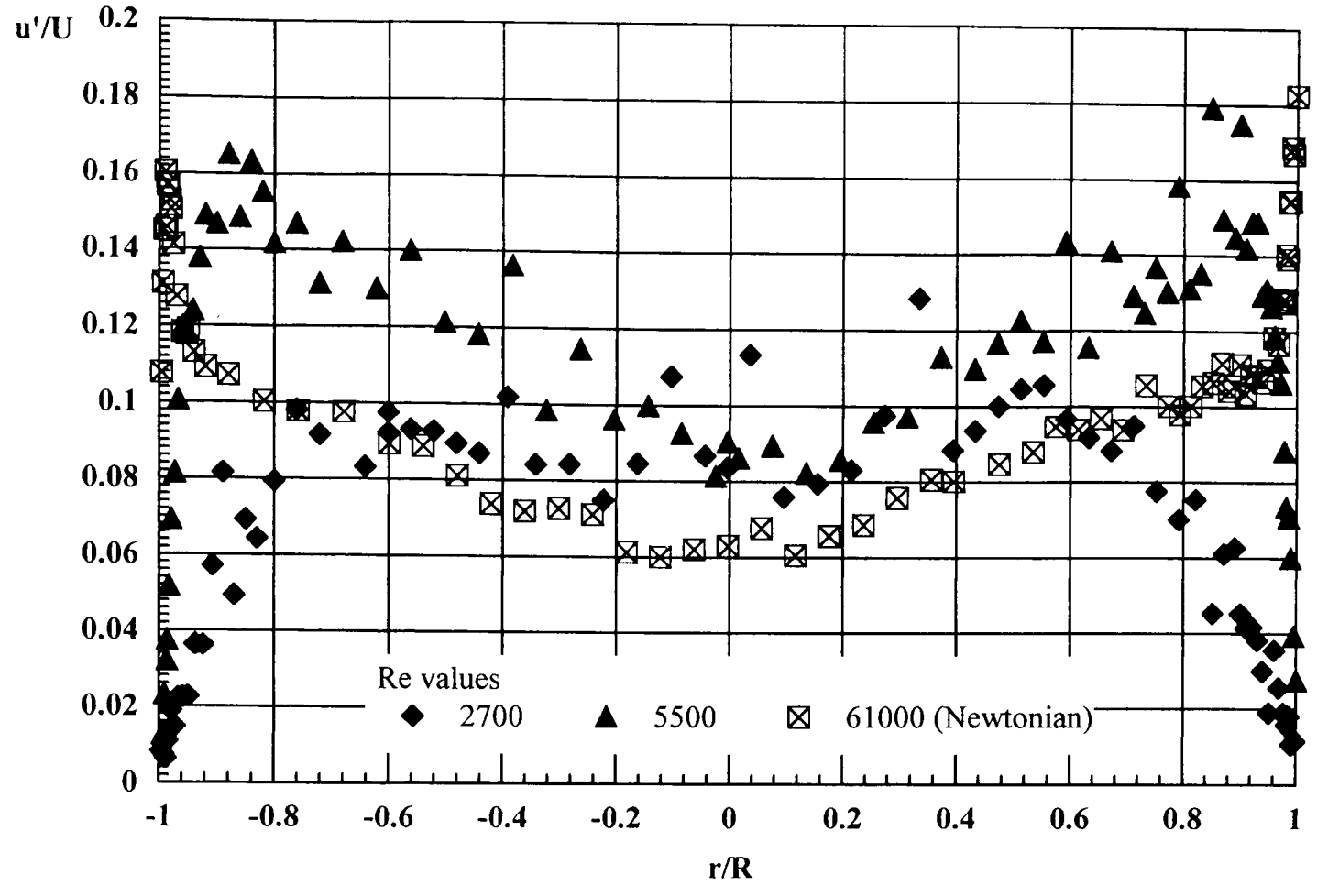

Figure 5.43(a) *Axial Turbulence Intensities For 0.4% CMC.*

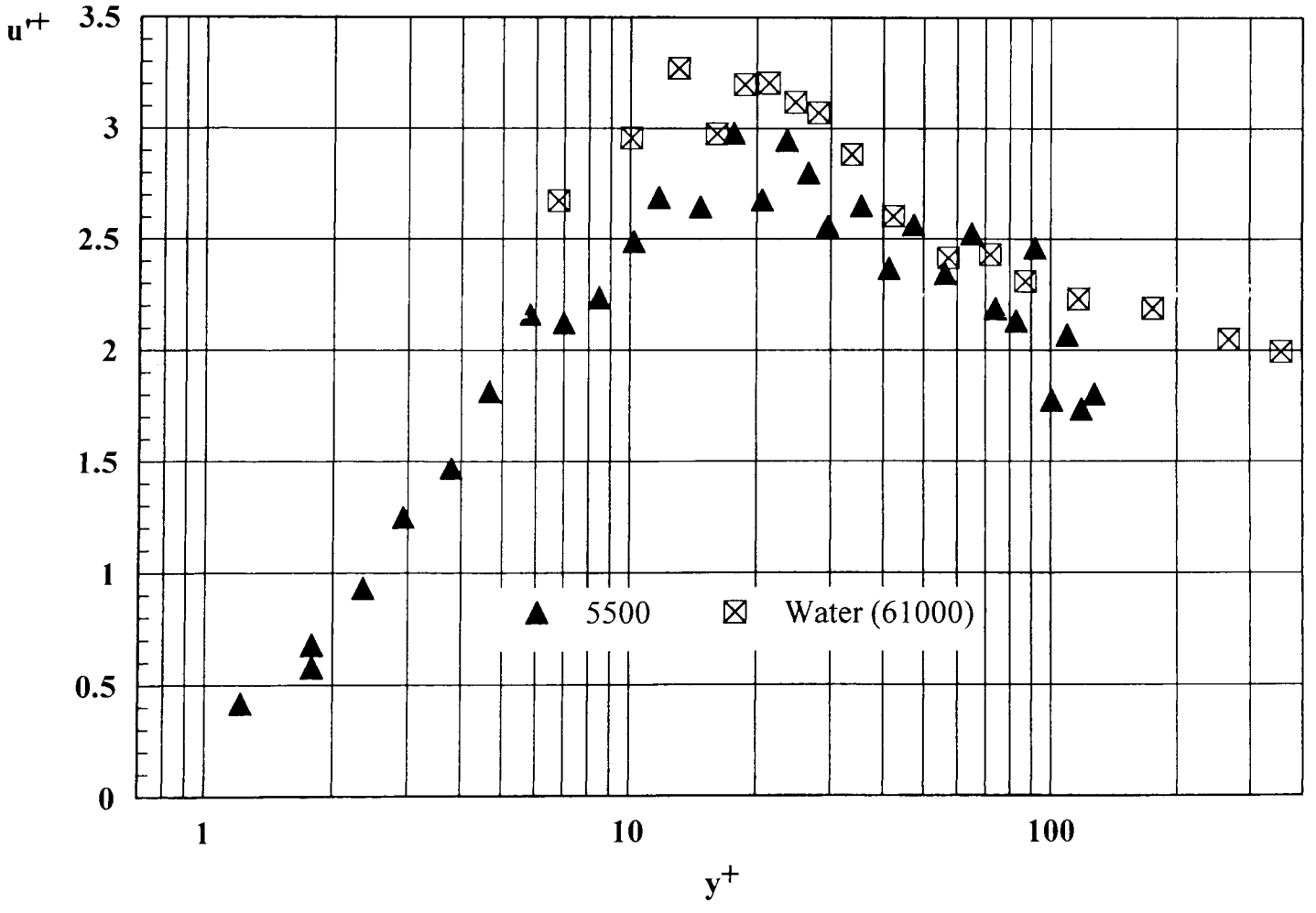

Figure 5.43(b) *Axial Turbulence Intensities in Wall Coordinates For 0.4% CMC.*

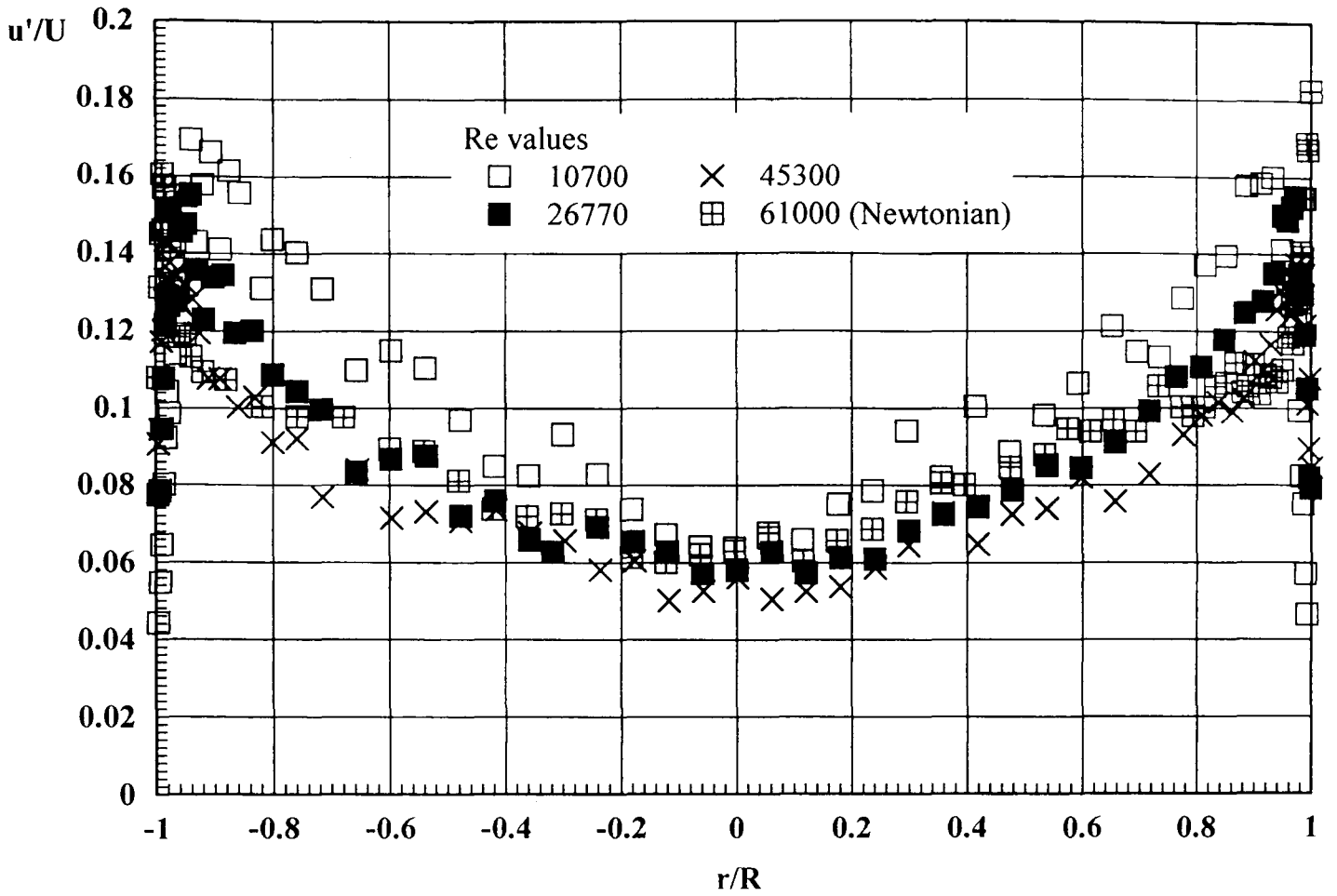

Figure 5.44(a) *Axial Turbulence Intensities For 0.09% CMC/0.09% XG.*

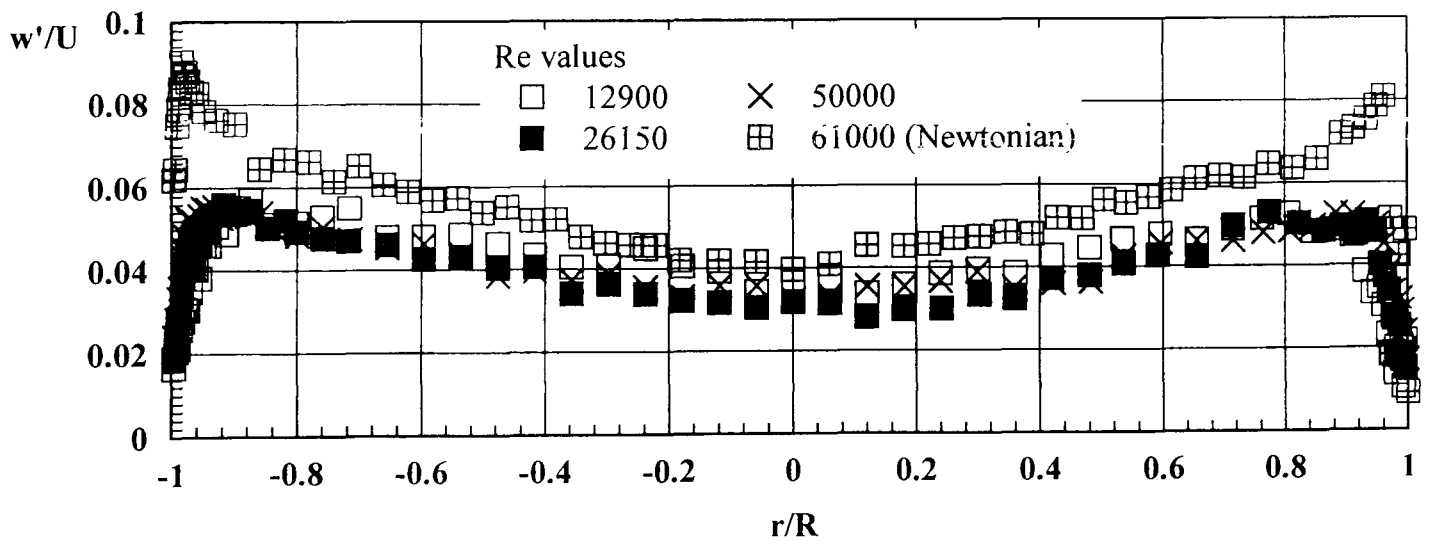

Figure 5.44(b) *Tangential Turbulence Intensities For 0.09% CMC/0.09% XG.*

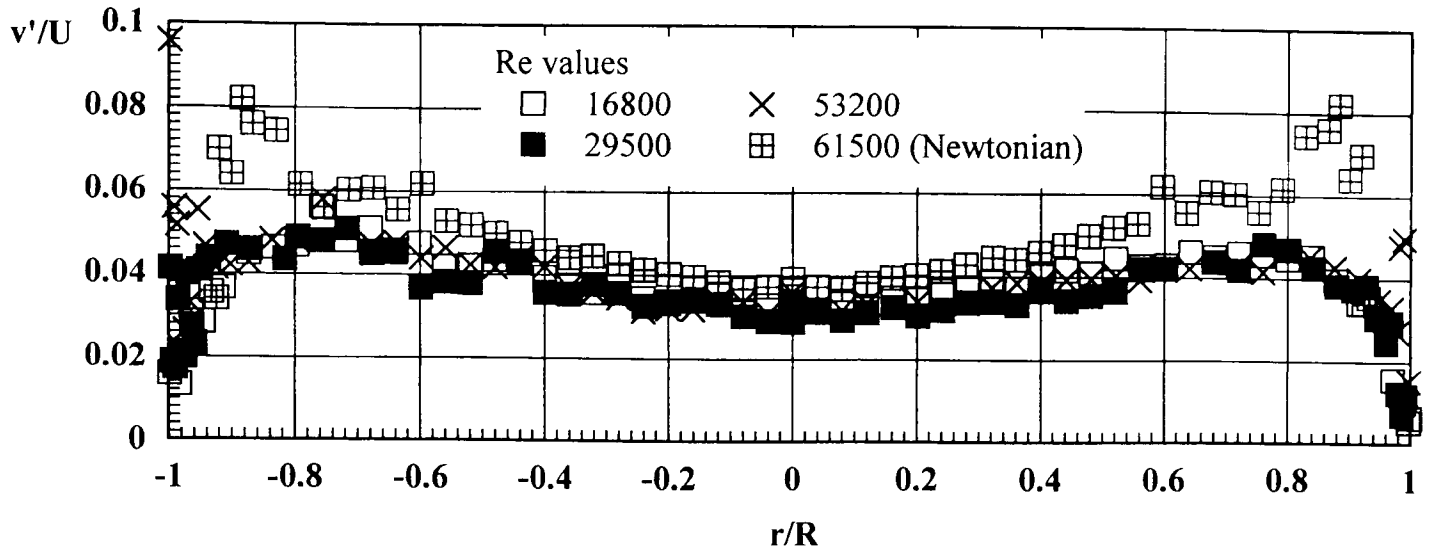

Figure 5.44(c) *Radial Turbulence Intensities For 0.09% CMC/0.09% XG.*

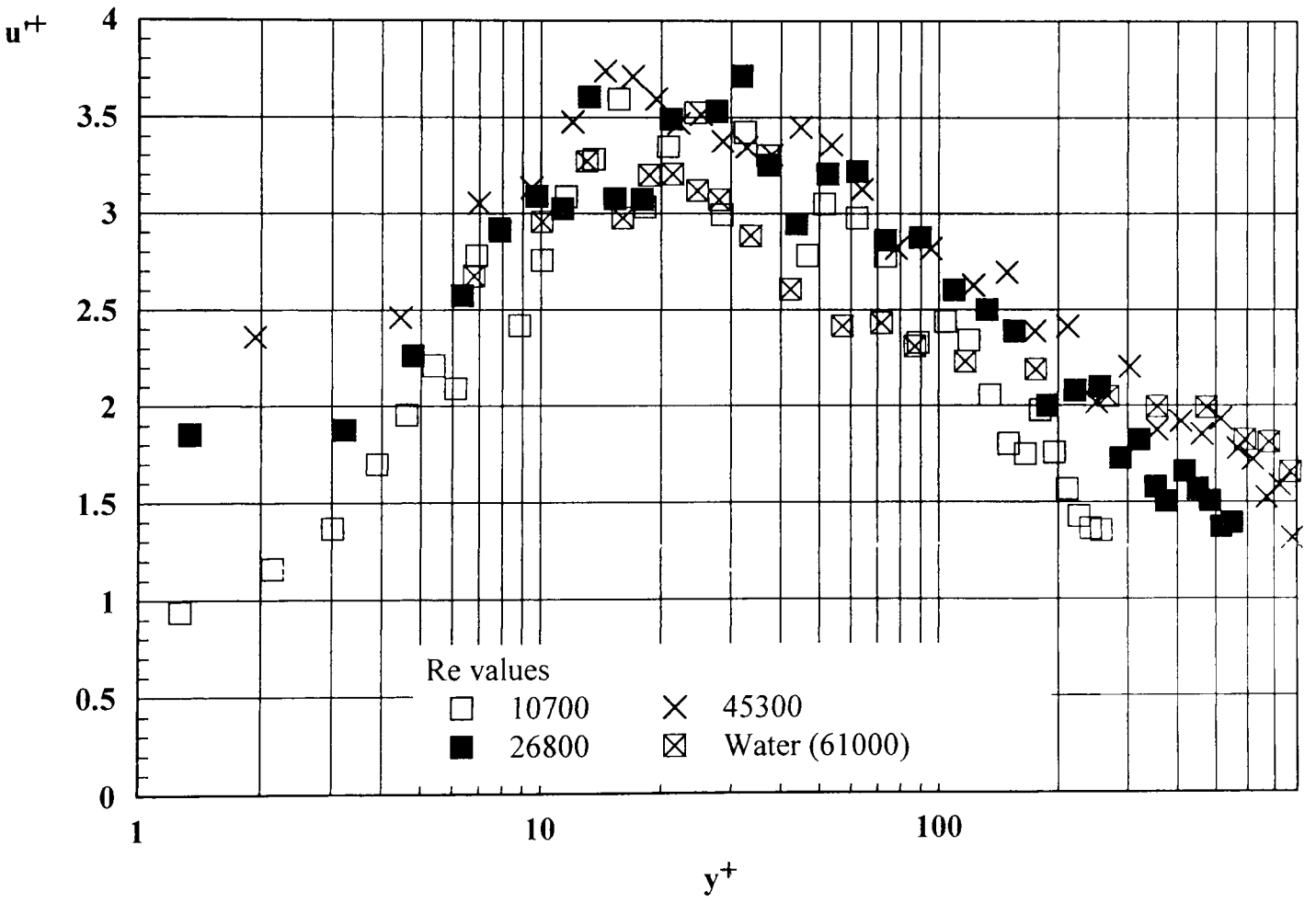

Figure 5.45(a) *Axial Turbulence Intensities in Wall Coordinates For 0.09% CMC/0.09% XG.*

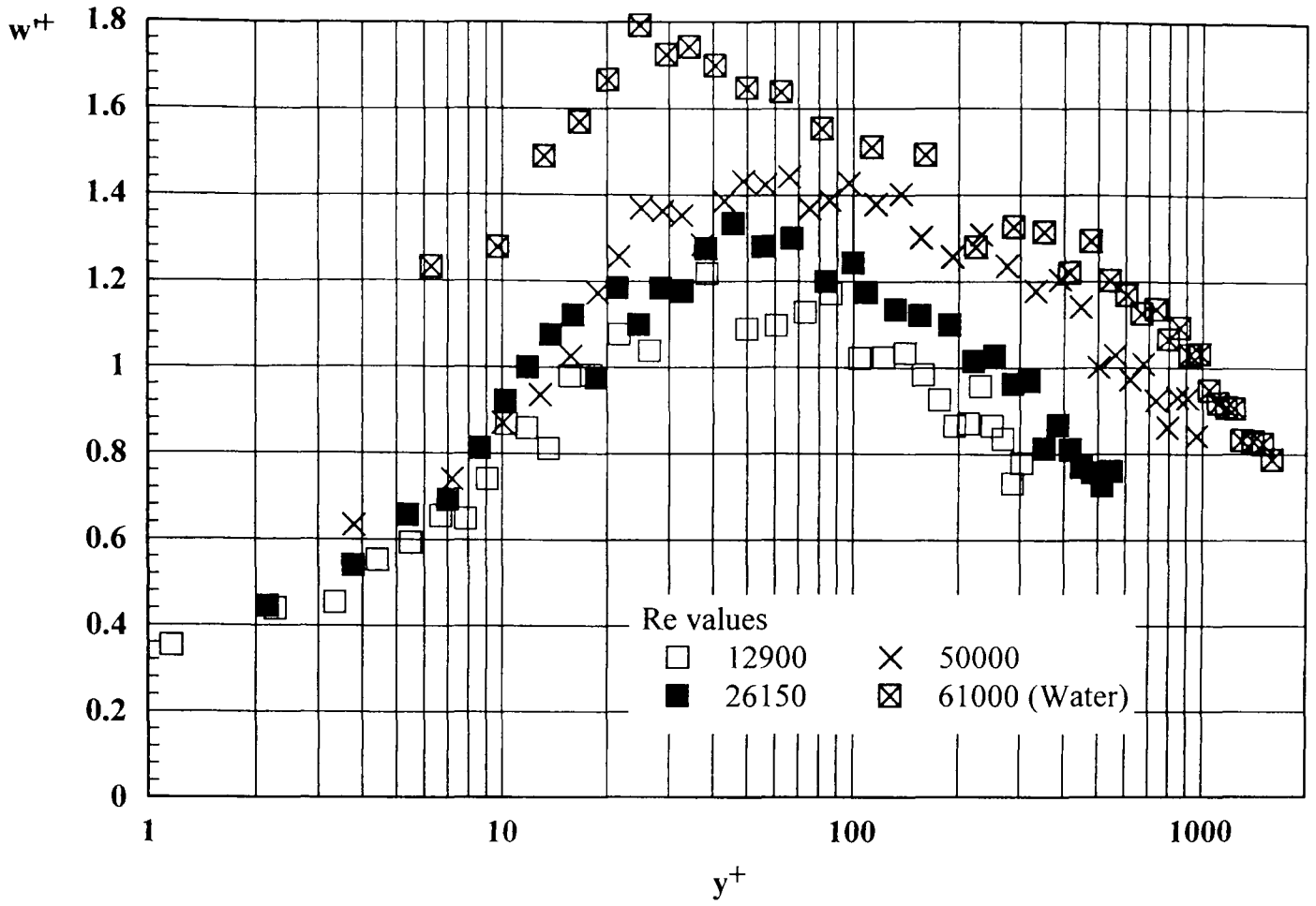

Figure 5.45(b) *Tangential Turbulence Intensities in Wall Coordinates For 0.09% CMC/0.09% XG.*

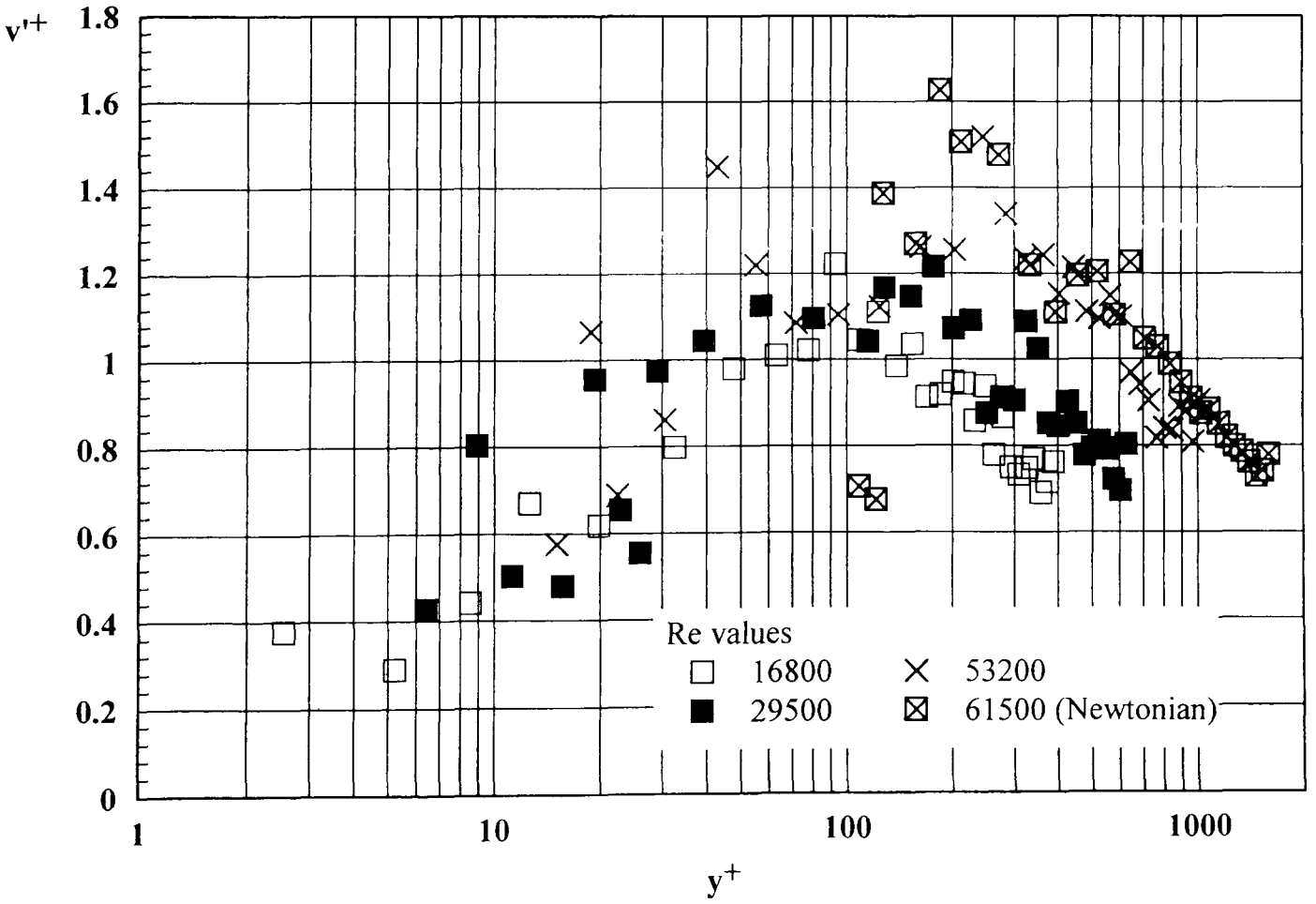

Figure 5.45(c) *Radial Turbulence Intensities in Wall Coordinates For 0.09% CMC/0.09% XG.*

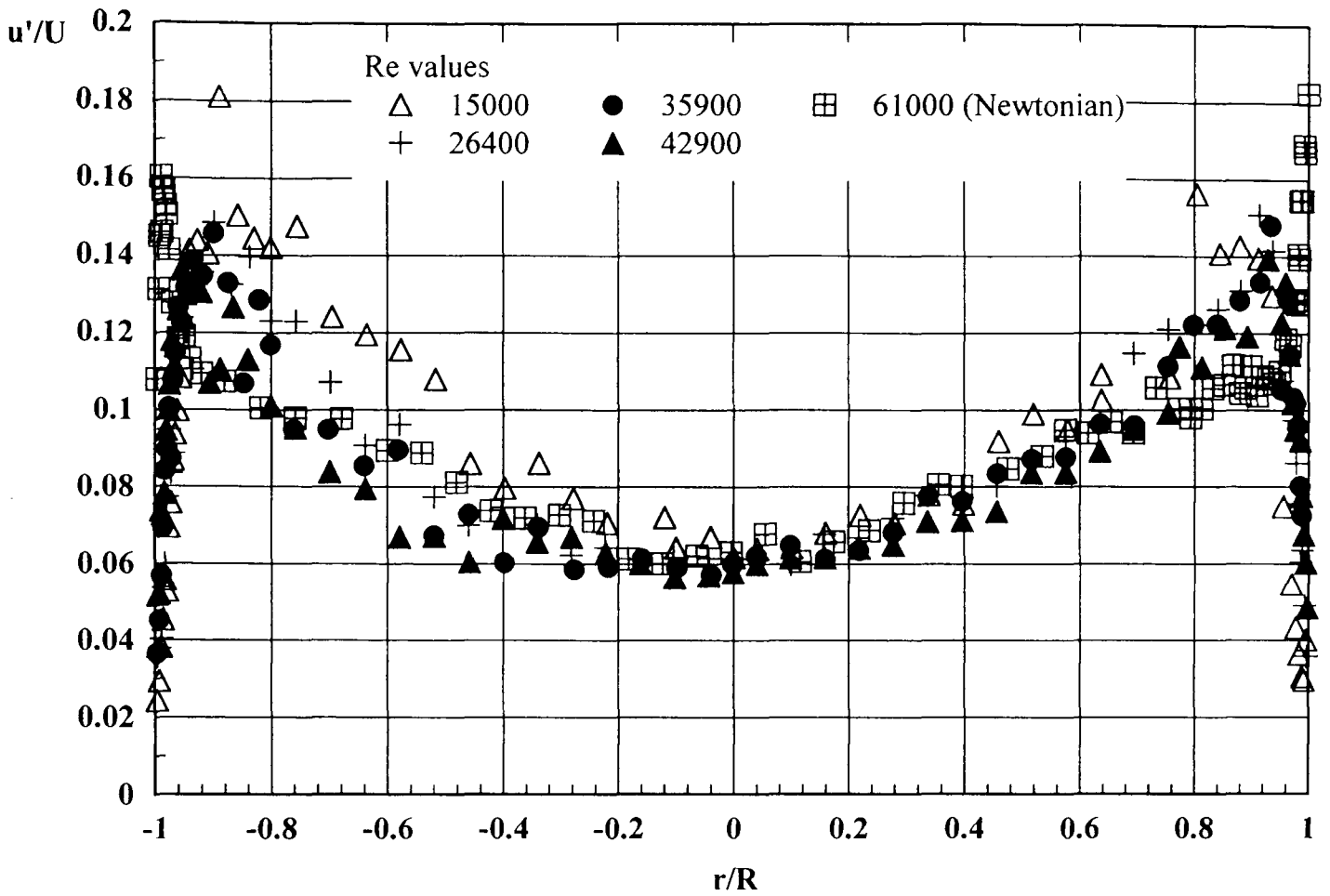

Figure 5.46(a) *Axial Turbulence Intensities For 0.125% PAA.*

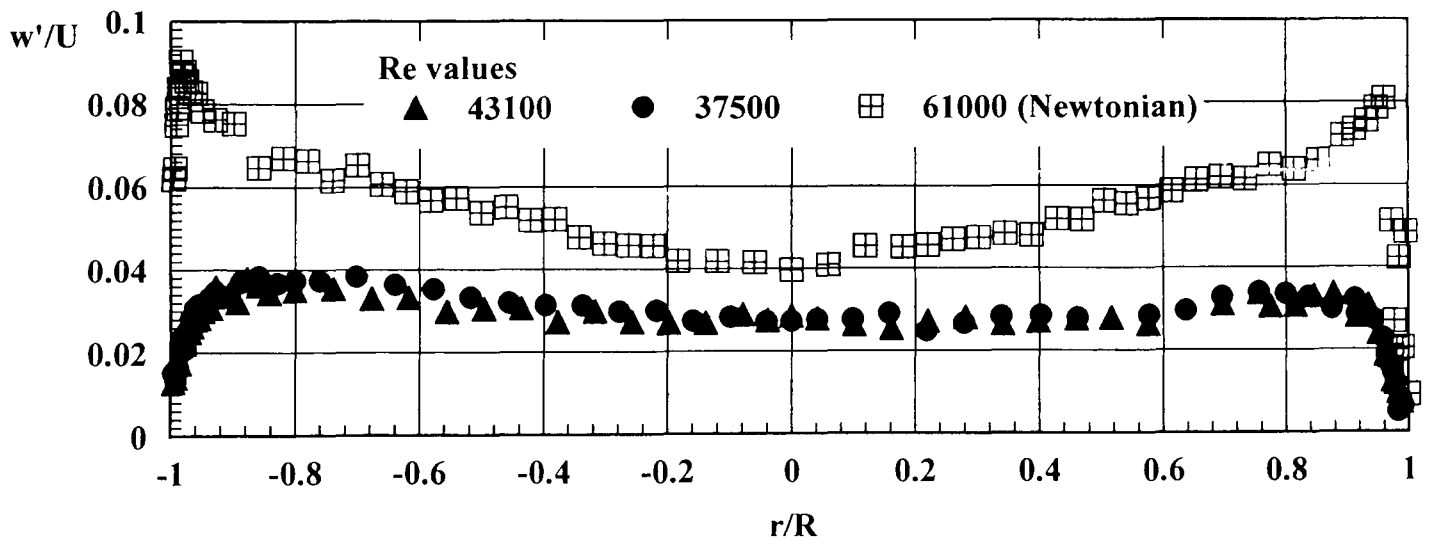

Figure 5.46(b) *Tangential Turbulence Intensities For 0.125% PAA.*

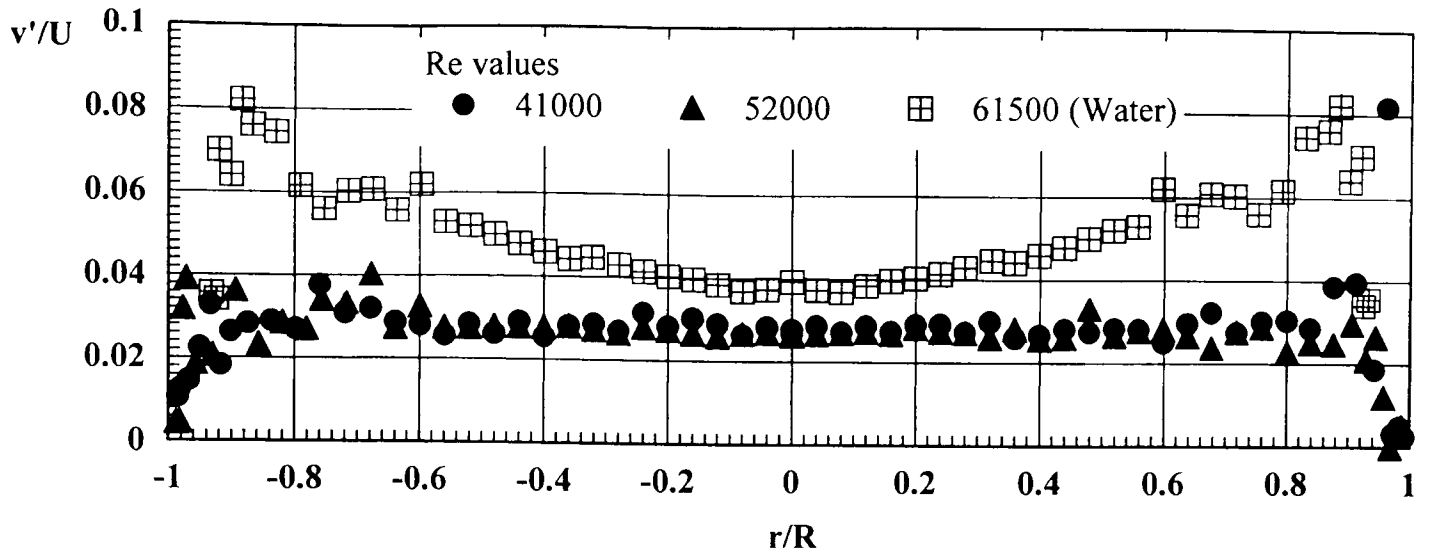

Figure 5.46(c) *Radial Turbulence Intensities For 0.125% PAA.*

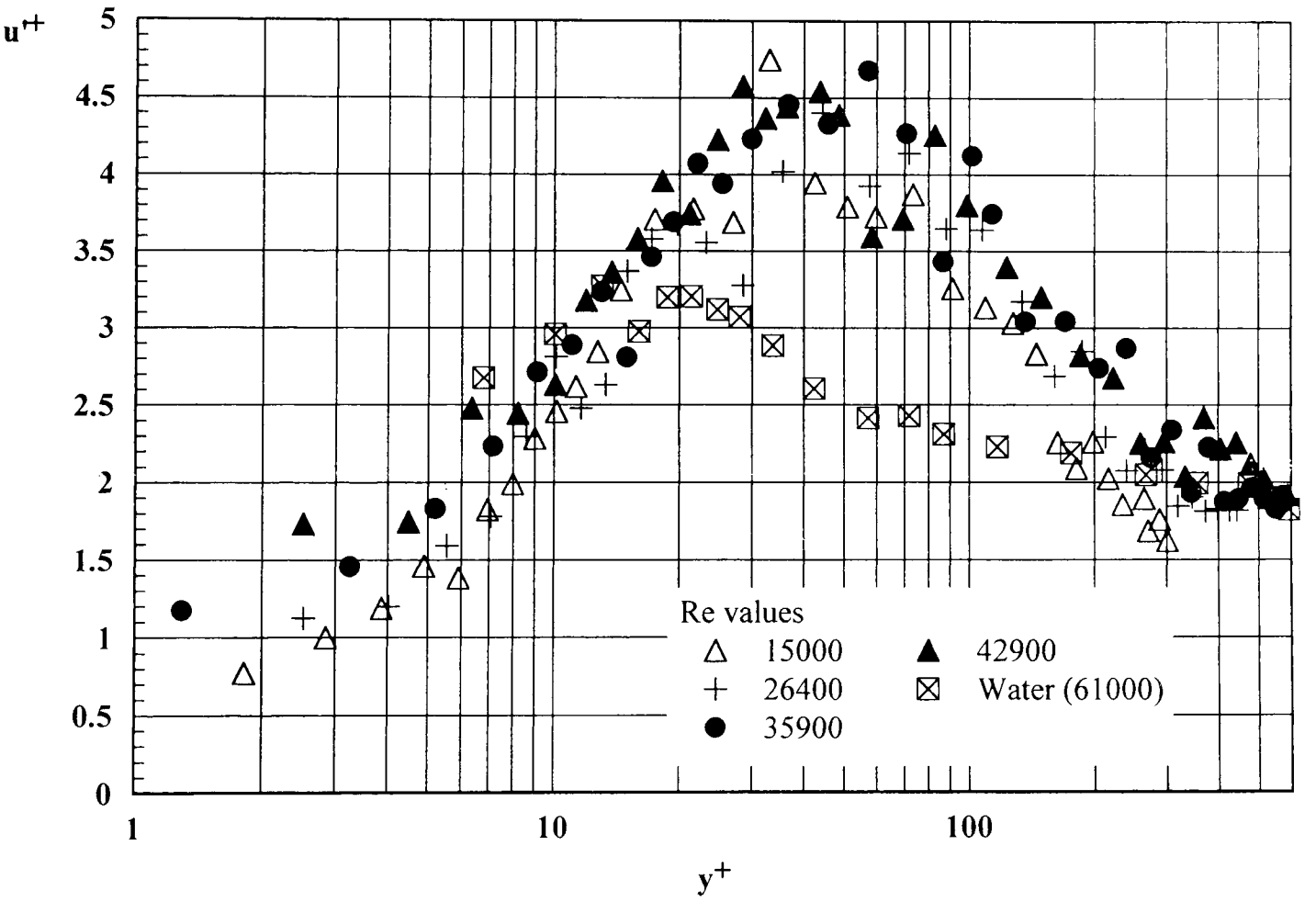

Figure 5.47(a) *Axial Turbulence Intensities in Wall Coordinates For 0.125% PAA.*

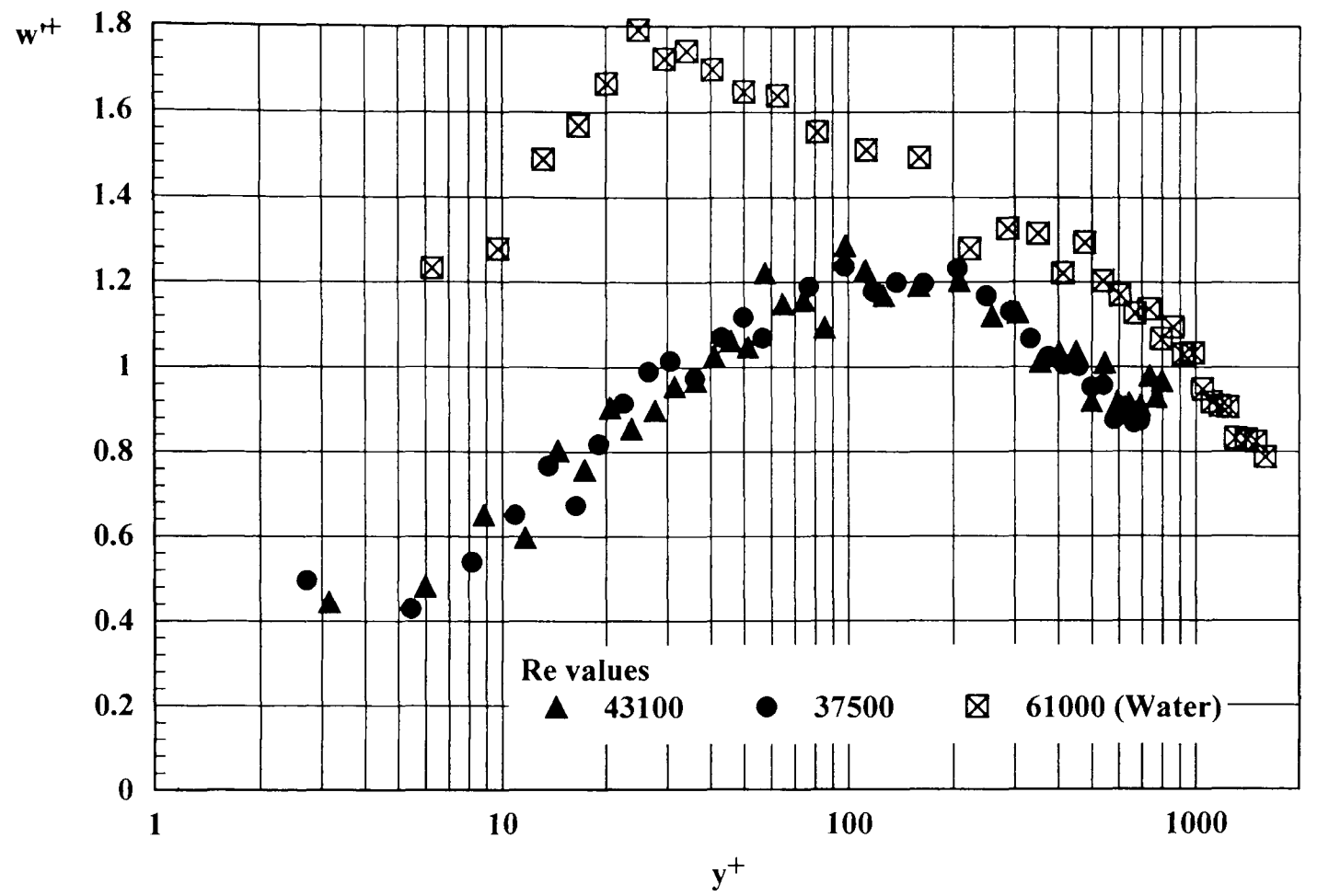

Figure 5.47(b) *Tangential Turbulence Intensities in Wall Coordinates For 0.125% PAA.*

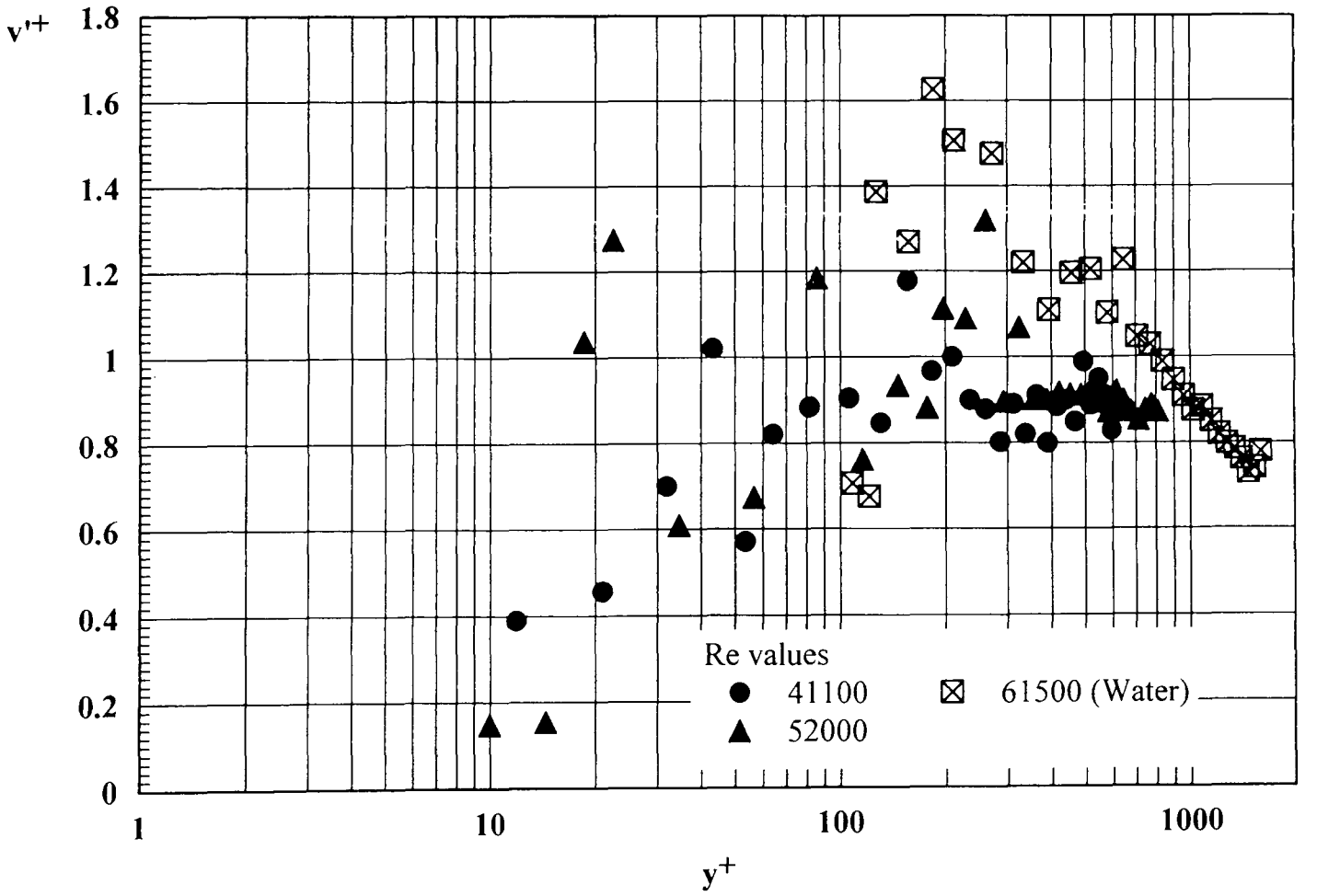

Figure 5.47(c) *Radial Turbulence Intensities in Wall Coordinates For 0.125% PAA.*

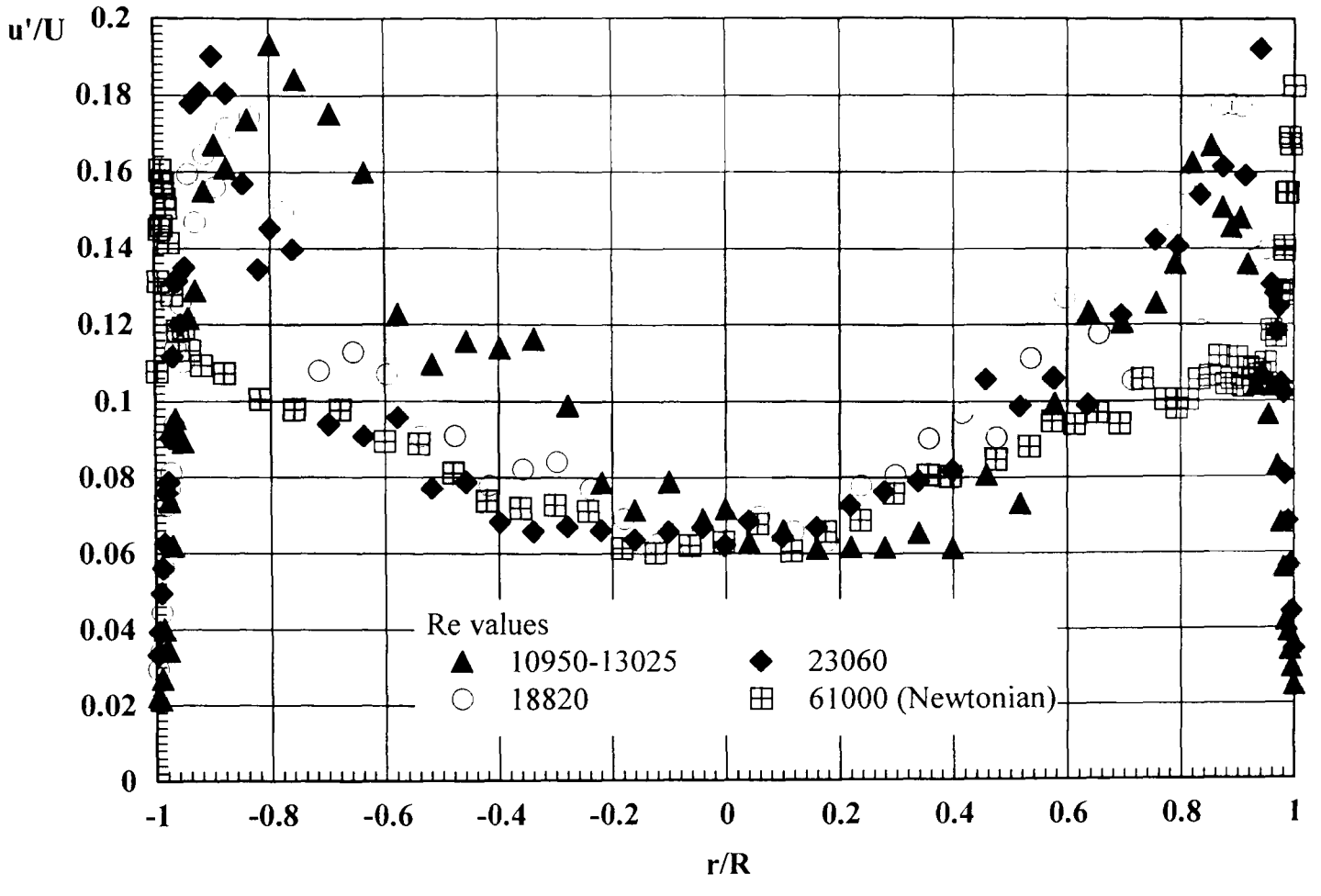

Figure 5.48(a) *Axial Turbulence Intensities For 0.2% PAA.*

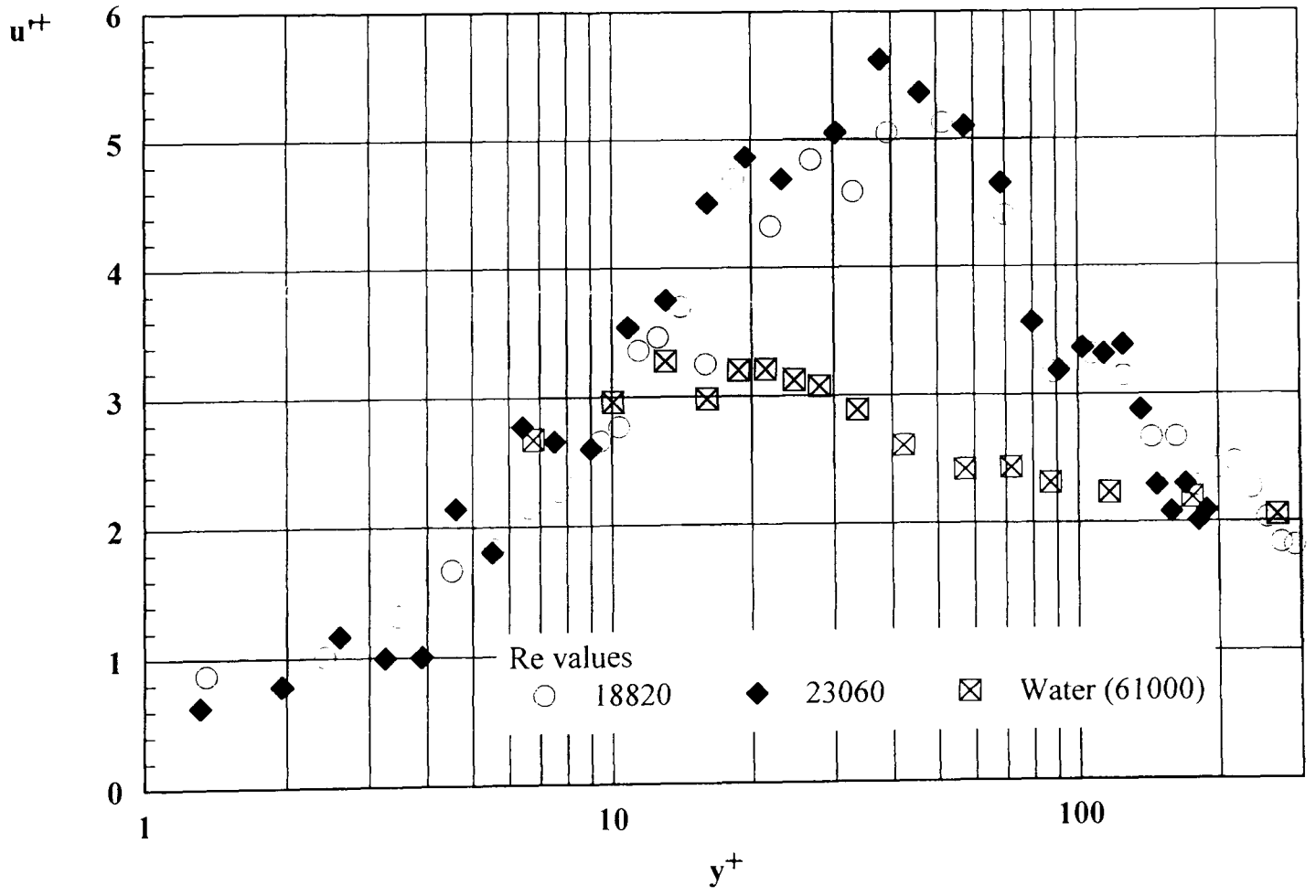

Figure 5.48(b) *Axial Turbulence Intensities in Wall Coordinates For 0.2% PAA.*

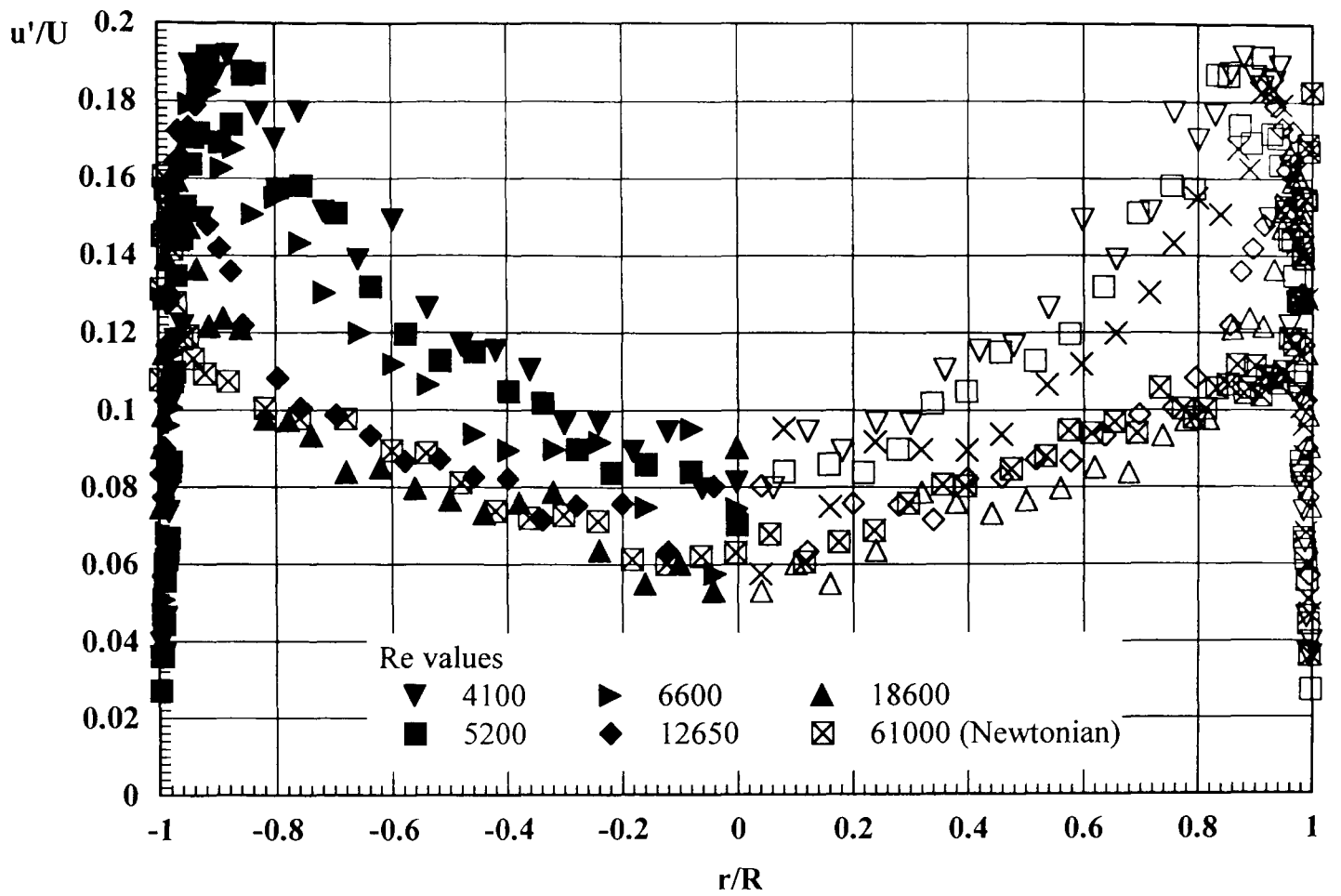

Figure 5.49(a) *Axial Turbulence Intensities For 0.14% Carbopol 934.*

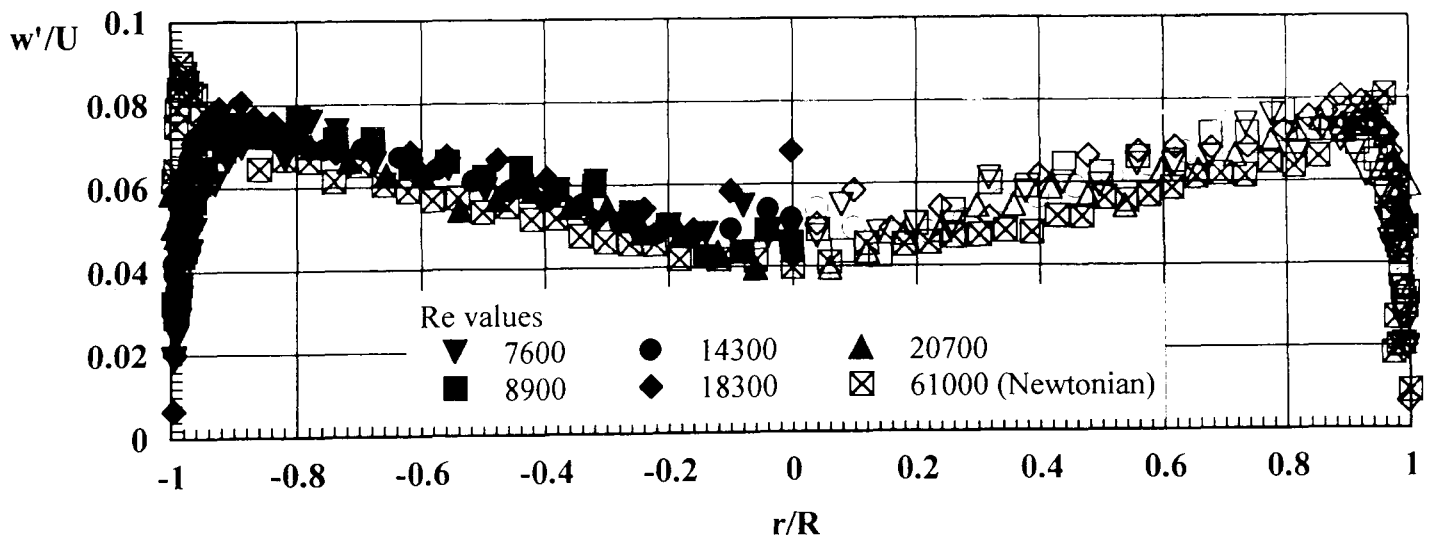

Figure 5.49(b) *Tangential Turbulence Intensities For 0.14% Carbopol 934.*

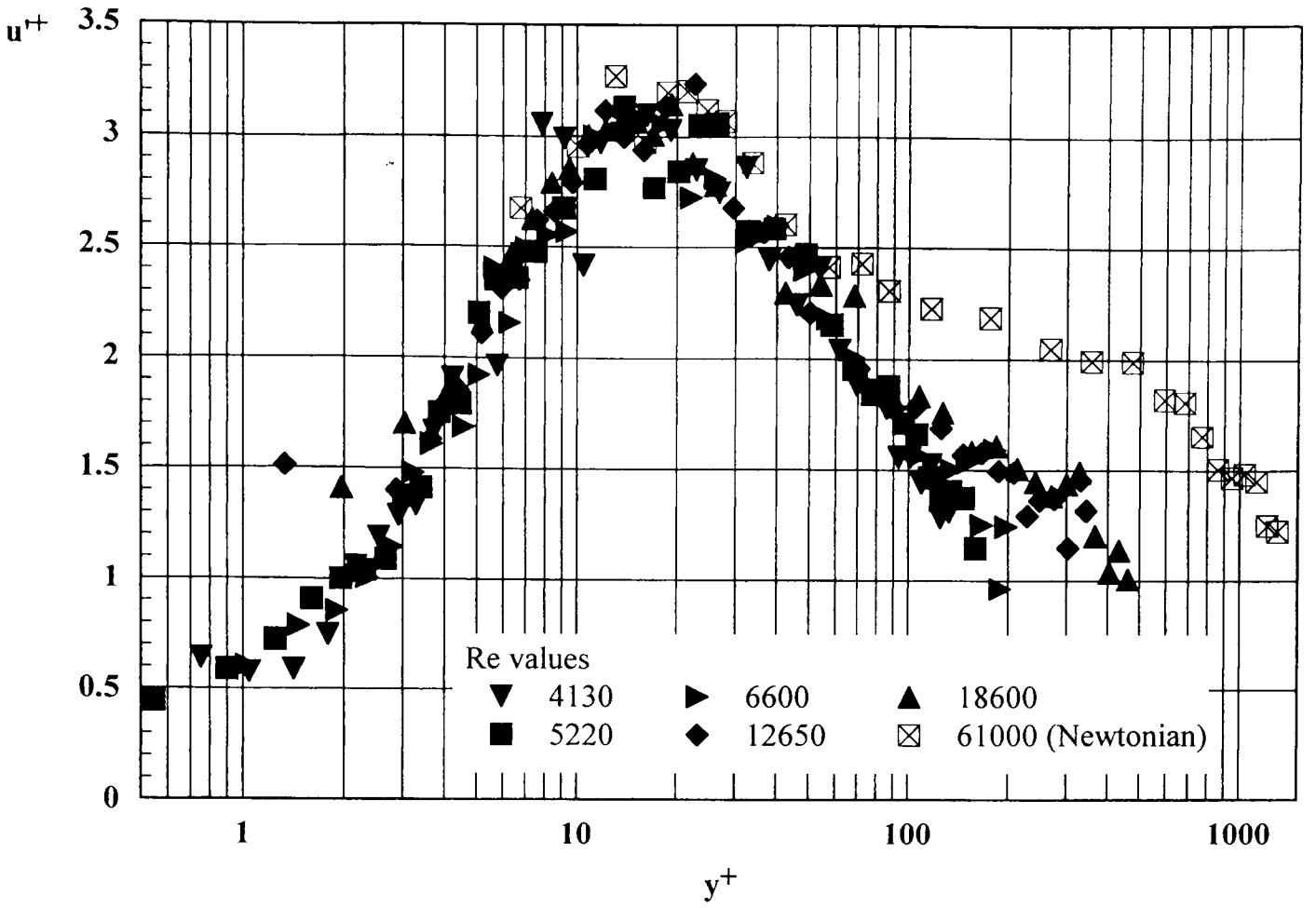

Figure 5.50(a) *Axial Turbulence Intensities in Wall Coordinates For 0.14% Carbopol 934.*

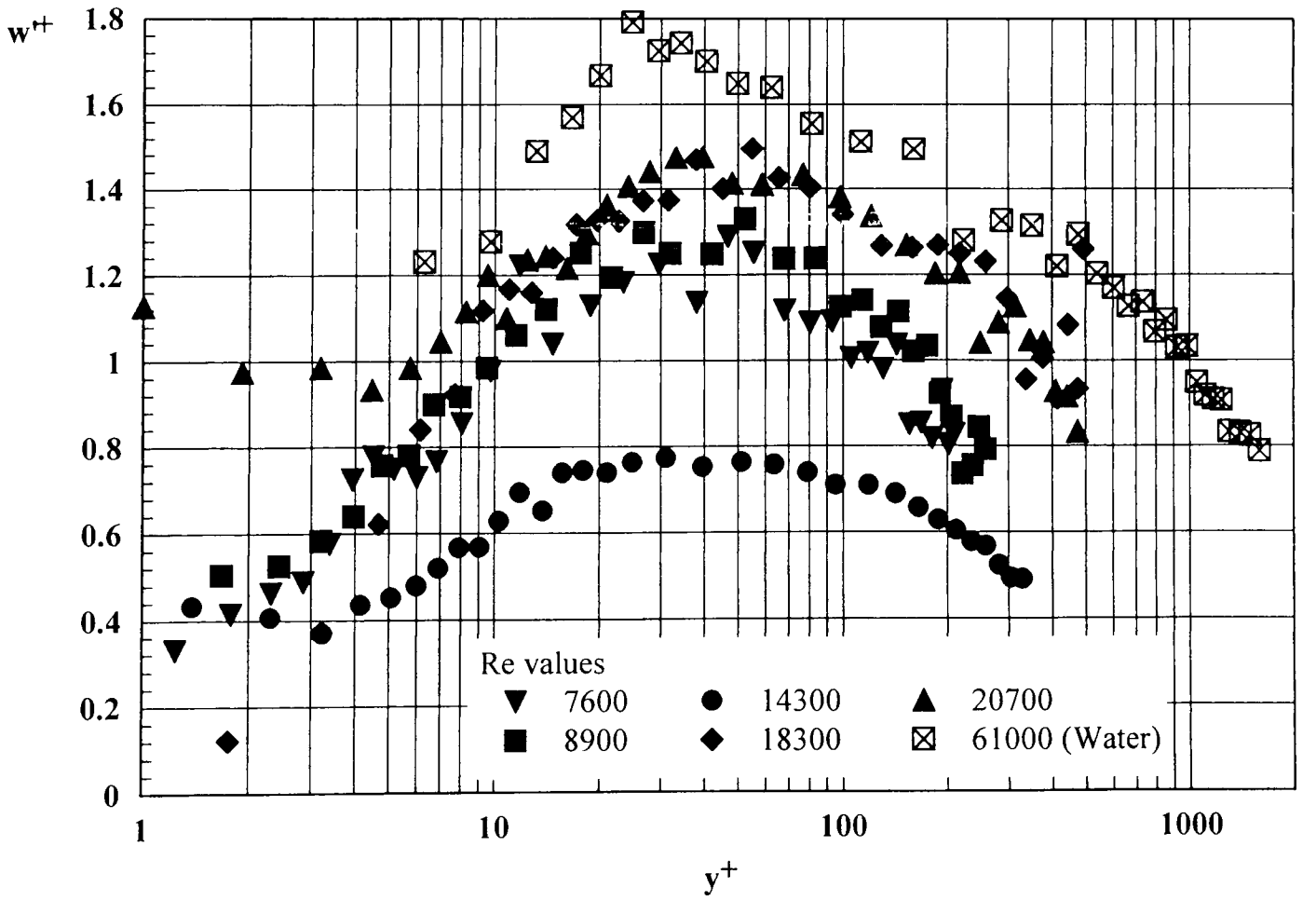

Figure 5.50(b) *Tangential Turbulence Intensities in Wall Coordinates For 0.14% Carbopol 934.*

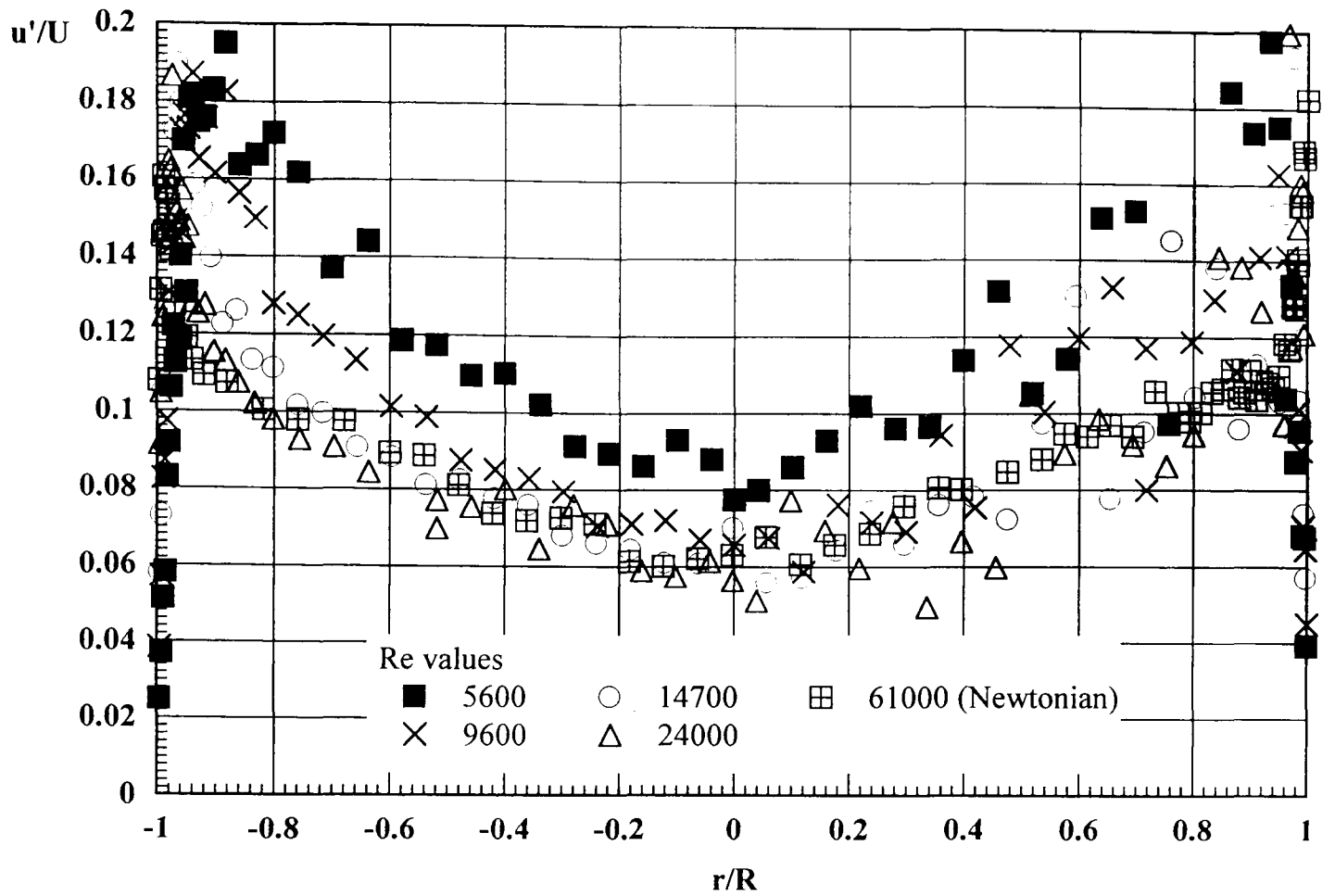

Figure 5.51(a) *Axial Turbulence Intensities For 0.1% Carbopol EZ1.*

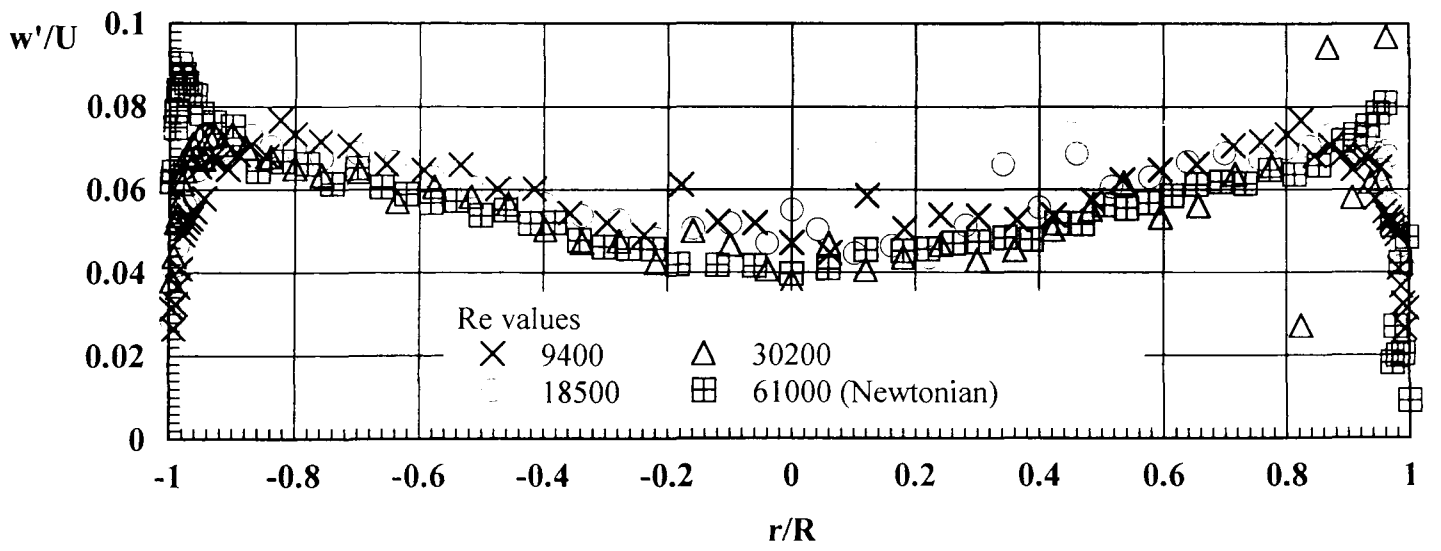

Figure 5.51(b) *Tangential Turbulence Intensities For 0.1% Carbopol EZ1.*

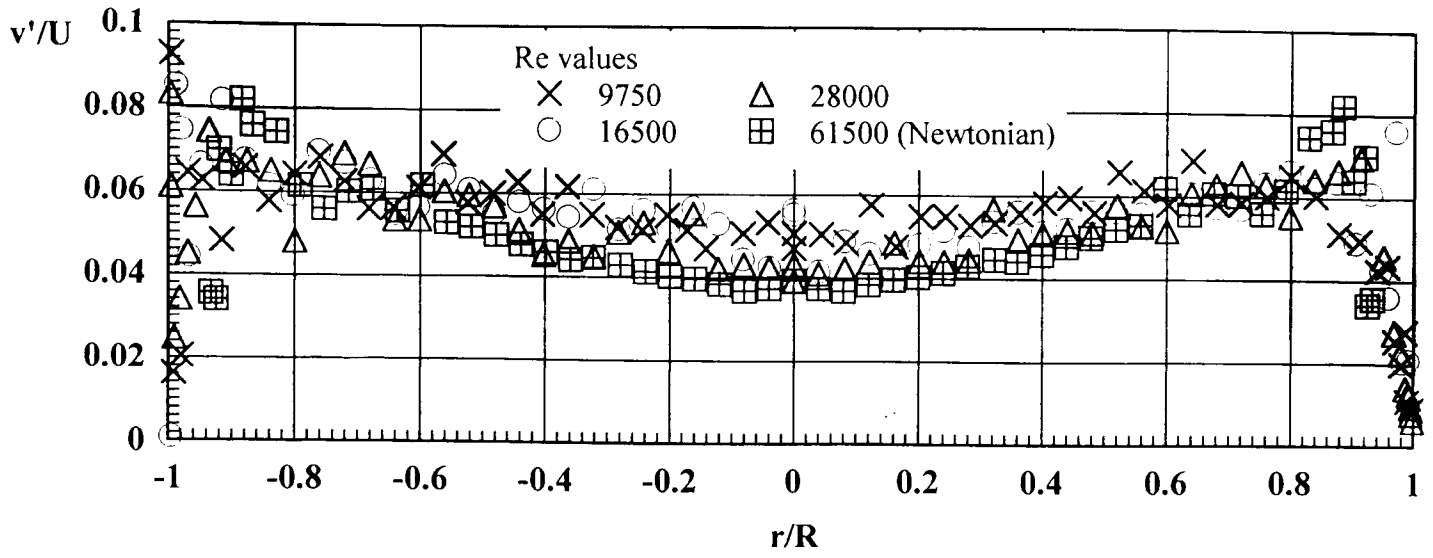

Figure 5.51(c) *Radial Turbulence Intensities For 0.1% Carbopol EZ1.*

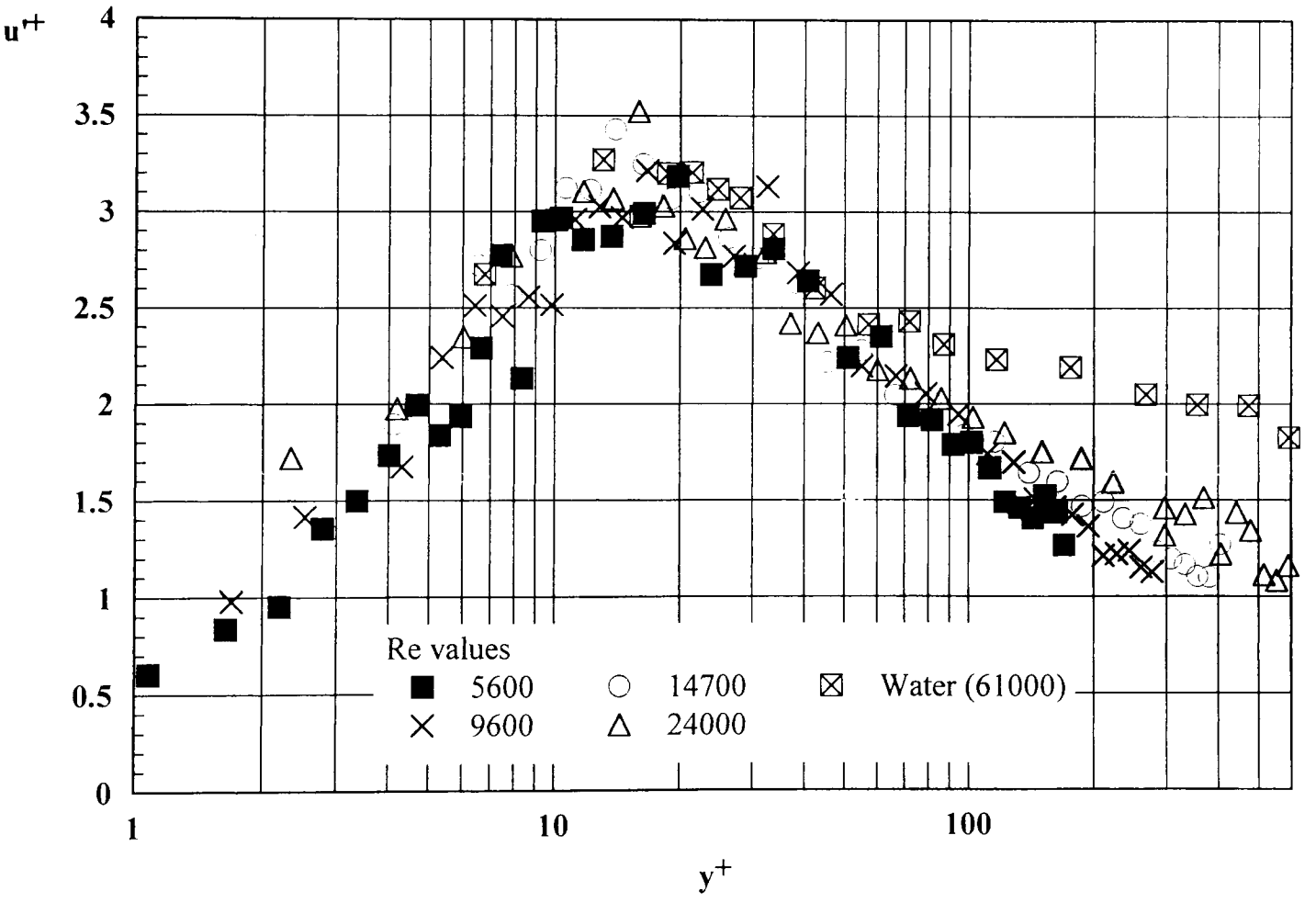

Figure 5.52(a) *Axial Turbulence Intensities in Wall Coordinates For 0.1% Carbopol EZ1.*

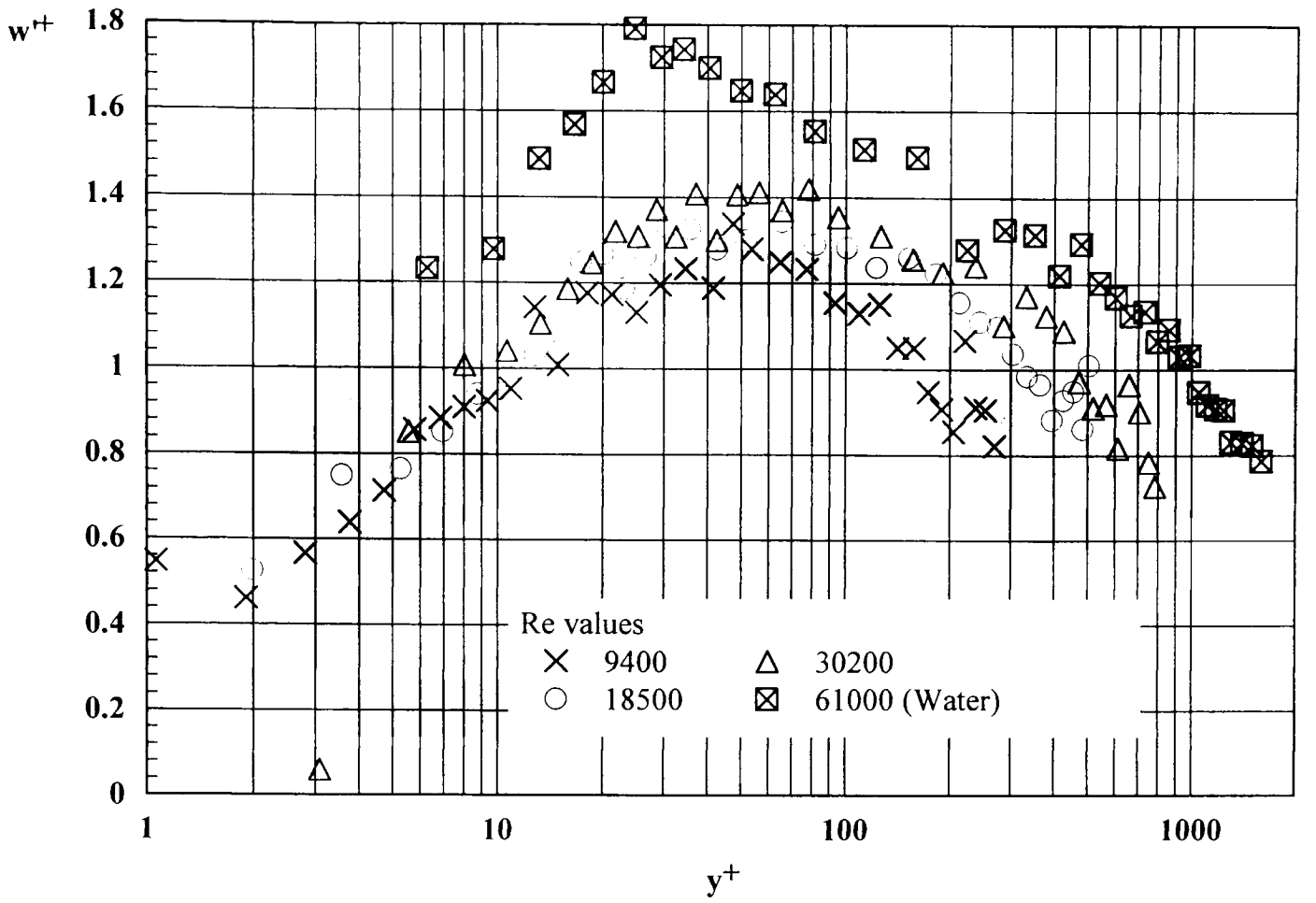

Figure 5.52(b) *Tangential Turbulence Intensities in Wall Coordinates For 0.1% Carbopol EZ1.*

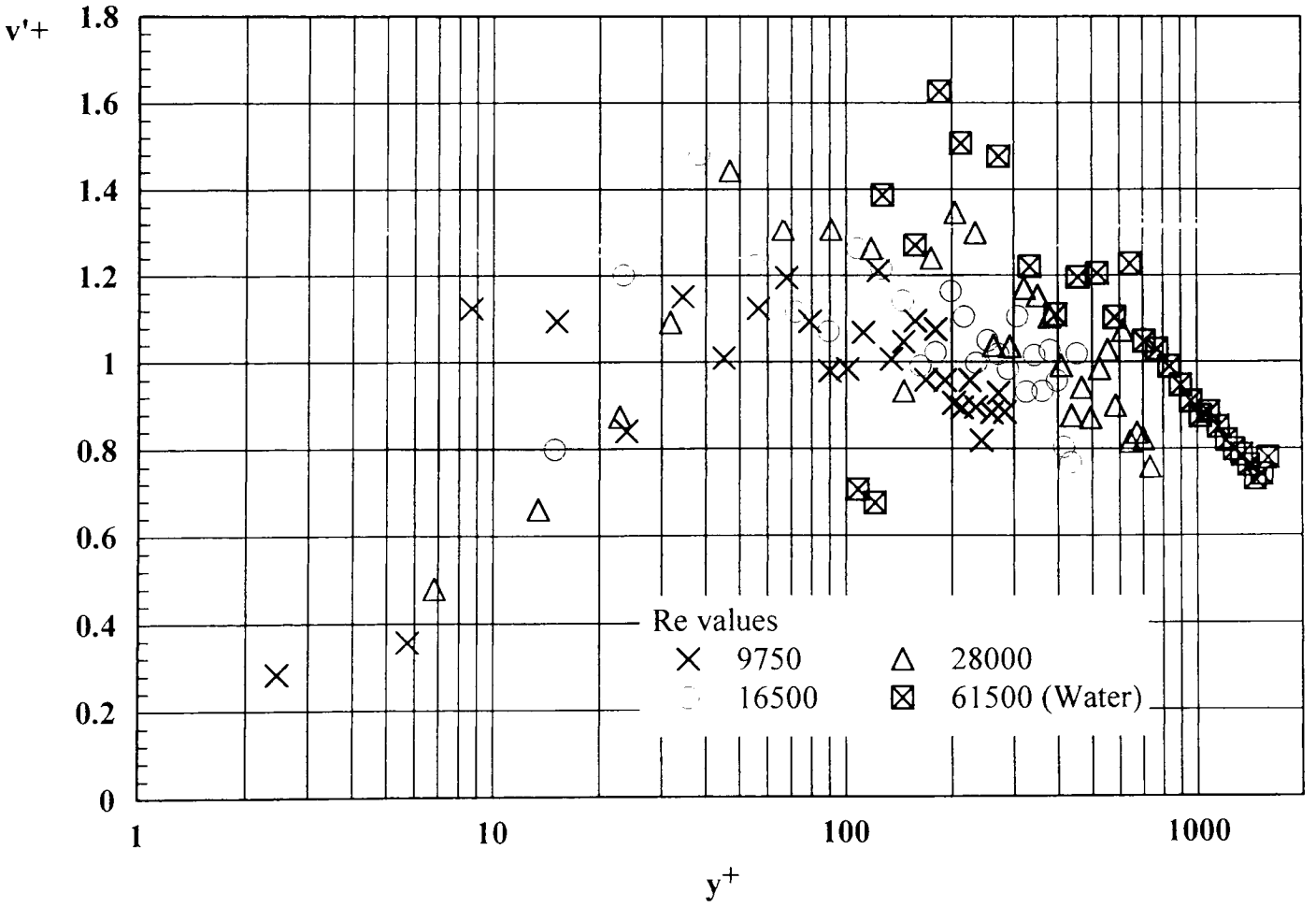

Figure 5.52(c) *Radial Turbulence Intensities in Wall Coordinates For 0.1% Carbopol EZ1.*

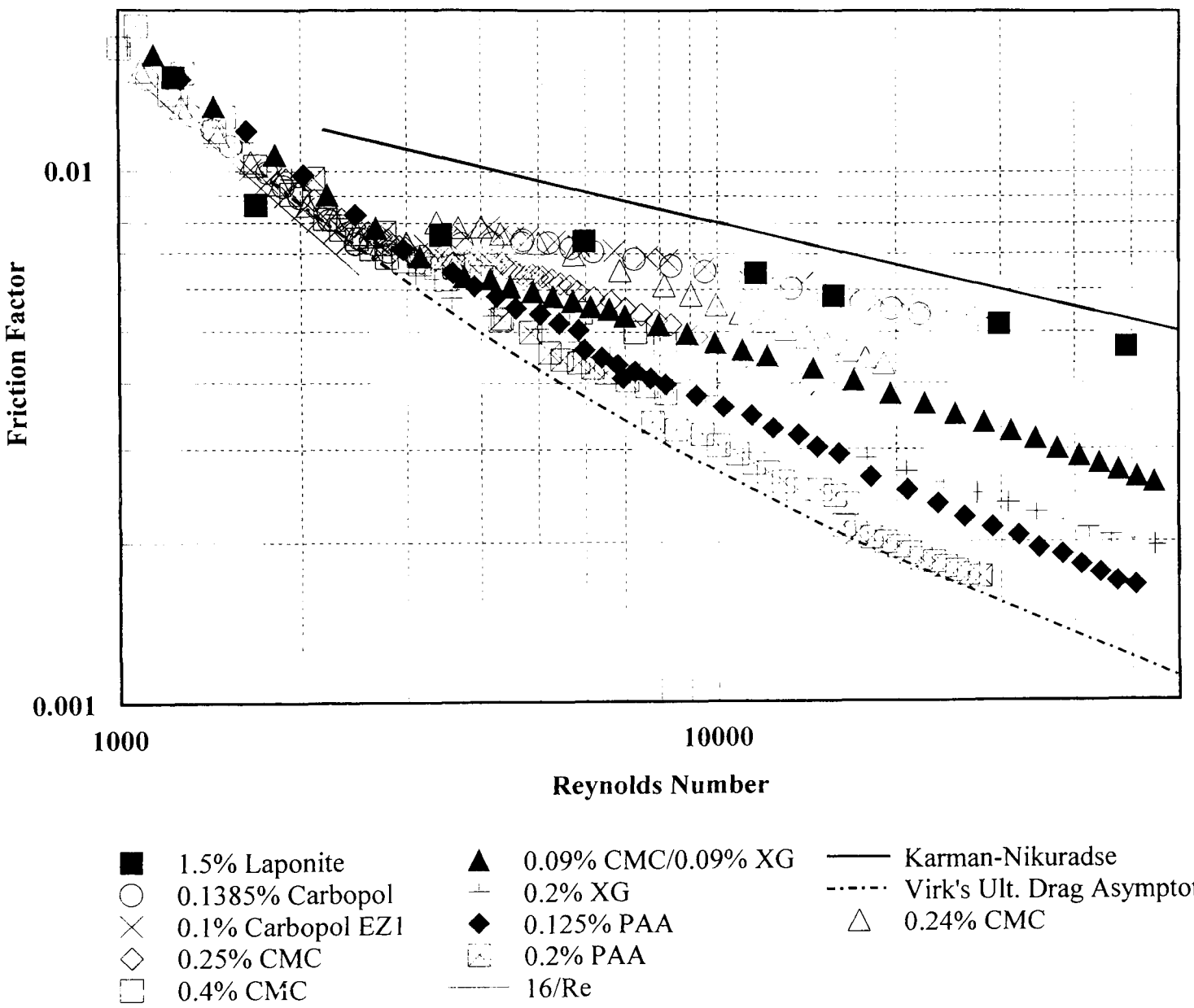

Figure 5.53 *Friction Factor versus Reynolds Number For All Test Fluids.*

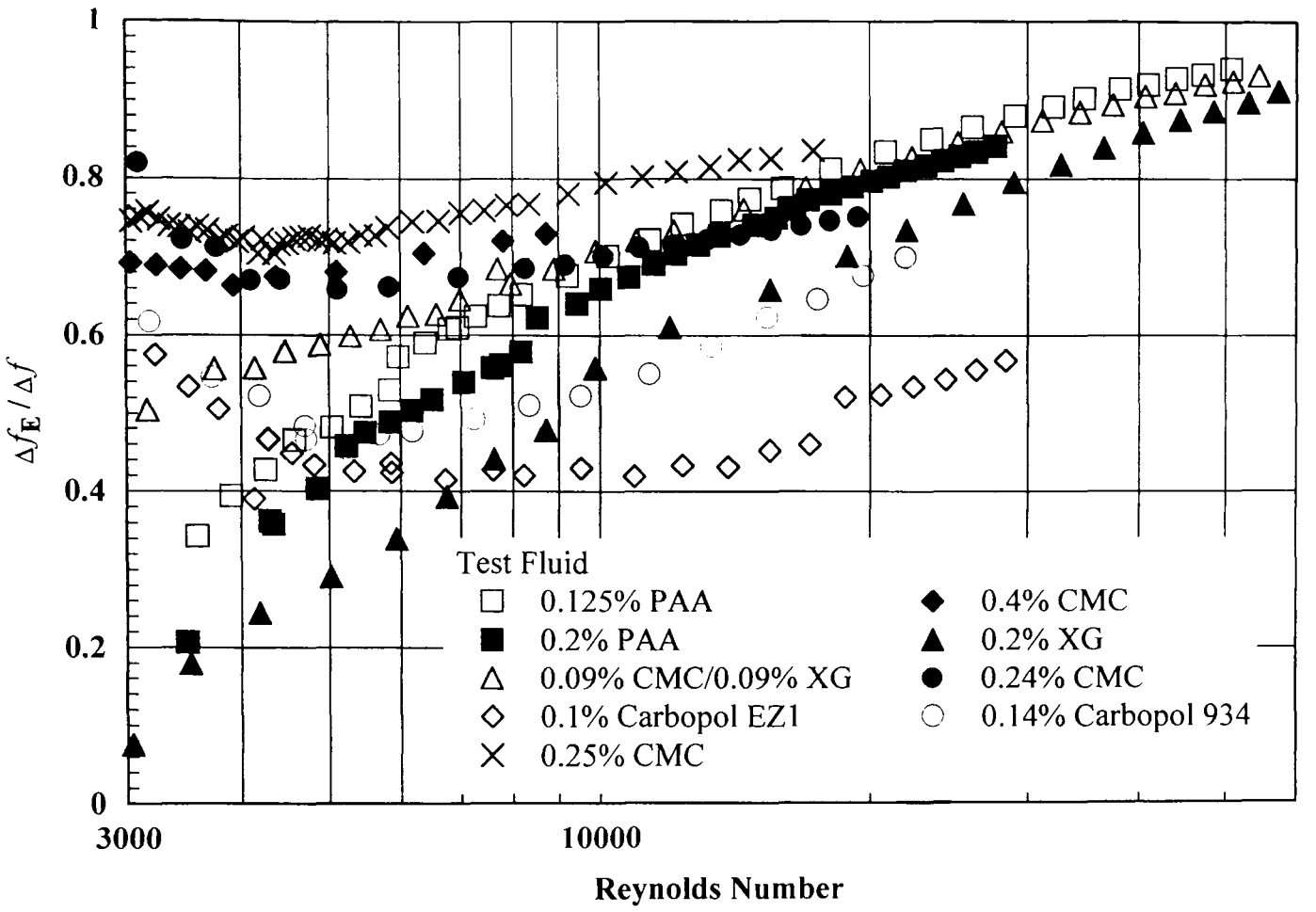

Figure 5.54 *Δf_E / Δf versus Reynolds Number For All Test Fluids.*

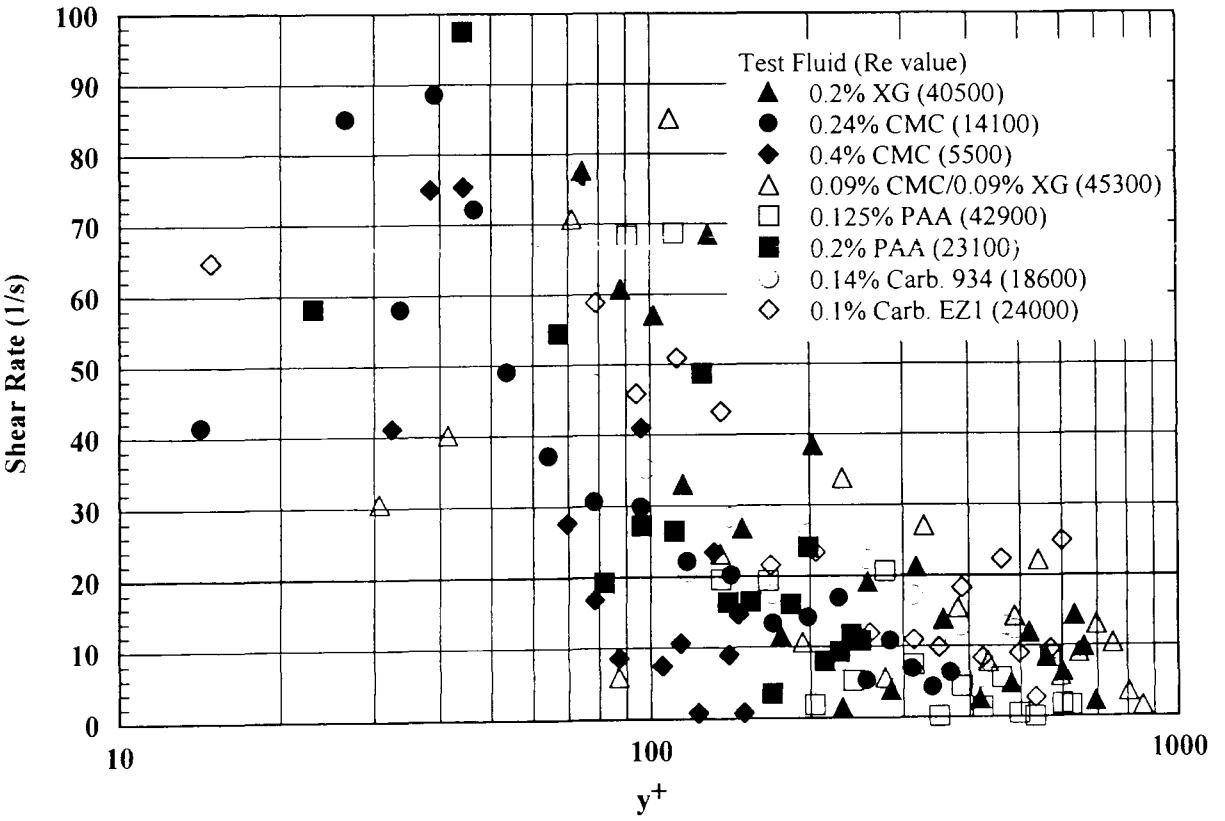

Figure 5.55 *Mean Shear Rate versus y^+ For All Test Fluids.*

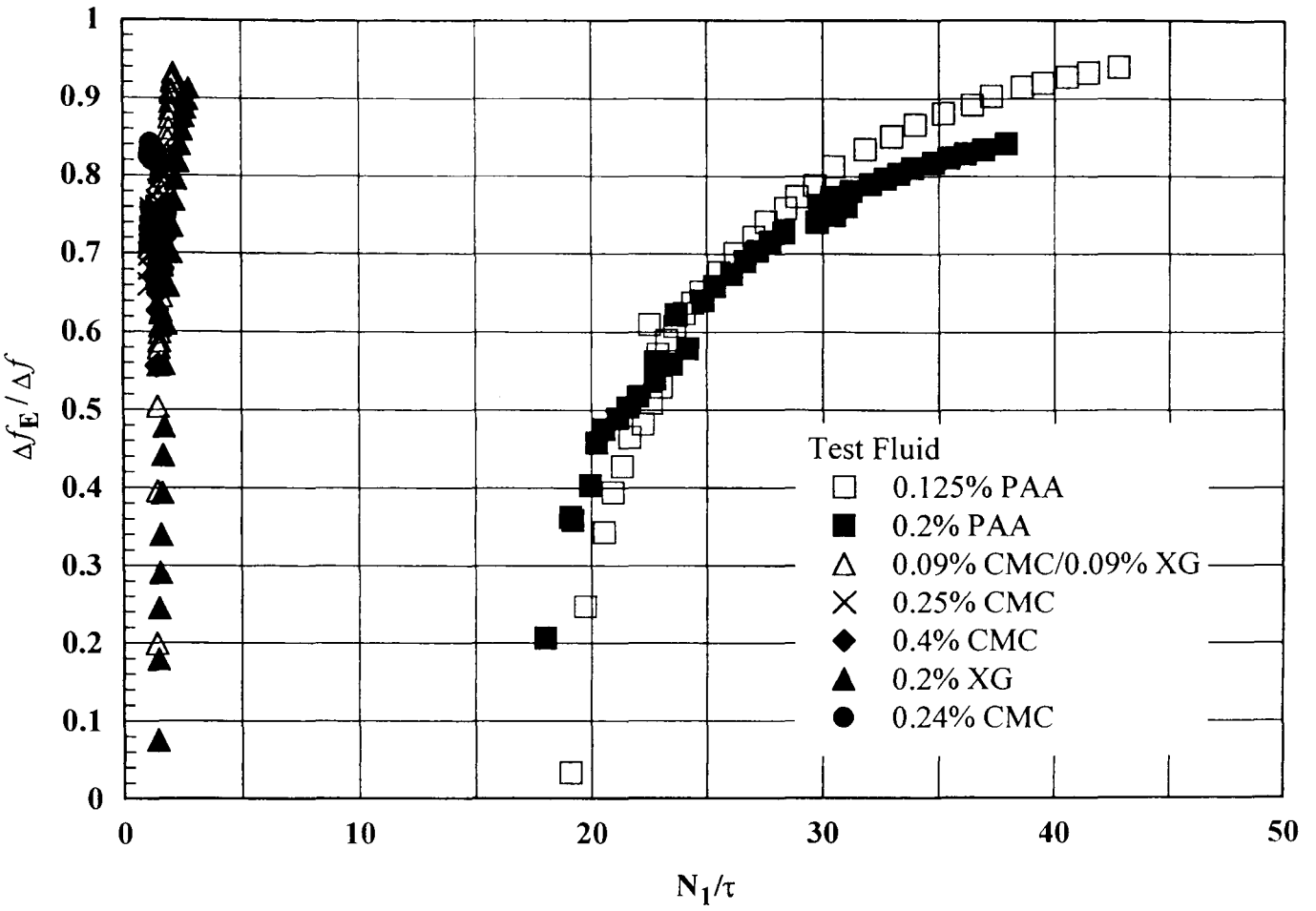

Figure 5.56 *Effect of Increasing Stress Ratio on the Elastic Part of the Total Reduction in Drag.*

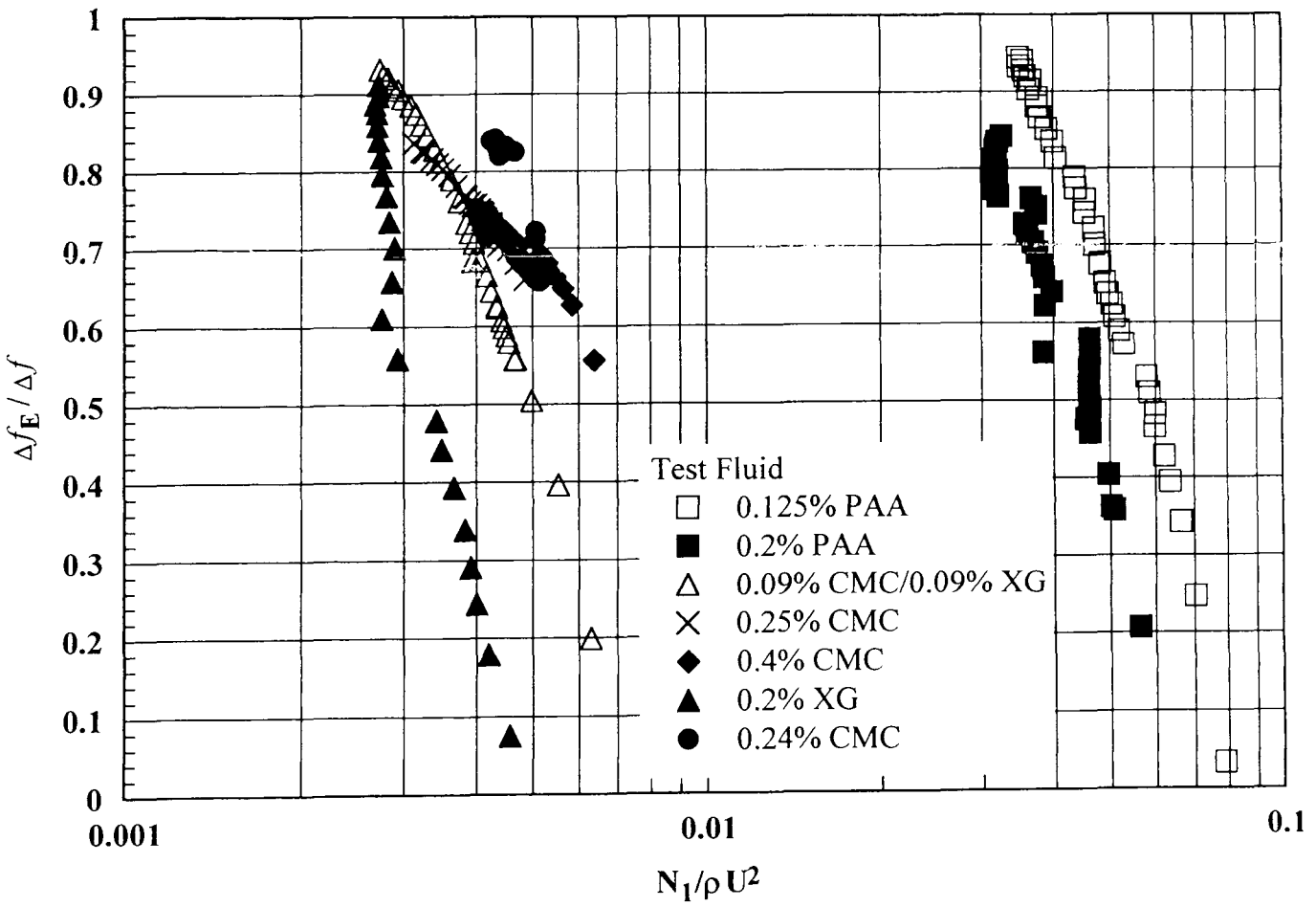

Figure 5.57 *Correlation Between Elastic Contribution to Drag Reduction and Non-Dimensional First Normal Stress Difference.*

6.0 PIPE FLOW OF A THIXOTROPIC LIQUID

This section provides a discussion on the pipe flow of a thixotropic fluid - Laponite RD - under laminar, transitional and turbulent flow conditions. Distributions of mean axial velocity and turbulence intensities together with friction factor *versus* Reynolds number (f-Re) data have been collected. The respective data have been compared with the measurements carried out for the Newtonian and non-Newtonian fluids as discussed in Chapter 5.

The first section of this chapter describes the basic molecular process associated with the behaviour of thixotropic fluids and also describes some of the theoretical relationships applied to thixotropic fluids flowing in a pipe. The remaining sections discuss the pipe flow measurements, of which their analysis have been categorised into velocity distribution data, universal law of the wall representations, turbulence intensities, f-Re data and transition identification data.

6.1 Introduction

Thixotropy is the term used to classify fluids for which there is an isothermal, time-dependent breakdown of some particulate (or general) structure under relatively high shear followed by structural build-up for lower shear (see Chapter 4.5.1(f)). As Nguyen and Boger (1985) point out, the applied shear acts to disrupt structural bonds interlinking fluid elements, which may be the primary particles and/or aggregates of such particles. At the same time, shear-induced collisions of the separated structural elements tend to reform part of the broken bonds so that a state of dynamic equilibrium is attained when these two processes balance. In the absence of sufficiently high shear, thixotropic fluids may gel and so exhibit a yield stress. As already mentioned (see Chapter 4.2), drilling muds are among the fluids that exhibit thixotropy [Alderman *et al.* (1988)].

The most relevant previous experimental work on the flow of non-Newtonian liquids in pipes, as discussed in the literature survey in Chapter 2, is that of Park *et al.* (1989),

Pinho and Whitelaw (1990), and Pereira and Pinho (1994). Park *et al.* presented LDA measurements for both laminar and turbulent flow of an oil-based transparent slurry with yield-power-law (Herschel-Bulkley) viscoplastic behaviour. Under fully developed laminar-flow conditions, their measurements revealed a velocity distribution with a core (ca 60% of the pipe diameter) of uniform velocity in good agreement with the theory of Soto and Shah (1976) for a Herschel-Bulkley fluid. It is convenient to reproduce here the equation representing this velocity distribution since, as will be seen, the Laponite solutions used in the present work are also well represented by this viscometric model although, quite clearly, it does not take into account the thixotropic nature of the fluid:

$$u = \left(\frac{n}{n+1}\right)\left(\frac{\tau_S}{K}\right)^{\frac{1}{n}} R\left[(1-\xi)^{\frac{n+1}{n}} - \left(\frac{r}{R} - \xi\right)^{\frac{n+1}{n}}\right] \text{ for } r \geq r_P\,, \tag{6.1}$$

where n and K are constants in the Herschel-Bulkley model (see **Table 4.1**):

$$\tau = \tau_Y + K\dot{\gamma}^{\,n} \tag{6.2}$$

and the non-dimensional radius ξ of the 'plastic' core is given by:

$$\xi = \frac{r_P}{R} = \frac{\tau_Y}{\tau_S} \tag{6.3}$$

where r_P is the radius of the region of flow denoted by the flat section in velocity profile. Also useful are expressions for the bulk velocity:

$$U = \left(\frac{n}{n+1}\right)\left(\frac{\tau_S}{K}\right)^{\frac{1}{n}} R\,(1-\xi)^{\frac{n+1}{n}}\left[1 - \frac{2n}{3n+1}(1-\xi) - \frac{2n^2\xi\,(1-\xi)}{(3n+1)\,(2n+1)}\right], \tag{6.4}$$

for the plug velocity:

$$\frac{u_P}{U} = \left[1 - \frac{2n}{3n+1}(1-\xi) - \frac{2n^2\xi(1-\xi)}{(3n+1)(2n+1)}\right]^{-1}, \quad \textbf{(6.5)}$$

and the friction factor - Reynolds number relationship:

$$\frac{4}{Re.f} = \left(\frac{n}{n+1}\right)(1-\xi)\left[1 - \frac{2n}{3n+1}(1-\xi) - \frac{2n^2\xi(1-\xi)}{(3n+1)(2n+1)}\right], \quad \textbf{(6.6)}$$

wherein the Reynolds number Re is defined as $2\rho UR/\mu_S$, μ_S being the viscosity corresponding to the surface shear stress (τ_S).

For turbulent flow, Park *et al.* (1989) found that the mean velocity distribution was almost indistinguishable from that for a Newtonian fluid although differences in the turbulence structure were apparent, particularly a reduction in the tangential intensity away from the immediate vicinity of the pipe wall and an increase in axial intensity near the wall. Unfortunately the data are presented in such a way that it is not possible to detect whether the slurry was drag reducing as is typical of other, primarily polymeric, shear-thinning liquids.

As previously explained in Chapter 4.5.1(f), the rheological behaviour of Laponite was anomalous to other fluids. An example of an anomaly associated with Laponite was a gradual increase in viscosity with time in contrast to a decrease in viscosity observed in all other polymer solutions, which for the latter case, were related to degradation effects. Structural equilibrium of the test-fluid within the test-section was never achieved, with the wall shear stress (τ_S) obtained from the pressure drop measurements, yielding an effective viscosity (η_S) based on near wall velocity measurements much lower than the apparent viscosity measured on the rheometer.

The following sections (Sections 6.2-6.6) detail the pipe flow measurements for Laponite under laminar, transitional and turbulent flow conditions.

6.2 Velocity Distribution Data

The measured mean velocity profiles (**Figure 6.1**) show a clear progression with increasing Reynolds number from laminar flow (a - d) through transition (e) into turbulent flow (f, g). At the two lowest Reynolds numbers the profiles are symmetrical with a well defined "plastic" plug, and are well represented by the theoretical profile for fully developed laminar flow of a Herschel-Bulkley fluid (see **Eq. (6.1)**), much the same as reported by Park *et al.* (1989) for their slurry flow. It must be recognised that the yield stress τ_Y is no more than a fitting parameter strongly influenced by the resolution of each of the rheometers at very low shear rates and also that some readers will prefer the term apparent yield stress. The theoretical profiles were fitted by determining values of ξ ($\equiv \tau_Y/\tau_S$) from u_P/U with n = 0.535. The rheological and flow parameters corresponding to the velocity profiles of **Figure 6.1** are listed in **Table 6.1**. It is evident from **Table 6.1** that τ_Y is increasing with Reynolds number. The increase in τ_Y is a result of an increase in fluid viscosity over a period of days during successive flow experiments as previously discussed in Chapter 4.5.1(f) and remains, in this case, solely a curve fitting parameter. For the asymmetric profiles (c, d), two Reynolds numbers are given corresponding to the wall shear rates ($\dot{\gamma}_S$, as explained below) on either "side" of the pipe. Although the value for the index n (= 0.535) corresponds to the equilibrium viscometric data of **Figure 6.2** (as previously described in Chapter 4.5.1(f)), it turns out that ξ is relatively insensitive to n. It could be argued that the close agreement between the data points and the theoretical velocity profile is somewhat misleading, since in normalised form (i.e. u/U *versus* r/R) the profile is not directly dependent upon K. Whilst it may seem quite remarkable that the measured profiles reveal nothing of the thixotropic nature of Laponite, in fact it is easily shown that the fluid residence time only approaches that required to reach equilibrium within about 10 μm of the pipe wall. As will be seen later, the clear indicator of thixotropic behaviour is that rheometric data (i.e. τ_Y and η_S) consistent with the velocity profiles are considerably different from the equilibrium values.

An entirely unexpected, but repeatable, feature of the velocity profiles for Reynolds numbers in the approximate range 1,300 - 3,000 (b - d) is a progressively increasing

degree of asymmetry, which would be consistent with a significant azimuthal variation of wall shear stress for a fluid of constant viscosity. In the same pipe-flow facility, the asymmetry was also observed for 0.2% XG, 0.2% PAA and 0.1% Carbopol EZ1. The asymmetry disappears once transitional or turbulent-flow conditions are established (profiles e - g), which suggests that an explanation for the asymmetry may be associated with the stability characteristics of the flow of a yield-stress fluid, of which the plastic plug is a consequence. It may be that the plug itself is initially deflected away from the centreline due, perhaps, to minor geometrical imperfections in the flow loop. A link with the flow geometry would be consistent with the asymmetry always being in the same orientation although it would seem unlikely that any significant upstream asymmetry would produce the symmetric profiles seen at lower Reynolds numbers. It is also the case that no change was observed when the downstream bend orientation was reversed. However, as previously explained from the observations made for 0.2% XG, 0.2% PAA and 0.1% Carbopol EZ1 in Chapter 5.3, the asymmetry was not constrained to one side of the pipe section. The skewed velocity profiles, also found for Reynolds numbers approaching those associated with transitional flow conditions, varied from fluid to fluid. Hence, it was suggested that the asymmetry is associated with transitional effects - a phenomena that has not been reported previously in literature.

Profile e corresponds to a Reynolds number of 3,400 and, when compared with both the laminar-flow data and also the profiles for fully turbulent conditions (f, g), it is evident that for this profile the flow state is transitional. There is no evidence of a gelled plug and the mean flow is practically symmetrical, albeit with a high degree of scatter associated with the intense velocity fluctuations which are typical of transition. The two profiles (f, g), for the highest Reynolds numbers, 13,400 and 25,300, are in close agreement with the curve which represents water flow at a Reynolds number of 61,000. The lower velocities for Laponite in the near-wall region are consistent with the degree of drag reduction, which was also noticed in the velocity profiles for the non-Newtonian fluids discussed in the previous chapter.

The Reynolds numbers here have been defined as $Re \equiv 2\rho UR/\mu_S$ with the viscosity μ_S evaluated from the shear stress τ_S and the shear rate ($\dot{\gamma}_S$ i.e. $\mu_S = \tau_S/\dot{\gamma}_S$), the subscript S

denoting conditions at the pipe surface. For the downstream half of the pipe run, within which all detailed measurements were made, the axial pressure gradient dp/dx was found to be constant within the limits of the transducer accuracy so that (-R.dp/dx)/2 should be an accurate estimate of τ_S. A constant axial pressure gradient is often taken to indicate that the hydrodynamic development of a flow is complete. However, a comparison of τ_S ($\dot{\gamma}_S$) with the data of **Figure 6.2** obtained from the two rheometers will show that (see below) in the case of Laponite the fluid rheology, and hence the flow itself, was in fact far from structural equilibrium. The high spatial resolution of the LDA system used for the present work permitted measurements very close to the pipe wall (well into the viscous sublayer for turbulent flow), which were then used to determine both the "true" origin (y = 0) for the velocity profile and also a value for the strain rate at the surface $\dot{\gamma}_S$. The foregoing procedure is clearly deficient for the asymmetric velocity profiles just prior to transition but has to suffice for obvious reasons.

It is instructive at this point to return to the data represented by the symbols in **Figure 6.2**, which correspond to values for $\dot{\gamma}_S$ deduced from near-wall velocity measurements (●, ■, ○). **Figure 6.3** shows all the **Figure 6.2** data re-plotted in the form of apparent viscosity (i.e. $\tau/\dot{\gamma}$) *versus* shear rate. At all flow rates it is apparent that the effective viscosity at the pipe wall corresponded to equilibrium values for τ and about twice the wall values, as is clear from the lines (——) of constant viscosity, e.g. that linking points A and B. Even close to the pipe wall, the fluid residence time is insufficient for the structure to build up to a viscosity consistent with the prevailing τ_S. For the particular case represented by point B, the equilibrium value for $\dot{\gamma}_S$ would be about 80% below the actual value if τ_S remained unchanged. In reality, if the structure were allowed to develop (e.g. in a much longer pipe) τ_S would also increase and an equilibrium state between A and C would ultimately be reached.

Another unexpected result is revealed from **Table 6.1** - the yield stress consistent with the laminar velocity profiles is not constant, as would be expected if it were a property

of the fluid in its gelled state, and is substantially lower than the value of 4.4 Pa obtained from the equilibrium viscometric data.

6.3 Universal Law of the Wall

The values obtained for μ_S permit the turbulent flow velocity profiles to be represented (**Figure 6.4**) in wall variables $U^+ \equiv u/u_\tau$ and $y^+ \equiv \rho u_\tau y/\eta_S$ (with the friction velocity $u_\tau \equiv \sqrt{\tau_S/\rho}$). As was evident from **Figure 6.1**, the profile for Re = 3,400 is clearly transitional, particularly as the data within the turbulent core region was not parallel with the Newtonian semi-logarithmic velocity profile [see **Eq. (5.9)** and Patel and Head (1969)]. However, the two main features evident from the mean velocity profiles for turbulent-flow conditions (Re = 13,400 and 25,300) transformed to these variables are the well-defined behaviour in the viscous sublayer and slight but definite upward shifts in the log-law region with the additive constant B increased from 5.5 to 7.1 for Re = 13,400 and to 6.5 for Re = 25,300 i.e. ΔB (see **Eq. (5.11)**) = 1.6 and 1.0 respectively. This is consistent with a low level of drag reduction associated with Laponite, as is discussed in Section 6.5, thereby suggesting that Laponite could be regarded as slightly elastic. It is, of course, the case that since the effective wall viscosity was taken as $\tau_S y/u$, it is inevitable that within the sublayer $U^+ = y^+$ provided u is proportional to y.

It is also instructive here, to make a quantitative assessment of the wall layer thickness (y_l^+) for Re = 13,400 and 25,300 as a consequence of an extended buffer region, which is associated with drag reducing flows. Based on the data illustrated in **Figure 6.4**, this was subjectively assessed as $25 < y_l^+ < 30$ for both turbulent flows, which is comparable with that associated with Newtonian fluids ($y_l^+ < 30$) [McComb (1990)]. Again, this is consistent with the low level of drag reduction displayed by the Laponite solution used in this study.

6.4 Turbulence Intensities

The distribution of normalised r.m.s. distributions (u′/U, w′/U and v′/U *versus* r/R) are shown in **Figure 6.5-6.7**. The normalised axial velocity fluctuation data shown in **Figure 6.5**, confirms that the transitional state is characterised by much higher levels than is typical for the fully turbulent flow, except in the immediate vicinity of the pipe surface, which is consistent with similar measurements for the non-Newtonian fluids discussed in the previous chapter. There is no great difference in the axial fluctuation levels for the fully turbulent flow of Laponite at Re = 25,300. However, for Re = 13,400, the peak in u′/U occurs at a larger distance away from the wall, which also displays a peak broadening effect. This is also consistent with the turbulent flow of Newtonian fluids whereas the normalised tangential w′/U (**Figure 6.6**) and radial v′/U (**Figure 6.7**) intensities for Laponite (at slightly different Reynolds numbers to the axial-flow data) fall well below the levels for water. These changes in the turbulence structure are entirely consistent with previous observations [see e.g. Soto *et al.* (1976) and Virk *et al.* (1970)] for polymers and are generally associated with drag reduction.

Figures 6.8 - 6.10 illustrate the normalised velocity fluctuations in wall co-ordinates (u'/u_τ, w'/u_τ and v'/u_τ *versus* y^+) for Laponite. **Figure 6.8** indicates that u'/u_τ increases with Reynolds number, with the peak range occurring within the extent of the buffer region ($y_1^+<30$) as previously identified in Section 6.3. The peak values of u'/u_τ and their corresponding locations are similar to that for a Newtonian fluid, which has also been shown for comparison reasons. A similar trend has been identified for the tangential velocity distribution as shown in **Figure 6.9**, though with peak values much reduced in comparison with the corresponding u'/u_τ values for similar Reynolds number. The peaks in w'/u_τ also occur at progressively larger distances from the wall than u'/u_τ as Reynolds number increases, which is consistent with the findings of Willmarth *et al.* (1987) and Tiederman (1988). For the radial velocity component (**Figure 6.10**), the peak values of v'/u_τ occur at similar distances from the wall as that for the tangential, though at slightly reduced levels by comparison respectively. These results have been summarised in **Table 6.2**, which allows direct comparisons to be

made with the data presented in the previous chapter for the other non-Newtonian fluids analysed in this study (see **Tables 5.4** and **5.5**).

6.5 Friction Factor *versus* Reynolds Number and Drag Reduction

Measurements of frictional pressure drop for flowrates covering the entire range of flow conditions are shown in **Figure 6.11** in the form of friction factor *versus* Reynolds number. Also shown on the same figure is the variation of axial turbulence intensity (u'/U) measured close to the pipe wall ($r/R = 0.8$). For each flowrate, the Reynolds number is again based upon an effective viscosity determined from the near-wall velocity variation using wall shear stress values calculated from the frictional pressure gradient. Data are shown from three series of experiments, carried out over a period of about six weeks. Values for f and Re, which correspond to the velocity profiles of **Figure 6.1**, are represented by large filled circles (●) as are data obtained from other profiles, which formed part of the same series of experiments. The laminar-flow friction factors lie between the classical $f.\mathrm{Re} = 16$ line [Schlichting (1978)] corresponding to fully developed flow of a Newtonian fluid and $f.\mathrm{Re} = 23.8$ and 26.3, which are consistent with the Herschel-Bulkley model with $n = 0.535$ and with $\xi = 0.3$ and 0.4, respectively. The turbulent flow data appear to be asymptoting towards the Blasius line ($f.\mathrm{Re} = 0.0791^{-1/4}$) with levels of drag reduction decreasing slightly with Reynolds number ($4{,}000 < \mathrm{Re} < 50{,}000$) from about 18% to 16%. This behaviour is anomalous to other non-Newtonian fluids discussed in the previous chapter where the level of drag reduction increased with Reynolds number. However, for the Carbopol solutions, a similar behaviour to that of Laponite was evident. The similarities in f-Re behaviour and corresponding drag reduction values are related to the analogous molecular formation of each fluid i.e. both are described as clay platelet suspensions in aqueous solution. This further substantiates the argument that a correlation clearly exists between drag reduction and molecular structure.

Since the Reynolds number is based upon μ_S, the true degree of drag reduction must be slightly higher than **Figure 6.11** would suggest: a generalised Reynolds number Re_N, formulated to ensure that in laminar flow $f.\mathrm{Re}_N = 16$, would inevitably be lower than Re.

The open circles (○) correspond to the data from a subsequent series of experiments for which it was found that the fluid viscosity was gradually increasing. As remarked earlier (see also Chapter 4.5.1(f)), the viscosity increase was most apparent at the low shear rates and so also corresponds to a decrease in the shear thinning index, which could explain why the degree of drag reduction is markedly higher (33% to 26%) for this set of data. The filled squares (■) correspond to an earlier data set obtained with only a few points to define the near-wall velocity profile. For low Reynolds number (laminar/transitional) flow the latter set may represent a flow which is still developing structurally (i.e. insufficient time was allowed for the fluid rheology to reach equilibrium throughout the system) whereas for turbulent flow conditions the data are entirely consistent with the data corresponding to **Figure 6.1**.

6.6 Transition Identification

As explained in Chapter 5.2, the axial-velocity fluctuation turbulence intensity u′ measured at a near-wall location provides a sensitive indicator of laminar/turbulence transition [Park *et al.* (1989)]; this is shown in **Figure 6.11** for Laponite (u′/U *versus* Re). In spite of a considerable degree of scatter in the data plotted, it is clear that transition to turbulent flow occurs in the range $1{,}500 < Re < 5{,}000$. These values of Reynolds correspond to Re_1 (onset of transition) and Re_2 (onset of turbulent flow, see Chapter 5.2), which are qualitatively assessed from the trend in u′/U data plotted in **Figure 6.11**. The generally accepted values for a Newtonian fluid are $Re_1 = 2{,}000$ and $Re_2 = 3{,}000$ (see **Figure 5.1**). Thus by comparison, this suggests that the onset of turbulent flow is indeed delayed to higher Reynolds numbers for Laponite, though the onset of transition flow occurs at a slightly lower Reynolds number respectively.

It was noted in Section 6.2 that in the region of $1{,}300 < Re < 3{,}000$, asymmetric velocity profiles were evident (profiles b-d in **Figure 6.1**). This region of flow corresponds closely to the transition region identified above ($1{,}500 < Re < 5{,}000$), thus providing substantiating evidence that transitional flow conditions for Laponite do occur at lower Reynolds numbers than that for Newtonian fluids ($Re < 2{,}000$). Also, in the region where the velocity profiles are asymmetric (profiles b-d), the u′ levels are generally

higher on the side where the velocity gradient is higher, which again suggests a link between the asymmetry and instability as mentioned in Section 6.2.

Tables And Figures

Table 6.1 *Rheological and Flow Parameters for Velocity Profiles of Figure 6.1*

Profile	U (m/s)	u_P/U	τ_S (Pa)	ξ	τ_Y (Pa)	Re	f
a	0.52	1.44	5.02	0.31	1.56	550	0.038
b	0.84	1.41	5.99	0.36	2.13	1300	0.017
c	0.90	1.37	6.30	0.40	2.53	1650-1245	0.016
d	1.06	1.39	6.39	0.38	2.40	2900-1270	0.012
e	1.09	-	4.54	-	-	3400	0.0076
f	1.60	-	7.66	-	-	13400	0.0060
g	2.03	-	10.9	-	-	25300	0.0053

Table 6.2 *Summary of Normalised Velocity Fluctuations for Laponite**

Axial			Tangential			Radial‡		
Re	**u′/U**	**r/R**	**Re**	**w′/U**	**r/R**	**Re**	**v′/U**	**r/R**
3,400	0.180	0.65	-	-	-	-	-	-
13,400	0.178	0.94	12,800	0.050	0.80	11,900	0.050	0.80
25,300	0.172	0.98	23,500	0.060	0.85	20,600	0.042	0.82
Re	**u'/u_τ**	**y^+**	**Re**	**w'/u_τ**	**y^+**	**Re**	**v'/u_τ**	**y^+**
3,400	2.9	11	-	-	-	-	-	-
13,400	3.2	11	12,800	1.05	40	11,900	1.05	38
25,300	3.1	10	23,500	1.25	50	20,600	1.00	30

* The data shown are maximum values and their corresponding location within the pipe (r/R or y^+) were determined from a subjective assessment of the trend in normalised velocity fluctuation data.

‡ Subjective assessments of the trend in data were difficult due to a large degree of scatter associated with low data rates and reduced quality of the LDA signal when taking radial measurements. The scatter in data is particularly evident when shown in wall co-ordinates (v'/u_τ *vs* y^+).

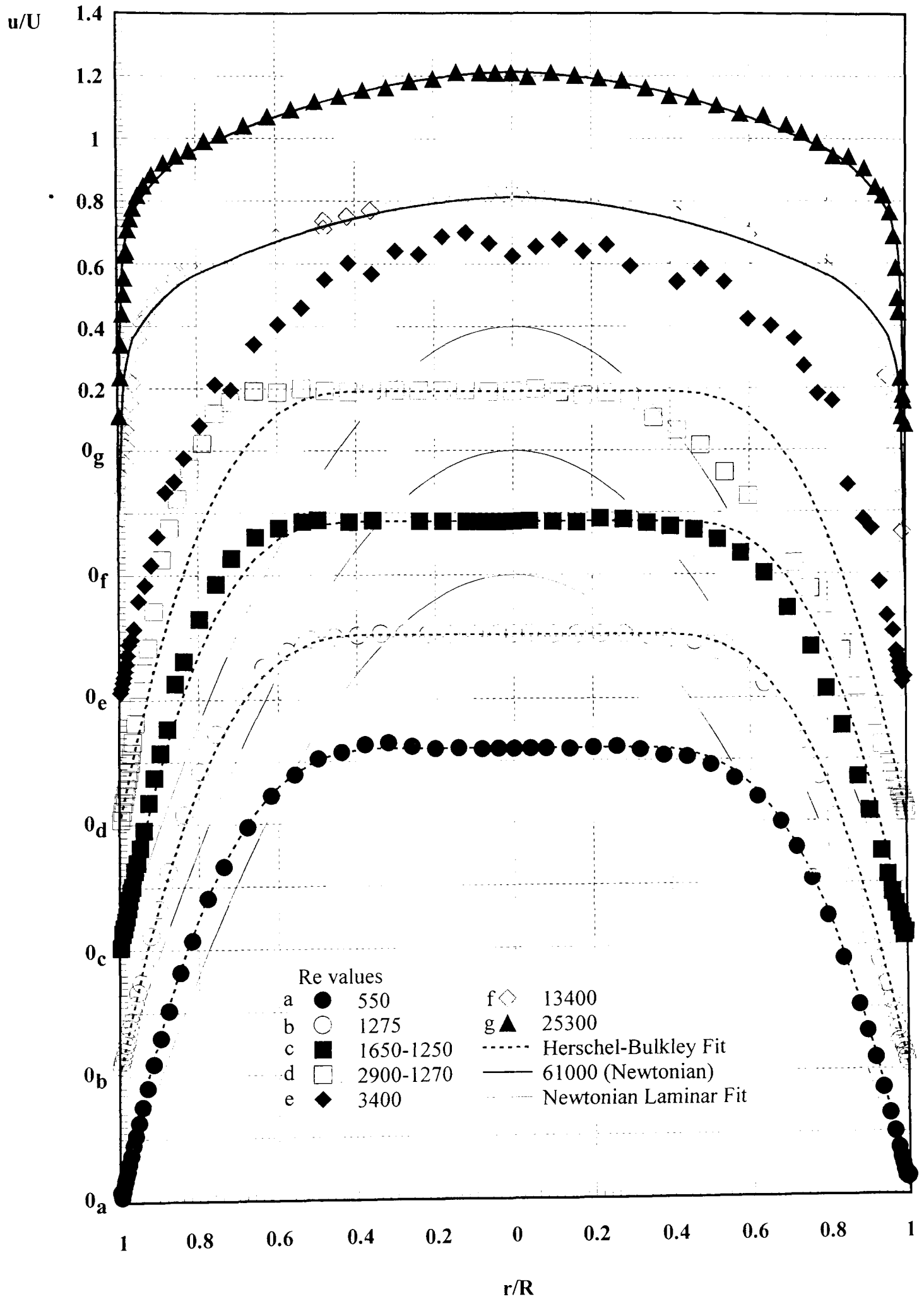

Figure 6.1 *Mean Velocity Profiles for Increasing Reynolds Number*

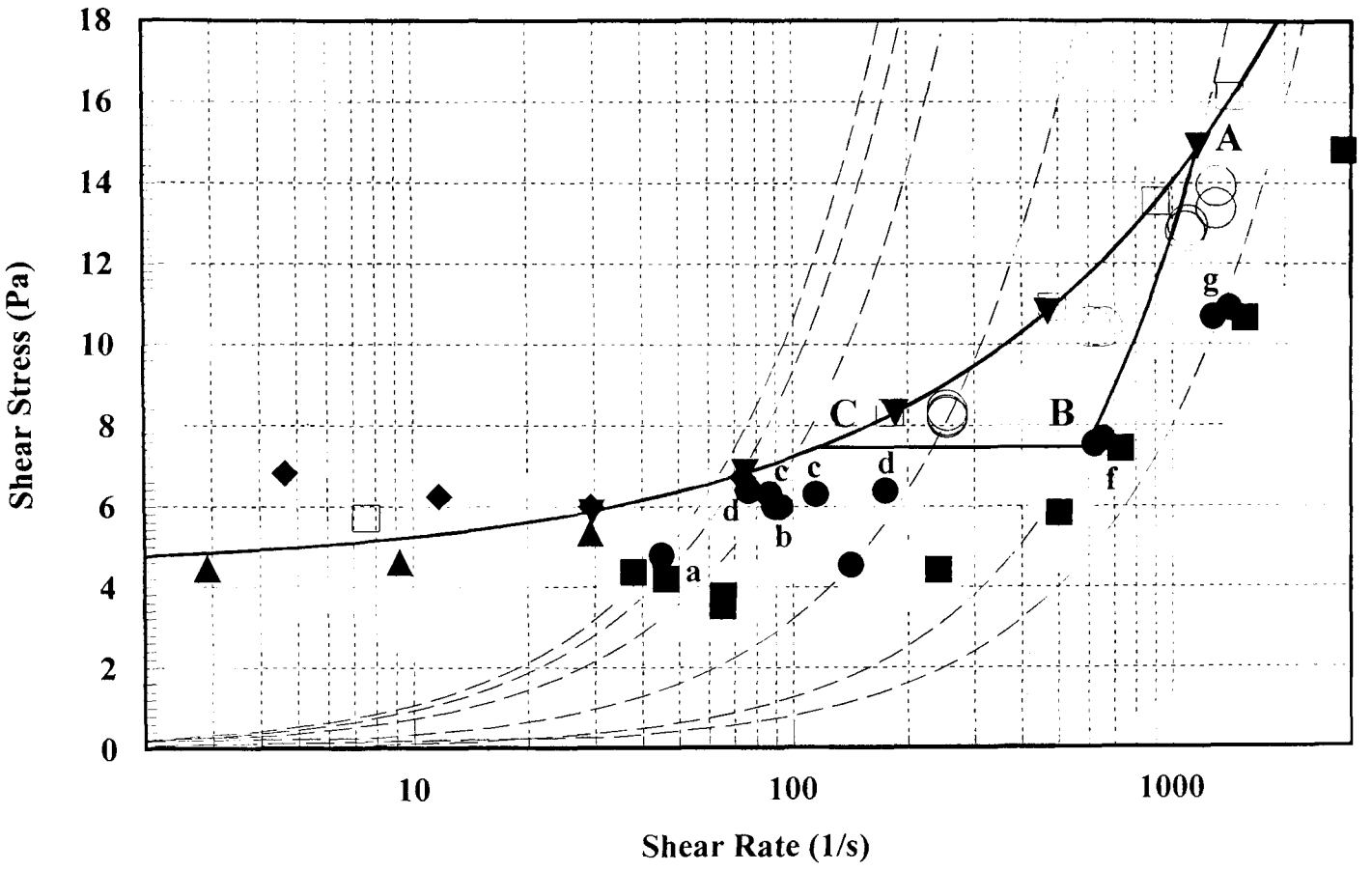

Figure 6.2 *Viscometric Data for 1.5% Laponite:* ▼, ▲, ◆, □ *rheometer data;* ■, ○, ● *velocity profile data;* ----- *lines of constant viscosity (see main text).*

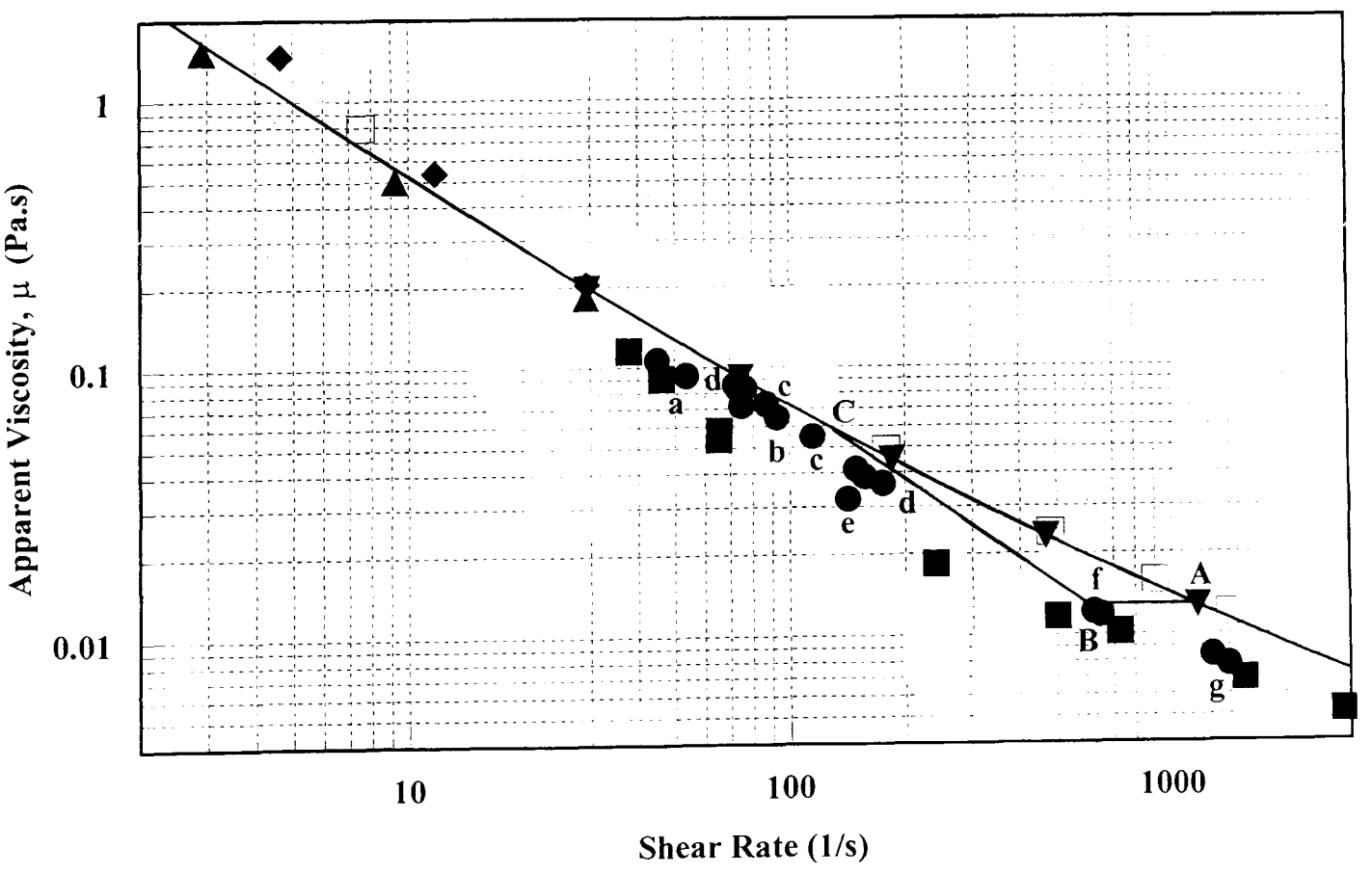

Figure 6.3 *Apparent Viscosity versus Shear Rate* (symbols as for **Figure 6.2**).

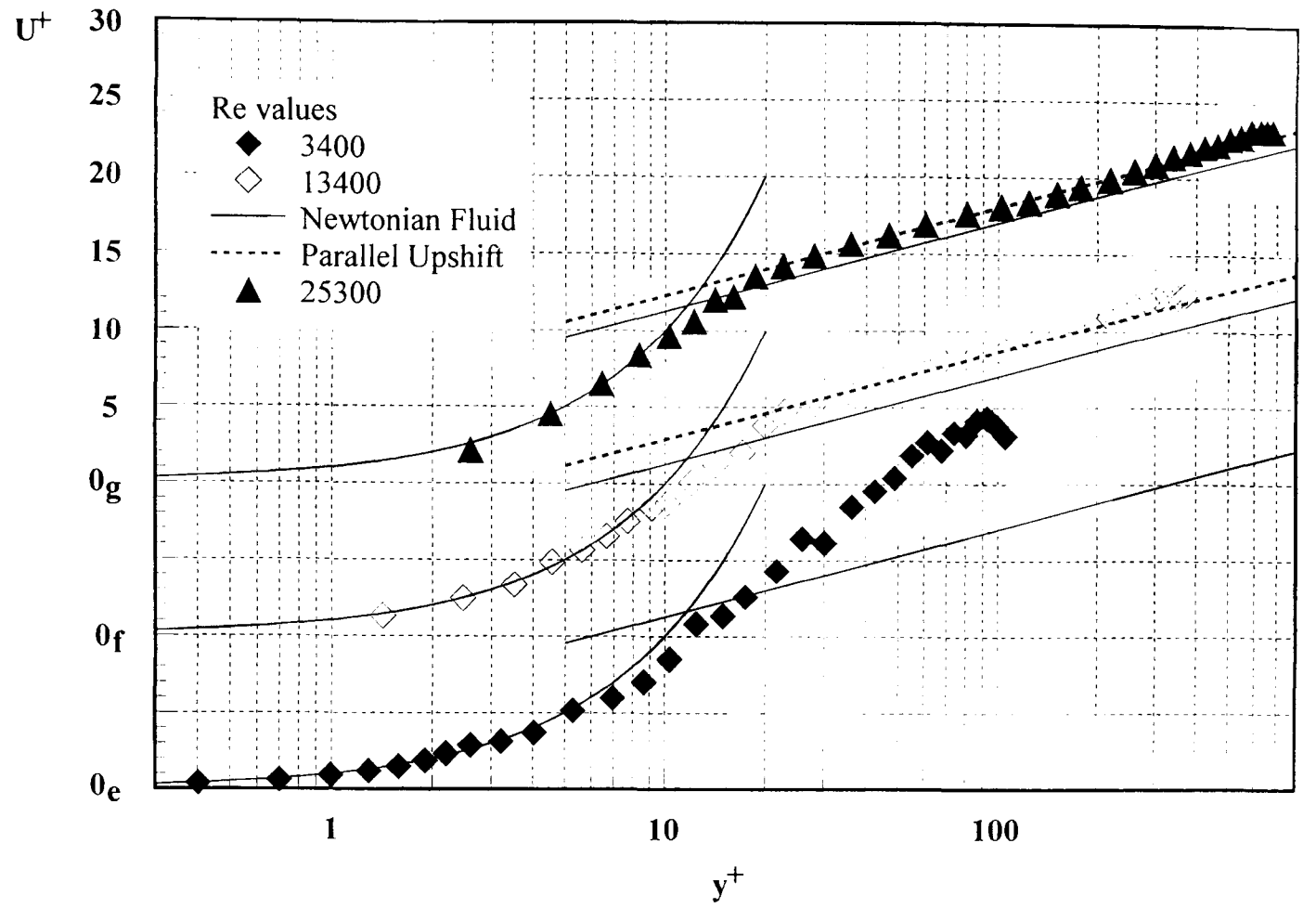

Figure 6.4 *Mean Velocity Profiles for Transitional (e) and Turbulent (f,g) Flow Conditions in Law-of-the-Wall Coordinates.*

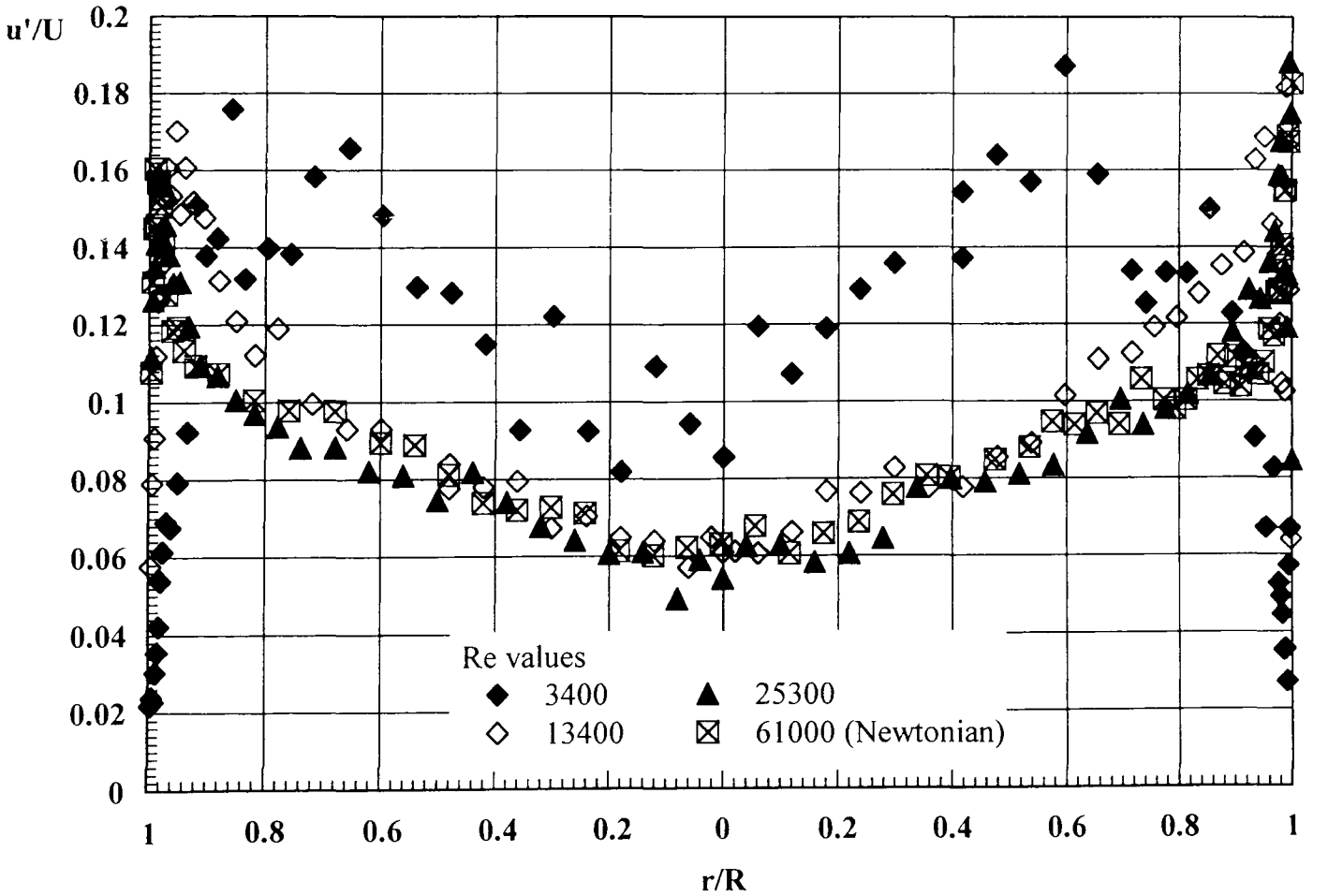

Figure 6.5 *Axial Velocity Fluctuations.*

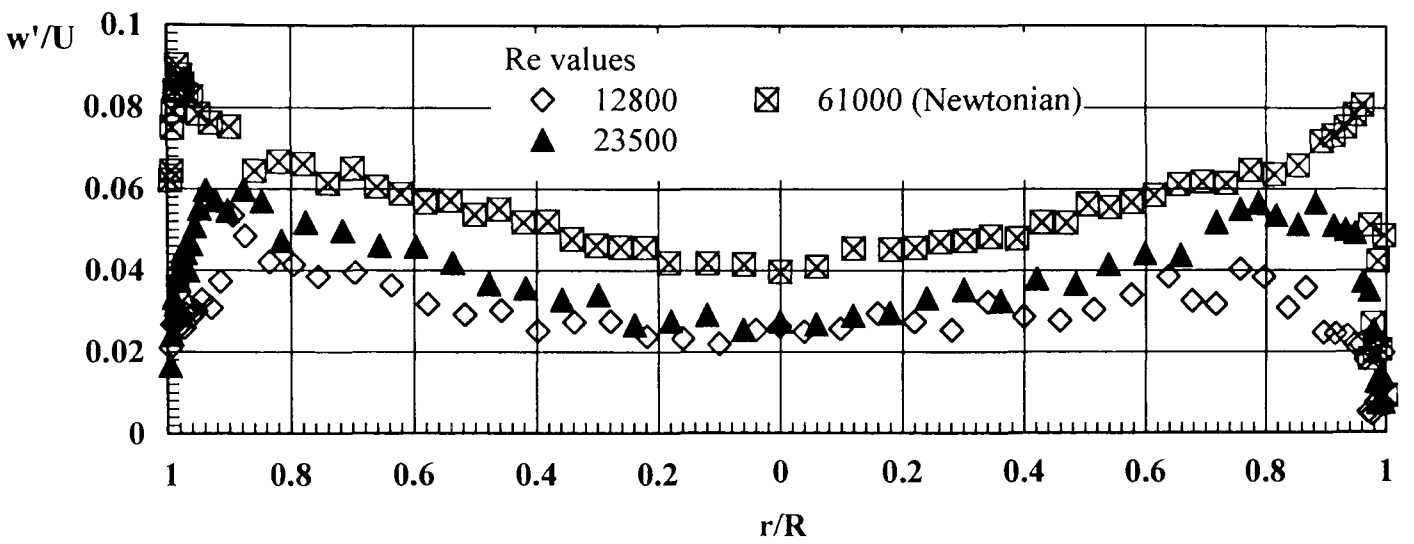

Figure 6.6 *Tangential Velocity Fluctuations.*

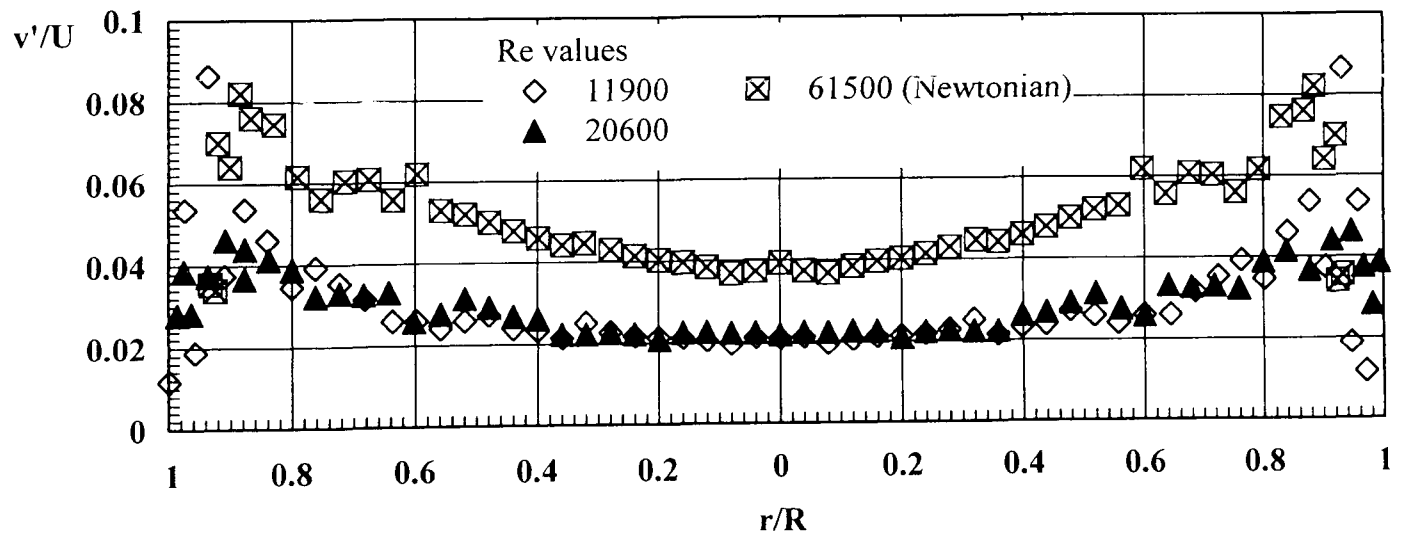

Figure 6.7 *Radial Velocity Fluctuations.*

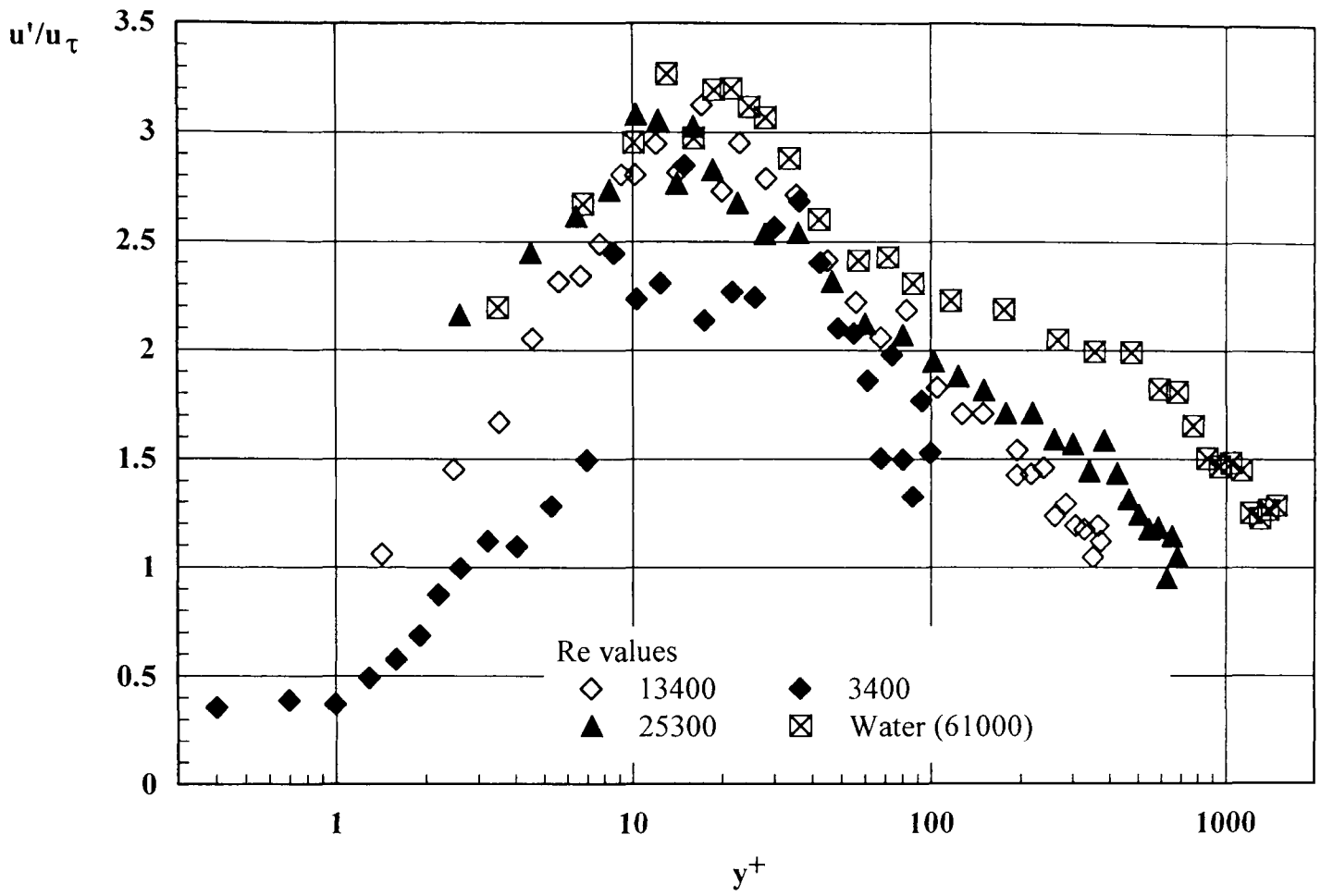

Figure 6.8 *Axial Velocity Fluctuations.*

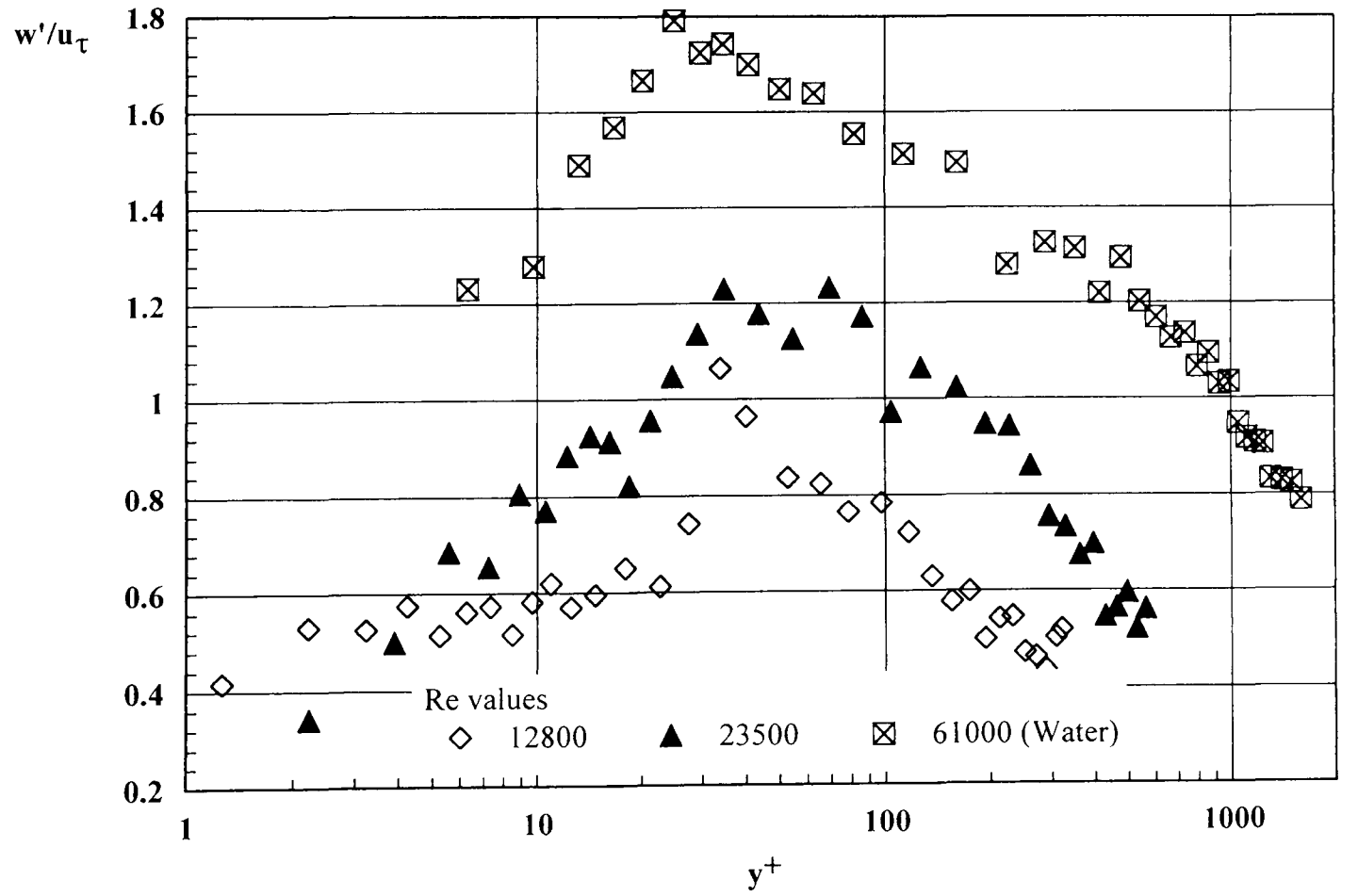

Figure 6.9 *Tangential Velocity Fluctuations.*

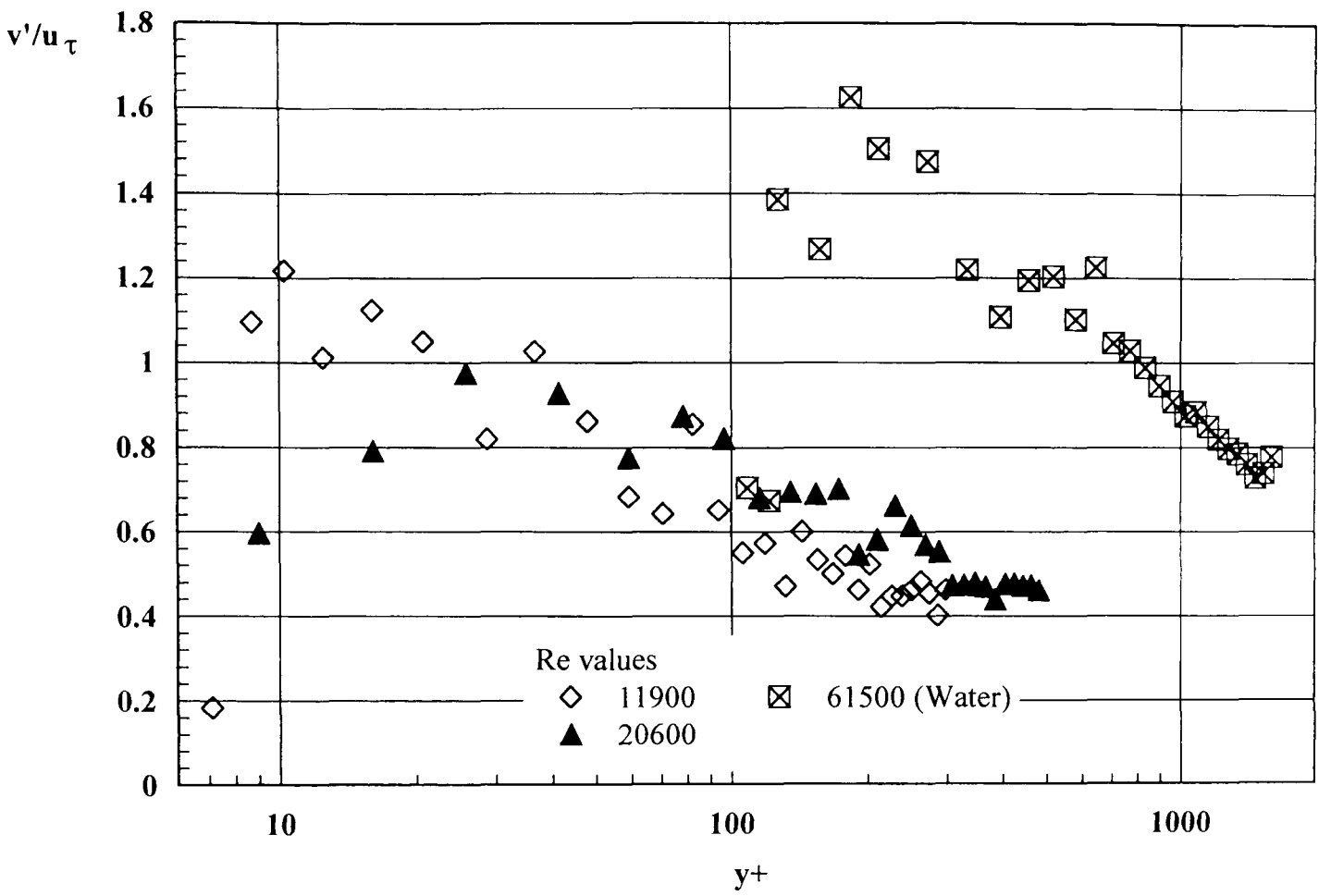

Figure 6.10 *Radial Velocity Fluctuations.*

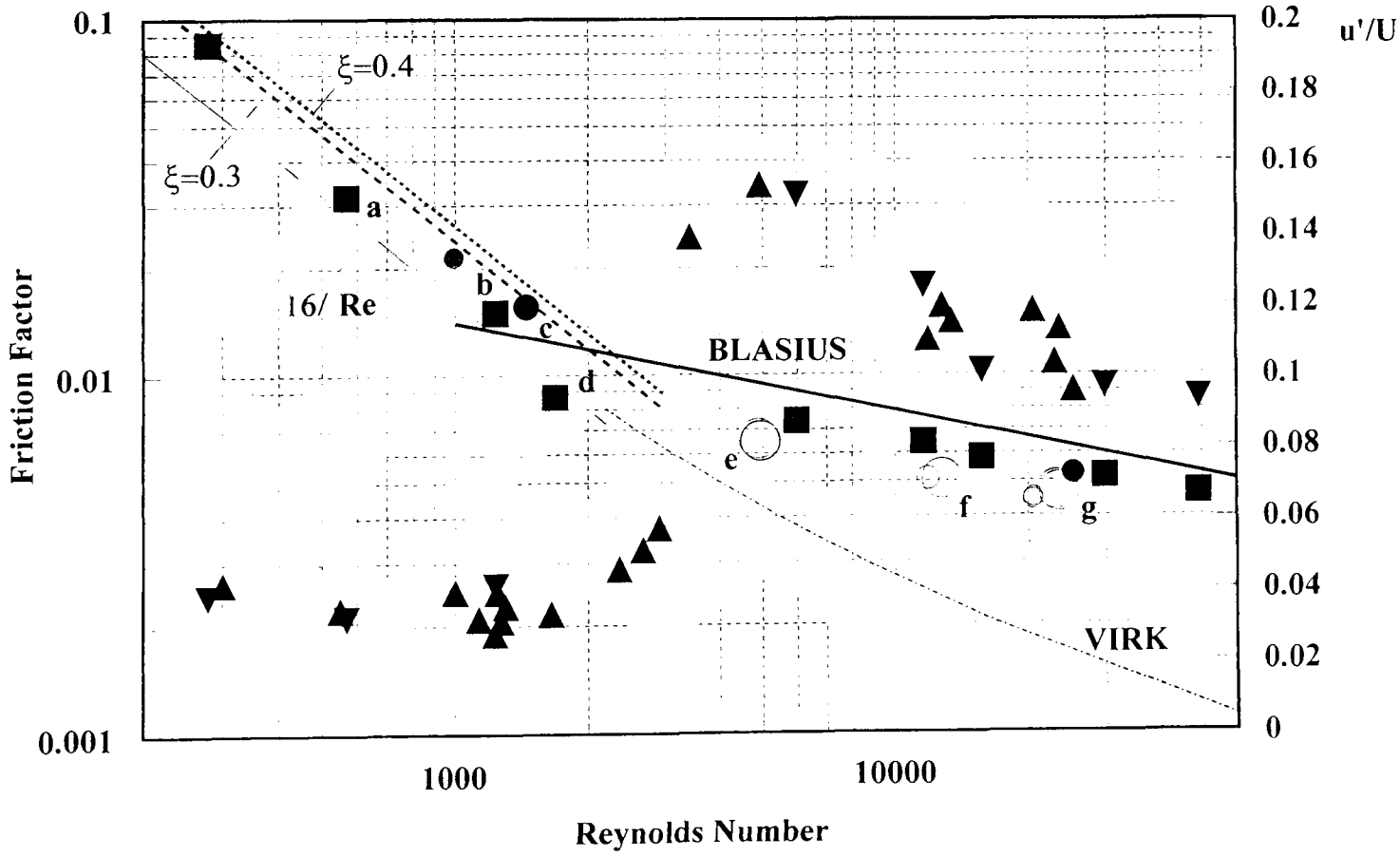

Figure 6.11 *Friction Factor (●, ■, ○) and near-wall turbulence intensity (▲, ▼) versus Reynolds Number (see main text).*

7.0 CONCLUSIONS

This section summarises the main conclusions from this extensive and detailed study, investigating the transitional and turbulent pipe flow behaviour of non-Newtonian fluids with rheological characteristics analogous to drilling fluids.

The first section provides a brief overview of the rheological assessments carried out for all working test fluids presented in Chapter 4. Section 7.2 concludes with the main findings from this study, based primarily on the pipe flow measurements discussed in Chapters 5 and 6. The possible correlation of a flow and rheological parameter is also discussed in Section 7.2. Finally, Section 7.3 provides suggestions for further work in areas deemed supportive to this study.

7.1 Rheology of Test Fluids

With the exception of Laponite, all non-Newtonian fluids displayed time-independent shear-thinning characteristics of various magnitudes, which were well represented by the Cross model. The thixotropic character of Laponite was apparent from values for the wall shear rate determined from velocity profile measurements, which, under all flow conditions, led to effective viscosity values considerably lower than would be consistent with the wall shear stress for a fluid in structural equilibrium. A second indicator of thixotropy is the apparent yield stress: the value consistent with the velocity profiles is much lower than that determined using a rheometer.

The test fluids selected for this study were reasonably resistant to degradation effects, showing negligible changes in viscometric behaviour before and after each flow test. However, the test fluids did degrade over a period of time ($< 43\%$ reduction in low shear rate viscosity over a 7 day period after approximately 30 hours of shearing). A consistent correlation was established between the level of degradation and the extent of drag reduction i.e. the greater the drag-reducing effectiveness of the fluids, the better resistance to degradation, for which no qualitative explanation could be found. An anomalous behaviour was found for the polymer-polymer blend of XG and CMC, where

the level of degradation was greater when compared with identical solutions containing only a single polymer additive.

Despite similarities arising when comparing fluids of similar viscometric flow curves, for example that of 0.09% CMC/0.09% XG and 0.125% PAA, the elastic components (first normal stress difference and storage modulus) can be markedly different resulting in different levels of drag-reducing effectiveness. These differences suggest that the elastic components of a fluid are more sensitive to variations in molecular structure than are the viscous components.

For XG, CMC and XG/CMC blend, there was a high dependence of the first normal stress difference (N_1) on shear stress, where the corresponding measurement data collapsed onto a single line irrespective of fluid concentration. However, for PAA, N_1 showed a greater dependence on concentration. For XG, CMC, XG/CMC and PAA, N_1 increased with shear rate. It was found that ranking fluids according to their elasticity provided some insight about drag-reducing effectiveness, as will be discussed in Section 7.2. Hence, when N_1 is shown as a function of shear stress, the following ranking was achieved: CMC, XG/CMC, XG and PAA, which is consistent with their corresponding levels of drag-reducing effectiveness. Using power-law master curves, which linked N_1 with τ, the normal-stress data was then translated to N_1 ($\dot{\gamma}$) using the viscometric flow curves. The results showed the same ranking as the normal-stress data for $\gamma < 20s^{-1}$ and subsequently also with the level of drag-reducing effectiveness.

The elastic ranking of fluids deduced from the oscillatory flow data was also consistent with the normal-stress ranking discussed above. Measurements from the oscillatory flow tests were, however, carried out under flow conditions that were not representative of transitional and turbulent flow and also lacked a general correlation with a pipe flow parameter. Nevertheless, from a ranking perspective, the data showed consistency between the various flow measurement techniques.

From the extensive rheological assessments carried out in this study, a possible correlation with the pipe flow behaviour was analysed as will be discussed in the following section.

7.2 Pipe Flow Measurements

The intensity of the axial velocity fluctuation measured at a fixed radial location (0.8 times the pipe radius) was a consistent indicator of transition. This is particularly valuable where there is such a high degree of drag reduction that there is little or no indication from the *f*-Re curve that transition has occurred. The delay in 'turbulent' flow follows a pattern similar to that of the increase in drag reduction. Interestingly, however, the onset of 'transitional' flow did occur at Reynolds number lower than that for a Newtonian fluid for 0.2% XG (Re = 1,600), 0.2% PAA (Re = 1,500), 0.14% Carbopol 934 (Re = 1,000), 0.1% Carbopol EZ1 (Re = 1,000) and 1.5% Laponite (Re = 1,500). The early transition for these fluids also manifested itself with asymmetric velocity profiles for Reynolds numbers approaching transitional flow conditions. Asymmetric velocity distributions were not evident for laminar flows with low Reynolds number and nor in flow regions extending into turbulent flow conditions. Such behaviour has not been reported previously in literature and is speculated to be related to the instability of such flows approaching transition.

Measurements of the mean velocity profiles in turbulent flow indicated progressively flatter profiles towards the centre of the pipe as the Reynolds number was increased with a resultant increase in velocity gradient near the pipe wall. The degree of flattening of the velocity profile and the velocity gradient near the wall were larger than that for the Newtonian fluid. However, for the Carbopol and Laponite solutions, the turbulent mean axial velocity distributions (u/U *versus* r/R) were very similar to that for the Newtonian fluid.

Under laminar flow conditions, the velocity profiles for all non-Newtonian fluids (with the exception of Laponite) were well represented by a power-law fit, with an increased plug-like nature for fluids exhibiting larger levels of shear-thinning. For Laponite, the

velocity profiles showed a well defined plastic plug towards the centre of the pipe, until transition occurred. The plug-like nature of the velocity distributions for Laponite were well represented to a very high degree of accuracy by profiles based upon the Herschel-Bulkley model for the fluid rheology. Agreement between the profile model and the laminar flow data was established provided the model parameters were matched to the prevailing flow conditions rather than the equilibrium state.

Universal velocity distributions for all test fluids used in this study confirmed that for $y^+ < 10$ the data faithfully followed the classic $U^+ = y^+$ distribution. Such a behaviour shows consistency between established theoretical relationships used in describing Newtonian flows in pipes and the measurement data presented in this study for non-Newtonian fluids. Perhaps this consistency between the Newtonian and non-Newtonian fluid behaviour within the viscous sublayer suggests that this region does not play a major role in the drag-reduction process. For $y^+ > 10$ the profiles were in reasonable agreement with Virk's asymptote prior to a gradual approach to an upshifted log-law region. Under turbulent flow conditions, the upward shift in log-law was consistent with the level of drag reduction, though it was clear for 0.2% PAA (and to a lesser extent for other relatively high drag-reducing test fluids), that the upward shift was not parallel to the Newtonian log-law profile.

A subjective assessment of the wall layer thickness (y_l^+) based on the law-of-the-wall representations of velocity distribution, indicated that the buffer region had extended further into the pipe for all non-Newtonian test fluids ($40 < y_l^+ < 160$) compared to that for a Newtonian fluid ($y_l^+ < 30$). The exception to this was that for Laponite, which showed a similar extent of wall layer thickness compared with that of a Newtonian fluid, though the log-law did shift upwards by a small amount consistent with progressively reducing levels of drag reduction as the Reynolds number was increased. For the remaining fluids, the extension of the buffer region, upward shift of the log-law and extended peak turbulence activity (as will be discussed below) provided the most significant changes in flow structure compared to the behaviour of a Newtonian fluid.

Distributions of turbulence intensities normalised against the mean bulk velocity (U), indicated peak values lower than those for a Newtonian fluid, with peaks also occurring over larger distances and further away from the wall. The peak axial turbulence intensity (u′/U) reduced progressively as the Reynolds number increased and peaked at distances closer to the wall for all fluids respectively. Corresponding lower peak values were also consistent with the drag-reducing effectiveness for each fluid. However, in the tangential and radial case, the normalised turbulence intensity distributions (w′/U and v′/U) were significantly reduced in comparison with u′/U and the corresponding levels for a Newtonian fluid. The radial normalised turbulence distributions fell below that for the respective tangential distributions. Based on a subjective assessment of the peak values for the tangential and radial turbulence intensities and their corresponding peak location using w′/U and v′/U *versus* r/R plots, there did not appear to be any significant dependence on Reynolds number. However, when the turbulence intensity distributions were plotted using wall coordinates (i.e. u'/u_τ, w'/u_τ and v'/u_τ *versus* y^+), the data indicated a dependence on Reynolds number. In this case, the peak in axial turbulence intensity, when normalised using the friction velocity, increases with drag-reducing effectiveness. Consequently, for 0.2% XG, 0.09% XG/0.09% CMC, 0.125% PAA and 0.2% PAA, values for u'/u_τ were greater in comparison with the corresponding Newtonian values, which is in contrast to the data normalised using the mean bulk velocity. The difference in peak values is partly a consequence of the drag-reducing effect resulting in a lower friction velocity, hence it is difficult to assert that the turbulence has been suppressed by the additive using these wall variables. These differences must be borne in mind when comparing data from previous experimental studies, which have often been conflicting by comparison. The tangential and radial turbulence intensities normalised with the friction velocity showed much lower values than the corresponding axial measurements and tended to increase with Reynolds number and at distances further away from the pipe wall. From the turbulence data normalised using u_τ, all the corresponding peak values occurred within the extended buffer region, with peak broadening effects consistent with the extent of wall-layer thickness.

From the observations made using law-of-the-wall coordinates, it seems that the mechanism for drag reduction is associated with the region of flow within and beyond the extended buffer region.

Reconsidering the ranking deduced from the rheological assessments of the normal-stress data, it was shown that the drag reduction behaviour was consistent for the most part with the first normal stress difference at low (ca $20s^{-1}$) shear rates. The same degree of consistency was lacking at higher shear rates. Since the shear rates in the viscous sublayer are between one and two orders of magnitude higher than the values for which there is a correspondence between the drag reduction and rheological behaviour, it maybe concluded that the drag reduction is indeed associated with the process occurring well beyond the viscous sublayer, in the buffer region and inner log-law region.

Although all test fluids produced increasing levels of drag reduction in turbulent flow with increased viscoelasticity, no qualitative correlation could be established between the level of drag reduction and a fluid/flow parameter. The trend for individual fluids was for a decrease in the elastic contribution (Δf_E) to the overall drag reduction with increasing $N_1/\rho U^2$. However, the representation of $\Delta f_E/\Delta f$ *versus* Reynolds number showed that the elastic effects increased with Reynolds number. In the absence of a general correlation, it was regarded as support for the hypothesis that drag reduction may be associated with the extensional viscosity (η_E), a fluid parameter that was outside the scope of the instrumentation available to this study.

7.3 Suggestions For Further Work

A better understanding of the macromolecular mechanism of polymer fluids could explain the large degree of drag-reduction at high Reynolds numbers, where it is known that the macromolecules are stretched from their equilibrium coiled configurations [den Toonder *et al.* (1997)]. It has been assumed that this stretching could be associated with drag-reducing behaviour. This inevitably leads to the requirement that extensional viscometric measurements would provide useful

supporting information that may assist in correlating the macromolecular behaviour of drag-reducing polymers with drag reduction.

Hence, the selection of test fluids could be classified upon the chemical composition of their molecular structure. For example, the following classifications could be used to classify polymer additives: molecular weight and molecular weight distribution, sensitivity to ionic content, complexity of molecular structure (e.g. number of side branches), etc.. Different types of solvent additives could be used to explain the differences in flow behaviour, which was evident when comparing the f-Re data for the polymer solutions with that for Carbopol and Laponite. A similar anomalous behaviour was observed when comparing the first normal stress difference data with the shear stress for PAA with other test fluids. Such classifications should involve experts who are able to provide some insight into the likely response of various solvent additives to simple induced shear flows from a macromolecular point of view.

The effect of increasing the concentration of the polymer additive would not, from the opinion of this study, provide any further insight into the mechanism of drag reduction. It is however recommended that scaling effects, such as varying the pipe diameter, could provide some indication of the change in flow structure associated with drag-reduction when compared with Newtonian fluids.

From the observations made within the transition region of flow, asymmetric velocity profiles were discovered for some of the fluids - a phenomena not reported previously. This could have important implications for flow-metering devices, which rely upon peak centreline velocities for determining the rate of flow. Clearly, further investigation is required in this region of flow, with the aim of also assisting the determination of the onset of transitional and drag-reducing flow.

An investigation of the turbulent flow characteristics using spectral analyses for example, particularly the turbulent 'burst' process [McComb (1990)] within the extended buffer region of flow associated with drag-reducing fluids, could provide further evidence of the mechanism for drag reduction. This investigation fell outside

the scope and time scale of the original programme set for this study and hence was not carried out.

8.0 REFERENCES

Year - Unknown

Tandon, P.N., Kulshreshtha, A.K. and Agarwal, R.: Rheological Study of Laminar-Turbulent Transition in Drag-Reducing Polymeric Solutions, *Dept. of Mathematics, H.B.T. Inst.*, Kanpur, (Year unknown), 459-477.

1941 - 1950

Toms, B.A.: Some Observations on the Flow of Linear Polymer Solutions Through Straight Tubes at Large Reynolds Numbers, *Proc. Intl. Congr. on Rheol.*, **II**, Amsterdam, (1949), 135-141.

1951 - 1960

Dodge, D.W. and Metzner, A.B.: Turbulent Flow of Non-Newtonian Systems, *AIChE. J.*, **5 (2)**, (1959), 189-203.

Kotaka, T., Kurata, M. and Tumara, M.: Normal Stress Effect in Polymer Solutions, *J. Appl. Phys.*, **30**, (1959), 1705-1712.

Laufer, J.: The Structure of Turbulence in Fully Developed Pipe Flow, *National Bureau of Standards Report,* Report 1174, (1954), 1-18.

Shaw, R.: The Influence of Hole Pressure Dimensions on Static Pressure Measurements, *J. Fluid Mech.*, (1959), 550-564.

Shaver, R.G. and Merrill, E.W.: Turbulent Flow of Pseudoplastic Polymer Solutions in Straight Cylindrical Tubes, *AIChE. J.*, **5**, (1959), 181-188.

1961 - 1970

Bird, R.B: Experimental Tests of Generalised Newtonian Models Containing a Zero-Shear Viscosity and a Characteristic Time, *Can. J. Chem. Eng.*, **1**, (1965), 161-168.

Cheng, D.C.H., Ray, D.J. and Valentine, F.H.H.: The Flow of Thixotropic Bentonite Suspensions Through Pipes and Pipe Fittings, *Trans. Inst. Chem. Engrs.*, **43**, (1965), 176-186.

Clark, J.A.: A Study Of Incompressible Turbulent Boundary Layers in Channel Flow, *J. Basic Eng.*, **90**, (1968), 445-468.

Ferry, J.D.: Viscoelastic Properties of Polymers, *Wiley (New York)*, 2nd Edition, (1970), Chapter 9.

Franklin, R.E., Wallace, J.M: Absolute Measurements of Static-Hole Error using Flush Transducers, *J. Fluid Mech.*, **42 (Part 1)**, (1970), 33-48.

Gadd, G.E.: Turbulence Damping and Drag Reduction Produced by Certain Additives in Water, *Nature*, May 1965, 463-467.

Hoyt, J.W. and Fabula, A.G.: Paper presented at the ONR-Skipsmodelltanken, *Fifth Symp. Naval Hydrodynamics,* Bergen, (Sept. 1964).

Jeanes, A., Pittsley, J.E. and Senti, F.R.: Polysaccharide B-1459: A New Hydrocolloidal Polyelectrolyte Produced from Glucose by Bacterial Fermentation, *J. Appl. Polym. Sci.*, **V-17**, (1961), 519-526.

Lumley, J.L.: Drag Reduction by Additives, *Ann. Rev. Fluid Mech.*, **1**, (1969) 367.

Metzner, A.B. and Metzner, A.P.: Stress Levels in Rapid Extensional Flows of Polymeric Fluids, *Rheol. Acta*, **9**, (1970), 174-181.

Metzner, A.B. and Park, M.G.: Turbulent Flow Characteristics of Viscoelastic Fluids, *J. Fluid Mech.*, **20**, (1964), 291-303.

Patel, V.C. and Head, M.R.: Some Observations on Skin Friction and Velocity Profiles in Fully Developed Pipe and Channel Flows, *J. Fluid Mech.*, **38**, (1969), 181-201.

Virk, P.S., Mickley, H.S. and Smith, K.A.: The Ultimate Asymptote and Mean Flow Structure in Tom's Phenomena, *J. Appl. Mech.*, **37**, (1970), 488-493.

1971 - 1980

Allan, J.J., Greated, C.C. and McComb, W.D.: Effect of Polymer Additives on the Small-Scale Structure of Grid Generated Turbulence, *J. Phys. D. Appl. Phys.*, **17**, (1977), 533-549.

Berman, N.S. and George, W.K.: Drag Reduction by Polymers, *Phys. Fluids*, **17**, (1974), 250.

Berman, N.S.: Flow Time Scales and Drag Reduction, *Phys. Fluids*, **20**, (1977), 168-174.

Bragg, R. and Oliver, D.R.: Triple Jet - New Method for Extensional Viscosity Measurements, *Nature Phys. Sci.*, **241**, (1973), 131.

Collyer, A.A.: Time Dependent Fluids, *Phys. Education*, **8**, (1973), 38-44.

Durst, F., Melling, A. and Whitelaw, J.H.: Principles and Practice of Laser Doppler Anemometry, *Academic Press*, 2nd Edition, (1976).

Higashitani, K.O., Lodge, A.S.: Hole Pressure Error Measurements in Pressure-Generated Shear Flow, *Trans. Soc. Rheol.*, **19:2**, (1975), 307-335.

Hoyt, J.W.: The Effect of Additives on Friction Factor, *J. Basic Eng.*, **94**, (1972), 258-285.

Hunston, D.L. and Reischman, M.M.: The Role of Polydispersity in the Mechanism of Drag Reduction, *Phys. Fluids*, **18**, (1975), 1626-1629.

International Association of Drilling Contractors: The Rotary Drilling Rig and its Components, Unit 3 Lesson 3, 3rd Edition, (1980), 1-21.

Hinze, J.O.: Turbulence, *McGraw-Hill*, 2nd Edition, (1975).

Higashitani, K.O., Lodge, A.S.: Hole Pressure Error Measurements in Pressure-Generated Shear Flow, *Trans. Soc. Rheol.*, **19:2**, (1975), 307-335.

Lawn, C.J.: The Determination of the Rate of Dissipation in Turbulent Pipe Flow, *J. Fluid Mech.*, **48**, (1971), 477-505.

McLaughlin, D.K. and Tiederman, W.G.: Biasing Corrections for Individual Realisation of Laser Anemometer Measurements in Turbulent Flows, *Phys. Fluids*, **16.12**, (1973), 2082-2088.

Mewis, J. and Metzner, A.B.: The Rheological Properties of Suspensions of Fibres in Newtonian Fluids Subjected to Extensional Deformations, *J.Fluid Mech.*, **62,** (1974), 593.

Mewis, J.: Thixotropy - A General Review, *J. of Non-Newtonian Fluid Mech.*, **6,** (1979), 1-20.

Nakano, A. and Minoura, Y.: Effects of Solvent and Concentration on Scission of Polymers with High Speed Stirring, *J. Appl. Polym. Sci.*, **19**, (1975), 2119.

Novotny Jr., E.J., Eckert, R.E.: Direct Measurement of Hole Error for Viscoelastic Fluids in Flow Between Infinite Parallel Plates, *Trans. Soc. Rheol.*, **17:2**, (1973), 227-241.

Schlichting, H.: Boundary Layer Theory, *Pergamon Press*, 7th Edition, (1978).

Soto, R.J. and Shah, V.L.: Entrance Flow of a Yield-Power Law Fluid, *Appl. Sci. Res.*, **32**, (1976), 73-85.

Tennekes, H. and Lumley,J.L.: A First Course in Turbulence, MIT Press, (1972).

Tiederman, W.G. and Reischman, M.M: Laser Doppler Anemometer Measurementsin Drag-Reducing Channel Flows, *J. Fluid Mech.*, **70**, (1975), 369-392.

Tung, T.T., Ng, K.S. and Hartnett, J.P.: Pipe Friction Factors for Concentrated Aqueous Solutions of Polyacrylamide, *Pergamon Press, Letters in Heat and Mass Transfer,* **5**, (1978), 59-69.

1981 - 1990

Allan, J.J., Greated, C.C. and McComb, W.D.: Laser Doppler Anemometer Measurements of Turbulent Structure in Non-Newtonian Fluids, *J. Phys. D. Appl. Phys.*, **17**, (1984), 533-549.

Alderman, N.J., Gavignet, A.A., Guillot, D. and Maitland, G.C.: High Temperature, High Pressure Rheology of Water Based Muds. *SPE* Paper 18035, (1988).

Barnes, H.A., Hutton, J.F. and Walters, K.: An Introduction to Rheology, *Elsevier*, 1st Edition, (1989).

Bewersdorff, H.W.: Effect of a Centrally Injected Polymer Thread on Drag in Pipe Flow, *Rheol. Acta*, **21**, (1982), 587-589.

Bewersdorff, H.W. and Berman, N.S.: The Influence of Flow Induced Non-Newtonian Fluid Properties on Turbulent Drag Reduction, *Rheol. Acta*, **27**, (1988), 130-136.

Bicen, A.F.: Refraction Corrections for LDA Measurements in Flows with Curved Boundaries, *TSI Quartely*, (1990).

Bird, R.B., Armstrong, R.C. and Hassager, O.: Dynamics of Polymeric Fluids, *Fluid Mech., John Wiley & Sons*, **1**, 2nd Edition, (1987).

Broadway, J.D. and Karahan, E.: Corrections of Laser Doppler Anemometer Readings for Refraction at Cylindrical Interfaces, *DISA*, **6**, (1981), 4-6.

Chang, H.D. and Darby, R.: Effect of Shear Degradation on the Rheological Properties of Dilute Drag-Reducing Polymer Solutions, *J. Rheol.*, **27 (1)**, (1983), 77-88.

Edwards, R.V.: Report of the Special Panel on Statistical Particle Bias Problems in Laser Anemometry, *J. Fluids Eng.*, **109**, (1987), 89-93.

Flannery, B.P., Deckman, B.P., Roberge, W.G. and D'Amico, K.L.: Three Dimensional X-Ray Microtomography, *Science*, **237**, (1987), 1439-1444.

Hartnett, J.P. and Kostic, M.: Anomalous Heat Transfer Behaviour of Aqueous Carbopol Solutions, *Minsk Int. Ht. Mass Transfer Forum*, Minsk (USSR), (1988), 78-89.

Hove, A.O., Nielsen, V. and Leknes J.: Visualisation of Xanthan Flood Behaviour in Core Samples by means of X-ray tomography, *SPE Reservoir Engineering*, **SPE 17342**, (1990), 475-480.

Huang, C.R., Characteristics of thixotropic fluids, in N P Cheremisnoff (Ed)., Encyclopedia of Fluid Mechanics, Rheology and Non-Newtonian Flows, **7**, *Gulf Publishing Co.*, Houston, (1988).

Kehoe, A.B. and Prateen V.Desai, P.V.: Compensation for Refractive-Index Variations in Laser Doppler Anemometry, *Appl. Optics*, **26 (13)**, (1987), 2582-2591.

Laun, H.M..: Prediction of Elastic Strains of Polymer Melts in Shear and Elongation, *J. Rheol.*, **30**, (1986), 459-501.

Luchik, T.S. and Tiederman, W.G.: Turbulent Structure in Low Concentration Drag-Reducing Channel Flows, *J. Fluid Mech.*, **190**, (1988), 241-263.

Massey, B.S.: Mechanics of Fluids, *Chapman and Hall*, 6th Edition, (1990).

McComb, W.D.: The Physics of Fluid Turbulence, University of Edinburgh, *Clarendon Press*, (1990).

Moffat, R.J. : Describing the Uncertainties in Experimental Results, *Exp. Thermal Fluid Sci.*, **1**, (1988), 3.

Nguyen, Q.D. and Boger, D.V., Thixotropic Behaviour of Concentrated Bauxite Residue Suspensions, *Rheol. Acta*, **24**, (1985), 427-437.

Park, J.T., Mannheimer, R.J., Grimley, T.A. and Morrow, T.B.: Pipe Flow Measurements of a Transparent Non-Newtonian Slurry, *J. Fluids Eng.*, **111**, (1989), 331-336.

Pinho, F.T.: Velocity Characteristics of Polymer Solutions in Ducts, Imp. Coll. (London), Mech. Eng. Dept., PhD Thesis, (1990).

Pinho, F.T. and Whitelaw, J.H.: Characteristics of Non-Newtonian Fluids, Imp. Coll. (London), Mech. Eng. Dept., Report FS/87/35, (1987).

Pinho, F.T. and Whitelaw, J.H.: Flow of non-Newtonian fluids in a pipe, *Journal of Non-Newtonian Fluid Mech*, **34**, (1990), 129-144.

Reddy, G.V. and Singh, R.P.: Drag Reduction Effectiveness and Shear Stability of Polymer-Polymer and Polymer-Fibre Mixtures in Recirculatory Turbulent Flow of Water, *Rheol. Acta*, **24**, (1985), 296-311.

Rochefort, W.E. and Middleman, S.: Rheology of Xanthan Gum: Salt, Temperatue and Shear Effects in Oscillatory and Steady Shear Experiments, *J. Rheol.*, **31(4)**, (1987), 337-369.

Soucemarianadin, A., Bourlion, M. and Lenormand, R.: Ultrasonic Saturation Mapping in Porous Media, *SPE Reservoir Engineering*, **SPE 16953**, (1989), 194-200.

Tiederman, W.G.: Review: The Effect of Dilute Polymer Solutions on Viscous Drag and Turbulence Structure, *Proc. IUTAM-Zurich*, (1988).

Vinegar, H.J. and Wellington, S.L.: Tomographic Imaging of Three-Phase Flow Experiments, *Rev. Sci. Instrum.*, **58 (1)**, (1987), 96-107.

Willmarth. W.W., Wei, T. and Lee, C.O.: Laser Anemometer Measurements of Reynolds Stress in a Turbulent Channel Flow with Drag Reducing Polymer Additives, *Phys. Fluids*, **30**, (1987), 933-935.

1991 - Present

Allen, E.: An Improved Viscosity Equation to Characterise Shear-Thinning Fluids, *SPE 28973*, (1995), 279-289.

Beris, A.N. and Dimitripoulos, C.D.: Pseudospectral Simulation of Turbulent Viscoelastic Channel Flow, *Comput. Methods Appl. Mech. Eng.*, **180**, (1999), 365-392.

Beris, A.N., Dimitripoulos, C.D., Sureshkumar, R. and Handler, R.D.: Direct Numerical Simulations of Polymer-Induced Drag Reduction in Viscoelastic Turbulent Channel Flows, *XIIIth Int. Congress on Rheol.*, Cambridge, (2000), 2.190-2.192.

Billingham, J. and Ferguson, J.W.J.: Laminar, Unidirectional Flow of a Thixotropic Fluid in a Circular Pipe, *J. Non-Newtonian Fluid Mech.*, **47**, (1993), 21-55.

Brown, G.O., Stone, M.L. and Gazin, J.E.: Accuracy of Gamma-Ray Compuetrized Tomography , *Water Resources Research*, **29 (2)**, (1993), 479-486.

Den Toonder, J.M.J., Kuiken, G.D.C and Nieuwstadt, F.T.M.: The Role of Elongational Viscosity in the Meachanism of Drag Reduction by Polymer Additives, *Appl. Sci. Res.*, **54**, (1995), 95-123.

Den Toonder, J.M.J., Hulsen, M.A., Kuiken, G.D.C and Nieuwstadt, F.T.M.: Drag Reduction by Polymer Additives in a Turbulent Pipe Flow: Numerical and Laboratory Experiments, *J. Fluid Mech.*, **337** (1997), 193-231.

Dimitripoulos, C.D., Sureshkumar, R. and Beris, A.N.: Direct Numerical Simulation of Viscoelastic Turbulent Channel Flow Exhibiting Drag Reduction: Effect of the Variation of Rheological Parameters, *J. Non-Newtonian Fluid Mech.*, **79**, (1998), 433-468.

Durst, F., Jovanovic, J. and Sender, J.: LDA Measurements in the Near-Wall Region of a Turbulent Pipe Flow, *J.Fluid Mech.*, **295**, (1995), 305-335.

Escudier, M.P., Jones, D.M. and Gouldson, I.W.: The Flow of Non-Newtonian Liquids Through a Concentric Annular Channel with Centrebody Rotation. Phase 1: Rheological Characterisation of Model Fluids, *University of Liverpool*, (1991), 1-20.

Escudier, M.P., Jones, D.M. and Gouldson, I.W.: Fully Developed Pipe Flow of Shear-Thinning Liquids, *Paper 1.3 presented at Sixth International Symposium on Applications of Laser Techniques to Fluid Mechanics*, Lisbon, (1992), 1.3.1-1.3.4.

Escudier, M.P., Gouldson, I.W. and Jones, D.M.: Flow of Shear-Thinning Fluids in a Concentric Annulus, *Exp. Fluids*, **18**, (1995a), 225-238.

Escudier, M.P., Gouldson, I.W. and Jones, D.M.: Taylor vortices in Newtonian and Shear-Thinning Liquids, *Proc. Roy Soc. A*, **449**, (1995b), 155-176.

Escudier, M.P. and Gouldson, I.W.: Concentric Annular Flow with Centrebody Rotation of a Newtonian and a Shear-Thinning Liquid, *Int. J. Ht. and Fluid Flow*, **16**, (1995c), 156-162.

Harder, K.J. and W.G.Tiederman, W.G.: Drag Reduction and Turbulence Structure in Two-Dimensional Channel Flows, *Phil. Trans. R. Soc. Lond.*, **A 336**, (1991), 19-34.

Hartnett, J.P.: Viscoelastic Fluid : A New Challenge in Heat Transfer, *J. Heat Transfer* (1992), **114**, 296-303.

Kelco (Manufacturers): Xanthan Gum, Suppliers Catalogue, 2nd Edition, (1991), 15-34.

Kokini, J.L. and Surmay, K.: Steady Shear Viscosity, First Normal Stress Difference and Recoverable Strain in Carboxymethylcellulose, Sodium Alginate and Guar Gum, *Carbohydrate Polymers*, **23**, (1994), 27-33.

Kostic, M.: On the Turbulent Drag and Heat Transfer Reduction Phenomena and Laminar Heat Transfer Enhancement in Non-Circular Duct Flow of Certain Non-Newtonian Fluids, *Int. J. of Ht. Mass Transfer*, **37**, (1994), 133-147.

Li, T.Q. and McCarthy, K.L.: Pipe Flow of Aqueous Polyacrylamide Solutions Studied by Means of Nuclear Magnetic Resonance Imaging, *J. Non-Newtonian Fluid Mech.*, **57**, (1995), 155-175.

Makrakis, A.: The Effect of Freezing and Thawing on Fluid Rheology, MEng. Report, *The University of Liverpool*, (1996).

Nelson, E.B.: Well Cementing, Developments in Petroleum Science, **28**, Elsevier, (1990).

Orlandi, P.: A Tentative Approach to the Direct Simulation of Drag Reduction by Polymers, *J. Non-Newtonian Fluid Mech.*, **60**, (1995), 277-301.

Pastor, M.V., Costell, E., Izquierdo, L. and Durn, L.: Effects of Concentration, pH and Salt Content on Flow Characteristics of Xanthan Gum Solutions, *Food Hydrocolloids*, **8 (3-4)**, (1994), 265-275.

Pearson, J.R.A.: Flow Curves with a Maximum, *J. Rheol.*, **38**, (1994), 309-331.

Pereira, A.Sá and Pinho, F.T.: Turbulent Pipe Flow Characteristics of Low Molecular Weight Polymer Solutions, *J. Non-Newtonian Fluid Mech.*, **55**, (1994), 321-344.

Sureshkumar, R., Beris, A.N. and Handler, R.A.: Direct Numerical Simulation of the Turbulent Channel Flow of a Polymer Solution, *Phys. Fluids*, **9 (3)**, (1997), 743-755.

Sursachem Limited, UK: Technical Correspondence with Sursachem Representative, *Sales Division*, (1995).

Ursin, J.R.: Detection of Fluid Saturations in Porous Media using Gamma-Ray Tomography, *J. Petrol. Sci. Eng.*, **7**, (1992), 297-308.

Vlassopoulos, D and Schowalter, W.R.: Characterisation of the Non-Newtonian Flow Behaviour of Drag-Reducing Fluids, *J. Non-Newtonian Fluid Mech.*, **49**, (1993), 205-250.

APPENDICES

ELSEVIER

J. Non-Newtonian Fluid Mech., 62 (1996) 291–306

Journal of Non-Newtonian Fluid Mechanics

Pipe flow of a thixotropic liquid

M.P. Escudier*, F. Presti

Department of Mechanical Engineering, University of Liverpool, P.O. Box 147, Liverpool, L69 3BX, U.K.

Received 14 October 1995; in revised form 17 November 1995

Abstract

Detailed measurements of mean velocity and velocity fluctuation levels (axial, tangential and radial) have been carried out using a laser Doppler anemometer for fully developed pipe flow of an aqueous solution of Laponite, a synthetic clay. The equilibrium rheological structure of this thixotropic liquid is well characterised by the Herschel–Bulkley model. Velocity profiles calculated for a Herschel–Bulkley fluid prove to be a very accurate representation of the measurements for laminar flow at Reynolds numbers below about 1500. The measured profiles develop an unexplained asymmetry for higher Reynolds numbers until the flow undergoes transition to turbulence. The fluid is drag reducing under turbulent flow conditions with relative levels of tangential and radial turbulence intensity suppressed in comparison with water whilst the axial turbulence intensity is little different. Under all flow conditions it is evident that the fluid rheology is far from structural equilibrium, with values for the apparent yield stress and effective viscosity determined from near-wall velocity measurements considerably below those obtained from a rheometer.

Keywords: Fully developed pipe flow; Herschel–Bulkley liquid; Thixotropy

1. Introduction

Thixotropy is the term used to classify fluids for which there is an isothermal, time-dependent breakdown of some particulate structure under relatively high shear followed by structural build-up for lower shear. As Nguyen and Boger [1] point out, the applied shear acts to disrupt structural bonds interlinking fluid elements which may be the primary particles and/or aggregates of such particles. At the same time, shear-induced collisions of the separated structural elements tend to reform part of the broken bonds so that a state of dynamic equilibrium is attained when these two processes balance. In the absence of sufficiently high shear, thixotropic

*Corresponding author.

SSDI 0377-0257(96)01417-9

fluids may gel and so exhibit a yield stress. Paints, clays, cement slurries, drilling muds, blood, ketchup, mayonnaise, toothpaste, shaving cream, crude oil and printing inks are among the many materials classed as thixotropic (see Collyer [2], Mewis [3], Huang [4]). Given the widespread nature of this list, and the commercial and technical significance of these materials, it is not surprising that numerous papers have been published on the rheological characteristics of thixotropic fluids: Mewis [3] put the figure at about a thousand nearly two decades ago. In contrast, the number of papers which are concerned with the flow of thixotropic fluids is small, a consequence of the extreme theoretical and experimental problems involved. The mathematical difficulty of dealing with such flows is exemplified by Pearson [5] who considers the general physics of the flow of thixotropic fluids and by the recent paper of Billingham and Ferguson [6] which analysed the relatively simple situation of laminar, unidirectional flow of a thixotropic fluid in a circular pipe. The experimental difficulties associated with the flow of thixotropic fluids are also readily apparent. For most laboratory installations and many practical situations, it can be anticipated that, except in the immediate vicinity of the surface, the timescales associated with structural breakdown and buildup for the fluid will be greatly in excess of residence times. An inevitable consequence is that the fluid viscosity is likely to be quite different from what would be consistent with the local shear stress if equilibrium had been reached. Global measurements of pressure drop vs. flow rate for flow through pipes and fittings, such as reported by Cheng et al. [7], are clearly inadequate for such complex situations but the very nature of thixotropic fluids precludes detailed measurements using conventional intrusive instrumentation such as pitot tubes or hot-wire anemometers. Since nearly all thixotropic fluids of practical interest are opaque, non-intrusive optical measuring techniques such as laser Doppler anemometry are also ruled out in most instances. The recent work of Li and McCarthy [8] on the flow of polyacrylamide is primarily of interest because they utilised nuclear magnetic resonance imaging, a technique which is not limited to optically transparent liquids. An exception to the statement about opacity is Laponite (a product of Laporte Industries Ltd.), a synthetic clay, and in this paper we discuss the results of measurements made using a laser Doppler anemometer (LDA) for pipe flow of Laponite RD under laminar, transitional and turbulent flow conditions.

The underlying motivation for the present work is the need to develop a better understanding of the mechanics of the flow of drilling fluids (muds) which are pumped down the drillpipe, through the drillbit, and up the annulus between the drillpipe and the borehole wall during the drilling of oil and gas wells. As already mentioned, drilling muds are among the fluids which may exhibit thixotropy (Alderman et al. [9]); most muds are also shear thinning and may well be viscoelastic. Previous work by the present authors and their colleagues has been concerned with the flow of a range of slightly elastic, shear-thinning liquids in an annular geometry with and without centrebody rotation (Escudier et al. [10,11], Escudier and Gouldson [12]) in partial simulations of mud flow in a wellbore during drilling operations. In the course of that work it became increasingly evident that more fundamental pipe-flow investigations of the fluids being used were required if progress was to be made in analysing and understanding the more complex situation of flow in an annulus.

The most relevant previous experimental work on the flow of non-Newtonian liquids in pipes is that of Park et al. [13], Pinho and Whitelaw [14], and Pereira and Pinho [15]. Park et al. presented LDA measurements for both laminar and turbulent flow of an oil-based transparent slurry with yield-power-law (Herschel–Bulkley) viscoplastic behaviour. Under fully developed

laminar-flow conditions, their measurements revealed a velocity distribution with a core (about 60% of the pipe diameter) of uniform velocity in good agreement with the theory of Soto and Shah [16] for a Herschel–Bulkley fluid. It is convenient to reproduce here the equation representing this velocity distribution since, as will be seen, the Laponite solutions used in the present work are also well represented by this viscometric model although, quite clearly, it does not take into account the thixotropic nature of the fluid:

$$u = \left(\frac{n}{n+1}\right)\left(\frac{\tau_S}{K}\right)^{1/n} R\left[(1-\xi)^{\frac{n+1}{n}} - \left(\frac{r}{R}-\xi\right)^{\frac{n+1}{n}}\right] \quad \text{for } r \geqslant r_P,$$

where n and K are constants in the Herschel–Bulkley model

$$\tau = \tau_Y + K\dot{\gamma}^n,$$

and the non-dimensional radius ξ of the "plastic" core is given by

$$\xi = r_P/R = \tau_Y/\tau_S.$$

Also useful are the expressions for the bulk velocity

$$V = \left(\frac{n}{n+1}\right)\left(\frac{\tau_S}{K}\right)^{1/n} R(1-\xi)^{\frac{n+1}{n}}\left[1 - \frac{2n}{3n+1}(1-\xi) - \frac{2n^2\xi(1-\xi)}{(3n+1)(2n+1)}\right],$$

for the plug velocity

$$\frac{u_P}{V} = \left[1 - \frac{2n}{3n+1}(1-\xi) - \frac{2n^2\xi(1-\xi)}{(3n+1)(2n+1)}\right]^{-1},$$

and the friction factor–Reynolds number relationship

$$\frac{4}{Ref} = \left(\frac{n}{n+1}\right)(1-\xi)\left[1 - \frac{2n}{3n+1}(1-\xi) - \frac{2n^2\xi(1-\xi)}{(3n+1)(2n+1)}\right],$$

wherein the Reynolds number Re is defined as $2\rho VR/\mu_S$, μ_S being the viscosity corresponding to the surface shear stress.

For turbulent flow, Park et al. [13] found that the mean velocity distribution was almost indistinguishable from that for a Newtonian fluid although differences in the turbulence structure were apparent, particularly a reduction in the tangential intensity away from the immediate vicinity of the pipe wall and an increase in axial intensity near the wall. Unfortunately the data are presented in such a way that it is not possible to detect whether the slurry was drag reducing as is typical of other, primarily polymeric, shear-thinning liquids.

The measurements of Pinho and Whitelaw [14] were for aqueous solutions of the polymer sodium carboxymethylcellulose (CMC) with w/w concentrations in the range 0.1–0.4% which they characterise by a power-law model. Their data showed a progressive approach with increasing polymer concentration to the asymptotic behaviour identified by Virk et al. [17], i.e. reduced drag in turbulent flow, delayed transition, reduced levels of radial and tangential turbulence intensity, and a mean velocity distribution with an extended sublayer and an increased additive constant B (in the range 8–12) in the law of the wall

$$u^+ = A \ln y^+ + B,$$

compared with the value of 5.5 for a Newtonian fluid whilst the Kármán constant A was unchanged at 2.5.

The recent study of Pereira and Pinho [15] was very similar in approach to that of Pinho and Whitelaw [14], but concerned with aqueous solutions (0.4–0.6% w/w concentration) of the low molecular weight polymer Tylose, a methylhydroxylcellulose. Pereira and Pinho concluded that their Tylose solutions, for which the viscometric data are well represented by the Carreau model, could be considered essentially inelastic, as is also the case for CMC at low concentrations. The hydrodynamic data showed turbulent-flow drag reductions of about half that for CMC together with a concomitant upshift in the log-law (i.e. an increase in B). A surprising feature of the turbulence measurements was an almost uniform distribution of both the radial and tangential turbulence intensities in the central core (80% of the diameter) of the flow at levels above those for a Newtonian fluid.

Some preliminary data for the pipe flow of CMC, xanthan gum, Laponite and a Laponite/CMC blend were presented by Escudier et al. [18]: the present paper considerably extends the scope of the earlier measurements for Laponite.

2. Experimental rig and instrumentation

The flow loop used for the experiments is shown schematically in Fig. 1. Flow is provided by a progressive cavity pump (1) (numbers in parentheses refer to the components shown in Fig. 1) (Mono type E101, maximum flowrate 0.025 $m^3\ s^{-1}$) fed directly from a 500 l capacity stainless steel tank (2). Three dampers (3) located immediately after the Mono pump outlet act to remove pulsations in the flow prior to entry into the test section (4). The latter consists of thirteen precision-bore borosilicate glass tubes (i.d. 100.4 ± 0.1 mm), each of which is assembled into a module with matched male/female stainless-steel flanges at alternate ends. Each glass tube is

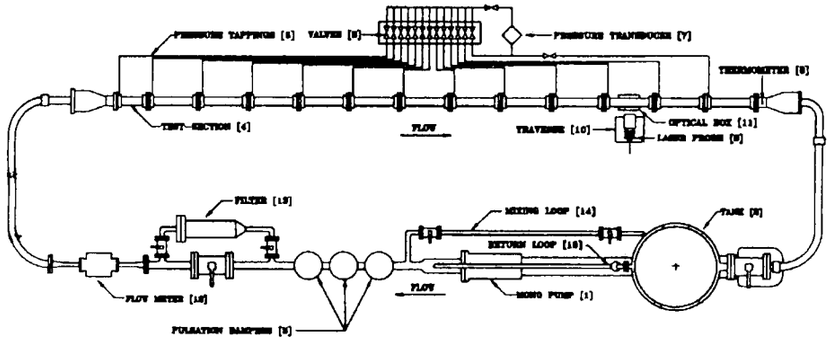

Fig. 1. Schematic diagram of pipe-flow facility (plan view).

separated from the stainless steel by a thin PTFE ring, and each end of a module (assembled in a jig) is fixed using Devcon urethane rubber. The modules are 1.027 m (±3 mm) in length, which gives an overall length of 13.35 m and a length:diameter ratio of 133. Pressure tappings of 1 mm diameter are provided on each mating flange pair with 2 mm internal diameter clear vinyl tubing (5), filled with deionised water, connecting each pressure tapping via a series of valves (6) to a Validyne differential pressure transducer (7) (DP15-26, 3448 Pa fsd). The valves are connected to the tappings in such a way as to permit measurement of the pressure drop over increasing numbers of pipe sections to assess the location at which the rate of flow development becomes negligible. Signal conditioning for the pressure transducers is provided by a Validyne CD223 digital transducer indicator with a BCD output connected to a data-logging computer (RCL 386 SX-33). The transducers were calibrated at periodic intervals using air against a Baratron 398HD-01000SP05 (1000 Torr fsd) high-precision differential pressure transducer with an accuracy over the calibration range of 0.01% of reading. The accuracy of the Validyne transducer is estimated to be better than ±0.25% of fsd. A platinum resistance thermometer (8) mounted in the endhousing downstream of the test section is used to monitor the fluid temperature to an accuracy of ±0.1°C.

Measurements were made of the radial distributions of the mean axial velocity and the axial, radial and tangential turbulence intensities using a Dantec Fibreflow LDA system comprising a 60 × 10 probe and 55 × 12 beam expander (9) together with a Dantec BSA 57N20 Enhanced Burst Spectrum Analyzer signal processor and an RCL 386 SX-33 PC microcomputer. The LDA optical parameters are as follows: beam separation at front lens 46.6 mm, lens focal length 160 mm, length of principal axis of measurement volume 0.21 mm and diameter 0.02 mm. In view of the small size of the measurement volume, it was not regarded necessary to make a gradient correction to the measured velocities or turbulence intensities. The probe head, housing both the transmitting and receiving optics, was mounted on a three-axis traverse (10) controlled by a microcomputer (IBM XT PS2 model 30) and having a spatial resolution of 15 μm. A flat-faced optical box (11), filled with water, was positioned over the pipe at the measurement location, 107 diameters from the pipe inlet, to minimise refraction of the beams at the curved surfaces.

A Fischer and Porter electromagnetic flowmeter (12) (model 10 D1) is incorporated in the return arm of the flow loop with the flowmeter output signal recorded via an Amplicon PS 30AT A/D converter on an RCL 386 SX-33 PC. Flow rates indicated by the flowmeter were found to be within 1% of values computed from the velocity profiles. In-house software was written to record flowrate, pressure drop and fluid temperature and to control and record the LDA probe location.

To permit filtering of the base solvent (tap water) prior to the addition of Laponite powder, a 125 μm filter (13) is incorporated into a by-pass loop through which the liquid can be diverted. Mixing of the powder is accomplished by circulating the fluid through a return loop (14) incorporated just before the pulsation dampers. A pressure relief (safety) valve and a second return loop (15) are located immediately after the pump outlet.

The viscometric characteristics of the test fluid in use were determined using both a CarriMed controlled-stress rheometer (CSL 100) with either a cone-and-plate or a parallel-plate geometry, and also a Bohlin VOR controlled shear-rate rheometer with similar geometries. The first rheometer was controlled from a CAF 386 SX-33 PC employing CarriMed's flow equilibrium software whilst the Bohlin VOR was controlled by a Compaq 486 DX2-66 PC running Bohlin's

BRS software. Fluid refractive indices were determined using an ABBE 60/ED high-accuracy refractometer. A Spirax Sarco conductivity meter (model MS1) was used to measure the conductivity of the working fluid.

3. Test fluid: description, preparation and rheology

Laponite is the trade name for a synthetic hectorite clay with a structure similar to that of sodium montmorillonite, a principal constituent in Wyoming Bentonite. When Laponite is dispersed in water, the exchangeable sodium ions hydrate, causing the clay to swell initially and to separate completely. This gives a clear colloidal dispersion (a sol) of anionic Laponite platelets and hydrated sodium ions in solution. The platelets carry a surface negative charge (due to lattice substitution) and a small positive charge on the edge due to the disruption of the lattice. In dilute solutions the surface negative charges are much larger than the small edge charges and repulsion occurs between the platelets so that no thickening occurs. As the ionic content of the water increases (either due to the addition of salt or to increasing Laponite level) the surface negative charge is reduced due to increasing association between this charge and the cations in solution. Repulsion between platelets, the primary Laponite clay particle, is reduced and the dominant force becomes the surface to edge attraction causing the dispersion to gel. The particle/particle bonds break down under the application of a shear stress giving rise to a highly thixotropic behaviour. In consequence, the rheology of Laponite suspensions is influenced greatly by solvent ionic strength and shear history.

The basic working fluid was prepared by slowly adding Laponite (grade RD) powder to cold (about 15°C) filtered Liverpool tapwater being circulated through the mixing loop (14) of the flow facility. In order to increase the yield stress of the fluid 60 ppm laboratory grade salt was added to produce a conductivity of about 0.74 mS cm^{-1} together with formaldehyde (100 ppm) to retard bacterial degradation of the fluid. Timiron particles (about 20 μm) were also added to improve LDA data rates and signal quality. Measurements of the viscometric properties were repeated at daily intervals over a period of about one week until their rate of change was negligible over the time required to carry out a single flow experiment. Fig. 2 shows the variation of shear stress versus shear rate from data obtained using both the Carri-Med controlled stress (□ 50 mm ϕ parallel plate) and the Bohlin controlled strain rate (▼ 25 mm ϕ high shear bob and cup, ◆ 5° cone/30 mm ϕ plate, ▲ 24 mm ϕ/27 mm ϕ double gap) rheometers. The fitted curve corresponds to a Herschel–Bulkley fluid with $\tau_Y = 4.4$ Pa, $K = 0.24$ Pa s^n and $n = 0.535$. These data correspond to equilibrium conditions whereby the fluid was sheared at a given shear stress until the shear rate remained essentially unchanged (about 30 min for each point) and are consistent for shear rates above 30 s^{-1} but become increasingly scattered for shear stresses close to the yield stress. (We recognise that the yield stress τ_Y is no more than a fitting parameter, strongly influenced by the resolution of our instrumentation at very low shear rates, and also that some readers will prefer the term apparent yield stress.) In addition to the anticipated difficulties of working with a shear-thinning thixotropic liquid, a further complication was associated with the tendency (confirmed by the manufacturer) for the viscosity of Laponite to gradually increase with time. This was particularly noticeable at low shear rates where a 30% increase in viscosity occurred over a period of 7 days. Also included in Fig. 2 are

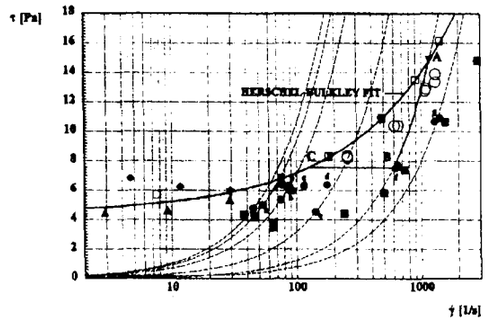

Fig. 2. Viscometric data for 1.5% Laponite: ▼, ▲, ◆, □ rheometer data; ●, ■, ○ velocity-profile data; - - - - lines of constant viscosity (see main text).

data deduced from measured velocity profiles (●, ■, ○) which will be discussed in Section 4. The thixotropic nature of Laponite is evident from Fig. 3 which shows the reduction in shear rate when the shear stress was reduced to 12 Pa after pre-shearing at 19 Pa for 15 min at 20°C. The two levels of shear stress correspond, respectively, to a typical wall shear stress for the pipe flow and the corresponding equilibrium stress for an asymptotic shear rate of 560 s^{-1}.

4. Results

The measured mean velocity profiles (Fig. 4) show a clear progression with increasing Reynolds number from laminar flow (a-d) through transition (e) into turbulent flow (f, g). At

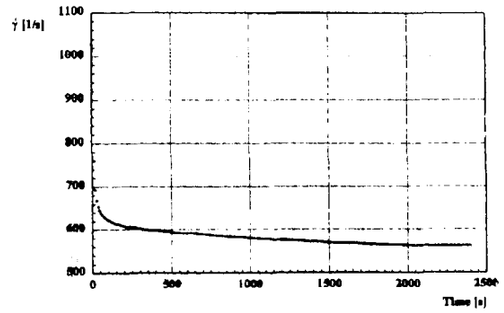

Fig. 3. Thixotropic behaviour of Laponite.

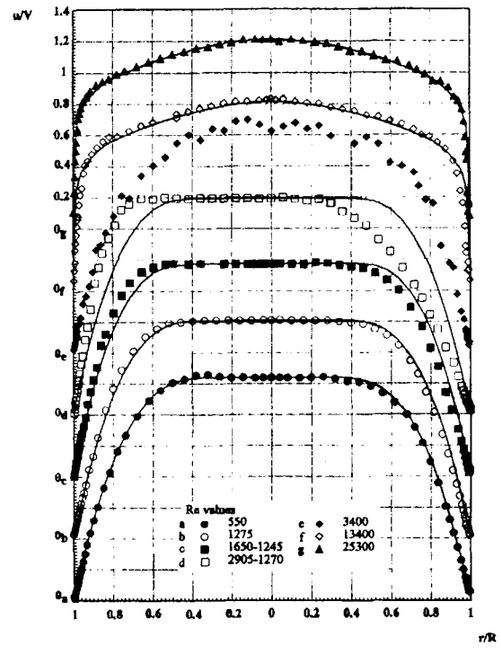

Fig. 4. Mean velocity profiles for increasing Reynolds numbers.

the two lowest Reynolds numbers the profiles are symmetrical with a well defined "plastic" plug, and are well represented by the theoretical profile for fully developed laminar flow of a Herschel-Bulkley fluid, much the same as reported by Park et al. [13] for their slurry flow. The theoretical profiles were fitted by determining values of ξ ($\equiv \tau_Y/\tau_S$) from u_p/V with $n = 0.535$. Although this value for the index n corresponds to the equilibrium viscometric data of Fig. 2, it turns out that ξ is relatively insensitive to n. It could be argued that the close agreement between the data points and the theoretical velocity profile is somewhat misleading, since in normalised form (i.e. u/V vs. r/R) the profile is not directly dependent upon K. Whilst it may seem quite remarkable that the measured profiles reveal nothing of the thixotropic nature of Laponite, in fact it is easily shown tht the fluid residence time only approaches that required to reach equilibrium within about 10 μm of the pipe wall. As will be seen later, the clear indicator of thixotropic behaviour is that rheometric data (i.e. τ_Y and μ_S) consistent with the velocity profiles are considerably different from the equilibrium values.

An entirely unexpected, but repeatable, feature of the velocity profiles for Reynolds numbers in the approximate range 1300–3000 Fig. 4 (c–e) is a progressively increasing degree of asymmetry which would be consistent with a significant azimuthal variation of wall shear stress for a fluid of constant viscosity. No such asymmetry has been observed for the flow of either Newtonian liquids or aqueous solutions of carboxymethylcellulose in the same pipe-flow facility. The asymmetry disappears once transitional or turbulent-flow conditions are established (profiles e–g) which suggests that an explanation for the asymmetry may be associated with the stability characteristics of the flow of a yield-stress fluid, of which the plastic plug is a consequence. It may be that the plug itself is initially deflected away from the centreline due, perhaps, to minor geometrical imperfections in the flow loop. A link with the flow geometry would be consistent with the asymmetry always being in the same orientation although it would seem unlikely that any significant upstream asymmetry would produce the symmetric profiles seen at lower Reynolds numbers. It is also the case that no change was observed when the downstream bend orientation was reversed.

Profile e of Fig. 4 corresponds to a Reynolds number of 3400 and, when compared with both the laminar-flow data and also the profiles for fully turbulent conditions (f, g), it is evident that for this profile the flow state is transitional. There is no evidence of a gelled plug and the mean flow is practically symmetrical, albeit with a high degree of scatter associated with the intense velocity fluctuations which are typical of transition. The two profiles (f, g), for the highest Reynolds numbers, 13400 and 25300, are in close agreement with the curve which represents water flow at a Reynolds number of 61000. The lower velocities for Laponite in the near-wall region are consistent with a degree of drag reduction.

The Reynolds numbers here have been defined as $Re \equiv 2\rho VR/\mu_S$ with the viscosity μ_S evaluated from the shear stress τ_S and the shear rate $\dot{\gamma}_S$ (i.e. $\mu_S = \tau_S/\dot{\gamma}_S$), the subscript S denoting conditions at the pipe surface. For the downstream half of the pipe run, within which all detailed measurements were made, the axial pressure gradient dp/dx was found to be constant within the limits of the transducer accuracy so that $(-R\, dp/dx)/2$ should be an accurate estimate of τ_S. A constant axial pressure gradient is often taken to indicate that the hydrodynamic development of a flow is complete. However, a comparison of $\tau_S(\dot{\gamma}_S)$ with the data of Fig. 2 obtained from the two rheometers will show that (see below) in the case of Laponite the fluid rheology, and hence the flow itself, was in fact far from structural equilibrium. The high spatial resolution of the LDA system used for the present work permitted measurements very close to the pipe wall (well into the viscous sublayer for turbulent flow), which were then used to determine both the "true" origin ($y = 0$) for the velocity profile and also a value for the strain rate at the surface $\dot{\gamma}_S$. The foregoing procedure is clearly deficient for the asymmetric velocity profiles just prior to transition but has to suffice for obvious reasons.

The values obtained for μ_S permit the turbulent flow velocity profiles to be represented (Fig. 5) in wall variables $u^+ \equiv u/u_\tau$ and $y^+ \equiv \rho u_\tau y/\mu_S$ (with the friction velocity $u_\tau \equiv \sqrt{\tau_S/\rho}$). As was evident from Fig. 4, the profile for $Re = 3400$ is clearly transitional whilst the two main features evident from the mean velocity profiles for turbulent-flow conditions ($Re = 13400$ and 25300) transformed to these variables are the well-defined behaviour in the viscous sublayer and slight but definite upward shifts in the log-law region with the additive constant B increased from 5.5 to 7.1 for $Re = 13400$ and to 6.5 for $Re = 25300$ consistent with a low level of drag reduction thereby suggesting that Laponite could be regarded as slightly elastic [14]. It is, of course, the

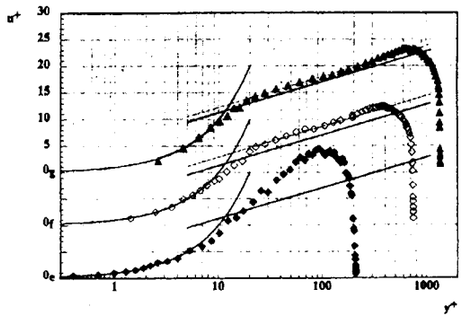

Fig. 5. Mean velocity profiles for transitional (e) and turbulent (f, g) flow conditions in law-of-the-wall coordinates. *Re* values: ◆ 3400; ◇ 13400; ▲ 25300.

case that since the effective wall viscosity was taken as $\tau_S y/u$, it is inevitable that within the sublayer $u^+ = y^+$ provided u is proportional to y.

The distribution of normalised rms values for the axial velocity fluctuation (Fig. 6) confirms that the transitional state is characterised by much higher levels than is typical for the fully turbulent flow, except in the immediate vicinity of the pipe surface. There is no great difference in the axial fluctuation levels for fully turbulent flow of Laponite and of water whereas the normalised tangential (Fig. 7) and radial (Fig. 8) intensities for Laponite (at slightly different Reynolds numbers to the axial-flow data) fall well below the levels for water. These changes in the turbulence structure are entirely consistent with previous observations ([14,15]) for polymers and are generally associated with drag reduction.

It is instructive at this point to return to the data represented by the symbols in Fig. 2 which correspond to values for $\dot{\gamma}_S$ deduced from near-wall velocity measurements (●, ■, ○). Fig. 9

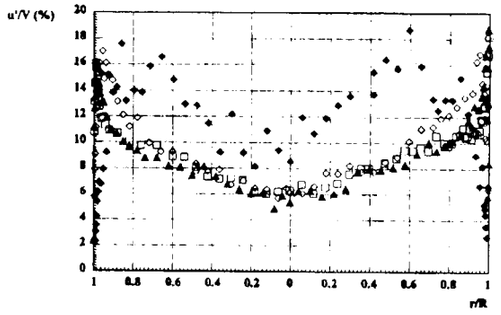

Fig. 6. Axial velocity fluctuations. *Re* values: ◆ 3400; ◇ 13400; ▲ 25300; □ 6100 (Newtonian).

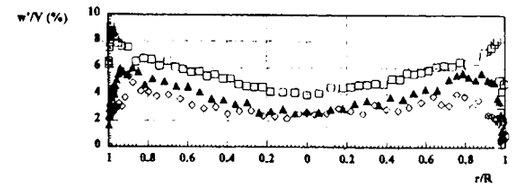

Fig. 7. Tangential velocity fluctuations. *Re* values: ◇ 12800; ▲ 23500; □ 61000 (Newtonian).

Fig. 8. Radial velocity fluctuations. *Re* values; ◇ 11900; ▲ 20600; □ 61500 (Newtonian).

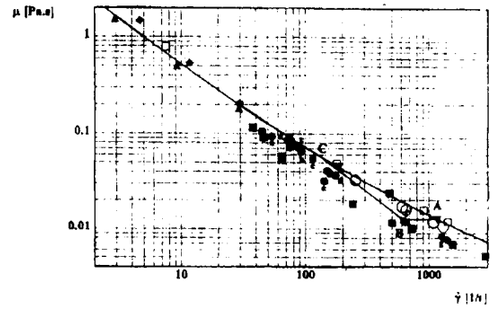

Fig. 9. Apparent viscosity vs. shear rate (Symbols as for Fig. 2 .

shows all the Fig. 2 data replotted in the form of effective viscosity (i.e. $\tau/\dot{\gamma}$) vs. shear rate. At all flow rates it is apparent that the effective viscosity at the pipe wall corresponded to equilibrium values for τ and $\dot{\gamma}$ about twice the wall values, as is clear from the lines of constant viscosity, e.g. that linking points A and B. Even close to the pipe wall, the fluid residence time is insufficient for the structure to build up to a viscosity consistent with the prevailing τ_s. For the particular case represented by point B, the equilibrium value for $\dot{\gamma}_s$ would be about 80% below the actual value if τ_s remained unchanged. In reality, if the structure were allowed to develop (e.g. in a much longer pipe) τ_s would also increase and an equilibrium state between A and C would ultimately be reached.

Values for the rheological and flow parameters corresponding to the velocity profiles of Fig. 4 are listed in Table 1 (with ξ evaluated assuming $n = 0.535$). For the asymmetric profiles (Fig. 4c, d), two Reynolds numbers are given corresponding to the shear rates on either "side" of the pipe. This table reveals another unexpected result — the yield stress consistent with the laminar velocity profiles is not constant, as would be expected if it were a property of the fluid in its gelled state, and is substantially lower than the value of 4.4 Pa obtained from the equilibrium viscometric data.

Measurements of frictional pressure drop for flowrates covering the entire range of flow conditions are shown in Fig. 10 in the form of friction factor vs. Reynolds number. Also shown on the same figure is the variation of axial turbulence intensity (u'/V) measured close to the pipe wall ($r/R = 0.8$). For each flowrate, the Reynolds number is again based upon an apparent viscosity determined from the near-wall velocity variation using wall shear stress values calculated from the frictional pressure gradient. Data are shown from three series of experiments, carried out over a period of about six weeks. Values for f and Re which correspond to the velocity profiles of Fig. 4 are represented by large filled circles (●) as are data obtained from other profiles which formed part of the same series of experiments. The laminar-flow friction factors lie between the classical $fRe = 16$ line corresponding to fully developed flow of a Newtonian fluid and $fRe = 23.8$ and 26.3 which are consistent with the Herschel–Bulkley model with $n = 0.535$ and with $\xi = 0.3$ and 0.4, respectively. The turbulent flow data appear to be asymptoting towards the Blasius line ($fRe^{1/4} = 0.0791$) with levels of drag reduction decreasing

Table 1
Rheological and flow parameters for velocity profiles of Fig. 4

Profile	V (m/s)	u_p/V	τ_s (Pa)	ξ	τ_Y (Pa)	Re	f
a	0.52	1.44	5.02	0.31	1.56	550	0.038
b	0.84	1.41	5.99	0.36	2.13	1275	0.017
c	0.90	1.37	6.30	0.40	2.53	1650-1245	0.016
d	1.06	1.39	6.39	0.38	2.40	2900-1270	0.012
e	1.09	–	4.54	–	–	3400	0.0076
f	1.60	–	7.66	–	–	13400	0.0060
g	2.03	–	10.9	–	–	25300	0.0053

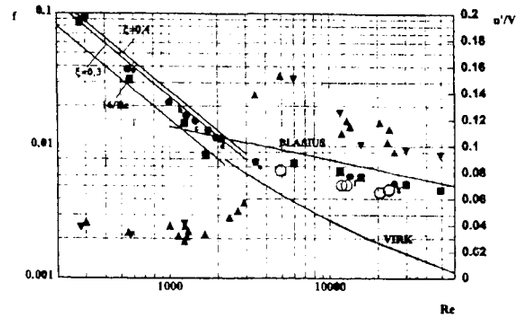

Fig. 10. Friction factor (●, ■, ○) and near-wall turbulence intensity (▲, ▼) vs. Reynolds number (see main text).

slightly with Reynolds number from about 18% to 16%. Since the Reynolds number is based upon μ_S, the true degree of drag reduction must be slightly higher than Fig. 10 would suggest: a generalised Reynolds number Re_N, formulated to ensure that in laminar flow $fRe_N = 16$, would inevitably be lower than Re. The open circles (○) correspond to the data from a subsequent series of experiments for which it was found that the fluid viscosity was gradually increasing. As remarked earlier, the viscosity increase was most apparent at the low shear rates and so also corresponds to a decrease in the shear thinning index which could explain why the degree of drag reduction is markedly higher (33% to 26%) for this set of data. The filled squares (■) correspond to an earlier data set obtained with only a few points to define the near-wall, velocity profile. For low Reynolds number (laminar/transitional) flow the latter set may represent a flow which is still developing structurally (i.e. insufficient time was allowed for the fluid rheology to reach equilibrium throughout the system) whereas for turbulent flow conditions the data are entirely consistent with the data corresponding to Fig. 4.

The u' data in Fig. 10 show an increase in the range $2000 < Re < 4000$ corresponding to transition from laminar to turbulent-flow conditions i.e., the Reynolds number for transition is not significantly different from that for a Newtonian fluid. In the region where the velocity profiles are asymmetric, the u' levels are generally higher on the side where the velocity gradient is higher, again suggesting a link between the asymmetry and instability. The behaviour of Laponite is clearly quite different from that for polymers for which the trend is for the percentage drag reduction to increase with Reynolds number and also for transition to be delayed to considerably higher Reynolds numbers than the value of 2300 associated with a Newtonian fluid.

6. Conclusions

Under fully developed laminar pipe flow conditions at low (<1300) Reynolds numbers, the shape of the velocity distribution for Laponite, a shear-thinning, slightly viscoelastic, thixotropic

fluid, can be represented to a very high degree of accuracy by profiles based upon the Herschel–Bulkley model for the fluid rheology provided the model parameters are matched to the prevailing flow conditions rather than the equilibrium state.

At higher Reynolds numbers ($1300 > Re > 3000$) the velocity profile for laminar flow becomes increasingly asymmetric, but with a well defined plastic plug, until transition occurs. It is speculated that the asymmetry is either associated with instability or that the plug is sucked towards the pipe wall at a circumferential location fixed by a minor geometrical imperfection in the flowloop.

The flow returns to symmetry at transition which occurs at a Reynolds number not significantly different to that for a Newtonian fluid. Under turbulent-flow conditions the log law is shifted upwards by a small amount consistent with progressively reducing levels of drag reduction as the Reynolds number is increased. The turbulence intensity distributions are also consistent with the characteristics exhibited by drag-reducing polymers, i.e. u'/V unchanged whereas v'/V and w'/V are reduced in comparison with the levels for a Newtonian fluid.

The thixotropic character of Laponite is apparent from values for the wall shear rate determined from velocity profile measurements, which, under all flow conditions, lead to effective viscosity values considerably lower than would be consistent with the wall shear stress for a fluid in structural equilibrium. A second indicator of thixotropy is the apparent yield stress: the value consistent with the velocity profiles is much lower than that determined using a rheometer.

Acknowledgement

The authors gratefully acknowledge financial support for the work reported here from EPSRC (GR/J/12062) and Unilever Research.

List of symbols

A, B	constants in the law-of-the-wall
f	friction factor $2\tau_S/\rho V^2$
K	constant in Herschel–Bulkley model (Pa s^n)
n	power-law exponent in Herschel–Bulkley model
Δp	pressure drop (Pa)
Q	volumetric flow rate (m^3/s)
r	radial location within pipe (m)
r_P	radius of constant-velocity plastic plug (m)
R	pipe radius (m)
Re	Reynolds number $2\rho VR/\mu_S$
Re_N	generalised Reynolds number
u	axial velocity (m/s)
u'	rms value of turbulent velocity fluctuations in axial direction (m/s)
u^+	non-dimensional velocity u/u_τ

u_τ friction velocity $\sqrt{\tau_S/\rho}$ (m/s)
V bulk mean velocity $Q/\pi R^2$ (m/s)
v' rms value of turbulent velocity fluctuations in radial direction (m/s)
w' rms value of turbulent velocity fluctuations in tangential direction (m/s)
y distance from pipe wall (m)
y^+ non-dimensional distance from pipe wall $\rho u_\tau y/\mu_S$

Greek letters

$\dot{\gamma}$ shear rate (s^{-1})
μ_S dynamic viscosity of fluid at pipe wall (kg m^{-1} s^{-1})
ξ r_p/R
ρ fluid density (kg/m^3)
τ shear stress (Pa)
τ_S surface shear stress (Pa)
τ_Y yield stress (Pa)

References

[1] Q.D. Nguyen and D.V. Boger, Thixotropic behaviour of concentrated bauxite residue suspensions, Rheol. Acta, 24 (1985) 427.
[2] A.A. Collyer, Time dependent fluids, Phys. Ed., 8 (1973) 38.
[3] J. Mewis, Thixotropy — A general review, J. Non-Newtonian Fluid Mech., 6 (1979) 1.
[4] C.-R. Huang, in N.P. Cheremisinoff (Ed.), Characteristics of thixotropic fluids, Encyclopedia of Fluid Mechanics, Vol. 7, Rheology and non-Newtonian Flows, Gulf Publishing Co., Houston, TX, 1988.
[5] J.R.A. Pearson, Flow curves with a maximum, J. Rheol., 38 (1994) 309.
[6] J. Billingham and J.W.J. Ferguson, Laminar, unidirectional flow of a thixotropic fluid in a circular pipe, J. Non-Newtonian Fluid Mech., 47 (1993) 21.
[7] D.C.-H. Cheng, D.J. Ray and F.H.H. Valentine, The flow of thixotropic bentonite suspensions through pipes and pipe fittings, Trans. Inst. Chem. Eng., 43 (1965) T176.
[8] T.-Q. Li and K.L. McCarthy, Pipe flow of aqueous polyacrylamide solutions studied by means of nuclear magnetic resonance imaging, J. Non-Newtonian Fluid Mech., 57 (1995) 155.
[9] N.J. Alderman, A.A. Gavignet, D. Guillot and G.C. Maitland, High temperature, high pressure rheology of water based muds, SPE paper 18035, 1988.
[10] M.P. Escudier, I.W. Gouldson and D.M. Jones, Flow of shear-thinning fluids in a concentric annulus. Exp. Fluids, 18 (1995) 225.
[11] M.P. Escudier, I.W. Gouldson and D.M. Jones, Taylor vortices in Newtonian and shear-thinning liquids. Proc R. Soc. A, 449 (1995) 155.
[12] M.P. Escudier and I.W. Gouldson, Concentric annular flow with centrebody rotation of a Newtonian and a shear-thinning liquid, Int. J. Heat Fluid Flow, 16 (1995) 156.
[13] J.T. Park, R.J. Mannheimer, T.A. Grimley and T.B. Morrow, Pipe flow measurements of a transparent non-Newtonian slurry, J. Fluids Eng., 111 (1989) 331.
[14] F.T. Pinho and J.H. Whitelaw, Flow of non-Newtonian fluids in a pipe, J. Non-Newtonian Fluid Mech., 34 (1990) 129.
[15] A. Sá Pereira and F.T. Pinho, Turbulent pipe flow characteristics of low molecular weight polymer solutions, J. Non-Newtonian Fluid Mech., 55 (1994) 321.
[16] R.J. Soto and V.L. Shah, Entrance flow of a yield-power law fluid, Appl. Sci. Res., 32 (1976) 73.

[17] P.S. Virk, H.S. Mickley and K.A. Smith, The ultimate asymptote and mean flow structure in Tom's phenomena, J. Appl. Mech., 37 (1970) 488.
[18] M.P. Escudier, D.M. Jones and I.W. Gouldson, Fully developed pipe flow of shear-thinning liquids, Paper 1.3 presented at Sixth International Symposium on Applications of Laser Techniques to Fluid Mechanics, Lisbon, Portugal, 1992.

A1.2 DRAG REDUCTION IN THE TURBULENT PIPE FLOW OF POLYMERS

ELSEVIER

J. Non-Newtonian Fluid Mech. 81 (1999) 197–213

Journal of Non-Newtonian Fluid Mechanics

Drag reduction in the turbulent pipe flow of polymers

M.P. Escudier*, F. Presti, S. Smith

Mechanical Engineering, Department of Engineering, University of Liverpool, Brownlow Hill, Liverpool, L69 3GH, UK

Received 12 January 1998; received in revised form 18 May 1998

Abstract

The paper concerns an experimental study of the fully developed turbulent pipe flow of several different aqueous polymer solutions: 0.25%, 0.3% and 0.4% carboxymethylcellulose (CMC), 0.2% xanthan gum (XG), a 0.09%/0.09% CMC/XG blend, 0.125% and 0.2% polyacrylamide (PAA). The flow data include friction factor vs. Reynolds number, mean velocity and near-wall shear rate distributions, and axial velocity fluctuation intensity u' at a fixed radial location as a laminar/turbulent transition indicator. For each fluid we also include measurements of shear viscosity, first normal-stress difference and extensional viscosity. At high shear rates we find that the degree of viscoelasticity increases with concentration (0.3% CMC is an exception) for a given polymer, and in the sequence XG, CMC/XG, CMC, PAA, whilst at low shear rates the ranking changes to CMC, CMC/XG, XG, PAA. The extensional viscosity ranking is XG/CMC, XG, CMC, PAA at high strain rates and the same as that for the viscoelasticity at low shear rates. We find that the observed drag-reduction behaviour is consistent for most part with the viscoelastic and extensional-viscosity behaviour at the low shear and strain rates typical of those occurring in the outer zone of the buffer region.

Although laminar/turbulent transition is practically indiscernible from the friction factor vs. Reynolds number plots, particularly for PAA and XG, the u' level provides a very clear indicator and it is found that the transition delay follows much the same trend with elasticity/extensional viscosity as the drag reduction.

1. Introduction

Drag-reducing polymers solutions are usually shear thinning, viscoelastic and either strain thinning or strain thickening, and to varying degrees each of these characteristics is thought to influence the level of drag reduction. In one of the earliest attempts to analyse this problem, Dodge and Metzner [1] developed a correlation between friction factor and Reynolds number for turbulent pipe flow of purely viscous shear-thinning liquids based upon a power-law representation of the rheology. A few years later Metzner and Park [2] achieved what they termed indicative success in attempting to correlate the degree of drag reduction in the turbulent flow of viscoelastic polymer solutions with the ratio of elastic to viscous stress, i.e. with N_1/τ_S where N_1 is the first normal-stress difference for a given wall shear rate $\dot{\gamma}$

* Corresponding author. Tel.: +44-1517944804; fax: +44-1517944848.

0377-0257/99/$ – see front matter
PII: S0377-0257(98)00098-6

and τ_S the corresponding wall shear stress. Although, the probable relative importance of viscoelasticity to the turbulence-suppression/drag-reduction mechanism continues to be argued (see e.g. [3]), a more persistent suggestion is that elongational (or extensional) viscosity is the crucial rheological property, possibly in combination with viscoelasticity. Gadd [4] was one of the first to suggest that the damping of turbulence by polymer additives is due to their high resistance to elongational strain which acts to suppress streak formation and bursting in the near-wall region. Lumley [5,6] was also an early proponent of the importance of extensional effects and more recently the case for extensional viscosity was succinctly argued by Bewersdorff and Berman [7]. A crucial feature of the extensional viscosity of drag-reducing polymers is that much higher values can be achieved than that of the solvent, even for dilute solutions which show appreciable levels of drag reduction. Other non-Newtonian properties, such as shear viscosity and the normal-stress differences, do not differ measurably from those of the solvent until polymer concentrations reach orders of magnitude well beyond what is needed for maximum drag reduction. Gyr [8] and Durst et al [9], have also attempted to provide extensional-viscosity models for the drag-reduction mechanism whilst Vlassopoulos and Schowalter [10] provide evidence in support of ranking drag-reduction effectiveness according to the degree of fluid elasticity inferred from oscillation-induced streaming. As Matthys [11] points out, since extensional viscosity and viscoelasticity have a common molecular origin, they are likely to be related. Also if, as seems to be the case, for concentrated polymer solutions both play a major role (in addition to the shear-thinning influence which Matthys terms pseudo-drag reduction) in the turbulence modifications associated with drag reduction, then parameters based on each are likely to be required to characterise their effects. Most recently Orlandi [12] and Den Toonder et al. [13,14] have reported numerical studies in which the roles of viscoelasticity, extensional viscosity and stress anisotropy have been investigated. Some of this work suggests that in spite of the recent emphasis on elongational viscosity it is premature to discard viscoelasticity as an influence in the drag-reduction mechanism: the numerical simulation of Den Toonder et al. [13] led to a drag increase rather than a decrease and these investigators inclined to the hypothesis of de Gennes [15], that polymer drag reduction is essentially an elastic rather than a viscous phenomenon.

Since it is only recently that a commercial instrument has become available for the routine measurement of extensional viscosity (Ng et al. [16]), it is hardly surprising that few measurements of the extensional viscosity of drag-reducing polymers have been reported. Although, far more measurements have been reported of the first normal-stress difference for polymers, some specifically with reference to drag reduction (e.g. [17]), even now the majority of papers reporting drag-reduction experiments include only the shear-viscosity flow curve (e.g. [18,19]). Even if both the viscoelastic and extensional viscosity characteristics were available for nominally the same fluids, the situation would still not be entirely satisfactory given the batch-to-batch variability of polymers, the influence of mixing, biological and mechanical degradation, ageing, etc.

In the present paper we report the results of a series of experiments for fully developed turbulent flow in a long (133 diameters) pipe of 100 mm internal diameter for seven different aqueous polymer solutions: 0.25%, 0.3% and 0.4% w/w sodium carboxymethylcellulose (CMC), 0.2% xanthan gum (XG), and a 0.09%/0.09% CMC/XG blend, all of which are polysaccharides, 0.125% and 0.2% polyacrylamide (PAA). For each fluid, measurements are reported of the shear viscosity and first normal-stress difference as functions of shear rate and of extensional viscosity versus strain rate. In addition to friction factor versus Reynolds number, the flow measurements carried out using a high-resolution laser Doppler anemometer (LDA) system include axial velocity fluctuation intensity at a

fixed location as a laminar/turbulent transition indicator and profiles of mean velocity. From this extensive and unique database, we attempt to detect qualitative trends in the rheometric characteristics which are mirrored in the flow behaviour.

2. Experimental rig and instrumentation

The flow loop used for the experiments is shown schematically in Fig. 1. Flow was provided by a progressive cavity pump (1)[1] (Mono type E101, maximum flowrate 0.025 m^3/s) fed directly from a stainless steel tank of 0.5 m^3 capacity (2). Three dampers (3) located immediately after the Mono pump outlet acted to remove pulsations in the flow prior to entry into the test section (4). The latter consisted of thirteen precision-bore borosilicate glass tubes (ID 100.4±0.1 mm), each of which was assembled into a module with matched male/female stainless-steel flanges at alternate ends. Each glass tube was separated from the stainless steel by a thin PTFE ring, and each end of a module (assembled in a jig) was fixed using Devcon urethane rubber. The modules were 1.027 m (±3 mm) in length, which gave an overall test-section length of 13.35 m and a length:diameter ratio of 133. Pressure tappings of 1 mm diameter were provided on each mating flange pair with 2 mm internal diameter clear vinyl tubing (5), filled with deionised water, connecting each pressure tapping via a series of valves (6) to a Validyne differential pressure transducer (7) (DP15-26, 3448 Pa fsd). The valves were connected to the tappings in such a way as to permit measurement of the pressure drop over increasing numbers of pipe sections to assess the location at which the rate of flow development became negligible. Signal conditioning for the pressure transducer was provided by a Validyne CD223 digital transducer indicator with a BCD output connected to a data logging computer. The transducer was calibrated at periodic intervals using air against a Baratron 398HD-01000SP05 (1000 Torr fsd) high-precision differential pressure transducer with an accuracy over the calibration range of 0.01% of reading. The accuracy of the Validyne transducer was estimated to be better than ±0.25% of fsd. A platinum resistance thermometer (8) mounted in the endhousing downstream of the test section was used to monitor the fluid temperature to an accuracy of ±0.1°C.

Measurements were made of the radial distribution of the mean axial velocity and of the axial turbulence intensity at a fixed radial location 10 mm from the pipe wall using a Dantec fibreflow laser Doppler anemometer system comprising of a 60X10 probe and 55X12 beam expander (9) together with a Dantec BSA 57N20 enhanced burst spectrum analyzer signal processor. The LDA optical parameters were as follows: beam separation at front lens 46.6 mm, lens focal length 160 mm, length of principal axis of measurement volume in the radial direction 0.21 mm and diameter 0.02 mm. All measurements were biased according to residence time. In view of the small size of the measurement volume, it was not felt necessary to make any gradient correction to the measured velocities. The probe head, housing both the transmitting and receiving optics, was mounted on a three axis traverse (10) controlled by a microcomputer and having a spatial resolution of 15 μm. A flat-faced optical box (11), filled with water, was positioned over the pipe at the axial measurement location, 107 diameters from the pipe inlet, to minimise refraction of the beams at the curved surfaces.

A Fischer and Porter electromagnetic flowmeter (12) (model 10 D1) was incorporated in the return arm of the flow loop upstream of the test section, with the flowmeter output signal recorded

[1] The numbers in parentheses refer to the components shown in Fig. 1.

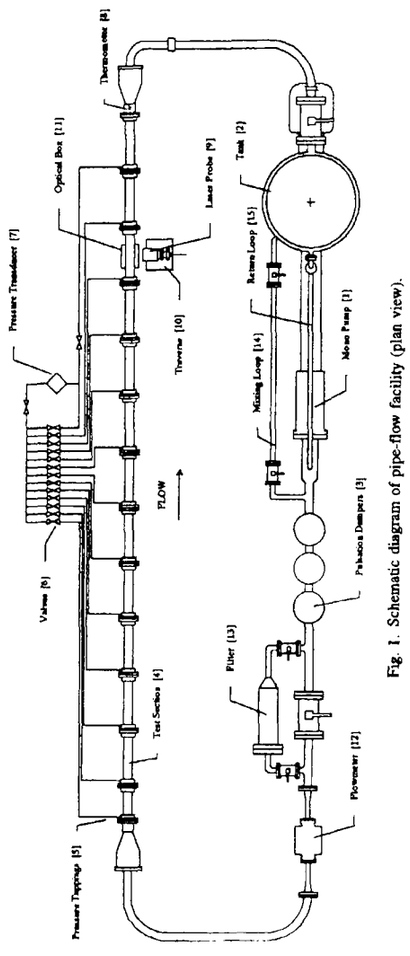

Fig. 1. Schematic diagram of pipe-flow facility (plan view).

via an Amplicon PS 30AT A/D converter. Flow rates indicated by the flowmeter were found to be within 1% of values computed from the velocity profiles. In-house software was written to record flowrate, pressure drop and fluid temperature and to control and record the LDA probe location.

To permit filtering of the base solvent (tap water) prior to the addition of polymer powder, a 125 μm filter (13) was incorporated into a by-pass loop through which the flow could be diverted. Mixing of the powder was accomplished by circulating the fluid through a return loop (14) incorporated just before the pulsation dampers. A pressure relief (safety) valve and return loop (15) were located immediately after the pump outlet.

The shear viscosity and first normal-stress difference characteristics of the test fluids were determined using a Bohlin VOR controlled shear-rate rheometer with either a concentric cylinder (double gap), a cone-and-plate or a parallel-plate geometry. The rheometer was controlled by a computer running Bohlin's BRS software. Measurements of the extensional viscosity were carried out on a Rheometrics RFX extensional rheometer controlled by RFX software. Fluid refractive indices were determined using an ABBE 60/ED high-accuracy refractometer and a Spirax Sarco conductivity meter (model MS1) was used to measure the conductivity of the working fluid.

3. Working fluid characteristics

The fluids used in the present work were aqueous solutions of the following polymers:

- sodium carboxymethylcellulose (CMC), a high-viscosity grade supplied by Aldrich Chemical Company,
- xanthan gum (XG), a food grade supplied by the Kelco Division of Merck and Co,
- polyacrylamide (PAA), Separan AP273 supplied by Floerger.

Each of these polymers has been used extensively in previous investigations of drag reduction and other non-Newtonian fluid-flow behaviour (see e.g. Pinho and Whitelaw [17], Escudier et al [20]). An important characteristic which influenced the selection of these polymers is that they remain optically transparent even at relatively high concentrations thereby facilitating LDA measurements.

3.1. Shear viscosity μ

The polymer solutions used are all well represented by the Cross model for a shear-thinning liquid:

$$\frac{\mu_0 - \mu}{\mu - \mu_\infty} = (\lambda\dot{\gamma})^m. \tag{1}$$

The values for the four parameters in Eq. (1) for each of the working liquids are listed in Table 1 and the experimental data are plotted in Fig. 2 together with the corresponding Cross-model fitted curves. Although the rheological measurements shown are for a temperature of 20°C, similar measurements were made over a range of temperatures so that the viscosity values used to evaluate Reynolds numbers corresponded to the liquid temperature measured during the flow experiments. A Newtonian plateau at

Table 1
Cross-model parameters at 20°C

Fluid Symbol	μ_0 (Pa s)	μ_∞ (Pa s)	λ (s)	m
0.25% CMC ■	0.112	2.39	0.0214	0.595
0.3% CMC ▲	0.149	6.83	0.0240	0.691
0.4% CMC ○	0.134	2.08	0.0305	0.575
0.09% CMC/0.09% XG □	0.267	2.00	1.34	0.512
0.2% XG ◆	0.578	2.76	1.30	0.724
0.125% PAA △	29.6	4.81	1090	0.664
0.2% PAA ●	165	8.04	1200	0.740

low shear rates is evident for the three CMC solutions. Otherwise, all fluids exhibit almost power-law structure except at the highest shear rates (>1000 s^{-1}) for PAA where the data are adversely affected by the onset of secondary flow.

3.2. First normal-stress difference N_1

At the concentrations used for the flow experiments, the first normal stress differences for CMC, XG and CMC/XG were below the sensitivity of the rheometer even at the highest shear rates. However, as suggested by Barnes et al. [21], at higher concentrations it was found that $N_1(\tau)$ followed a power-law master curve for each fluid, practically independent of concentration, from which it was possible to extrapolate to lower concentrations. This procedure is not ideal but has to suffice in the absence of either a direct measurement or a more sophisticated extrapolation algorithm. The data plotted in Fig. 3(a)–(c) result in the empirical expressions

$N_1 = 0.85\,\tau^{1.25}$, 0.6–1.5% CMC,
$N_1 = 0.97\,\tau^{1.47}$, 1.0–1.5% XG,
$N_1 = 1.35\,\tau^{1.18}$, 0.4/0.4–1.5/1.5% CMC/XG.

According to Barnes et al. a recoverable shear (i.e. $N_1/2\tau$) greater than 0.5 indicates a highly elastic state. For the three polymer solutions considered here, this condition corresponds to shear stresses in excess of 1.9 Pa (CMC), 1.1 Pa (XG) and 0.2 Pa (CMC/XG).

For PAA it was possible to obtain $N_1(\dot{\gamma})$ data directly because even at the lower concentration (0.125%) the N_1 values were above the resolution of the rheometer. As can be seen from Fig. 3(d) there is a strong dependence on concentration. The data are well represented by

$N_1 = 16.3\,\tau^{1.48}$, 0.125% PAA,
$N_1 = 6.07\,\tau^{1.90}$, 0.2% PAA,

so that 0.125% PAA can be said to be highly elastic for $\tau > 0.003$ Pa and 0.2% PAA for $\tau > 0.13$ Pa.

With the exception of the CMC/XG blend, for which previous data are unavailable, the results here confirm that the elasticity ranking is CMC, XG, CMC/XG and PAA, though with the lower

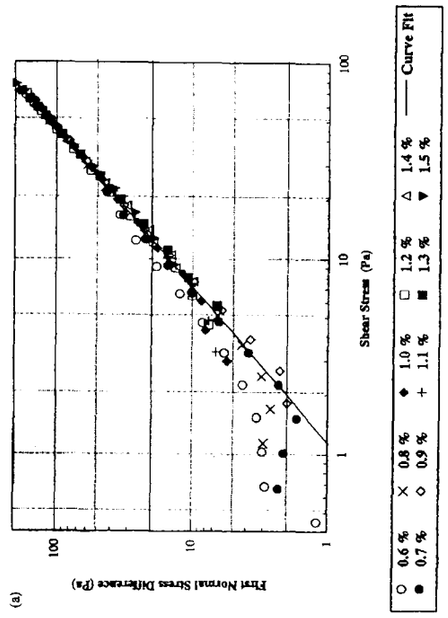

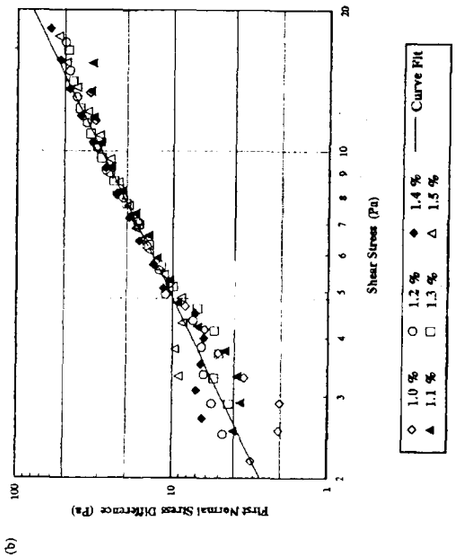

Fig. 3. Viscoelastic characteristics: N_1 versus τ_r. (a) CMC (b) XG (c) CMC/XG (d) PAA.

Fig. 2. Flow curves: μ vs. $\dot{\gamma}$. ■ 0.25% CMC; ▲ 0.3% CMC; ○ 0.4% CMC; □ 0.09% CMC/0.09% XG; Δ 0.125% PAA; ● 0.2% PAA.

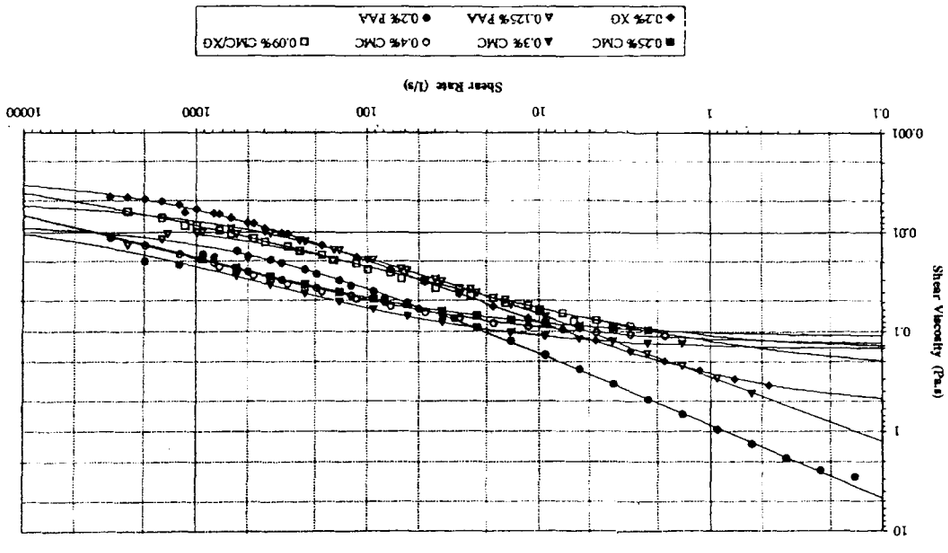

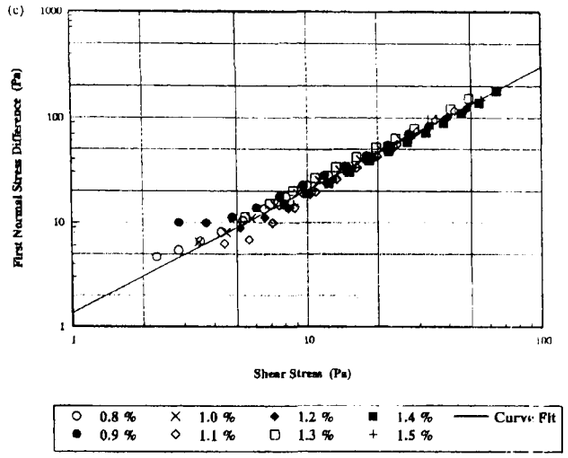

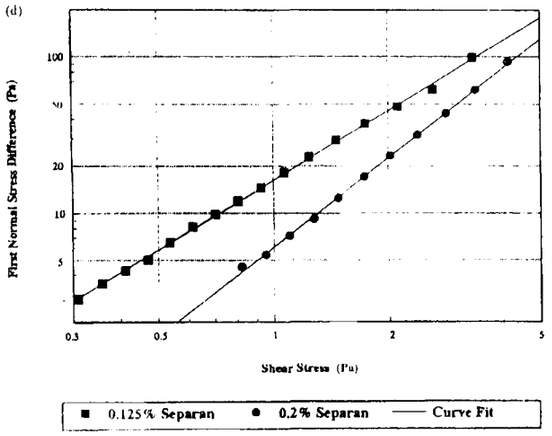

Fig. 3 (*Continued*)

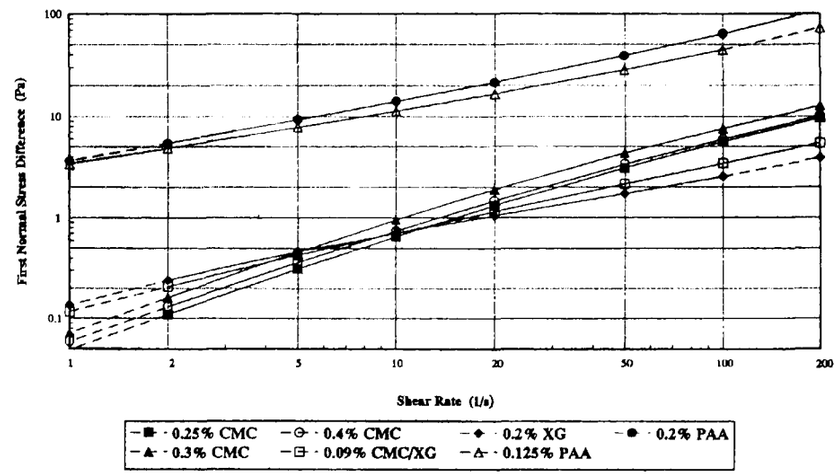

Fig. 4. Viscoelastic characteristics for working fluids: N_1 vs. $\dot{\gamma}$.

concentration for PAA being the more elastic. The normal-stress characteristics $N_1(\dot{\gamma})$ for all of the fluids investigated are shown in Fig. 4.

3.3. Extensional viscosity

Unlike the normal stress situation, it was possible to obtain extensional viscosity measurements for all of the polymer solutions at the concentrations actually used in the flow experiments. These measurements were carried out using a Rheometrics RFX opposed nozzle rheometer, with nozzle diameters 0.5, 1, 2, 3, 4 and 5 mm, the majority of measurements being made using the 1, 3 and 5 mm nozzles. For each rheometer setting, at least three measurements were made and only those data retained which produced consistent values for the extensional viscosity. The final results, shown in Fig. 5, reveal several important qualitative trends. At the highest strain rates ($>100\ s^{-1}$) the ranking is CMC/XG, XG, CMC, PAA whereas at intermediate strain rates CMC falls below XG and for the lowest strain rates ($<5\ s^{-1}$) the trend suggests CMC will also fall below CMC/XG. The sequence for both the first normal stress difference and the extensional viscosity is thus the same at low shear and strain rates, whereas, at the highest shear and strain rates the relative position of PAA is completely reversed. So far as XG and CMC/XG are concerned, as we have seen, the blend is the more elastic on the basis of both recoverable shear and N_1 at high shear rates. At low shear rates and all strain rates however, the N_1 values and the extensional viscosities for CMC/XG fall below XG.

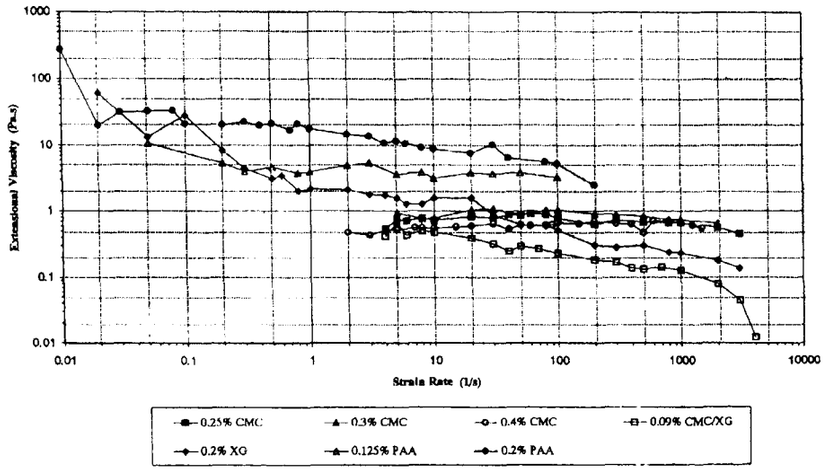

Fig. 5. Extensional viscosity vs. strain rate.

4. Friction factors and drag reduction

The definitions for the friction factor f and the pipe Reynolds number Re used here are as follows

$$f \equiv \frac{\tau_S}{\rho U^2} \quad \text{and} \quad \mathrm{Re} \equiv \frac{\rho U D}{\mu_S},$$

where ρ is the liquid density, U is the bulk mean velocity, D is the internal diameter of the pipe and the wall shear stress τ_S was calculated from the measured pressure gradient along the pipe. The value of the apparent dynamic viscosity at the pipe wall μ_S is then obtained directly from the flow curves (Fig. 2). The plots of friction factor versus Reynolds number (Fig. 6) show the levels of drag reduction for each fluid in the turbulent flow regime. As for the rheological properties of the polymer solutions, it is instructive to identify the drag-reduction ranking: at high Reynolds number (>20000) this is 0.3% CMC, 0.09% CMC/0.09% XG, 0.25% CMC, 0.2% XG, 0.125% PAA, 0.2% PAA. At lower Reynolds numbers the curves for XG and 0.125% PAA cross over. The behaviour of CMC is confusing, particularly the reversal between 0.25% and 0.3% and also the higher level of drag reduction for 0.25% and 0.4% CMC compared with CMC/XG. If the results for CMC are temporarily excluded from consideration, we see that the drag reduction ranking matches that for the first normal stress difference at low shear rates (<10 s^{-1}) and that for the extensional viscosity at all strain rates. The first of these conclusions partially confirms that of Vlassopoulos and Schowalter [10] 'that ranking additives according to elasticity provides information about drag-reducing effectiveness' . It is suggested that the

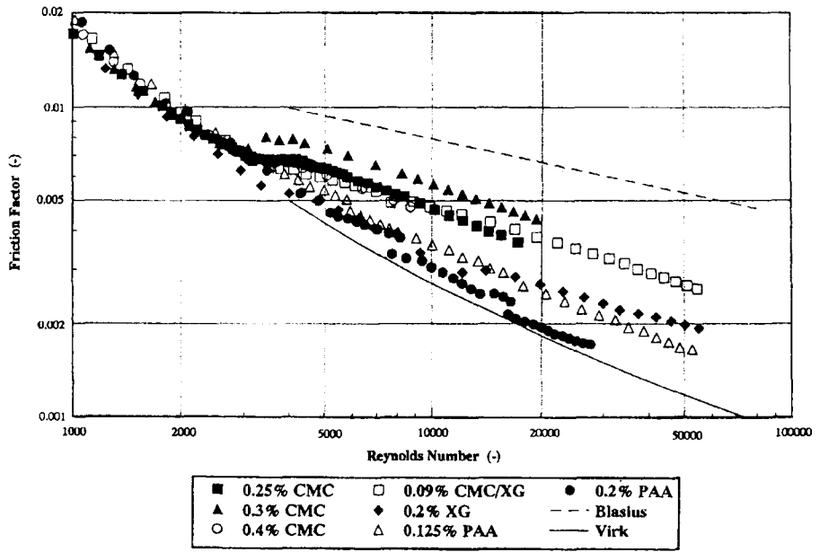

Fig. 6. Friction factor vs. Reynolds number.

tendency for the CMC elongational viscosity curves to cross over those for XG and CMC/XG at low strain rates provides a clue to the apparently anomalous drag-reduction behaviour for CMC. On balance it seems safe from these ranking considerations to conclude that the mechanism for drag reduction must be associated with strain and/or shear rates of order 10 s^{-1} or lower. Shear rates of this magnitude are considerably lower than the wall shear rates and are comparable to what can be estimated from the mean velocity distributions just beyond the buffer region ($65< y^+ <250$) (see Figs. 7 and 8). Our observations seem to be consistent with the view of Tiederman et al. [23] who argued that the viscous sublayer plays a passive role in the drag-reduction process and that polymer additives have a direct effect on flow structures in the buffer layer.

5. Mean velocity profiles and shear rates

Mean velocity profiles in the universal u^+ ($\equiv u/U_\tau$ where the friction velocity $U_\tau \equiv \sqrt{\tau_S/\rho}$) versus y^+ ($\equiv \rho U_\tau y/\mu_S$) form are shown in Fig. 7 for the highest Reynolds numbers for each fluid (i.e. profiles corresponding with the highest levels of drag reduction). The evaluation of μ_S is explained in the previous section. Both the velocity variation within the viscous sublayer and also the extent of the sublayer are not significantly different from the standard $u^+ = y^+$ ($y^+ \leq 10$) form, once again

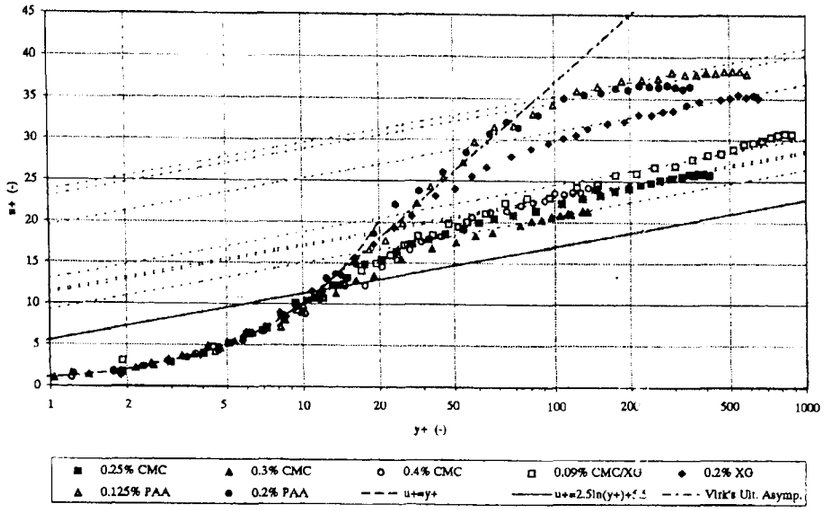

Fig. 7. Mean velocity profiles: u^+ vs. ln y^+. ■ 0.25% CMC, Re =16600; ▲ 0.3% CMC, Re =4300; ○ 0.4% CMC, Re =5500; □ 0.09% CMC/0.09% XG, Re =45300; ◆ 0.2% XG, Re =40500; △ 0.125% PAA, Re =42900; ● 0.2% PAA, Re =23060.

suggesting that this region does not play a major role in the drag-reduction process. As many previous studies have shown, the buffer region increases in thickness with increasing levels of drag reduction, and the velocity distribution is close to Virk's [24] asymptote. Fig. 8 shows the near-wall distribution of the shear rate $\dot{\gamma}$ versus y^+ evaluated from the mean velocity profiles. It becomes apparent from Figs. 7 and 8 that shear rates of the order 10 s^{-1} are not reached until well into the buffer region or even the log-law region itself. An upshifted log-law region of limited extent can be identified for CMC, CMC/XG and XG and 0.125% PAA but not for 0.2% PAA. Although the progressive increase in the upshift is again consistent with earlier work, the slope in each case exceeds the standard value ($1/\kappa$=2.5), by as much as 40%. Previous opinion on this issue has been divided, with the majority of workers inferring that the log law was negligibly affected by drag-reducing polymers. However, such an increase in slope is evident in the polyacrylamide data of Bartes et al. [25] and Den Toonder et al. [14] also reported both measurements and numerical simulations showing a significantly increased slope.

6. Transition identification

It is frequently impossible to detect from an f–Re curve the Reynolds number corresponding to transition from laminar to turbulent flow. In fact, for strongly drag-reducing polymers, such as 0.2%

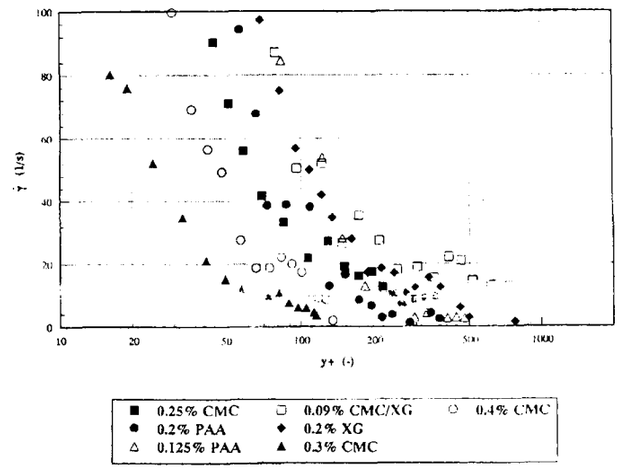

Fig. 8. Mean shear rate $\dot{\gamma}$ vs. ln y^+

PAA (see Fig. 6), it is not apparent that transition has occurred. In our experiments we have systematically used the suggestion of Park et al. [22] that the rms value of the axial-velocity fluctuation intensity u′ measured at a near-wall location (80% radius) is a sensitive indicator of laminar/turbulence transition. In spite of a considerable degree of scatter in the data plotted in Fig. 9, also evident in the paper of Park et al., it is clear that transition to turbulent flow does occur in all cases. What is also apparent is that the onset of transition is slightly but progressively delayed in the sequence CMC, CMC/XG, XG, PAA by a factor of about two in Reynolds number i.e. according to the low shear rate, low strain rate ranking of the elasticity and extensional viscosity. Polymer concentration appears to have little influence, and the Reynolds number at which transition is complete is about 5000 for all fluids except PAA where the transition regime occupies the range 4000< Re <10000. Also apparent is that the peak level of u'/U is very much the same in all cases. Finally, the curve for 0.3% CMC is much steeper than for all other fluids, which is yet another indicator that the behaviour of this fluid is anomalous.

7. Conclusions

We have provided and analysed an extensive set of experimental data for the turbulent pipe flow of shear-thinning polymer solutions. The drag reduction behaviour is shown to be consistent for the most part with the first normal stress difference and extensional viscosity at low (ca 10 s^{-1}) shear and strain rates. The same degree of consistency is lacking at higher shear and strain rates. Since the shear rates in the viscous sublayer are between one and two orders of magnitude higher than the values for which

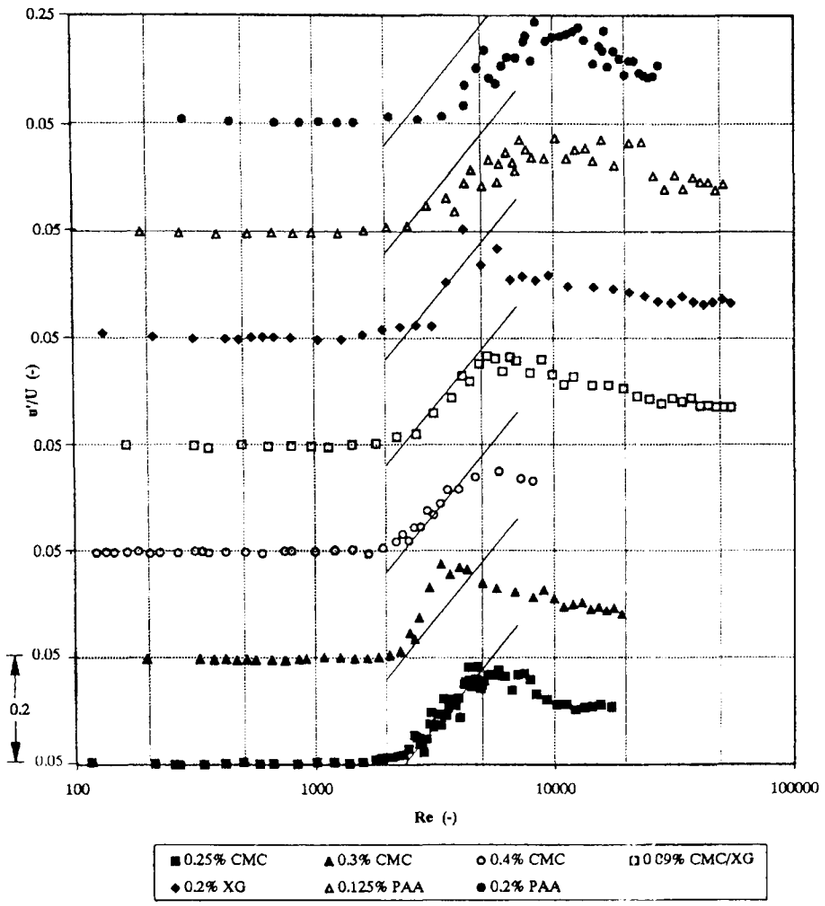

Fig. 9. Use of u'/U at y=10 mm to indicate transition.

there is a correspondence between the drag reduction and rheological behaviour, we conclude that the drag reduction is associated with the processes occurring well beyond the viscous sublayer, in the buffer region and inner log-law region.

Measurements of the mean velocity confirm that for $y^+ < 10$ the data faithfully follow the classic $u^+ = y^+$ distribution. Beyond $y^+ = 10$ the profiles are in reasonable agreement with Virk's asymptote prior to a gradual approach to an upshifted log–law region.

We have found that the intensity of the axial velocity fluctuation measured at a fixed radial location (0.8 times the pipe radius) is a consistent indicator of transition and so is particularly valuable when there is such a high degree of drag reduction that there is little or no indication from the f–Re curve that transition has occurred. The delay in transition follows a pattern similar to that of the increase in drag reduction.

Acknowledgements

The work described here was supported by EPSRC Research Grant GR/J15841. The authors also acknowledge the assistance of Dr. J. Meadows of North East Wales Institute in making available to us the Rheometrics RFX extensional viscometer.

References

[1] D.W. Dodge, A.B. Metzner, Turbulent flow of non-Newtonian systems, AIChEJ 5 (1959) 189.
[2] A.B. Metzner, M.G. Park, Turbulent flow characteristics of viscoelastic fluids, J. Fluid Mech. 20 (1964) 291.
[3] M. Renardy, On the mechanism of drag reduction, J. Non-Newtonian Fluid Mech. 59 (1995) 93.
[4] G.E. Gadd, Turbulence damping and drag reduction produced by certain additives in water, Nature 206 (1965) 463.
[5] J.L. Lumley, Drag reduction by additives, Ann. Rev. Fluid Mech. 1 (1969) 367.
[6] J.L. Lumley, Drag reduction in two phase and polymer flows, Phys. Fluids 20 (1977) 564.
[7] H.W. Bewersdorff, N.S. Berman, The influence of flow-induced non-Newtonian fluid properties on turbulence drag reduction, Rheologica Acta 27 (1988) 130.
[8] A. Gyr, Direct evidence that drag reduction is an effect of the elongation of the polymer molecules in drag reduction, in: Proc 3rd Int. Conf., Drag Reduction, Bristol, 2–5 July 1984, B 10-1.
[9] F. Durst, R. Haas, W. Interthal, Laminar and turbulent flows of dilute polymer solutions: a physical model, Rheologica Acta 21 (1982) 572.
[10] D. Vlassopoulos, W.R. Schowalter, Characterisation of the non-Newtonian behaviour of drag-reducing fluids, J. Non-Newtonian Fluid Mech. 49 (1993) 205.
[11] E.F. Matthys, Heat transfer, drag reduction and characterisation for turbulent flow of polymer solutions: recent results and research needs, J. Non-Newtonian Fluid Mech. 38 (1991) 313.
[12] P. Orlandi, A tentative approach to the direct simulation of drag reduction by polymers, J. Non-Newtonian Fluid Mech. 60 (1995) 277.
[13] J.M.J. Den Toonder, F.T.M. Nieuwstadt, G.D.C. Kuiken, The role of elongational viscosity in the mechanism of drag reduction by polymer additives, Appl. Sci. Res. 54 (1995) 95.
[14] J.M.J. Den Toonder, M.A. Hulsen, G.D.G. Kuiken, F.T.M. Nieuwstadt, Drag reduction by polymer additives in a turbulent pipe flow: numerical and laboratory experiments, J. Fluid Mech. 337 (1997) 193.
[15] P.G. de Gennes, Introduction to Polymer Dynamics, Cambridge University Press, Cambridge, 1990.
[16] S.L. Ng, R.P. Mun, D.V. Boger, D.F. James, Extensional viscosity measurements of dilute solutions of various polymers, J. Non-Newtonian Fluid Mech. 65 (1996) 291.
[17] H.W. Bewersdorff, R.P. Singh, Rheological and drag reduction characteristics of Xanthan gum solutions, Rheologica Acta 27 (1988) 617.
[18] F.T. Pinho, J.H. Whitelaw, Flow of non-Newtonian fluids in a pipe, J. Non-Newtonian Fluid Mech. 34 (1990) 129.
[19] A. Sá Pereira, F.T. Pinho, Turbulence pipe flow characteristics of low molecular weight polymer solutions, J. Non-Newtonian Fluid Mech. 55 (1994) 321.

[20] M.P. Escudier, I.W. Gouldson, D.M. Jones, Flow of shear-thinning fluids in a concentric annulus, Experiments in Fluids 18 (1995) 225.
[21] H.A. Barnes, J.F. Hutton, K. Walters, An Introduction to Rheology, Elsevier, Amsterdam, 1989.
[22] J.T. Park, R.J. Mannheimer, T.A. Grimley, T.B. Morrow, Pipe flow measurements of a transparent non-Newtonian slurry, ASME J. Fluids Eng. 111 (1989) 321.
[23] W.G. Tiederman, T.S. Luchik, D.G. Bogard, Wall-layer structure and drag reduction, J. Fluid Mech. 156 (1985) 419.
[24] P.S. Virk, H.S. Mickley, K.A. Smith, The ultimate asymptote and mean flow structure in Toms' phenomenon, Trans. ASME J. Appl. Mech. 1970, 488.
[25] P.V. Bartels, A. Markus, J.M. Smith, The turbulent mixing of viscoelastic fluids in pipe flow, in: Proc. IUTAM Symp. Essen, 1984, The influence of polymer additives on velocity and temperature fields, Springer, 1985.

APPENDIX 2
REFRACTION CORRECTIONS FOR LDA MEASUREMENTS

This section details the positional corrections applied to the measurement control volume of the LDA system when performing traverses that measure the axial, tangential and radial velocity components. These positional corrections are derived from Snell's law of refraction and geometric considerations. The refraction of beams through the measurement system (see Chapter 3.3) results in a change of the laser beam intersection angle, hence changing the pattern of the interference field of the measurement control volume (namely that of the fringe spacing d_f). As explained in the following sections, the change in the interference field pattern requires a correction factor to be applied to the measured velocities, however, for the axial case the correction factor is shown to be unity.

A2.1 Axial Refraction Corrections

For the measurement of axial velocity (u), the optical system is oriented such that both beams are in a plane which passes through the axis of the cylinder, whilst the bisector between the beams is at a right angle to the axis (see **Figure 3.12**). In this case, refraction takes place only in the axial direction and the refracting surface is perpendicular to the beam bisector. **Figure A2.1** illustrates a plan view of the refraction of laser beams when measuring the axial velocity component of flow in the axial direction. The laser beams emerging from the inner wall of the test pipe intersect at an angle of φ. Interference at the beam intersection gives rise to an interference field (see **Figure 3.6(b)**) with the fringe spacing d_f given by [Durst *et al.* (1976)]:

$$d_f = \frac{\lambda / n_5}{2 \sin \varphi / 2} = \frac{\lambda / n_1}{2 \sin \theta_1} \qquad \textbf{(A2.1)}$$

where $n_1 = 1$ for air.

From Snell's law of refraction, it follows that:

$$n_1 \sin\theta_1 = n_5 \sin\varphi/2 \qquad \textbf{(A2.2)}$$

due to which, the change of the intersection angle compensates exactly for the change of wavelength (λ/n_5). Hence, using this traverse mode for determining the axial velocity component, no corrections were applied to the LDA measurements.

However, the relationship between the actual traverse motion within the axial plane and the precise location of the beam intersection within the test pipe is still required. The intersection location is determined by using ray tracing as shown in **Figure A2.1** and is obtained by considering the decomposition of d/2:

$$d/2 = (t+S+\rho+T)\tan\theta_1 = l\tan\varphi/2 + \ldots\ldots\ldots \qquad \textbf{(A2.3)}$$
$$\rho\tan\theta_4 + S\tan\theta_3 + t\tan\theta_2$$

Applying Snell' law to **Figure A2.1**, we obtain:

$$n_1 \sin\theta_1 = n_2 \sin\theta_2 = n_3 \sin\theta_3 = \ldots\ldots\ldots \qquad \textbf{(A2.4)}$$
$$n_4 \sin\theta_4 = n_5 \sin\varphi/2$$

Hence, using **Eq.s (A2.3)**, **(A2.4)** and trigonometric functions, a linear relationship is obtained between the location of the beam intersection l and the traversation distance T:

$$T = \left(\frac{l}{\sqrt{n_5^2 - \sin^2\theta_1}} + \frac{\rho}{\sqrt{n_4^2 - \sin^2\theta_1}} + \frac{S}{\sqrt{n_3^2 - \sin^2\theta_1}} \ldots\ldots\ldots \right. \qquad \textbf{(A2.5)}$$
$$\left. + \frac{t}{\sqrt{n_2^2 - \sin^2\theta_1}} \right) \cos\theta_1 - \rho - S - t$$

The axial positional corrections derived above were subsequently incorporated within the traverse control programme.

A2.2 Tangential Refraction Corrections

Ray tracing for measurements of the tangential velocity component (w) is shown in **Figure A2.2**. The calculations used to determine the location of the beam intersection and also the fringe spacing are presented below, where the symbols on the left denote the quantities to be calculated from the equations on the right-hand-side of the colon.

For the beams shown in **Figure A2.2** we obtain:

θ_3:

$$n_1 \sin\theta_1 = n_3 \sin\theta_3 \qquad \textbf{(A2.6)}$$

d_1, r_1:

$$\frac{|D - d_1|}{L - r_1} = \tan\theta_3 \qquad \textbf{(A2.7)}$$

$$d_1^2 + r_1^2 = (R + \rho)^2 \qquad \textbf{(A2.8)}$$

φ_1:

$$\frac{d_1}{(R + \rho)} = \sin(\theta_3 \pm \varphi_1) \qquad \textbf{(A2.9)}$$

φ_2:

$$n_3 \sin\varphi_1 = n_4 \sin\varphi_2 \qquad \textbf{(A2.10)}$$

l:

$$R^2 = l_2^2 + (R + \rho)^2 - 2l(R + \rho)\cos\varphi_2 \qquad \textbf{(A2.11)}$$

ε_2:

$$l_2^2 = R^2 + (R + \rho)^2 - 2l_2(R + \rho)\cos\varepsilon_2 \qquad \textbf{(A2.12)}$$

d_2, r_2:

$$\frac{d_2}{r_2} = \tan(\theta_1 \pm \varphi_1 \pm \varepsilon_2) \qquad \textbf{(A2.13)}$$

$$d_2^2 + r_2^2 = R^2 \qquad \textbf{(A2.14)}$$

$\varphi/2$:

$$n_4 \sin(\varepsilon_2 \pm \varphi_1) = n_5 \sin(\varepsilon_2 + \varphi_1 \pm \theta_3 \mp \varphi/2) \qquad \textbf{(A2.15)}$$

In **Eq.s (A2.9)**, **(A2.13)** and **(A2.15)** the upper sign holds for $\varepsilon_1 > \theta_3$, and the lower sign holds for $\varepsilon_1 < \theta_3$.

The location (ΔT) of the beam intersection can be determined from:

$$d_2 / (r_2 + \Delta T) = \tan(\varphi/2) \qquad \textbf{(A2.16)}$$

The tangential velocity component (w) is then related to the Doppler frequency (f_D) by:

$$w = f_D \cdot d_f = f_D \frac{\lambda / n_5}{2 \sin(\varphi/2)} \qquad \textbf{(A2.17)}$$

where the beam intersection angle is obtained from **Eq. (A2.15)**. The interference fringe spacing d_f (w) for the tangential velocity component varies linearly with both the position (ΔT) of the laser-beam intersection along the x-axis, and the actual traversation position of the LDA probe. Therefore, at different positions within the pipe, it is necessary to correct for deviations of d_f (w) from the free space value d_f i.e. fringe spacing within the unrefracted interference field of the measurement control volume in air. Consequently, the following correction factor C_w was applied to the measured tangential velocities:

$$w_{corrected} = w_{measured} \cdot C_w, \text{ where } C_w = \frac{n_1}{n_5} \cdot \frac{\sin\theta_1}{\sin\varphi/2} \qquad \textbf{(A2.18)}$$

where φ/2 varies with the radial traversation position within the test pipe. Hence, for each traverse location, the corresponding correction factor was determined and applied to each measured velocity. These velocity correction factors were carried out in a separate computer programme, whilst the positional corrections were incorporated within the traverse control programme.

A2.3 Radial Refraction Corrections

Ray tracing for measurements of the radial velocity component (v) is shown in **Figure A2.3**. The calculations used to determine the location of the beam intersection and also the fringe spacing have been presented below in a similar manner to those for the tangential measurements described above.

For the lower beam in the third quadrant we obtain:

θ_{23}:

$$n_1 \sin\theta_{21} = n_3 \sin\theta_{23} \qquad \textbf{(A2.19)}$$

d_{21}, r_{21}:

$$\frac{|D_{21} - d_{21}|}{L - r_{21}} = \tan\theta_{23} \qquad \textbf{(A2.20)}$$

$$d_{21}^{\,2} + r_{21}^{\,2} = (R + \rho)^2 \qquad \textbf{(A2.21)}$$

φ_{21}:

$$\frac{d_{21}}{(R + \rho)} = \sin(\theta_{23} \pm \varphi_{21}) \qquad \textbf{(A2.22)}$$

φ_{22}:

$$n_3 \sin\varphi_{21} = n_4 \sin\varphi_{22} \qquad \textbf{(A2.23)}$$

l_2:

$$R^2 = l_2^{\,2} + (R + \rho)^2 - 2R(R + \rho)\cos\varphi_{22} \qquad \textbf{(A2.24)}$$

ε_{22}:

$$l_2^{\,2} = R^2 + (R + \rho)^2 - 2l_2(R + \rho)\cos\varepsilon_{22} \qquad \textbf{(A2.25)}$$

d_{22}, r_{22}:

$$\frac{d_{22}}{r_{22}} = \tan(\theta_{23} \pm \varphi_{21} \pm \varepsilon_{22}) \quad \textbf{(A2.26)}$$

$$d_{22}^2 + r_{22}^2 = R^2 \quad \textbf{(A2.27)}$$

ν_b:

$$n_4 \sin(\varepsilon_{22} \pm \varphi_{22}) = n_5 \sin(\varepsilon_{22} + \varphi_{21} \pm \varphi_{22} \mp \nu_b) \quad \textbf{(A2.28)}$$

In **Eq.s (A2.22)**, **(A2.26)** and **(A2.28)** the upper sign holds for $\varepsilon_{21} > \theta_{23}$, and the lower sign holds for $\varepsilon_{21} < \theta_{23}$. For the upper beam, an analogous set of equations can be obtained.

The location (x_o, y_o) of the beam intersection can be determined from:

$$\frac{d_{22} - y_o}{r_{22} + x_o} = \tan \nu_b \quad \textbf{(A2.29)}$$

$$\frac{-d_{22} - y_0}{y_{12} + x_o} = \tan \nu_a \quad \textbf{(A2.30)}$$

As can be seen from **Figure A2.3**, the bisector of the beam intersection is inclined to the y-axis by an angle χ:

$$\chi = \frac{(\nu_a + \nu_b)}{2} \quad \textbf{(A2.31)}$$

therefore changing the orientation of the radial velocity component. Hence, the measured radial velocity becomes influenced by a tangential velocity component according to the equation below [Broadway and Karahan (1981)]:

$$v_{measured} = v \cos \chi + w \sin \chi \quad \textbf{(A2.32)}$$

For the radial velocity measurements, the dependence of the inclination angle χ and the laser-beam intersection location y/R is shown in **Figure A2.4**. For y/R < 0.8, it can be shown using the tangential velocity distribution data, that the tangential influence (w cos χ) is less than 3% of the measured velocity ($v_{measured}$) and therefore can be ignored. However, for y/R > 0.8, the influence of the tangential velocity component increases (< 25% of $v_{measured}$), though due to an optical path length difference (as explained below) the total level of uncertainty associated with the radial velocity measurements close to the wall could not be determined accurately.

The radial velocity component (v) was then related to the Doppler frequency (f_D) by:

$$v = f_D.d_f = f_D \frac{\lambda / n_5}{2 \sin(\nu_a + \nu_b)/2} \qquad \textbf{(A2.33)}$$

As for the tangential velocity component (see **Eq. (A2.18)**), a velocity correction factor, C_v was applied to the measured radial velocities to account for only the change in interference field pattern of the measurement control volume:

$$v'_{corrected} = v'_{measured} \cdot C_v \text{ , where } C_v = \frac{n_1}{n_5} \cdot \frac{\sin\theta_1}{\sin(\nu_a + \nu_b)/2} \qquad \textbf{(A2.34)}$$

Finally, in determining the radial velocity component, an optical path length difference [see e.g. Bicen (1990)] is created between the beams for $y \neq 0$ (see **Figure (A2.3)**). The optical path length difference is caused by different levels of refraction between each of the transmitted beam wavefronts as they propogate through the measurement system. The path length difference leads to weaker modulation signals of the LDA measurement with resultant reductions in signal-to-noise ratios when compared with axial and tangential velocity measurements. This is due to the plane wavefronts at the beam waist (described by the Gaussian beam theory) [Durst *et al.* (1976)] of one of the beams intersecting with the spherical wavefronts of the other (i.e. not at the beam waist). Consequently, there is a distortion of interference fringes

thus creating a level of uncertainty in the radial component of velocity measurement. The level of uncertainty manifests itself as a greater degree of scatter in the radial velocity distribution measurements as illustrated in Chapter 5. This effect becomes attenuated as the optical path length difference of the refracting beams increase at measurement locations approaching the inner wall. The extent of uncertainty associated with this distortion is outside the scope of this study and hence was not determined during the course of this work, though qualitatively, it may be assumed that the main conclusions from this study are not affected respectively.

Figures

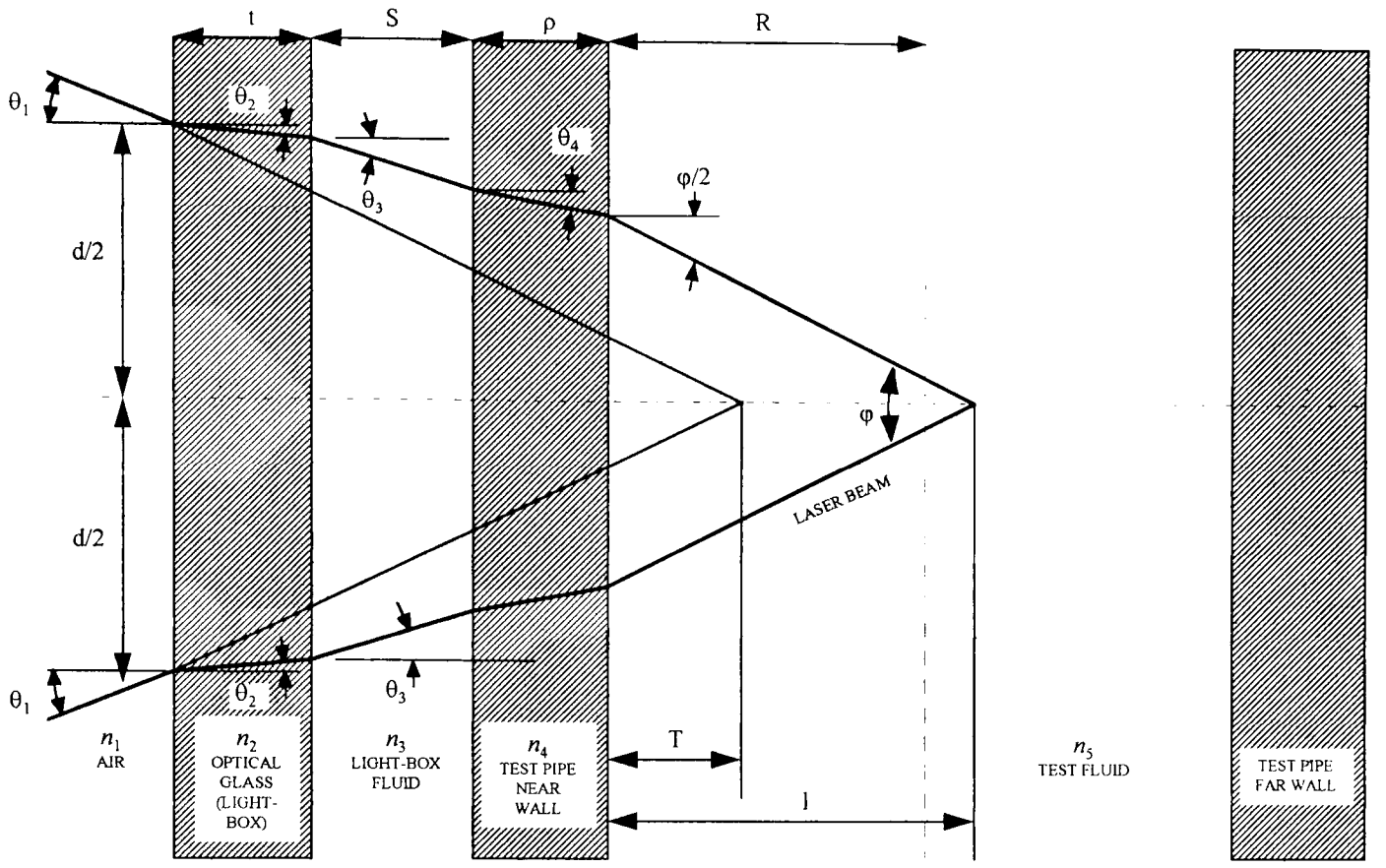

Figure A2.1 *Axial Refraction - Ray Tracing Method for Positional Corrections (Plan View).*

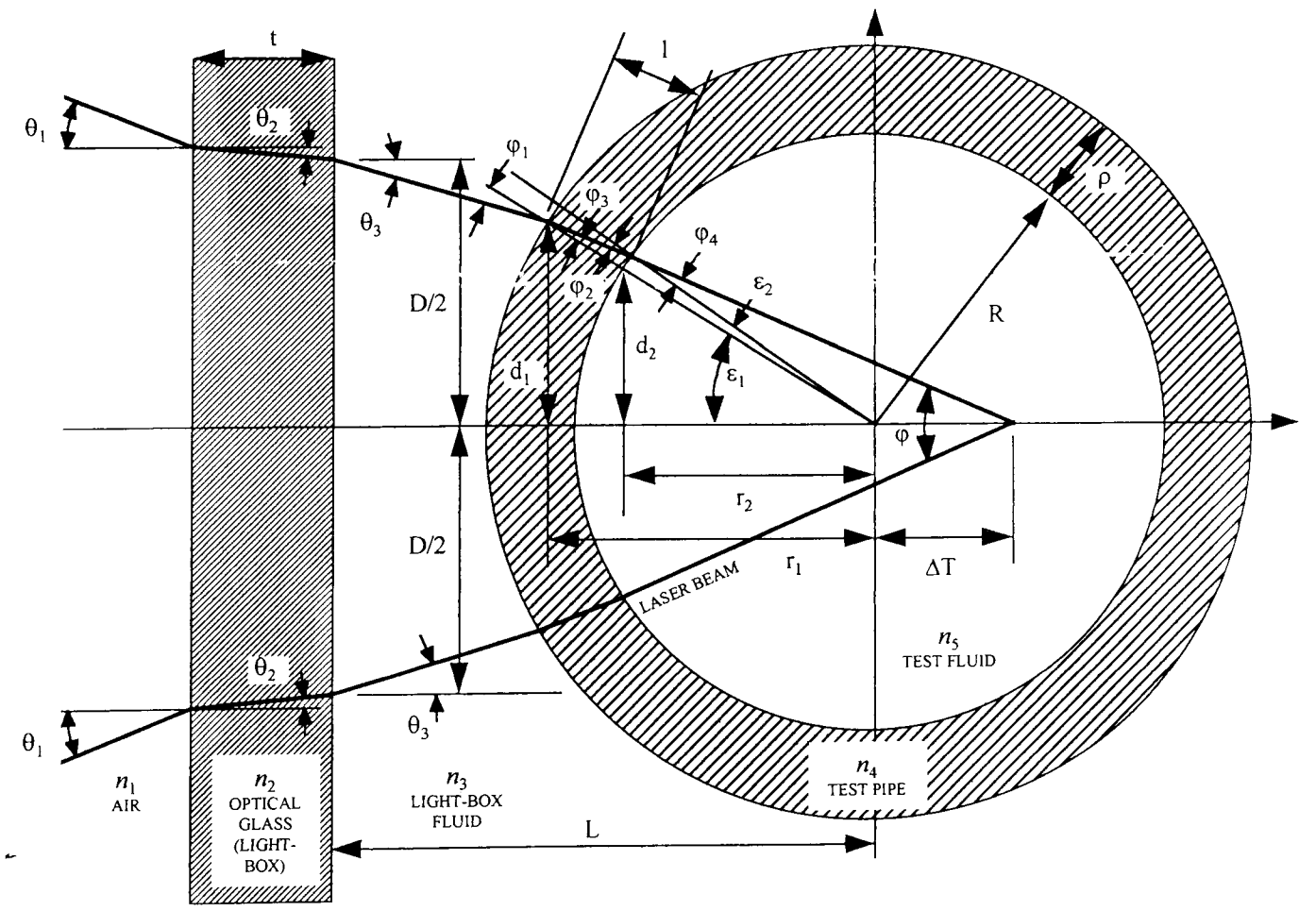

Figure A2.2 *Tangential Refraction - Ray Tracing Method for Positional Corrections.*

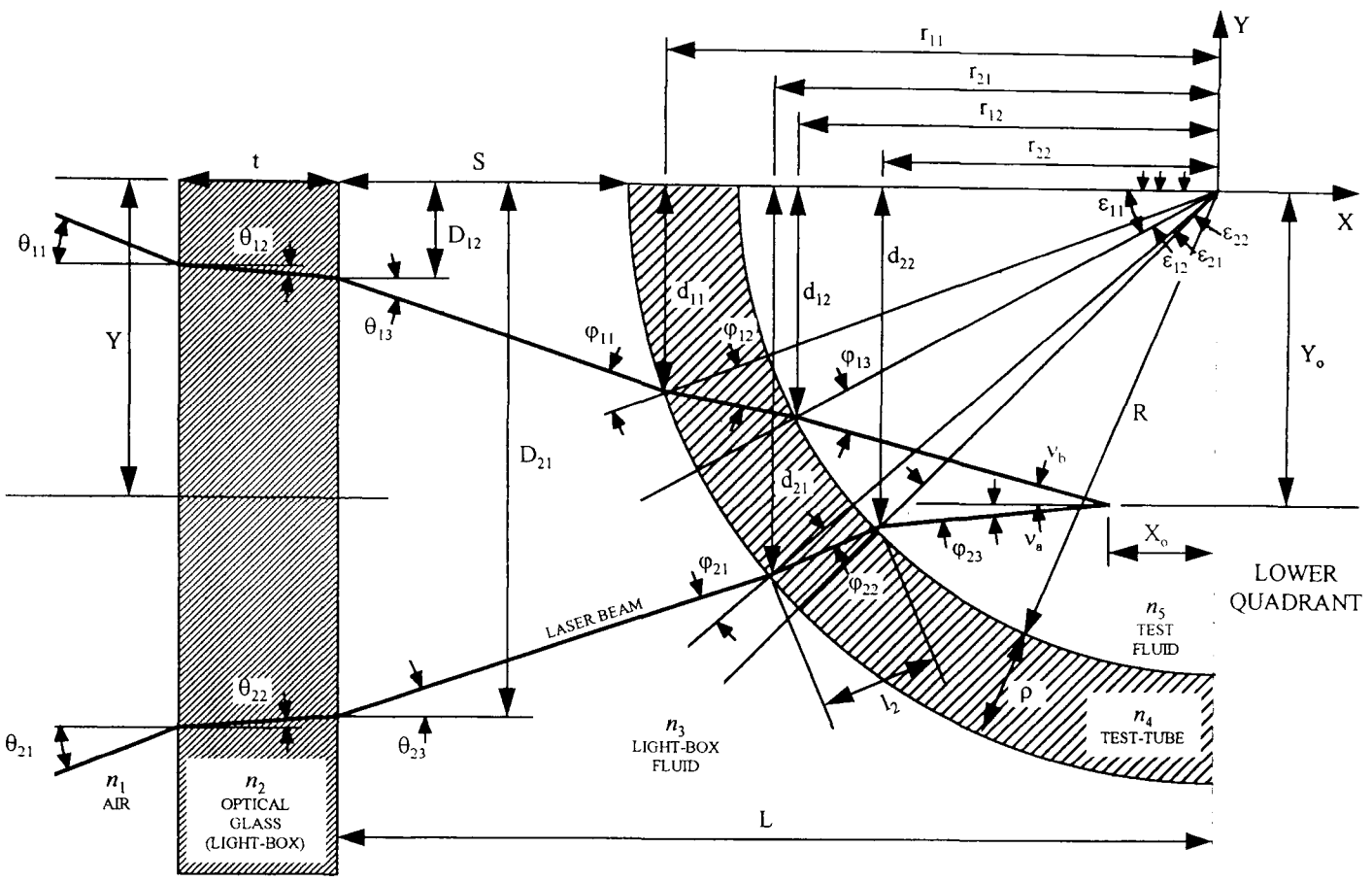

Figure A2.3 *Radial Refraction - Ray Tracing Method for Positional Corrections.*

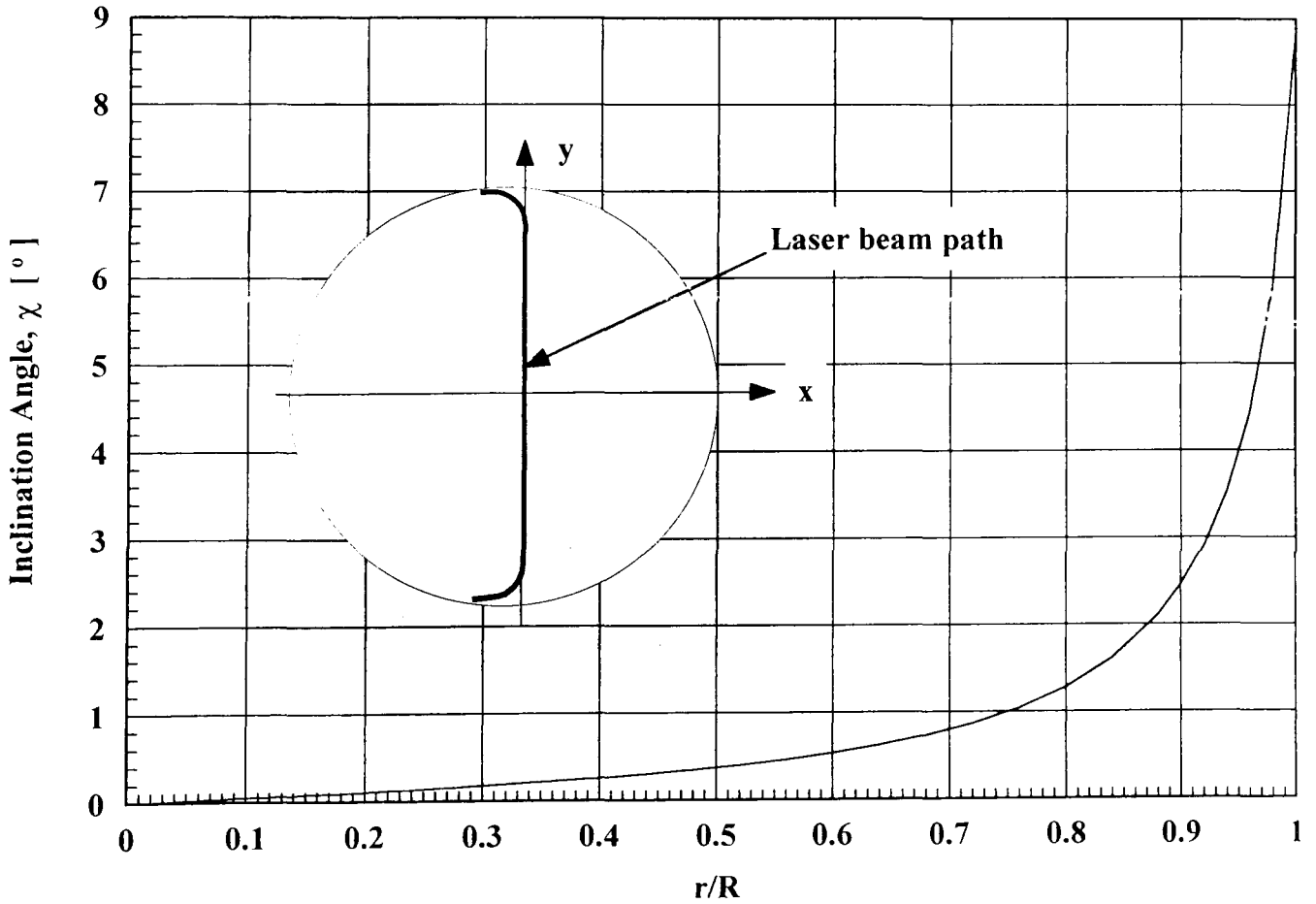

Figure A2.4 *Bisector of the Beam Intersection - Angle of Inclination with the Y-Axis versus r/R for the Radial Traverse.*

APPENDIX 3
RHEOLOGICAL CHARACTERISATION OF FLUIDS USING OSCILLATION FLOW TECHNIQUES

Oscillatory analysis of samples requires very little perturbation of the test material. Analyses of the structural elements are performed in very fast response times. The stress applied in oscillatory shear experiments varies in a sinusoidal manner as opposed to linearly when compared with steady shear flow.

The essence of oscillatory analysis is to test various structures in the sample (e.g. cross-links) non-destructively [Barnes *et al.* (1989)]. By varying the frequency of the stress applied at these low amplitudes (so as not to breakdown any structure), will cause the various elements to respond when their characteristic times match the change in stress applied at a particular frequency.

When a sinusoidal stress pattern is applied to the sample, there are two possible resulting waveforms i.e. a sinusoidal or a distorted waveform. Distortion occurs by structural forces or interactions within the sample's structure that are essentially governed by non-linear relationships. The rheometers (CarriMed and Bohlin VOR) used in the rheological analyses carried out for this work were only able to manage oscillatory flow data successfully in the linear viscoelastic region.

The resultant wave may vary in phase to the input, thus providing information to the type of response (elastic or viscous) that the sample is showing. A purely elastic response is characterised by a zero phase angle (0°) and a purely viscous response by a 90° phase difference (see **Figure A3.1**), where a viscoelastic response lies in between these two extremes.

The main parameter measured is the Complex Modulus, G^* (ratio of stress amplitude to strain amplitude). Due to its sinusoidal nature, it is a trigonometric function described by two components in complex form. The two components are referred to as the Storage Modulus, G' and the Loss Modulus, G''. The former is a measure of the

elastic structural components in a sample where energy is stored as elongation occurs and released when the stress applied is removed and the sample is allowed to relax. The viscous elements, however, dissipates the applied stress as strain, so the loss modulus quantifies this energy dissipation [Ferry (1970)].

From **Figure A3.1**, it can be seen that the two moduli are related to the phase angle (δ) via a cosine (G') or sine (G") term:

$$G^* = G' + iG'' \qquad \textbf{(A3.1)}$$

and

$$\tan \delta = G'' / G' \qquad \textbf{(A3.2)}$$

An increase in G' for a given G*, for example, results in tan δ decreasing so that the strain curve tends to become in phase with respect to the stress curve. The opposite occurs for a decrease in G' for a given G*, where tan $\delta \rightarrow 90°$.

Figures

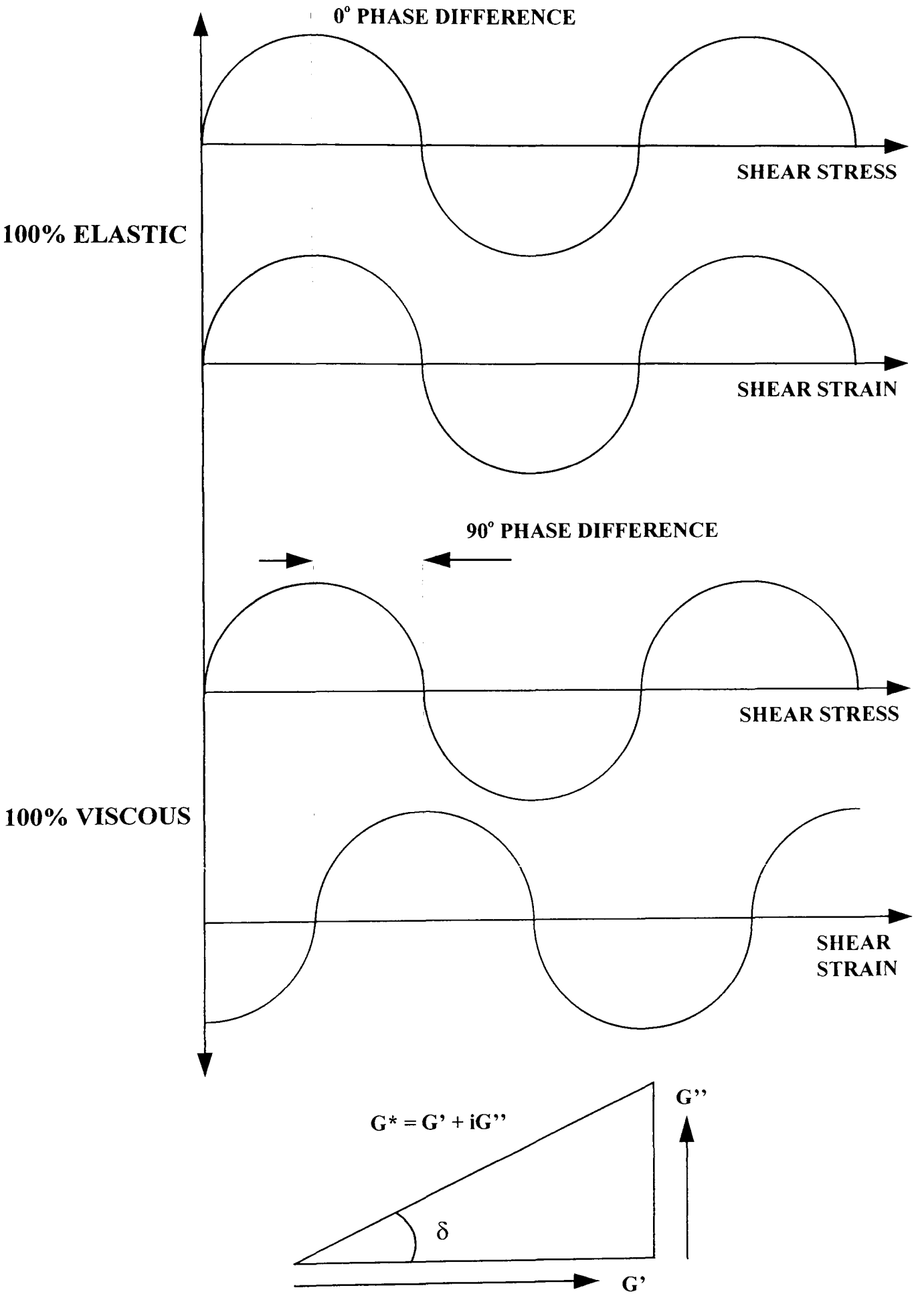

Figure A3.1 *Basic Principles Applied to Steady Oscillating Shear Flows used in Rheometric Techniques.*

APPENDIX 4

EFFECT OF FREEZING AND THAWING ON TEST FLUID RHEOLOGY

As discussed in Section 4.5.2, all fluids analysed in this study exhibited variations in rheological behaviour over a period of time. These effects were primarily caused by various mechanisms of degradation or, in the case for Laponite, were related to time dependent effects. As a consequence, rheometrical studies for each test fluid were limited to periods relating to their pipeflow experiments. Thus, as insurance to carry out further rheological investigations on the test fluids, batches of each fluid ($2\times150ml$ samples taken directly from the flow loop during Day 1 of testing) were frozen at temperatures of $-10°C < T < 0°C$. There is no available data in literature at present concerning the effects of freezing on the rheology of non-Newtonian fluids. Consequently, an additional study was carried out during the research programme to investigate the viscometric effects of various fluid types and blends subjected to numerous freezing/thawing cycles.

Various fluid samples were prepared specifically for these tests using the methodology described in Section 4.3.3. The fluids selected were of the same type as those used in the pipeflow experiments, though of much higher concentration to improve the accuracy of the rheological measurements. The viscometric measurements for each of these samples were carried out over a range of shear rates (at 20°C) before and after each of the four freezing/thawing cycles.

For CMC (BDH, UK), the viscometric flow curve remained constant after consecutive cycles of freezing and thawing. A slight increase in viscosity was observed after the first freeze/thaw cycle, though the discrepancy was comparable with the repeatability of the rheometer. The corresponding data has been illustrated in **Figure A4.1**.

An aqueous mixture of glucose syrup was also prepared (50% water, w/w) and tested as above. The fresh sample (not exposed to any freeze/thaw cycle) had a viscosity of 0.1190 Pa.s (at 20°C). However, after each cycle, the viscosity of the solution increased slightly, eventually reaching a value of 0.1214 Pa.s (20°C) after four cycles:

a total increase of 2%. This increase was systematic, however, the measurements were comparable with the repeatability of the rheometer and hence the solution was regarded as stable.

This investigation was verified and extended by Makrakis (1996) during the course of this study, which included oscillatory flow measurements. Makrakis found that the viscometric flow curves for XG, CMC/Glucose blend and Laponite solutions also remained stable through each freezing/thawing cycle. The oscillatory flow data also remained consistent between each cycle, thus indicating the elastic influences were not being affected. For frozen samples of PAA and XG/CMC blend, which were not tested for freezing/thawing influences, their rheology could be analysed and directly compared with previous data before carrying out any further examinations.

Figures

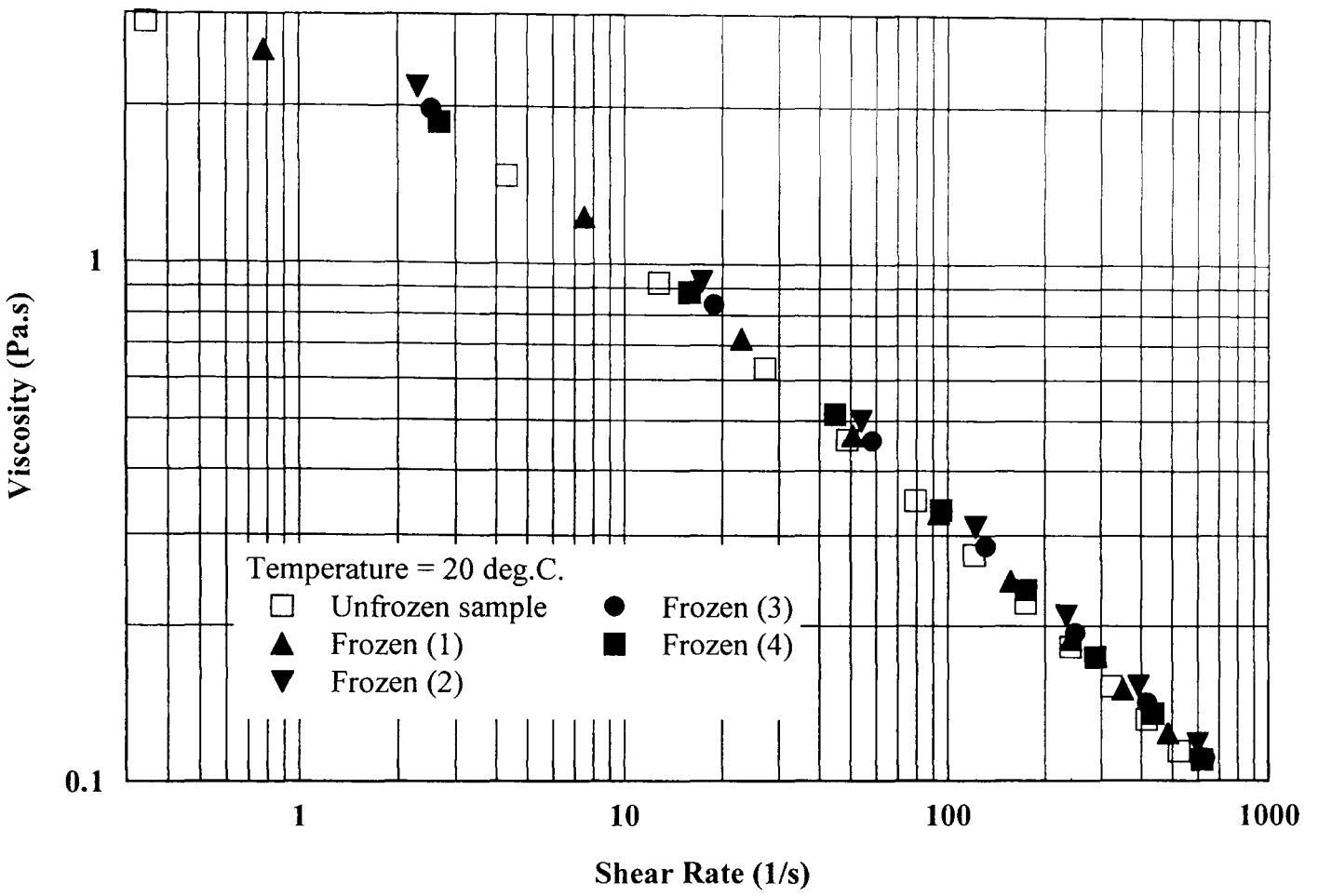

Figure A4.1 *Effect of Freezing and Thawing on the Viscometric Behaviour for 1% CMC (BDH).*